Forschungszentrum Jülich
in der Helmholtz-Gemeinschaft

50 Jahre Zukunft

Scientific Report 2004/2005

Festkörperforschung

Institut für Festkörperforschung

Institute of Solid State Research

IFF

Institute of Solid State Research

Scientific Report

2004/2005

Contents

Department IFF

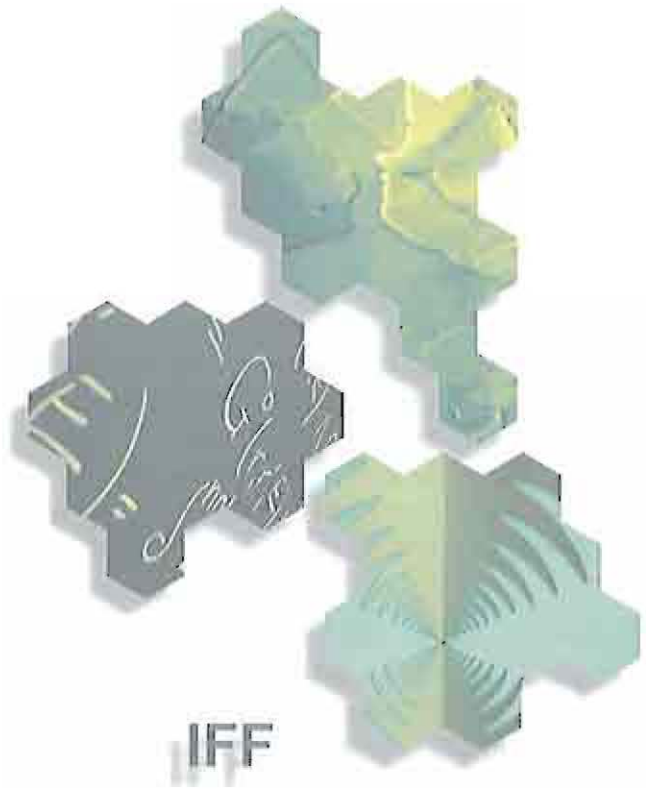

comprising the Institutes

Theory I	–	Prof. Dr. Stefan Blügel
Theory II	–	Prof. Dr. Gerhard Gompper
Theory III	–	Prof. Dr. Heiner Müller-Krumbhaar
Neutron Scattering	–	Prof. Dr. Dieter Richter
Electronic Materials	–	Prof. Dr. Rainer Waser
Scattering Methods	–	Prof. Dr. Thomas Brückel
Soft Condensed Matter	–	Prof. Dr. Jan K. G. Dhont
Microstructure Research	–	Prof. Dr. Knut Urban
Electronic Properties	–	Prof. Dr. Claus M. Schneider

The **Institute of Solid State Research (Institut für FestkörperForschung – IFF)** is devoted to condensed matter physics. The scientific success of the IFF owes much to the conception of its founders that new discoveries are made at boundaries of disciplines: this is as true today as it was then.

In its more than thirty years of existence, the IFF has grown into a versatile and successful organism. It has pioneered topics such as magnetoelectronics and set trends towards multi- und cross-disciplinary research. This was manifest in the foundation of the Institutes of "Electronic Materials" and "Scattering Methods", as well as by the establishment of a young interdisciplinary field at the boundaries of modern physics – "Soft Condensed Matter".

The IFF pursues research into the fundamental principles of the physics of condensed matter in the solid and liquid state. In its application-oriented research, the Institute realizes ideas for technological innovations. These challenges are tackled from three directions: we investigate the *phenomena of condensed matter*, perform *material-oriented studies of complex systems*, and we develop and improve *experimental and theoretical methods*.

Statistical physics and quantum mechanics form the physical basis of IFF research. On a microscopic scale, they determine the interaction of electrons and atomic building blocks and how they react to external influences. Particular strengths of the IFF include the theory of electronic structure, clusters and polymer physics, the dynamics of structure formation and phase transitions, materials and phenomena of magneto- and nanoelectronics, spintronics, high-temperature superconductivity, electron microscopy and spectroscopy, as well as the instrumentation of synchrotron and neutron sources and their application to the study of matter.

Dedicated state-of-the-art laboratories and facilities are available for the preparation of polymers, colloids and ceramics, and for growing thin films and crystals. In addition to standard methods for materials characterization, highly sophisticated techniques are used and further developed. These techniques range from superconducting microscopy to femtosecond laser spectroscopy. The associated *Ernst Ruska-Centre for Microscopy and Spectroscopy with Electrons* develops and operates the most advanced transmission electron microscopes in the world. As a complement to local research opportunities, instruments are constructed and operated at external neutron and synchrotron radiation sources in Germany and abroad. Within the newly founded *Jülich Center for Neutron Science (JCNS)* the IFF operates experimental stations at the FRM-II in Munich, the ILL in Grenoble, France, and the SNS in Oak Ridge, USA. All facilities are open to scientists of every nation.

The international networking of the IFF is a pillar of its success: the Institute initiated, e.g., two EU Networks of Excellence (NoE). It is partner of more than one hundred universities and research institutions from all continents. Within Germany, the Institute cooperates closely with nearby universities and maintains intensive relations with scientists in all parts of the country. The IFF co-founded the Centre of Nanoelectronic Systems for Information Technology (CNI). Furthermore, in recent years the IFF has become partner of major companies such as Bosch, Infineon, DaimlerChrysler, Thomson, ExxonMobil, Agilent, and Philips.

The research groups of the IFF cannot be regarded separately: the Institute has a departmental structure comprising six experimental and three theoretical divisions, as well as joint service facilities. The IFF is an institute of the Research Centre Jülich in the Hermann von Helmholtz Association of German Research Centres (HGF). On campus, it collaborates closely with the Institute of Thin Films and Interfaces (ISG) and the Institute of Biological Information Processing (IBI).

Collaborating closely with the other members of the Hermann von Helmholtz Association the IFF makes key contributions to the strategic mission of the HGF within the following research programmes

- Information Technology with Nanoelectronic Systems,
- Condensed Matter,
- Large Scale Facilities for Research with Photons, Neutrons and Ions
- Scientific Computing

IFF researchers utilize the Central Department of Technology and the Central Electronics Laboratory and the supercomputers of the John von Neumann Institute for Computing (NIC). The IFF can also draw on its own technical and administrative infrastructure, an important requirement for designing and constructing scientific instruments, such as synchrotron beamlines, neutron spectrometers, sputtering facilities, or crystal growth facilities.

The success of the Institute is based on the inventiveness and initiative of its more than three hundred staff members. The IFF supports independent research by encouraging the responsibility of its individual members, a philosophy that contributes greatly to the stimulating atmosphere in the department. In order to sustain this level in the long term, special encouragement is given to the younger generation, examples being the internationally renowned IFF Spring School and the laboratory course on neutron scattering.

The casual observer is struck by the wide range of topics and extensive networking at the IFF, whose strength is to link complex topics together with its scientific and industrial partners. In the sixties, Germany seemed to be about to miss the boat in solid state research. The success of the IFF demonstrates how a leading position worldwide can be achieved by a modern research strategy.

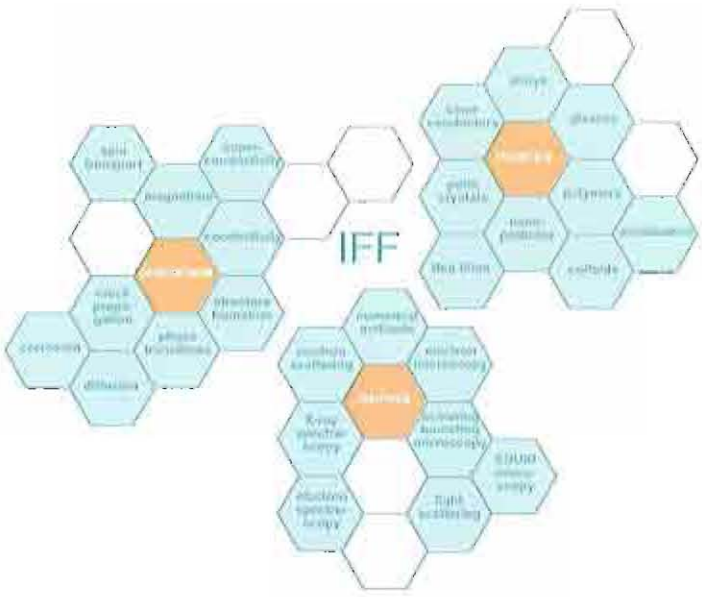

Theory I

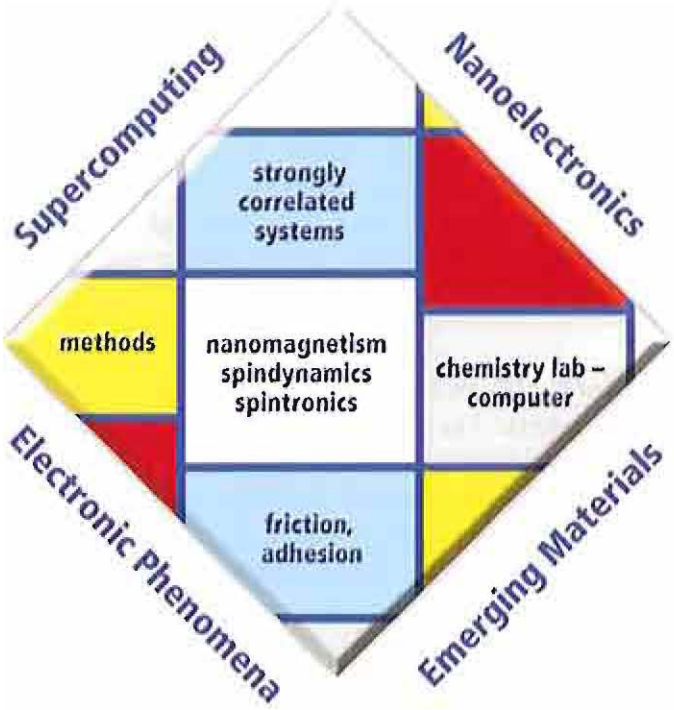
Supercomputing
Nanoelectronics
strongly correlated systems
methods
nanomagnetism spindynamics spintronics
chemistry lab – computer
friction, adhesion
Electronic Phenomena
Emerging Materials

A major focus at "Theory I" is the analysis and computation of structural, electronic, and magnetic properties and processes in molecules and solids, in terms of both basic research and practical applications. The goal is to achieve a microscopic understanding of such complex phenomena.

Our research covers key areas of condensed matter theory and computational materials science. We explore the electronic and structural properties of systems from large organic (including biological) molecules, low-dimensional magnets, and magnetic multilayers, to complex solids. We consider transport properties across interfaces, electronic excitations, and dynamical properties of atomic and molecular clusters, solids, and solid surfaces, as well as the quasiparticle behaviour of semiconductors, oxides, and transition metals that results from electronic correlations. We analyze the physics of strongly correlated materials, such as transition-metal oxides and molecular crystals paying particular attention to complex ordering phenomena. Other areas include nanoscale tribology, including friction, plastic deformation, adhesion, and brittle fracture, as well as nonlinear processes in the atmosphere and agrosphere.

A major asset of our institute is the competence in developing conceptual and computational methods based on density functional theory, molecular dynamics simulations, and Quantum Monte Carlo methods.

Theory II

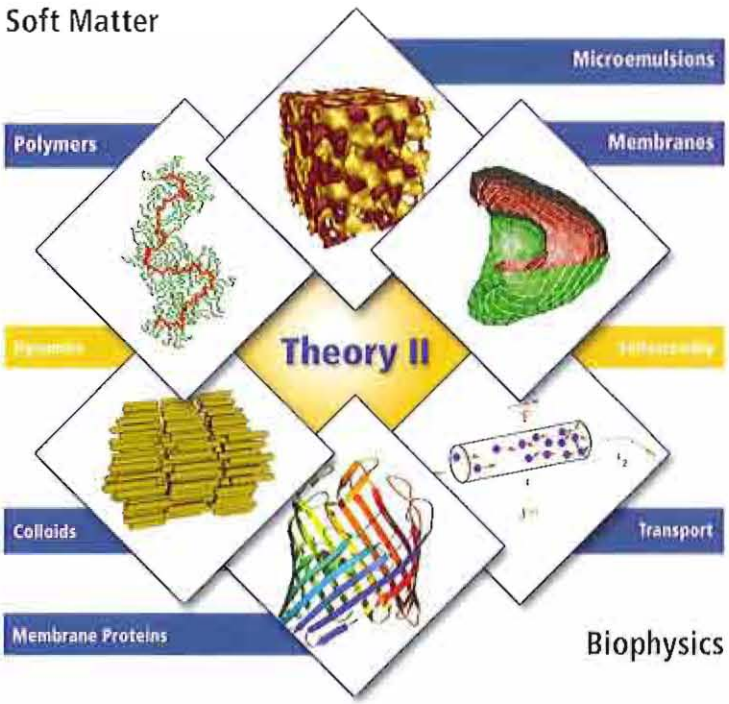
Soft Matter
Microemulsions
Polymers
Membranes
Theory II
Colloids
Transport
Membrane Proteins
Biophysics

The Institute "Theory II" focuses on soft matter studies. The main research topic of the Institute is the theory of complex fluids and soft matter systems. Soft matter physics is an interdisciplinary research area encompassing statistical physics, materials science, chemistry, and biology. Our systems of interest include polymer melts and liquid crystals, as well as colloidal suspensions. Recently the focus has shifted to more complex systems ranging from colloids in polymer solutions or liquid crystals to mixtures of surfactants and amphiphilic block copolymers. This brings the systems closer to applications in materials science or biology.

At "Theory II" a large variety of methods are applied. In fact, a combination of analytical and numerical methods is often required to successfully characterize the properties of these complex systems. In particular, simulation methods (Monte Carlo, molecular dynamics), computational hydrodynamics, field theory, perturbation theory, and exact solutions are employed. Since the building blocks of soft matter systems often contain a large number of molecules, "simplified" mesoscale modelling is typically required, which is then linked to the molecular architecture.

A characteristic feature of soft-matter research is the fruitful interaction between theory and experiment. IFF "Theory II" closely cooperates with the Institute for Neutron Scattering (Richter) and the Institute for Soft Matter (Dhont) to successfully tackle many of the essential aspects of the systems investigated..

Theory III

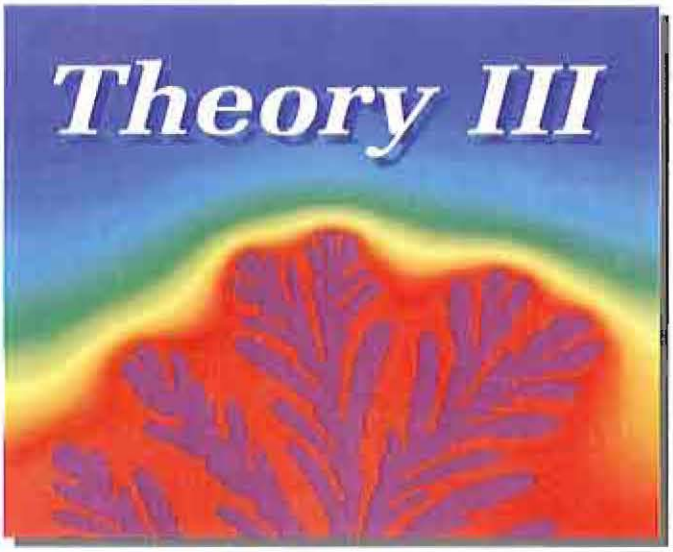

The research of institute Theory III is concerned with the mechanisms of the formation of structures and their consequences in condensed matter. The investigations start from electronic properties which define the shortest length and time scales, but they also encompass the macroscopic consequences. The analytical and numerical studies are in many ways closely connected to experimental research performed in other groups of the IFF, but also to activities in other institutes of the Research Center Juelich (FZJ). The institute contributes mainly to the research-programs "Condensed Matter" and "Nanoelectronic Systems" of FZJ.

Central points of interest for the research in Theory III are in the field of electronic structure of solids, in particular effects of strong electronic correlations. A specific interest concerns materials relevant for information technology. A second mainstream is formed by cooperative phenomena in condensed matter. Questions here aim at the dynamics of structure and pattern formation and the statistical mechanics of order and disorder processes. Specific activities concern the effect of long-range interactions like elastic effects in solids, friction and fracture phenomena, or hydrodynamic interactions in solid-liquid systems.

The research of Theory III employs all analytical and numerical techniques applicable to many-body problems of equilibrium and non-equilibrium phenomena in condensed matter. In addition, the development of new methodological concepts and numerical procedures is part of our research interest. The development of parallel program codes adapted to massively parallel computers has received special attention in recent years.

Neutron Scattering

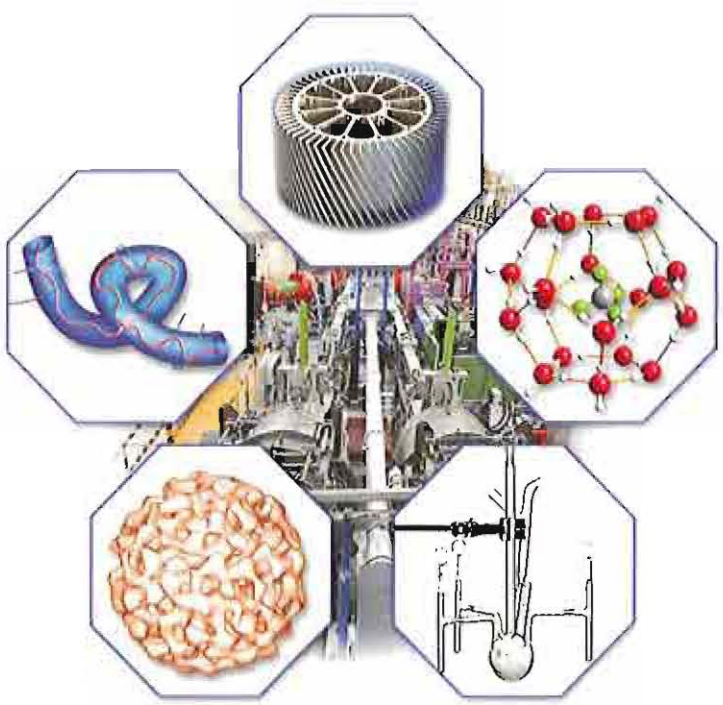

The "Neutron Scattering" Institute is concerned with neutron research placing major emphasis on soft condensed matter. Materials that react strongly to weak forces are termed soft.

Apart from their structure, we are interested in the glass dynamics of amorphous polymers and the dynamics of systems like polymers in melts and solutions (e.g. gels, rubbery networks, aggregates). Another field of interest is complex liquids such as microemulsions or colloid systems. The Institute has modern chemical laboratories for the synthesis and modification of soft matter.

The Institute for Neutron Scattering operates several scattering instruments at the DIDO reactor (FRJ-2) and in the associated ELLA neutron guide laboratory including experimental stations for small-angle scattering (SANS), neutron spin echo spectroscopy (NSE), reflectometry and backscattering spectroscopy (BSS1). These instruments are available to researchers on request (Instruments). Another focus of research is the development of neutron instrumentation for research reactors and future spallation sources worldwide. This includes the new Munich reactor (FRM-II) and the megawatt spallation source SNS at Oak Ridge (USA).

Electronic Materials

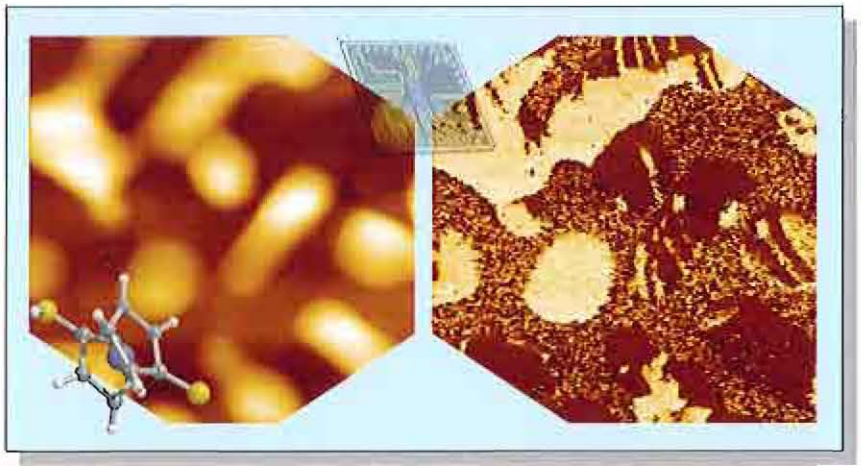

The research areas of the "Electronic Materials" Institute comprise (1) technologies for the integration of electroceramic materials into micro- and nanoelectronics, (2) dielectric and ferroelectric properties of oxide ceramics, and (3) the defect structure in oxides in the vicinity of internal and external interfaces.

These key areas are complementary to the research activities of the Institute for Electronic Materials (IWE 2) at RWTH Aachen University. Both labs are managed by one and the same director. The project teams are often formed by staff members and students from both institutes.

Specialized state-of-the-art laboratories and facilities exist for the preparation of ceramics, as well as for growing thin films and structures under clean room conditions (e.g. CSD, MOCVD, RIE). In addition, standard methods for materials characterization and highly sophisticated techniques are used and are being constantly further developed.

The Institute is one of the seven founders of the Centre of Nanoelectronic Systems for Information Technology (CNI). The idea is to strengthen the bridge between IFF and ISG (Institute for Thin Layers and Interfaces) on campus, and research groups close to Jülich. These partners form a "virtual" centre of internationally recognized competence in nanoelectronics with joint projects and facilities.

Scattering Methods

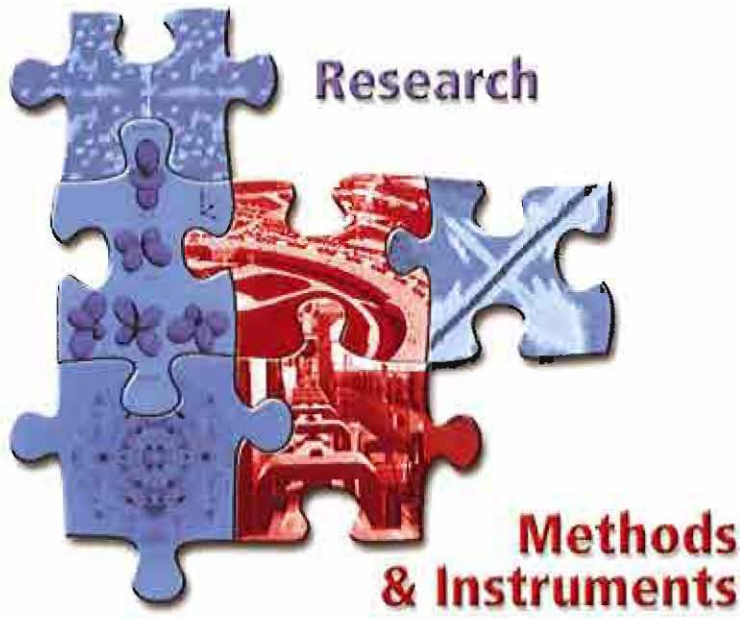

At the Institute for Scattering Methods, we focus on the investigation of structural and magnetic order, fluctuations and excitations in complex or nano-structured magnetic systems and highly correlated electron systems. Our research is directed at obtaining a microscopic atomic understanding based on fundamental interaction mechanisms. The aim is to relate this microscopic information to macroscopic physical properties. To achieve this ambitious goal, we employ the most advanced synchrotron X-ray and neutron scattering methods and place great emphasis on the complementary use of two probes. Some of our efforts are devoted to dedicated sample preparation and characterization from thin films and multilayers via nano-patterned structures to single crystals for a wide range of materials from metals to oxides.

A significant part of our activity is devoted to the development of novel scattering techniques and the construction and continuous improvement of instruments at large facilities. Within the MuCAT consortium, we operate a sector at the Advanced Photon Source APS in Argonne, USA. And in the frame of the recently founded *Jülich Centre for Neutron Science JCNS*, we operate neutron instruments at three leading facilities, the research reactor FRM-II in Garching, the Institute Laue-Langevin ILL in Grenoble, France and the Spallation Neutron Source SNS in Oak-Ridge, USA. All these instruments are accessible through a peer-review system to general users.

Soft Condensed Matter

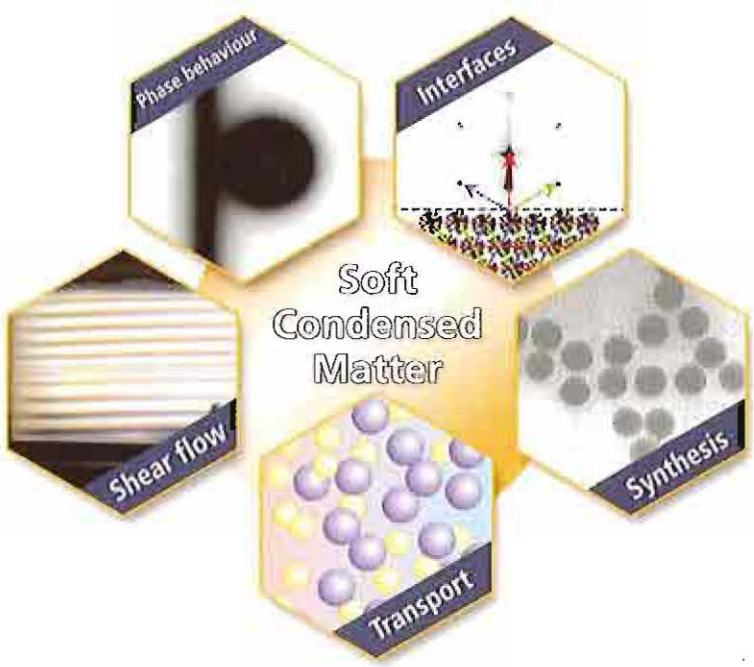

The Soft Matter group investigates the chemistry and physics of colloidal systems, some times in combination with other soft matter components like polymers and surfactants.
Colloidal systems can be regarded as solutions of very large molecules (typically 10 nm - 10 micron). Colloidal particles are still small enough to exhibit thermal motion, and therefore obey the same laws of thermodynamics and statistical physics as simple molecular systems. In particular, colloidal systems exhibit phase transitions and show non-equilibrium phenomena that are also found for simple molecular systems. Due to the slow dynamics of colloids and the tunable interactions between the colloidal particles, however, there are many transitions and non-equilibrium phenomena that do not occur in simple molecular systems, like gellation and shear-band formation..
The aim is to understand macroscopic phenomena that are found in various colloidal systems on a microscopic basis with an open eye for possible technological applications.
The main topics that are studied are :

- The phase behaviour, pattern formation, phase separation kinetics and dynamics of suspensions of spherical and rod-like colloids under *shear flow*, with an emphasis on crystallization and the isotropic-nematic phase transition.
- Mass transport induced by *temperature gradients*, also referred to as themodiffusion, where both single particle diffusion and the effect of interactions between colloids are of interest.
- Dynamics and micro-structural properties of colloidal systems near *walls and interfaces*, of spherical, plate-like and rod-like particles.
- The effects of *pressure* on interactions, the location of phase transition lines and gellation transitions and the dynamics of colloids and polymers under high pressure.
- Response of colloids to external *electric fields*, where the phase behaviour, phase separation kinetics and dynamics is of interest.
- The equilibrium phase behaviour of *mixtures of colloids and polymer-like systems*, including depletion interactions induced by these various types of polymer-like depletants.
- *Dynamics* of various types of colloidal systems in equilibrium, such as mixtures of spherical colloids, suspensions of rods and tracer diffusion of spherical particles in networks of rods both in the isotropic and nematic state.
- The *synthesis of new colloidal model particles*, with specific surface properties, interaction potentials and particle geometries. Different specific properties are required in order to conduct the various above mentioned investigations.

Most of the equipment that is used for our research is home built. The available equipment includes scattering equipment (dynamic and static light scattering, small angle scattering, evanescent-wave scattering, forced Rayleigh scattering and Brillouin scattering), optical set ups (like dichroism, birefringence and tandem interferometry), microscopes (like internal total reflection microscopy and confocal microscopy) and various shear cells and pressure cells for scattering and microscopy.

Microstructure Research

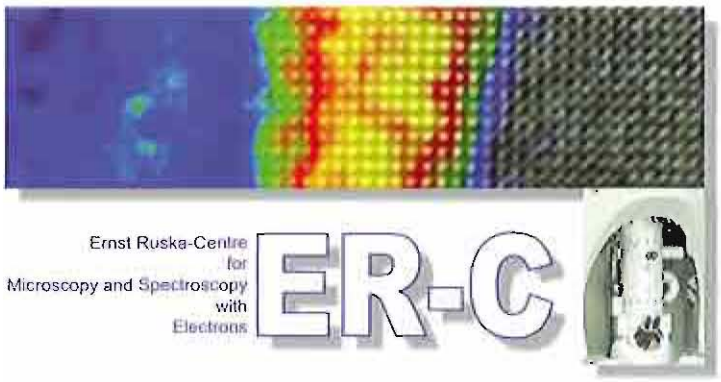

The Institute "Microstructure Research" of Prof. Urban focuses on the atomic and microstructural understanding of crystalline material properties with a special emphasis on electroceramics, metal alloys, nanostructured semiconductors and oxide superconductors.

In some of these fields, the competence covers the whole range from basic research to the development and preparation of prefabricated technical devices. In other fields, access to novel material classes and intricate problems is provided by qualified collaborations. Current reseach programmes, performed either exclusively at the institute or in the framework of international cooperations, range from pure material preparation carried out hand in hand with all-embracing electron microscopic analyses to the design of electronic circuits and the development of advanced structural analysis techniques.

Over and above these general physics and technology-related projects, as a globally established organization, the institute continuously focuses and complements special competence in the field of advanced transmission electron microscopy techniques accompanied by the development of novel investigation methods. For these purposes, the institute operates and maintains the *Ernst Ruska-Centre for Microscopy and Spectroscopy with Electrons*, which, as a supraregional user facility, benefits from the unique scientific expertise in the field of transmission electron microscopy, which is being continuously extended at the institute.

Electronic Properties

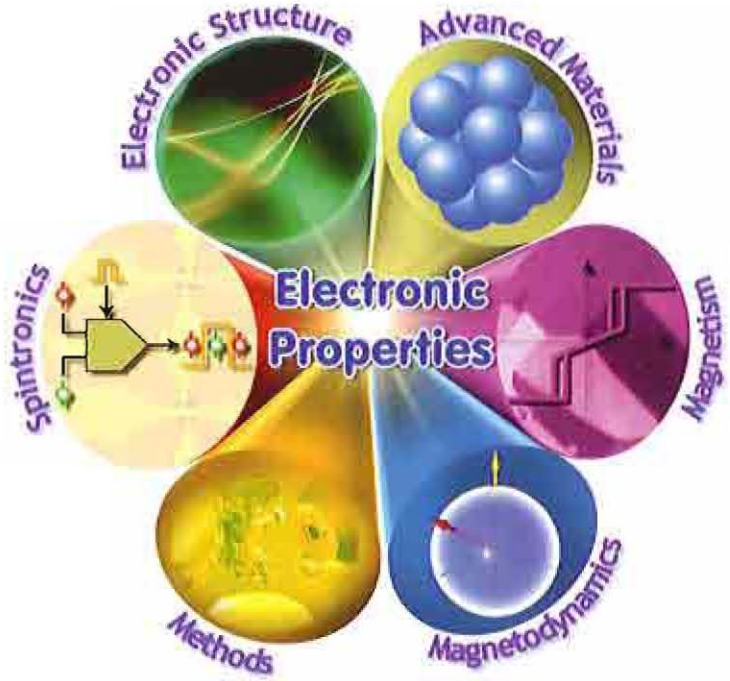

At the Institute "Electronic Properties" we explore the intricate and multifaceted interrelations between the electronic structure and the physical properties of matter. The current focus of our research lies on magnetism, magnetic phenomena, and their exploitation in nanoscience and information technology. The systems of interest range from ultrathin films and thin film layer stacks through quantum wires and dots to clusters and molecules.

Magnetism is a many-electron phenomenon and is characterized by a complicated interplay of interactions taking place on different length, energy, and time scales. Thus, hybridization and correlation effects dominate the electronic structure of a magnetic system. We are particularly interested in the influence of reduced dimensionality on the magnetism and the formation of quantum effects in nanoscale magnetic structures. The crosslinks between electronic structure and magnetism are addressed by a variety of spectroscopic techniques, ranging from high-resolution photoelectron spectroscopy to x-ray absorption spectroscopies. In order to study the spin state of matter directly spin-resolving approaches, such as spin-polarized photoemission and x-ray magnetooptics (circular and linear magnetic dichroism, x-ray resonant magnetic scattering) are employed. These experiments are carried out at proprietary beamlines operated at the synchrotron radiation facilities BESSY (Berlin) and DELTA (Dortmund).

A second major topic of interest concerns the behavior of magnetic systems on short and ultrashort time scales. In the nano- and picosecond regime, different magnetodynamic processes such as domain nucleation, magnetization rotation and precession occur. These processes are experimentally investigated by a variety of pump-probe techniques and interpreted via micromagnetic simulations. Laser-based approaches provide a high time-resolution, whereas time-resolved photoemission microscopy combines high lateral resolution with large magnetic sensitivity and element selectivity. On the sub-picosecond regime, we are interested in the energy and angular momentum transfer processes taking place between the electron, spin, and lattice subsystems. Understanding these processes provides an access to fundamental spin-dependent interactions, such as spin-orbit and exchange coupling. Such experiments are performed by femtosecond pump-probe methods.

The third main topic in the IEE is Spintronics, i.e., the physics of spin-dependent transport processes. Resting on a long-standing experience with giant (GMR) and tunnel-magnetoresistive (TMR) phenomena, the current studies concentrate on the fundamental physics of spin transport and transfer phenomena. This also includes the development of new magnetic materials systems for the use as electrodes, such as, e.g., magnetic semiconductors or halfmetallic ferromagnets. A particular emphasis is put on the development of smart magnetic switching alternatives. In this context, we explore magnetic switching processes and magnetization dynamics induced by spin-polarized electrical currents. The interest in these current-induced magnetic switching phenomena is just one facet of the broader activities on Nanospintronics, which are occupied with the spin transport through nanostructures, such as magnetic point contacts or carbon nanotubes.

With these activities, the IEE contributes to two major HGF research programmes, namely *Condensed Matter* and *Informationtechnology with Nanoelectronic Systems*.

Research Reports

Condensed Matter

Electronic and Magnetic Phenomena

The inverse problem of Electrical Impedance Tomography
H. Lustfeld, A.Erven,, A. Kemna, M. Reissel, C. Schwarzbach,

Polymerization of proteins actin and tubulin: the role of nucleotides ATP, GTP
R.O. Jones, P. Ballone, and J. Akola

The Principal net chemical reaction occurring in the whole world: DF study of hydrolysis of ATP at the active site of actin
R.O. Jones and J. Akola

Impurity-Vacancy Complexes in Si and Ge
H. Höhler, N. Atodiresei, K. Schroeder, R. Zeller, and P.H. Dederichs

Rashba effect at magnetic metal surfaces
G. Bihlmayer, S. Blügel, K. Starke, and O. Krupin

Non-collinear magnetism in 3d nanostructures on Ni(001) and Fe on $Fe_3ML/Cu(001)$
S. Lounis, Ph. Mavropoulos, P.H. Dederichs, and S. Blügel

Dynamical Correlations in the homogeneous electron gas: Double plasmon excitations in simple metals
H. Lustfeld and K. Sturm

Dephasing by Kondo impurities: Exact results
T. Micklitz, A. Altland, T.A. Costi, and A. Rosch

Effect of dynamical Coulomb correlations on the Fermi surface of $Na_{0.3}CoO_2$
H. Ishida, M.D. Johannes, and A. Liebsch

Orbital-selective Mott transitions in the nonisotropic two-band Hubbard model
A. Liebsch

Static versus dynamical mean field theory of Mott antiferromagnets
G. Sangiovanni, A. Toschi, E. Koch, K. Held, M. Capone, C. Castellani, and O. Gunnarsson

Magnetic Structure and Crystal-field of Pyrochlore $Ho_2Ru_2O_7$
L.J. Chang, W. Schweika, W. Schäfer, E. Jansen, M. Prager, and Th. Brückel

Magnetic structures in [Er/Tb] multilayers: a combined neutron and x-ray study
J. Voigt, E. Kentzinger, U. Rücker, W. Schweika, Th. Brückel, W. Schmidt, and D. Wermeille

Magnetization reversal in exchange biased multilayers depending upon applied field direction
A. Paul, E. Kentzinger, U. Rücker, D.E. Bürgler, Th. Brückel

Unraveling complex ordering in $La_{1-x}Sr_xMnO_3$ ($x \sim 1/8$) with synchrotron X-rays from below 1 keV to above 100 keV
Y. Su, H.F. Li. D. Wermeille, J. Perßon, P. Meuffels, S. Mattauch, A. Nefedov, J. Grabis, H. Zabel, D. Prabhakaran, A.T. Boothroyd, V. Kaiser, and Th. Brückel

Strain Relief of Heteroepitaxial Bcc-Fe Films on Mg(001)
G. Wedler and C.M. Schneider

Sub-Nanosecond Time-Resolving X-Ray Photoemission Electron Microscopy: Incoherent Magnetization Rotation Observed in Permalloy Microstructures
C.M. Schneider and A. Kuksov

Magnetic domains in mesoscopic ferromagnets: simulations and experiments
R. Hertel

Self-Trapping of Magnetic Oscillation Modes
A.Krasyuk, F. Wegelin, S.A. Nepijko, H.J. Elmers, G. Schönhense, M. Bolte, and C.M. Schneider

Fast Magnetization Dynamics in Cobalt Thin Films Structures
R. Adam, R. Hertel, A. Rzhevsky, and C.M. Schneider

Magnetization induced second harmonic generation in epitaxial Fe_3O_4/MgO(100)
A.A. Rzhevsky, B.B. Krichevtsov, A.D. Rata, C.F. Chang, R. Sutarto, L.H. Tjeng, and C.M. Schneider

Time-resolved photoelectron spectra of $Pt^2(N^2)^-$
M. Neeb, J. Stanzel, N. Pontius, W. Eberhardt, G. Lüttgens, P.S. Bechthold, C. Friedrich

The inverse problem of Electrical Impedance Tomography

H. Lustfeld[+])
IFF, Institute Theory I
[+]) *in cooperation with A.Erven,*
IFF und FH Aachen, Abt. Jülich,
A. Kemna, ICG IV, M. Reissel,
FH Aachen, Abt. Jülich, C. Schwarzbach,
Inst. f. Geophysik der Bergakademie Freiberg

The different resistivity of soil or rock layers has often been used to determine the position and thickness of these layers by injecting currents, measuring the electric potentials at different places and comparing these results with finite element calculations in which the resistivity of the soil is a parameter in each finite element. As is typical of tomographic problems the number of equations is not sufficient for determining these parameters. Theoretically an even over-determined set of equations can be obtained by using not only dc currents but ac currents with arbitrary many frequencies. We show: this need not be true in reality and we give relative noise level requirements for achieving a relevant information gain when using ac currents. It turns out that very low noise levels are needed to get essentially more information out of ac current measurements than of dc current measurements

The different resistivity of different soil or rock layers makes it possible - at least in principle - to determine the soil structure by measuring electrical potentials[1][2][3]. To achieve this, electrodes are distributed close to the surface of the soil and arranged along cables in small drilling holes. From some electrodes (positive and negative) currents are injected into the soil. The remaining electrodes are used to measure the electric potential at the electrode positions cf FIG.1). These measurements

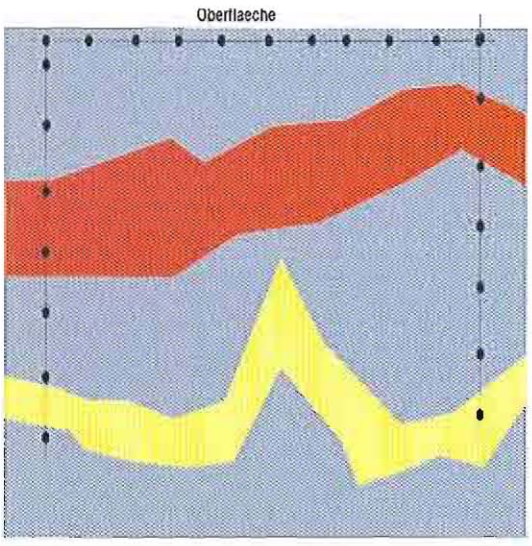

FIG. 1: *Sketch of layers and electrodes. The electrodes have a distance between* $1m$ *and* $10m$ *and the cables reach a depth of* $20m$ *till* $500m$.

are compared with numerical results obtained from finite elemente computations[1][4]. Typical in such cases is the underdetermination of the problem.

A modified approach[1][2] consists in applying ac currents. At first sight this is very promising since the impedance of typical soils depends distinctively on (low) frequencies. Thus measuring the electrical potential for arbitrary many frequencies transforms the problem of getting the soil structure from an under-determined one to an over-determined one.

We have shown[6] that the relevant information (which is equivalent to the number of relevant equations) is limited and depends sensitively on the precision of the measurements. We argue as follows: The frequency dependence of many soil and rock impedances can be fitted by the *Cole-Cole parameters*[5]. So the computed potential Ψ is a function of all the Cole-Cole parameters $\mathbf{c}$, the frequency ω and the location r: $\Psi = \Psi(\mathbf{r}, \omega, \mathbf{c})$. The cost function[7] E is given by

$$E = \frac{1}{2N_S} \sum_{i,k,l} \frac{|\Phi(\omega_l)_{ik} - \Psi_i(\mathbf{r}_k, \omega_l, \mathbf{c})|^2}{|\eta_{ikl}|^2} \qquad (1)$$

where $\Phi(\omega_l)_{ik}$ are the measured electric potentials, N_S is a normalization constant and the η_{ikl} are weight factors.

We concentrate on the situation in which the Cole-Cole parameters of the model agree - up to a small deviation $\delta\mathbf{c}_p$ - completely with the real ones. Thus $E \approx 0$. This can be achieved by choosing an exemplary model structure, cf FIG.2). From the deviation between computed and given values for the electric potential we get a set of equations determining the estimated correction $\delta\mathbf{c}$. We obtain $\delta\mathbf{c} = \delta\mathbf{c}_p$ if the set contains a sufficient number of relevant equations. This is always true if the number of frequencies is large enough and the relative noise level of the given values is infinitely small. However, in realistic cases the situation is quite different. E.g. data obtained from a frequency close to an already used one will not lead to new information if the data are noisy. This consideration can be placed on firm mathematical ground by applying the method of singular value decompositions to the matrix $\partial\Psi_i(\mathbf{r}_k, \omega_l, \mathbf{c})/\partial\mathbf{c}$. The results for the system

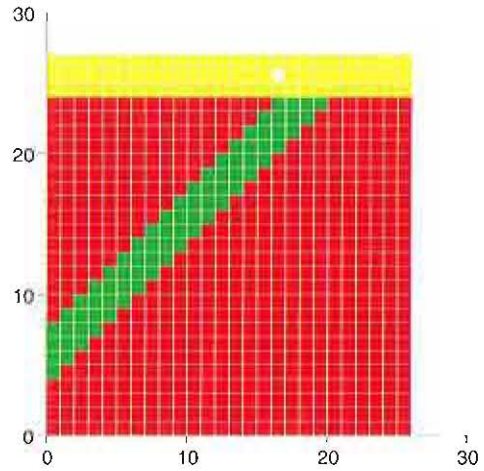

FIG. 2: *Sketch of an exemplary subsurface structure, it is assumed that all layers are running perpendicular to the plane (i.e. there is no y dependence of the structure). Surface layer: overburden, bulk layer: host rock, inclined layer: fracture zone.*

relative noise level	10^{-2}	10^{-3}	10^{-4}	10^{-5}
1 frequency	73	127	174	214
40 frequencies	122	268	456	690

table I *number of relevant equations obtained for data of only one frequency ($\nu = 10^{-3}Hz$) and of 40 frequencies in the interval $[10^{-3}Hz, 1000Hz]$ (the distance of the frequencies is logarithmic*

of Fig.2 are contained in table I and II. In table I the number of relevant equations are determined when measuring only at *one* frequency and when measuring at 40 frequencies respectively. Note the sensitive dependence

number of frequencies	relative noise level			
	10^{-2}	10^{-3}	10^{-4}	10^{-5}
1	73	127	174	214
2	99	218	315	402
5	100	220	390	559
10	100	220	391	560
15	100	220	392	560

table II *Number of relevant equations as function of the relative noise level and of the number of frequencies in the interval $[10^{-3}Hz, 1Hz]$ (the distance of the frequencies is logarithmic)*

on the relative noise level. Table II shows the maximum information that can be obtained when increasing the number of measurements in a given frequency interval. Increasing the frequency does not lead to an increase of relevant equations to the same extent. On the contrary saturation occurs beyond that further measurements in that frequency interval become useless.

In conclusion we can state that doing measurements at many frequencies increases the number of relevant equations. But that number saturates at a value depending sensitively on the relative noise level. This means that the tomographic problem changes from an underteter-mined one (when using dc current) to an ill posed problem (when using ac currents) and the usual methods such as regularization procedures are still required.

[1] A. Kemna: Tomographic inversion of complex resistivity, der Andere Verlag, Osnabrück (2000)
[2] D. Kretzschmar: Untersuchungen zur Inversion von spektralen IP-Daten unter Berücksichtigung elektromagnetischer Kabelkopplungseffekte, thesis, TU Berlin (2001)
[3] A. Kemna, J. Vanderborght, B. Kulessa, H. Vereecken, J. Hydrology, **267** 125 (2002)
[4] C. Schwarzbach: optimization and generalization of Kemna's code (2-3d solutions of Poisson equation as function of impedances), private communication (2004)
[5] K.S. Cole and R.H. Cole: J. Chem. Phys. **9**, 341 (1941)
[6] A. Erven: Diplom thesis (supervisor M. Reissel, H. Lustfeld), FH Aachen, Abt. Jülich (2005)
[7] Note that the Cole-Cole parameter are discrete which means that the cost function E can be looked at as the Hamiltonian of a generalized Ising model.

Polymerization of proteins actin and tubulin: the role of nucleotides ATP, GTP

R. O. Jones, P. Ballone[†], and J. Akola
Institute Theory I

The polymerizing proteins actin and tubulin are found in almost all cells and are crucial to important biological processes. Polymerization in both requires complexation by a nucleotide (adenosine triphosphate (ATP) and guanosine triphosphate (GTP), respectively), whose role is not understood in detail. Both reactions are entropy-driven, and we suggest that this arises from the softening on polymerization of vibrational modes localized near ATP and GTP. Simulations for a mesoscopic model based on particles and harmonic oscillators reproduce the transition from a dilute, gas-like state at low T to filaments at high T and support this assignment.

F&E-Nr: *E2310207*

After earlier studies of polymerization in liquid sulphur and phosphorus, we turn to the biological molecules actin and tubulin. Although an atomistic study of polymerization in not yet possible, we have developed a model that indicates the origin of the transition. Reversible polymerization of proteins is essential to cell motility and replication [1] and has motivated much study of both molecules. The monomers (Fig. 1) show important parallels: The actin monomer (G-actin, molecular weight 42 kDa, Fig. 1(a)) consists of four subdomains with a cleft containing a bound nucleotide (adenosine triphosphate ATP or diphosphate ADP) and a divalent cation Mg^{2+} or Ca^{2+} [2, 3]. Polymerization to F-actin is followed by hydrolysis of the ATP molecule [3] to ADP and an inorganic phosphate group P_i. The $\alpha\beta$-tubulin dimer (molecular weight 55 kDa, Fig. 1(b)) [4] is the basic unit of microtubules, which are essential components in all eukaryotic cells and show dynamic instability that is based on binding and hydrolysis of a related nucleotide (guanosine triphosphate GTP). Such instabilities are the likely origin of some forms of cancer.

The measured $T\Delta S$ in actin polymerization exceeds the reaction enthalpy ΔH [5], and entropy as a driving force is consistent with the increased polymerization rate in actin and tubulin solutions as temperature T increases [6]. The source of entropy driving these transitions is unclear. We focus on the dynamical properties of actin-ATP and propose that entropy provided by the softening of ATP vibrational modes offsets the loss of translational entropy and the increase in potential energy upon aggregation. This picture is supported by simulations of a model that includes essential features of actin-ATP and displays an equilibrium phase diagram similar to those measured. A related mechanism should be active in tubulin.

In the (classical) harmonic approximation, the vibrational entropy of actin-ATP is:

$$S/K_B = -\sum_{i=1}^{k} \log[\hbar\omega_i/K_B T] \qquad (1)$$

where K_B is the Boltzmann constant, and k is the number of vibrational modes with frequency ω_i. If a single mode in G-actin changes frequency from ω_G to ω_F on aggregation, the entropy change per monomer is:

$$\Delta S = S_F - S_G = K_B \log[\omega_G/\omega_F], \qquad (2)$$

Grouping monomers into $N' = N/P$ polymers of length P will raise translational entropy by ΔS_{ideal} dependent on the thermodynamic conditions. If ΔU is the

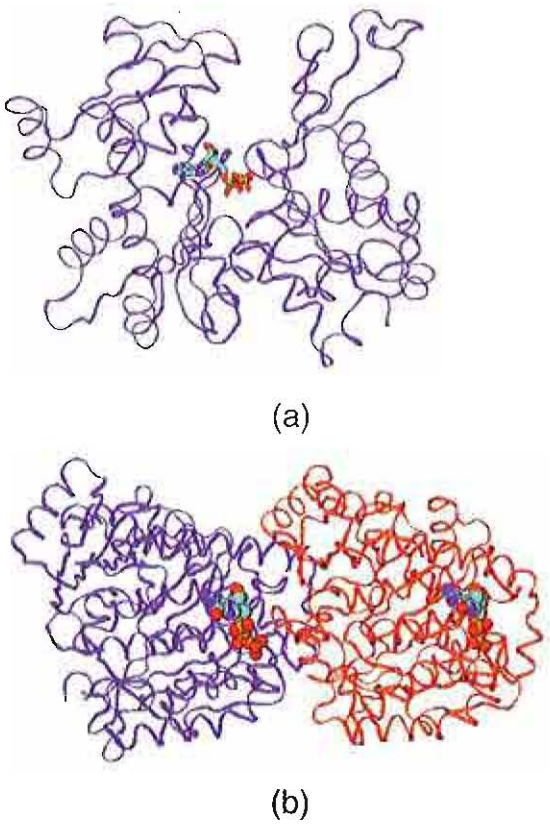

FIG. 1: Ribbon diagrams of monomers of (a) actin (with ATP, after Ref. 3) and (b) tubulin (with GTP and GDP, after Ref. 4).

increase in internal energy upon polymerization, and the monomer-monomer interaction is repulsive, polymerization is possible above the floor temperature $T_f = \Delta U/[\Delta S_{ideal} + \Delta S_{vib}]$ whenever $\Delta S_{ideal} + \Delta S_{vib} < 0$.

The harmonic stretching frequency of the ADP–P_i covalent bond is predicted our density functional calculations to be $\omega_G = 924$ cm^{-1}, and the dramatic reduction of the ADP–P_i stretching frequency in F-actin ($\omega_F \sim 0$) could provide a free energy contribution at high T large enough to overcome the ΔU and ΔS_{ideal} contributions of opposite sign.

We have developed a model comprising N spherical "particles" (the protein monomers) that interact with a pair potential supplemented by bending contributions. A purely repulsive pair potential is adopted to emphasize the relative roles of potential energy and entropy. Each particle carries s intramolecular (vibrational) degrees of freedom, for which we use harmonic oscillators $\{r_{i,I}, I = 1, ..., N; i = 1, ..., s\}$, whose dynamics depend on the particle coordination. Full details of the model are given elsewhere [7], and we show that it leads to ordered aggregates in an initially disordered configuration as T is increased. A suitable choice of functional form and parameters results in long, semiflexible polymers reminiscent of the actin and tubulin [8]. Simulations have been performed for systems of 4000 atoms at a range of temperatures and densities, using molecular dynamics (MD) in the NVT ensemble and a 2D geometry. The simulation cell is a square of side L in all cases.

Repeated quenches and annealing cycles at low density led at T = 0 to a disordered configuration of isolated particles with separations greater than R_c. Increasing the kinetic energy results initially in nearly elastic collisions, followed by the separation of the particles, and then to more persistent changes. The degree of polymerization shows a monotonic rise with increasing T, reaching 80 % of the total mass at T = 0.6 (reduced units).

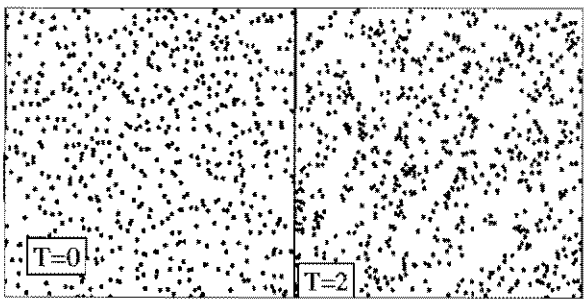

FIG. 2: Snapshots from simulations of the basic model.

Short linear units (dimers, trimers, etc.) predominate at T $\sim$ 0.1, and larger aggregates of 10-15 particles seldom occur. At intermediate (T $\sim$ 0.5) and high temperatures (T $\geq$ 1) the dominant species are medium-size ($\sim$ 20 particles) open chains (see Fig. 2); larger molecules (up to 80 particles) are also present. The simulation results depend strongly on density, with even slight increases greatly favoring aggregation, which takes place at lower T and produces much larger molecules. On the other hand, no visible aggregation takes place at the lowest density over the temperature range we have explored.

Polymerization in tubulin is also enhanced by increasing T and density. One non-exchangeable molecule of GTP is bound to α-tubulin, and β-tubulin can hydrolyze its bound GTP to GDP–P_i, release P_i, and exchange bound GDP for GTP. The microtubule is stabilized at the ends by caps of GTP-subunits. Tubulin, however, shows collective dynamic effects leading to the sudden collapse of microtubules, even at equilibrium, which suggest that the description of tubulin polymerization requires additional ingredients.

Our model focuses on the dependence of intramolecular (vibrational) modes on the environment, and the simulations show intriguing similarities to the behavior of proteins polymerizing with increasing T. The results suggest that actin polymerization arises from the softening of intramolecular vibrational modes (particularly of ADP-P_i) caused by the docking of actin monomers. The essential role of ATP is that the affected modes are localized near this molecule [3], as well as water molecules in the first hydration shell [10]. The loss of phosphate by F-actin, often identified with ATP hydrolysis, is here of secondary importance. This picture could be tested by comparing the full vibrational spectra of actin-ATP in filaments and in the isolated monomers. This is a formidable challenge, but the investigation of the actin-ATP vibrational properties is an exciting and important subject.

[†] Permanent address: Università degli Studi di Messina, Dipartimento di Fisica, I-98166 Messina, Italy.

[1] L. Stryer, *Biochemistry*, Fourth Edition (Freeman, New York, 1995).
[2] W. Kabsch, *et al.*, Nature **347**, (1990).
[3] S. Vorobiev, *et al.*, Proc. Natl. Acad. Sci. USA **100**, 5760 (2003).
[4] R. B. G. Ravelli, *et al.*, Nature **428**, 198 (2004).
[5] M. Kasai, Biochim. Biophys. Acta **180**, 399 (1969).
[6] D. K. Fygenson, E. Braun, and A. Libchaber, Phys. Rev. E **50**, 1579 (1995).
[7] P. Ballone, J. Akola, and R. O. Jones (submitted).
[8] I. Fujiwara, *et al.*, Nature Cell Biology **4**, 666 (2002).
[9] T. D. Pollard and A. G. Weeds, FEBS Lett. **170**, 94 (1984).
[10] N. Fuller and R. P. Rand, Biophys. J. **76**, 3261 (1999).

"The principal net chemical reaction occurring in the whole world": DF study of hydrolysis of ATP at the active site of actin

R. O. Jones and J. Akola[†]
Institute Theory I

Adenosine 5′-triphosphate (ATP) is a basic energy carrier in cellular metabolism. As a high-energy intermediate, it provides a way to convert energy from one biochemical process to another via an environment-dependent hydrolysis reaction. Actin is a protein that occurs in most mammalian cells, and it is crucial for muscle contraction and many other processes. Density functional calculations for four possible paths of the hydrolysis reaction at the active site of actin show that the lowest energy barrier (21.0 kcal/mol) is found for a dissociative reaction where the terminal phosphate breaks on approaching the catalytic water.

F&E-Nr: E2310207

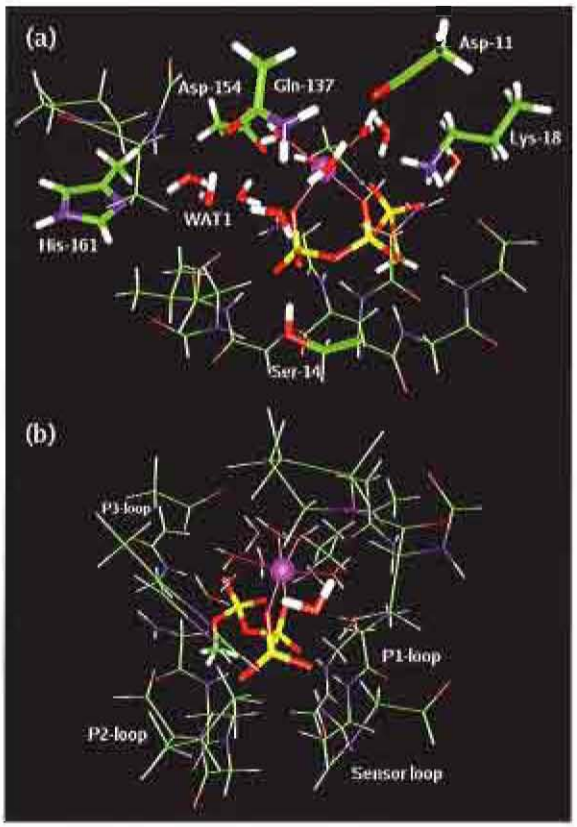

FIG. 1: Active site of actin: (a) Front view: Triphosphate tail of ATP, water molecules, and residue side chains are plotted in licorice representation. Magenta sphere is an Mg cation. (b) Side view: Triphosphate and catalytic water are emphasized (note location of WAT1), and β-hairpin segments of actin are labeled. Color key: H, white; C, green; N, blue; O, red; and P, yellow.

Adenosine 5′-triphosphate (ATP), the universal energy carrier in the living cell, consists of adenosine linked to three phosphate groups. Removal of the outermost γ-phosphate group to form adenosine diphosphate (ADP) provides energy for use in other reactions. With provision of energy, the inorganic phosphate group P_i can be bound to ADP to form ATP. The formation and use of ATP is "the most prevalent chemical reaction in the human body" and "the principal net chemical reaction occurring in the whole world" [1]. It will come as no surprise that it has been studied in a vast array of contexts, and we focus here on the mechanism of this reaction at the active site in the protein actin (Fig. 1).

Actin (molecular weight 43,000) comprises two domains connected by an α-helix link, and the overall shape resembles a cloverleaf with a deep interdomain cleft that can bind one adenine nucleotide (ADP or ATP) complexed with a divalent cation (Mg^{2+} or Ca^{2+}). ADP/ATP is essential for the stability of actin under physiological conditions [2]. Actin is involved in muscle contraction, cellular motility and division (cytokinesis), vesicle transport, and the establishment and maintenance of cell morphology. It is also an essential component of structures such as the intestinal brush border or the sensory cells of the inner ear (stereocilia). The versatility of actin is a consequence of the dynamic nature of filamentous actin (F-actin) assemblies that form in living organisms. In the cytoplasm of a cell, a microscopic network of actin filaments (cytoskeleton) is formed via polymerization of actin monomers (G-actin). The contribution of the ATP/ADP reaction to determine the structure, function, and dynamics of actin is crucial in this context, and most actin subunits hydrolyze a single molecule of ATP to ADP during the lifetime of F-actin.

We have published the results of density functional (DF) calculations of the hydrolysis of ATP to yield ADP and P_i in an aqueous environment [3], and we have now extended this work to ATP hydrolysis at the active site of actin. DF calculations incorporate details of the electronic structure of ATP, water molecules, and the active site without introducing adjustable parameters, and our goal is to provide an atomistic description of plausible reaction paths. The protein plays a crucial role, since it affects the properties of ATP, and the coordination of the end products provides valuable information for the subsequent phosphate migration process that completes

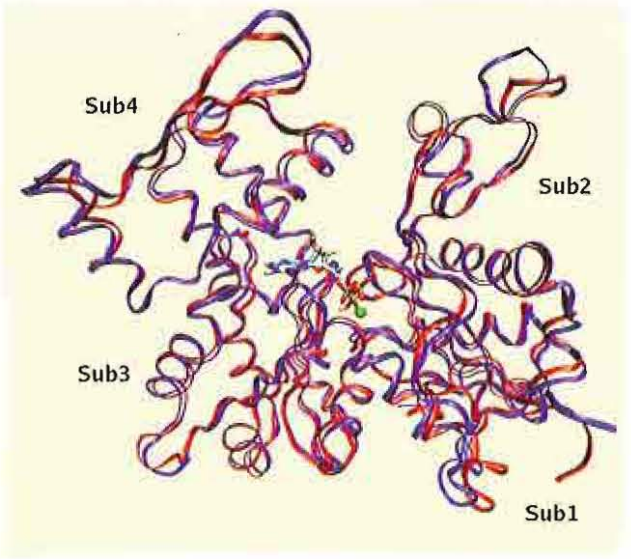

FIG. 2: Snapshot of ADP·P_i-actin after 5 ns of molecular dynamics (blue ribbons) compared with the initial crystal structure of ATP-actin (red ribbons). The actin subdomains are labeled according to the standard notation. ADP^{3-} and $H_2PO_4^-$ are shown in licorice format, and the Mg cation is represented by a green sphere (simulation).

the hydrolysis.

In order to obtain information about the possible conformational changes due to hydrolysis, we have performed in addition 5 ns of classical molecule mechanics for the ATP-actin (ADP·P_i-actin) system embedded in an orthorhombic box of water (altogether 38700 atoms). We used the ORAC simulation package [4], which employs a multiscale time step, and the AMBER99 force field for biomolecules [5]. For ATP, a recently developed force field [6] is applied with classical point charges derived from the DF calculations of this study.

The reactions have been studied using DF calculations and applying constraints to coordinates to allow phosphate stretching, attack by the catalytic water molecule (WAT1), and OH^- formation via water deprotonation. The lowest energy barrier (21.0 kcal/mol) is found for a dissociative reaction where the terminal phosphate breaks on approaching the catalytic water, followed by proton release. Stretching the terminal bridging P-O bond results in rupture with an energy barrier of 28.8 kcal/mol. The calculations also demonstrate the role of the neighbouring residues in the reaction. Gln-137 and His-161, for example, take no significant part in the process.

The immense complexity of the system (a single molecule of actin has a molecular weight of 43,000, and the aqueous environment is of central importance) means that a combination of classical force field and DF calculations has distinct advantages over the use of either approach alone. Classical force fields allow us to perform much longer simulations on many particles (see Fig. 2), but cannot yet provide a convincing picture of reaction mechanisms. The latter is the realm of density functional calculations. Details of the present calculations, as well as DF calculations of molecules related to ATP, are provided elsewhere [7].

[†] Present address: Nanoscience Center, University of Jyväskylä, FIN-40014 Jyväskyklä, Finland.

[1] Boyer, P. D. *Nobel Lectures, Chemistry 1996-2000*, Ed. Grenthe, I. (World Scientific Publishing, Singapore), p. 120 (2003).

[2] E. M. De La Cruz and T. D. Pollard, Biochemistry **34**, 5452 (1995).

[3] J. Akola and R. O. Jones, J. Phys. Chem. B **107**, 11774 (2003).

[4] P. Procacci, T. A. Darden, E. Paci, M. Marcchi, J. Comput. Chem. **18**, 1848 (1997). ATP-actin system (5840 atoms) is solvated by 10950 water molecules in an orthorhombic box of 61.2×79.5×79.5 $Å^3$.

[5] W. D. Cornell, P. Cieplak, C. I. Bayly, I. R. Gould, K. M. Merz, D. M. Ferguson, D. C. Spellmeyer, T. Fox, J. W. Caldwell, P. A. Kollman, J. Am. Chem. Soc. **117**, 5179 (1995).

[6] K. L. Meagher, L. T. Redman, H. A. Carlson, J. Comput. Chem. **24**, 1016 (2003).

[7] J. Akola and R. O. Jones, J. Phys. Chem. B (submitted).

Impurity-Vacancy Complexes in Si and Ge

H. Höhler, N. Atodiresei, K. Schroeder, R. Zeller, and P. H. Dederichs
Institute Theory III

We have investigated the electronic and geometrical structure of impurity-vacancy complexes for sp-impurities in Si and Ge, using the pseudopotential plane wave (PPW) and the all-electron Kohn-Korringa-Rostoker (KKR) methods. For oversized impurities, in particular of the 5sp and 6sp series we find a new configuration in the form of a split-vacancy, while impurities of the 3sp and 4sp series prefer the usual substitutional complex (except Al, which prefers a split complex in Si). These trends strongly correlate with the lattice relaxations of nearest neighbors around the isolated (without vacancy) substitutional impurities. For Cd and Sn, where experimental PAC and EPR data exist, our calculated hyperfine parameters agree well with these data.

Intrinsic defects and their complexes with impurities play an important role in semiconductor physics. Particularly interesting systems are vacancy-impurity complexes in Si and Ge. From experiments on Sn in Si (EPR [1]) and on Cd in Ge (PAC [2]) it was suggested that in these systems an exotic configuration is preferred: a split-vacancy complex with the Sn (Cd) atom on the bond-center position and the vacancy split into two half-vacancies on the nearest neighbor (NN) sites. Previous ab initio calculations [3] for Sn in Si found a very small energy preference (0.045 eV) for the split-vacancy complex compared to the substitutional-Sn-vacancy pair on NN sites.

Here we present a systematic study of impurity-vacancy complexes in Si and Ge. Our results show that as a general rule oversized impurities form split-vacancy complexes, while impurities with sizes comparable to the host atoms prefer the usual substitutional complex. In the calculations we have used two different density functional methods (for details see [4]). The pseudopotential plane wave (PPW) method has been used to investigate the configuration and stability of the impurity-vacancy complexes. The stable configurations for the Cd and Sn impurity-vacancy complexes and the relaxations of the neighboring atoms have been recalculated by the KKR-Green-function method, which as an all-electron method allows to calculate the electric field gradients, isomer shifts and hyperfine fields.

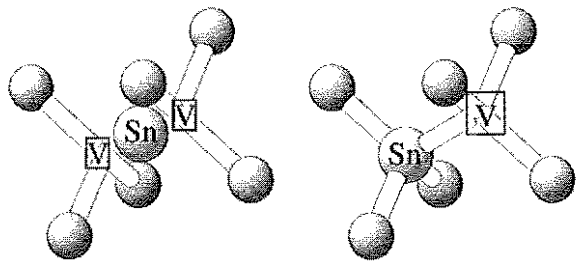

FIG. 1: The Sn-split-vacancy configuration (left) and the usual substitutional Sn-vacancy configuration (right).

We have found that both in Si and Ge the substitutional Cd (and Sn) vacancy-complex is instable and relaxes into the highly symmetrical split-vacancy complex, where the vacancy is split into two "half-vacancies" on neighboring sites and the Cd or Sn atom occupies the bond-center position in between (Fig. 1). This configuration is about 1eV lower in energy than the substitutional configuration (see Table II). The local density of states (LDOS) at the impurity site of the split-vacancy complex in Ge is shown in Fig. 2, where the energies are given relative to the Fermi level chosen at the top of the valence band $E_F = E_{val}$. The different peaks are labeled by the irreducible subspaces A_{1g}, A_{2u}, E_u and E_g of the D_{3d} point group symmetry of the complex. Compared to the Cd complex (d-level at about -9 eV), the d-level of Sn is fully localized and at much lower energies, otherwise the level scheme is very similar: the A_{1g} state at relative low energies, the A_{2u} and the doubly degenerate E_u state slightly below the gap, the doubly degenerate E_g state in the gap and, for Sn, a second A_{1g} state at higher energies. Since the occupied A_{1g}, A_{2u} and E_u states accommodate 8 electrons, of which the 6 neighboring host atoms provide 6 (one dangling bond each), the vacancy complex with Cd (with 2 valence electrons) is neutral ($[CdV]^0$), and the complex with Sn (with 4 valence electrons) is doubly positively charged ($[SnV]^{2+}$). As discussed in [4], the level sequence is basically the same as for the divacancy. The Cd and Sn-atoms can be considered as Cd^{2+} and Sn^{4+} ions inserted in the center of the divacancy and only weakly hybridize with the 6 nearest neighbors. The attractive ionic potentials shift the divacancy states to lower energies, in particular the fully symmetrical A_{1g} state. This effect is naturally stronger for the Sn^{4+} ion than for the Cd^{2+} ion. The same level sequences is expected for other 5sp impurities.

By occupying the E_g state in the gap, different charge states of the complexes are realized, i.e. $[SnV]^+$, $[SnV]^0$, ..., and analogously $[CdV]^-$, $[CdV]^{2-}$. Both the $[SnV]^+$ and the $[SnV]^0$ complexes are magnetic with total moments of 1 and 2 μ_B, and with small local moments of 0.045 μ_B (0.008 μ_B) and 0.091 μ_B (0.016 μ_B) on the Sn site in Si (Ge). The calculations have shown that sizable relaxations of the neighboring host atoms toward the Sn (Cd) atoms exist, which increase with the electronic charge.

The hyperfine parameters for the Cd-split-vacancy complexes are listed in Table I. In the split configuration the weak hybridization of the impurity atoms with

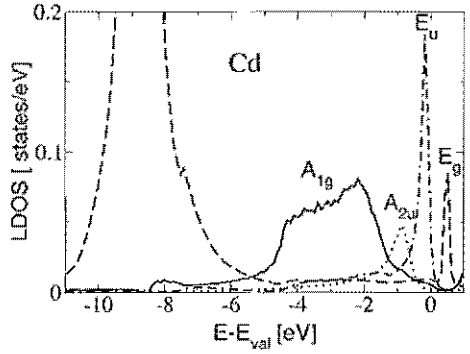

FIG. 2: LDOS projected on the irreducible subspaces of the D_{3d} group at the Cd site for the impurity split-vacancy complex in Ge.

the six NN atoms results in a nearly isotropic charge density and a unusually small EFG. Our results are in good agreement with PAC measurements [2] and allow a unique assignment of the measured Cd EFG values to the Cd-split-vacancy complex in the charge state $[CdV]^-$.

For the neutral Sn-split-vacancy complex our results are in good agreement with available EPR data. The measured hyperfine field (-91.02 kG) [1] at the neighboring Si atoms adjacent to a SnV complex agrees well with our calculated value -82.96 kG for the neutral complex. The measured hyperfine field at the Sn atom [5] is close to our calculated value for the neutral Sn-split-vacancy complex [4]. The calculated isomer shifts agree well with unpublished measurements of R. Sielemann.

TABLE I: Hyperfine fields HF and electric field gradients EFG at the Cd site for the Cd-split-vacancy complexes in Si and Ge.

	Si host		*Ge host*	
system	*HF [kG]*	*EFG [Mhz]*	*HF [kG]*	*EFG [MHz]*
$[V\|Cd\|V]^0$		*-6.97*		*-32.69*
$[V\|Cd\|V]^{1-}$	*21.8*	*-27.99*	*8.5*	*-55.69*
$[V\|Cd\|V]^{2-}$		*-49.47*		*-79.64*
EXP [2, 6]		*± 28.00*		*± 54.00*

We have calculated the structure of impurity-vacancy complexes for other impurities, in particular for heavy impurities with larger sizes than Si or Ge atoms. For the elements Cd, In, Sn and Sb of the 5sp series and the even heavier element Bi we have found that the split-vacancy impurity complex is preferred over the substitutional one by energies between 0.5 to 1 eV (see Table II). This suggests that this complex is the stable one for all oversized impurities in Si and Ge.

On the other hand, we find that impurities of the 3sp and 4sp series, with the exception of Al in Si, prefer the substitutional complex, in most cases rather distorted by a sizable relaxation of the impurity toward the bond center (see Table II). In order to discuss the importance of impurity size for the relative stability of the substitutional and split configurations we have calculated the lattice relaxations of the isolated impurities of the 3sp, 4sp, and 5sp series. In general, we have found a good qualitative correlation of sign and size of the NN relaxations of the single impurities with the stability of the two configurations, although a strict one-to-one correspondence is not valid. As a rule of thumb we can define an impurity as "oversized", yielding a stable split-vacancy complex, if the NN relaxation exceeds 3%. There are two exceptions: substitutional Al shows only 2% NN relaxation in Si, yet we find the Al-split-vacancy complex stable, and Se shows a NN relaxation larger than 5% in both Si and Ge, yet the distorted substitutional complex is stable.

TABLE II: Relaxations of neutral impurity-vacancy complexes and substitutional impurities in Si and Ge. The forces F (in mRy/a.u.) on the impurity atom are given for the undistorted substitutional-vacancy complex, a negative sign means forces directed toward the bond center. The energy differences ΔE (in eV) are between the fully relaxed split-vacancy and distorted substitutional-vacancy complex. The stable positions r of the impurities in (111) direction are also given; 0.5 is the bond-center and 1.0 the substitutional position. The values Δr^* refer to the NN relaxation of the isolated impurities (in % of the NN-distance).

	Si host				*Ge host*			
	F	ΔE	*r*	Δr^*	*F*	ΔE	*r*	Δr^*
Al	*-22.4*	*-0.15*	*0.50*	*+2.03*	*-0.96*	*+0.03*	*0.82*	*-0.51*
Si					*-4.50*	*+0.30*	*0.88*	*-1.51*
P	*-11.5*	*+1.27*	*0.95*	*+0.04*	*-11.7*	*+0.81*	*0.93*	*-0.73*
Ga	*+5.37*	*+0.22*	*1.04*	*+0.32*	*+14.6*	*+1.11*	*1.04*	*-1.65*
Ge	*-21.7*	*+0.30*	*0.87*	*+1.13*				
As	*-41.7*	*+0.82*	*0.90*	*+2.52*	*-44.1*	*+0.41*	*0.87*	*+1.80*
Se	*-44.9*	*+0.55*	*0.92*	*+7.09*	*-37.6*	*+0.35*	*0.91*	*+5.65*
Cd	*-85.2*	*-1.04*	*0.50*		*-69.6*	*-1.01*	*0.50*	
In	*-77.2*	*-0.69*	*0.50*	*+6.02*	*-43.2*	*-0.47*	*0.50*	*+3.17*
Sn	*-105.*	*-0.83*	*0.50*	*+6.24*	*-79.0*	*-0.60*	*0.50*	*+4.18*
Sb	*-129.*	*-0.68*	*0.50*	*+7.91*	*-109.*	*-0.64*	*0.50*	*+6.32*
Bi	*-182.*	*-0.92*	*0.50*	*+10.37*	*-152.*	*-0.86*	*0.50*	*+8.68*

[1] Watkins, G. D., *Phys. Rev. B* **12** (1975), 4383-4390
[2] H. Haesslein, R. Sielemann and Ch. Zistl, Phys. Rev. Lett. **80** , 2626, (1998).
[3] A. N. Larsen et al., Phys. Rev. B **62**, 4535 (2000); M. Kaukonen et al., Phys. Rev. B **64**, 245213 (2001).
[4] H. Höhler, N. Atodiresei, K. Schroeder, R. Zeller, and P. H. Dederichs, Phys. Rev. B **70**, 155313 (2004) and **71** 035212 (2005).
[5] M. Fanciulli and J. R. Byberg, Phys. Rev. B **61**, 2657 (2000).
[6] D. Forkel, F. Meyer, W. Witthuhn, H. Wolf, M. Deicher and M. Irisher, Hyperfine Interactions **35** , 715, (1987).

Rashba effect at magnetic metal surfaces

G. Bihlmayer,[1] S. Blügel,[1] K. Starke,[2] and O. Krupin[2]
[1]*Institute Theory I*
[2]*Institut für Experimentalphysik, Freie Universität Berlin, Germany*

In semiconductor heterostructures the Rashba effect allows the manipulation of spin-polarized electrons in a two dimensional electron gas by an external electric field. This tiny effect is difficult observe directly or to access with *ab initio* calculations. But on some metal surfaces the Rashba effect can be observed as spin-orbit splitting of the surface state. Our first-principles calculations of the clean and O covered Gd(0001) surface show a Rashba spin-orbit splitting for the exchange-split surface state in good agreement with experimental data. We can manipulate the strength of this splitting by adsorption of O on this surface, as has also been shown experimentally.

Exploring the possibility to use the electron-spin degree of freedom for storage, processing and transfer of information is a current focus of condensed matter physics research [1]. The key issue of future spintronic devices is to control and manipulate the electron spin without the need to apply an external magnetic field, which becomes exceedingly difficult to be integrated in high-density devices. Rashba had realized early on [2] that, due to relativistic effects, electron-spin manipulation could as well be done using an electric field since it acts as a magnetic field in the rest frame of a moving electron. This effective interaction is described by the Rashba Hamiltonian

$$\mathcal{H}_R = \alpha\,(\mathbf{e}_z \times \mathbf{k}) \cdot \underline{\sigma} \qquad (1)$$

and is largest when electron momentum k, its spin given by the Pauli matrices $\underline{\sigma}$ and the electric field along the unit vector $\mathbf{e}_z$ are perpendicular to each other. The Rashba constant α comprises intra-atomic spin-orbit coupling and the effective electric field strength seen by the electron. It is obvious from Eq.(1) that this interaction exists only when inversion symmetry is broken, either due to an external field or due to the local crystal symmetry, e.g. at an interface. Based on this concept Datta and Das [3] proposed a scheme of a FET type spin transistor, in which the electron spin is controlled through the gate voltage and, both, source and drain are made of magnetic electrodes through which spin polarized electrons ought to be injected into and detected from a two-dimensional electron gas, respectively [3].

The requirement of structural inversion asymmetry for non-vanishing Rashba effect is met par excellence by surface (interface) states in which electron propagation is confined to a plane perpendicular to the surface (interface) potential gradient (along z), i.e. $\mathbf{e}_z \perp \mathbf{k}_\parallel$ is naturally fulfilled (cf. Eq.(1)). The Rashba effect leads to a measurable splitting of (spin-degenerate) surface bands when the Rashba constant α in Eq.(1) is sufficiently large, i.e. when both, the spin-orbit interaction and the electric field are large in the surface (interface) region. Extremely large effects have recently been found theoretically and experimentally on Bi surfaces [4]. The fact, that also on a nonmagnetic surface the electron has a spin-direction

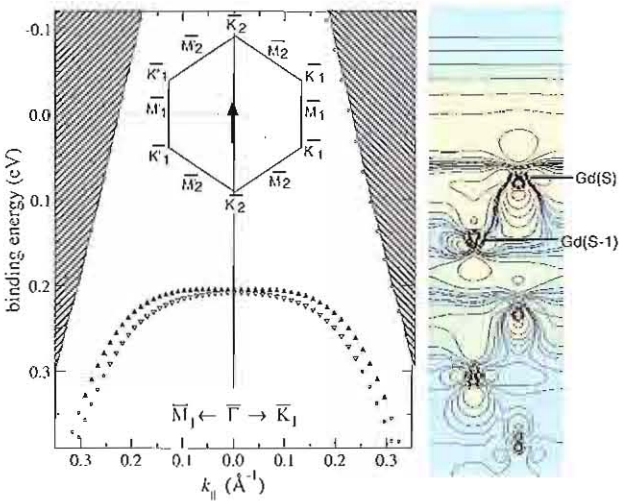

FIG. 1: Calculated surface state dispersion (left) and charge density (right) of Gd(0001). The two lines correspond to surface states on the upper (empty symbols) and lower (full symbols) surface of the Gd film. The inset shows the magnetic surface Brillouin zone (BZ) for the indicated magnetization direction.

given by Eq.(1) can even be observed in STM images [5]. Here, we show the existence of a sizable Rashba splitting at magnetic metal surfaces. Experiment and *ab initio* calculations reveal a sizable Rashba splitting of the d–derived surface state at the ferromagnetic Gd(0001) surface, which increases substantially upon formation of the ordered $O(1 \times 1)$/Gd(0001) surface monoxide [6].

Calculations were performed using density functional theory in the local density approximation. We use the full-potential linearized augmented planewave method in film-geometry [7] as implemented in the FLEUR program. Spin-orbit coupling is included self-consistently as described in Ref. [8]. The Gd surface was simulated by a relaxed 10-layer film embedded in semi-infinite vacua. O was adsorbed on the fcc site and its relaxed position was 0.78Å above the topmost Gd layer. This outermost metal layer shows a strong (18%) outward relaxation upon O adsorption, while the inner layers remain nearly unperturbed. The magnetic moment was always

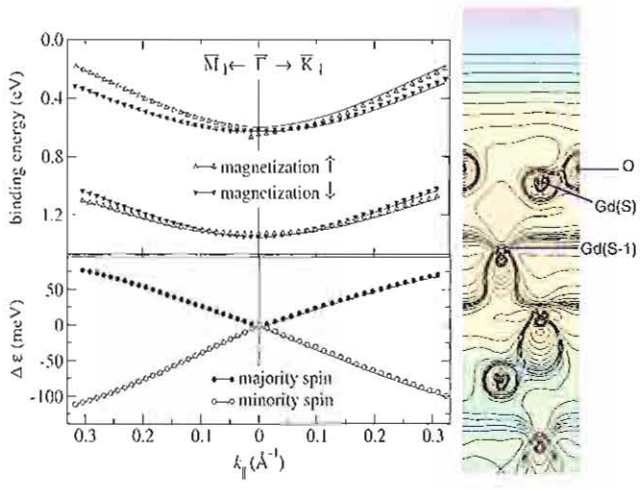

FIG. 2: Calculated surface state dispersion (left) and charge density (right) of O/Gd(0001). The difference of the energy dispersion of the two surface states on the upper and lower surface is shown in the lower panel.

assumed to be in the surface plane in (1000) direction.

We see in Fig. 1 the spin-orbit split surface state of Gd(0001), the splitting being linear in k. Comparison with experimental data shows that the size of the Rashba splitting is in good agreement with the experimental values. The dispersion was measured for opposite magnetization directions showing two branches are oppositely shifted in $\Delta k_\parallel$ w.r.t. BZ center. In the calculation, the surface was simulated by a thin film having an upper and a lower surface. Since the potential gradients on these two surfaces are opposite, we observe the upper and the lower surface state with the same Rashba splitting that would result from two calculations of a surface state on one of these surfaces but with opposite magnetization.

Adsorption of oxygen leads to formation of an O layer on the Gd(0001) surface which exhibits an exchange-split pair of surface bands originating from hybridization between Gd $5d$ and Op states [9]. The calculation shows that O adsorption strongly modifies the electronic structure of the surface Gd atom (see Fig. 2). The O atom draws charge from the surface Gd (Gd(S) in Fig. 2). Furthermore, the surface state is now pushed to the subsurface Gd layer (cf. right side of Fig. 2) so that it might be considered as an interface state between the (bulk) Gd and the (surface monoxide) GdO layer. In good agreement with the experimental data we find now the majority and minority surface state occupied and dispersing upwards. The Rashba splitting of the surface states is found to be more than twice as large for the O covered surface than for clean Gd(0001), again in very good agreement with the experimental data. Note, that now the shift is opposite for opposite spins and, also experimentally, it changes sign upon magnetization reversal.

From Eq.(1) it is evident that the sign of the interaction will change by reversing either the magnetization direction or electron momentum. The interaction thus leads to a separation in momentum space of electrons with equal energies and opposite spins, causing the splitting of the spin degenerated band into two bands. As the surface state of Gd(0001) is of pure majority spin character, experimentally no spin-resolved detection method is needed to observe the Rashba effect which, as expected, is rather a shift of the band than a splitting. For the O-induced surface states, both, minority and majority states are present and well separated in energy. The opposite spin character of the states results in opposite signs of the Rashba interaction, cf. Eq.(1).

From the calculated charge densities and the decomposition of the wavefunction in p and d-character, the increase of the observed Rashba-splitting can be traced back to a change in the shape of the wavefunction of the surface state. Since the Rashba constant is largely determined by the intra-atomic spin-orbit coupling constant, a slight increase of p-character of the wavefunction increases the Rashba splitting. From Fig. 2 we see further, that both the splitting and the dispersion is a bit larger for the minority than for the majority surface state.

Although the (Rashba) spin-orbit splitting of the Gd(0001) and O/Gd(0001) surface states in $\bar{\Gamma} - \bar{M}$ and $\bar{\Gamma} - \bar{K}$ direction appear very similar to the splitting of the Au(111) surface state [10] with an additional (Zeeman) spin-splitting, one has to keep in mind one important difference: Whereas on a nonmagnetic surface the spin polarization of an electron is always perpendicular to the electric field and the direction of propagation (k), in the present magnetic case it is defined by the magnetization direction. Therefore, in the case of Au(111) the Rashba-splitting is identical in all $k_\parallel$ directions, while on Gd(0001) it is zero, when the global magnetization direction coincides with the propagation direction of the electron (i.e. $\bar{K}_2$ in Fig. 1).

[1] S. A. Wolf, D. D. Awschalom, R. A. Buhrman, et al., Science **294**, 1488 (2001).
[2] E. I. Rashba, Sov. Phys. Solid State **2**, 1109 (1960).
[3] S. Datta and B. Das, Appl. Phys. Lett. **56**, 665 (1990).
[4] Y. M. Koroteev, G. Bihlmayer, J. E. Gayone, et al., Phys. Rev. Lett. **93**, 046403 (2004).
[5] J. I. Pascual, G. Bihlmayer, Y. M. Koroteev, et al., Phys. Rev. Lett. **93**, 196802 (2004).
[6] O. Krupin, G. Bihlmayer, K. Starke, et al., Phys. Rev. B **71**, 201403(R) (2005).
[7] E. Wimmer, H. Krakauer, M. Weinert, et al., Phys. Rev. B **24**, 864 (1981).
[8] C. Li, A. J. Freeman, H. J. F. Jansen, et al., Phys. Rev. B **49**, 5433 (1990).
[9] C. Schüssler-Langeheine, R. Meier, H. Ott, et al., Phys. Rev. B **60**, 3449 (1999).
[10] S. LaShell, B. A. McDougall, and E. Jensen, Phys. Rev. Lett. **77**, 3419 (1996).

Non-collinear magnetism in 3d nanostructures on Ni(001) and on Fe_{3ML}/Cu(001)

S. Lounis, Ph. Mavropoulos, P. H. Dederichs, and S. Blügel
Institut für Festkörperforschung, Forschungszentrum Jülich, D-52425 Jülich, Germany

Magnetic nanostructures on non-magnetic or magnetic substrates have attracted strong attention due to the development of new experimental methods with atomic resolution. Motivated by this progress we have extended the full-potential Korringa-Kohn-Rostoker (KKR) Green function method to treat non-collinear magnetic nanostructures on surfaces. We focus on the complex magnetism of 3d impurity nanoclusters, sitting as adatoms on or in the first surface layer of the ferromagnetic Ni(001) surface. While clusters of Fe, Co, Ni atoms are magnetically collinear, non-collinear magnetic coupling is expected for Cr and Mn clusters on the surfaces of elemental ferromagnets. The origin of frustration is the competition of the antiferromagnetic exchange coupling between the Cr or Mn atoms with the antiferromagnetic (for Cr) or ferromagnetic (for Mn) exchange coupling between the impurities and the substrate. We discuss also similar non-collinear configurations for Cr-trimers and tetramers on the *fcc* Fe/Cu(001) surface.

During the last years, extensive theoretical and experimental work has been carried out in the area of complex non-collinear magnetism, particularly for bulk systems, but recently also for surfaces and nanostructures. In fact a lot of interesting physics would be missed if only collinear magnetic structures were considered. Magnetic nanostructures on magnetic or nonmagnetic substrates are attractive to the scientific community due to their novel and unusual properties[1] being of relevance both for theory as well as for the device applications. One of these properties is the non-collinear magnetic order occurring for geometrically frustrated magnetic systems, e.g. on a triangular lattice, in disordered systems, exchange bias systems, and molecular magnets, or for other systems which exhibit either competing exchange interactions, or an interplay between exchange interaction and strong spin-orbit coupling.

The aim of this work is to investigate small 3d clusters of adatoms on the ferromagnetic Ni(001) and Fe_{3ML}/Cu(001) surfaces or as impurities (inatoms) within the first layer of these surfaces. We use the full-potential KKR Green function method[2] which we recently have extended to treat non-collinear magnetic states[3].

The basic difference between non-collinear and collinear magnetism is the absence of a natural spin quantization axis common to the whole crystal. The density matrix is not anymore diagonal in spin space as in the case of collinear magnetism. Instead, in any fixed frame of reference it has the form

$$\rho(\vec{r}) = \begin{bmatrix} \rho_{\uparrow\uparrow}(\vec{r}) & \rho_{\uparrow\downarrow}(\vec{r}) \\ \rho_{\downarrow\uparrow}(\vec{r}) & \rho_{\downarrow\downarrow}(\vec{r}) \end{bmatrix} = \frac{1}{2}\left[n(\vec{r}) + \vec{\sigma}\cdot\vec{m}(\vec{r})\right] \qquad (1)$$

Here, $\vec{\sigma} = (\sigma_x, \sigma_y, \sigma_z)$ are the Pauli matrices, $n(\vec{r})$ is the charge density and $\vec{m}(\vec{r})$ is the spin density vector, the direction of which is spatially varying.

3d single adatoms and inatoms

Natural candidates for magnetic adatoms are elements of the 3d series. As the calculations show, the early 3d atoms Sc, Ti, V and Cr couple antiferromagnetically (AF) to the Ni substrate moments, while Mn, Fe, Co and Ni atoms couple ferromagnetically (FM). Clearly the AF-FM transition occurs when the adatom atomic number changes from Cr (Z = 24) to Mn (Z = 25). As regards the adatom moments, due to its half filled d band, on Ni(001) the Mn adatom carries the highest magnetic moment (4.09 μ_B) followed by Cr (3.48 μ_B) and Fe (3.24μ_B). In case of inatoms, the general trend is similar to the adatom behavior, and the local impurity moments are only slightly reduced.

Adatom and inatom dimers on Ni(001)

We focus our discussion here on Cr and Mn first neighbor dimers. For the dimers with other 3d impurities the local moments are parallel aligned and couple either ferromagnetically (Fe, Co, Ni) or antiferromagnetically (V, Ti) to the substrate moments. Thus the behavior is dominated by the adatom–substrate interaction and no significant amount of frustration exists so that the magnetic configuration is collinear. However both the Cr- as well as the Mn-dimer adatoms couple strongly antiferromagnetically to each other, which is in competition with the interaction with the substrate atoms, favoring a parallel alignment of the dimer moments and being either of antiferromagnetic nature, for the Cr-dimer, or of ferromagnetic one for the Mn-dimer. Thus frustration occurs and non-collinear structures can be expected. The important configurations are shown in Fig. 1. Here Fig. 1(a) shows the magnetic ground state for the Cr- and Mn-dimer in a collinear calculation. The dimer moments couple antiferromagnetic to each other and are collinear to the substrate moments. In this configuration the two dimer moments are no longer equivalent, resulting in a ferrimagnetic state. The results of non-collinear calculations are shown in Fig. 1(b) for the Cr-dimer and in Fig. 1(c) for the Mn-dimer. In this configuration the Cr-(Mn) adatom moments are aligned antiparallel to each other and basically perpendicular to the substrate moments. However, the weak AF(FM) interaction with the substrate causes a slight tilting towards the substrate, leading to an angle of 94.2°(72.6°) instead of 90°. We also observe a

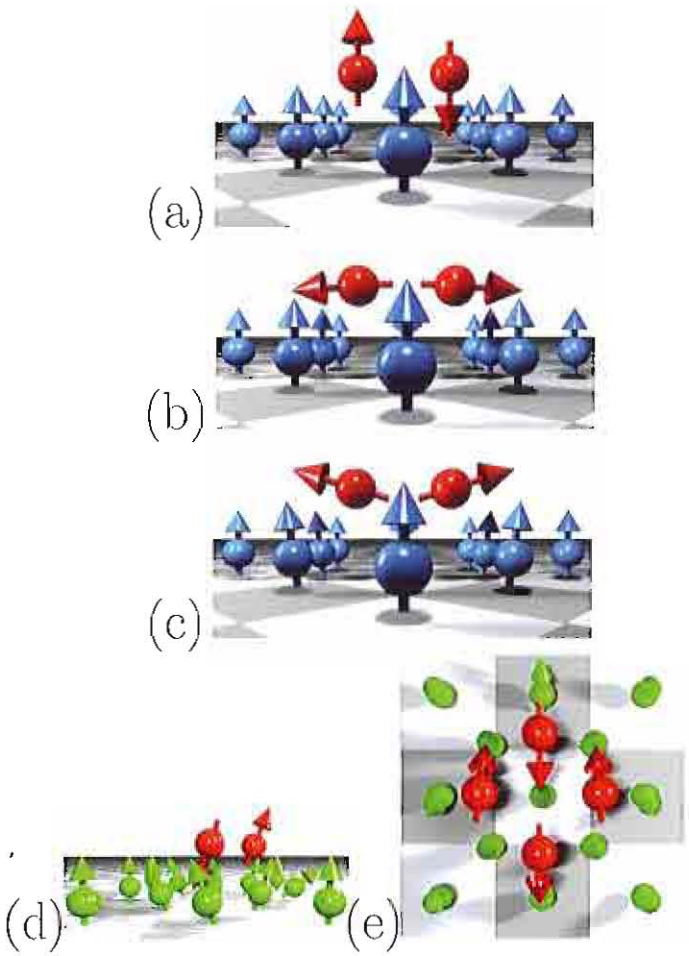

FIG. 1: Most stable configurations of Cr and Mn dimer on Ni (in blue) obtained with (a) the collinear KKR method and (b)-(c) the non-collinear KKR method. For Cr(Mn) the rotation angle with respect to the z axis is equal to 94.2°(72.6°) and the collinear(non-collinear) state is the ground state (see text). (d) shows a side view of the stable Cr trimer on the fcc Fe(001) surface (in green), with two Cr atoms pointing down (the second one cannot be seen), one Cr atom pointing up. (e) shows the stable Cr tetramer on the same fcc Fe surface.

small tilting 0.3° (7.4°) of the magnetic moments of the four outer Ni atoms neighboring the Cr-(Mn-) dimer (the two inner Ni atoms do not tilt for symmetry reasons). After performing total energy calculations we find that for Cr-dimer the ground state is collinear as in Fig. 1(a) whereas the Mn-dimer prefers the non-collinear configuration (Fig. 1(c)) as ground state (total energy difference $\Delta E_{Ncol-Ferri} = -13.45$ meV).

For an estimate of the total energy differences, it is interesting to compare these non-collinear ab initio results with calculations based on the Heisenberg model. We assume a classical spin Hamiltonian in terms of the tilting angles θ_1 and θ_2 of the two dimer atoms with respect to the substrate moments (the azimuthal angles ϕ do not enter the expression because of symmetry reasons):

$$H = -J_{Cr-Cr}\cos(\theta_1-\theta_2) - 4J_{Cr-Ni}(\cos\theta_1+\cos\theta_2). \quad (2)$$

We can evaluate the interatomic exchange constants J via a fit to the total energy obtained from collinear calculations of the FM, AF, and Ferri configurations. One directly finds, that the 90° orientation as in Fig. 1(b) is energetically degenerate with the collinear configuration in Fig. 1(a), since in both cases the interaction with the substrate vanishes. However only the configuration of Fig. 1(a) is an energy minimum or extremum. For the 90° configuration a small variation of the angles θ_1 and θ_2 from the 90° values leads to a linear change of the energy $\sim \Delta\theta$, such that exchange interaction energy with the substrate atoms can be gained by tilting either towards the substrate, as for the Cr-dimer, or away from the substrate, as for the Mn-dimer. The calculated tilting angles are in good agreement with the ab initio results.

In order to evaluate the effect of changes in coordination and hybridization, we have also studied first neighbor dimers in the first layer (inatom dimers). In both cases we found again a collinear solution as in Fig. 1(a) and non-collinear solutions as in Fig. 1(b) for Cr and in Fig. 1(c) for Mn, with similar tilting angles. However in both cases the collinear solution has a lower energy.

Cr Trimer and Tetramer on fcc Fe(001)

In response to recent measurements we have extended these calculations to Cr multimers on Fe_{3ML}/Cu(001), i.e. the Cu(001) surface covered with three ferromagnetic monolayers of f cc Fe. Here in general the hybridization with the substrate is much stronger than for Ni, and the different non-collinear configurations can be well explained by the Heisenberg model. The ground state for the trimer is basically collinear, since for three Cr atoms there is always an uncompensated interaction with the substrate, which does not occur for the 90° configuration. Nevertheless by tilting of the wrongly aligned third Cr moment some more energy can be gained, so that also this configuration is non-collinear. Fig. 1(e) shows the ground state for the Cr-tetramer. As one might have guessed from the dimer results on Ni(001), all neighboring Cr moments are antiferromagnetically aligned in-plane, with the directions slightly tilted towards the substrate to gain some exchange interaction energy.

[1] J. T. Lau, A. Fölisch, R. Nietubyć, M. Reif, and W. Wurth, Phys. Rev. Lett. **89**, 57201, (2002).
[2] N. Papanikolaou, R. Zeller, and P. H. Dederichs, J. Phys.: Condens. Matter. **14**, 2799 (2002).
[3] S. Lounis, Ph. Mavropoulos, P. H. Dederichs, S. Blügel, preprint: cond-mat/0509760.

Dynamical Correlations in the homogeneous electron gas: double plasmon excitations in simple metals

H. Lustfeld and K. Sturm
IFF, Institute Theory I

Dynamical correlations in the homogeneous electron gas are investigated by evaluating exactly the leading correction to the RPA proper polarizability that defines the frequency ω and wavevector $\mathbf{k}$ dependent dielecric function $\epsilon(\mathbf{k},\omega)$. *Outside* the particle-hole (ph) spectrum predicted peaklike structures in the high frequency tail of the dynamic structure factor due to double plasmon excitations were recently observed in inelastic x ray scattering spectroscopy (IXSS) on *Al* and *Na*. The evaluation of $\epsilon(\mathbf{k},\omega)$ *inside* the ph spectrum is in progress. This will enable us to analyze further experimental observations inside the ph spectrum of simple metals and assess the quality of the approximation by checking sum rules and the ground state theorem.

Dynamical correlations in the homogeneous electron gas are central to time dependent density functional theory, a very active area of research. The aim of the present investigation is to obtain exact results for dynamical correlation effects with the $\mathbf{k}$ and ω dependent dielectric function $\epsilon(\mathbf{k},\omega)$ of the jellium model in the high density limit. We write $\epsilon(\mathbf{k},\omega)$ in terms of the proper polarizability $\pi_p(\mathbf{k},\omega)$, i.e.

$$\epsilon(\mathbf{k},\omega) = 1 + v(\mathbf{k})\pi_p(\mathbf{k},\omega) \qquad (1)$$

In many body perturbation theory $\pi_p(\mathbf{k},\omega)$ is defined as the sum of irreducible diagrams. The leading correction to the RPA bubble are depicted in Fig.1 It was

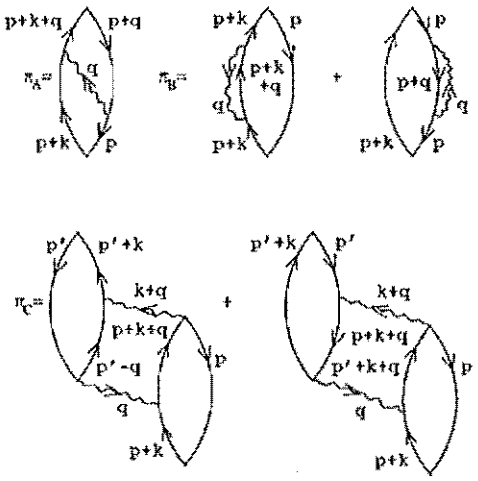

FIG. 1: *The π_A, π_B and π_C diagrams are lowest order corrections to the RPA bubble. The wavy lines signify the dynamically screened Coulomb interaction. p, p', q and $\mathbf{k}$ are 4 dimensional vectors including frequency.*

demonstrated long ago [1] that a consistent set of diagrams generated in selfconsistent approximation (SCA) must include the π_C diagrams. It will then give the correct r_s dependence of the compressibility sum rule. Thus we have

$$\begin{aligned}\epsilon(\mathbf{k},\omega) &= 1 + v(\mathbf{k})[\pi_0(\mathbf{k},\omega + \\ &\quad + \pi_A(\mathbf{k},\omega) + \pi_B(\mathbf{k},\omega) + \pi_c(\mathbf{k},\omega) + \cdots] \qquad (2)\end{aligned}$$

$\pi_0(\mathbf{k},\omega)$ defines the well knonw Lindhard dielectric function $\epsilon_L(\mathbf{k},\omega) = 1 + v(\mathbf{k})\pi_0(\mathbf{k},\omega)$. Although these formal results were obtained long ago [2] the corresponding expressions of π_A, π_B and π_C involve seven-dimensional integrals whose numerical evaluations is a formidable task that prevented computation for arbitrary $\mathbf{k}$ and ω until recently [3]. There it was realized that the seven-dimensional integrals could be reduced to three-dimensional integrals by analytical means. Nevertheless the numerical evaluation of the diagrams is very complicated and as a first step the imaginary part $Im\,\epsilon(\mathbf{k},\omega)$ for $(\mathbf{k},\omega)$ *outside* the ph spectrum was computed, cf Fig.2. Since $Im\,\pi_0(\mathbf{k},\omega)$ vanishes in that regime we have

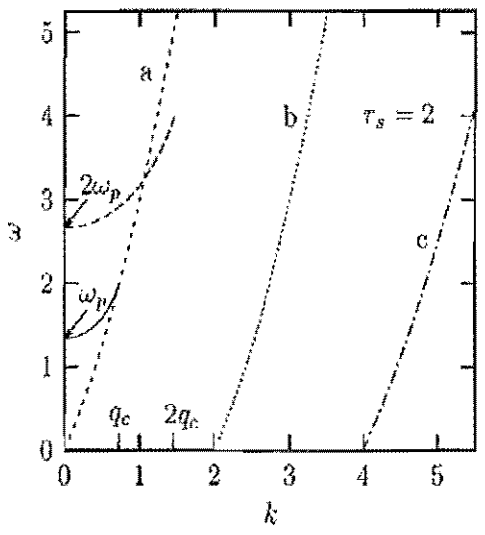

FIG. 2: *Excitation spectrum of the homogeneous electron gas. a: upper bound of the ph spectrum $\omega = \mathbf{k}^2 + 2\mathbf{k}$; b: lower bound of the ph spectrum $\omega = \mathbf{k}^2 - 2\mathbf{k}$; c: lower bound of the ph-ph spectrum $\omega = \mathbf{k}^2/2 - 2\mathbf{k}$. ω_{pl} denotes the onset of the RPA plasmon dispersion $\omega_{pl}(\mathbf{k})$ with the cutoff wavenumber q_c. The line $2\omega_{pl}(\mathbf{k}/2)$ marks the onset of pl-pl excitations [4].*

$$\begin{aligned}Im\,\epsilon(\mathbf{k},\omega) &= v(\mathbf{k})Im\,[\pi_A(\mathbf{k},\omega) + \pi_B(\mathbf{k},\omega) + \pi_C(\mathbf{k},\omega)] \\ &\equiv Im\,(\epsilon_{ABC}(\mathbf{k},\omega) \qquad (3)\end{aligned}$$

Dynamical correlations that constitute $Im\,\epsilon_{ABC}(\mathrm{k},\omega)$ outside the ph spectrum were found to consist of ph-ph excitations, ph-plasmon (ph-pl) excitations and pl-pl excitations. Comparisons with existing experimental data on simple metals were very satisfying. Contributions to the plasmon half width [5]

$$\Delta E_{1/2}(\mathrm{k}) = 2\left(Im\,\epsilon_{ABC}(\mathrm{k},\omega)\times\left|\frac{\partial\epsilon_L(\mathrm{k},\omega)}{\partial\omega}\right|^{-1}\right)_{\omega=\omega_{pl}(\mathrm{k})}, \quad (4)$$

the high frequency tail of the dynamical structure factor

$$S(\mathrm{k},\omega) = \frac{\hbar k^2}{4\pi^2 e^2 n_0} Im\left[\frac{-1}{\epsilon(\mathrm{k},\omega)}\right], \quad (5)$$

and optical absortion of alkali metals [6]

$$\sigma(\omega) = \frac{4}{3}\frac{|V^s_{\mathrm{G}_{110}}|^2|\mathrm{G}_{110}|^4}{\omega^3} Im\,\epsilon_{ABC}(\mathrm{G}_{110},\omega) \quad (6)$$

were considered. These successes stimulated further experimental investigations on simple metals. In particular, the predicted peaklike structures in the high frequency tail of $S(\mathrm{k},\omega)$ resulting form pl-pl excitations were recently observed experimentally by IXSS [7] on *Al* and *Na*, cf. Fig.3 and Fig.4. The rather successful comparison with various experimental obseravations is the impetus behind our effort to complete the evaluation of $\epsilon(\mathrm{k},\omega)$ by computing $Im\,\epsilon(\mathbf{k},\omega)$ inside the ph spectrum as well as $Re\,\epsilon(\mathbf{k},\omega)$. This is the most difficult part of the computation because of the singular nature of the integrands in this (k,ω) regime. Work is in progress. When this is achieved not only structures *inside* the ph spectrum observed in experiments can be analysed and compared with the calculated result but also the quality of the considered approximation could be assessed by checking Kramers-Kronig relations and sum rules such as

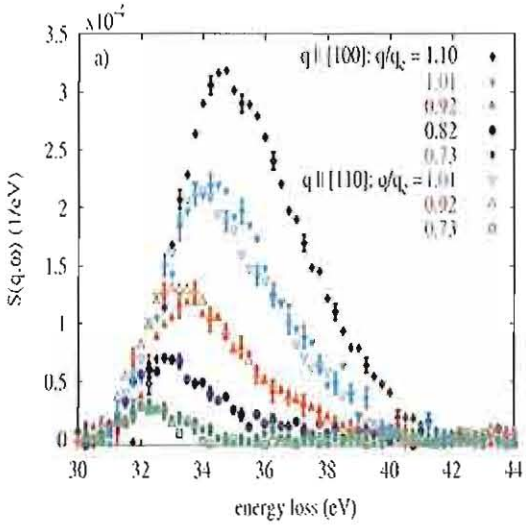

FIG. 3: *Al pl-pl correlation peak extracted from the experimental* $S(\mathrm{q},\omega)$ *spectra.*

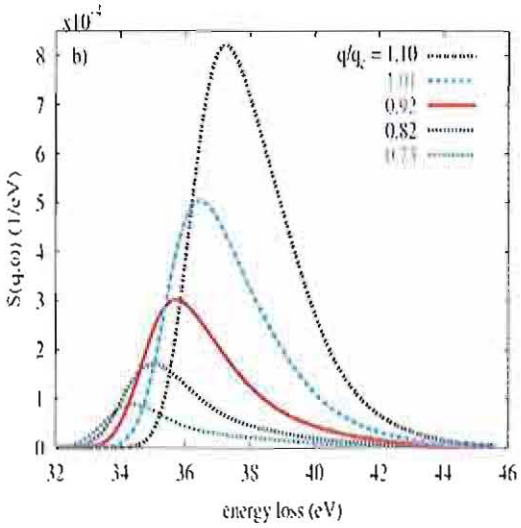

FIG. 4: *Calculated Al pl-pl correlation peak for* $r_s = 2.07$ *on an absolute scale, broadened by the experimental resolution.*

the f-sum rule, the conductivity sum rule, the third frequency moment sum rule and the ground state theorem that relates the excitation spectrum to the ground state energy [8]. This will also shed light on the importance of diagrams not considered in the present approximation, such as e.g. second order exchange diagrams which might be responsible for the discrepancy in the intensity of pl-pl excitations between theory and experiment, cf. Fig.3 and Fig.4.

---

[1] D.J.W. Geldart and S.H. Vosko, Can. J. Phys. **44**, 2137 (1966).

[2] V.I. Perel' and G. Éliashberg, Zh. Eksp. Teor. Fiz. **41**, 886 (1961), Sov. Phys. JETP **14** 633 (1962)

[3] K. Sturm and A. Gusarov, Phys.Rev. **B 62**, 6474 (2000)

[4] Frequencies are measured in units of the free electron Fermi energy and the wavevectors in units of the Fermi wave number.

[5] The plasma frequency $\omega_{pl}(\mathrm{k})$ is the solution of $\epsilon_L(\mathrm{k},\omega) = 0$.

[6] $V^s_{\mathrm{G}_{110}}$ is the screened psudopotential, $\mathbf{G}_{110}$ is a BCC reciprocal lattice vector.

[7] C. Sternemann, S. Huotari, G. Vanko, M. Volmer, G. Monaco, A. Gusarov, H. Lustfeld, K. Sturm, and W. Schülke, Phys.Rev.Lett. **95**, 157401 (2005)

[8] D.Pines, *Elemantary Excitations in Solids*, W.A. Benjamin, Inc. N.Y., Amsterdam (1963)

Dephasing by Kondo impurities: Exact results

T. Micklitz[1], A. Altland[1], T. A. Costi[2], and A. Rosch[1]
[1] *Institute for Theoretical Physics, University of Cologne, 50937 Cologne, Germany*
[2] *Institut für Festkörperforschung, Forschungszentrum Jülich, 52425 Jülich, Germany.*
(*Dated: December 8, 2005*)

We calculate the dephasing rate due to magnetic impurities in a weakly disordered metal as measured in a weak localization experiment. If the density n_S of magnetic impurities is sufficiently low, the dephasing rate $1/\tau_\varphi$ is a universal function, $1/\tau_\varphi = (n_S/\nu) f(T/T_K)$, where T_K is the Kondo temperature and ν the density of states. We show that inelastic vertex corrections with a typical energy transfer ΔE are suppressed by powers of $1/(\tau_\varphi \Delta E) \propto n_S$. Therefore the dephasing rate can be calculated from the *inelastic cross section* proportional to $\pi\nu \mathrm{Im}T - |\pi\nu T|^2$, where T is the T-matrix which is evaluated numerically exactly using the numerical renormalization group.

Dephasing, i.e. the loss of wave coherence, is a ubiquitous phenomenon in the quantum mechanics of complex systems. It is of relevance to any experiment where both interference and interactions play a role and is, therefore, of profound importance in all areas of nanoscopic and mesoscopic physics.

In weakly disordered metals, the interference of electronic wave functions on time-reversed paths leads to a characteristic reduction (or enhancement in the presence of spin-orbit interactions) of the conductivity[1]. The magnitude of this effect is controlled by the dephasing time τ_φ the typical time-scale over which electrons get entangled with their environment (phonons, other electrons or dynamical impurities) thereby loosing the ability to interfere. Even small magnetic fields break time-reversal invariance thus prohibiting the interference of time-reversed paths. Fitting the magnetoresistivity to weak localization (WL) theory is a means to determine the dephasing rate $1/\tau_\varphi$ with high precision.

Experiments [2] show a puzzling saturation of the dephasing rate at the lowest experimentally accessible temperatures T, while theoretically it is expected that in the limit $T \to 0$ all inelastic process freeze out when the system approaches its (time-reversal invariant and unique) ground-state. This has lead to an intense discussion [2 4, 6] as to whether quantum fluctuations can induce dephasing at T = 0. We believe that the presence of a few parts-per-million (ppm) of dynamical impurities — realized by atomic two-level systems [7] or by magnetic impurities [8–11] — may be an alternative cause of the saturation phenomenon.

We consider the Hamiltonian $H = H_0 + H_S$, where

$$H_0 = \int \mathrm{d}^d x\, c_\sigma^\dagger(x)\Big[\frac{\hat{p}^2}{2m} - \mu + V(x)\Big] c_\sigma(x) \qquad (1)$$

describes electrons in a weak non-magnetic disorder potential V, modeled for convenience by Gaussian white noise: $\langle V(x)V(x')\rangle_V = \frac{1}{2\pi\nu\tau}\delta(x-x')$ where ν is the density of states (DOS), $\tau = l/v_F$ the elastic scattering time and l the elastic mean free path. The coupling of the electrons to a small concentration n_S of spin-1/2 impurities

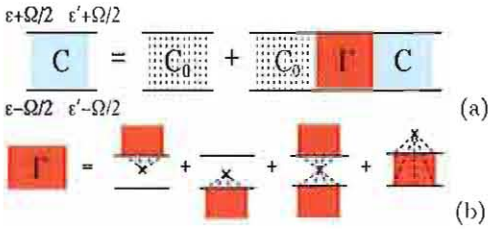

FIG. 1: Bethe-Salpeter equation for the Cooperon C in the presence of (dilute) magnetic impurities to linear order in n_S. C_0 is the bare Cooperon in the absence of interactions and Γ the irreducible vertex obtained by adding self-energy, elastic- and inelastic vertex contributions. The crosses with attached dashed lines denote the averaging over impurity positions x_i, the squares the interactions to arbitrary order in J.

is described by the Kondo Hamiltonian

$$H_S = J \sum_i \hat{S}_i c_\sigma^\dagger(x_i)\sigma_{\sigma\sigma'} c_{\sigma'}(x_i). \qquad (2)$$

To calculate physical quantities, we have to average over $V(x)$ and the positions x_i of the spins, taking into account the exchange coupling J to all orders.

We wish to explore the impact of dynamic impurity scattering on the WL corrections to the electric conductivity. This amounts to computing the impurity generated 'self energy' or 'mass' of the Cooperon describing the coherent propagation of an electron and a time-reversed hole in the disordered environment. As justified in detail in [5], mixed interaction/disorder diagrams can be neglected and the problem reduces to the solution of the Bether-Salpeter equation depicted diagrammatically in Fig. 1(a). To linear order in n_S, the two-particle irreducible vertex Γ shown in Fig. 1(b) can be separated into three distinct contributions: self-energy diagrams (the first two terms in Fig. 1(b)), an 'elastic' vertex correction with no energy transfer between upper and lower line, and an 'inelastic' vertex where interaction lines connect the two lines.

Since self-energy and elastic vertex contributions conserve the energy of single electron lines, the solution of the reduced Bethe-Salpeter amounts to a straightforward

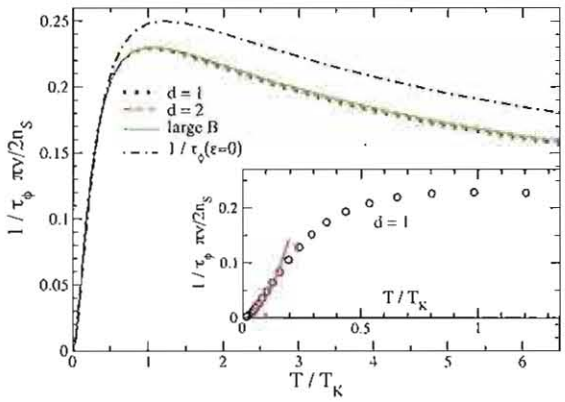

FIG. 2: Universal dephasing rate calculated via NRG. Accidentially, there is almost no dependence on the dimension d. Nevertheless, the ϵ-dependence of $1/\tau_\varphi(\epsilon, T)$ is important as can be seen from the comparison to the $1/\tau_\varphi(\epsilon = 0, T)$ curve (dot-dashed line). The low-T behavior of $1/\tau_\varphi$ (for $d = 1$) is shown in the inset together with the analytic result for $T \ll T_K$ (solid line).

summation of a geometric series. Setting the center-of-mass frequency Ω (see Fig. 1) to 0, the Cooperon obtains as $C^{\mathrm{q}}_{\Omega=0}(\epsilon, \epsilon') = \frac{1}{2\pi\nu\tau^2}\delta(\epsilon - \epsilon')/[D\mathrm{q}^2 + 1/\tau_\varphi(\epsilon, \mathrm{T})]$ and the WL correction to the conductivity is given by

$$\frac{\Delta\sigma_{\mathrm{WL}}}{\sigma_{\mathrm{Drude}}} = 2\tau^2 \int \mathrm{d}\epsilon\, f'(\epsilon) \int \mathrm{d}^{\mathrm{d}}\mathrm{q}\, \frac{1}{D\mathrm{q}^2 + 1/\tau_\varphi(\epsilon)}, \qquad (3)$$

with the T and ϵ dependent dephasing rate

$$\frac{1}{\tau_\varphi(\epsilon, \mathrm{T})} = \frac{2\mathrm{n_S}}{\pi\nu}\left[\pi\nu\,\mathrm{Im}[\mathrm{T}^{\mathrm{R}}(\epsilon)] - |\pi\nu\,\mathrm{T}^{\mathrm{R}}(\epsilon)|^2\right]. \qquad (4)$$

The many-body T-matrix [defined by the Green function $G_{\mathbf{x}\mathbf{x}'}(\epsilon) = G^0_{\mathbf{x}\mathbf{x}'}(\epsilon) + G^0_{\mathbf{x}0}(\epsilon)\mathrm{T}(\epsilon)G^0_{0\mathbf{x}'}(\epsilon)$] describes the scattering of electrons from a single magnetic impurity. Together with the numerical evaluation of $1/\tau_\varphi$ and the analytic estimate of the leading corrections [5], Eq. (4) is the main result of this work.

Fitting to $\Delta\sigma = 2\tau^2\sigma_{\mathrm{Drude}}\int \mathrm{d}^{\mathrm{d}}\mathrm{q}(D\mathrm{q}^2 + \tau_\varphi^{-1}(\mathrm{T}))^{-1}$, we next relate our results to the T–dependent dephasing rates, $\tau_\varphi^{-1}(\mathrm{T})$ extracted from experiments. Comparison with the energy–resolved representation (3) gives

$$\frac{1}{\tau_\varphi(\mathrm{T})} = \begin{cases} \left[-\int \mathrm{d}\epsilon\, f'(\epsilon)\tau_\varphi(\epsilon, \mathrm{T})^{-\frac{2}{2-d}}\right]^{\frac{2-d}{2}} & , \mathrm{d} = 1, 3 \\ \exp\left[-\int \mathrm{d}\epsilon\, f'(\epsilon)\ln\tau_\varphi(\epsilon, \mathrm{T})\right] & , \mathrm{d} = 2 \\ -\int \mathrm{d}\epsilon\, f'(\epsilon)/\tau_\varphi(\epsilon, \mathrm{T}) & , \omega_B\tau_\varphi \gg 1, \end{cases}$$

where the last line applies to the case where a strong magnetic field is present and the Cooperon can be expanded in $1/(\omega_B\tau_\varphi)$. (ω_B is the "cyclotron" frequency of the Cooperon.)

The T-matrix in Eq. 4 can be evaluated for arbitrary values of $\mathrm{T/T_K}$ and $\epsilon/\mathrm{T_K}$ using the numerical renormalization group for dynamical quantities [16] (with modifications suggested in [17]). The result is shown in Fig. 2 where we define and determine the Kondo temperature $\mathrm{T_K} = \mathrm{T_K^{(0)}}$ from the $\mathrm{T} = 0$ susceptibility $\chi = (g\mu_B)^2/(4\mathrm{T_K^{(0)}})$. For $\mathrm{T} \gg \mathrm{T_K}$, we confirm (up to numerical prefactors [9, 13]) $1/\tau_\varphi \approx 3\pi\mathrm{n_S}/(8\nu\ln^2[\mathrm{T/T_K}])$ giving rise to a very weak T dependence for $\mathrm{T} \gtrsim \mathrm{T_K}$. For $\mathrm{T} \lesssim 0.3\,\mathrm{T_K}$ one observes a crossover regime where $1/\tau_\varphi$ varies almost linear in T while at lowest T one obtains the expected T^2 behavior.

In conclusion, we have shown that the dephasing rate due to diluted magnetic impurities can be calculated directly from the inelastic cross section (4) introduced in [14]. This result is valid for all types of diluted dynamical impurities as long as typical energy transfers remain larger than $1/\tau_\varphi$. A measurement of τ_φ for spin-1/2 impurities along with an independent experimental determination of $\mathrm{T_K}$ and $\mathrm{n_S}$ would put our theory to a parameter–free test.

[1] B. L. Altshuler and A. G. Aronov, in *Electron-Electron Interaction in Disordered Systems*, edited by A. L. Efros and M. Pollak (North-Holland, Amsterdam, 1985)

[2] P. Mohanty, E. M. Q. Jariwala and R. A. Webb, Phys. Rev. Lett. **78**, 33663369 (1997); P. Mohanty and R. A. Webb, Phys. Rev. B **55**, R13452 (1997).

[3] D. S. Golubev and A. D. Zaikin, Phys. Rev. Lett. **81**, 1074 (1998).

[4] I. L. Aleiner, B. L. Altshuler and M. E. Gershenson, Waves in Random Media **9**, 201 (1999).

[5] T. Micklitz, A. Altland, T. A. Costi and A. Rosch, cond-mat/0509583, submitted to PRL.

[6] J. v. Delft, J. Phys. Soc. Jpn., Suppl. A, **72**,24 (2003).

[7] A. Zawadowski, J. v. Delft and D.C. Ralph, Phys. Rev. Lett. **83**, 2632 (1999).

[8] P. Mohanty, R. Webb, Phys. Rev. Lett. **84**, 4481 (2000).

[9] C. Van Haesendonck, J. Vranken and Y. Bruynseraede Phys. Rev. Lett. **58**, 19681971 (1987).

[10] F. Schopfer *et al.*, Phys. Rev. Lett. **90**, 056801 (2003).

[11] F. Pierre *et al.*, Phys. Rev. B **68**, 085413 (2003).

[12] B. L. Altshuler, A. G. Aronov and D. E. Khmelnitsky, J. Phys. C: Solid State Phys., **15**, 7367-7386 (1982).

[13] M. G. Vavilov and L. I. Glazman, Phys. Rev. B **67**, 115310 (2003); M. G. Vavilov, L. I. Glazman, A. I. Larkin, Phys. Rev. B **68**, 075119 (2003).

[14] G. Zaránd, L. Borda, J. v. Delft and N. Andrei, Phys. Rev. Lett. **93**, 107204 (2004).

[15] More precisely, $\Delta E \approx T$ in the Fermi liquid regime $T \ll T_K$ while for $T \gg T_K$, $\Delta E \approx T/\ln^2[T/T_K]$ is given by the life-time of the spin. Comparing this with $1/\tau_\varphi \sim n_S/\nu$ at $T \sim T_K$, we obtain the criterion stated in the text.

[16] T. A. Costi, A. C. Hewson and V. Zlatic, J. Phys.: Condens. Matter **6**, 2519 (1994).

[17] W. Hofstetter, Phys. Rev. Lett. **85**, 1508 (2000).

Effect of Dynamical Coulomb Correlations on the Fermi Surface of $Na_{0.3}CoO_2$

H. Ishida[1], M.D. Johannes[2], and A. Liebsch[3]
[1] *College of Humanities and Sciences, Nihon University, Sakura-josui, Tokyo 156, Japan*
[2] *Code 6391, Naval Research Laboratory, Washington, D.C. 20375, USA*
[3] *Theorie I, Institut für Festkörperforschung, Forschungszentrum Jülich, 52425 Jülich, Germany*

The t_{2g} quasi-particle spectra of $Na_{0.3}CoO_2$ are calculated within the dynamical mean field theory. It is shown that as a result of dynamical Coulomb correlations charge is transfered from the nearly filled $e_{g'}$ subbands to the a_{1g} band. This charge flow is intimately coupled to the spectral weight transfer from the coherent peaks near the Fermi level to the Hubbard bands and cannot be understood within the static LDA+U method which favors a charge transfer from a_{1g} to $e_{g'}$ states.

The intercalated layer compound Na_xCoO_2 has been intensely studied during the recent years since as a function of Na doping it exhibits a variety of fascinating properties. The relevant valence bands near the Fermi level consist of Co t_{2g} states with occupancy d^{5+x}. For $x \approx 0.50 - 0.75$ an unusually large thermopower is observed; for $x \approx 0.3$ hydration gives rise to a superconducting transition at 4.5 K. In a narrow region near $x = 0.5$ the material undergoes a metal insulator transition; the end-member at $x = 0$ with a single hole per Co atom might be a Mott insulator. In the limit $x = 1$, since the filled t_{2g} bands are separated by about 1.5 eV from the empty e_g bands, one finds a band insulator.

In the metallic phase the hexagonal Fermi surface consists of a large electron sheet centered at Γ and six small hole pockets near K (see Fig. 1). Because of the layered structure the t_{2g} levels split into a a_{1g} level and doubly degenerate $e_{g'}$ levels. The large Fermi surface stems mainly from the a_{1g} bands while the small hole pockets have predominantly $e_{g'}$ character. The existence of these hole pockets is thought to be crucial for the superconducting phase. On the other hand, recent angle resolved photoemission data for $x \approx 0.7$ provide evidence only for a_{1g} bands crossing the Fermi level. To address the question of possible modifications of the Fermi surface via Coulomb correlations not included in the local density approximation (LDA), several theoretical studies were carried out within the LDA+U approach. Typically, a gradual filling of the $e_{g'}$ subbands with increasing U is found. In the metallic phase, however, it is well known that correlations have an important dynamical component not captured within the LDA+U.

The aim of this work [1] is to elucidate the possibility of modifying the Fermi surface of $Na_{0.3}CoO_2$ via dynamical Coulomb correlations. More specifically we focus on the charge transfer between the paramagnetic t_{2g} subbands. Since only the total electron number is conserved when correlations are taken into account, the occupations of individual subbands may vary with the strength of the local intra- and inter-orbital Coulomb energies. In a single band picture, the typical effect of dynamical fluctuations is the spectral weight transfer from the quasi-particle peak near E_F to the incoherent satellites associated with the lower and upper Hubbard bands. In a multi-band material, this spectral weight transfer will in general be orbital dependent, opening the intriguing possibility of redistributing electronic charge among the valence orbitals and thereby modifying the shape of the Fermi surface.

To investigate these kinds of multi-band correlation effects we use the dynamical mean field theory (DMFT) combined with the Quantum Monte Carlo (QMC) method. The remarkable result of this work is that in the metallic domain of Na_xCoO_2 near $x = 0.3$

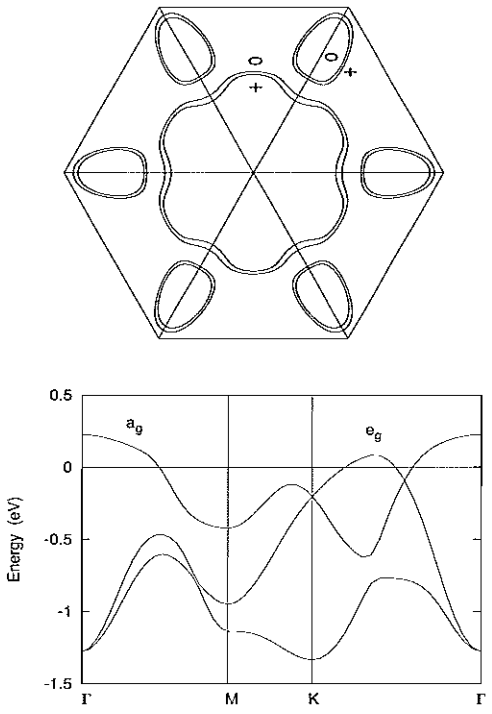

FIG. 1: Upper panel: Fermi surface of $Na_{0.3}CoO_2$. LDA: o symbols; DMFT: + symbols (schematic). Lower panel: tight-binding fit to LDA band structure of $Na_{0.3}CoO_2$; $E_F = 0$. The $e_{g'}$ states near K just above E_F give rise to the small hole pockets of the Fermi surface.

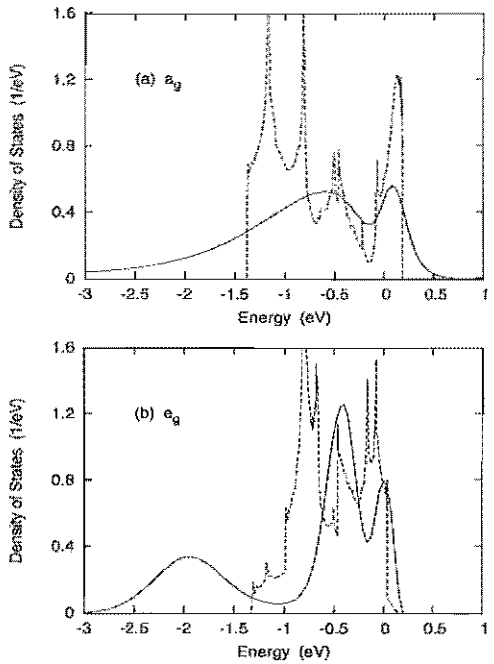

FIG. 2: Quasi-particle spectra for metallic $Na_{0.3}CoO_2$ calculated within the DMFT (solid curves) for $U = 2$ eV, $J = U/4$; T = 770 K, $E_F = 0$. Dashed curves: LDA local density of states. (a) a_{1g} states; (b) $e_{g'}$ states.

dynamical correlations shift charge from the $e_{g'}$ states to the a_{1g} bands, thereby stabilizing the $e_{g'}$ hole pockets and slightly reducing the a_{1g} Fermi surface. The key reason for the charge transfer from $e_{g'}$ to a_{1g} states is the fact that both quasi-particle distributions exhibit important incoherent regions. Since with increasing Coulomb interaction both a_{1g} and $e_{g'}$ spectra consist of incoherent contributions of approximately equal intensity, their occupations must approach one another.

Fig. 2 shows the a_{1g} and $e_{g'}$ quasi-particle spectra for $Na_{0.3}CoO_2$ as calculated within the DMFT. The spectra show the characteristic band narrowing near E_F and the transfer of weight from the coherent to the incoherent spectral region. In the case of the slightly narrower $e_{g'}$ band dynamical correlations are large enough to give rise to a lower Hubbard band. Also noticeable is the substantial lifetime broadening of valence states caused by excitation of electron hole pairs. The subband occupations are: $z_a = 0.842$, $z_e = 0.902$, which should be compared to the LDA values $n_a = 0.797$, $n_e = 0.927$.

This trend is in striking contrast to the one found in the LDA+U which favors integer occupations and leads to a reduction or elimination of the $e_{g'}$ pockets. For a paramagnetic t_{2g} complex with one-fold a_{1g} and two-fold $e_{g'}$ subbands, the orbital dependent potential is given by the non-diagonal element of the Hartree Fock self-energy in the t_{2g} basis [2]: $\Sigma^{HF}_{i\neq j} = \delta(U - 5J)$, with $\delta = (n_e - n_a)/3$. Thus, $\Sigma^{HF}_{i\neq j} > 0$ for $U > 5J$ if $n_e > n_a$, leading to a separation of a_{1g} and $e_{g'}$ band energies. Dynamical correlations associated with the narrowing of the quasi-particle peak near and the transfer of spectral weight to the incoherent region, which are the prominent characteristics of the DMFT, are absent from the LDA+U.

The correlation induced band narrowing is consistent with infrared optical data which show transitions within the t_{2g} manifold at lower energies than predicted by the LDA. Also, the dynamical correlations for $x = 0.3$ might play a role in the metallic range at larger Na concentrations. For $x \approx 0.7$, however, additional effects such as bi-layer splitting of t_{2g} bands and transition to a half-metallic magnetic phase must be taken into account. Furthermore, for the interpretation of photoemission spectra surface induced single-particle and correlation features need to be considered [3]. It is not clear, therefore, whether the results obtained here for $x = 0.3$ are in conflict or not with photoemission data for $x \approx 0.7$.

In summary, we have explored the modification of the Fermi surface of $Na_{0.3}CoO_2$ as a result of dynamical Coulomb correlations not included in the LDA nor LDA+U. The main effect of these fluctuations is the spectral weight transfer from the quasi-particle peak near E_F to the incoherent part of the spectrum associated with the Hubbard bands. In a multi-band material, these dynamical processes are orbital dependent. In particular, they can give rise to charge transfer between subbands induced via hybridization and interband Coulomb interactions. The highlight of the LDA band structure of $Na_{0.3}CoO_2$ is the distinctly different filling of the t_{2g} bands, with the nearly full $e_{g'}$ subbands yielding characteristic hole pockets of the Fermi surface. Accounting for correlations within the dynamical mean field theory we have shown that electronic charge is shifted from the $e_{g'}$ subbands to the a_{1g} band, thus slightly enlarging the hole pockets and reducing the main electron sheet of the Fermi surface. It would be very interesting to perform photoemission and quantum oscillation experiments to verify the existence of the $e_{g'}$ pockets at 0.3 Na concentration. It would also be desirable to extend the present dynamical calculations to the more complex metallic phase near $x \approx 0.7$ in order to analyze the existing photoemission data.

[1] H. Ishida, M. D. Johannes, and A. Liebsch, submitted to Phys. Rev. Lett.
[2] A. Liebsch and A. I. Lichtenstein, Phys. Rev. Lett. **84**, 1591 (2000).
[3] A. Liebsch, Phys. Rev. Lett. **90**, 96401 (2003); Eur. Phys. J. **32**, 477 (2003).

Orbital-Selective Mott Transitions in the Nonisotropic Two-Band Hubbard Model

A. Liebsch
Institut für Festkörperforschung, Forschungszentrum Jülich, 52425 Jülich, Germany

The Mott transition in a two-band Hubbard model involving subbands of different widths is studied as a function of temperature using dynamical mean field theory combined with exact diagonalization. The phase diagram is shown to exhibit two successive first-order transitions if the full Hund's rule coupling is included. In the absence of spin-flip and pair-exchange terms the lower transition remains first-order while the upper becomes continuous.

The nature of the metal insulator transition in materials involving subbands of different widths has been intensively debated during the recent years. This issue is relevant for the understanding of the effect of strong local Coulomb interactions in systems such as $Ca_{2-x}Sr_xRuO_4$. The pure Sr compound is superconducting below 1.5 K. Iso-electronic replacement of Sr by Ca leads to an effective band narrowing due to octahedral distortions and a metal insulator transition. In this layer perovskite the partially filled Ru t_{2g} bands for $x = 2$ consist of wide d_{xy} and narrow $d_{xz,yz}$ bands. Since the onsite Coulomb energy lies between the subband widths: $W_{xz,yz} < U < W_{xy}$, the usual criterion with the parameter U/W as a measure of the importance of correlations must be generalized [1, 2]. As a consequence of non-cubic crystal fields many other transition metal oxides also involve non-equivalent partially occupied subbands.

A key question in these materials is whether the wide and narrow subbands exhibit separate Mott transitions or whether single-particle hybridization and inter-orbital Coulomb interactions ensure a single transition for all bands simultaneously. In the present work [3] we combine finite temperature dynamical mean field theory (DMFT) with exact diagonalization (ED) to determine the phase diagram of a two-band Hubbard model consisting of non-hybridizing, half-filled subbands with semi-circular density of states of width $W_1 = 2$ eV and $W_2 = 4$ eV. The subbands interact via intra- and interorbital Coulomb matrix elements U and $U' = U - 2J$, where J is the Hund's rule exchange integral. In contrast to the multi-band Quantum Monte Carlo (QMC) approach, which includes only Ising-like exchange terms to avoid sign problems at low temperatures, ED permits also the consideration of spin-flip and pair-exchange interactions. To be specific we take $J = U/4$ which is approximately satisfied in several transition metal oxides.

The main result of this work is that the T/U phase diagram in the presence of the full Hund's rule exchange exhibits *two successive first-order phase transitions*, with separate hysteresis loops and coexistence regions. The intermediate region corresponds to the $T > 0$ analog of the orbital-selective Mott (OSM) phase obtained at $T = 0$ in [4]. If spin-flip and pair-exchange terms are omitted, we find a *single first-order transition succeeded by a non-Fermi-liquid phase*, in agreement with previous QMC results [5, 6].

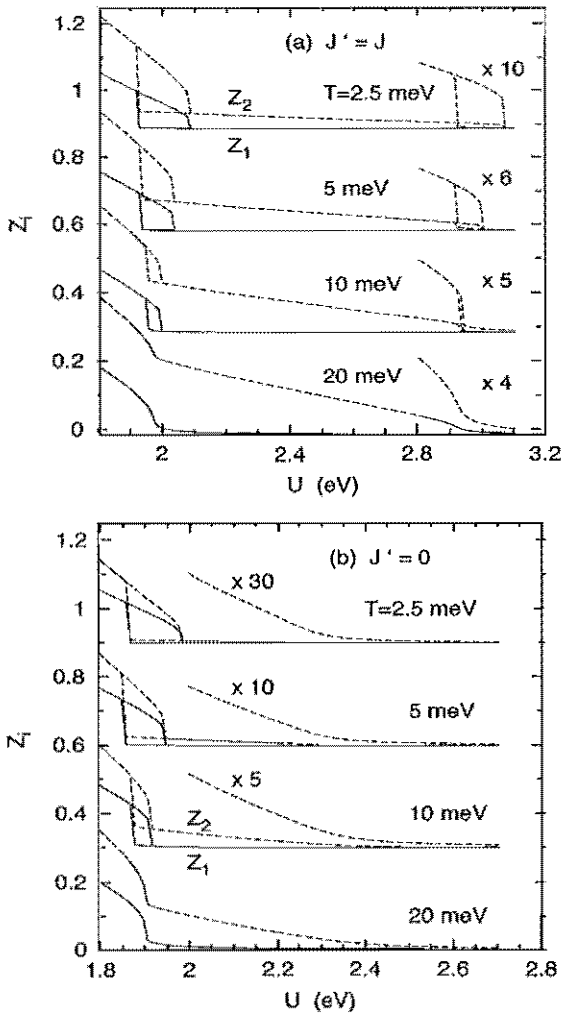

FIG. 1: $Z_i(U)$ of nonisotropic two-band Hubbard model, calculated within ED/DMFT. (a) $J' = J = U/4$, (b) $J' = 0$, $J = U/4$. Solid (dashed) curves: narrow (wide) band. Results for different T are displaced vertically by 0.3.

Fig. 1(a) shows quasiparticle weights $Z_i(U)$ for $J' = J = U/4$, where J' denotes spin-flip and pair-exchange terms. Two critical regions can be identified, each with hysteresis loops characteristic of first-order phase transitions. At the lower transition both bands undergo first-order transitions – but in fundamentally different ways:

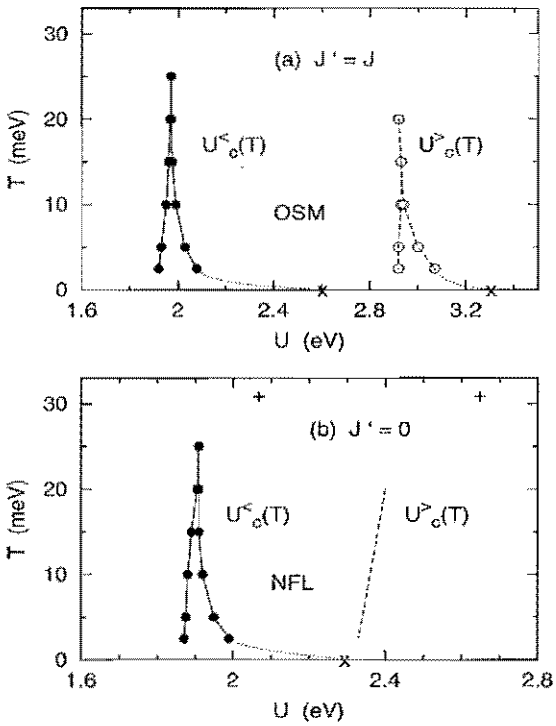

FIG. 2: Phase diagram for nonisotropic two-band Hubbard model, calculated within ED/DMFT. (a) $J' = J = U/4$, (b) $J' = 0$, $J = U/4$. Solid dots in (a), (b): stability boundaries of both subbands near lower first-order transition. Open dots in (a): stability boundaries of wide band near upper first-order transition. Dashed line in (b): approximate location of continuous transition of wide band. Symbols (x): T = 0 transitions obtained in [4, 7]; (+): results for T = 31 meV [5]. Lines are guides to the eye.

$Z_1(U)$ becomes very small while $Z_2(U)$ drops to a finite value. The narrow band therefore undergoes a 'complete' metal/insulator transition, whereas the wide band exhibits an 'incomplete' transition to a new, considerably more correlated phase. This band becomes fully insulating near 3.0 eV, where it exhibits a weak second hysteresis loop.

Fig. 1(b) shows $Z_i(U)$ for $J' = 0$, $J = U/4$, i.e., in the absence of spin-flip and pair-exchange terms. The results are similar to those in Fig. 1(a), with the important exception that the wide band above the lower transition is even more correlated and the upper transition is now continuous at smaller U. The lower transition remains first-order for both subbands. The results in Fig. 1(b) confirm the picture obtained previously within the QMC for $T > 0$, $J' = 0$ [5], showing a single first-order transition near $U = 2.1$ eV, at which the narrow band becomes insulating, followed by a mixed insulating/bad-metallic phase until the wide band becomes insulating at $U = 2.7$ eV.

The phase diagrams deduced from the ED results for $T \geq 2.5$ meV are shown in Fig. 2. For $J' = J$ as well as $J' = 0$ the transition at $U_c^<(T)$ is first-order for both subbands. The subsequent transition of the wide band at $U_c^>(T)$ is first-order for $J' = J$ but continuous for $J' = 0$. At $U_c^<(T)$ the metal/insulator transition is complete only for the narrow band. The wide band first undergoes a transition to a more strongly correlated phase and becomes truly insulating at the second transition at $U_c^>(T)$. The overall shape of the phase diagram for $J' = J$ agrees with the one recently obtained by Inaba et al. [8].

Quasiparticle spectra derived within the QMC/DMFT for $J' = 0$ [5] showed that in the intermediate phase the self-energy of the wide band at small ω_n deviates significantly from metallic $\sim \omega_n$ behavior. Accordingly, the quasi-particle spectra show a pseudogap which for larger U gets more pronounced, indicating progressive bad-metal, non-Fermi-liquid properties. A true gap opens at $U_c^>(T)$. As indicated in Fig. 2(b), in the absence of spin-flip and pair-exchange the intermediate phase is a mixed insulating/NFL phase and not an OSM phase with coexisting insulating and Fermi-liquid-metallic subbands. The same trend is found using the $T > 0$ ED/DMFT. Thus, the OSM phase in Fig. 2(a) is the $T > 0$ analog of the orbital-selective Mott phase identified first by Koga el al. [4] at T = 0.

For the analysis of experimental data of materials such as $Ca_{2-x}Sr_xRuO_4$ it is necessary to account also for hybridization between orbitals. Moreover, spatial fluctuations and deviations from half-filling might play a decisive role close to the Mott transition. More work is needed to investigate whether both first-order transitions persist in the presence of these effects, or whether the weak first-order behavior of the upper transition disappears and only the dominant lower transition survives as the common first-order Mott transition for all bands.

[1] A. Liebsch and A. I. Lichtenstein, Phys. Rev. Lett. 84, 1591 (2000).
[2] A. Liebsch, Europhys. Lett. 63, 97 (2003).
[3] A. Liebsch, Phys. Rev. Lett. 95, 116402 (2005).
[4] A. Koga, N. Kawakami, T. M. Rice, and M. Sigrist, Phys. Rev. Lett. 92, 216402 (2004).
[5] A. Liebsch, Phys. Rev. B 70, 165103 (2004).
[6] A. Liebsch, Phys. Rev. Lett. 91, 226401 (2003).
[7] A. Koga, N. Kawakami, T. M. Rice, and M. Sigrist, cond-mat/0406457.
[8] K. Inaba et al., cond-mat/0506151.

Static versus dynamical mean field theory of Mott antiferromagnets

Giorgio Sangiovanni,[1] Alessandro Toschi,[1] Erik Koch,[2] Karsten Held,[1] Massimo Capone,[3] Claudio Castellani,[3] and Olle Gunnarsson[1]

[1] *Max-Planck Institut für Festkörperforschung, Heisenbergstr. 1, D-70569 Stuttgart, Germany*
[2] *Institut für Festkörperforschung, Forschungszentrum Jülich, D-52425 Jülich, Germany*
[3] *Dipartimento di Fisica Università di Roma "La Sapienza", piazzale Aldo Moro 5, I-00185 Roma, Italy*

(Dated: December 18, 2005)

Studying the antiferromagnetic phase of the Hubbard model by dynamical mean-field theory reveals striking differences to the static (Hartree-Fock) mean-field: The Slater band is strongly renormalized and spectral weight is transferred to spin-polaron side bands. Already for intermediate values of the interaction U the overall bandwidth is larger than in Hartree-Fock, and the gap is considerably smaller. Such differences survive any renormalization of the interaction strength.

In order to understand strongly correlated materials, one needs to go beyond the conventional local density approximation (LDA) [1]. Methods have been developed like LDA+U [2], where the LDA is supplemented by a local Coulomb interaction U treated in the static Hartree-Fock (HF) mean field theory, and its sibling LDA+DMFT [3], which employs the more sophisticated dynamical mean-field theory (DMFT) [4]. While it is generally accepted that LDA+DMFT deals more accurately with strongly correlated metals, the computationally simpler LDA+U is considered to be sufficient for insulators with a large U – at least in the presence of magnetic or orbital ordering. Indeed, LDA+U is widely employed for the calculation of various physical properties of such strongly correlated insulators. To assess in how far this approach is appropriate, we analyze the differences between the static and dynamical mean-field treatment of insulators with long-range order at intermediate to strong Coulomb interaction U. Studying the antiferromagnetic (AF) phase of the one-band Hubbard model, we demonstrate that at large U dynamic properties and the structure of excited states are strikingly different in the Slater (HF) and the DMFT antiferromagnet. More specifically the Slater bands are strongly renormalized, most of the spectral weight is transferred to spin-polaron side bands, and the overall bandwidth is proportional to the non-interacting width, instead of shrinking like $1/U$ in HF.

We focus on large values of U. This is made possible by exploiting technical advances in the methodology and by the unique capabilities of the JUMP computer. Thereby we improve the accuracy of the DMFT calculation to the point that we can make definite statements not only about the size of the AF gap but also regarding the inner structure of the (Hubbard or Slater) bands below (and above) the gap. In the large U limit, we can even make contact with the t-J model which has been studied in DMFT by Strack and Vollhardt. We recover the spin-polaron peaks of [5] which are however dispersive in our calculation – an effect occurring in order t^2/U^2 and hence absent in Ref. [5].

We solve the DMFT equations for the one-band Hubbard model with on-site coulomb repulsion U and a semi-circular density of states $N(\omega) = (2/\pi D^2)\ \sqrt{D^2-\omega^2}$ with half-bandwidth D, using the Lanczos algorithm at $T = 0$ for the associated Anderson impurity model (AIM). A continued fraction expansion of the DMFT Weiss fields [7] allows us to obtain reliable spectra in the intermediate-to-large U region. Moreover, in the AF phase we can push the number of AIM sites N_s to much larger values than commonly possible.

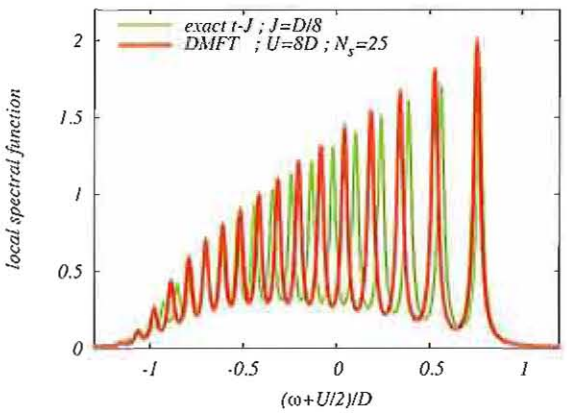

FIG. 1: Spectral function of the lower Hubbard band. Red: DMFT solution of the Hubbard model for $U = 8D$ and $N_s = 25$; green: exact solution of the t-J model for $J = D^2/U$. Both spectra have been plotted using the same broadening.

Fig. 1 shows the comparison between the spin-averaged local spectral function for the Hubbard model, calculated with DMFT for $U = 8D$ and $N_s = 25$ (red curve), and the exact spectral function of the infinite-dimensional ($d = \infty$) t-J model with $J = D^2/U$ [5]. In both cases, we show only the negative frequency part of the spectrum, i.e., the lower Hubbard band centered around $\omega = -U/2$ (the x axis is shifted correspondingly). The shape and the position of the lowest energy peaks in the DMFT spectrum are almost independent on N_s, reflecting the fact that, contrary to the case of the paramagnetic insulating phase, in the AF phase the peaks do not originate from the discreteness of the impurity model but have a true physical meaning [5, 6]: If we start with a half-filled antiferromagnet and take an electron out (lower Hub-

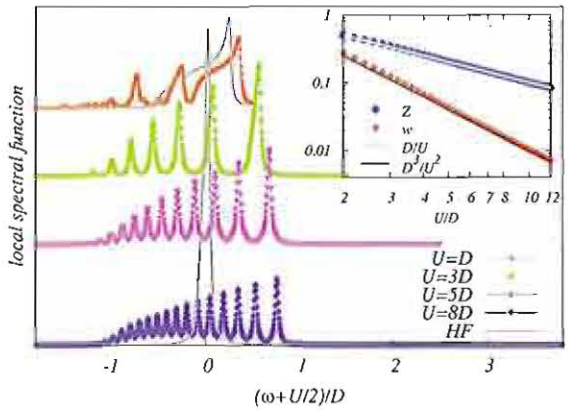

FIG. 2: Evolution of the lower Hubbard band with U/D. The solid gray lines represent the HF spectrum for $U = D$ and $U = 8D$. In the inset the spectral weight and the quasiparticle dispersion are shown as a function of U/D.

bard band), the hole can propagate through the crystal without creating double occupancies and hence without the cost of U. When moving, the hole breaks however AF bonds, with an energetic cost proportional to nJ where n is the length of the path through the lattice. As a consequence, discrete peaks appear at distance J which can be interpreted as spin-polaron side bands [8] for dispersionless spinwaves [9]. In the $U \to \infty$ ($J \to 0$) limit, these spin-polaron peaks become dense and the lower Hubbard band recovers the shape and the width of the non-interacting density of states, with the important difference that the states are now incoherent. The difference between the position of the DMFT and t-J peaks in Fig. 1, which is of order D^2/U^2 (i.e., neglected in the t-J model).

It is now interesting to see whether and to what extend the t-J-like features survive with decreasing U. In Fig. 2, we show four different cases ranging from $U = 8D$ to $U = D$. The spin-polaron structure turns out to be surprisingly robust: It is present all the way down to $U = 3D$, where the spectrum still is qualitatively similar to the spectrum at large U. Only for $U \sim D$, the spectrum resembles the Hartree-Fock one (full grey line).

A deeper insight can be gained by analyzing the leading peak of the Hubbard band (the right-most peak in Figs. 1 and 2): We find that it continuously evolves from the weak-coupling Slater (HF) peak. However, its spectral weight Z is dramatically reduced when increasing U since more and more spectral weight is transferred to the spin-polaron side bands. As shown in the inset of Fig. 2, Z scales as D/U for $U \gtrsim 2D$. Althought a similar scaling can be found measuring the weight of the first peak in the t-J spectrum, there is a profound difference in the nature of the peak: In the Hubbard model it has a finite dispersion, while in the t-J in $d = \infty$ it is completely dispersionless [5]. We find that the effective bandwidth w of this quasiparticle excitation scales as D^3/U^2, for large U, as shown in the inset of Fig. 2. This behavior can be understood as an effect of the second-order hopping terms $\mathcal{O}(1/U^2)$ neglected in the mapping to the t-J Hamiltonian. Consequently, we have a quasiparticle renormalization of the Slater (HF) peak (see Fig. 2). The width of this peak shrinks like D^2/U and is further reduced by $Z \simeq D/U$ so that altogether $w \simeq Z D^2/U = D^3/U^2$.

Another striking difference between the Slater and the DMFT spectrum is the size of the spectral gap. In HF (see again Fig. 2), the Slater peak is located roughly at the center of the DMFT lower Hubbard band (whose width is of order W and which is structured by spin-polaron side bands). Hence, the magnitude of the spectral gap is reduced from the HF value, at large U from U to $U - W$. This shortcoming of HF questions the reliability of static mean-field calculations for describing spectra at intermediate or large U. On the other hand, the wide use of LDA+U for antiferromagnets or orbitally-ordered phases with a large gap seems to be supported by the fact that HF and DMFT yield the same results for static groundstate properties, such as magnetization, kinetic and potential energy. In practice, U is often used as an adjustable parameter, e.g., adjusting the LDA+U results to the experimental gap. As we have demonstrated, this is very dangerous since the static properties then become wrong.

[1] W. Kohn and L.J. Sham, Phys. Rev. **140**, A1133 (1965); R.O. Jones and O. Gunnarsson, Rev. Mod. Phys. **61**, 689 (1989).

[2] V.I. Anisimov, J. Zaanen, and O.K. Andersen, Phys. Rev. B **44**, 943 (1991); V.I. Anisimov, F. Aryasetiawan, and A.I. Lichtenstein, J. Phys. Cond. Matter **9**, 767 (1997).

[3] V.I. Anisimov *et al.*, J. Phys. Cond. Matter **9**, 7359 (1997); A.I. Lichtenstein and M.I. Katsnelson, Phys. Rev. B **57**, 6884 (1998).

[4] W. Metzner and D. Vollhardt, Phys. Rev. Lett. **62**, 324 (1989); A. Georges, G. Kotliar, W. Krauth, and M. Rozenberg, Rev. Mod. Phys. **68**, 13 (1996).

[5] R. Strack and D. Vollhardt, Phys. Rev. B **46**, 13852 (1992).

[6] W.F. Brinkman and T.M. Rice, Phys. Rev. B **2**, 1324 (1970); L.N. Bulaevskii *et al.*, Sov. Phys.-JETP **27**, 838 (1968).

[7] Q. Si *et al.*, Phys. Rev. Lett. **72**, 2761 (1994).

[8] K.J. von Szczepanski *et al.*, Phys. Rev. B 41, 2017 (1990); C. Martínez and P. Horsch, Phys. Rev. B **44**, 317 (1991).

[9] E. Cappelluti and S. Ciuchi, Phys. Rev. B **66**, 165102 (2002).

Magnetic Structure and Crystal-field of Pyrochlore $Ho_2Ru_2O_7$

L.J. Chang [1], W. Schweika[1], W. Schäfer[2], E. Jansen[2], M. Prager[3], and Th. Brückel[1]
[1] *Institute for Scattering Methods, IFF*
[2] *University of Bonn*
[3] *Institute for Neutron Scattering*

The magnetic structure of the pyrochlore compound $Ho_2Ru_2O_7$ was investigated by neutron scattering techniques. In $Ho_2Ru_2O_7$, Ho and Ru form two individual networks of corner-sharing tetrahedrons giving rise to frustration. Magnetic order of Ru^{4+} was observed below 95 K. By means of neutron diffraction, we had found the Ho^{3+} ions are ordered below 1.7 K and have spin-ice q = 0 magnetic structure. By the neutron time-of-flight experiments performed on DNS and SV-29, we had observed the transitions from excited states at 1.7 and 4.5 meV, and the transitions from ground states at 22 and 27 meV. We therefore conclude that the crystal-field in $Ho_2Ru_2O_7$ is nearly identical to that of spin-ice pyrochlore $Ho_2Ti_2O_7$.

Pyrochlore oxides of the chemical formula $A_2B_2O_7$, where A is a rare-earth ion and B is a transition-metal ion, have the face-centered-cubic structure with space group *Fd3m* and eight molecules of this general formula in a unit cell. $A_2B_2O_7$ has attracted much attention on account of the unusual structure of corner-sharing tetrahedrons which can produce geometrical frustration and interesting low-temperature magnetic properties, leading to extensive studies by both experimental and theoretical physicists. For example, $Ho_2Ti_2O_7$ had been identified as a spin ice configuration and has been modelled with an Ising-like anisotropy and a net ferromagnetic interaction[1]. $Tb_2Ti_2O_7$ is a fluctuating spin liquid state at low temperature as explained by an antiferromagnetic Heisenberg model[2].

In $RE_2Ru_2O_7$ (RE = rare earth and Y), Ru has a partially filled 4*d* shell and possesses a magnetic moment, while RE and Ru form two individual networks of corner-sharing tetrahedrons. It was reported that all the $RE_2Ru_2O_7$ show a specific heat jump in the temperature range 75-160 K which is correlated with the rare-earth ionic size[3,4]. Neutron diffraction studies[5] on $Y_2Ru_2O_7$ and $Nd_2Ru_2O_7$ show growing integrated intensity at peaks (111) and (220) with decreasing temperature. The magnetic order is attributed to the Ru^{4+} ions because the exchange interaction between the inner 4*f* electrons of rare earth ions is expected to be much weaker than the interaction of the 4*d* electrons of Ru^{4+}. The magnetic moments of Ru^{4+} are estimated to be 1.36 μ_B and 1.18 μ_B in $Y_2Ru_2O_7$ and $Nd_2Ru_2O_7$, respectively. Magnetic effects of $Y_2Ru_2O_7$ and $Nd_2Ru_2O_7$ were also observed in specific heat measurements[3]. It was explained as antiferromagnetic correlated Ru moments, but macroscopically exhibiting a spin-glass-like behavior due to geometrical frustration. In $Ho_2Ru_2O_7$, susceptibility data[4] show slight irreversibility in zero field cooled and field cooled data below 95 K, which is in very good agreement with the report of measurements of specific heat[3]. It is interesting to investigate the ordering mechanism of Ru^{4+} and the most likely orderings in RE^{3+} in the $RE_2Ru_2O_7$ family, and furthermore to study the possible interaction between Ru^{4+} and RE^{3+}.

$Ho_2Ru_2O_7$ polycrystalline samples were synthesized by solid-state reaction methods. High purity starting materials Ho_2O_3 and RuO_2 were mixed in stoichiometric proportions, heated at 850°C for 24 h, pressed into pellets, and then sintered at 1150°C for 48 h. Because of the high volatility of RuO_2, the sintering process was performed in a sealed quartz tube. The powder x-ray diffraction patterns reveal no impurity in the samples within sensitivity limits of a few percent, and show the samples to have cubic structure and a lattice parameter of 10.122 Å at room temperature.

Powder diffraction experiments were performed at SV-7 using both closed-cycle and orange cryostats for different temperature ranges from 1.7 K to room temperature. A neutron wavelength of 1.096 Å was selected for the diffraction experiments.

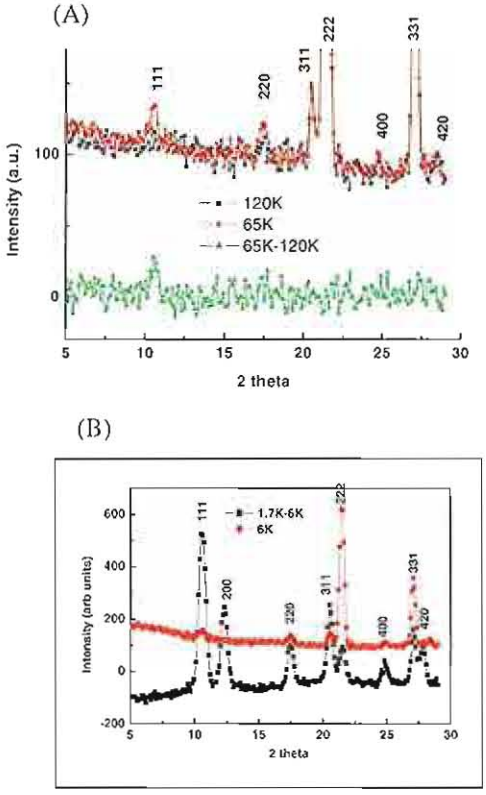

Fig. 1 (A) A weak magnetic peak occurs between 120 K and 65 K at 111 position. (B) Strong magnetic peaks observed below 1.7 K.

Fig. 1 (A) shows the magnetic ordering from Ru^{4+} which is consistent with the reported ordering temperature at 95 K. Fig. 1 (B) indicates an additional magnetic phase transition occurring at 1.7 K
magnetic peaks, we conclude that the magnetic ordering comes from Ho^{3+}. The magnetic peaks can be indexed in the q = 0 structure meaning the magnetic unit cell is identical to the chemical unit cell. The best results of ***Fullprof*** fit for the magnetic peaks at 1.7 K has an R-factor of 3.57, and m_x = 4.69 μ_B, m_y = 3.40 μ_B, m_z = 0.67 μ_B for the moments along x, y and z directions respectively, as shown in Fig. 2.

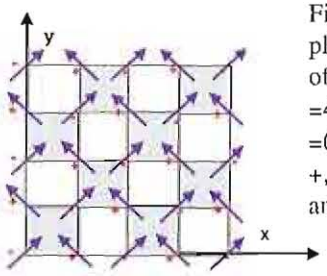

Fig. 2 the projection on x-y plan of the magnetic structure of Ho^{3+} on $Ho_2Ru_2O_7$, m_x =4.69 μ_B ,m_y =3.40 μ_B , m_z =0.67 μ_B , M=5.85 μ_B , R=3.57. +, - mean the directions on +z and –z axis respectively.

In order to understand the nature of the magnetic order and the ground-state spin dynamics, it is important in any heavy rare-earth system to determine the single ion crystal-field splittings. We therefore carried out inelastic neutron scattering measurements to investigate the low lying crystalline electric field energy levels of $Ho_2Ru_2O_7$. Neutron diffuse scattering experiments were performed at DNS by using closed-cycle apparatus for temperatures from 10 K to room temperature. Neutron wavelengths of 3.3 Å and 5.25 Å were selected for the time-of-flight experiments.

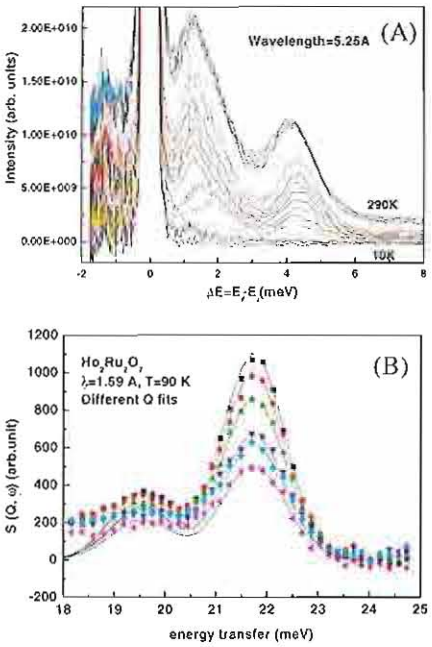

Fig. 3 Time-of-flight spectra taken at (A) DNS using wavelength 5.25 Å, temperature from 10 to 290 K (B) SV-29 using wavelength 1.58 Å, temperature 90 K for different Qs and their Gaussian fits

Fig. 3 (A) shows the inelastic time-of-flight spectra taken at DNS using the neutron wavelength 5.25 Å. The intrinsic transitions from the excited states are observed at 1.7 and 4.5 meV and the intensities of the peaks are growing with increasing temperature. This result is very similar to the published transitions between crystal-field levels in $Ho_2Ti_2O_7$[6]. In $Ho_2Ti_2O_7$, the first ground state transition is at an energy of about 20 meV, which is far above the energy range DNS can reach. Neutron time-of-flight experiments were carried out at SV-29 between temperature 2 to 120 K in an orange cryostat for the purpose of investigating the excitations at higher energy levels. Fig. 3 (B) shows the spectra for different Q values at 90 K for neutron wavelength 1.58 Å at SV-29. Two ground state excitations have been observed at 19.4 and 22 meV. Those peaks are following well the Ho^{+3} form factor intensity decay with Q. Another ground state excitation was found at 27 meV. We have good evidence to believe that the crystal field splittings of $Ho_2Ru_2O_7$ and $Ho_2Ti_2O_7$ are nearly identical.

Since the long range ordering occurs below 2.9 K, the spin ice delicate balance in the system has been broken so that the Ho^{3+} moments no longer lie exactly along the <111> direction as observed in $Ho_2Ti_2O_7$. The moment canting and long range order may come from the influence of Ru^{4+}. Further experiments are necessary to understand the interactions between Ho^{3+} and Ru^{4+}. Studies on $Ho_2Ru_xTi_{2-x}O_7$ may also be a good approach to investigate the broken balance of the spin ice state at low temperature. Another mystery in our studies is the crystal field splittings below the ordering temperature 2.9 K. The data from SV-29 show the crystal field splitting in $Ho_2Ru_2O_7$ without observable change from temperature 2 K up to 120 K even though long range order occurs at 2.9 K. In addition to the static magnetism studies, spin echo experiments had been proposed to observe the dynamical magnetism in $Ho_2Ru_2O_7$.

[1] S.T. Bramwell, and M.J. Harris, *J. Phys.: Condens. Matter* **10**, L215 (1998).

[2] M.J.P. Gingras, B.C. den Hertog, M. Faucher, J.S. Gardner, S.R. Dunsinger, L.J. Chang, B.D. Gaulin, N.P.Raju, and J.E. Greedan, *Phys. Rev. B* **62**, 6496 (2000).

[3] M. Ito, Y. Yasui, M. Kanada, H. Harashina, S. Yoshi, K. Murata, M. Sato, H. Okumura, and K. Kakurai, *J. Phys. Chem. Solids* **62**, 337 (2001)

[4] C. Bansal, H. Kawanaka, H. Bando, and Y. Nishihara, *Phys. Rev. B* **66**, 52406 (2002)

[5] M Ito, Y. Yasui, M. Kanada, H. Harashina, S. Yoshii, K. Murata, M. Sato, H. Okumura, and K. Kakurai, *J. Phys. Soc. Jpn.* **69**, 888 (2000)

[6] S. Rosenkranz, A.P. Ramirez, A. Hayashi, R.J. Cava, R. Siddharthan, and B.S. Shastry, *J. App. Phys.* **87**, 5914 (2000).

Magnetic structures in [Er|Tb] multilayers: a combined neutron and x-ray study

J. Voigt,[1] E. Kentzinger,[1] U. Rücker,[1] W. Schweika,[1] Th. Brückel,[1] W. Schmidt,[2] and D. Wermeille[3]

[1] *IFF, Institut für Streumethoden*
[2] *IFF, Institut für Neutronenstreuung*
[3] *Advanced Photon Source, Argonne National Lab, Argonne, USA*

The magnetic properties of $[Er_{n_{Er}}|Tb_{n_{Tb}}]$ superlattices have been studied for a series of different compositions (indices denote the number of atomic layers). Modulated magnetic order –as found in the bulk systems– is short range and restricted to the Er layers for all samples beside the $[Er_{20}|Tb_5]$ superlattice, the sample with the smallest Tb layer thickness. We observe antiferromagnetic coupling between single ferromagnetic Tb layers in all samples, with the onset of this ordering depending on the Tb layer thickness. We argue that the exchange coupling is limited to the interface near region due to competing anisotropies. Therefore long range modulated magnetic order is observed in the $[Er_{20}|Tb_5]$ superlattice only, where the interface regions overlap.

The magnetic coupling and its influence on the electronic properties in artificial superlattices attract the interest of scientists from a fundamental and a applied point of view. The different magneto-resistive effects are used for example in read-heads of hard disks or sensors for the anti-skid system in cars. But the basic physics behind the effects are still subject of investigations.
Magnetic superlattices containing RE metals were among the first systems, when the field of magnetic interlayer coupling came up in the middle of the eighties. Majkrzak et al. [1] and Salamon et al. [2] report on long range ordered magnetic phases throughout a multilayer stack, even if the magnetic layers are separated by non-magnetic spacer layers. The thickness of a bilayer D ranges from 10-100 atomic planes. This coupling was explained

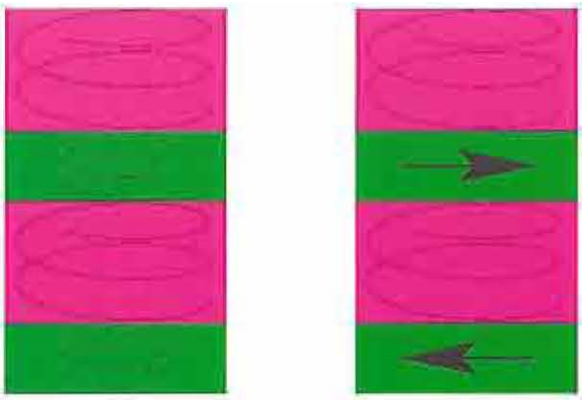

FIG. 1: Schematic view of two bilayers from a superlattice sample. The left sketch shows shows a modulated magnetic structured, e.g. a helix, in both layers. The right one indicates a ferromagnetic ordering in one layer and a helical order in the second layer.

in terms of an extension to the conventional RKKY interaction, which is responsible for the magnetic order in RE metals. The conduction electrons in the spacer layer are polarized by the magnetic moments of the magnetic layers and mediate the magnetic information to the next bilayer. Complications arise, if one combines two magnetic layers with different magnetic structures. How does the resulting magnetic structure look like? The structure is determined not only by the RKKY interaction, but anisotropy and magneto-elastic forces must be taken into account.
We have investigated the magnetic structure of the [Er|Tb] system. The two materials have fairly different magnetic properties. Tb orders at a temperature of $T_N = 230$ K in a helical structure, i.e. the magnetic moments in one basal plane of the hexagonal lattice are aligned parallel within the plane and turn by a given angle propagating along the c-direction. At $T_c = 220$ K the structure changes to a ferromagnetic alignment of all planes. In Er the anisotropy favors the alignment of magnetic moments perpendicular to the basal plane. At $T_N = 82$ K the c-axis component of the moment orders with a sinusoidal modulation when propagating along the c-direction. Below $T_{N1} = 54$ K a basal plane component develops, which is aligned in a helical way. A third phase transition at $T_C = 20$ K leads to a cone structure, i.e. the c-axis component orders ferromagnetically, while the basal plane component stays helical [3].

Neutron diffraction and resonant x-ray magnetic scattering (RXMS) were used to determine the magnetic structure for a series of superlattices with different compositions. The neutron diffraction yields an overview of the existing magnetic structures. The resonant magnetic scattering can probe the magnetic structure element specific, if the photon energy is tuned to absorption edge of the respective element. The different periodicities of the superlattice and modulated magnetic structures give rise to a large number of diffrac-

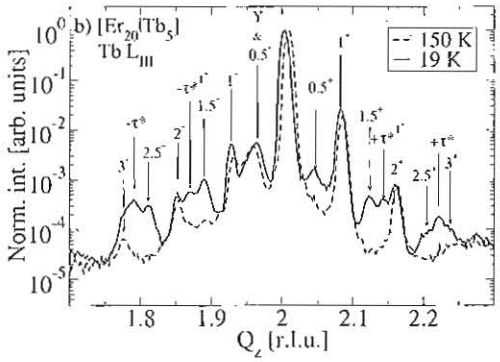

FIG. 2: RXMS as a function of Q_z measured in $\sigma \rightarrow \pi$ geometry at different temperatures, normalized to the maximum intensity: RXMS from the $[Er_{20}|Tb_5]$ sample close to the Tb L_{III} absorption edge ($E = 7.518$ keV).

tion peaks as can be seen from the RXMS of the $[Er_{20}|Tb_5]$ superlattice in Fig 2. The reflections labelled with $n^{\pm}$ correspond to the bilayer thickness (see Fig 1). From the intensities we deduce the structural properties like interface width, lattice constants in the different layers etc.. The reflections labeled with $(2n+1)/2^{\pm}$ correspond to twice the bilayer thickness. Their origin is purely magnetic. Therefore we conclude that the Tb layers order ferromagnetically with an antiferromagnetic coupling to the next Tb layer as indicated in the right part of Fig. 1. Finally we observe reflections labeled with τ^*. They correspond to the modulated magnetic structure, schematized by the screwline in Fig. 1. The additional reflections labeled with $\tau^{*n\pm}$ show, that the modulated magnetic structure is coherent across several bilayers. For the samples with thicker Tb layers, broad τ^* reflections exist. With RXMS, these broad reflections can be detected only at the Er absorption edge. We conclude that in these cases the magnetic modulation is limited to a single Er layer. We argue that the exchange interaction, which is responsible for the modulated magnetic order, is limited to the interface region. Here the elements form a kind of an anisotropic alloy. If two interface regions do not overlap, the different anisotropies prevent an exchange coupling to the next layer. For the ferromagnetic layers, the coupling can be mediated by dipolar interactions, which lead to an antiferromagnetic coupling. For details we refer to the our recent publications [4, 5].

Surprisingly, we find in the $[Er_{20}|Tb_5]$ superlattice a coexistence of the modulated magnetic order and the antiferromagnetically coupled ferromagnetic layers in both elements Er and Tb. To resolve this issue we studied recently the diffuse polarized neutron scattering under grazing incidence. As an example we present the scattering of neutrons that kept the initial polarization at 22 K, after the sample has been cooled in zero field. At this temperature we observed before the coexistence of modulated magnetic order and coupled ferromagnetic order. The broad intensity distribution yields the information about the correlation length of the magnetic order in the growth direction of the superlattice and in plane. As the next step we will deduce the domain structure from a modeling of the intensity of all spin channels.
In conclusion, neutron scattering and RXMS elucidated the origin of the different magnetic phases found in a series of [Er|Tb] superlattices. The neutrons uncovered the magnetic structure, while the RXMS allowed the investigations of the competing interactions in Er and Tb, respectively. The combination of both methods has proven to be extremely valuable for studies of magnetic nanostructures consisting of different magnetic species.

[1] C. F. Majkrzak, J. W. Cable, J. Kwo, M. Hong, D. B. McWhan, Y. Yafet, J. V. Waszczak, and C. Vettier, Phys. Rev. Lett. **56**, 2700 (1986).
[2] M. B. Salamon, S. Sinha, J. J. Rhyne, J. E. Cunningham, E. R. W., J. Borchers, and C. P. Flynn, Phys. Rev. Lett. **56**, 259 (1986).
[3] W. C. Koehler, *Magnetic Properties of Rare Earth Metals* (Plenum Press, New York, 1972), chap. 3.
[4] J. Voigt, E. Kentzinger, U. Rücker, W. Schweika, W. Schmidt, D. Hupfeld, D. Wermeille, and Th. Brückel, Europhys. Lett. **65**, 560 (2004).
[5] J. Voigt, E. Kentzinger, U. Rücker, W. Schweika, D. Wermeille, W. Schmidt, and Th. Brückel, submitted to Eur. Phys. J. B.

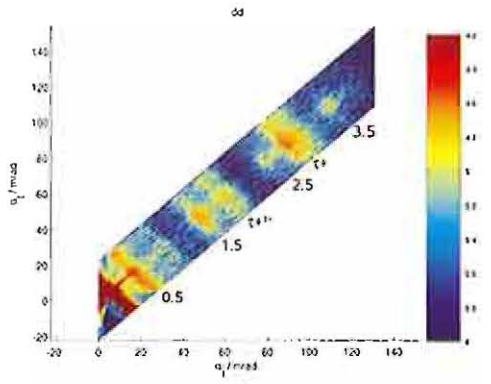

FIG. 3: Diffuse scattering of polarized neutrons at grazing incidence at 22 K as a false color plot. The color code refers to the logarithmic normalized intensity.

Magnetization Reversal In Exchange Biased Multilayers Depending Upon Applied Field Direction

A. Paul[1], E. Kentzinger[1], U. Rücker[1], D. E. Bürgler[2], Th. Brückel[1]
[1] *Institute for Scattering Methods* [2] *Institute for Electronic Properties*
(Dated: January 19, 2006)

Reversal mechanisms for exchange coupled ferromagnet/antiferromagnet (FM/AF) multilayer systems have been observed to depend upon the directions (θ) of the applied field with respect to the unidirectional anisotropy direction. All FM layers switches *sequentially* (layer by layer) either by nonuniform mode (via domain formation) or uniform mode (via coherent rotation) and also *simultaneously* which is by uniform mode only. The different remagnetization behavior is observed by specular and off-specular scattering of polarized neutrons. We explain these findings within a general and simple model by the angular dependencies for reversal guided by the relative strengths of exchange, Zeeman and anisotropy energies.

I. INTRODUCTION

When a bilayer system of ferromagnet (FM) layer in direct contact with an antiferromagnet (AF) layer is cooled below the Néel temperature a shift in the hysteresis loop is observed. This shift is by an exchange bias field which is crucial for designing thin film magnetic sensors as spin-valves. The magnetization reversal in such systems is complex and are subject to recent studies.

Asymmetric hysteresis loops due to different magnetization reversal processes in different branches of the hysteresis loop are common [1] in exchange coupled FM(ferromagnet)/AF(anti-ferromagnet) layers. Theoretically Beckmann *et. al* [2] showed that depending on θ, the angle between applied field H_a and the AF anisotropy axis or the field cooling axis H_{FC}, the reversal mode is either by coherent rotation (uniform reversal mode) for both loop branches or asymmetric with a nonuniform reversal for the increasing branch. Here nonuniform refer to the reversal of magnetization with no component perpendicular to the H_a direction which is essentially reversal by domain nucleation and growth.

Neutron scattering under grazing incidence with polarization analysis has proven to be an extremely powerful and unique technique for the investigation of this phenomenon (see Ref. [3] and references therein). For one dimensional analysis four different cross sections can be distinguished, namely non-spin flip (R_{++} and R_{--}) and spin flip (SF) channels (R_{+-} and R_{-+}). Here, the indices + and - to the intensity R represent the polarization parallel and antiparallel to the guiding field. Magnetization rotation is identified by a significant increase of the specular reflectivities in the SF channels, which correspond to in-plane magnetization components perpendicular to the guiding field H_a applied collinear to H_{FC}. Reversal by domain nucleation and propagation does not provide enhanced SF intensities, because the magnetization is always collinear to H_a (shows up in NSF channels only).

Recently we observed sequential reversal of the FM layers in $[IrMn/CoFe]_{10}$ [3] and also in $[Co/CoO]_{20}$ multilayers (MLs) [4] which was directly related to the evolution of the grain size along the stack. The nonuniform reversal of each CoFe layer was found to proceed symmetrically via domain wall motion for both remagnetization directions. This reversal mode – symmetric, but nonuniform – corresponds to the situation for $\theta = 0°$ for our polycrystalline ML specimens, unlike usually observed asymmetric reversals in epitaxial bilayer specimens [1].

II. EXPERIMENT AND DISCUSSION

In the present case we measure specular and off-specular Polarized Neutron Scattering from the $[IrMn/CoFe]_{10}$ specimen along each full magnetization loop: increasing (negative to positive) and decreasing (positive to negative) field sweeping direction of the H_a for the hysteresis loop with respect to the direction of H_{FC}. We show the measurements with θ =15° for increasing and decreasing fields with respect to H_{FC} direction in Fig. 1. The specular intensity along the line $\alpha_i = \alpha_f$ shows first order and weaker second order Bragg peaks at $\alpha_{i,f} \approx 25$ and 50 mrad respectively corresponding to the bilayer thickness.

The fitting of the specular reflectivities for the NSF and SF channels are done taking into account the non-ideal polarization efficiencies. Each layer rotates or flips independently and *sequentially* with field strength, fanning around in different directions in a certain field which shows the layer resolved magnetization direction with respect to the H_a direction. On the decreasing field branch: the bottom layers start flipping first followed by the top layers as we increase the field strength. On the increasing branch: the top layers rotate in different directions while the bottom layers flip back. The flipping and rotation of layers are seen by the presence/absence of SF signals of different intensities as we sweep the field strength on both branches of the loop.

For θ=90° and 45°, we observe a large specular SF signal all along the hysteresis loop, indicating uniform magnetization reversal by coherent rotation. The fits to the data are done considering all the layers to rotate *coherently* with the field. The variation is monotonic and gradually follows the H_a direction with increasing field strengths.

For a finite angle θ, the strength of the anisotropy field

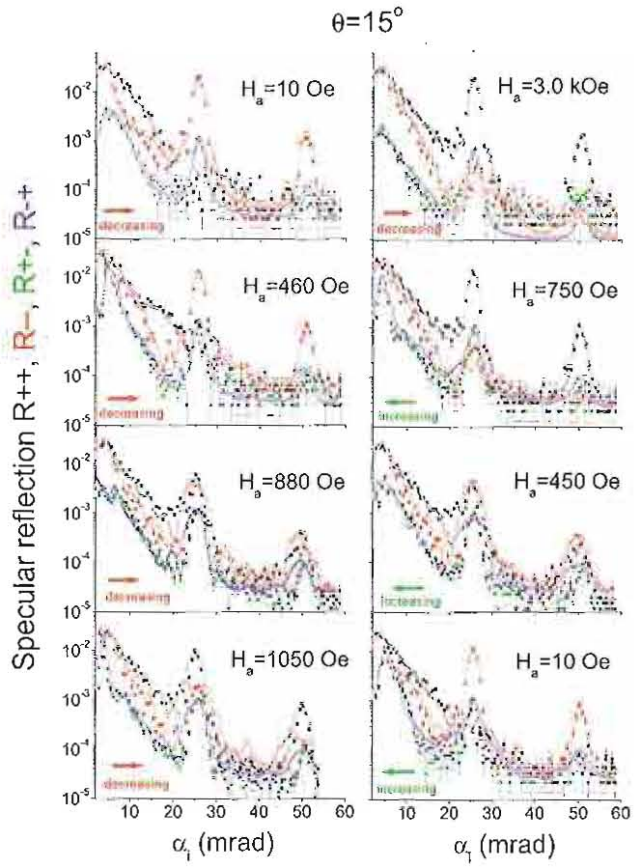

FIG. 1: NSF and SF specular reflectivity patterns (solid symbols) along with their fits (open circle) for $[Ir_{20}Mn_{80}(6.0\ nm)/Co_{80}Fe_{20}(3.0\ nm)]_{10}$ ML with θ=15° for increasing and decreasing branches of the field.

H_A (depends on the projection of the FM magnetization onto the easy axis) and that of the exchange field of the AF (H_X) decide on the angle (ϕ) between the effective field H_{eff} and the M_{FM} direction. In our system, for θ=15°, we see uniform/non-uniform reversal depending upon the relative strengths of H_X and H_A fields of each layer, which is increasing from bottom to top of the ML. The H_{eff} : acted upon each layer, make different angles $\phi_{1,2}$ with M_{FM}, which decides upon the strength of the torque for the reversal. Thus, we observe a layer-by-layer reversal mechanism in the stack. A sketch showing the angles for θ=15° when $H_X > H_A$ is presented in Fig. 2. The angle at equilibrium ϕ_1 for the increasing branch of the hysteresis loop (a) makes a large angle with M_{FM}. As the sign of FM magnetization (decreasing branch of the hysteresis loop) reverses so does the anisotropy field and the corresponding angle ϕ_2 (b) can be very close to 180° thus a small angle with M_{FM}. Larger angle means larger torque which favors rotation of the magnetization whereas a small angle favors flipping by domain wall motion.

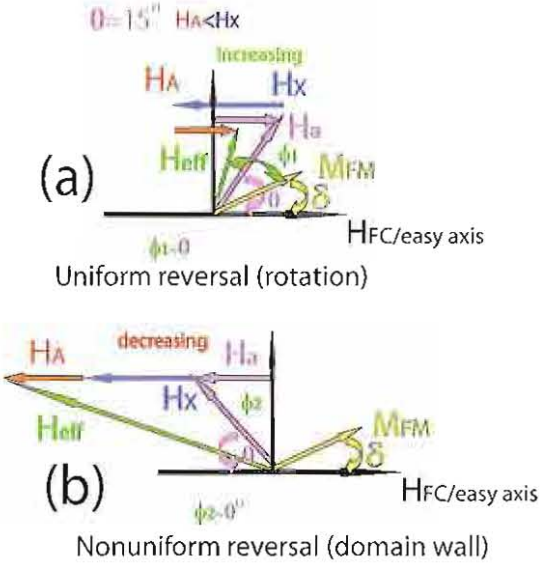

FIG. 2: Sketch showing the H_{eff} (green) when $\theta \approx 15°$ and H_X (blue) > H_A (red). The M_{FM} (yellow) and H_a (violet) are making an angle δ and θ respectively with the easy axis which is the H_{FC} direction. The effective angles ϕ_1 and ϕ_2 decide upon the torque for magnetization reversal via (a) rotation or (b) domain wall.

III. CONCLUSION

The above observations therefore are understood in general terms of the torque exerted on the system due to different effective field strengths and the corresponding angles with the magnetization axis. We systematically varied the relative strengths of the exchange and uniaxial anisotropies in a single multilayered system which is particularly possible due to *sequential* switching of layers with increasing N. All reversal modes are accompanied by small scale fluctuations of the perpendicular component of the in-plane magnetization on a length scale comparable to the grain size thus indicating the domain to domain fluctuations in the system. Our measurements show a gradual crossover from layer flipping (domain wall motion) for low torque regimes to coherent rotation for high torque regimes. Our experimental findings finally unravel the mysteries of magnetization reversal of exchange coupled systems and explain earlier observations of asymmetric and symmetric hysteresis loops.

[1] M. R. Fitzsimmons *et al.*, Phys. Rev. Lett. **84**, 3986 (2000).
[2] B. Beckmann *et al.*, Phys. Rev. Lett. **91**, 187201 (2003).
[3] A. Paul *et al.*, Phys. Rev. B **70**, 224410 (2004).
[4] A. Paul *et al.*, (submitted).

Unraveling complex ordering in $La_{1-x}Sr_xMnO_3$ (x~1/8) with synchrotron X-rays from below 1 keV to above 100 keV

Y. Su[1], H.F. Li[1], D. Wermeille[3], J. Perßon[1], P. Meuffels[2], S. Mattauch[1], A. Nefedov[4], J. Grabis[4], H. Zabel[4], D. Prabhakaran[5], A.T. Boothroyd[5], V. Kaiser[6] and Th. Brückel[1]

[1]*Institute for Scattering Methods, IFF* / [2]*Institute for Electronic Materials, IFF*
[3]*MuCAT, APS, ANL, U.S.A.* / [4]*Institut für Experimentalphysik/Festkörperphysik, Ruhr-Universität Bochum*
[5]*Department of Physics, University of Oxford, U.K.* / [6]*Institut für Kristallographie, RWTH-Aachen*

New insights on complex low-temperature charge and orbital ordering and associated structural modulations in $La_{1-x}Sr_xMnO_3$ (x~1/8) have been gained from our latest resonant scattering experiments carried out in the soft X-ray (~ 600 eV) and hard X-ray (~6-7 KeV) range, and quantitative high-energy X-ray (~ 100 KeV) diffraction measurements.

Lightly doped $La_{1-x}Sr_xMnO_3$ (x~1/8) compound exhibits a very intriguing ferromagnetic insulating (FMI) phase at low temperatures. The exact nature of this FMI behavior is still being strongly debated in spite of intensive investigations carried out during last couple of years [1-4]. Nevertheless, the consensus on the importance of charge and orbital degrees of freedom has been reached, the central argument is now focused on how charge and orbital ordering take place. The latest suggestion is that the localized holes and surrounding e_g orbitals in adjacent Mn cation sites are organized in the form of so-called orbital polarons, the ordering of such orbital polarons would lead to a FMI phase [2-3]. There exist several alternative charge/orbital ordering models [4-5]. Therefore, this compound also represents an outstanding example to tackle complex ordering phenomena in highly correlated transition-metal oxides (TMO).

To directly detect charge and orbital ordering in a scattering experiment is far from trivial due to their small perturbation to the average charge density of a lattice. The resonant X-ray scattering (RXS) technique has been tipped to have unique sensitivity to charge and orbital ordering due to its spectroscopic characteristics. On the other hand, non-resonant scattering methods will provide accurate information on the charge-density distributions of core electrons, and therefore are sensitive to lattice modulations. To disentangle complex ordering phenomena, an integral approach has to be chosen.

The situation concerning charge ordering in this compound is among the most puzzling. According to the classic ionic charge-ordering scenario Mn^{3+} and Mn^{4+} order periodically, and they can be distinguished via the chemical shift of the 1*s* core level. This chemical shift will lead to the occurrence of resonant enhancement of a charge-ordering reflection at the Mn K-edge via a $1s \rightarrow 4p$ dipolar transition.

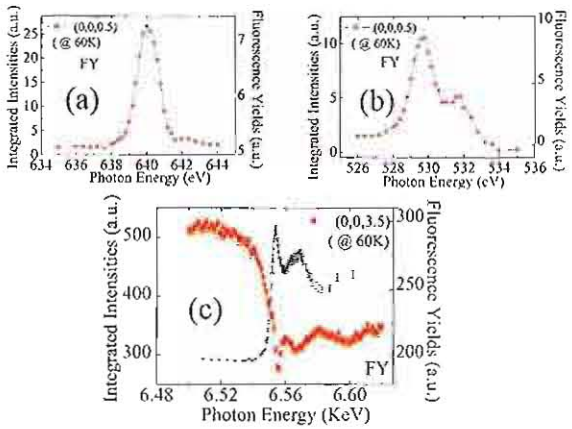

Fig. 1 Observation of charge ordering by soft X-ray resonant scattering (above), while no signal is observed at the Mn K-edge (below).

However, as shown in Fig. 1(c), no resonance at the charge-ordering reflection with q = (0,0,0.5) is observed in our RXS experiment carried out at the Mn K-edge (~ 6.554 KeV), despite the proposed models predicted that the charge ordering should take place at q = (0,0,0.5) [4-5]. To clarify the nature of charge ordering in the FMI regime of this compound, we carried out soft X-ray resonant scattering experiments in a UHV scattering chamber at BESSY-II. This technique has unique sensitivity to the charge ordering of 3*d* electrons via a dipolar transition to an unoccupied 3*d* band, instead of via indirect chemical shift effects. As shown in Fig. 1(a), a clear resonant enhancement of q = (0,0,0.5) can be observed near the Mn L_3-edge i.e. at ~ 640 eV. Furthermore, an extraordinary resonance was also observed near the so-called pre-edge region (~ 530 eV) of the O K-edge. The pre-edge spectroscopic feature is in

general interpreted as originating from strong hybridization of the O $2p$ orbitals with unoccupied Mn $3d$ orbitals. Therefore, just similar to the case in high-T_C superconducting cuprates, the charge degree of freedom in manganites will possess a strong $2p$ character. In fact, it is quite astonishing to notice that the character as a charge-transfer insulator (CHI) has been largely ignored in the physics of manganites. Our observations with soft X-rays clearly indicate that the charge ordering does take place in this compound, however, in a different form. The classic ionic ordering with integer $3d^n$ configurations of cations and fully filled oxygen $2p$ shells has to be challenged.

Orbital ordering of 3d electrons can be observed by RXS at the Mn K-edge, since the orbital occupancy of single e_g electron in manganites is always accompanied by local distortions. This local anisotropic structure effects will lead to the occurrence of anisotropic anomalous scattering, also called the Tempelton scattering. Comprehensive RXS experiments on this compound have been undertaken at MuCAT, Advanced Photon Source (APS), USA. As shown in Fig. 2(a), significant resonant enhancement can be observed in the reciprocal space with q = $(H,0,L/2)$ (H,L ~ odd), when the photon energy is tuned to the Mn K-edge at ~ 6.554 KeV. The energy dependence of several superstructure reflections with q = $(H,0,L/2)$ (H,L ~ odd) is shown in Fig. 2(b). All resonant reflections disappear when warming the sample above ~ 140 K. The characteristic azimuthal-angle dependence has also been confirmed, indicating that this resonant behavior is caused by an anisotropic effect i.e. orbital ordering.

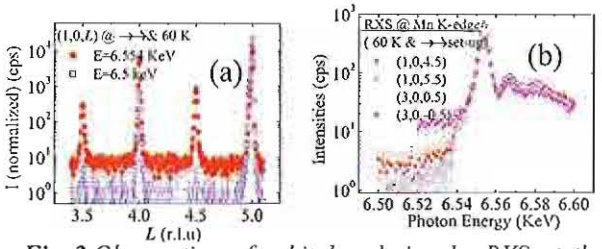

Fig. 2 Observation of orbital ordering by RXS at the Mn K-edge.

It has been known that $La_{1-x}Sr_xMnO_3$ (x~1/8) undergoes several complex lattice modulations and structural phase transitions in the FMI regime. However, the nature of these structural modulations has not been well established. Therefore, high-energy X-ray diffraction experiments were undertaken at the 6-ID-D undulator beamline of MuCAT, APS to investigate the complex lattice modulations with photon energy chosen at near or above 100 keV (see Fig. 3).

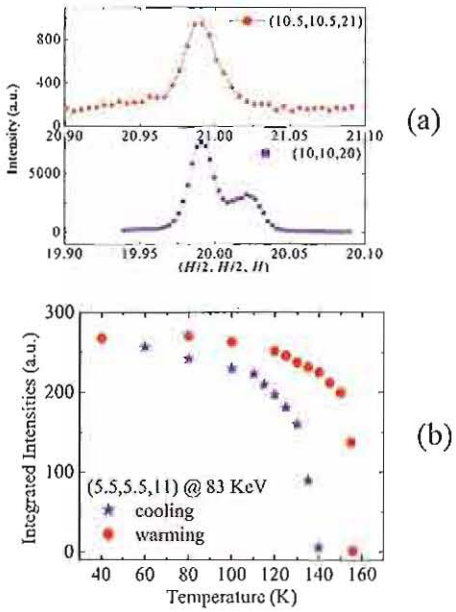

Fig. 3 Investigation of complex lattice modulations by high energy X-ray diffraction.

A superstructure lattice modulation with q = $(H/2,H/2,H)$ (H~odd) has be observed up to reciprocal positions with very high q e.g. at (10.5,10.5,21) below ~ 140 K. This observation leads us to suspect that q = $(H/2,H/2,H)$ (H~odd) represents a coherent strain wave modulation. The strain wave modulation will help to stabilize an orbital ordering pattern through elastic interactions.

In summary, comprehensive synchrotron X-ray scattering experiments on one of the most challenging and complex correlated electron systems – lightly doped $La_{1-x}Sr_xMnO_3$ (x~1/8) have been undertaken, which enable us to finally confirm the occurrence of charge ordering in this compound by soft X-ray resonant scattering. New insights on the orbital ordering and unusual lattice modulations were obtained.

We acknowledge BESSY-II and APS for providing excellent synchrotron beams, and technical staffs at IFF for their full supports.

[1] Y. Endoh, *et al.*, Phys. Rev. Lett. **82**, 4328 (1999)
[2] J. Geck, *et al.*, New Journal of Physics **6**, 152 (2004)
[3] R. Kilian and G. Khaliullin, Phys. Rev. B **60**, 13458 (1998)
[4] T. Mizokawa, *et al.*, Phys. Rev. B **61**, R3776 (2000)
[5] M. Korotin, *et al.*, Phys. Rev. B **62**, 5696 (2000)

Strain Relief of Heteroepitaxial Bcc-Fe Films on Mg(001) *

G. Wedler and C.M. Schneider
Institut f. Festkörperforschung "Elektronische Eigenschaften", Forschungszentrum Jülich, D-52425 Jülich, Germany

We have investigated the strain relief in heteroepitaxial bcc-Fe(001) iron films grown on Mg(001) by means of scanning tunneling microscopy. We find that the tensile misfit strain is relieved during coalescence of flat, mainly 2–3 monolayers (ML) high Fe islands at the high thickness of ~ 20 ML. To accommodate the misfit between merging strain-relaxed islands, a network of $\frac{1}{2}[111]$ screw dislocations is formed.

The system Fe/MgO/Fe(001) is highly interesting with respect to spin-dependent tunneling processes. Theoretical predictions have identified a coherent tunneling mechanism based on the symmetry of specific wave functions, which should lead to extremely high tunneling magnetoresistance (TMR) [1]. Recently, experimental evidence for an enhanced TMR of up to $\sim 220\,\%$ at room temperature has been found in epitaxial and polycrystalline highly textured layer structures containing MgO tunneling barriers [2, 3]. As the crystalline orientation and the interfacial perfection plays an important role in this spin-polarized tunneling phenomenon, the growth and morphology of the individual layers – also of the magnetic electrodes – in the Fe/MgO/Fe(001) sandwich are important issues. For this reason, we investigated the growth and the strain relief mechanism of Fe-films on MgO(001).

Epitaxial layer growth often leads to a strain caused by the lattice mismatch of substrate and film. This strain may result in structural instability, thus affecting growth mode and/or film morphology. The Stranski-Krastanov growth mode is one pathway to reduce the strain by the formation of 3D islands on top of a continuous wetting layer [4]. Another mechanism is the introduction of misfit dislocations without the formation of 3D islands [5].

Whereas the strain relief in epitaxial films has been studied extensively for fcc-type systems, the respective behavior of the bcc-class is less well known. A major difference of the bcc to the fcc lattice is a higher activation barrier for dislocation glide. This results in a low mobility of $(a/2)\langle 111\rangle$ screw dislocations in the plastic deformation of bcc bulk materials, and may also affect the nucleation and glide of dislocations in bcc films. Indeed, previous thickness dependent stress measurements in the Fe/MgO(001) system revealed a relief of the tensile strain only *above* a thickness of 2–3 nm (15–20 atomic layers) [6], which is more than twice the critical thickness expected from energy considerations [5]. Since the substrate has an fcc structure, the transmission of dislocations between substrate and film is suppressed. Thus, the dislocations are confined to the bcc-Fe film, which allows us to study the dislocations in the film itself. Our *in-situ* scanning tunneling microscopy (STM) studies (Fig. 1) reveal the merging of 2–3 monolayer thick islands at the surface of the 2–3 nm films, in the course of which a network of screw dislocations is formed, as the dominant

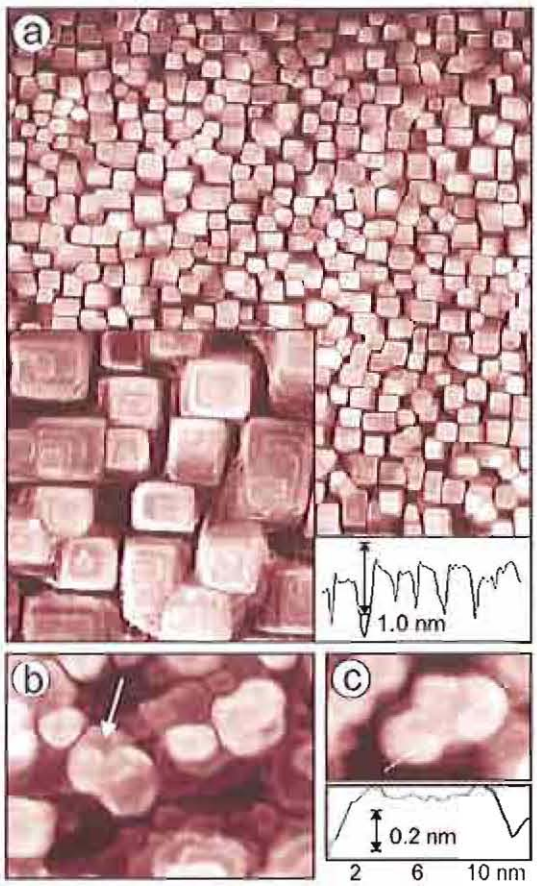

FIG. 1: Strain relaxation in Fe/MgO(001) as seen by STM: (a) $600 \times 600\,\mathrm{nm}^2$ image – 7.5 nm Fe film grown @ 570 K; film surface showing a dense array of ~ 1 nm high (cf. line scan) square islands on top of a 6 nm thick continuous layer; each island contains screw dislocations. Inset: $180 \times 180\,\mathrm{nm}^2$ zoom of the screw dislocations. (b) $36 \times 26\,\mathrm{nm}^2$ image – 5 nm Fe film grown @ 520 K: formation of screw dislocations (arrow) during island coalescence. (c) Respective $19 \times 12\,\mathrm{nm}^2$ image – island with borders raised by ~ 0.03 nm due to lattice contraction (cf. Fig. 2); single scan along dashed line.

*work performed in collaboration with A. Trampert and R. Koch (Paul-Drude-Institut für Festkörperelektronik, Berlin)

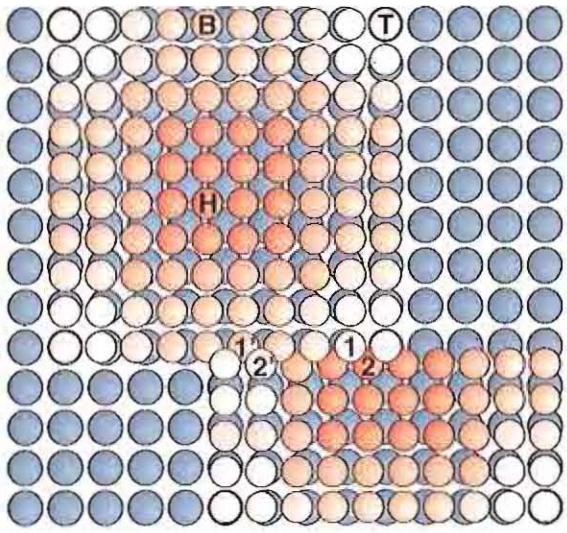

FIG. 2: Sphere model (top view) illustrating the mechanism of strain relaxation in Fe/MgO 001: The blue spheres represent the uppermost (001) plane of the expanded and thus highly strained continuous Fe(001) layer (misfit is exaggerated for reasons of clarity, see text). Upon coalescence of the two strain-relaxed 2D islands (bright spheres) a screw dislocation is formed in the contact region.

mechanism of strain relaxation.

The strain investigations in Ref. [6] showed that the Fe-films are highly strained up to a thickness of $t \approx 2-3$ nm. Our STM study proves the Fe films to be continuous for $t > 1.3$ nm; at lower thickness steps of the insulating substrate inhibit long-range conductivity necessary for STM investigations. Fig. 1(a) displays an STM image of a 7.5 nm thick Fe film grown at 570 K to MgO(001). According to the strain data, at this thickness the Fe film is in a stage where the relief of misfit strain progresses. Interestingly, the entire film surface is patterned by a dense array of square islands with heights of about 1 nm [cf. line scan of Fig. 1(a)], sitting on top of a continuous Fe layer of about 6 nm. The mean island length is ~ 28 nm. Each island contains at least one, often two (right- and lefthanded), screw dislocations [cf. inset of Fig. 2(a)]. Our STM studies thus clearly disclose that in the case of bcc-Fe(001) films – in contrast to fcc films – a large number of screw dislocations is formed upon strain relaxation. At thicknesses $t < 2.5$ nm no screw dislocations were found.

Fig. 2 sketches a realistic mechanism for the insertion of screw dislocations into a growing (001) film. The blue spheres in Fig. 2 represent the uppermost (001) plane of the biaxially expanded continuous Fe layer (~ 6 nm thick). For reasons of clarity we increased the misfit of the sphere model to $\sim 11\,\%$, i.e., requiring an additional row every nine rows for complete relief of the misfit strain. For comparison, in Fe/MgO 001 with a misfit of 3.5 % insertion of an additional row every 29 lattice distances (~ 9 nm) is sufficient. The two 2D islands in Fig. 2 – growing on top of the strained (001) plane – have relaxed the strain. Due to the reduced lattice spacing, only the atoms in the center of the square upper island of Fig. 2 sit in the fourfold hollow sites of the bcc lattice (indicated by H). Atoms near the step edges are shifted to energetically less favorable bridge sites (B) as well as to on-top sites in the four corners (T). In the lower part of Fig. 2 a second 2D island coalesces with the upper island. At the contact region atoms of the lower island (marked by 2) have moved beneath the edge and the corner atoms of the upper island (marked by 1), thus pushing them upwards onto top sites of the bcc lattice. Due to the strain relaxation in the lower island, a reversed situation is observed farther to the left in Fig. 2, where atoms of the square island lie underneath (i.e., 1' below 2'). A closer look reveals that the restructuring of the contact region has created two screw dislocations with $(a/2)\langle 111\rangle$ Burgers vectors, suggesting that island coalescence may provide a natural way to insert screw dislocations in Fe/MgO(001).

That island coalescence indeed plays a crucial role in the formation of screw dislocations is supported by the data in Fig. 1(b). It shows a 5 nm thick Fe film, grown at a lower temperature of 520 K. Due to the reduced surface diffusion at 520 K the island shapes are less regular and therefore still contain information of the island coalescence. The marked island (arrow) – being only one example out of many – has emerged from coalescence of two smaller islands. In agreement with our model (Fig. 2) two screw dislocations have formed, with their cores lying in the boundary region. Notice also the island in Fig. 1(c) with its borders raised by ~ 0.03 nm, thus indicating the lattice contraction as illustrated in Fig. 2.

Our results (details cf. [7]) lead to a conclusive picture of the strain relief in a bcc-metal film. Coalescence of islands of appropriate height provides an energetically favorable path for the nucleation of dislocations, whereby screw dislocations accommodate the misfit between merging islands is. Interestingly, there is a pronounced preference for forming screw dislocations which is in clear contrast to the strain relief in fcc films. The strong barrier for dislocation glide – which is typical for bcc metals – is most likely responsible for the delayed onset of strain relief in Fe/MgO(001). In fact, strong barriers for dislocation glide might provide a general explanation for the large kinetic barriers to inject dislocations in heteroepitaxial systems.

[1] W. H. Butler *et al.*, Phys. Rev. B **63** (2001) 054416.
[2] S. S. P. Parkin *et al.*, Nature Materials **3** (2004) 862.
[3] S. Yuasa *et al.*, Nature Materials **63** (2004) 868.
[4] E. Bauer, Z. Kristallogr. 110 (1958) 372.
[5] J. H. Van der Merwe, J. Appl. Phys. **34** (1962) 123.
[6] R. Koch *et al.*, J. Magn. Magn. Mater. **159** (1996) L11.
[7] G. Wedler *et al.*, Phys. Phys. Lett. **93** (2004) 236101.

Sub-Nanosecond Time-Resolving X-Ray Photoemission Electron Microscopy: Incoherent Magnetization Rotation Observed in Permalloy Microstructures*

C.M. Schneider and A. Kuksov
Institut f. Festkörperforschung "Elektronische Eigenschaften", Forschungszentrum Jülich, D-52425 Jülich, Germany

We carried out time-resolved X-ray photoemission electron microscopy (TR-XPEEM) on Permalloy microstructures. The stroboscopic experiments feature a time-resolution of $\Delta\tau \leq 130$ ps. We observe a strong influence of incoherent magnetization rotation processes, leading to a significant transient stray-field formation at the edges of the microstructure.

A solid understanding of the micromagnetic processes which determine the dynamics of magnetization reversal is mandatory for a further improvement of existing devices and the evaluation of new magnetic writing strategies. These processes comprise domain nucleation, domain wall motion, or incoherent and coherent magnetization rotation. Although some knowledge can be gained from spatially integrating over the sample response, a much more detailed picture will emerge from laterally resolving techniques. Direct imaging of fast magnetization reversal remains a considerable experimental challenge and has long been a domain of magnetooptical techniques [1]. However, recent years have witnessed the advancement of new powerful magnetic microscopy techniques based on the use of synchrotron radiation [2, 3]. The successful implementation of nanosecond time-resolution into X-ray photoemission microscopy (XPEEM) was demonstrated just recently [4-6].

We describe stroboscopic XPEEM studies on Permalloy microstructures with a time resolution of 130 ps. The TR-XPEEM experiments have been performed at the elliptical undulator beamline ID 08 at the ESRF using a dedicated photoemission electron microscope. The experiments described below employed ESRF's "16-bunch" mode, which delivers light pulses of about 106 ps width and about 176 ns repetition time. A bunch marker from the storage ring was used to trigger a magnetic field pulse of about 10 ns width. The time delay between field and light pulse was set by a switchable delay unit (see scheme in Fig. 1).

The samples comprised 100 μm wide Cu microstrip lines of 200 nm thickness. The magnetic sample was placed on top of the stripline and consisted of a bilayer (40 nm $Ni_{81}Fe_{19}$, 2 nm Cu), which had been lithographically patterned into elements of different geometrical shapes and sizes (see also Ref. 4). A short current pulse through the micro stripline generated a transient in-plane magnetic field at the position of the microstructures.

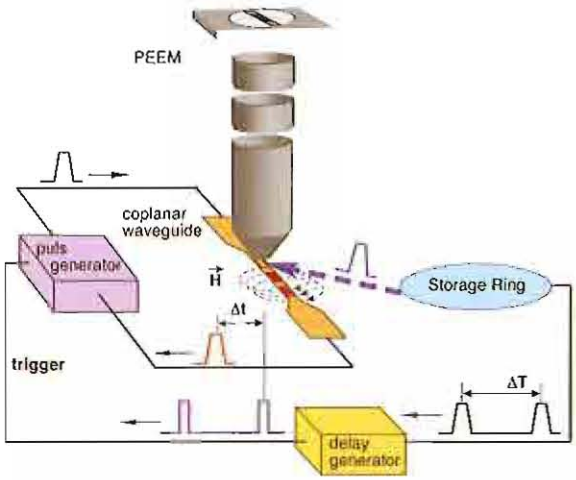

FIG. 1: Principal set-up of the time-resolved XPEEM experiment.

In Fig. 2 we show a sequence of domain images (Ni L_3 XMCD contrast) taken along the rising edge of the field pulse ($\Delta B/\Delta t \sim 1$ mT/ns) with a delay step width of $\Delta t = 125$ ps. Prior to the field pulse, both elements reveal Landau-like domain patterns [7]. This proves the sample to reproducibly be driven back into the same state after each field pulse cycle by the demagnetizing field. With increasing strength of the transient field, we start to see characteristic changes in the domain configuration, which are highlighted by forming differences of subsequent images (Fig. 2, bottom row). The difference images exhibit clear structures indicating an actual time resolution well below the chosen delay step width.

We note that the dominant changes in Fig. 2, i.e. the formation of stripe-like domains, appear alternatingly in the triangular domains on the right and left hand side of the bar, respectively. In the static case, these domains have a magnetization vector $\vec{M}$ opposite to the direction of the transient field $\vec{H}(t)$ generated by the current pulse through the stripline. Domains with $\vec{M} \parallel \vec{H}(t)$ exhibit only a homogeneous contrast level. A magnetic field pulse of opposite sign creates a stripe-like pattern in the opposing triangles, clearly demonstrating the orientation between $\vec{M}$ and $\vec{H}(t)$ to be responsible for this behavior. Similar observations are made with a bipolar pulse.

*work performed in collaboration with A. Krasyuk, A. Oelsner, D. Neeb, S. A. Nepijko, G. Schönhense (J.-Gutenberg Universität Mainz), J. Morais (Instituto de Fisica - UFRGS, Porto Alegre, Brazil), C. de Nadaï, and N. B. Brookes (ESRF, France)

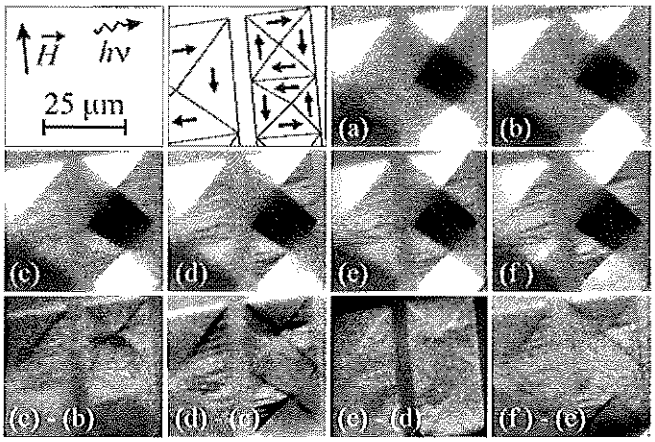

FIG. 2: TR-XPEEM domain images of $Ni_{81}Fe_{19}$ rectangular bars ($20\,\mu m \times 80\,\mu m$ and $40\,\mu m \times 80\,\mu m$ size) taken along the rising edge of a unipolar magnetic field pulse at $t = 0$ (a), 125 (b), 250 (c), 375 (d), 500 (e) and 625 ps (f). Directions of light incidence and pulse field $\vec{H}$ are given, together with a sketch of the particle domain structure in the initial state. Bottom row: subsequent differences between images (b) to (f).

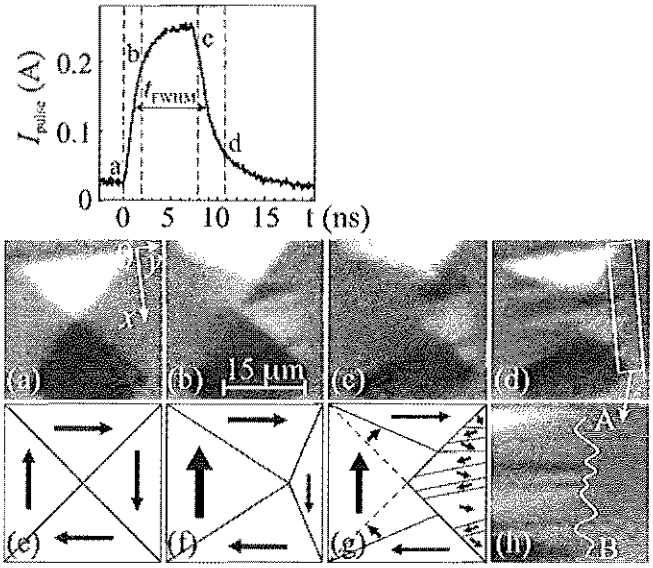

FIG. 3: Domain images of the upper part of the narrow rectangle in Fig. 2 mapping the field pulse (top panel) at $t = 0$ (a), 1.750 (b), 7.875 (c) and 10.875 ns (d). Area marked by rectangle in (d) is stretched $\times 5$ in horizontal direction (h). Schematic images of expected behavior of the Landau structure (e) in a slowly varying field (f) and formation of a stripe pattern at $t = 7.875$ ns after the leading edge of the pulse (g). White line in (h) traces the deformation profile AB along the particle edge.

Images taken at smaller field of view reveal more details of the dynamic behavior. Fig. 3 shows the domains in the upper part of the narrow bar at $t = 0$ (a), 1.75 (b), 7.875 (c) and 10.875 ns (d) after the onset of the field pulse (upper panel). The Landau pattern (Fig. 3e) at $t = 0$ (Fig. 3a) proves the fully relaxed initial state. For comparison, the changes expected during a *slow* reversal process are given in Fig. 3f. The applied field $\vec{H}$ should move the domain walls, expanding the domain with $\vec{M} \parallel \vec{H}$ on the expense of the others. In particular, the domain with $\vec{M} \uparrow\downarrow \vec{H}(t)$ should shrink, causing the central vortex to shift to the right. Also in the pulsed-field case, the domain with $\vec{M} \parallel \vec{H}(t)$ grows in the applied field, while domains with $\vec{M} \perp \vec{H}(t)$ shrink. The domain with $\vec{M} \uparrow\downarrow \vec{H}(t)$, however, breaks up into stripes, which cover almost the same area as the original domain. As a consequence, the vortex seems to split up into substructures, which move along the initial position of the domain walls with inceasing field strength. Reconstructing the magnetization distribution from the grey levels in Fig. 3c reveals a complex transient domain pattern (Fig. 3g).

The explanation or our findings rests on recent work of the Freeman group [8, 9]. We attribute our observations to the action of incoherent rotation processes in the magnetization. The important difference to the above time-resolved Kerr microscopy experiments of Freeman *et al.* is the lack of a static guiding field. Its role is taken by the demagnetizing field of the element, which stabilizes the Landau structure. In an incoherent rotation process, the homogeneous magnetization breaks up into a system of elongated regions, in each of which the local magnetization vector rotates into an orientation close to $\vec{M} \perp \vec{H}(t)$. The rotation is not restricted to the film plane, as the transient domain patterns observed by the Freeman group revealed also sizable components of $\vec{M}$ normal to the film plane. Probing these components will be an interesting aspect in future vectorial TR-XPEEM investigations. The microscopic origin of this incoherent rotation is not yet fully understood. We suggest, however, that it may be associated with structural (edge roughness) or magnetic inhomogeneities (magnetization ripple) of the sample. Further details may be found in Ref. [10].

[1] M. R. Freeman and W. K. Hiebert, in *Spin Dynamics in Confined Magnetic Structures I*, eds. B. Hillebrands and K. Ounadjela (Springer-Verlag, Berlin, 2002).
[2] C. M. Schneider and G. Schönhense, Rep. Prog. Phys. **65** (2002) R1785.
[3] P. Fischer *et al.*, J. Phys. D: Appl. Phys. **35** (2002) 2391.
[4] A. Krasyuk *et al.*, Appl. Phys. A **76** (2003) 863.
[5] J. Vogel *et al.*, Appl. Phys. Lett. **82** (2003) 2299.
[6] S.-B. Choe *et al.*, Science **304** (2004) 420.
[7] A. Hubert and R. Schäfer, *Magnetic Domains: The Analysis of Magnetic Microstructures* (Springer-Verlag, Berlin, 1998).
[8] M. R. Freeman *et al.*, J. Appl. Phys. **83** (1998) 6217.
[9] W. K. Hiebert *et al.*, J. Appl. Phys. **92** (2002) 392.
[10] C. M. Schneider *et al.*, Appl. Phys. Lett. **85** (2004) 2562.

Magnetic domains in mesoscopic ferromagnets: simulations and experiments

Riccardo Hertel
Institute of Solid State Research (IFF), Research Center Jülich, D-52425 Jülich, Germany

Micromagnetic simulations are an indispensible tool to the study the magnetization in mesoscopic particles. A comprehensive picture of magnetic domain structures can be obtained by combining accurate simulation results with high-resolution magnetic imaging techniques. Magnetic structures in lithographicallly prepared rectangular Co thin-film elements and in self-assembled, monocrystalline Fe/Mo(110) particles have been imaged with X-ray magnetic circular dichroism with photoemission electron microscopy (XMCD-PEEM). The results of the micromagnetic simulations are in excellent agreement with the experimental observations. In addition, the simulations provide information that is not available experimentally. This includes the *energy* of the magnetization states and a fully *three-dimensional* description of the magnetization field. The latter point is particularly important in samples of mesoscopic lateral size and of elevated thickness (ca. 100 nm and more).

The size and the shape of a ferromagnetic particle can have a drastic influence on its magnetic properties and on its magnetic domain structure. The influence of the particle size appears most clearly in the so-called single-domain limit [1], which describes the transition from a virtually homogeneous, single-domain arrangement of the magnetization into a multi-domain, flux-closure magnetization structure with increasing particle size. The importance of the particle size is connected with the existence of a material-specific length scale, the so-called exchange length. In soft-magnetic materials, the exchange length $\delta = \sqrt{2A/\mu_0 M_s^2}$ (M_s: saturation magnetization, A: ferromagnetic exchange constant) represents a measure for the extension of magnetic inhomogeneities like domain walls or vortices and is typically in the order of several nm. When the particle size is significantly below or significantly above the exchange length, the magnetic structure is in a single-domain or in a multi-domain state, respectively. This is obviously only a rough estimation, and accurate computer simulations are required to establish the precise single-domain limit [2], which does not only depend on the particle size but also on its shape.
In sub-micron sized, soft-magnetic thin-film elements of a few hundred nm size and several nm thickness, a relatively large but finite number of magnetization states can occur. The lateral confinement of the magnetization limits the number of possible magnetization states, since only a few domain walls can be sustained in such small particles and their position inside the sample is determined by finite-size effects. A theoretical understanding of the occurence of different magnetization states in mesoscopic, soft-magnetic thin-film elements is important from a technological point of view, because such elements are employed in modern magneto-electronic devices. But it is also of fundamental importance for the study of the magnetization in confined magnetic structures.

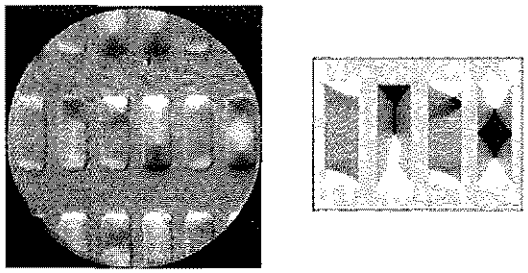

FIG. 1: Magnetic domain structures in Co thin-film elements: Experiment (left) and simulation (right). The size of the particles is 1200 nm x 400 nm x 20 nm. The simulated structures correspond almost exactly to the contrast obtained in the XMCD-PEEM experiment.

The zero-field magnetic structures in rectangular 20nm-thick Co elements with aspect ratios of 1:1, 1:2 and 1:3 and widths of 200, 400 and 600 nm have been investigated experimentally by means of XMCD-PEEM and simulated with a custom-developed micromagnetic code based on the finite-element method. Several different (metastable) magnetization states can occur in such particles. The first aim of the study was to investigate and categorize all of these domain structures. In a second step the probability of finding each magnetization state for different aspect ratios and sizes has been determined with a statistical evaluation of the experimental data. The micromagnetic simulations are finally used to investigate to which extent this probability is connected with the energy of the magnetization state. In ferromagntic particles, the magnetization state is usually determined by hysteretic effects, *i.e.* by the magnetic history of the sample. If the particles were exposed to a strong magnetic field, they would remain in a magnetized state after the field is switched off. Several metastable magnetization states would then not be accessible due to an insurmountable energetic barrier. To observe these magnetization states and to obtain a meaningful statiscs it is therefore essential that the particles are in the so-called virgin state, *i.e.* that they have not been exposed to a magnetic field after their fabrication.

The samples consisted of lithographically fabricated arrays of particles of same size and thickness. The number of elements ranged from 100 for the smallest (200 nm width and 1:1 aspect ratio) to 18 for the largest (600 nm width and 1:3 aspect ratio). The spacing between the el-

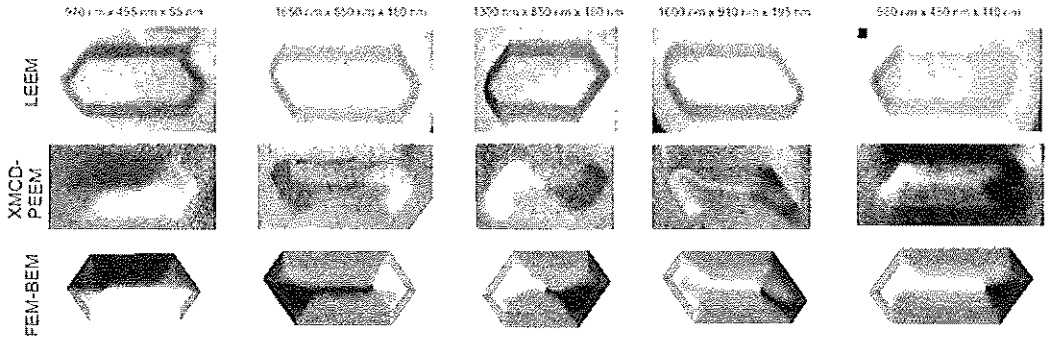

FIG. 2: Topography, magnetic domain structure and simulated magnatization distribution in five Fe/Mo(110) islands of different size and shape. The XMCD-PEEM images (middle row) reveal unusual, distorted magnetic domain patterns on the top of the islands. This observation is reproduced by the simulations (bottom row).

ements was sufficiently large to safely rule out any significant stray field coupling. In the simulations, ten different magnetization states have been obtained, all of which have also been found in the experiment. Fig. 1 shows a typical example of experimental results and simulated structures [3]. The different domain states observed in the arrays have been counted and their frequency of occurrence has been compared with the computed energy of the structures. The results indicate the existence of a correlation between these two quantities: The magnetization state with the lowest energy is most frequently found, while high-energy states occur much more rarely. In spite of this qualitative correlation, some exceptions have also been found. The statistical correlation between the energy of a magnetization state and its probability of observation must therefore be considered to be rather a tendency than as a strict correspondence. A more detailed discussion on this study and on the results is reported in Ref. [3].

In a technically similar, but topically quite different study, magnetic domain structures in three-dimensional, mesoscopic Fe particles have been investigated by combining finite-element micromagnetic simulations with high-resolution XMCD-PEEM imaging. The motivation of this study was to extend the relatively well established knowledge of two-dimensional magnetization structures in thin-film elements to particles of elevated thickness. As a model system to study three-dimensional magnetization structures in mesoscopic particles, self-assembled, monocrystalline Fe islands of about 1.5 μm size and several 100 nm thickness have been grown on an atomically flat Mo(110) substrate. The shape of the sample has been determined by means of low-energy electron microscopy (LEEM), and the magnetic contrast was obtained with the same instrument by means of XMCD-PEEM. A large number of Fe islands of different shape, size and thickness has been examined. Typical LEEM images of such particles are displayed in the top row of Fig. 2. The corresponing XMCD-PEEM images and the simulated magnetic structures are shown in the rows below. The sample shape obtained from the LEEM images was used in the simulations to create a finite-element model of the sample. The geometrical flexibility of the finite element method is particularly important in this case, since the irregular, hexagonal shape of the particles and the inclined lateral facets of the islands are very difficult to simulate with the frequently used finite-difference method. Adaptive mesh refinement methods have been used to locally increase the accuracy in regions of strong magnetic inhomogeneities, thereby obtaining precise solutions of the three-dimensional vector field of the magnetization.

The XMCD-PEEM results, which display one magnetization component on the top surface of the island, yield unusual, asymmetric domain patterns. In contrast to this, the well-known Landau-type flux closure patterns in thin-film elements are almost perfectly symmetric, as shown, *e.g.*, in the second image in the right panel of Fig. 1. The simulation results are again in perfect agreement with the experimental observations. However, the simulations provide a complete three-dimensional description of the magnetization inside the sample, which is not accessible in the experiment. This possibility to analyze the internal structure of the magnetization is essential for understanding the surprisingly asymmetric magnetic structures observed in the experiment. A detailed description of this extensive study is reported in Ref. [4].

[1] A. Yamasaki, W. Wulfhekel, R. Hertel, S. Suga, and J. Kirschner, Phys. Rev. Lett. **91**(12), 1272011 (2003).
[2] R. Hertel, Z. Metallkd. **93**(10), 957–962 (2002).
[3] S. Cherifi, R. Hertel, J. Kirschner, H. Wang, R. Belkhou, A. Locatelli, S. Heun, A. Pavlovska, and E. Bauer, J. Appl. Phys. **98**, 0430901 (2005).
[4] R. Hertel, O. Fruchart, S. Cherifi, P.-O. Jubert, S. Heun, A. Locatelli, and J. Kirschner, Phys. Rev. B **72**, 214409 (2005).

Self-Trapping of Magnetic Oscillation Modes

A. Krasyuk,[1] F. Wegelin,[1] S. A. Nepijko,[1] H. J. Elmers,[1] G. Schönhense,[1] M. Bolte,[2] and C. M. Schneider[3]

[1] *Universität Mainz, Institut für Physik, D-55128 Mainz, Germany*
[2] *Institut für Angewandte Physik, Universität Hamburg, D-20355 Hamburg, Germany*
[3] *Institut für Festkörperforschung, Forschungszentrum Jülich GmbH, D-52425 Jülich, Germany*

Under the influence of an oscillatory magnetic field the Néel wall in an initial classical Landau pattern may shift quasistatically away from the center, corresponding to an induced magnetic moment perpendicular to the exciting field. This effect is caused by a self-trapping of the dominating spin-wave mode when the system is excited just below the resonance frequency, the basic driving mechanism being entropy maximization.

The magnetodynamics in nanostructures is a key issue in magnetic data storage technology. The high frequency limit has recently attracted considerable attention [1–5], as advanced magnetic recording concepts push the switching time into the gyromagnetic regime. In mesoscopic elements the high frequency behavior is dominated by confined spin-wave eigenmodes. So far, most studies have addressed the simplest case of quasi-monodomain elements, whereas in larger microstructures multidomain configurations prevail. Thin rectangular platelets of Permalloy ($Ni_{80}Fe_{20}$), for example, often exhibit a Landau flux-closure structure comprising a Néel wall in the center [6].

In our studies we focused on the magnetodynamics in 16μm×32μm Permalloy platelets with 10 nm thickness, being excited by a *periodic* field $\vec{H}_x(t)$. The time-dependent response of the magnetization $\vec{M}(\vec{r})$ was imaged with a photoemission electron microscope (PEEM) [7] at BESSY (Berlin), exploiting the x-ray magnetic circular dichroism (XMCD) contrast. As a surprising result we found a magnetic moment induced perpendicular to $\vec{H}_x(t)$. This effect occurs for a Landau flux-closure structure excited slightly off-resonance. The induced perpendicular moment – leading to a domain wall shift despite zero local torque – is caused by a self trapping of an oscillating mode thus maximizing the energy exhausted off the exciting field.

For the time-resolved studies the Permalloy platelets were placed on a coplanar waveguide and imaged stroboscopically. An externally triggered pulse generator synchronized with the x-ray pulses from the synchrotron injected a periodic train of high-frequency current pulses into the waveguide. The timing between magnetic field pulse ("pump") and x-ray pulse ("probe") was adjusted by a variable delay. The actual pulse shape for different amplitudes [see curves I, II, and III] is displayed in Fig. 1(a). The maximum field values were of the order of 2 Oe [Fig. 1(a)]. In effect, this excitation corresponds to a 500 MHz AC signal with substantial higher harmonic components [Fig. 1(b)].

The time evolution of the platelet's magnetization $\vec{M}$ comprising a Landau pattern is shown in Fig. 2 (field pulse I). Domains oriented parallel and antiparallel to

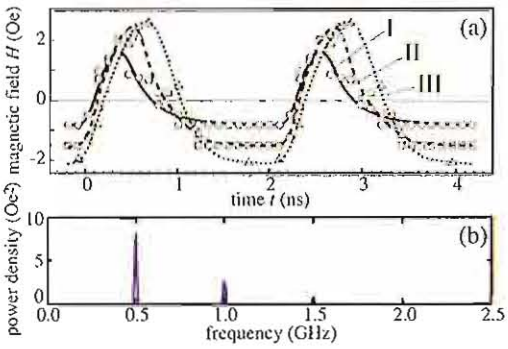

FIG. 1: (a) Time dependence of the exciting magnetic field $H_x(t)$. Two periods are shown in order to emphasize the repetition rate. (b) Fourier transformation of 50 periods of amplitude I into frequency space.

the light vector $\vec{P}$ appear black and white, while the two domains with $\vec{M} \perp \vec{P}$ both appear grey. A 180°-Néel wall along the y-axis separates the two large domains with $\vec{M}$ up- (left) and downward (right). In the Néel wall $\vec{M}$ points to the left, thus the Néel wall appears black. The high driving frequency of 500 MHz renders the image at $t = 0$ to already reflect a dynamical state of the magnetization. Between pulses the system does not have enough time to relax back into the equilibrium ground state.

At $t = 600$ ps the intensity in the left and right domains has increased, indicating a rotation of $\vec{M}$ *towards* the direction of the applied field, i.e. CW in the left domain and CCW in the right domain. At $t = 1100$ ps the left and right domain appear dark, because $\vec{M}$ has rotated in the *opposite* direction. A second oscillation is indicated by the snapshot at $t = 1400$ ps. This oscillatory response appears qualitatively also in micromagnetic simulations.

The main excitation mode in the experiment is a precession of the magnetization in the two large domains. It is excited by the condition $\vec{H}_x(t) \perp \vec{M}$ in these domains. The presence of two pronounced maxima of $\vec{M}_x(t)$ confirms the dynamical motion of $\vec{M}$. In our case $\vec{H}_x(t)$ can be described as an oscillating field with sizable overtones. Thus, the system resembles a driven oscillator and we observe the dynamical answer of the system to

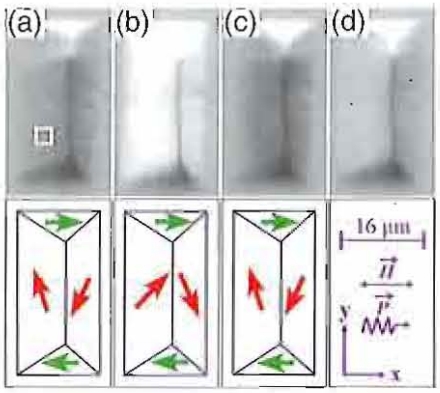

FIG. 2: Selected XMCD images showing the time evolution of $\vec{M}_x$ (bright areas magnetized to the right, dark areas to the left) in the Permalloy platelet for delay times $t = 0$ ps (a), 600 ps (b), 1100 ps (c) and 1400 ps (d). Exciting AC field and photon polarization $\vec{P}$ are oriented in x-direction. Second row shows sketches of the corresponding domain patterns.

the periodic excitation instead of a damped oscillatory relaxation to equilibrium. To determine the frequencies of this driven oscillation, we analyzed the rotation angle $\phi(t) = \pm \arccos(M_x/M)$, which can be extracted from the image contrast. For the left domain we found a value of 1.25 GHz, i.e., just in between the 2^{nd} and 3^{rd} harmonic in Fig. 1(b).

We briefly note that the domain walls and particularly the 180°-Néel wall move only very little throughout the series shown in Fig. 2(a-d). Close to the field pulse maximum at $t = 600$ ps the upper triangular domain ($\vec{M} \parallel \vec{H}(t)$) grows on the expense of the lower black domain. This occurs through a bulging of the 90° domain walls downwards. This bulging behavior is similar to observations in square particles [1].

The most intriguing phenomenon is the mean shift ϵ of the 180°-Néel wall out of its symmetric position to the right [see Fig. 3(a-c)]. This shift increases with the amplitude of the exciting field. It cannot be caused by $\vec{H}_x(t)$ directly, because the field is directed parallel to the magnetization in the domain wall and thus causes no torque. Moreover, the field is oscillating and the mean field averaged over one cycle disappears. We can also exclude magnetic fields along the y-axis. Given our experimental situation we estimate the external field needed to shift the domain wall to the right edge to $H_y \sim 3$ Oe, i.e. the same order of magnitude as the field amplitude H_x. Such a large field component cannot be caused by a misalignment of the particle and the waveguide or by stray fields from the leads. The presence of static fields can also be ruled out, as the domain wall shift should then be independent of the exciting field. However, Fig. 3 clearly shows the shift to increase with $\vec{H}_x(t)$. At the largest field amplitudes the platelet is nearly saturated with the magnetization vector pointing upwards [Fig. 3(c)].

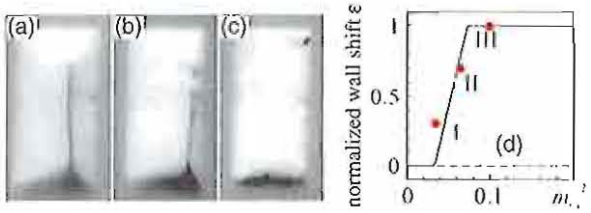

FIG. 3: Domain patterns at the time $t = 600$ ps excited with three different amplitudes [see Fig. 1(a)] denoted as I (a), II (b) and III (c). A comparison of the experimentally determined mean domain wall shift ϵ to a numerical simulation is shown in (d).

The observed effect can be explained by the following argument: A periodically excited system with a continuous source (exciting field) and sink (spin damping) of power assumes a state with maximum energy stored in the system and thus maximizes the entropy production. The energy stored in our particle is mainly given by the magnetization precession in the large domains. The system is excited with a sizable RF field component at 1 GHz, i.e. just below the resonance frequency ν_r of the free-running system (~ 1.25 GHz). Shifting the domain wall to the right will reduce the effective field determining the precession frequency and consequently lower ν_r in the left domain and raise ν_r in the right domain. As a consequence the precession amplitude will increase in the left domain and decrease in the right domain. Thus, the total energy has increased, as the precession energy is proportional to the square of the amplitude. Moreover, the domain with the larger amplitude has grown, which also helps to increase the stored energy. The stored precession energy is finally balanced by the stray field energy, because of the resulting finite magnetic moment of the particle. The initial domain wall movement can occur to the left or to the right. However, we observed exclusively a shift to the right. Small inhomogeneities or a small vortex motion as described in Ref. [3] could be the reason.

More details on the results of this experiment may be found in Ref. [9].

[1] J. Raabe et al., Phys. Rev. Lett. **94**, 217204 (2005).
[2] K. Perzlmaier et al., Phys. Rev. Lett. **94**, 057202 (2005).
[3] S.-B. Choe et al., Science **304**, 420 (2004).
[4] H. Stoll et al., Appl. Phys. Lett. **84**, 3328 (2004).
[5] J. P. Park et al., Phys. Rev. B 67, 020403(R) (2003).
[6] See, e.g., A. Hubert and R. Schäfer, *Magnetic Domains* (Springer, Berlin, 1998).
[7] C. M. Schneider et al., Appl. Phys. Lett. 85, 2562 (2004).
[8] C. M. Schneider et al., Rep. Prog. Phys. **65**, 1785(R) (2002).
[9] A. Krasyuk et al., Phys. Rev. Lett. **95**, 207201 (2005).

Fast Magnetization Dynamics in Cobalt Thin Film Structures

Roman Adam, R. Hertel, A. Rzhevsky, and C. M. Schneider
Institut für Festkörperforschung, Forschungszentrum Jülich, D-52425 Jülich, Germany
(Dated: December 21, 2005)

Detailed understanding of the fast magnetization dynamics in thin ferromagnetic films is essential for the further development of high speed spintronic devices. The magnetization dynamics in nanosecond time scale has been recently tested by several groups. Magnetization dynamics in picosecond time scale, however, is still the hot topic of the current magnetodynamics research. In our experiments we studied cobalt thin film structures exposed to a very short magnetic pulse (~20 ps FWHM) employing time-resolved magneto-optic Kerr effect (TR-MOKE). The average magnetization showed fast damped oscillations with a period of ~100 ps and ~1 ns relaxation time. Micromagnetic finite-element simulations indicate that separate parts of the sample respond differently to the pulse field perturbation and that the domain walls near the edge of the microstructure respond particularly strongly to the excitation.

I. INTRODUCTION

Several experimental techniques have been employed recently to address dynamics [1], [2], [3]. One of the frequently applied techniques exploits the time-resolved magnetooptic Kerr effect to detect instantaneous magnetization variations after the short pulse excitation. Substantial insight can be gained by combining the experimental data with micromagnetic simulations.

II. EXPERIMENTAL SETUP

In this report, we present measurements and micromagnetic finite-element simulations of the magnetodynamics of a patterned cobalt film on the ps time scale. Our structures were fabricated on top of an GaAs substrate covered with 1.5-m-thick GaAs film grown at 250°C using molecular beam epitaxy. Such a low-temperature-grown GaAs (LT-GaAs) film shows very short photoresponse (<1 ps) which makes it the material of choice for ultrafast pump-probe experiments. After the film growth Ti/Au coplanar waveguide (CPW) transmission lines were patterned onto the LT-GaAs surface using photolithography. Each transmission line was terminated by a photoconducting switch with a photoresponse of ~20 ps FWHM. After the CPW completion 20-nm-thin cobalt structures with dimensions ranging from $2 \times 6\ \mu m^2$ to $150 \times 200\ \mu m^2$ were patterned on top of the CPW central line. Fig. 1 shows a microscope picture of the sample. A pulsed mode-locked Ti:sapphire laser was used to generate a short excitation pulse as well as to measure the time-resolved MOKE signal. To obtain synchronized pump and probe pulses we split the laser beam into two paths. The first beam (pump) was directed at the photoconducting switch to trigger the magnetic pulses. The second beam (probe) was reflected from the cobalt surface under the incidence angle of 30 degrees to detect the TR-MOKE signal. The sample was mounted inside an optical cryostat between the poles of an electromagnet and measurements were performed at 100 K.

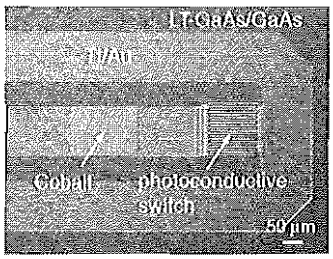

FIG. 1: Coplanar waveguide transmission line with integrated LT-GaAs photoconducting switch and cobalt film patterned on top of the central line.

III. TIME-RESOLVED MEASUREMENTS OF MAGNETIZATION DYNAMICS

During the TR-MOKE measurements the direction of the field pulse generated by the switch was always parallel to the surface of the sample and perpendicular to the CPW lines. The direction of the static external field was either parallel or perpendicular to the direction of

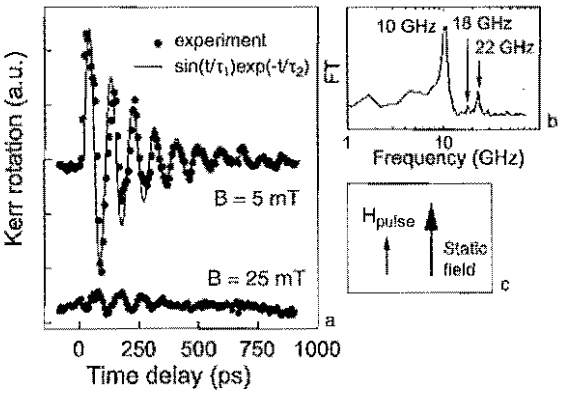

FIG. 2: a) Experimentally measured TR-MOKE signal at B = 5 mT and B = 25 mT b) Fourier transform of the signal at B = 5 mT c) magnetic field alignment schematics.

the pulsed magnetic field. Fig. 2 shows the TR-MOKE measurements at B = 5 mT, and B = 25 mT at the static magnetic field parallel to the pulse field. After the pulse excitation at small static fields (<10 mT) the TR-MOKE signal shows a sharp initial increase followed by damped oscillations with ~100 ps period and ~1 ns relaxation time. At static fields exceeding ~25 mT, however, only an extremely weak TR-MOKE signal is observed due to the almost saturated sample. The oscillatory transients can be fit by a damped sine function $y \sim \sin(t/\tau_1)+\exp(t/\tau_2)$ with $\tau_1 = 95$ ps and $\tau_2 = 200$ ps. The Fourier transform of the TR-MOKE signal at B = 5 mT reveals the presence of two strong oscillatory modes at 10 GHz and 22 GHz and one weaker mode at 18 GHz. Fig. 3 shows the TR-MOKE measurements at B = 80 mT with the static magnetic field aligned perpendicular to the pulse field. The signal shows again oscillatory transients with ~100 ps oscillation period. Contrary to the parallel field configuration, however, the signal shows a longer relaxation time and a more gradual increase of the signal amplitude after the excitation. Most significantly, amplitude of the oscillatory signal shows no significant changes with the static magnetic field variation.

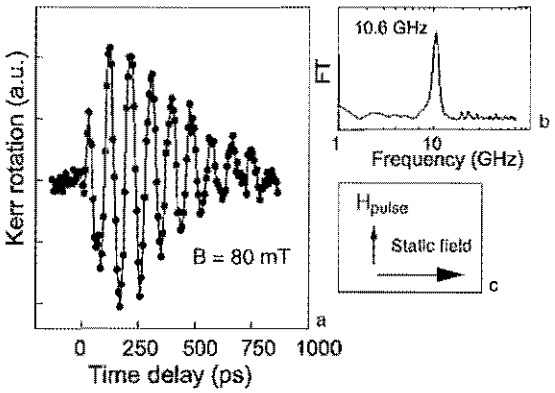

FIG. 3: a) Experimentally measured TR-MOKE signal at B = 80 mT b) Fourier transform of the signal c) magnetic field alignment schematics.

IV. SIMULATIONS

To account for the observed data we employed micromagnetic modelling to simulate the magnetization dynamics in a 20-nm-thin 600 × 200 nm^2 rectangular cobalt element subjected to ~20 ps magnetic pulse. We solved the Gilbert equation that describes the dynamics of the magnetization vector $\vec{M}$ in an effective field $\vec{H}_{eff}$ [4]. Fig. 4a shows the initial equilibrium magnetization. A snapshot of the m_z magnetization component of the microstructure 400 ps after pulse excitation is shown in Fig. 4b. Several regions with distinct magnetization dynamics can be identified. The domain walls close to the end of the rectangle show a particularly strong oscillatory response to the perturbation. The oscillations of the domain walls appear to act as a source generating spin waves propagating across the central part along the long axis of the sample. Fig. 4c and d show the temporal evolution of the volume-averaged magnetization component m_z and the Fourier transform of the $m_z(t)$ signal showing good qualitative agreement with the experiment. The differences in oscillation frequencies can be attributed to the different physical dimensions of the sample. In conclusion, we performed ultrafast TR-MOKE experiments and micromagnetic finite-element simulations to study the spin dynamic in ferromagnetic cobalt thin film structures. Measured signal showed damped oscillations with ~100 ps period and ~1 ns relaxation time. The simulations showed that separate parts of the sample respond differently to the pulse field perturbation and that the domain walls near the edge of the microstructure respond particularly strongly to the excitation. Our simulations indicate that a simple macrospin model is insufficient to account for details of magnetization dynamics.

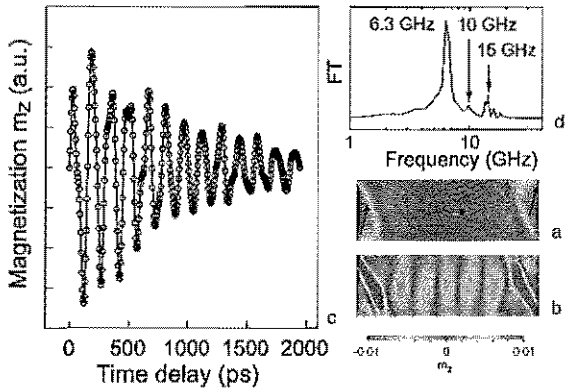

FIG. 4: a) Initial equilibrium magnetization m_z b) snapshot of magnetization 400 ps after the pulse excitation c) calculated temporal evolution of the volume averaged m_z d) Fourier transform of the signal.

[1] Th. Gerrits, H. A. M. van den Berg, J. Hohlfeld, L. Bär, Th. Rasing, Nature **418**, 509 (2002).

[2] W. K. Hiebert, L. Lagae, J. Das, J. Bekaert, R. Wirix-Speetjens, and J. De Boeck, J. Appl. Phys. **93**, 6906 (2003).

[3] A. V. Kimel, A. Kirilyuk, P.A. Usachev, R. V. Pisarev, A. M. Balbashov, and Th. Rasing, Nature **435**, 655 (2005).

[4] W. F. Brown Jr., Micromagnetics, Wiley Interscience, New York, London, 1963.

Magnetization induced second harmonic generation in epitaxial Fe_3O_4/MgO(100)

A. A. Rzhevsky,[1,2] B. B. Krichevtsov,[2] A. D. Rata,[1] C. F. Chang,[3] R. Sutarto,[3] L. H. Tjeng,[3] and C. M. Schneider[1]

[1] *Institut für Festkörperforschung, Forschungzentrum Jülich, 52425 Jülich, Germany*
[2] *Ioffe Physical Technical Institute, Russian Academy of Sciences, 194021 St.Petersburg, Russia*
[3] *Physikalisches Institut II, Universität zu Köln, 50937 Köln, Germany*

Surface and interface magnetic properties often markedly differ from those of the respective bulk system, and may dominate the magnetic behavior of thin films. Discriminating the surface and interfacial contributions to the magnetism is thus both an experimental challenge and of importance to understand thin film magnetism, in particular, in complex systems such as magnetic transition metal alloys. We have employed nonlinear optical second harmonic generation to probe the surface magnetic and structural properties of magnetite thin films in the high (centrosymmetric, O_h) and low (noncentrosymmetric, C_1) temperature phases. We observe azimuthal variations of the nonlinear response reflecting the influence of a cubic magneto-crystalline anisotropy and a symmetry reduction due to a magnetically modified surface layer.

Magnetite - Fe_3O_4 - is a strongly correlated valence-mixed transition metal compound. Due to electron correlation it displays many interesting phenomena, the most prominent being a metal-insulator transition (Verwey) at $T_V = 125$ K. Promising high values of the spin polarization at the Fermi level, Fe_3O_4 thin films recently attract a lot of attention as electrode material in spintronics. Thus, surface and interfacial magnetic and structural properties of these films are of considerable interest, but remain unclear in many aspects up to now [1]. We report on studies of the surface structural and magnetic properties of Fe_3O_4 thin films by the method of magnetization-induced second harmonic generation (MSHG).

Magnetite films with a thickness of 50 nm were grown by MBE on MgO(100) substrates. The temperature dependencies of the conductivity and magnetization were measured by a two-point probe method and SQUID magnetometry, respectively. A sharp Verwey transition was observed around 118 K (see Fig.1).

Azimuth variations of the odd $\Delta I(2\omega) = I(H+) - I(H-)$ (MSHG) and even $I^e(2\omega) = (I(H+) + I(H-))/2$ on magnetization contributions to the second harmonic

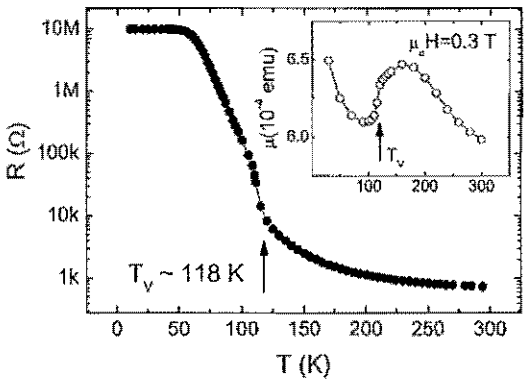

FIG. 1: Electrical resistivity vs temperature in Fe_3O_4/MgO films. Inset shows temperature dependence of magnetization.

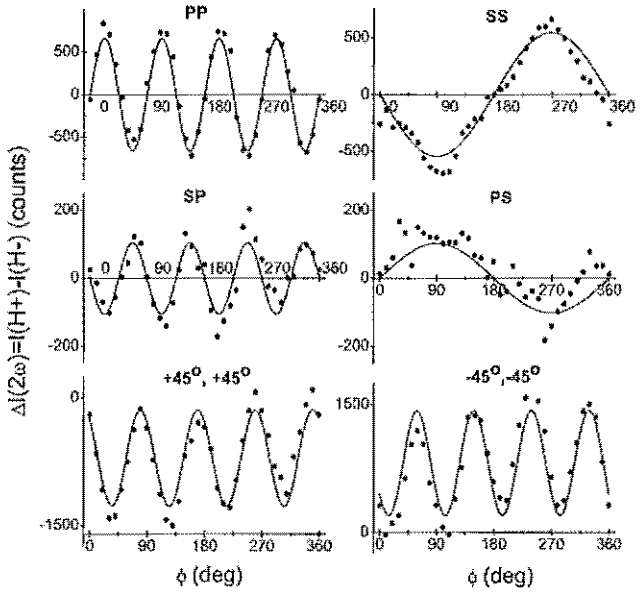

FIG. 2: Azimuthal variations of magnetically induced SHG for different polarization combinations of input (ω) and output (2ω) light in Fe_3O_4/MgO (100) films.

generation signal (SHG) were studied in reflection for a nearly normal ($\theta \sim 5°$) light incidence, using light from a Ti:Sapphire fs-laser in the spectral region of the charge transfer ($Fe^{2+} \longrightarrow Fe^{3+}$) transitions for different polarization combinations of incoming ($E = 1.55$ eV) and outgoing ($E = 3.1$ eV) light. The anisotropy measurements were carried out at 300 K in longitudinal geometry in magnetic fields H up to 0.3 T.

The azimuthal variations of ΔI are given in Fig.2. Taking into account the large value of the absorption coefficient at 2ω ($\sim 2 \times 10^5 cm^{-1}$), we consider the nonlinear response to arise from the surface only. For *pp* and *sp* configurations ΔI is proportional to $\sim \sin 4\phi$, where ϕ is the angle between the magnetic field **H** and the [100] direction of the film. In contrast to that, ΔI in *ps* and *ss*

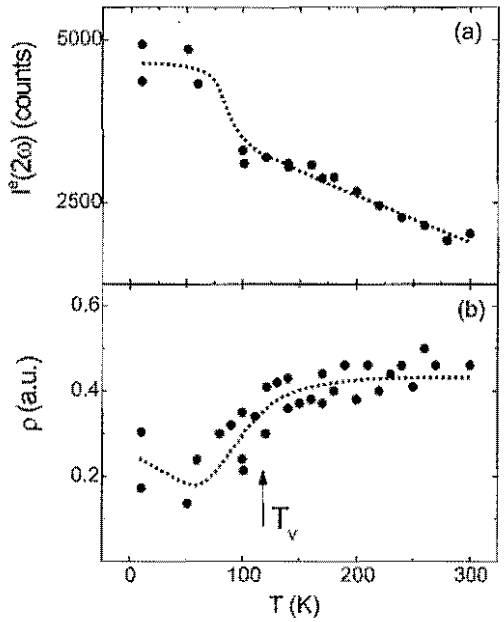

FIG. 3: Even on magnetization contribution to SHG (a) and magnetic contrast (b) vs temperature in *ss* configuration. Dashed line is guide for eyes.

configurations is described by a first harmonic $\sin\phi$. The amplitudes of ΔI for *pp* and *sp* and also for *ps* and *ss* configurations differ in sign. For intermediate configurations (45°,45°) and (−45°,−45°) ΔI is follows a combination of a constant and a forth harmonic term $\sim \sin 4(\phi \pm \delta)$. The sign of both constant term and phase shift (δ) in these configurations differs. The magnitude of the magnetic contrast defined as $\rho = \Delta I/I^e$ is remarkable and reaches its maximal value of $\sim 80\%$ for *ss* configuration.

Fe_3O_4 is centrosymmetric at $T = 294$ K. Thus, bulk electric-dipole SHG contributions are forbidden and the symmetry breaking at the surface and high-order mechanisms reflecting quadrupole or magnetic dipole symmetries act as sources of SHG. For the C_{4v} symmetry corresponding to the (100) face the MSHG in longitudinal geometry is described by a tensor χ^m_{ijk}, which contains ten nonvanishing elements, whereby five of them are even and five odd under magnetization reversal. Using the general expression given in Ref. [2], which relates the components of light at ω and 2ω, we found that in *pp* and *sp* configurations ΔI is related to the magnetization component $M_y = \beta \sin 4\phi$, which is perpendicular to the external field **H**. The existence of this component follows from the cubic magneto-crystalline anisotropy of magnetite and correlates with torque measurements of $Fe_3O_4(100)$ thin films [3]. The parameter β depends on the magnetic anisotropy constants K_1, K_2 and the magnetic field as $1/H$. In configurations (45°,45°) and (−45°,−45°) M_y provides an azimuthal variation of $\Delta I \sim \sin 4\phi$ of the same amplitude, but without any phase shift ($\delta = 0$). The component M_x in these geometries gives rise to a constant term of opposite sign in accordance with experiment. To explain the non-zero value of δ we may also take into account an azimuthal variation of M_x like $M_x = M_x^0 + \xi \sin^2 2\phi$, where M_x^0 is the magnetization for **H** along [100] direction. Such a M_x variation is related to different magnetization values, when magnetite is magnetized along middle [110] and hard [100] directions. It should be noted that in contrast to bulk Fe_3O_4 thin films reach saturation only in high magnetic fields ~ 7 T [3].

In *ss* and *ps* configurations the azimuthal variations of components M_x and M_y should not show any magnetic contrast. The $\Delta I \sim \sin\phi$ experimentally observed in these geometries can be explained by accounting for a changed magnetization $\mathbf{M}_1$ (or an antiferromagnetic moment) directed normal to [100], which is strongly pinned and cannot be switched by the external field. In this case the components M_{1x} and M_{1y} vary upon rotation of the film as $M_{1x} = M_1 \sin\phi$ and $M_{1y} = M_1 \cos\phi$. The interference of the magnetic SHG signals induced by the magnetization components **M** and $\mathbf{M}_1$ gives rise to the appearance of $\Delta I \sim \sin\phi$. In the *pp* and *sp* geometries $\mathbf{M}_1$ does not contribute to ΔI. Another source of the first harmonic in ΔI may arise from surface areas with a symmetry lower then C_2. The non-magnetic contribution to SHG from these areas can involve terms proportional to $\sin\phi$. The modification at the surface could be due to a different surface termination or a coexistence of different magnetic iron-oxide phases.

To study structural and magnetic changes across the Verwey transition we have measured the temperature variations of ρ and I^e (Fig. 3). The Verwey transition manifests itself in an increase of I^e by 25%. This increase is accompanied by a $\sim 50\%$ decrease of ρ. At first sight, one may expect a stronger increase of the I^e, since the Verwey transition is known to be a transition from a high temperature centrosymmetric (O_h) to a low-temperature triclinic (C_1) phase, where a strong contribution from the bulk should be expected. However, taking into account only very small changes in angles and bondings giving rise to a distortion of 0.2° along (110) axis, this result seems to be plausible. The $\sim$ 50% drop of the magnetic contrast observed is much bigger then the drop of the magnetic moment observed in SQUID measurements (Fig. 1). This fact can be explained by the difference of dc and magneto-optical susceptibilities.

Further details on these experiments and results can be found in Ref. [4].

[1] B. Stanka, W. Hebenstreit, U. Diebold, S. A. Chambers, Surf. Sci. **448**, 49 (2000).
[2] H. Hübner and K. H. Bennemann, Phys. Rev. B **52**, 13411 (1995)
[3] D. T. Margulies *et al.*, Phys. Rev. B **53**, 9175 (1996).
[4] A. A. Rzhevsky *et al.*, J. Appl. Phys. (accepted).

Time-resolved photoelectron spectra of $Pt_2(N_2)^-$

M. Neeb[1], J. Stanzel[1], N. Pontius[1], W. Eberhardt[1], G. Lüttgens[2], P.S. Bechthold[2], C. Friedrich[3]
[1]*BESSY GmbH, Berlin;* [2]*IFF-Elektronische Eigenschaften,* [3]*IFF-Theorie I, Jülich*

Pump-probe photoelectron detachment spectra of $Pt_2(N_2)^-$ have been measured using two subsequent fs-laser pulses. The time-resolved spectra show two parallel dissociation channels: photoinduced thermal desorption of N_2 as well as a breaking of the intermetallic Pt-Pt bond. For both fragmentation channels the dissociation energy is less than 1.5 eV. Density-functional calculations predict a linear geometry of neutral and anionic $Pt_2(N_2)$. The calculated electron affinity of the neutral linear cluster (3.2 eV) agrees with the experimental value of (2.8 ± 0.2) eV. An intermetallic dissociation energy of 0.4 eV has been estimated from the measured dissociation rate.

Small transition metal clusters may provide new and efficient catalysts. Even a metal which is chemically inactive in its bulk form, like gold, can promote chemical reactions if it is used in form of small clusters [1]. Besides others there are two principal prerequisites that a cluster can be used as a catalyst: The intermetallic cluster bonds must be stable enough to avoid breaking of the metal-metal bonds and, secondly, the metal-product bond must be weak enough so as to facilitate thermal desorption of the product. This finally recovers the pristine metal cluster at the end of a catalytic cycle.

Photoinduced thermal desorption is a stochastic process which needs a sufficient number of degrees of freedom for thermalization. Such statistical evaporation has recently been observed for small Pt- and Au-Carbonyl clusters [2]. The complete energy dissipation pathway from the athermal photoexcited cluster, the generation of secondary hot-electrons, an energy transfer into the vibronic system as well as a final energy release by desorption of a CO molecule, has been followed in real time by pump-probe photodetachment spectroscopy [2].

In general, free clusters are well suited for studying thermal photodesorption as the energy is locally stored and distributed over a limited number of degrees of freedom. This raises the probability that the thermalized energy redistributes onto a particular metal-ligand coordinate, e.g. a repulsive state, while similar experiments on surfaces are complicated by the fact that the energy dissipates into the bulk. Furthermore, transition metal clusters with open d-shells have a relatively large density of states near the Fermi edge which facilitates excitation by narrow-band laser wavelengths and thermalization of the photoabsorbed energy among the internal degrees of freedom [3].

$Pt_2(N_2)^-$ shows not only an evaporation of the ligand molecule but also a breaking of the intermetallic bond as a competing fragmentation channel.

Platinum clusters are produced in a laser-vaporization source (50 Hz) using a pulsed He-carrier gas (10 bar backing pressure)[4]. Gaseous N_2 is injected via a second solenoid valve downstream of the cluster condensation zone. Anionic $Pt_n(N_2)_m^-$ clusters are mass-selected from the cluster beam using a time-of-flight mass spectrometer. When the desired cluster enters a time-of-flight magnetic-bottle electron spectrometer, an electron is detached from the cluster via two subsequent fs-laser pulses. The fundamental (1.5 eV) and second harmonic of a Ti:sapphire laser were used as pump (≈1 mJ, ≈80 fs, 4 mJ/cm^2) and probe (≈0.3 mJ) pulses, respectively. The delay was controlled by a motor-driven microcontroller where the optical path of the pump pulse is altered relative to the probe pulse. The point of zero delay has been determined by polarization gating using the rear quartz window of the spectrometer chamber.

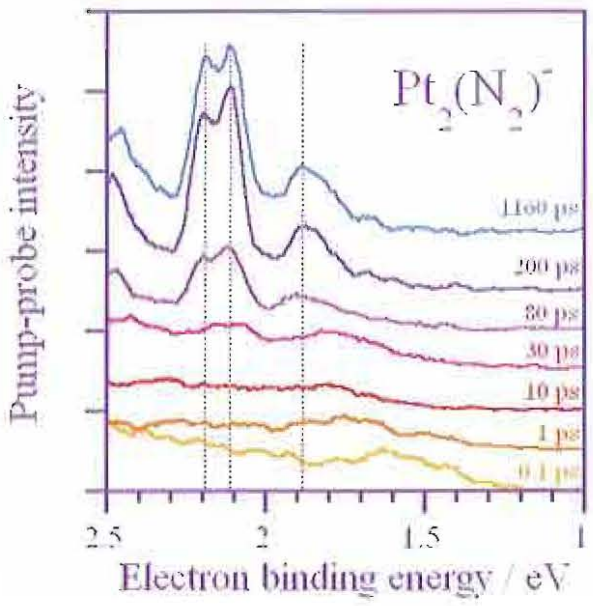

FIG. 1: Normalized and background corrected pump-probe photoelectron spectra of $Pt_2(N_2)^-$. The pump-probe delay varies from 100 fs to 1 ns from bottom to top. The pump-photon energy is 1.5 eV while 3 eV-photons were used for probing the excited clusters. The peaks evolving at 2.15 and 1.9 eV arise from photodissociation processes [5].

Time-resolved photodetachment spectra of $Pt_2(N_2)^-$ are displayed in Fig. 1. The binding energy refers to excited electrons. A double peak at 2.15 eV evolves after ≈10 ps. In addition, a small, but distinct feature develops at 1.9 eV. The double feature at 2.15 eV fits the

adiabatic peak doublet of Pt_1^- as well as the split photoelectron feature of Pt_2^-. Additionally, the small feature at 1.9 eV is equal to the energy of the adiabatic peak of Pt_2^-. For comparison, ordinary photodetachment spectra of Pt_1^- and Pt_2^- are shown together with a time-resolved photodetachment spectrum of $Pt_2(N_2)^-$ in Fig. 2. The normal photoelectron spectra (single-photon) have been taken with a Nd:YAG laser (3.49 eV) while, in this case, the time-resolved spectrum of $Pt_2(N_2)^-$ has been taken with an electronically synchronized Ti:Sa (pump-pulse) and Nd:YAG laser (probe, ≈10 ns pulse width). Due to the high probe-photon energy of the YAG laser (3.49 eV) an additional peak of the Pt atom is seen at 2.9 eV. The peaks of the Pt monomer and dimer fit perfectly with the evolving peaks in the $Pt_2(N_2)^-$ spectrum. From this we conclude that $Pt_2(N_2)^-$ photodissociates in either Pt_2^- and N_2 or Pt_1^- + PtN_2. The metal dimer results from a metal-ligand bond disrupture while the Pt atom results from an intermetallic bond breakage

(I) $Pt_2(N_2)^- + 1.5\ eV \rightarrow Pt_1^- + Pt(N_2)$;

(II) $Pt_2(N_2)^- + 1.5\ eV \rightarrow Pt_2^- + N_2$.

The negative charge locates in both cases at the metal fragment as the electron affinity of the Pt-atom and the dimer is quite high, namely 2.1 and 1.9 eV (see the adiabatic peak of Pt_1^- and Pt_2^- in Fig. 2).

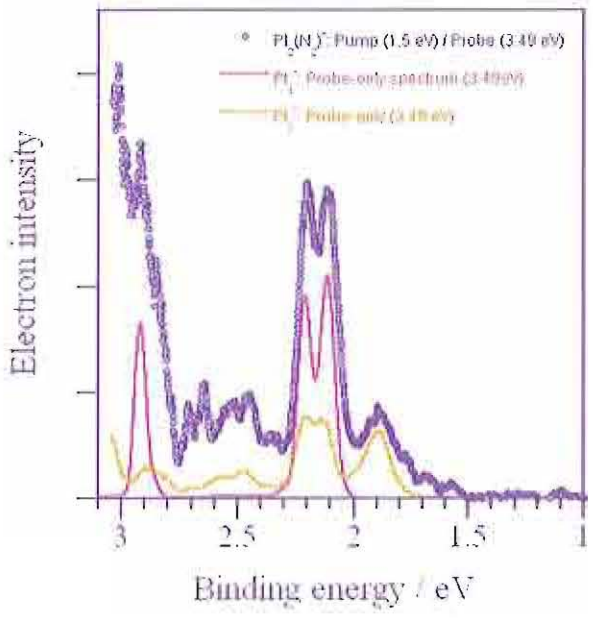

FIG. 2: Pump-probe photoelectron spectrum of $Pt_2(N_2)^-$. For this spectrum a Ti:Sa laser is synchronized with a frequency-doubled Nd:YAG laser. The pump photon is 1.5 eV (Ti:Sa) while the probe photon in this case is 3.49 eV (Nd:YAG). Due to the pulse width of the Nd:YAG laser a delay of a few ns is intrinsically given. The photodetachment spectra of Pt_1^- and Pt_2^- have been taken with the Nd:YAG laser alone. Note the similarity between the time-resolved spectrum of $Pt_2(N_2)^-$ and the spectra of the two metal fragments.

The dissociation is initiated by a single pump photon as shown by the dependence of the fragment-peak intensity on the pump power. The fragment peaks do not change either their envelope or energy. Only the detachment peak of the final product, i.e. the completely dissociated fragment, is observed. Intermediate structures, where the bond is elongated but not disrupted, can not be identified in the spectra. This indicates statistical photodesorption processes where the energy of the pump photon first thermalizes over all internal vibronic degrees of freedom, before the thermalized energy is statistically reunified on a particular reaction coordinate leading to fragmentation. Therefore, the evolution of the fragment peak at 2.15 eV has been interpreted by a statistical photodesorption process and a dissociation time constant $\tau_{diss} = (78 \pm 25)$ ps has been deduced. Using the experimentally determined rate constant, $k(E^*) = 1/\tau_{diss}$, the intermetallic dissociation energy can be estimated from a quantum-statistical RRK analysis (Rice-Ramsperger-Kassel). In this approach the Pt-Pt dissociation energy is estimated to be (0.4±0.1) eV [5].

Density-functional calculations predict a linear geometry ($C_{\infty v}$) of $Pt_2(N_2)$ and $Pt_2(N_2)^-$ as well. The calculated electron affinity of the neutral cluster (3.2 eV) agrees reasonably well with the experimental value of (2.8±0.2) eV. The frontier orbitals of both the anion and the neutral are σ-like and non degenerate. The HOMO of the anion is strongly antibonding with respect to the intermetallic Pt-Pt bond which makes the observed fragmentation of the intermetallic bond plausible. In contrast to $Au_2(CO)$ [2, 6] the LUMO of $Pt_2(N_2)$ is non degenerate. Therefore no bending occurs in $Pt_2(N_2)^-$ while $Au_2(CO)^-$ is bent by ≈ 132°. The bending of the latter is due to a Renner-Teller distortion, because in the linear geometry neutral $Au_2(CO)$ has degenerate frontier orbitals.

[1] A. Sanchez, S. Abbet, U. Heiz, W.D. Schneider, H. Häkkinen, R.N. Barnett, U. Landman, J. Phys. Chem. **A 103**, 9573 (1999); L. D. Socaciu, J. Hagen, T.M. Bernhardt, L. Wöste, U. Heiz, H. Häkkinen, U. Landman, J. Am. Chem. Soc. **125**, 10437 (2003).

[2] G. Lüttgens, N. Pontius, P.S. Bechthold, M. Neeb, and W. Eberhardt, Phys. Rev. Lett. **88**, 076102 (2002).

[3] N. Pontius, M. Neeb, G. Lüttgens P.S. Bechthold, W. Eberhardt, Phys. Rev. **B. 67**, 034425 (2003).

[4] N. Pontius, P.S. Bechthold, M. Neeb, W. Eberhardt, Appl. Phys. **B 71**, 351 (2000).

[5] M. Neeb, J. Stanzel, N. Pontius, W. Eberhardt, G. Lüttgens, P.S. Bechthold, C. Friedrich, J. Electron Spectr. Rel. Phen., **144-147**, 91-96 (2005)

[6] H. Häkkinen, U. Landman, J. Am. Chem. Soc. **123**, 9704 (2001).

Condensed Matter

From Matter to Materials

Rubber friction on wet rough substrates at low sliding velocity: the sealing effect
B.N.J. Persson

Influence of frozen capillary waves on contact mechanics
B.N.J. Persson

Pressure dependence of the Boson peak in amorphous materials
V.L. Gurevich, D.A. Parshin, and H.R. Schober

Phase Field Modeling of Fast Crack Propagation
R. Spatschek, M. Hartmann, E. Brener, and H. Müller-Krumbhaar, K. Kassner

Velocity selection problem for combined motion of melting and solidification fronts
Efim A. Brener and D. E. Temkin

Plasticity of the complex metallic alloy phase $Al_{13}Co_4$
M. Heggen and M. Feuerbacher

Strategies for Aberration Control in Sub-Angstrom HRTEM
A. Thust, J. Barthel, L. Houben, C.L. Jia, M. Lentzen, K. Tillmann, and K. Urban

Atomic configuration at a $SrTiO_3$ dislocation core
C.L. Jia et al.

Contrast Transfer Theory for Transmission Electron Microscopes Equipped with a Wien-Filter Monochromator
M. Lentzen and A. Thust

Metadislocation reactions and metadislocation networks
M. Heggen and M. Feuerbacher

[010] dislocations in the complex metallic alloy ξ'-Al-Pd-Mn
M. Feuerbacher

Scaling effects in nanocrystalline $BaTiO_3$ and $NaNbO_3$
C. Pithan, Y. Shiratori, R. Waser, A. Magrez, K. Kasezawa

The reaction of high density $SrTi_{0.6}Fe_{0.4}O_{(3-\delta)}$ ceramics with traces of propane in oxidizing atmospheres
P. Meuffels

Diffusion and jump-length distribution in liquid and amorphous $Cu_{33}Zr_{67}$
M. Kluge and H. R. Schober

Condensate Formation and Vortex Generation in Bose Gas upon Cooling
E. A. Brener, S.V. Iordanskii, R.B. Saptsov

Deriving nonequilibrium interface kinetics from variational principles
Robert Spatschek

Multilayer relaxation sequence of stepped Cu surfaces
J.L.F. da Silva, K. Schroeder, S. Blügel

Vertical attachment of molecules via carboxylate group: Formate on Cu(110)
N. Atodiresei, K. Schroeder, S. Blügel

Rubber friction on wet rough substrates at low sliding velocity: the sealing effect

B.N.J. Persson[1]

[1] *IFF, FZ-Jülich, 52425 Jülich, Germany*

Rubber friction on wet rough substrates at low velocities is typically $20-30\%$ smaller than for the corresponding dry surfaces. This cannot be due to hydrodynamics, and we propose a novel explanation based on a sealing effect exerted by rubber on substrate "pools" filled with water. Water effectively smoothens the substrate, reducing the major friction contribution due to induced viscoelastic deformations of the rubber by surface asperities. The theory is illustrated with applications related to tire-road friction.

81.40.Pq, 62.20-x

The study of sliding friction has attracted increasing interest during the last decade thanks also to the development of new experimental and theoretical approaches[1]. While some understanding has been gained about the origin and qualitative properties of friction, first principle calculations of friction forces (or friction coefficients) for realistic systems are in general impossible. The basic reason for this is that friction usually is an interfacial property, often determined by the last few uncontrolled monolayers of atoms or molecules at the interface. An extreme illustration of this is diamond friction: the friction between two clean diamond surfaces in ultra high vacuum is huge because of the strong interaction between the surface dangling bonds. However, when the dangling bonds are saturated by monolayers of hydrogen atoms (as they invariably are in real life conditions), friction becomes extremely low[2]. Since most surfaces of practical use are covered by several monolayers of contamination molecules of unknown composition, the quantitative prediction of sliding friction coefficients is generally impossible. An exception to this may be rubber friction on rough surfaces, which is the topic of the present paper.

Rubber friction is a topic of extreme practical importance, e.g., in the context of tires, wiper blades, conveyor belts and sealings. Rubber friction has several remarkable properties. First, it may be huge, sometimes resulting in friction coefficients much higher than unity. Secondly, on very rough surfaces, e.g., in the context of a tire sliding on a road surface, it is mainly a bulk property of the rubber. That is, the substrate (or road) asperities exert pulsating forces onto the rubber surface which, because of its high internal friction at the appropriate frequencies, results in a large dissipation of energy in the rubber bulk (hysteretic contribution)[3, 4]. Finally, rubber friction is very sensitive to temperature because of the strong temperature dependence of the viscoelastic bulk properties of rubber-like materials.

For very rough surfaces the adhesive contribution to rubber friction will be much smaller than for smooth surfaces, mainly because of the small contact area. For a tire in contact with a road surface, for example, the actual contact area between the tire and the substrate is typically only $\sim 1\%$ of the nominal footprint contact area[3]. We have shown recently that the observed friction when a tire is sliding on a dry road surface can be calculated accurately by assuming it to be due entirely to internal damping in the rubber (the hysteretic contribution)[3, 4]. This theory takes into account the pulsating forces acting on the rubber surface from road asperities on many different length scales, from the length scale $\lambda_0 \sim 1$ cm, corresponding to the largest road asperities, down to micro-asperities characterized by a wavelength λ_c of order $\sim 1-10$ μm (theory shows that shorter wavelength roughness is unimportant), and gives friction coefficients of order unity, as indeed observed experimentally.

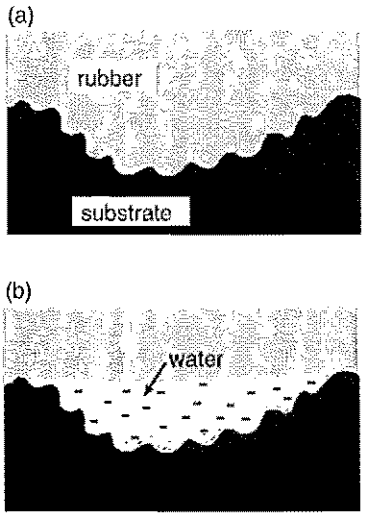

FIG. 1: A rubber block sliding on a rough hard substrate. (a) The rubber penetrates into a large substrate valley and explores the short wavelength roughness in the valley. The pulsating rubber deformations induced by the short-wavelength roughness contribute to the friction force. (b) On a wet substrate the water trapped in the large valley forms a pool preventing the rubber from penetrating into the valley. It will hence remove the valley contribution to the friction force This rubber *sealing effect* reduces the sliding friction.

Here I study rubber friction at low sliding velocities on wet rough substrates, where it has been observed that the friction typically is 20 – 30% smaller than for the corresponding dry surfaces. We have recently shown that this cannot be a hydrodynamic effect (see also below)[5], and in this paper we propose a novel explanation based on the rubber sealing off pools, namely regions on the substrate filled with water as shown in Fig.1. The water effectively smoothens the substrate surface, and thus reduces the viscoelastic deformation contribution to the rubber friction from the surface asperities.

The contribution to rubber friction from the viscoelastic deformation of the rubber surface by the substrate asperities depends only on the complex frequency-dependent viscoelastic modulus $E(\omega)$ of the rubber and on the substrate surface roughness power spectrum $C(q)$. The power spectra of a dry asphalt road is shown in Fig. 2 (upper curve).

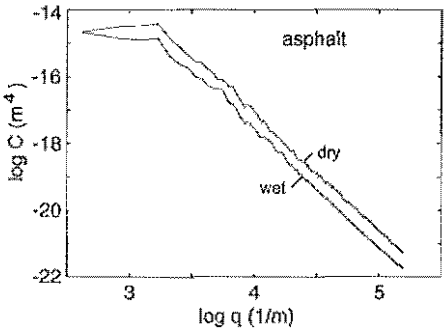

FIG. 2: The logarithm of the surface roughness power spectra $C(q)$ for a dry and a wet asphalt road surface, as a function of the logarithm of the wavevector q.

In general, the hysteretic contribution to rubber friction increases with increasing magnitude of $C(q)$. However, the friction depends on $C(q)$ over a wide range of wave vectors q. For example, the rubber friction on asphalt road surfaces depends on $C(q)$ for $q_0 < q < q_1$, where typically $q_0 \approx 10^3$ m^{-1} and $q_1 \approx 10^6$ m^{-1}. For a wet road surface, the rubber will seal some surface areas filled with water (pools) as indicated in Fig. 1, and this leads to an effective smoothening of the substrate and to a reduced power spectrum. The power spectra of a wet asphalt road surface (the same asphalt road considered above), is shown in Fig. 2 (lower curve).

Consider a tire rolling or sliding on a wet road surface. In Ref. [5] we have shown at low velocities (say v < 60 km/h), there is a negligible hydrodynamic water build up between the tire and the road surface. Thus, if v < $(\sigma/\rho)^{1/2}$, where σ is the perpendicular stress in the tire road contact area and ρ the water mass density, there is sufficient time for the water to be *squeezed* from the contact regions between the tire and the road surface, except for water trapped in road cavities and sealed off by the road-rubber contact at the upper boundaries of the cavities (see Fig. 1). Thus, in what follows we will only focus on the smoothing effect on the road profile by the sealed off water pools.

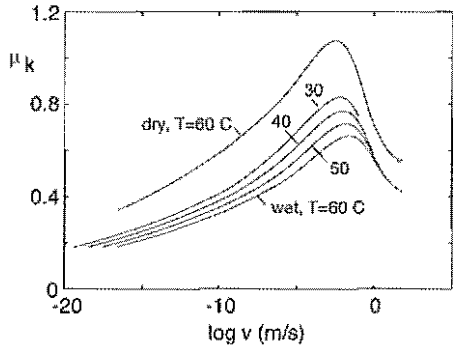

FIG. 3: Kinetic friction coefficient as a function of the logarithm of the sliding velocity, calculated for a standard tread compound and an asphalt substrate

We now present numerical results related to tire friction on dry and wet substrates, calculated using the theory presented in Ref. [3, 4]. In Fig. 3 we show the kinetic friction coefficient calculated for the dry surface at $T = 60°$ C (a typical tire temperature during driving on a dry road), and for the wet surface at four different temperatures, namely $T = 30$, 40, 50, and 60° C. Note that on a wet road the tire temperature is generally lower than on the dry surface, typically of order 30° C. The decreased friction with increasing temperature shown in Fig. 3 is always observed for rubber, and result from the shift in the viscoelastic spectrum to higher frequencies with increasing temperature (temperature makes rubber more elastic and less viscous), which in turn reduces rubber friction.

[1] B.N.J. Persson, *Sliding Friction: Physical Principles and Applications* 2nd edn (Heidelberg: Springer, 2000)
[2] R.J.A. van der Oetelaar and C.F.J. Flipse, Surface Science **384**, L828 (1997).
[3] B.N.J. Persson, J. Chem. Phys. **115**, 3840 (2001).
[4] B.N.J. Persson, to be published
[5] B.N.J. Persson, U. Tartaglino, O. Albohr and E. Tosatti, to be published

Influence of frozen capillary waves on contact mechanics

B.N.J. Persson
IFF, FZ-Jülich, 52425 Jülich, Germany

Free surfaces of liquids exhibit thermally excited (capillary) surface waves. We show that the surface roughness which results from capillary waves when a glassy material is cooled below the glass transition temperature can have a large influence on the contact mechanics between the solids. The theory suggest a new explanation for puzzling experimental results [L. Bureau, T. Baumberger and C. Caroli, arXiv:cond-mat/0510232] about the dependence of the frictional shear stress on the load for contact between a glassy polymer lens and flat substrates. It also lend support for a recently developed contact mechanics theory.

Many technological applications require surfaces of solids to be extremely smooth. For example, window glass has to be so smooth that no (or negligible) diffusive scattering of the light occur (a glass surface with strong roughness on the length scale of the light wavelength will appear white and non-transparent because of diffusive light scattering). For glassy materials, e.g., silicate glasses, or glassy polymers, e.g., Plexiglas, extremely flat surfaces can be prepared by cooling the liquid from well above the glass transition temperature T_g, since in the liquid state the surface tension tends to eliminate (or reduce) short-wavelength roughness.

However, surfaces of glassy materials prepared by cooling the liquid from a temperature above T_g cannot be perfectly (molecularly) smooth, but exhibit a fundamental minimum surface roughness, with a maximum height fluctuation amplitude of typically 10 nm, which cannot be eliminated by any changes in the cooling procedure. The reason is that at the surface of a liquid, fluctuations of vertical displacement are caused by thermally excited capillary waves (ripplons). At the surface of very viscous supercooled liquids near the glass transition temperature these fluctuations become very slow and are finally frozen in at the glass transition[1].

The roughness derived from the frozen capillary waves is unimportant in many practical applications, e.g., in most optical applications as is vividly evident for glass windows. However, in other applications they may be of profound importance. Here I show that they are of crucial importance in contact mechanics, even for elastically relative compliant solids such as Plexiglas (PMMA). The results presented below suggest a new explanation for the puzzling experimental result of Bureau et al[2] for PMMA, and in addition lends support for a recently developed contact mechanics theory[3].

The most important property of a rough surface is the surface roughness power spectrum which is the Fourier transform of the height-height correlation function:

$$C(q) = \frac{1}{(2\pi)^2}\int d^2x\ \langle h(x)h(0)\rangle e^{-iq\cdot x}$$

Here $z = h(x)$ is the height of the surface at the point $x = (x, y)$ above a flat reference plane chosen so that $\langle h(x)\rangle = 0$. The angular bracket $\langle ...\rangle$ stands for ensemble averaging. Neglecting gravity, the surface roughness power spectra due to capillary waves is of the form

$$C(q) = \frac{1}{(2\pi)^2}\frac{k_BT}{\gamma q^2 + \kappa q^4} \qquad (1)$$

where γ is the surface tension, κ the bending stiffness, and ρ the mass density of the glassy melt. The mean of the square of the surface height fluctuation is given by

$$\langle h^2\rangle = \int d^2q\ C(q) = \frac{k_BT}{2\pi\gamma}\ln\left[\frac{q_1}{q_0}\left(\frac{q_0^2+q_c^2}{q_1^2+q_c^2}\right)^{1/2}\right] \qquad (2)$$

where $q_c = (\gamma/\kappa)^{1/2}$ is a cross-over wavevector. For the polymer surface which interests us below (PMMA), Eq. (2) gives the rms roughness ≈ 0.5 nm which correspond to a maximum roughness amplitude of about 3 nm. I will now show that even this small roughness has a large influence on the contact mechanics.

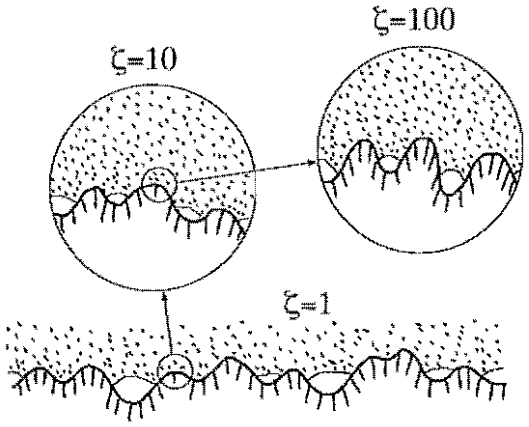

FIG. 1: An elastic (e.g., rubber) block (dotted area) in adhesive contact with a hard rough substrate (dashed area). The substrate has roughness on many different length scales and the rubber makes partial contact with the substrate on all length scales. When a contact area is studied at low magnification ($\zeta = 1$) it appears as if complete contact occurs in the macro asperity contact regions, but when the magnification is increased it is observed that in reality only partial contact occurs.

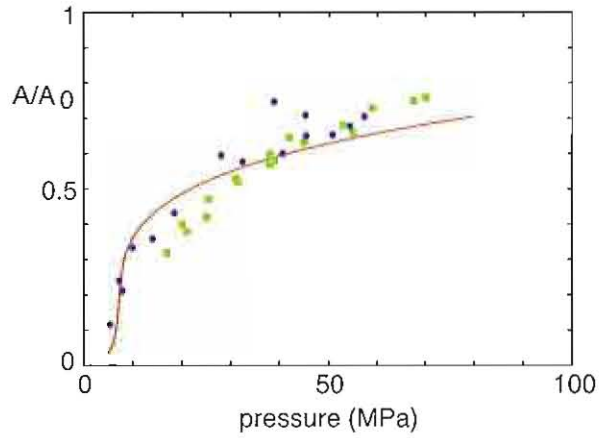

FIG. 2: Solid line: the calculated relative contact area as a function of the (nominal) pressure p_{nom}. Circles: the normalized, (nominal) shear stress σ/σ_f for PMMA sliding on TMS as a function of the (nominal) pressure. The nominal shear stress σ has been divided by $\sigma_f = 50$ MPa, which is the (measured) shear stress in the area of real contact (see text). Squares: the normalized, (nominal) shear stress σ/σ_f (with $\sigma_f = 5$ MPa) for PMMA sliding on OTS as a function of the (nominal) pressure.

Recently, a contact mechanics theory has been developed which is valid not only when the area of real contact is small compared to the nominal contact area, but which is particularly accurate when the squeezing force is so high that nearly complete contact occurs within the nominal contact area[3, 4]. All other contact mechanics theories were developed for the case where the area of real contact is much smaller than the nominal contact area. The theory developed in Ref. [3, 4] can also be applied when the adhesional interaction is included. The theory describes how the (apparent) contact between two solids change with increasing resolution ζ.

Fig. 1 shows the contact between two solids at increasing magnification ζ. At low magnification ($\zeta = 1$) it looks as if complete contact occurs between the solids at many macro asperity contact regions, but when the magnification is increased smaller length scale roughness is detected, and it is observed that only partial contact occurs at the asperities. In many cases the local pressure at asperity contact regions at high magnification will become so high that the material yields plastically before reaching the atomic dimension. In these cases the size of the real contact area will be determined mainly by the yield stress of the solid.

In the experiment by Bureau et al.[2], the PMMA lens were prepared by cooling a liquid drop of PMMA from 250 °C to room temperature. In the liquid state the surface fluctuations of vertical displacement are caused by thermally excited capillary waves (ripplons). When the liquid is near the glass transition temperature T_g (about 100 °C for PMMA), these fluctuations become very slow and are finally frozen in at the glass transition. Thus, the temperature T in (1) is not the temperature where the experiment was performed (room temperature), but rather the glass transition temperature T_g.

The solid line in Fig. 2 shows the calculated relative contact area as a function of the (nominal) pressure $p_{nom} = F_N/A_0$ (where F_N is the squeezing force). In the calculation we have used the equations above with the measured elastic (Young) modulus $E = 2.9$ GPa and surface tension $\gamma = 0.04$ J/m^2. We have also used the glass transition temperature $T_g \approx 370$ K, the short-distance cut-off wavevector $q_1 = 7 \times 10^9$ m^{-1} and $q_c = 1.7 \times 10^9$ m^{-1}. The cross-over wavevector q_c (or the bending stiffness κ) has not been measured for PMMA, but has been measured for other systems. Thus, for alkanes at $T \approx 100$ °C for C20 and C36, $q_c \approx 4.4 \times 10^9$ and $\approx 2.7 \times 10^9$ m^{-1}. The interfacial binding energy $\Delta\gamma$ can be estimated using $\Delta\gamma \approx 2(\gamma_1\gamma_2)^{1/2} \approx 0.07$ J/m^2, where $\gamma_1 = \gamma \approx 0.04$ J/m^2 is the surface energy of PMMA and $\gamma_2 \approx 0.02$ J/m^2 the surface energy of the (passivated) substrate. In the calculations we used $\Delta\gamma = 0.06$ J/m^2.

If one assumes that, in the relevant pressure range (see below), the frictional shear stress σ_f between PMMA and the substrate is essentially independent of the normal stress p in the asperity contact regions, then the calculated curve in Fig. 2 is also the ratio between the nominal (or apparent) shear stress σ and the true stress σ_f; $A/A_0 = \sigma/\sigma_f$ (note: the friction force $F_f = \sigma_f A = \sigma A_0$).

The circles and squares in Fig. 2 show the measured data of Bureau et al.[2] for σ/σ_f. They performed experiments where a PMMA lens, prepared by cooling a liquid drop of PMMA, was slid on silicon wafers (which are nearly atomically smooth) covered by a grafted silane layer. Two different types of alkylsilanes were employed for surface modification, namely a trimethylsilane (TMS) and octadecyltrichlorosilane (OTS). The circles in Fig. 2 are the shear stress, divided by $\sigma_f = 50$ MPa, for PMMA sliding on TMS as a function of the (nominal) pressure p_{nom}. The shear stress $\sigma_f = 50$ MPa was deduced from multi-contact experiments (where the local pressure in the asperity regions is so high as to give rise to local plastic deformation) using $\sigma_f \approx \sigma H/p_{nom}$, where $H \approx 300$ MPa is the hardness (yield stress) of PMMA as determined from indentation experiments. This equation follows from $\sigma A_0 = \sigma_f A$ and $AH = A_0 p_{nom}$. The squares in Fig. 2 show σ/σ_f for PMMA sliding on OTS as a function of the (nominal) pressure p_{nom}.

[1] J. Jäckle and K. Kawaski, J. Phys.: Condens. Matter **7**, 4351 (1995).
[2] L. Bureau, T. Baumberger and C. Caroli, arXiv:cond-mat/0510232 v1.
[3] B.N.J. Persson, J. Chem. Phys. **115**, 3840 (2001).
[4] B.N.J. Persson, Eur. Phys. J. **E8**, 385 (2002).

Pressure dependence of the Boson peak in amorphous materials

V. L. Gurevich[1], D. A. Parshin[2], and H. R. Schober[3]
A. F. Ioffe Institute,Saint Petersburg, Russia[1]
Saint Petersburg State Technical University,
Saint Petersburg, Russia[2]
Institute IFF-Theory III[3]
(Dated: December 21, 2005)

One of the most characteristic properties of amorphous materials and glasses is the "boson peak", a maximum in the inelastic scattering intensity at low frequencies where the crystalline counterparts show only a much lower and frequency independent intensity due to the sound waves (Debye contribution). The position and intensity of the boson peak are highly susceptible to pressure which could not be explained by previous theories. We have shown previously that any broad distribution of low frequency quasi-localized (resonant) vibrations results in a boson peak. Such quasi-localized vibrations are a signature of structural disorder. Exploiting the theory further we find a characteristic shift of the boson peak frequency under applied pressure, $\omega_b \propto p^{1/3}$. This pressure dependence has been verified in a recent experiment giving further support to our interpretation.

I. INTRODUCTION

One of the most characteristic properties of glasses is a maximum in the low frequency part of their inelastic scattering intensities. [1] This maximum, the Boson peak (BP), originates from a maximum of the ratio $g(\omega)/\omega^2$ where $g(\omega)$ is the density of vibrational states which itself often has no corresponding maximum. The BP shows an excess of low frequency vibrations above the Debye contribution of the sound waves. It is observed in experiments on Raman scattering of light and inelastic neutron scattering within the frequency interval 0.5 — 2 THz as well as in the temperature dependence of the specific heat. It is considered to be one of the universal properties of glasses and is found also in a number of other disordered systems — see Ref. [2] and references therein where also other approaches to the problem of the Boson peak are discussed.

For the proper interpretation of the BP, the key problem is the nature of the vibrations that contribute to $g(\omega)$. Since the term BP frequently is used for any peak in the low frequency inelastic scattering intensity one has to distinguish between different cases. In some materials the BP is ascribed to low lying optical or transverse acoustic modes of parental crystals or to librations of some molecules in plastic crystals. If these excitations have a small frequency spread they will show as a peak in $g(\omega)$. The role of disorder is merely to broaden modes which exist already without disorder.

In the opposite case the excess of low frequency modes is caused by disorder itself. A simple example is realized in a metallic like model glass where the the parent crystal is fcc [3]. In the present paper we discuss this latter case. Between these two extreme cases of well defined low frequency modes, broadened by disorder, and no such modes before disorder, there is a range of materials having aspects of both.

In a glass one has a finite concentration of quasi-localized vibrations (QLV's). As discussed in our paper[2], this has a profound effect on their density of states (DOS). The interaction of the QLV's with the sound waves induces an elastic dipole interaction between them. First, the interaction of soft QLV's with surrounding QLV's of higher frequency may lead in harmonic approximation to unstable modes. Stability is restored by the anharmonic terms. This leads to a linear density of states, $g(\omega) \propto \omega$, for $\omega < \omega_c$ where ω_c is determined by the typical interaction strength and typically is several times the frequency of the boson peak maximum, ω_b.

Secondly, these renormalized low frequency QLV's interact with each other. In effect this means that the QLV's are subject to random forces, f , (internal forces). Due to the high susceptibility of low frequency vibrations their low frequency DOS is changed to $g(\omega) \propto \omega^4$ for $\omega < \omega_b$. This is a general property of the low frequency DOS of non-Goldstone bosonic excitations in random media [4]. It is associated with the so-called sea-gull singularity in the distribution of the stiffness constants of the QLV [5, 6] in the soft potential model.

By the crossover between the two limiting regimes of the DOS the BP is formed and obtains a "universal" shape. The frequency of the BP, ω_b, is determined by the interaction strength and thus by the characteristic value of the internal forces, f .

Under an applied hydrostatic pressure additional forces are exerted on the QLV which will shift the boson peak. From Hook's law one gets

$$\varepsilon_{ik} = -(\mathrm{P}/3K)\delta_{ik} \qquad (1)$$

where ε_{ik} is the strain tensor and $1/K$ is the compressibility of the glass.

The interaction of a QLV with the strain is bilinear

$$\mathcal{H}_{\mathrm{int}} = \Lambda_{ik}\varepsilon_{ik}\mathrm{x} = -(\mathrm{P}/3K)\Lambda_{ii}\mathrm{x} \qquad (2)$$

where Λ_{ik} is the deformation potential tensor and x is the coordinate of the QLV. For simplicity we will write in the following Λ instead of Λ_{ii}. Thus the additional contribution to the random force due to applied pressure is proportional to the pressure

$$\Delta\mathrm{f} = (\mathrm{P}/3K)\Lambda. \qquad (3)$$

The deformation potential Λ of a QLV is a random quantity. In particular, it has a random sign, so that the corresponding distribution function $D(\Lambda)$ is an even function of Λ. As a result, the distribution of the random forces $\tilde{f}$ in the glass remains an even function of $\tilde{f}$ when the pressure is applied.

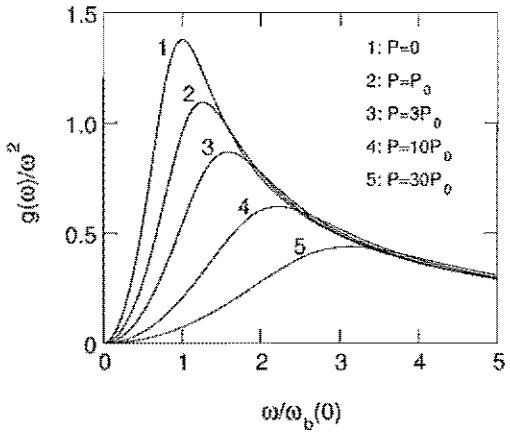

FIG. 1: Boson peak intensity for different applied pressures, excluding the low frequency Debye contribution. Lorentzian distributions were assumed for both internal and pressure induced forces.

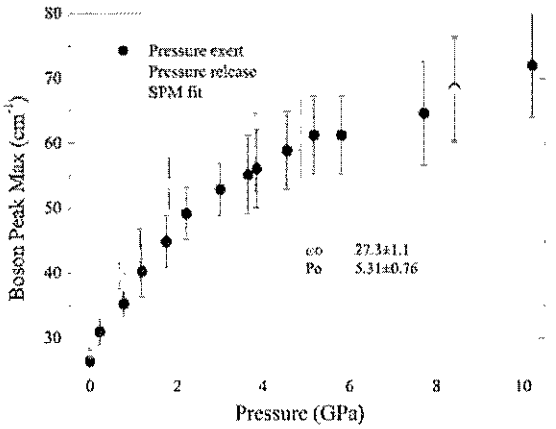

FIG. 2: Boson peak frequency in As_2S_3 as function of pressure measured by Raman scattering. Solid line: present theory. (K. S. Andrikopoulos, D. Christofilos, G. A. Kourouklis and S. N. Yannopolous to be published)

The total random force on the QLV, $\tilde{f}$, is then the sum of two contributions the internal forces f , present before pressure was applied, and the pressure induced forces |Deltaf

$$\tilde{f} = f + \Delta f . \tag{4}$$

If the distribution of the internal forces f is $Q(f)$ then the distribution of the total random force $\tilde{f}$ in a glass under pressure is given by the convolution

$$F_P(\tilde{f}) = \int_{-\infty}^{\infty} d\Lambda\, Q\left(\tilde{f} - \frac{\Lambda}{3K}P\right) D(\Lambda). \tag{5}$$

For $P = 0$ it reduces to the unperturbed distribution $Q(f)$ since the distribution $D(\Lambda)$ is normalized to unity.

The evaluation evolves some lengthy but straightforward mathematics, see Ref. [7]. Fig. 1 shows the resulting dependence of the boson peak excess intensity. For the shift of the of the maximum frequency we find

$$\omega_b(P) = \omega_b(0)\left(1 + \frac{|P|}{P_0}\right)^{1/3}. \tag{6}$$

Here we assumed Lorentzian force distributions. The dependence on the exact shape of the distribution is weak. in a recent experiment on As_2S_3 this dependence of ω_b on pressure has been quantitatively verified, Fig. 2.

The boson peak intensity is predicted to decay $\propto 1/\omega_b$ which is also in good agreement with experiment.

This is the first time that a theory of the boson peak has been able to predict the pressure shift. This gives strong supporting evidence to our explanation of the BP in terms of interacting QLVs. In previous work we have shown that these QLV are linked to tunneling and relaxations in glasses. Thus our work is a major step towards a unified picture of glassy dynamics.

[1] *Amorphous Solids. Low Temperature Properties*, edited by W. A. Phillips, (Springer-Verlag, Berlin:1981).
[2] V. L. Gurevich, D. A. Parshin and H. R. Schober, Phys. Rev. B **67**, 094203 (2003).
[3] H. R. Schober, J. Phys.: Condens. Matter **16**, S2659 (2004).
[4] V. Gurarie and J. T. Chalker, Phys. Rev. Lett. **89**, 136801 (2002); Phys. Rev. B **68**, 134207 (2003).
[5] M. A. Il'in, V. G. Karpov, D. A. Parshin, Sov. Phys. JETP **65**, 165 (1987).
[6] U. Buchenau, Yu. M. Galperin, V. L. Gurevich, and H. R. Schober, Phys. Rev. B **43**, 5039 (1991).
[7] V. L. Gurevich, D. A. Parshin and H. R. Schober, Phys. Rev. B **71**, 014209 (2005).

Phase Field Modeling of Fast Crack Propagation

Robert Spatschek, Miks Hartmann, Efim Brener, and Heiner Müller-Krumbhaar
Institut für Festkörperforschung, Forschungszentrum Jülich, D-52425 Jülich, Germany

Klaus Kassner
Institut für Theoretische Physik, Universität Magdeburg, D-39016 Magdeburg, Germany

We present a continuum theory which predicts the steady state propagation of cracks. The theory overcomes the usual problem of a finite time cusp singularity of the Grinfeld instability by the inclusion of elastodynamic effects which restore selection of the steady state tip radius and velocity. We developed a phase field model for elastically induced phase transitions; in the limit of small or vanishing elastic coefficients in the new phase, fracture can be studied. The simulations confirm analytical predictions for fast crack propagation.

Understanding the day-to-day phenomenon of fracture is a major challenge for solid state physics and materials science. Usually, the motion of cracks is understood on the level of breaking bonds at sharp tips, and obviously theoretical predictions depend sensitively on the underlying empirical models of the atomic properties (see for example [1]). Plastic effects, however, lead to extended crack tips (finite tip radius r_0), and it is conceivable that for example fracture in gels can be described macroscopically. Then a full modeling of fracture should not only determine the crack speed but also the crack shape self-consistently.

Recent phase field models go beyond the microscopic limit of discrete models with broken translational and rotational symmetry, and encompass much of the expected behavior of cracks [2]. However, the scale of the appearing patterns is always dictated by the phase field interface width, and thus these models have problems in the sharp interface limit. Other descriptions are based on macroscopic equations of motion but suffer from inherent finite time singularities which do not allow steady state crack growth unless the tip radius is limited by the phase field interface width [3].

It is therefore highly desirable to look for minimal models of fracture which are free from microscopic details and which are based on well established thermodynamical concepts. This is also motivated by experimental results showing that many features of crack growth are rather generic [4]; among them is the saturation of the steady state velocity appreciably below the Rayleigh speed and a tip splitting for high applied tension.

Based on our previous publication [5], we propose an approach which describes crack growth in brittle materials by a phase transition model. In fact, it produces a non-trivial dynamical selection of the radius of the crack tip. Instead of cracks filled with vacuum, we consider for the moment a soft condensed phase inside the crack which is growing at the expense of a brittle material [3].

The difference in the chemical potentials between two phases at an interface is $\Delta\mu = \Omega\,(\sigma_{jk}\epsilon_{jk}/2 - \gamma\kappa)$, provided that the soft phase is stress free because of negligible elastic moduli. Then the surface of the crack is free of normal and shear stresses. We assume for simplicity the mass density ρ to be equal in both phases and the elastic displacements to be continuous at the interface, which means that the two phases are coherent. Also, we assume a two-dimensional geometry. The interfacial energy per unit area is γ, and the interface curvature κ is positive if the crack shape is convex. Ω is the atomic volume, σ_{jk} and ϵ_{ik} stress and strain tensor respectively.

For phase transitions, the motion of the interface is locally expressed by the normal velocity $v_n = D\Delta\mu/\gamma\Omega$ with a kinetic coefficient D with dimension $[D] = \mathrm{m}^2\mathrm{s}^{-1}$.

We developed a phase field code together with elastodynamics to describe phase transformations under stress, including for example also martensitic transformations. In the limit of vanishing shear modulus in one of the phases, this approach can be used to study melting and solidification processes which are induced by elastic forces [3]. For a very soft secondary phase, crack propagation can be studied in the framework of a continuum theory, since then the usual boundary conditions of vanishing normal and shear stress are recovered. Let ϕ denote the phase field with values $\phi = 0$ for the soft and $\phi = 1$ for the hard phase. The energy density contributions are $f_{el} = \mu(\phi)\epsilon_{ij}^2 + \lambda(\phi)(\epsilon_{ii})^2/2$ for the elastic energy, with $\mu(\phi) = h(\phi)\mu^{(1)} + (1-h(\phi))\mu^{(2)}$ and $\lambda(\phi) = h(\phi)\lambda^{(1)} + (1-h(\phi))\lambda^{(2)}$, where $h(\phi) = \phi^2(3-2\phi)$ interpolates between the phases and the superscripts denote the bulk values. The surface energy is $f_s(\phi) = 3\gamma\xi(\nabla\phi)^2/2$ with the interface width ξ. Finally, $f_{dw} = 6\gamma\phi^2(1-\phi)^2/\xi$ is the well-known double well potential. Thus the total potential energy is

$$U = \int dV\,(f_{el} + f_s + f_{dw})\,. \tag{1}$$

The equations of motion are

$$\rho\ddot{u}_i = -\frac{\delta U}{\delta u_i}, \qquad \frac{\partial\phi}{\partial t} = -\frac{D}{3\gamma\xi}\frac{\delta U}{\delta\phi}. \tag{2}$$

These equations lead in the limit $\xi \to 0$ to the correct sharp interface limit.

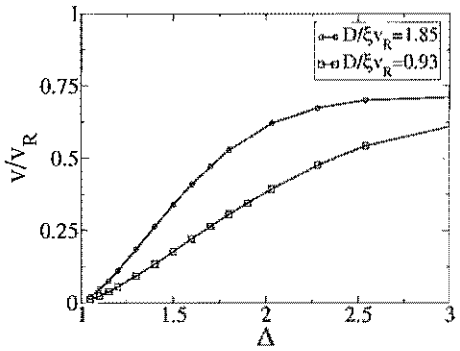

FIG. 1: Steady state velocity versus dimensionless driving force Δ; $\Delta = 1$ is the Griffith point.

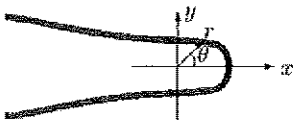

FIG. 2: Steady state growth of a crack in a strip, as obtained from phase-field simulations. A constant displacement is prescribed at the upper and lower boundary of the system.

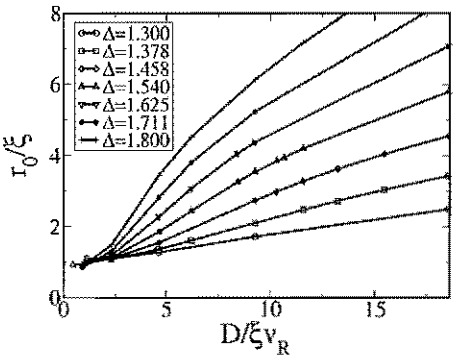

FIG. 3: Tip radius r_0 as function of the kinetic coefficient D for different driving forces Δ. In the intermediate linear regime the length scales are well separated.

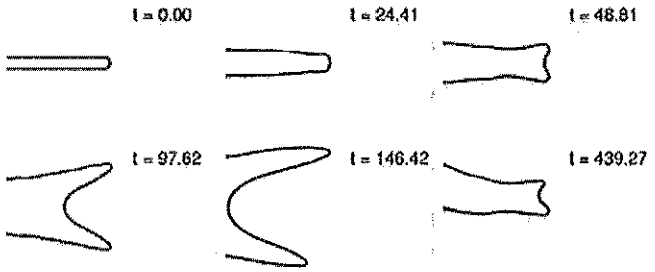

FIG. 4: Irregular tip splitting scenario. We used $D/\xi v_R = 1.85$ and $\Delta = 3.6$; the system size is 600×400. Time is given in units D/v_R^2. Minor numerical noise breaks the symmetry of the competing sidebranches.

First, we studied the growth of cracks in the vicinity of the Griffith point. Here, the tip radius in not determined by the length scale D/v_R but by the phase field interface width ξ. In the strip geometry, the dimensionless driving force is $\Delta = u_0^2(\lambda + 2\mu)/4L\gamma$ with the fixed vertical displacement u_0 applied to the strip. As a nontrivial test, the numerical results validate the analytical prediction of the Griffith point $\Delta = 1$ in the framework of the model, as the propagation velocity tends to zero (see Fig. 1).

The main goal was to approve that elastodynamics allows steady state growth without collapsing into the finite time cusp singularity of the Grinfeld instability [6], selecting both a non-zero tip radius and a propagation velocity below the Rayleigh speed. The simulations confirm this prediction, and a typical steady state shape is shown in Fig. 2. Obviously, the tip radius is not determined by the intrinsic phase field length scale ξ. This can also be seen in Fig. 3, where we plotted the steady state tip radius r_0 as function of the kinetic coefficient D for various driving forces Δ. Only for very low kinetic coefficients, the tip radius is cut off by the interface width ξ, otherwise it is fairly bigger; for high kinetic coefficients the saturation is induced by the system size. In between, however, the scales are well separated and the radius r_0 is a linear function of D, in good agreement with the theoretical analysis.

Snapshots of a typical tip splitting scenario for relatively high driving forces are shown in Fig. 4. Repeated irregular splitting of the crack tip occurs, followed by symmetrical growth of the sidebranches. After a while, one finger wins the competition, moves back to the center of the strip and can finally split again.

This work has been supported by the Deutsche Forschungsgemeinschaft under grant SPP 1120.

[1] J. Hauch et al., Phys. Rev. Lett. **82**, 3823 (1999).
[2] A. Karma, D. Kessler, and H. Levine, Phys. Rev. Lett. **87**, 045501 (2001); A. Karma and A. Lobkovsky, Phys. Rev. Lett. **92**, 245510 (2004); H. Henry and H. Levine, Phys. Rev. Lett. **93**, 105504 (2004).
[3] K. Kassner et al., Phys. Rev E **63**, 036117 (2001).
[4] J. Fineberg and M. Marder, Phys. Rep. **313**, 1 (1999).
[5] E. A. Brener and R. Spatschek, Phys. Rev. E **67**, 016112 (2003).
[6] R. J. Asaro and W. A. Tiller, Metall. Tran. **3**, 1789 (1972); M. A. Grinfeld, Sov. Phys. Dokl. **31**, 831 (1986).

Velocity selection problem for combined motion of melting and solidification fronts

Efim A. Brener and D. E. Temkin
Institut für Festkörperforschung, Forschungszentrum Jülich, D-52425 Jülich, Germany

We discuss a free boundary problem for two moving solid-liquid interfaces that strongly interact via the diffusion field in the liquid layer between them. This problem arises in the context of liquid film migration (LFM) during the partial melting of solid alloys. In the LFM mechanism the system chooses a more efficient kinetic path which is controlled by diffusion in the liquid film, whereas the process with only one melting front would be controlled by the very slow diffusion in the mother solid phase. The relatively weak coherency strain energy is the effective driving force for LFM. As in the classical dendritic growth problems, also in this case an exact family of steady-state solutions with two parabolic fronts and an arbitrary velocity exists if capillary effects are neglected [7]. We develop a velocity selection theory for this problem, including anisotropic surface tension effects.

The early observations of liquid film migration (LFM) were made during sintering in the presence of liquid phase [1] or during partial melting of alloys [2] (see [3] for a review). Nowadays LFM is a well established phenomenon of great practical importance. In LFM one crystal is melted and another one is solidified. Both solid-liquid interfaces move together with the same velocity. In the investigated alloys systems the migration velocity is of the order of $10^{-6} - 10^{-5}$ cm/s and it is controlled by the solute diffusion through a thin liquid layer between the two interfaces [4]. The migration velocity is much smaller than the characteristic velocity of atomic kinetics at the interfaces. Therefore, both solids should at the interfaces be locally in thermodynamic equilibrium with the liquid phase. On the other hand, these local equilibrium states should be different for the two interfaces to provide the driving force for the process. It is by now well accepted (see, for example, [3, 4]) that the difference of the equilibrium states at the melting and solidification fronts is due to the coherency strain energy, important only at the melting front because of the sharp concentration profile ahead the moving melting front (diffusion in the solid phase is very slow and the corresponding diffusion length is very small). The solute atoms diffuse ahead of the moving film and the coherency strain energy in such frontal diffusion zone arises from the solute misfit (for the schematic diagram of liquid film migration see Fig. 11 in [5]). If such a frontal diffusion zone is sufficiently small due to the very slow diffusion in the solid phase, the coherency strain energy is not relaxed due to the possible nucleation of misfit dislocations [3] (for an alternative point of view see also [6]). Thus, the equilibrium liquid composition at the melting front, which depends on the coherency strain energy and on the curvature of the front, differs from the liquid composition at the unstressed and curved solidification front. This leads to the necessary gradient of the concentration across the liquid film and the process is controlled by the diffusion in the film.

If only the melting front existed, the melting process would be controlled by the very slow diffusion in the mother solid phase and elastic effects would be irrelevant. In the LFM mechanism the system chooses a more efficient kinetic path which is controlled by the much faster diffusion in the liquid film. However, in this case the relatively weak coherency strain energy is involved as effective driving force for this process. In this respect the LFM mechanism is similar to other well-known phenomena such as diffusion induced grain boundary migration and cellular precipitation [3]. In these processes a relatively fast diffusion along the grain boundaries controls the kinetics and the coherency strain energy plays also a controlling role.

Thus, a theoretical description of LFM requires the solution of a free boundary problem for two combined moving solid-liquid interfaces with a liquid film in between. In Ref.[7] this problem was considered for simplified boundary conditions: the temperature and the chemical composition along each interface were kept constant. Their values are different for the melting and solidification fronts and differ from those far from the migrating liquid film. This means that any capillary, kinetic and crystallographic effects at the interfaces were neglected. It was found that under these simplified boundary conditions two co-focal parabolic fronts can move together with the same velocity. The situation is rather similar to a steady-state motion of one parabolic solidification front into a supercooled melt [8, 9] or one parabolic melting front into a superheated solid. In this approximation the Peclet numbers were found, but the steady-state velocity remained undetermined at that stage. Thus, the problem of velocity selection arises.

Solvability theory has been very successful in predicting certain properties of pattern selecting in dendritic growth and a number of related phenomena (see, for example, [10–12]). This theory has been extended to the three-dimensional case [13, 14]. We note that capillarity is a singular perturbation and the anisotropy of the surface energy is a prerequisite for the existence of the solution.

We discuss the two-dimensional problem of the steady-state motion of a thin liquid film during the process of isothermal melting of a binary alloy, see Fig.1. We assume that the diffusion in the solid phases is very slow

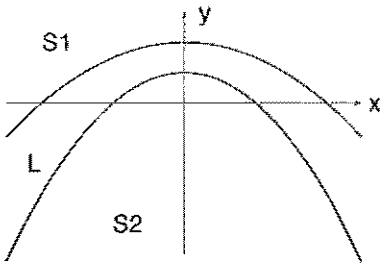

FIG. 1: Schematic presentation of two moving nearly parabolic fronts; S1 and S2 are the melting and growing solids, and L is the liquid film.

and the concentration c in the liquid film obeys the Laplace equation. We introduce the normalized concentration $C = (\mathrm{c} - \mathrm{c}_L)/(\mathrm{c}_L - \mathrm{c}_S)$ with c_L and c_S being the liquidus and solidus concentrations of the equilibrium phase diagram at a given temperature. Then the equilibrium concentration and the mass balance conditions at the solidification front read

$$C = \mathrm{d}_2 K_2, \qquad V_\mathrm{n} = -D\partial C/\partial \mathrm{n}. \tag{1}$$

At the melting front the equilibrium concentration is changed by the presence of the elastic coherency strain energy [3] and also the diffusional flux changes because in the solid ahead of the melting front the concentration is c_0 which is different from c_S:

$$C = -\mathrm{b}\Delta^2 - \mathrm{d}_1 K_1, \qquad V_\mathrm{n}(1-\Delta) = -D\partial C/\partial \mathrm{n}. \tag{2}$$

Here V_n is the normal velocity; D is the diffusion coefficient in the liquid film; K is the curvature assumed to be negative for the interfaces in Fig.1; $\Delta = (\mathrm{c}_0 - \mathrm{c}_S)/(\mathrm{c}_L - \mathrm{c}_S)$ is the dimensionless driving force; $\mathrm{b} = Y\Omega(\mathrm{da}/\mathrm{dc})^2/\mathrm{a}^2\mathrm{f}''_L$ is the dimensionless constant which describes the coherency strain energy [4], Ω is the atomic volume, Y is the bulk elastic modulus, a is the atomic constant, $\mathrm{f}_L(\mathrm{c})$ is the free energy of the liquid phase per atom, f''_L is the second derivative of $\mathrm{f}_L(\mathrm{c})$ at $\mathrm{c} = \mathrm{c}_L$; d_i are the anisotropic chemical capillary lengths:

$$\mathrm{d}_i(\theta) = \mathrm{d}_0[1 - \alpha\cos 4(\theta - \theta_i)], \quad \mathrm{d}_0 = \gamma\Omega/\mathrm{f}''_L(\mathrm{c}_L - \mathrm{c}_S)^2 \tag{3}$$

with the isotropic part of the surface energy γ and the anisotropy parameter $\alpha << 1$; θ is the angle between the normal to the interface n and the direction of motion, θ_i is the direction of the minimum of $\mathrm{d}_i(\theta)$ for each of the interfaces.

We measure all lengths in the units of the radius of curvature of the Ivantsov parabolic solidification front, R_2. Introducing a parabolic coordinates system,

$$y = (\eta^2 - \beta^2)/2, \qquad \mathrm{x} = \eta\beta, \tag{4}$$

we look for a solution of the Laplace equation for the concentration field $C(\eta, \beta)$. $C_0(\eta) = -\mathrm{b}\Delta^2(\eta - 1)/(\eta_0 - 1)$ is the solution without surface tension which satisfies the boundary conditions: $C_0(1) = 0$ and $C_0(\eta_0) = -\mathrm{b}\Delta^2$. The balance equations at the interfaces, $2P = 2P(1 - \Delta)\eta_0 = -\partial C_0/\partial\eta$ lead to the relations for the Peclet number and η_0:

$$\mathrm{P} = \frac{VR_2}{2D} = \frac{\mathrm{b}\Delta^2}{2(\eta_0 - 1)}, \quad \eta_0 = \sqrt{\frac{R_1}{R_2}} = \frac{1}{1-\Delta}. \tag{5}$$

These relations can also be obtained in the proper limit of Eqs.(27)-(28) of Ref. [7] and give the expressions for the radii of curvature for the two interfaces, R_1 and R_2, for a given velocity V which remains undetermined at this stage.

The surface tension plays a crucial role in the velocity selection problem. The details of the solution of this selection problem are given in [15]. The result is:

$$\sigma = \sigma^* \sim \Delta\alpha^{5/4}, \qquad \Delta << \sqrt{\alpha}.$$

$$\sigma = \sigma^* \sim \alpha^{7/4}, \qquad \Delta >> \sqrt{\alpha}, \tag{6}$$

where $\sigma = \mathrm{d}_0/\mathrm{P}\,R_2$ is the usual stability parameter.

In conclusion, we developed a selection theory for the process of liquid film migration where the strong diffusion interaction between melting and solidification fronts plays a crucial role. This process is very important in practical applications, in particular during sintering in the presence of the liquid phase [1, 3].

[1] D. N. Yoon, and W. J. Hupmann, Acta Metall 27, 973 (1979).
[2] T. Muschik T, W. A. Kaysser, and T. Hehenkamp, Acta Metall 37, 603 (1989).
[3] D. N. Yoon, Int. Mater. Rev. 40, 149 (1995).
[4] D. N. Yoon, J. W. Cahn, C.A. Handwerker, J. E.Blendell, and Y. J. Baik, In: Interface Migration and Control of Microstrucutres. Am Soc. Metals. Park. Ohio (1985), pp. 19-31.
[5] W. A. G. McPhee, G. B. Schaffer, and J. Drennan, Acta Metall 51, 3701 (2003).
[6] J. S. Kirkaldy, Acta mater. 46, 5127 (1998).
[7] D.E. Temkin , to be published in Acta Materialia.
[8] G. P. Ivantsov, Dokl. Akad. Nauk SSSR 58, 567 (1947).
[9] G. P. Ivantsov, Dokl. Akad. Nauk SSSR 83, 573 (1952).
[10] Y. Saito, Statistical Physics of Crystal Growth, World Scientific Publishing, Singapore, 1996.
[11] D. Kessler, J. Koplik, and H. Levine, Adv. Phys. 37, 255 (1988).
[12] E. A. Brener, and V. I. Mel'nikov, Adv. Phys. 40 53 (1991).
[13] M. Ben Amar, and E. Brener, Phys. Rev. Lett 71, 589 (1993).
[14] E. Brener, Phys. Rev. Lett. 71, 3653 (1993).
[15] E. Brener and D. Temkin, Phys. Rev. Lett. 94, 184501 (2005).

Plasticity of the complex metallic alloy phase $Al_{13}Co_4$

M. Heggen, M. Feuerbacher

Institut für Mikrostrukturforschung

Plastic deformation experiments were performed on single crystals of the orthorhombic $Al_{13}Co_4$ complex metallic alloy phase. The material was compression tested in a temperature range between 600 and 800 °C and shows a pronounced yield-drop effect followed by a regime of weak work hardening. Incremental experiments like stress-relaxation tests and temperature changes were conducted in order to determine thermodynamic activation parameters of the deformation process. Microstructural investigations by means of transmission electron microscopy reveal that dislocation motion on (0 0 1) planes is the basic mechanism of plastic deformation. The dislocations have [0 1 0] Burgers-vector direction, [1 0 0] line direction and are structurally related to Metadislocations [1].

Complex metallic alloys (CMAs) are characterized by a high structural complexity and large lattice parameters. They posses a high number of atoms per unit cell, ranging from some tens to some thousands [2]. The plasticity of these novel materials is largely unknown and a field of intense current research activity. Conventional mechanisms of plastic deformation are prone to failure in such structures, essentially due to the occurrence of large lattice parameters. For instance, the movement of perfect dislocations, i.e. dislocations with a Burgers vector corresponding to a translationally invariant distance, in CMAs would be connected to high elastic line energies exceeding physically reasonable values.

The material in the present investigation is $Al_{13}Co_4$, an orthorhombic phase (space group $Pmn2_1$) with lattice parameters a = 8.2 Å, b = 12.3 Å, and c = 14.5 Å [3]. The structure has been well characterized by different authors [e.g. 3]. The unit cell contains 102 atoms. The main structural features are pair-connected pentagonal prismatic channels which extend along the [1 0 0]-direction. In this sense $Al_{13}Co_4$ is structurally related to a group of other CMAs of which orthorhombic $Al_{13}Fe_4$ is the most prominent phase [4]. In $Al_{13}Co_4$ the occurrence of metadislocations was proposed [5], however, experimental evidence for the existence of metadislocations was so far only given for the phase ξ′-Al-Pd-Mn [1]. Therefore, besides the characterization of the macroscopic plastic deformation behaviour, the present investigation is an important jigsaw piece to determine the role of metadislocations in the plastic deformation mechanism of CMAs.

$Al_{13}Co_4$ single crystals were grown by means of the Bridgman technique. The grain sizes achieved were of the order of 1 to 2 cm^2. The quality of the material was characterized by phase contrast optical microscopy, scanning electron microscopy, and transmission electron microscopy. For mechanical testing we used a modified Zwick Z050 machine under closed loop control at constant strain rate of 10^{-5} s^{-1}. After deformation, the samples were rapidly unloaded and quenched on a cold metal plate to preserve their microstructural state. They were cut into slices and prepared for transmission electron microscopy. The microstructural investigations were carried out using a JEOL 4000FX transmission electron microscope (TEM).

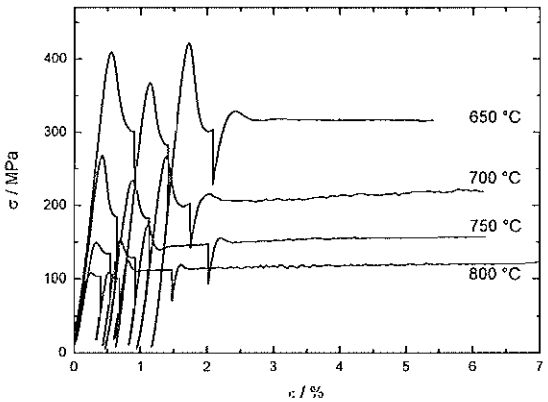

Fig 1: Stress-strain curves of $Al_{13}Co_4$ at different temperatures.

Figure 1 shows stress-strain curves of $Al_{13}Co_4$ at temperatures between 650 and 800 °C. We have conducted a similar series of stress-relaxation tests and temperature-cycling tests in order to determine thermodynamic activation parameters of the deformation process [6]. At all temperatures the curves have common qualitative features. After the elastic regime, a strong yield-point effect is observed in the strain range between 0.25 and 0.55 % which can be most probably attributed to dislocation multiplication at the onset of plastic deformation. Another feature is the occurrence of slight work hardening at higher strain. After plastic deformation the $Al_{13}Co_4$ samples show localised shear zones which correspond to crystallographic (0 0 1) planes.

The macroscopic plastic deformation behaviour of the well investigated CMA ξ′-Al-Pd-Mn [7] shows clear differences to $Al_{13}Co_4$. First of all the deformation of ξ′-Al-Pd-Mn is homogeneous. No localized shear zones are observed on deformed samples. Furthermore almost no yield drop effect can be found and work softening is observed at higher strain rather than work hardening. The homologous temperature range, i.e. the temperature range related to the melting temperature of the material, where plastic deformation experiments are performed is different. $Al_{13}Co_4$ is deformable at much lower homologous temperatures than ξ′-Al-Pd-Mn.

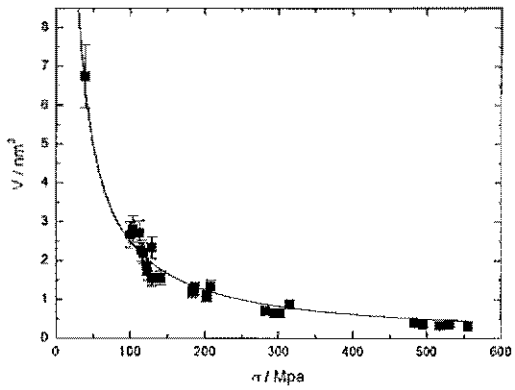

Fig 2: Experimental activation volume (squares) evaluated from stress-relaxation tests and hyperbolic fit curve (solid line).

In Figure 2 the activation volume of $Al_{13}Co_4$ evaluated from stress-relaxation tests [6] is shown. It shows a hyperbolic stress dependence (solid line in Figure 2). The activation volumes are bigger by about a factor of 2 than those of the CMA ξ′-Al-Pd-Mn and the icosahedral Al-Pd-Mn quasicrystal [7]. Conclusions can be drawn from the large values of the activation volume on the mechanism of plastic deformation. A detailed discussion on this topic is given elsewhere [8].

The activation enthalpy ζH [6] was calculated and has a mean value of 2.2 eV. The work term ζW [6], i.e. the part of the energy which is supplied by the applied stress, amounts to 0.4 eV in the temperature range considered. Hence, the work term is distinctly lower than the activation enthalpy, which indicates that dislocation motion is a thermally activated process. The mean value of the activation enthalpy is lower than the corresponding values of 5 eV for ξ′-Al-Pd-Mn [7].

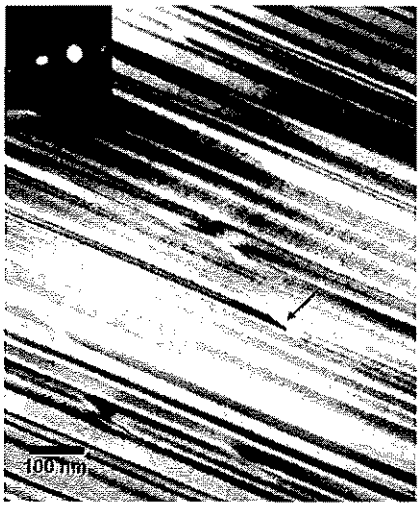

Fig 3: Bright field micrograph of a deformed sample (see text).

Figure 3 shows an electron micrograph of a deformed sample under two-beam bright-field conditions. It reveals the presence of stacking faults at very high density. They can be noticed as parallelly oriented stripes covering the whole image area. The planes of the stacking faults were determined by specimen tilting and correspond to (0 0 1) planes. Furthermore a high density of dislocations is observed in the deformed sample. The black arrow in Figure 3 points at a dislocation terminating a planar defect. The dislocation density in a sample deformed at 700 °C and 10^{-5} s^{-1} to 6.2 % was determined as 1.4 (± 0.2) × 10^9 cm^{-2}, which is about 50 times higher than the dislocation density of an undeformed reference sample. The dislocations are aligned parallely and have [1 0 0] line direction. Furthermore, contrast extinction experiments revealed that the Burgers vectors of most of the dislocations and the displacement field of all planar defects observed in the present study are parallel to the [0 1 0] direction.

The present microstructural investigations clearly indicate that the movement of [0 1 0] dislocations on (0 0 1) planes trailing stacking faults is a basic mechanism of plastic deformation in $Al_{13}Co_4$. This deformation mechanism is different to the Metadislocation-mediated deformation mechanism of ξ′-Al-Pd-Mn. Although the Burgers-vector direction is equivalent, the planes of the planar defects are different. It is a fundamental feature of Metadislocations in ξ′-Al-Pd-Mn that they are connected to phason planes possessing (0 0 1) habit planes [1]. In $Al_{13}Co_4$ these planes correspond to (0 1 0) planes [8]. In the present study, planar faults of any kind possessing (0 1 0) habit planes were not observed. Accordingly, despite the structural relatedness of ξ′-Al-Pd-Mn and $Al_{13}Co_4$, our present results on the latter phase show that we can exclude the deformation mechanisms operating in ξ′-Al-Pd-Mn.

However, a current investigation by our group shows that the core structure of the dislocations in $Al_{13}Co_4$ corresponds to those of metadislocations proposed for this material [8]. This study comprises a investigation of the dislocation core using high-resolution electron microscopy. Despite of the microstructural differences, first of all the lack of phason planes in $Al_{13}Co_4$, this investigation shows that the dislocations found in $Al_{13}Co_4$ are structurally related to metadislocations. It indicates for the first time that metadislocation related defects are found in different types of CMAs and that they are a powerful concept to describe the mechanisms of plastic deformation in those materials.

[1] H. Klein, M. Feuerbacher, P. Schall and K. Urban, Phys. Rev. Lett, 82, 3468 (1999).
[2] K. Urban and M. Feuerbacher, J. Non Cryst. Sol. 331 - 335, 143 (2004).
[3] J. Grin, U. Burkhardt, M. Ellner, K. Peters, J. Alloys & Comp. 2006, 243 (1994a)
[4] J. Grin, U. Burkhardt, M. Ellner, K. Peters, Z. Kristallogr. 209, 479 (1994b).
[5] M. Feuerbacher, and M. Heggen, Phil. Mag., in press (2005b).
[6] A.G. Evans, and R.D. Rawlings, Phys. Stat. Sol. 34, 9, (1969).
[7] M. Feuerbacher, H. Klein, and K. Urban, Phil. Mag. Lett. 81, 639 (2001).
[8] M. Heggen, D. Deng, M. Feuerbacher, in preparation (2005).

Strategies for Aberration Control in Sub-Angstrom HRTEM

A. Thust, J. Barthel, L. Houben, C.L. Jia, M. Lentzen, K. Tillmann and K. Urban

Institute of Solid State Research, Forschungszentrum Jülich GmbH, D-52425 Jülich, Germany

High-resolution transmission electron microscopes (HRTEMs) of the most recent generation will allow one to enter the sub-Angstrom resolution regime on a routine basis. However, in order to be able to interpret the sub-Angstrom information, an extremely precise control of residual optical aberrations will be required. The precision of existing aberration measurement procedures is by far not sufficient for this purpose. We developed software procedures, which exceed the precision of existing solutions by an order of magnitude, enabling for the first time a reproducible access to the sub-Angstrom regime. The measured aberrations can be either removed by hardware before experiment or more completely via phase-retrieval methods after experiment.

With the upcoming transmission electron microscopes equipped with a monochromator it is possible to access the sub-Angstrom resolution regime on a routinely basis. Apart from the high demands on the instrumental stability and on the specimen quality, the precise measurement and the correction of residual higher-order lens aberrations is a primary challenge in order to be able to take advantage of the extra resolution offered by such microscopes. Just in the same way as the resolution jump enabled by field emission guns in the early nineties required a precise correction of axial coma, two- and threefold astigmatism, the resolution jump enabled now by monochromators requires the control of many more aberrations than have been considered so far. A graphical overview of aberrations, which are expected to play a role in the resolution regime around 0.8 Angstrom, is given in Fig. 1.

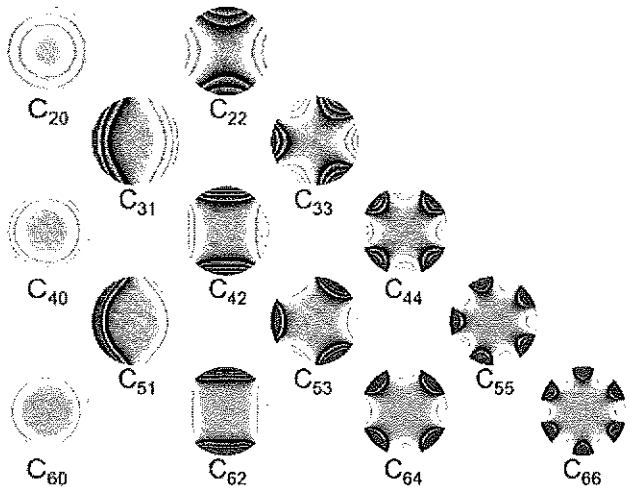

Figure 1 Schematic wave optical display of lens aberrations in Fourier space up to the sixth order of the spatial frequency g. The notation C_{mn} is chosen in such a way that the index m denotes the order of the spatial frequency, whereas n denotes the rotational symmetry. Bright areas indicate a positive phase, dark areas a negative phase, discontinuities highlight multiples of π. E.g. C_{20} denotes the defocus, C_{22} the 2-fold astigmatism, C_{40} the spherical aberration, C_{mm} in general a m-fold astigmatism.

While the introduction of a hardware corrector for the spherical aberration (C_S) yields a drastic improvement in the image quality, our experience with the C_S corrected CM200 FEG instrument installed in Jülich shows that a parallel integration and even a further development of software solutions is helpful or even necessary in order to fully overcome the aberration problem.

Firstly, the aberration measurement software, which is based on a diffractogram analysis and which is currently delivered with the CEOS hardware corrector [1], is by far not robust and precise enough for a corrector alignment aiming at a target resolution around 0.8 Angstrom. Moreover, error limits, which are traditionally given only for single aberrations (see e.g. Ref. 1) are no longer realistic in the case of a large ensemble of potential aberrations as is shown in Fig. 1. For this purpose we developed a new software suite for ultra-precise aberration measurement, which includes numerous novel insights and approaches for the recognition of diffractograms as well as a correct error propagation analysis. First experiments with the new software running in parallel with the CEOS software on the Jülich microscope show a drastic improvement by a full order of magnitude in the precision of the diffractogram recognition. Due to this essential progress in the software methodology a reliable corrector alignment for target resolutions well below one Angstrom is now possible for the first time.

Secondly, the fact that aberrations, which can be potentially corrected by hardware, may vary with time, and the fact that many higher-order aberrations cannot be corrected by hardware at all, suggest to combine an incomplete hardware correction with an a-posteriori software correction via phase-retrieval methods [2]. A comparison of a C_S corrected image with the corresponding phase image, which was retrieved by focal-series reconstruction, is shown in Fig. 2. Apart from the improvement of the signal-to-noise ratio, the a-posteriori elimination of residual aberrations from the retrieved wave function leads to an apparent improvement of the optical quality, allowing for a direct interpretation of the atomic details belonging to the imaged defect structure [3,4,5,6].

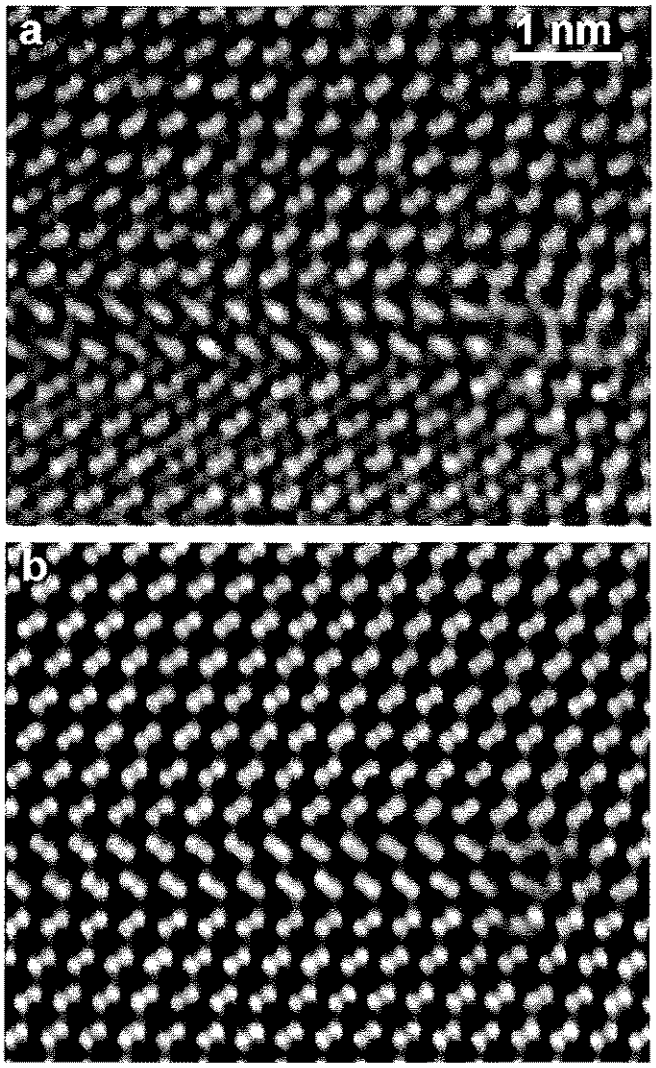

Figure 2 (a) Image of a stacking fault in GaAs taken along a [110] crystal axis with a C_S corrected microscope under bright atom contrast conditions. Although the microscope is already corrected for spherical aberration by hardware, the image does not reveal a direct structure projection due to the existence of unwanted further aberrations. (b) Phase of the electron wave function reconstructed from a focal series after a-posteriori software correction of residual aberrations C_{20}, C_{22}, C_{31}, C_{33} and C_{40}. The artificial kidney-shaped distortion of the dumbbell contrast and the blurred appearance of the fault, as observed in (a), are absent in the reconstructed aberration-free phase.

[1] S. Uhlemann and M. Haider, Ultramicroscopy 72 (1998) 109.

[2] A. Thust, M.H.F. Overwijk, W.M.J. Coene and M. Lentzen, Ultramicroscopy 64 (1996) 249.

[3] K. Tillmann, A. Thust and K. Urban, Microsc. Microanal. 10 (2004) 185.

[4] K. Tillmann, A. Thust, A. Gerber, M. P. Weides and K. Urban, Microsc. Microanal. 11 (2005) 534.

[5] A. Thust, J. Barthel, L. Houben, C.L. Jia, M. Lentzen, K. Tillmann and K. Urban, Microsc. Microanal. 11 (Suppl 2) (2005) 58.

[6] C. L. Jia, A. Thust, and K. Urban, Phys. Rev. Lett. 9, (2005) 225506.

Atomic configuration at a $SrTiO_3$ dislocation core

C.L. Jia, A. Thust and K. Urban

Institut für Mikrostrukturforschung

The atomic structure of a $SrTiO_3$ dislocation is revealed directly by phase-retrieval electron microscopy. In particular, atomic columns of light oxygen are observed simultaneously with the columns of considerably heavier Sr and Ti. A distinct structural modification of the oxygen octahedra at the dislocation core as well as a significant nonstoichiometry, including a deficiency of oxygen, are observed. Deviations from the bulk chemical concentration are quantified column-by-column by means of structure modelling and quantum-mechanical simulations of the electron scattering process.

Dislocations, which appear almost unavoidably in many materials, have been at the focus of materials research for a long time. The electrical properties of functional materials applied in electronics depend crucially on the density and nature of the dislocations involved [1,2]. Dislocation structures in oxides, especially in perovskite oxides, which play a key role in industrial nanoelectronics, are still not well known due to their intrinsic structural and chemical complexity. The ability to determine the geometrical and chemical distribution of light anions with atomic resolution in the presence of heavy cations has been so far an unsolved challenge in microstructure research.

High-resolution transmission electron microscopy (HRTEM) has proven to be a powerful tool for the characterisation of lattice defects. In the present work, we take advantage of two advanced techniques, the negative Cs imaging (NCSI) technique [3] and the wave function reconstruction from a focal series of images [4], for investigating the atomic structure of a dislocation core in $SrTiO_3$. The emphasis of this investigation is not only on the spatial arrangement of the heavy cations Sr and Ti but also on the detailed arrangement of the considerably lighter oxygen atoms.

[110] oriented specimens were prepared from a single crystal of $SrTiO_3$ for the HRTEM investigation. Twenty images of a dislocation were recorded under NCSI conditions ($C_S = -40$ µm) with a nominal focal step size of −1.8 nm in the Philips CM200 FEG microscope equipped with a C_S-corrector. The exit-plane wave function was retrieved from the recorded image series using the Philips/Brite-Euram software package for focal-series reconstruction. The modelling of the core structure and the simulations of the wave function and images required for the subsequent quantitative comparisons were carried out with the CrystalKit and MacTempas software packages.

Figure 1a displays image no. 9 belonging to a series of high-resolution images containing a dislocation core. This image was recorded at a defocus value of +8.8 nm, which is close to the optimum phase contrast under NCSI conditions. In this image all types of atomic columns, i.e. SrO, Ti, and O, are directly revealed by bright dots on a dark background, as

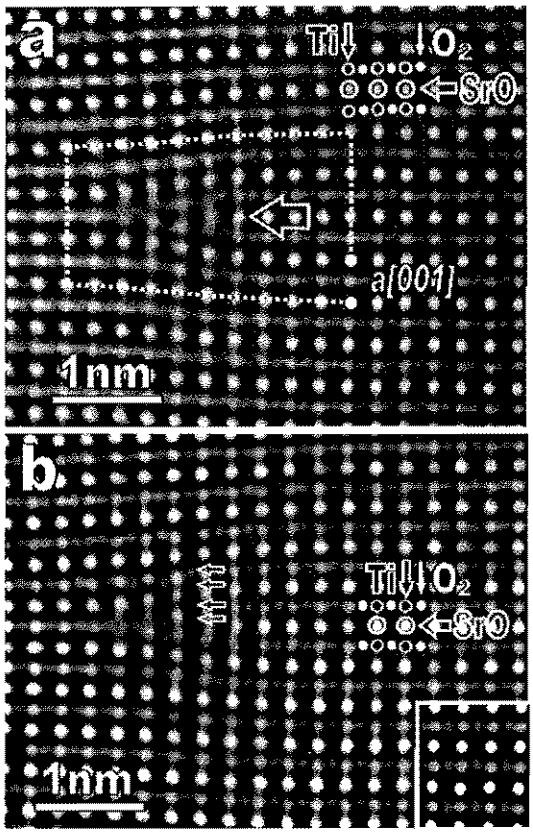

FIG. 1. (a) Image no. 9 of a focal series of 20 images containing a dislocation core in [110] oriented $SrTiO_3$. (b) Numerically retrieved phase from the same region after elimination of residual aberrations. The inset in the periodic area shows the simulated phase for a sample thickness of 4.3 nm. Pairs of arrows highlight the splitting of oxygen columns.

is marked by circles in the periodic lattice area. The arrows denote the dislocation with a Burgers vector a[001]. Whereas the cation columns in the core area can be identified in a quite straightforward manner from the Cs-corrected image, the contrast of the oxygen columns is buried in comparatively strong noise. Figure 1b shows the corresponding phase image

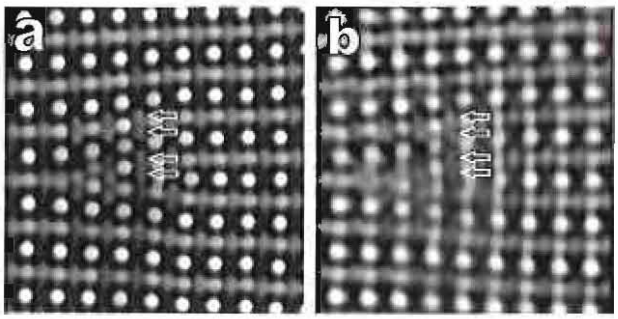

FIG. 2. Comparison between (a) the simulated phase image based on the structure model shown in Fig. 3 and (b) the phase image retrieved numerically from experimental data.

retrieved from the focal series of 20 images, which is delocalisation-free due to an additional a-posteriori elimination of all residual aberrations. The details of the oxygen arrangement at the dislocation core are sufficiently well resolved after the numerical reconstruction and can now be studied column-by-column. From Fig. 1b it is clearly seen that the dislocation is characterised by the termination of two atomic planes, a (001) SrO plane and a (001) TiO_2 plane. The core area extends over about 0.8 nm, one and a half [110] periods between the different termination points of these two atomic planes. At this distance two Ti-O planes directly face each other, forming a structure of double Ti-O planes. This structure can be also considered as a short-distance dissociation of the dislocation.

The most prominent feature of the oxygen signal in the core region is a doubling of the phase maxima, as is marked by two pairs of small horizontal arrows in Fig. 1b. Moreover, the phase peaks at the oxygen positions in the core region are in general considerably lower than those in the surrounding perfect lattice. Extensive simulations of the wave phase showed that the prominent doubling of phase maxima cannot be caused by a single column of oxygen, indicating that indeed two oxygen columns are responsible for the observed maximum doubling. A corresponding structure model was set up and further refined by adjusting the occupancy of the atomic columns in order to obtain as small a discrepancy as possible between simulated and experimentally retrieved phase. Figure 2a displays the simulated phase image of the dislocation core based on the refined structure model. For direct comparison, Fig. 2b displays the experimentally retrieved phase image of the core area. It is already obvious from visual inspection that the details of the phase images displayed in Figs. 2a and 2b mutually match each other to a high degree. A more quantitative comparison based on the specific shape of phase profiles shows also the excellent resemblance between the experimental and the simulated phase profiles supports in detail the validity of the refined structure model of the dislocation core [5].

Figure 3a shows the structure model of the dislocation core viewed along the [110] direction. Figure 3b

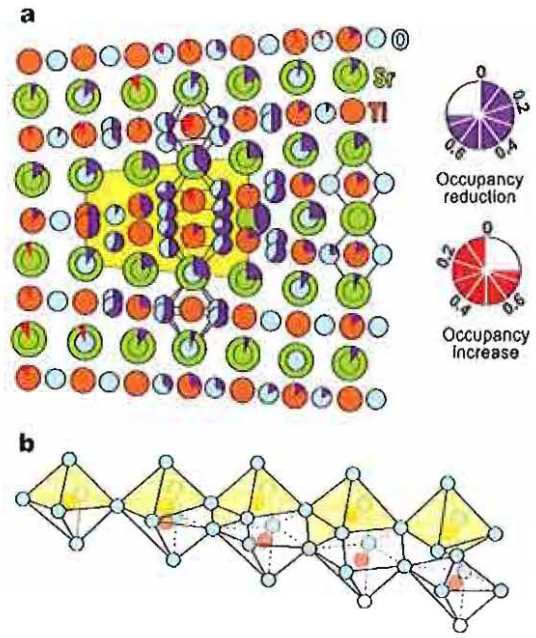

FIG. 3. (a) Structure model of the dislocation core refined by matching the simulated phase to the experimentally retrieved phase. The violet segments at the atomic columns indicate the occupancy reduction relative to a fully occupied reference column of 4.3 nm height. The red segments indicate a slight formal over-occupancy due to experimental noise and local thickness variations with respect to the reference level. (b) Perspective view of the oxygen configuration at the dislocation core.

schematically shows the modification details of the octahedra at the dislocation core in a perspective view.

From the refinement of the structure model, it is found that most of the columns in the core region have a tendency to be under-occupied. This holds for both the cation and oxygen columns. One can therefore calculate a relative occupancy ratio, i.e. the ratio between the number of cation atoms and oxygen atoms for neighbouring atom columns. In the region of the dislocation core marked by the yellow background colour, one obtains the atom ratio of 0.51 : 1.00 : 2.29 for Sr : Ti : O. In comparison to the stoichiometry of the $SrTiO_3$ the core is thus Sr- and O-deficient. It is known that the concentration of cations can vary for different dislocation types. The relatively low concentration of oxygen could result in a positively charged dislocation core.

[1] M.-W. Chu *et al. Nat. Mater.* **3**, 87 (2003).
[2] S.P. Alpay *et al., Appl. Phys. Letts.* **85**, 2044 (2004).
[3] C.L. Jia, M. Lentzen, and K. Urban, *Science* **299**, 870 (2003).
[4] A. Thust *et al.*, Dyck, *Ultramicroscopy* **64**, 211 (1996).
[5] C.L. Jia, A. Thust and K. Urban, *Phys. Rev. Lett.* **95**, 225506 (2005).

Contrast Transfer Theory for Transmission Electron Microscopes Equipped with a Wien-Filter Monochromator

M. Lentzen, A. Thust
Institute of Solid State Research and Ernst Ruska Centre for Microscopy and Spectroscopy with Electrons

A key limit to the resolution of transmission electron microscopes is the energy distribution of the electron source, which induces via the chromatic aberration of the objective lens an unavoidable "blur" of object details in the imaging plane. The future generation of sub-Ångström electron microscopes will be equipped with so-called gun-monochromators, which reduce the source energy spread by electron-optical filtering and hence improve the information limit. One of these devices, the Wien-filter monochromator, induces into the illumination system of the microscope a new shape of the effective source. This work extends the traditional contrast transfer theory, which describes high-resolution image formation, by a new damping envelope taking the energy dispersion of the illumination into account. The impact of the new envelope for sub-Ångström contrast-transfer is evaluated for the case of a modern aberration-corrected 300-kV instrument. The envelope simulation shows a defocus-dependent asymmetric loss of high-frequency structure information.

The past two decades have seen major improvements of transmission electron microscopes with respect to the information limit and the interpretable resolution of structure images. The combined use of new instrumentation, such as field-emission sources, more stable lens and high-voltage power supplies, and, eventually, spherical-aberration correctors, provides an interpretable resolution just penetrating the sub-Ångström scale.

Attempts for further improvement are made today by reducing the deleterious influence of the chromatic aberration through the use of gun monochromators. These devices reduce the energy spread of electrons emitted by the source at the cost of brightness. One of the new monochromators, of the Wien-filter type [1], images incoming electrons into an energy dispersive plane, cuts out electrons of a desired small energy interval by means of a slit, and lets the outgoing electrons pass through the high-voltage accelerator and the illumination system to form the illumination cross-over, for example above the specimen under investigation.

The illumination cross-over of a Wien-filter monochromator has a shape much different from that of traditional illumination systems. The linear energy dispersion introduced is still present at the cross-over plane, that is, electrons of different energy appear to impinge from different directions onto a certain point in the object plane. Figure 1 displays a model of the resulting effective source: Electrons with energy E_0 travel straight on, those with energies larger than E_0 are incident from the right, and those with an energy smaller than E_0 are incident from the left. The respective change of the wavevector K is traced by the wavevector Q. The vector q traces an additional direction change, still present for each energy, due to the finite size of the field-emission source.

The traditional imaging model for the contrast transfer under partially coherent illumination [2, 3] is hence no more valid, because it assumes identical illumination disks, spanned by q, for different electron energies. This work was dedicated to a full recalculation of the contrast transfer using the transmission cross-coefficient formalism to describe high-resolution imaging for a microscope equipped with a Wien-filter monochromator [4], using the illumination model described before.

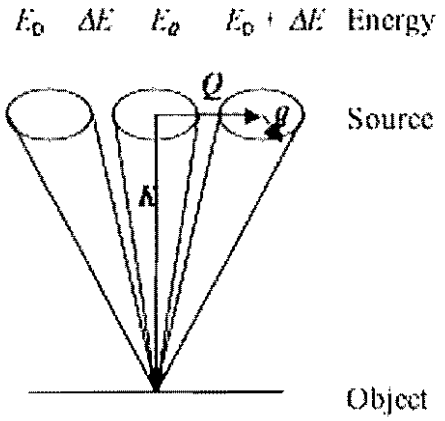

Figure 1 The effective source for an illumination system equipped with a Wien-filter monochromator. An image of the field-emission source, traced by q, is displaced by a wavevector Q related to an energy change of ζE. Thus electrons with energy $E_0+\zeta E$ have an apparent illumination tilt of Q/K.

The most prominent change to the standard high-resolution imaging model [2, 3], which will affect not only future image calculations but also wave function restoration using electron holography or through-focus series reconstruction, has to be made for the damping envelopes describing the effects of partial coherence. The well-known envelopes for spatial and temporal coherence, $E_S(\boldsymbol{g}, \boldsymbol{h})$ and $E_F(\boldsymbol{g}, \boldsymbol{h})$, for the two-beam interference of diffracted beams $\boldsymbol{g}$ and $\boldsymbol{h}$, stay unchanged, but an additional new envelope $E_M(\boldsymbol{g}, \boldsymbol{h})$ occurs, due to the dispersion of the effective source. The resulting formulae for the first-order expansion are lengthy; therefore we display here, due to limited space, only the envelopes for the linear interferences:

$$E_S = \exp\left(\pi^2 q_0^2 |\nabla\chi|^2 \right),$$

$$E_F = \exp\left(-\pi^2 \Delta_F^2 \left(\frac{\partial\chi}{\partial Z} \right)^2 \right),$$

$$E_M = \exp\left(-\pi^2 \Delta_M^2 \left(\frac{\partial Q}{\partial Z} \nabla\chi \cdot \vec{e}_Q + \frac{\partial\chi}{\partial Z} \right)^2 \right),$$

with the aberration-function $\chi(g)$ of the objective lens, the lens defocus Z, the semi-convergence angle of the field-emission source q_0, the effective defocus spread ζ_F due to high-voltage and lens-current instabilities, the effective defocus spread $\zeta_M = C_C\, \zeta E_M/E_0$ due to the energy spread ζE_M left over by the monochromator, the constant of the chromatic aberration C_C, the dispersion of the effective source $\partial Q/\partial Z$, and a unit vector e_Q along the disperison axis.

The simulation of the combined effect of the three envelope functions, displayed in Figure 2, shows a notable effect of the new illumination system: For a spherical-aberration corrected microscope with an information limit of 0.08 nm the contrast transfer becomes asymmetrical for diffraction vectors g and $-g$ upon defocussing the objective lens, here by a moderate value of ±50 nm. Depending on the amount of defocus high spatial frequencies belonging to one half of the diffraction plane are transmitted poorer. That is, details of the object structure may appear asymmetrical to the operator, and work with such an instrument is restricted to a defocus interval around Gaussian defocus, depending on the strength of the dispersion. The worst of the mentioned effects is, however, the loss of valuable high-resolution information.

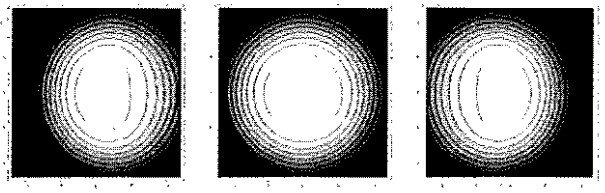

Figure 2 The envelope $E_S(g)$ $E_F(g)$ $E_M(g)$ of the linear interferences for E_0 = 300 keV, defoci –50 nm (left), 0 nm (centre), +50 nm (right), and an information limit of 0.08 nm. The frame coordinates run from -12 nm^{-1} to $+12$ nm^{-1}; white denotes a transmission of 1, black a transmission of 0.

[1] P.C. Tiemeijer, Inst. Phys. Conf. Ser. 161 (1999) 191.

[2] K. Ishizuka, Ultramicroscopy 5 (1980) 55.

[3] H. Pulvermacher, Optik 60 (1981) 45.

[4] M. Lentzen, A. Thust, Microsc. Microanal. 11 (Suppl. 2) (2005) 2145.

Metadislocation reactions and metadislocation networks

M. Heggen and M. Feuerbacher

Institut für Mikrostrukturforschung

Metadislocations are novel structural defects firstly observed in the complex metallic alloy ξ′-Al-Pd-Mn. We present a transmission electron microscopy study on metadislocation reactions and networks. It is shown that metadislocations can dissociate into partials, which leads to a decrease of the elastic line energy. Connected groups of metadislocations can assume large and complex network structures with large total Burgers vectors. However, the local elastic strain at the individual metadislocation cores as well as the fault-plane energies remain small. By this mechanism, effective large Burgers vectors, contributing massively to plastic strain, can be distributed over a large portion of the material.

The mechanisms of plastic deformation of complex metallic alloys (CMAs) and the defects mediating their plastic deformation are largely unknown. Due to the large lattice parameters encountered in these materials, the concepts that are used to describe the plastic deformation of simple crystalline materials fail since the introduction of a perfect dislocation into a CMA would lead to a high elastic line energy exceeding physically reasonable values.

In the complex intermetallic phase ξ′-Al-Pd-Mn a novel mechanism of plastic deformation involving a new type of structural defect called metadislocation (MD) [1] was found. Metadislocations (MDs) do not introduce high elastic line energies, since their Burgers vectors are much smaller than the lattice constant (Table 1). Nevertheless, due to their particular structure, slip of MDs does not involve the creation of planar faults as ordinary partials would do [2]. To date, the investigation of defects in ξ′-Al-Pd-Mn is limited to the structure and properties of single MDs [1,2,3]. However, frequently MDs are observed as parts of complex network structures. These networks are particularly found in deformed materials. Therefore the understanding of the properties of MD networks is essential for the comprehension of the plasticity of ξ′-Al-Pd-Mn.

The material used in the present investigation, a ξ′-Al-Pd-Mn single crystal, was grown by means of the Bridgman technique. A sample of approximately 5×2×2 mm^3 in size was cut for mechanical testing; the long axis of the deformation specimen was oriented in a 45° angle to the [0 1 0] direction. The sample was uniaxially deformed in compression along the long specimen axis at 700 °C to about 0.5 % strain. After mechanical testing the sample was quenched on a cold metal plate and prepared for transmission electron microscopy (TEM) by standard techniques. The microstructural investigation was performed in a JEOL 4000EX electron microscope.

Figure 1 shows a simple example of interacting MDs. Two MDs of opposite sign sharing six (1,2) and ten (3,4) phason planes are seen. Their Burgers vectors are ±1.83 and ±1.13 Å, respectively All associated phason planes of the MDs are mutually connected. Hence these defect can be interpreted as a MD dipoles. Figure 2 shows an example of MD splitting. A MD with ten phason planes (1) is connected to a MD with six phason planes (2). They share six phason planes, hence four phason planes are remaining on the left hand side of the defect. Adding the Burgers vectors of both MDs yields (1.83+1.13) Å = 2.96 Å, which corresponds to the Burgers vector of a MD possessing four phason planes. Therefore the situation shown in Figure 2 can be interpreted as a MD with four phason planes which has split into MDs with six and ten phason planes, respectively. By this means, the local elastic strain at the dislocation core is reduced. On the other hand, the six shared phason planes are additionally introduced. Hence the process of MD splitting has to be treated similarly as splitting of dislocations into partials in ordinary materials, and the total energy balance of all defects involved has to be considered.

Figure 3 shows a MD network. For the sake of clarity, the location and orientation of MDs are indicated by triangles. Furthermore, the numbers and the arrows indicate the number of associated phason planes and the direction and length of the Burgers vector, respectively. This is an example for a complex MD network, formed by the mutual interconnec-

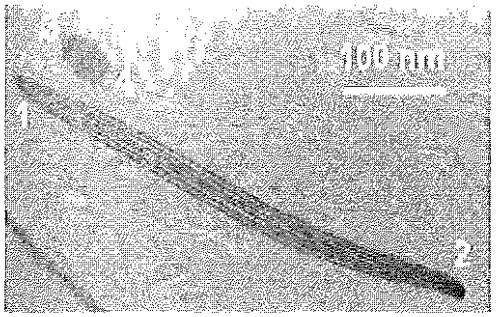

Fig. 1: MD dipoles sharing six (1,2) and ten (3,4) phason planes

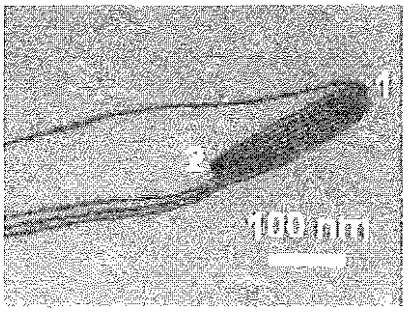

Fig. 2: MD splitting. A MD associated to ten (1) and six phason planes (2) are indicated.

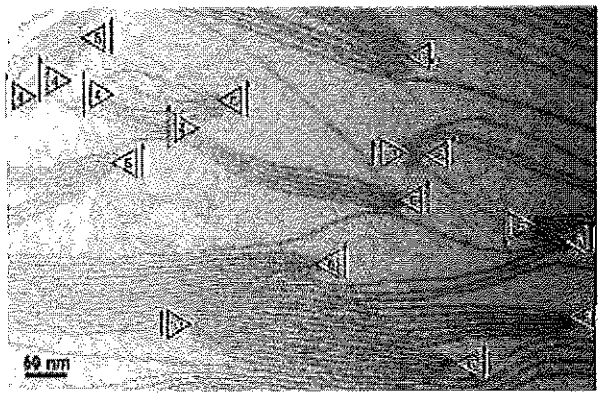

Fig. 3: Example of a complex MD network.

tion of MDs via their associated phason planes. A remarkable fact in this network is that the Burgers vectors of almost all MDs are oriented in the same direction and add up to a large amount of 27.61 Å. The arrangement of MD in networks hence can create objects with large total Burgers vectors. The movement of these objects through the structure leads to strong straining of the sample and is therefore for a highly effective means of plastic deformation. On the other hand, a MD network is more favourable than an arrangement of single MDs for energetic reasons as will be demonstrated below.

Figure 4 a shows a scheme of a MD with two phason planes, which introduces a small number of fault planes and hence a low fault-plane energy. However due to its relatively large Burgers vector of 4.80 Å the local elastic strain energy is high. Figure 4 b shows an example of a simple MD network. Two MDs with four phason planes are connected to a MD with six phason planes on the right hand side. Hence six phason planes are terminated by the MDs and two phason planes are left and reach into the bulk. This MD network introduces a small number of fault planes and a low fault plane energy. Additionally it introduces low local strain at the MDs (b = 2.96 and 1.83 Å). Nevertheless the Burgers vectors add up to a very large amount 7.75 Å. Analogously, higher numbers of metadislocations can add up to larger networks in order to achieve long total Burgers vectors (i.e. effective means of plastic deformation) and simultaneously reduce the total energy cost of local elastic strains and fault planes. MD arrangements as shown in

Number of phason half-planes	Burgers vector	Lattice mismatch in units of $c_{\xi'}$
16	- 0.70 Å	- 0.056
10	1.13 Å	0.090
6	- 1.83 Å	- 0.146
4	2.96 Å	0.236
2	- 4.80 Å	- 0.382

Table 1: Burgers vectors of MDs associated to different numbers of phason half-planes.

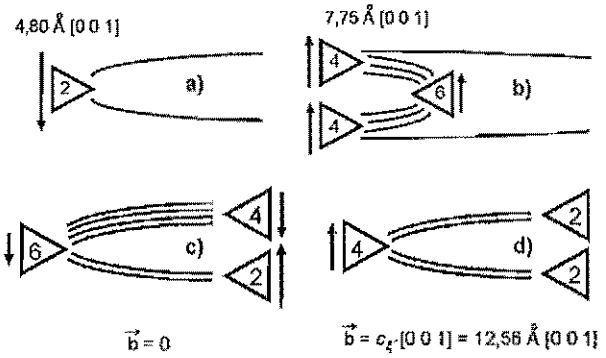

Fig. 4: Schematics of simple MD networks. See text.

Figure 4 b are frequently found in plastically deformed ξ′-Al-Pd-Mn samples [4].

A special case of a MD network is the "closed" network in the sense that all phason planes are terminated at MD cores within the network. A Burgers circuit can be performed around such type of MD network entirely in one phase, the ξ′-phase. Figures 4 c and d schematically show simple examples of such MD networks. The phason planes are shown as black lines. Figure 4 a shows a MD network with a MD associated to 6 phason planes on the left side and two MDs with four and two phason planes on the right side. All phason planes are terminated within this small network. The Burgers vector can be easily calculated according to Table 1: the Burgers vector modulus is 0.146 $c_{\xi'}$ - (0.236 $c_{\xi'}$ - 0.382 $c_{\xi'}$) = 0 $c_{\xi'}$, where $c_{\xi'}$ is the lattice constant of ξ′-Al-Pd-Mn. Hence a Burgers circuit without a closure failure can be performed around the object. Figure 4 d shows a MD network containing one MD associated to four phason planes on the left side and two MD with two phason planes on the right side. The modulus of the Burgers vector is 0.236 $c_{\xi'}$ - (2 × -0.382 $c_{\xi'}$) = $c_{\xi'}$ = 12.56 Å. Hence the total Burgers vector is $\mathbf{b} = c_{\xi'}$ [0 0 1], i.e. this MD network is a perfect dislocation in the ξ′-phase. The latter case is another example for a highly effective means of plastic deformation. Analogously, larger closed networks can be constructed.

In conclusion we have shown that MDs can form dipoles or dissociate into partials with smaller Burgers vectors which leads to a decrease of the total elastic energy. MDs can form complex networks by the mutual interconnection via their associated phason planes. MD networks are highly effective means of plastic deformation since they possess large total Burgers vectors and small local elastic strain at the individual MD cores.

[1] H.Klein, M. Feuerbacher, P.Schall and K.Urban, *Phys. Rev. Lett.*, **82**, 3468 (1999)

[2] H. Klein, M. Feuerbacher, P. Schall, and K. Urban, *Phil. Mag. Lett.*, **80**, 11, (2000)

[3] H. Klein and M. Feuerbacher, *Phil. Mag.*, **83**, 4103, (2003)

[4] M. Heggen, M. Feuerbacher, *Mat. Sci. Eng. A*, in press.

[010] dislocations in the complex metallic alloy ξ'-Al-Pd-Mn

M. Feuerbacher

Institut für Mikrostrukturforschung

The observation and characterization of dislocations with (010) habit planes in the complex intermetallic alloy ξ'-Al-Pd-Mn was investigated by means of transmission electron microscopy. Contrast-extinction experiments show that the Burgers vectors of the dislocations are parallel to the [010] direction, which reveals that they are prismatic edge dislocations. Their movement is shown to take place by pure climb. The [0 1 0] dislocations are split into two pairs of partials. It is argued that the Burgers vector length of the full dislocations amounts to 16.56 Å and that of the individual partials to 4.14 Å.

The class of Complex metallic alloys (CMAs) latterly attracts increasing interest [1]. Although a number of CMAs are well characterized considering their phase diagrams and their crystallographic structure only few investigations on their physical properties have been carried out yet. CMAs distinguish themselves by their large unit cells comprising some hundred to some thousand atoms and by the presence of local atomic coordinations which substantially differ from those found in simple metals. In the present paper dislocations in ξ'-Al-Pd-Mn, an orthorhombic material (space group *Pnma*) with a unit cell containing about 320 atoms are investigated. The cell parameters are $a = 23.54$ Å, $b = 16.56$ Å, and $c = 12.34$ Å [2]. The structure of ξ'-Al-Pd-Mn can be described in terms of overlapping Mackay-type clusters of local icosahedral symmetry containing about 54 atoms. ξ'-Al-Pd-Mn is the basis of a family of superstructures with equal a and b cell parameters, but larger cell parameters along the c direction. A superstructure with $c = 57.0$ Å, referred to as Ψ-Al-Pd-Mn and others with $c = 32.4$, 44.9, and 70.1 Å have been identified. In ξ'-Al-Pd-Mn, Klein et al. [3] have discovered a novel class of defects, the metadislocations, which allow for partial-dislocation motion without alteration of the structure. Macroscopic plastic deformation studies were carried out on ξ'-Al-Pd-Mn by means of uniaxial deformation by Feuerbacher et al. [4]. These studies demonstrated that ξ'-Al-Pd-Mn is plastically deformable at elevated temperatures. In the present paper the observation and characterization of another, substantially different type of dislocation in ξ'-Al-Pd-Mn is described.

Single crystals of final composition $Al_{73.9}Pd_{22.2}Mn_{3.9}$ were grown by means of the Bridgman. Oriented specimens with [010] plane normals were prepared for transmission electron microscopy (TEM) investigation from the as-grown material. Contrast-extinction experiments under bright- and dark-field Bragg-contrast conditions in order to characterize grown-in dislocations and in-situ heating experiments for the study of moving dislocations using a GATAN double-tilt high-temperature specimen holder were carried out. In these experiments, the as-grown sample is slowly heated under continuous observation. Under the induced thermal stresses, local dislocation motion and multiplication is induced.

Fig. 1 a) to c) shows a part of a dislocation loop under various imaging conditions, which all fulfill the extinction criterion $\boldsymbol{g}\cdot\boldsymbol{b} = 0$ where $\boldsymbol{b}$ is the Burgers vector of the dislocation. All reflections used for imaging correspond to reciprocal lattice vectors perpendicular to the [0 1 0] zone axis. It is obvious that only the facets fulfilling the additional critierion $\boldsymbol{g}\cdot\boldsymbol{b}\times\boldsymbol{u} = 0$, where $\boldsymbol{u}$ is the dislocation line direction of the corresponding facet are extinct, while the other facets show strong residual contrast. From these contrast exctintion experiments we can conclude that the Burgers vector of the dislocation investigated is parallel to the [0 1 0] direction, i.e. it is perpendicular to the (0 1 0) habit plane.

Fig. 1 d) shows a bright-field image of a similar dislocation in a thinner specimen area. The image clearly shows that the dislocation is split into four partials, which arrange in two pairs. The splitting distance between the two pairs amounts to about 67 nm whereas the splitting distance within the pairs amounts to about 13 nm. In the in-situ heating experiments at 610 °C it was observed the movement and growth of loops of the dislocations investigated. The velocities of the facets were determined to amount between 90 and 140 nm/s and the habit planes of the dislocations could be unambiguously determined as (0 1 0) planes.

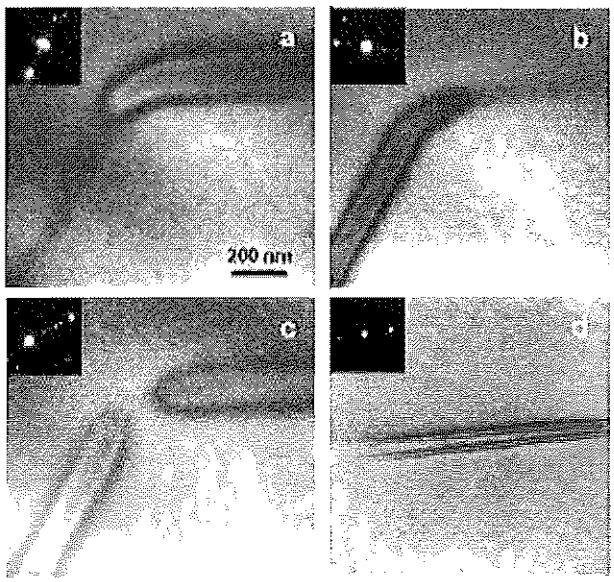

Fig. 1: Contrast exctinction experiments (a) to (c) and splitting of the dislocations (b). See text.

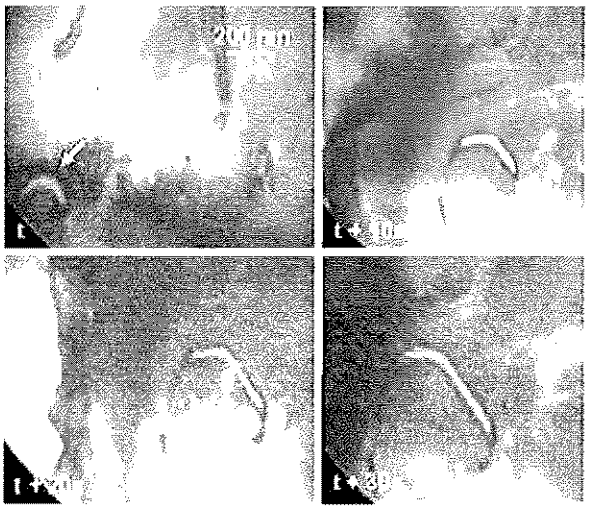

Fig. 2: In-situ observation of the expansion of a dislocation loop.

The contrast-extinction experiments show that the Burgers-vector direction of the dislocations considered is parallel to the [0 1 0] direction. The habit planes of the dislocations were identified as (0 1 0) planes. Hence all segments of the dislocations have pure edge character. The dislocation line and the Burgers vector define a cylindrical surface. Therefore the dislocations considered are prismatic dislocations. Fig 2 shows a series of video frames taken at about 610 °C. In the first image, taken at t = 0, a small dislocation loop can be seen in the lower left corner (arrow). This dislocation loop expands during the sequence. In the final stage shown here, at t = 30 s, the loop has clearly increased in size and has developed facets. The Burgers vector of the dislocation loop imaged is parallel to the viewing direction, i.e. the loop expands perpendicular its Burgers-vector direction.

The results directly show that the [0 1 0] dislocations move by pure climb. Prismatic dislocations, if their movement takes place by pure climb, directly and effectively contribute to the plastic deformation of a material. In this geometry, all segments of a dislocation loop are equivalent and equally mobile. Correspondingly, in the in-situ experiments (Fig. 2) we observe expansion of the loops without substantial changes of their shape.

Since the experimental determination of the Burgers vector length is highly difficult if not impossible the authors rely on the value deduced according to the following arguments: The study of the grown-in dislocations shows that the [0 1 0] dislocations are not terminating planar faults. Accordingly, in the in-situ studies they do not create faults upon moving. Hence we can conclude that the full [0 1 0] dislocations, i.e. the assembly of the four partials, are perfect. Their Burgers vector then is a lattice vector of the ξ'-Al-Pd-Mn structure. It is plausible to assume that the Burgers vector length equals the [0 1 0] lattice parameter amounting to 16.56 Å, i.e. the shortest translational invariant distance along the [0 1 0] direction. Burgers vectors of this length, however, must be considered energetically not

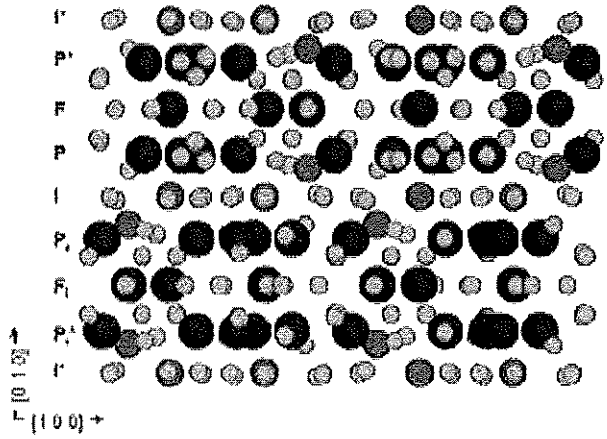

Fig. 2: [0 0 1] projection of one unit cell according to the structure model of Boudard et al [2]

favorable, and we expect splitting into partials as observed experimentally.

Fig. 3 shows a schematic representation of the structure of ξ'-Al-Pd-Mn [2]. The Al, Mn, and Pd atoms are shown as small bright, medium gray, and large dark spheres, respectively. According to this model, only very minor next-neighbor discrepancies occur for the ½(010) dislocations. For the next-next and higher neighbor distances, larger discrepancies occur, since then e.g. a P_i*-layer takes the position of a P layer, which due to their mirror symmetry, causes e.g. shorter distances between Mn-Mn pairs on both sides of the I or I* layer. With the ¼ [0 1 0] dislocations we introduce stronger discrepancies already in the first neighbor positions since we now exchange the positions of an I (or I*) layer and an F (or F_i) layer. Furthermore we obtain discrepancies in next-next and higher neighboring distances, since P and P_i or P* and P_i* layers replace each other. According to these considerations, we expect that the stacking fault necessarily introduced between the two ½ [0 1 0] partials should be energetically less costly than those introduced between the ¼ [0 1 0] partials. Consequently, we expect the splitting distance between the ½ [0 1 0] partials to be wider than that between the ¼ [0 1 0] partials. This finding is in full agreement with the experimental observations (see Fig. 4).

Furthermore it was observed that parallelly moving [0 1 0] dislocations tend to agglomerate in the later stages of the in-situ experiments even though they have Burgers vectors of equal sign. These observations could be explained in terms of attractive forces between the edge loops caused by the presence of the TEM specimen surfaces [5].

[1] K. Urban and M. Feuerbacher, *J. Non Cryst. Sol.* **334 – 335**, 143 (2004)

[2] M. Boudard, H. Klein, M. de Boissieu, M. Audier and H. Vincent, *Phil. Mag. A*, **74**, 939 (1996)

[3] H.Klein, M. Feuerbacher, P.Schall and K.Urban, *Phys. Rev. Lett.*, **82**, 3468 (1999)

[4] M. Feuerbacher, H. Klein, and K. Urban, *Phil. Mag. Lett.*, **81**, 639 (2001)

[5] M. Feuerbacher and D. Caillard, *Acta Mat.*, **52**, 1297 (2004)

Scaling Effects in Nanocrystalline $BaTiO_3$ and $NaNbO_3$

C. Pithan, Y. Shiratori, R. Waser
Institut für Festkörperforschung

A. Magrez
Laboratoire des Nanostructures et des Nouveaux Matériaux, EPFL, (Switzerland)

K. Kasezawa
Department of Applied Chemistry, Ritsumeikan University, Kusatsu (Japan)

Nanocrystalline particles of the perovskite type phases $BaTiO_3$ and $NaNbO_3$ have been prepared by applying microemulsion mediated synthesis. The products have be characterized structurally by scattering methods (neutron- and X-ray diffraction) in combination with Raman-spectroscopy (temperature and pressure tuning) and morphologically using electron microscopy (HRSEM, TEM und HRTEM). The results of these studies indicate some new aspects of scaling effects on the crystallographic structure and consequently on the dielectric, ferroelectric and piezoelectric properties of these materials. In the case of nanocrystalline $BaTiO_3$-particles (average particle size of 10 nm) und -ceramics (average grain size of 35 nm) evidence for a at least partial tetragonality of the lattice could be given for the first time. For nanocrystalline $NaNbO_3$ a series of phase transformations including two new polymorphs described by the space groups $Pmc2_1$ and $Pnma$ has been found.

The ongoing trend in the miniaturization of passive electronic modules based on the manufacturing by ceramic multilayer technology requires at present and in future a continuous reduction of the minimum layer thickness well below 1 µm and the use of nanocrystalline powders. This concerns in particular polar oxides for the application in MLCCs (Multilayer Ceramic Capacitors), MEMS (Micro-Electro-Mechanical Systems) or LTCC-modules (Low Temperature Cofired Ceramics). The crystallographic structure and here with many of the dielectric, ferroelectric and piezoelectric properties depend strongly from the size of the particles or grains, a phenomenon, which is often denoted by the term "scaling effect". The results summarized in this report, show new insights in nanocrystalline $BaTiO_3$ and $NaNbO_3$, which have been prepared by microemulsion mediated synthsis [1-3] and characterized using scattering methods and Raman spectroscopy [4-6].

It is well established that the tetragonal distortion of the unit cell for the crystal lattice of $BaTiO_3$, being one of the preconditions for ferroelectricity, shrinks and finally vanishes below a certain critical grain size. From dielectric measurement [7] ceramic grains are considered to consist of a tetragonal ferroelectric core, which is covered by a thin (8 Å) dead layer of superparaelectric, pseudocubic phase. Due to the enormous mechanical stresses in nanocrystalline ceramics, which stabilize the cubic high temperature phase this very thin thickness of the dead layer, however, does not seem to be very realisitic. Recently Zhao et al. [8] reported on $BaTiO_3$ ceramics with an average grain-size of 50 nm a dead layer thickness of 2 to 3 nm. According to their calorimetric and structural studies the critical grain-size in $BaTiO_3$ is between around 20 and 30 nm. In the present study nanocrystalline $BaTiO_3$ with an average particle diameter of 10 nm were prepared using a microemulsion as reaction medium [1,3]. Nanocrystalline ceramics with an average grain-size were prepared by pressure assisted consolidation. Raman spectroscopy was employed to study the true crystallographic structure in both nanocrystalline powders and ceramics. The results are shown in figure 1. The measurements shown here clearly reveal that in nonclamped $BaTiO_3$ nanocrystals of 10 nm tetragonality is still present.

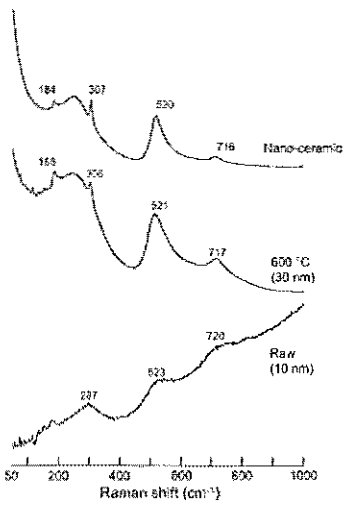

Figure 1: Raman spectra obtained for $BaTiO_3$ in the form of (bottom) nanocrystalline powders (10 nm average diameter), (middle) coarse powders (100 nm average diameter) and (top) nanocrystalline ceramics (35 nm average diameter).

The perfect cubic lattice of $BaTiO_3$ indicates no Raman active modes. The tetragonal lattice of the ferroelectric modification of $BaTiO_3$, however, crystallizes in the space group C_{4v}^1 and shows the Raman active normal modes represented by $3A_1+B_1+4E$. Some of these split up into TO and LO and consequently a complicated peak profile with typical bands at around 180 cm^{-1}, 270 cm^{-1}, 305 cm^{-1},

520 cm^{-1} and 720 cm^{-1} appears. The profile obtained for 10 nm $BaTiO_3$ particles shows these features, which are also demonstrated in figure 1 for a coarse reference powder. The same is true in the case of bulk nanoceramics with an average grain-size of 35 nm. The present study clearly showed that the critical size for the disappearance of tetragonality in powdereous $BaTiO_3$ derived from microemulsion mediated synthesis must be below the value documented in the literature [8]. We also showed that the critical size in dense ceramics with clamped grains must be below the value reported by Buscaglia et al [8].

The second material system of interest has been $NaNbO_3$. Nanocrystalline powders of approximately 30 nm in size were again prepared by microemulsion mediated synthesis and subsequently annealed at different temperatures in order to form particles of various sizes. X-ray diffraction in combination with neutron diffraction and Raman spectroscopy [6] confirmed three different orthorhombic polymorphs, depending on particle size (figure 2). For coarse powders the space group *Pbcm* with a=5.5071 Å, b=5.5698 Å and c=15.5245 Å was found. In the case of submicron sized particles this structure changes to the space group $Pmc2_1$, the lattice parameter being a=7.7673 Å, b=5.5150 Å and c=15.5245 Å. Nanocrystalline powders with an average particle size smaller than 70 nm revealed the space group *Pmma* with a=5.5235 Å, b=7.7951 Å and c=5.5235 Å. Interestingly the intermediate structure looses in contrast to both the nanocrystalline and bulk structure its center of symmetry and consequently enhanced piezoactivity for the under normal conditions antiferroelectric compound may be expected. The exact atomic positions for all three polymorphs were evaluated by refining the corresponding XRD patterns by the Rietveld method and are reported elsewhere [6].

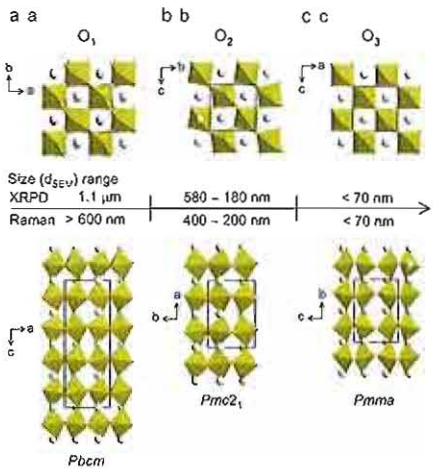

Figure 2: Illustration of the differences between the three different polymorphs observed for (a) micro-, (b) submicron- and (c) nanocrystalline $NaNbO_3$.

Figure 3 shows results from temperature turning and pressure turning Raman studies on the phase transition behaviour of the non-centrosymmetric polymorph $Pmc2_1$ of $NaNbO_3$. A recent qualitative analysis of these data indicates a hysteretic transformation from the metastable non-centrosymmetric structure into the thermodynamically stable new phases of the same composition.

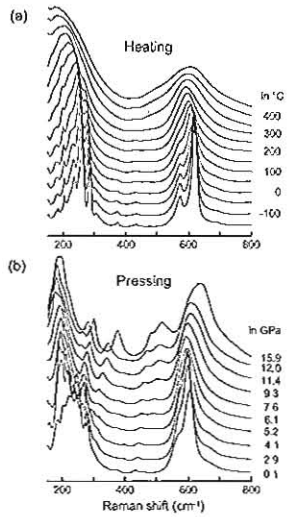

Figure 3: Evolution of Raman spectra with (a) increasing temperature (from –100 to 400 °C) and (b) increasing pressure from 0. 1 GPa up to 15.9 GPa recorded for submicron $NaNbO_3$.

[1] C. Pithan, D. Hennings, R. Waser: „Progress in the Synthesis of Nanocrystalline $BaTiO_3$ Powders for MLCC" *Int. J. Appl. Ceram. Technol.* **2** (2005) 1-14.

[2] C. Pithan, Y. Shiratori, J. Dornseiffer, F.-H. Haegel, A. Magrez, R. Waser: „Microemulsion Mediated Synthesis of Nanocrystalline $(K_x,Na_{1-x})NbO_3$ Powders" *J. Cryst. Growth* **280** (2005) 191-200.

[3] C. Pithan, Th. Schneller, Y. Shiratori, S.B. Majumder, F.-H. Haegel, J. Dornseiffer, R. Waser: „Microemulsion Mediated Synthesis of Nanocrystalline $BaTiO_3$: Possibilities, Potential and Perspectives" einger. bei *Z. Metallkde.*

[4] Y. Shiratori, A. Magrez, C. Pithan: „Phase Transformation of $KNaNb_2O_6$" *Chem. Phys. Lett.* **391** (2004) 288-292.

[5] Y. Shiratori, A. Magrez, C. Pithan: „Particle Size Effect on the Crystal Structure Symmetry of $K_{0.50},Na_{0.50})NbO_3$" *J. Europ. Ceram. Soc.* **25** (2005) 2075-2079.

[6] Y. Shiratori, A. Magrez, J. Dornseiffer, F.-H. Haegel, C. Pithan, R. Waser: „Polymorphism in micro-, submicro- and nanocrystalline $NaNbO_3$" *J. Phys. Chem. B* **109** (2005) 20122-20130.

[7] M.H. Frey, Z. Xu, P. Han, D.A. Payne: "The Role of Interfaces on an Apparent Grain Size Effect on the Dielectric Properties of Ferroelectric Barium Titanate Ceramics" *Ferroelectrics* **206-207** (1998) 337-353.

[8] Z. Zhao, V. Buscaglia, M. Viviani, M. T. Buscaglia, L. Mitoseriu, A. Testino, M. Nygren, M. Johnson, P. Nanni: "Grain-Size Effects on the Ferroelectric Behaviour Dense Nanocrystalline $BaTiO_3$ Ceramics" *Phys. Rev. B* **70** (2004) 024107—1-8.

The reaction of high density $SrTi_{0.6}Fe_{0.4}O_{(3-\delta)}$ ceramics with traces of propane in oxidizing atmospheres

P. Meuffels
Institut für Festkörperforschung, Elektronische Materialien

Because of their usually simple design which makes mass production feasible solid-state gas sensors have the potential to play an influential role in meeting future environmental objectives. Recent studies have shown that semi-conducting $SrTi_{(1-x)}Fe_xO_{(3-\delta)}$ compounds are of interest as novel materials for applications as resistive hydrocarbon gas sensors. As the underlying gas-sensing mechanism is still in question, thermogravimetric analysis was performed on high density (>99 %) $SrTi_{0.6}Fe_{0.4}O_{(3-\delta)}$ ceramic specimens in order to investigate whether bulk properties are affected by the catalytic oxidation of propane at the materials surface. At temperatures 250 – 400 °C oxygen content of the material was found to significantly decrease upon exposure to traces of propane in a background atmosphere of 20 % O_2/80 % Ar. Lattice oxygen anions are sufficiently mobile in $SrTi_{0.6}Fe_{0.4}O_{(3-\delta)}$ so that reducing surface reactions are followed by a change in oxygen stoichiometry even at low or moderate temperatures. The sensitivity of $SrTi_{(1-x)}Fe_xO_{(3-\delta)}$ artefacts towards hydrocarbon gases seems thus to mainly result from modifications in the bulk defect chemistry of the material.

Demand for chemical sensors has been growing at a consistent pace in recent years due to stringent environmental regulations that are coming into effect to reduce hazardous emissions. Because of their usually simple design which makes mass production feasible resistive solid-state gas sensors have the potential to play an influential role through applications in several sectors. Much research has focused on sensors based on SnO_2 technology, but other oxides – including ternary ones with perovskite-related structures – are receiving increased attention.

Recently, it has been reported that the electrical resistance of porous thick films based on p-type conducting $SrTi_{(1-x)}Fe_xO_{(3-\delta)}$ compounds is sensitive to traces of hydrocarbon gases in surrounding atmospheres [1]. These oxides appear thus to be of interest as novel materials for hydrocarbon gas sensor applications. There are various ways how reactive gaseous species can affect the resistivity of oxide materials [2,3], but in the case at hand some open questions remain with respect to the underlying mechanism.

Traces of hydrocarbon gases in otherwise oxidizing atmospheres can have an influence on the resistance of semiconducting oxides as a result of fast catalytic surface reactions. When trace reducing gases arrive on catalytically active surfaces they react with chemisorbed and/or lattice oxygen in outermost surface layers thus interfering with equilibrium exchange reactions between gaseous oxygen and surface oxygen species. If the catalytic surface processes proceed fast enough, a new non-equilibrium state can be established which is characterized by a kinetically determined decrease in the concentration of negatively charged surface oxygen species [3]. As a consequence, charge is transferred to the material. In the case of p-type conducting oxides, this leads to the consumption of holes, i.e. one would expect the overall resistance to increase.

Oxide-based, solid-state gas sensors for trace reactive gases typically operate at temperatures below 500 °C. If lattice oxygen anions are immobile at the sensor operating temperature resistance will be modified only to a certain depth at the surface. In this case, $SrTi_{(1-x)}Fe_xO_{(3-\delta)}$ would work as a gas-sensitive resistor provided the material is presented in a high surface-to-bulk form, viz. artefacts with open porosity or very thin, dense films. If, however, lattice oxygen anions are sufficiently mobile surface reactions are followed by a change in bulk oxygen content and the resistance of the entire artefact becomes modified. In this case, $SrTi_{(1-x)}Fe_xO_{(3-\delta)}$ would work as a gas-sensitive resistor even though the material is presented in a high density form.

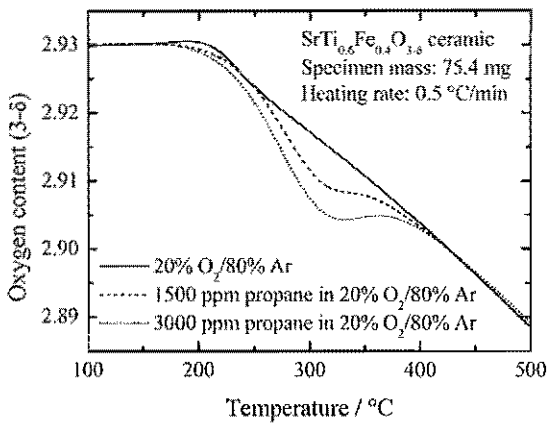

Fig. 1. Changes in oxygen deficiency of a STF40 ceramic disc of mass 75.4 mg and thickness 415 µm as a function of temperature obtained on heating up at 0.5 °C/min in background atmospheres of 20 % O_2/80 % Ar (solid line) and of 1500 ppm (dashed line) and 3000 ppm propane (dotted line) in 20 % O_2/80 % Ar.

A good indicator of such a type of response is the weight loss resulting from the oxygen departure from the sensor sample. Thermogravimetric analysis (TGA) was thus performed on high density $SrTi_{0.6}Fe_{0.4}O_{(3-\delta)}$ (STF40) ceramic specimen in order to investigate whether the oxygen stoichiometry is affected by the catalytic oxidation of hydrocarbons at the materials surface. Work has focused on this particular composition to compare with published data [1].

The STF40 ceramic specimens were made by a standard mixed-oxide process and ceramics with densities > 99 % of the theoretical density could be produced. The TGA measurements were conducted with a Netzsch 439 TGA system where the specimens could be exposed to gas flows of varying composition. A mixture of 20 % O_2/80 % Ar was used as the reference gas. Propane was selected as the reducing gaseous agent.

When STF40 ceramics are heated up in atmospheres that contain different amounts of propane, one observes significant differences in the temperature dependent changes in oxygen deficiency. Representative results are shown in fig. 1. The solid line depicts the oxygen deficiency of a thin STF40 disc of mass 75.4 mg and thickness 415 µm as function of temperature obtained on heating up at a rate of 0.5 °C/min in the pure reference gas. The dashed and dotted lines represent results of similar measurements on the same sample by the time the propane concentration in the reference gas was adjusted to 1500 and 3000 ppm, respectively.

It is quite obvious that the presence of propane gives rise to pronounced deviations from the reference measurement (solid line) at temperatures 250 – 400 °C. The irreversible oxidation of propane by oxygen from the surface proceeds thus fast enough to effectively interfere with the equilibration process. Concentration of surface oxygen species is lowered compared to that in the reference state becoming manifest in an additional reduction of the material. Presuming a surface oxygen density of about $10^{15}/cm^2$, this effect cannot be explained by a sole surface reduction. It is related to a redox mechanism, i.e. partial reduction of outermost surface layers proceeds into the bulk in that lattice oxygen anions diffuse out of the material.

It should be emphasised here that one is faced with a system that is driven into a non-equilibrium steady-state. The additional reduction of the material has no relation to slight shifts in oxygen partial pressure because of gas-phase reactions with the trace reducing agent. It is an outcome of a locally reduced chemical potential of oxygen at the materials surface owing to fast catalytic surface reactions. This is the reason why the "non-equilibrium" curves set in to approach the reference curve at higher temperatures. Interfacial exchange reactions between surface oxygen species and gaseous oxygen become now fast enough to gradually overcome the influence of the trace reducing agent so that an equilibrium state can be re-established.

On the basis of the TGA measurements one can anticipate that the resistance of dense and bulky STF40 specimens will also be affected by traces of propane. Fig. 2. displays the resistance response of a STF40 ceramic disc of thickness 480 µm at 350 °C upon altering the propane concentration in the reference gas. As expected for p-type conducting oxides, sample resistance increases due to the presence of reducing gases in the surrounding atmosphere.

The above results show that surface reactions with propane affect the whole volume of the material. Hence, lattice

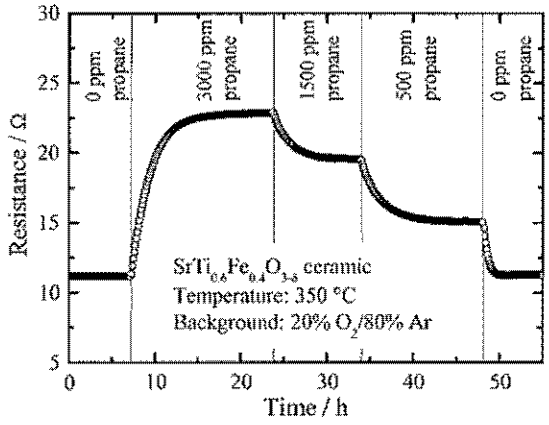

Fig. 2. Resistance response of a STF40 ceramic disc of thickness 480 µm at 350 °C to varying concentrations of propane in a background of 20 % O_2/80 % Ar.

oxygen anions are sufficiently mobile in STF40 so that reducing surface reactions can be followed by a change in oxygen stoichiometry even at low or moderate temperatures. It can thus be concluded that the sensitivity of porous $SrTi_{(1-x)}Fe_xO_{(3-\delta)}$ artefacts towards hydrocarbon gases mainly originates from modifications in the bulk defect chemistry of the material.

High oxygen diffusivities at low or moderate temperatures do not seem to be a surprising finding in the case of $SrTi_{(1-x)}Fe_xO_{(3-\delta)}$ compounds. Previous work has shown that the formation of micro-domains is a non-unusual characteristic of non-stoichiometric perovskite-related oxides[4,5]. Domain walls are potential short-circuit pathways for oxygen diffusion. Overall reduction/oxidation processes can thus be accelerated as a result of long-range fast oxygen transport along micro-domain walls, followed by slow diffusion over short distances within the domains

Acknowledgement

Work was performed in collaboration with K. Sahner (Universität Bayreuth) within the framework of a joint project (Universität Bayreuth, Forschungszentrum Jülich GmbH, National Research Council of Canada) supported by a joint international program of the Helmholtz Gemeinschaft and the National Research Council of Canada (project 01SF0201/9.1).

[1] K. Sahner, R. Moos, M. Matam, J. J. Tunney, M. Post, Sens. Actuators, B 108 (2005) 102.

[2] S. R. Morrison, Sens. Actuators 2 (1982) 329.

[3] D. E. Williams, Sens. Actuators, B 57 (1999) 1.

[4] M. González-Calbet, M. A. Alario-Franco, M. Vallet-Regí, Cryst. Latt. Def. and Amorph. Mat. 16 (1987) 379.

[5] A. Nemudry, E. L. Goldberg, M. Aguirre, M. Á. Alario-Franco, Solid State Sci. 4 (2002) 677.

Diffusion and jump-length distribution in liquid and amorphous $Cu_{33}Zr_{67}$

M. Kluge and H. R. Schober
Institut für Festkörperforschung, Theorie III

Using molecular dynamics simulation of $Cu_{33}Zr_{67}$ near the glass transition temperature, we show that the distribution of atomic jumps lengths can be described by a temperature independent exponential of the length and an effective activation energy plus a contribution of elastic displacements at short distances. No indication of an enhanced probability to jump over a nearest neighbour distance was found. We find a smooth transition from flow in the liquid to jumps in the glass. The drop of diffusion below the Arrhenius value is traced to a decrease of the correlation factor with decreasing temperature.

Metallic glasses are the paradigm of dense random packing and hence of great fundamental interest for the understanding of disorder. At the same time they are of great technological importance. They can be designed to combine properties of ordinary glasses (e.g. isotropy) with typical properties of metals (e.g. electric conductivity, magnetism and mechanic ductility). During the past few years considerable effort has been spent to gain an understanding of the processes governing the glass transition. The most successful theory which has evolved so far is the statistic mode coupling theory (MCT). It predicts a freezing in of density fluctuations, a dynamical phase transition, at a critical temperature T_c, well above the thermodynamic glass transition temperature T_g. It does not identify the underlying processes on an atomic scale. Furthermore, in order to account for diffusion below T_c, still in the undercooled liquid state, additional atomic hopping processes have to be postulated. The connection between the "flow motion", dominating above T_c, and the hopping is unclear.

Diffusion has proved a powerful tool to elucidate the atomistic nature of motion in the glass and undercooled liquid see Ref. [1] for a review. Both by experimental isotope effect measurements and by computer simulation it has been shown that diffusion in the undercooled liquid and in the glass is by a collective mechanism involving more than ten atoms. Upon cooling from a hot melt this collectivity evolves well above T_c and T_g and no obvious transition was seen [2,3]. Monitoring the activation volume, the pressure dependence of the diffusion coefficient, as a function of temperature a pronounced cusp at T_c is observed [4], in agreement with MCT. Both in the glass and the undercooled melt the activation volume was found to be around 0.3 atomic volumes which again is compatible with collective motion.

On the other hand, hopping diffusion below T_g is often depicted by jumps over typical nearest neighbour distances. Indeed based on the time evolution of the atomic autocorrelation function, diffusion in the $Cu_{33}Zr_{67}$, studied here, can be described by such jumps and a small residual of flow motion [5]. The aim of the present work was to resolve this seeming discrepancy. For details and more information see Ref. [6].

We simulated with molecular dynamics $Cu_{33}Zr_{67}$ described by a modified embedded atom interaction developed earlier. Three samples of 1000 atoms were quenched in steps, with intermittent aging stages. The mode coupling temperature is found as $T_c = 1025$ K and the quench rate dependent glass transition is at $T_g \approx 970$ K. Extrapolating to experimental quench rates we find $T_g \approx 750$ K, in excellent agreement with experiment. Before studying diffusion each ensemble was aged at each temperature to reduce aging effects. As far as possible the aging times were chosen to give similar mean square displacements at each temperature. At $T = 900$ K, e. g., the total quench plus aging time was ≈ 20 ns.

Fig. 1 shows the calculated diffusion coefficients together with the MCT fit. Above T_c one observes usual the drop from the Arrhenius behaviour. In the glassy state diffusion follows again an Arrhenius law. Other than in the similar NiZr or the often studied binary Lenard-Jones system, the diffusion coefficients of the two components do not evolve in parallel in the undercooled liquid.

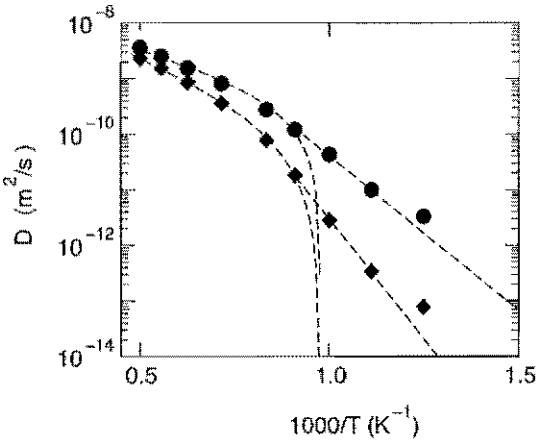

FIG. 1. Diffusion coefficients in $Zr_{67}Cu_{33}$ (Zr: diamonds, Cu: spheres) The dashed lines represent a fit with MCT, using the same temperature T_c for both components, in the undercooled melt and an Arrhenius fit in the glass.

To study the atomic motions during diffusion, we developed an algorithm to extract for each atom its "jumps". In dense packed materials an atomic jump can-

not be understood as a ballistic motion from one site to another. The atoms follow rather complicated reaction paths. In crystals these are restricted by symmetry. In amorphous materials there is no such restriction. We record as "jump" a motion of an atom in a time window of 2.5 ps. To distinguish between vibrational and jump motion, initial and final configurations are averaged over 2.5 ps. For details of the algorithm see Ref. [6].

From the recorded jumps we can calculate how often and how far each atom jumped during the observation time. This defines the average atomic jump rates

$$\gamma^j_{\rm jump}(\ell_{\rm cut}) = \frac{1}{N^j t_{\rm obs}} \sum_{\ell<\ell_{\rm cut}} N^j_{\rm jump}({\rm T}, \ell, t_{\rm obs}) \qquad (1)$$

where $N^j_{\rm jump}({\rm T}, \ell, t_{\rm obs})$ is the number of jumps of atoms of species j with jump length in the interval $[\ell - \delta\ell/2, \ell + \delta\ell/2]$ with $t_{\rm obs}$ and T the observation time and temperature,respectively. The probability that an atom jumps over a distance ℓ we define by

$$P^j({\rm T}, \ell)\delta\ell = \frac{1}{N^j t_{\rm obs}} N^j_{\rm jump}({\rm T}, \ell, t_{\rm obs}). \qquad (2)$$

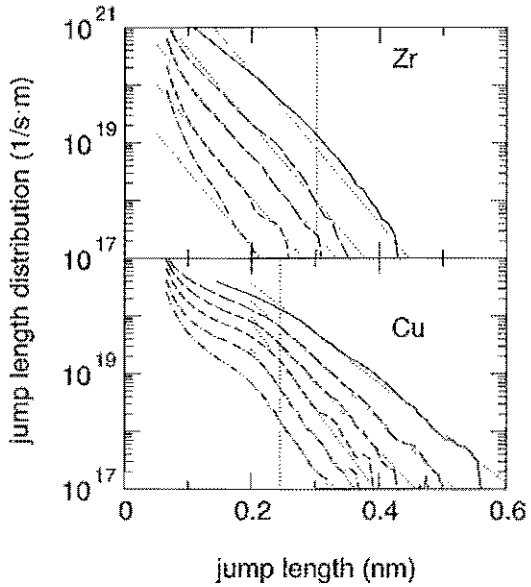

FIG. 2. Distribution of jumps/second over jump length for Zr (top) and Cu (bottom). Temperatures from top to bottom: 1400, 1200, 1100, 1000 and 900 K. The dotted lines indicate the fits by exponential jump length distributions, see text. The respective nearest neighbor distances for the two components are indicated by the vertical dotted lines.

Fig. 2 shows the distribution of the numbers of jumps per second against jump length for the larger majority component Zr for temperatures ranging from 900 to 1400 K (top) and for the smaller minority component Cu for temperatures ranging from 800 to 1400 K (bottom). For Zr one clearly sees no indication of a preferred jump length. The distribution can be fitted with a simple form

$$P_{\rm jump}({\rm T}, \ell) = A_{\rm jump} {\rm e}^{-E_{\rm jump}/kT} {\rm e}^{-\ell/\ell_{\rm jump}} \qquad (3)$$

with $A^{\rm Zr}_{\rm jump} = 1.83 \cdot 10^{28}$ 1/(m·s), $E^{\rm Zr}_{\rm jump} = 1.51$ eV and $\ell^{\rm Zr}_{\rm jump} = 0.033$ nm. The apparent activation energy $E^{\rm Zr}_{\rm jump}$ agrees within some 10% with the diffusional one in the glassy state. In the undercooled melt it corresponds to the apparent activation energy at 1140 K. As shown by the dotted line this fit works well in the whole temperature range investigated which spreads over both T_g and T_c. Of course $E^{\rm Zr}_{\rm jump}$ has to be interpreted as an effective activation energy. There will be a spread of activation energies which is absorbed by the prefactor $A^{\rm Zr}_{\rm jump}$. The probability of jumps over a nearest neighbour distance is two orders of magnitude less than the one for jumps over half that distance. The distribution for the minority Cu-atoms is slightly more complicated [6]. For both components jumps over nearest neighbour distances play only a minor role.

The absence of a preferred jump length might, prima facie, be taken as a contradiction to the time evolution of the van-Hove self correlation function where, in the undercooled liquid, clearly a secondary peak at the nearest neighbour distance evolves. Combining this and the present results one can conclude that the secondary peak in the van-Hove function indicates preferred resting positions for the Cu-atoms in the Zr-matrix which is rigid on the time scale of the Cu diffusion. At the lower temperature the same holds also (to a lesser extend) for the Zr-atoms. Due to dynamic heterogeneity the more movable Zr-atoms are embedded in a matrix of the others.

For uncorrelated jumps the distributions $P_{\rm jump}({\rm T}, \ell)$ would result in Arrhenius laws for the diffusion coefficients. Studying the correlations between successive jumps we find a drop of the correlation factor with falling temperature. The ratio between forward and backward jumps changes. This is in accordance with energy landscape pictures where more and more paths are closed upon cooling.

Our work shows that diffusion both above and below T_c can be described by atomic jumps which in accordance with collectivity have no typical jump length.

[1] F. Faupel, W. Frank, M.-P. Macht, H. Mehrer, V. Naundorf, K. Rätzke, S. K. Sharma, H. R. Schober, and H. Teichler, Rev. Mod. Phys. **75**, 237 (2003).
[2] M. Kluge and H. R. Schober, Phys. Rev. E **62**, 597 (2000).
[3] H. R. Schober, Solid State Commun. 119, 73 (2001).
[4] H. R. Schober, Phys. Rev. Lett. **88**, 145901 (2002).
[5] C. Gaukel and H. R. Schober, Solid State Commun. 107,1 (1998).
[6] M. Kluge and H. R. Schober, Phys. Rev. B **70**, 224209 (2004).

Condensate Formation and Vortex Generation in Bose Gas upon Cooling

E. A. Brener [1], S. V. Iordanskii [2], and R. B. Saptsov [2]
Institut für Festkörperforschung, Forschungzentrum Jülich, 52425 Jülich, Germany [1]
Landau Institute for Theoretical Physics, Russian Academy of Sciences, Chernogolovka, Moscow region, 142432 Russia[2]

The mechanism of transition of a Bose gas to the superfluid state via thermal fluctuations under the condition of external cooling at a temperature above the transition point is considered. The probability of formation of such critical fluctuations (instantons) is calculated; it is found that this probability increases as the system approaches the transition temperature. It is shown that the evolution of an individual instanton is impossible without the formation of vortices in its superfluid part.

The ideas of the kinetics of phase transitions have been thoroughly developed for first-order phase transitions and envisage the existence of the metastable phase itself and an equilibrium critical nucleus. The corresponding theory was worked out in [1, 2] and described in detail in [3]. However, theoretical concepts concerning the kinetics of second-order phase transitions, where these two facts do not exist, have been developed insufficiently. Lifshits [4] proposed a certain special model for the formation of an ordered phase after the fast phase-transition stage in the short-range order in the presence of only two types of ordering. The interest in the problem of a phase transition upon a fast change in external parameters (e.g., temperature) has been aroused in connection with the cosmological ideas of the Big Bang, where the rapidly expanding U niverse must be cooled and pass through a series of phase transformations accompanied by a change in the symmetry of physical fields [5]. It was proposed that the kinetics of these transformations can be modeled in condensed matter [6]. Zurek [7] proposed a theory of the second-order phase transition upon a rapid change in temperature in liquid He_4. The main assumption in the proposed mechanism is about the "critical retardation" of all processes in the vicinity of the transition temperature and "fast" formation of the nuclei of a new phase upon the subsequent cooling. This gives rise to a large number of defects on the order of the number of fluctuations far above the transition point. However, no retardation in the formation of a new phase has been detected experimentally; the critical retardation is associated with the duration of the equilibration process at macroscopic distances, which is insignificant for the nonuniform process of formation of a new phase.

In this work, we consider the transition to a new phase via the evolution of fluctuations on scales much smaller than the correlation length, which can occur quite rapidly even in the vicinity of the critical temperature. The transition kinetics in this case are found to be directly related to the cooling process itself. We will consider the formation of a condensate in the model of a weakly nonideal Bose gas with external cooling and demonstrate a certain analogy with the first-order phase transitions. The standard theory of a weakly nonideal Bose gas involves a Hamiltonian of the form

The entire kinetics is essentially determined by the Bose-gas cooling mechanism. We will consider a simple model where the Bose gas is in a certain solid matrix with which it only slightly interacts. Such a situation may take place, for example, for the exciton gas in a crystal. The crystal can be rapidly cooled to a low temperature; in this case, the Bose-gas cooling proceeds via phonon emission. Assuming that the heat capacity of the crystal is large compared to the Bose gas, we can disregard the presence of thermal phonons in the crystal and their effect on the Bose gas. As a result, we obtain a uniform energy-loss mechanism, which is described by a phenomenological quantity T/τ_{ph}. The other models of cooling necessitate the analysis of heat transfer at the sample boundaries, which is a much more complicated problem. The loss rate $1/\tau_{ph}$ is determined by the collisions of particles with each other and by the interaction with phonons, which will be regarded as weak. This allows us to consider the problem of fluctuation kinetics within the framework of the theory of hydrodynamic fluctuations by supplementing the hydrodynamic equations with the energy flux carried away as a result of phonon emission. In view of the constancy of pressure, we can describe the evolution of temperature fluctuations by the heat conduction equation

$$\frac{\partial T}{\partial t} = \chi \nabla^2 T + \Theta(T_c - T)\frac{T - T_c}{\tau_{ph}},$$

where the energy flux carried away by phonons is added. Here χ is the thermal diffusivity; T_c is the transition temperature; $\Theta(x)$ is the step function. We assume here that the phonon induced flux is much larger in the superfluid state [8]. We are interested in the temperature-field fluctuations and their time evolution. To analyze these fluctuations, we must introduce random heat fluxes q [3, 9], i.e., the Langevin term ∇q. These fluxes are delta-correlated (i.e., correlated at distances and time intervals smaller than the hydrodynamic scales). It is well known that the probability $W_t(T(r))$ of realizing the given configuration T(r) of fluctuation field at time t obeys the

Fokker-Planck equation in variational derivatives [10]:

$$\frac{\partial W}{\partial t} = \int \frac{\delta}{\delta T(r)} \left[\frac{\chi T_\infty^2}{n c_p} \nabla^2 \frac{\delta}{\delta T(r)} W + \left[\chi \nabla^2 T + \Theta(T_c - T) \frac{T - T_\infty}{\tau_{ph}} \right] W \right] d^3 r$$

We assume that fluctuations occur at a fixed temperature $T_\infty > T_c$. Fluctuations with $\Delta T = T - T_\infty << T_\infty$ occur quite frequently and are characterized by a certain (in fact, stationary) spatial distribution that determines the value of $W_t(T)$. In view of the normalization, the latter quantity gives the number of small fluctuations in a unit volume. However, rare large-amplitude fluctuations with $\Delta T \sim (T_c - T_\infty)$ also sometimes occur, initiating the effective cooling by phonons, so that the fluctuation becomes irreversible and the nucleus of a new phase appears. Our goal is to calculate the probability of such fluctuations in a unit volume per unit time. Since they are infrequent and the distribution at small $T_\infty - T$ is stationary, one can use the method of characteristics to determine the exponentially low probability of formation of such a nucleus (instanton for the Fokker-Planck equation). An important difference from the theory of nucleation in the first-order phase transition is that the probability of instanton formation in this case is determined by the cooling process.

This problem was solved by us in [8] and we found that the number of critical fluctuations arising per unit time in a unit volume is:

$$\frac{dN}{dt} \sim \exp\left[-s_0 (\chi \tau_{ph})^{3/2} \frac{n c_p (T_\infty - T_c)^2}{T_\infty^2} \right]$$

The constant s_0 is of otherder unity and can be determined numerically. It is a universal number corresponding to the extrema of action and is independent of the values of physical parameters.

Analysis of the subsequent growth of the instanton requires the solution of hydrodynamic equations for a superfluid liquid, because a superfluid core appears in the developing fluctuation. We qualitatively considered the phenomena that arise in this case in [8]. A singularity appears in the superfluid core. This singularity indicates that the quasi-stationarity conditions are violated , and a complex nonstationary superfluid flow with the intense vortex formation in an instanton should appear upon the transition to the normal liquid at $T > T_c$.

Thus, we have shown that, in contrast to [7], a transition to the superfluid phase can occur through an independent growth of critical fluctuations (instantons) at temperatures above the critical point ($T > T_c$) immediately in the course of external cooling. These fluctuations subsequently transform into macroscopic formations. The growth of the nucleus of the superfluid state is accompanied by vortex generation in its external part. Consequently, vortex defects appear both due to the independent nucleation with an arbitrary phase upon cooling (the Zeldovich-Kibble hypothesis) and directly during the growth of each superfluid nucleus. This vortex-generation mechanism during the growth of an instanton significantly differs from the mechanism determined in [11], where the existence of a superfluid flow interacting with the heated normal regions was presumed. In [11], an attempt was made to explain the results of experiments [12], in which 3He was bombarded by neutrons. As a result, regions heated to temperatures above T_c appeared. These regions were cooled by the surrounding superfluid ^3He, and the formation of vortices was detected. Thus, nonuniform cooling took place that differs considerably from the model used in our study. In the critical fluctuation considered here, heating takes place due to its nonsuperfluid surroundings. Consequently, it is advantageous for the fluctuation to preserve its spherical symmetry to reduce this heating. In the case of cooling of a heated region with superfluid surroundings [12], the interface must obviously be unstable against its shape distortions, because this leads to a faster cooling. However, the stability, as well as the phase-transition mechanism itself, under such conditions (which, in contrast to [11], are not associated with the existence of an external superfluid flow) calls for detailed investigations.

[1] R. Becker and W. Doering, Ann. Phys. (Leipzig) 24, 719 (1935).

[2] Ya. B. Zeldovich, Zh. ksp. Teor. Fiz. 112, 525 (1942).

[3] J. S. Langer, Ann. Phys. (N.Y.) 54, 258 (1962).

[4] I. M. Lifshits, Zh. ksp. Teor. Fiz. 42, 1354 (1962) [Sov. Phys. JETP 15, 939 (1962)].

[5] Ya. B. Zeldovich, I. Yu. Kobzarev, and L. B. Okun, Zh. ksp. Teor. Fiz. 67, 3 (1974) [Sov. Phys. JETP 40, 1 (1975)].

[6] T. W. Kibble, J. Phys. A 9, 1387 (1976).

[7] W. H. Zurek, Phys. Rep. 276, 177 (1996).

[8] E.A. Brener, S.V. Iordanskii, and R.B. Saptsov, JETP Lett. 79, 410 (2004)

[9] E. M. Lifshitz and L. P. Pitaevskioe, Course of Theoretical Physics, Vol. 9: Statistical Physics, 2nd ed. (Fizmatlit, Moscow, 2002; Pergamon, New York, 1980), Part 2, Chap. 9.

[10] V. I. Klyatskin, Stochastic Equations by the Eyes of a Physicist (Fizmatlit, Moscow, 2001).

[11] I. S. Aranson, N. B. Kopnin, and V. M. Vinokur, Phys. Rev. Lett. 83, 2600 (1999).

[12] V. H. M. Ruutu, V. B. Eltsov, A. J. Gill, et al., Nature 382, 334 (1996).

Deriving nonequilibrium interface kinetics from variational principles

Robert Spatschek
Institut für Festkörperforschung, Forschungszentrum Jülich, D-52425 Jülich, Germany
(Dated: February 8, 2005)

Nonequilibrium dynamics at interfaces is generally driven by a chemical potential. Here we demonstrate a generic technique to derive the basic equations of motion, boundary conditions and the chemical potential in a consistent way from fundamental variational principles. As a particular example, we consider a solid surface with elastodynamic effects, together with surface energy and tension. We apply the generic results to perform a linear stability analysis of a planar front subjected to uniaxial stress (Asaro-Tiller-Grinfeld instability [1]), here also with surface tension.

I. INTRODUCTION

The quest for the correct equations of motion describing a system is an essential task of each problem in all branches of physics. The procedure is well-known for mechanical systems, where for example the appropriate Lagrangian has to be found, from which the (Newtonian) equations of motion can be derived using variational principles. This method can in particular be applied to continuum mechanics, generating the usual bulk equations and boundary conditions.

However, for more complicated dissipative systems, these straightforward and general methods are usually not applicable. Bulk diffusion, friction, and also irreversible phase transitions are important examples. In the framework of linear nonequilibrium thermodynamics, the "process velocity" is proportional to the deviation of an energy functional from its equilibrium value.

If we consider for example diffusion processes, then the flux of material is typically $j = -D\nabla\mu$ with the diffusion coefficient D and a chemical potential μ. The Asaro-Tiller-Grinfeld (ATG) instability is a particular example of these processes [1]. Here strong surface tension and also dynamical effects become relevant, but they are not taken into account in conventional descriptions.

The main goal of the current paper is therefore to provide a method to derive all describing quantities in a consistent way from variational principles. A particular illustration is the Grinfeld instability with surface tension.

II. ACTION AND LAGRANGIAN

We consider a solid body in vacuum under the influence of external forces, linear elastodynamics, surface energy and tension. The Lagrangian is given by

$$L = \int\limits_{V(t)} (T - U_b)\, dV - \int\limits_{\partial V(t)} U_s\, d\tau = L_b + L_s, \qquad (1)$$

where $V(t)$ is the time-dependent volume of the elastic body and $\partial V(t)$ its boundary with elements $d\tau$. The expressions for kinetic and potential energy densities are

$$T = \frac{1}{2}\rho \dot{u}_i \dot{u}_i, \qquad U_b = \frac{1}{2}\sigma_{ik} u_{ik}, \qquad (2)$$

$$U_s = \alpha + \beta u_{\tau\tau} - \sigma^{(0)}_{ni} u_i. \qquad (3)$$

Here ρ denotes the mass density, u_i is the displacement field, σ_{ik} the stress, u_{ik} the strain tensor, α is the surface energy density and β the surface tension coefficient. The stresses $\sigma^{(0)}_{ij}$ are the given external forces which may act on some parts of the boundary; everywhere else they are zero. We assume the volume to be two-dimensional; τ is the tangential and n the normal direction at the interface.

Stress and strain are connected by Hooke's law. For simplicity, we restrict it to the isotropic case,

$$\sigma_{ij} = \frac{E}{1+\nu}\left(u_{ij} + \frac{\nu}{1-2\nu}\delta_{ij} u_{kk}\right), \qquad (4)$$

with E being the elastic modulus and ν the Poisson ratio. The action is given by the time integral

$$S = \int\limits_{t_0}^{t_1} L\, dt = S_b + S_s \qquad (5)$$

with arbitrary initial and end times t_0, t_1.

III. THE FUNDAMENTAL EQUATIONS

The Euler-Lagrange conditions demand that the variation of the action with respect to the displacements has to vanish [5]. Here we also take into account that the volume can change in time due to other processes. This leads to the elastodynamic equations and boundary conditions with surface tension

$$\frac{\partial \sigma_{ij}}{\partial x_j} = \rho \ddot{u}_i, \qquad (6)$$

$$\sigma_{nn} = -v_n \rho \dot{u}_n + \beta\kappa + \sigma^{(0)}_{nn}, \qquad (7)$$

$$\sigma_{n\tau} = -v_n \rho \dot{u}_\tau + \sigma^{(0)}_{n\tau}. \qquad (8)$$

The velocity dependent term in the boundary conditions ensures momentum conservation.

The elastic motion as "mechanical" process describes the motion of individual atoms due to Newton's law; in contrast, the "chemical" processes are related to a (local) change of the number of atoms and consequently of the shape of the body.

Demanding that the solid body is in equilibrium not only with respect to variations of the displacement vector but also with respect to this new degree of freedom, the interface position, leads to the requirement that $\delta S = 0$ holds also for variations of the surface position in normal direction by an interface shift δn. Otherwise, small deviations from the condition $\delta S = 0$ initiate thermodynamical processes, driven by the chemical potential

$$\mu = -\Omega \frac{\delta L}{\delta n}. \tag{9}$$

Therefore the total chemical potential reads after some tedious calculations involving complicated differential geometry,

$$\mu = \Omega \left[\frac{1}{2}\sigma_{ik}u_{ik} - \frac{1}{2}\rho \dot{u}_i^2 - \alpha\kappa + \beta \left(\frac{\partial u_{\tau\tau}}{\partial n} - u_{\tau\tau}\kappa - 2\frac{du_{n\tau}}{d\tau} \right) \right]. \tag{10}$$

Inertial effects enter in an unexpected way, because instead of the *sum* of elastic and kinetic energy density their *difference* appears here. Surface tension gives rise to three contributions: At first, the term $\partial u_{\tau\tau}/\partial n$ reflects the change of the strain $u_{\tau\tau}$ when the solid extends in normal direction, and $u_{\tau\tau}\kappa$ expresses the elongation of a curved surface element. Without dynamical effects and external forces, the last term in the surface tension contribution vanishes, because, by virtue of the boundary condition (8) and Hooke's law, also $u_{n\tau} = 0$. This full derivative appears only if both inertial contributions and surface tension are taken into account, leading to a coupling of both effects.

The chemical potential can also be introduced by consideration of the dissipation rate,

$$\frac{dE}{dt} = \frac{1}{\Omega} \int\limits_{\partial V(t)} \mu v_n \, d\tau \tag{11}$$

with the same expression (10). In particular, we clearly see that the density of the bulk *Lagrangian* instead of the total *energy* is relevant for the dynamics.

IV. GRINFELD INSTABILITY WITH SURFACE TENSION

A straightforward application of the preceding results is the Grinfeld instability [1]; similar to [2] we also include surface tension here and neglect inertial effects [3, 4].

The geometrical situation is sketched in Fig. 1. The

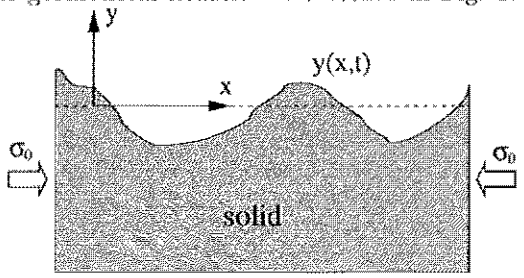

FIG. 1: The Grinfeld instability.

horizontally applied uniaxial loading $\sigma_{xx}^{(0)} = \sigma_0$ can be compressive or tensile. Our goal is to calculate the stability of an originally flat surface. Therefore we study the evolution of a slightly perturbed interface, $y(x,t) = \Delta \cos kx$.

The elastic problem is solved by the means of an Airy function, and this step is not demonstrated here. The total chemical potential at the interface is therefore to first order in Δ

$$\mu = \Omega \left(\frac{(1-\nu^2)\sigma_0^2}{2E} + k\Delta \cos kx \left[-2\sigma_0^2 \frac{1-\nu^2}{E} + \alpha k - k\frac{\beta(1-\nu^2)}{E}(3\sigma_0 + 2\beta k) \right] \right) + \mathcal{O}(\Delta^2).$$

In the particular case of surface diffusion, $v_n = D\partial^2\mu/\partial\tau^2/\alpha\Omega$, with a kinetic coefficient D, the amplitude evolution, $\Delta = \Delta_0 \exp(\lambda t)$, leads up to linear order to the spectrum

$$\lambda = Dk^3 \left(2\sigma_0^2 \frac{1-\nu^2}{E\alpha} - k + k\frac{\beta(1-\nu^2)}{E\alpha}(3\sigma_0 + 2\beta k) \right), \tag{12}$$

assuming $k \geq 0$. Obviously, the surface tension favors the Grinfeld instability; the self-stress due to surface tension leads to an instability even without external loading σ_0.

[1] R. J. Asaro and W. A. Tiller, Metall. Trans. **3**, 1789 (1972); M. A. Grinfeld, Sov. Phys. Dokl. **31**, 831 (1986).
[2] J. Grilhe, Acta metall. mater. **41**, 909 (1993).
[3] E. A. Brener and R. Spatschek, Phys. Rev. E **67**, 016112 (2003).
[4] K. Kassner and C. Misbah, Europhys. Lett. **28**, 245 (1999).
[5] L. D. Landau and E. M. Lifshitz, *Theory of Elasticity*, Pergamon Press, Oxford, 1987.

Multilayer relaxation sequence of stepped Cu surfaces

Juarez L. F. Da Silva[1], K. Schroeder, S. Blügel[1]
IFF-Theory III and [1] *IFF-Theory I*

We performed density-functional theory (DFT) calculations, employing the all-electron full-potential linearized augmented plane-wave (FLAPW) method, for the multilayer relaxations of the vicinal, high-Miller-index Cu(210), Cu(211), and Cu(331) surfaces, for the flat, low-Miller-index Cu(100), Cu(110), and Cu(111) surfaces, as well as for more open surfaces such as for Cu(320) and Cu(410). Generally, it is expected that the interlayer relaxation-sequence at stepped metal surfaces with n surface atom rows in the terraces exposed to the vacuum show $n-1$ contractions (indicated by $-$) followed by one expansion (indicated by $+$). While this so-called atom-rows trend holds true for closed stepped surfaces it does not apply for more open surfaces such as for Cu(320) and Cu(410). For these surfaces we found relaxation-sequences like $---+-\cdots$, instead of the expected $--+-\cdots$ and $---+-\cdots$, respectively. Our results show that the relaxation-sequences of eleven stepped Cu surfaces, namely, (110), (311), (331), (211), (511), (210), (221), (711), (911), (410), and (320), follow the more general nearest-neighbor coordination trend, which correlates the relaxation-sequence of the topmost interlayer spacings with the nearest-neighbor coordination number of the topmost surface atomic layers. Therefore, the reduction of the atomic coordination plays a more important role in the relaxation-sequences of stepped metal surfaces than the number of atoms exposed to the vacuum region.

A microscopic understanding of many physical and chemical processes which take place at solid surfaces such as heterogeneous catalysis, electrochemistry, corrosion, lubrication, etc., requires as a prerequisite an atom level understanding of surface defects like adatoms, vacancies, kinks, atomic steps, etc., (for reviews see Ref. 2). In particular, atomic steps are always present on real solid surfaces, and hence, there is a clear interest to understand their atomic structure. To reach that goal, the study of high-Miller-index surfaces (vicinal or stepped), which have a periodic distribution of atomic steps separated by terraces of a low-Miller-index orientation (see Fig. 1), is the most simple and convenient approach. [3]

Based on results of quantitative low-energy electron diffraction (LEED) intensity analysis and some theoretical semi-empirical as well as first-principles calculations, Tian *et al.* [4] suggested that there is a correlation between the interlayer relaxation-sequence of the topmost interlayer spacings and the number of atom-rows in the terrace of a stepped metal surface: For a stepped metal surface with n atom-rows in the terrace exposed directly to the vacuum region, the topmost $n-1$ interlayer spacings (d_{12}, $\cdots$, $d_{n-1,n}$) contract compared with the unrelaxed interlayer distances, while the nth and $(n+1)$th interlayer spacings, i.e., $d_{n,n+1}$ and $d_{n+1,n+2}$, expand and contract, respectively.

Recently, Sun *et al.* [5, 6] suggested that the multilayer relaxation-sequences of the topmost interlayer spacings of a stepped metal surfaces correlates with the number of nearest neighbors of all atoms with coordination smaller than those in the bulk: each pair of layers with coordination smaller than in the bulk contracts.

We performed density-functional theory (DFT) calculations employing the all-electron full-potential linearized augmented plane-wave (FLAPW) method for stepped Cu surfaces: a series of low index surfaces, Cu(111), Cu(110) and Cu(100); several surfaces with (111) terraces and

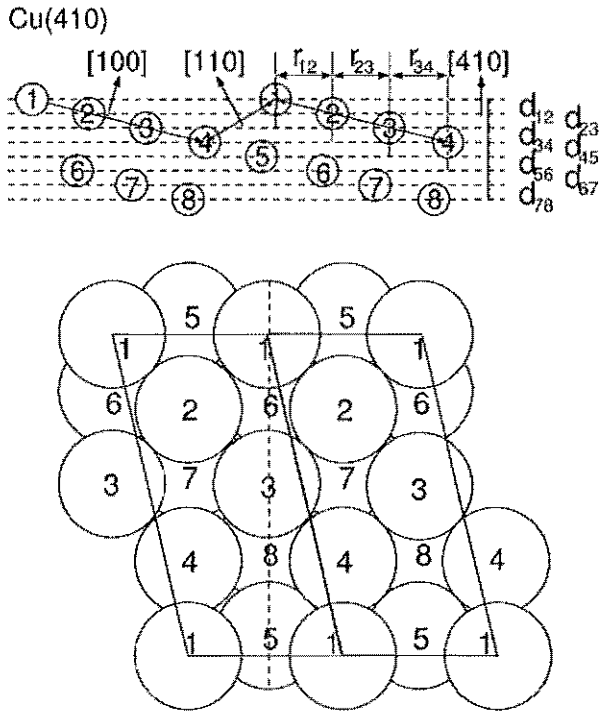

FIG. 1: Schematic views of the stepped Cu(410) surface (upper panel side view, lower panel top view). The Cu atoms are indicated by spheres with radius of half of the first-neighbors distance and the numbers inside indicate the surface layer number (increasing for deeper layers). In the side view the direction normal to the surfaces, terraces, and steps are indicated. The interlayer and registry distances are also indicated In the top view The (1×1) surface unit cell are indicated by solid lines, while the dashed lines indicate the mirror plane symmetry.

TABLE I: Multilayer relaxation and coordination sequences for Cu surfaces. The second column indicates the number of atom-rows in the (*hkl*) terrace exposed to the vacuum region, which are separated by (*uvw*) steps. The fifth column indicates the sequence of coordination numbers (number of nearest-neighbors (*NN*)) for the outermost surface layers down to where the bulk fcc coordination (i.e., 12) is obtained. N_c indicates the number of surface layers for which the coordination is smaller than the bulk Cu coordination. The last column summarizes the multilayer relaxation-sequence for several stepped Cu surfaces as calculated with the all-electron FLAPW method in our work. [7, 8]

Surface	Atom-rows in the terraces	Terrace (*hkl*)	Step (*uvw*)	first-neighbors coordination sequence	N_c ($NN < 12$)	multilayer relaxation-sequence
Cu(*110*)	2			7, *11*, *12*, *12*, ⋯	2	$-+-\cdots$
Cu(3*11*)	2	(*100*)	(*111*)	7, *10*, *12*, *12*, ⋯	2	$-+-\cdots$
Cu(33*1*)	3	(*111*)	(*111*)	7, 9, *11*, *12*, *12*, ⋯	3	$--+-\cdots$
Cu(*211*)	3	(*111*)	(*100*)	7, 9, *10*, *12*, *12*, ⋯	3	$--+-\cdots$
Cu(5*11*)	3	(*100*)	(*111*)	7, 8, *10*, *12*, *12*, ⋯	3	$--+-\cdots$
Cu(*210*)	3	(*110*)	(*100*)	6, 9, *11*, *12*, *12*, ⋯	3	$--+-\cdots$
Cu(*221*)	4	(*111*)	(*111*)	7, 9, 9, *11*, *12*, *12*, ⋯	4	$---+-\cdots$
Cu(7*11*)	4	(*100*)	(*111*)	7, 8, 8, *10*, *12*, *12*, ⋯	4	$---+-\cdots$
Cu(9*11*)	5	(*100*)	(*111*)	7, 8, 8, 8, *10*, *12*, *12*, ⋯	5	$----+-\cdots$
Cu(4*10*)	4	(*100*)	(*110*)	6, 8, 8, 9, *11*, *12*, *12*, ⋯	5	$----+-\cdots$
Cu(3*20*)	3	(*110*)	(*100*)	6, 7, 9, *11*, *11*, *12*, *12*, ⋯	5	$----+-\cdots$

(100) or (111) steps, Cu(211), Cu(221), and Cu(331); a series of surfaces with varying width (100) terraces and (111) steps, Cu(311), Cu(511), Cu(711), Cu(911); and the more open surfaces showing terraces or steps of (110) orientation, Cu (221), Cu(320), Cu(410).[7, 8] Fig. 1 shows the layer sequence and surface geometry for the open Cu(410) surface. The open surfaces can be considered as important test cases for the suggested atom-rows and nearest-neighbors trends.

Our theoretical calculations are based on DFT within the generalized gradient approximation. The Kohn-Sham equations are solved using the all-electron FLAPW method, as it is implemented in the FLEUR code, [9] in which solid surfaces are modeled using a film geometry. Careful tests were made with respect to all parameters determining the layer relaxation (basis set, i.e. number of k-points and energy cut-off for plane-wave basis; number of layers), and we made sure that comparable accuracy was achieved for all systems considered.

The multilayer relaxation-sequences of eleven Cu surfaces are summarized in Table I, along with the number of atom-rows in the (hkl) terrace and the nearest-neighbors coordination sequence of the topmost atomic layers. We found that the multilayer relaxation-sequences of the (110), (311), (331), (211), (511), (210), (221), (711), and (911) Cu surfaces follow the atom-rows trend, however, the same was not found for (320) and (410). For example, the (410) and (320) Cu surfaces have four and three atom-rows in the terraces, hence, according to the atom-rows trend, one expects relaxation-sequences like $---+-\cdots$ and $--+-\cdots$, respectively. However, we found a multilayer relaxation-sequence like $----+-\cdots$ for both surfaces, which is expected for a stepped surface with five atom-rows in the terrace such as for Cu(911). The (410) and (320) Cu surfaces have an irregular behavior with respect to the the atom-rows trend, i.e., the relaxation-sequence does not correlate with the number of atom-rows in the terrace.

However all considered surfaces do follow the nearest-neighbor coordination trend. As one can note from Table I the atom-rows trend is a particular case of the nearest-neighbor coordination trend. We want to point out that the nearest-neighbor coordination trend is a simple consequence of the chemist's concept of bond-order bond-length correlation, which correlates the contraction of the topmost surface layer to the reduction of coordination of the surface atoms. [10] As we have checked, the reduction of the coordination number drastically changes the density of states of the surface atoms, e.g. the bandwidth is decreased for the topmost surface layer.[8]

---

[1] present address: Institut für Chemie, Arbeitsgruppe Quantenchemie, Humboldt-Universität zu Berlin.

[2] For a retrospective of surface science, see Surf. Sci. **500**, 1-1053 (2002).

[3] M. -C. Desjonquères and D. Spanjaard, *Concepts in Surface Science*, Springer (1995).

[4] Y. Tian, K. -W. Lin, and F. Jona, Phys. Rev. B **62**, 12844 (2000).

[5] Y. Y. Sun, H. Xu, J. C. Zheng, J. Y. Zhou, Y. P. Feng, A. C. H. Huan, and A. T. S. Wee, Phys. Rev. B **68**, 115420 (2003).

[6] Y. Y. Sun, H. Xu, Y. P. Feng, A. C. H. Huan, A. T. S. Wee, Surf. Sci. **548**, 309 (2004).

[7] J. L. F. Da Silva, K. Schroeder, and S. Blügel, Phys. Rev. B **69**, 245411 (2004).

[8] J. L. F. Da Silva, K. Schroeder, and S. Blügel, Phys. Rev. B **70**, 245432 (2004).

[9] http:\\www.flapw.de.

[10] P. J. Feibelman, Phys. Rev. B **46**, 2532 (1992).

Vertical attachment of molecules via carboxylate group: iFormate on Cu(110)

N. Atodiresei[1], K. Schroeder, S. Blügel[1]
IFF-Theory III and [1]IFF-Theory I

We have investigated the interaction of formate molecules with the Cu(110)-surface by using density functional theory (DFT) calculations. We found that in the most stable structures the formate molecules are always sitting perpendicular to the Cu(110)-surface, and they are adsorbed in a bridge position, i.e. the O-C-O group forms a bridge between two Cu atoms. Other tested configurations are less stable by at least 0.9 eV per formate molecule. We have shown that there is an attractive interaction between adsorbed formate molecules at the copper surface. In the case of oxygen precovered Cu(110)-surface the higher formate coverage (two molecules in a (2×2) unit cell) is enforced through favorable reaction of the formic acid deprotonation by the preadsorbed oxygen. Our results are consistent with experimental observations and help in the understanding of the different adsorption domains formed by formate molecules on copper surface.

Surface reaction involving organic molecules have attracted increasing attention recently. Apart from the traditional use in a vast number of economically important surface processes such as catalysis in chemical production, corrosion, the fabrication of computer chips or magnetic storage devices, the behavior of biomaterials and organic functionalisation of the metallic surfaces has important applications.[1] In addition, electronic transport involving organic molecules adsorbed on metal surfaces is attracting increasing interest. The inclusion of biological active molecules and the concept of bioelectronic devices add further weight to this idea. Within such a technological complex, it is clear that the development of future organic/inorganic interfaces is critically dependent on establishing a fundamental understanding of the various bonding mechanismus and lateral interactions that govern the ultimate orientation, conformation and two dimensional organization of these molecules at the surface.

Recent developments have enabled the chemistry field of surface science to progress from the study of simple adsorbates to the investigation of bigger and more complicated molecules, e.g. organic acids and aminoacids. The carboxyl group is well known to be an anchoring group for the chemical binding to the metal surfaces used by a large variety of organic molecules.[1–3, 9]

From the theoretical point of view the understanding of the binding to metal surfaces of the simplest molecule that contains the carboxyl group (which is the formic acid) is a first step for the treatment of more complex molecular structures.

Formic acid adsorption has been studied experimentally on both clean and oxygen precovered surfaces of copper. At elevated temperatures (300-450°C) formate molecules are chemically adsorbed at the Cu surface by dehydrogenation (clean surface) or release of water (oxygen precovered surface)[4]. To determine the formate adsorption structures, several experimental methods have been used: near-edge X-ray-absorption fine structure spectroscopy (NEXAFS), surface extended X-ray-absorption fine structure (SEXAFS), low-energy electron diffraction (LEED), Auger electron spectroscopy, temperature programmed desorption (TPD), scanning tunneling microscopy (STM), reflection-absorption infrared spectroscopy (RAIRS) and in-situ infra-red reflection-absorption spectroscopy (IRAS)[4–8].

With some of the experimental methods it was difficult to determine how the formate molecules are chemisorbed on the copper surface. The distinction between an upright or tilted geometry, or the bidentate or monodentate geometry (for the monodentate case the oxygen forms a single bond with a copper atom, for the bidentate geometry the oxygen atoms are bound to the copper atoms) cannot be made unambiguously. Only NEXAFS and SEXAFS have suggested specific geometries[5]: the molecules are adsorbed with their molecular plane perpendicular to the metal surface, and the molecules are arranged in rows with the plane formed by the carboxylic group along the direction $[1\bar{1}0]$.

Ab initio calculations of the molecular and electronic structure of adsorbed organic molecules on Cu(110)-surface are done using our projector-augmented wave (PAW) code [10]. Although we can use ultrasoft pseudopotentials and plane-wave cut-off energies less than 25 eV with the PAW-method, the computer demands are quite high, since the adsorption assemblies of larger molecules yield rather large unit cells.

We have used the Perdew-Burke-Ernzerhof implementation of the general gradient approximation for the exchange-correlation functional. The calculations for formate molecules adsorbed on Cu(110)-surface have been performed using an inversion symmetric slab containing five copper layers. The unit cell has the dimensions $4a\sqrt{2}$ (perpendicular to the surface), and $2a$, $a\sqrt{2}$ (parallel), with $a = 3.641$Å being the bulk lattice constant of the Cu-fcc. An energy cutoff of 25 Ry and a 1x3x4 k-point set have been used. In all calculated structures the molecules and the first two layers have been allowed to relax without any constraint. In the starting configurations the positions of the copper atoms are corresponding to those of the optimized (1×1) unit cell of the Cu(110)-surface. For the molecules the relaxed atom positions of the for-

mate free radical have been used as starting positions.

Several geometries corresponding to low and high coverages of formate molecules in a (2×2) unit cell on clean and oxygen-precovered Cu surface have been optimized. For all configurations we found that the molecule is sitting with its molecular plane perpendicular to the Cu(110)-surface. For low coverage (one formate molecule in the unit cell) we found that in the stable configuration the molecule is in a bridge position (each oxygen of the carboxylate group binds a single copper atom so that the carboxylate group forms a bridge between two nearest-neighbor copper atoms along to $[1\bar{1}0]$ direction). The Cu surface atoms that are not binding directly to oxygen atoms show inward relaxations as on the clean Cu(110) surface. In contrast, nearly no relaxation relative to the ideal unrelaxed Cu(110) surface is found for the Cu atoms that are forming the bonds with O atoms. At high coverage (two formate molecules in the unit cell) the most stable configuration is the one with both molecules in bridge positions. The Cu-surface atoms show outward relaxations larger than in the low coverage case.

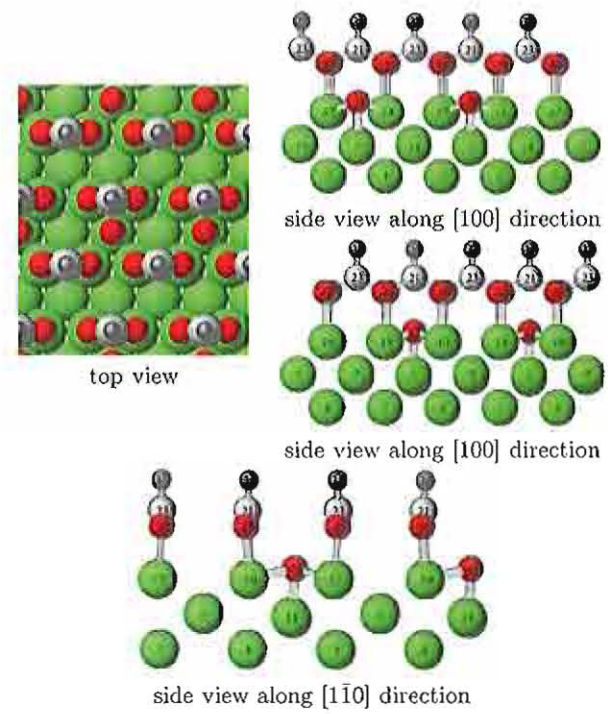

Figure 1: Adsorption geometry of two formate molecule in (2x2) unit cell on a 0.25ML oxygen precovered Cu(110) surface: the bridge-bridge position (C^{21} on bridge between Cu^{15}-Cu^{19} and C^{23} on bridge between Cu^{13}-Cu^{17}). (Cu-green, O-red, C-gray, H-dark grey)

In the case of oxygen-precovered Cu-surface (see figure 1), at high coverage of formate molecules, we find again that the stable configuration is the one with both molecules in bridge positions. A large outward relaxation of the Cu surface layer is found. The molecular geometry of the formate molecules does not change significantly and it is similar as in the previously discussed systems. The Cu-O bond length is practically the same in all configurations and does not depend on the coverage ratio. The oxygen adsorption does not influence the binding of the oxygen atoms of the carboxylate group with the first layer of the Cu-surface. With increasing coverage the first Cu-surface layer relaxes towards the positions corresponding to the unrelaxed (110) surface, and for the oxygen precovered surface the inward relaxation for the clean Cu(110) surface is over-compensated and turned into a large outward relaxation.

We consider these calculations as the starting point of a series, in which we will consider the adsorption of larger and more complicated organic molecules, containing a longer C-backbone, e.g. additional five-membered heterocycles. This introduces more degrees of freedom, e.g. the orientation of the plane of the heterocycle rings with respect to the COO bonding group. One example is 3-thiophene-carboxylate ($(CH)_3SCCOO$) which is formed by adding a thiophene five-atom-ring to formate. This molecule is found experimentally to sit vertical on the Cu(110) surface and the heterocycle ring is rotated as we also found theoretically. Other examples are the five-membered heterocycles containing as heteroatom: O (furoic acid), Se (selenophene carboxylic acid) and Te (tellurophene carboxylic acid). Thus the following questions should be answered by *ab initio* calculations: (i) What is the overall geometric arrangement of the adsorbed molecules? (ii) What is the registry of the bonding of the functional group with respect to the Cu surface atoms? (iii) Do the bonding geometry and adsorption energies depend on the heteroatom of the heterocycle?

[1] R. Raval, Current Opinion in Solid State and Materials Science, **7**, 67 (2003).
[2] V. Humblot, S. Haq, C. Muryn, W. A. Hofer, R. Rava, J. Am. Chem. Soc. **124(3)**, 503 (2002).
[3] L. A. M. M. Barbarosa, P. Sautet, J. Am. Chem. Soc. **124(27)**, 6639 (2001).
[4] F. M. Leibsle, Surf. Sci., **311**, 45 (1994).
[5] A. Puschmann, J. Haase, M. D. Crapper, C. E.Riley, D. P. Woodruff, Phys. Rev. Lett.,**54(20)**, 2250 (1985).
[6] S. Poulston, R. A. Bennett, A. H. Jones, M. Bowker, Phys. Rev. B., **55(19)**, 12888 (1997).
[7] P. Stone, S. Poulston, R. A. Bennet, Nicola J. Price, M. Bowker, Surf. Sci., **418**, 71 (1998).
[8] S. L. Silva, A. A. Patel, T. M. Pham, F. M. Leibsle, Surf. Sci., **441**, 351 (1999).
[9] S.M.Barlow and R.Raval, Surf. Science Reports **50**, 201-341 (2003).
[10] Winfried Kromen, "Die Projector Augmented Wave-Methode: Ein schnelles Allelektronenverfahren für die *ab initio* Molekulardynamik", Dissertation RWTH Aachen, Oktober 2000

Condensed Matter

Soft Matter and Biophysics

Proton Pathways in a Biological Proton Pump
S. Grudinin, G. Büldt, V. Gordeliy, and A. Baumgärtner

Sphere Overcharging by Wrapped Polyelectrolyte
R. G. Winkler and A.G. Cherstvy

Depletion interaction of anisotropic colloidal particles in polymer solutions
E. Eisenriegler

Dynamics of fluid vesicles in flows
H. Noguchi and G. Gompper

Broken ergodicity in one-dimensional systems with short-range interaction?
M. Paessens, A. Rakos, G.M. Schütz

Shape and Motility of a Model Cell
S.V.M. Satyanarayana and A. Baumgärtner

Universal properties of complexes of oppositely charged polyelectrolytes
R.G. Winkler

Hysteresis in one-dimensional reaction-diffusion systems
A.Rakos, M. Paessens, and G.M. Schütz

Single Protein dynamics in natural and denaturated state
R. Biehl, Z. Bu, B. Hoffmann, M. Monkenbusch, D.J.E. Callaway

Protein diffusion in PEO networks
R. Biehl, M. Monkenbusch, A. Radulescu, J. Allgaier, D. Richter, G. Kali, X. Guo, R.K. Prud'homme

Hydrophilic polymers equipped with short hydrophobic stickers as efficiency boosters for microemulsions
Ch. Frank, J.A. Allgaier, H. Frielinghaus

Tuning the membrane properties in bicontinuous microemulsions with homopolymers and diblock copolymers probed with NSE and SANS
H. Frielinghaus, O. Holderer, D. Byelov, M. Monkenbusch, J. Allgaier, and D. Richter

Hierarchical structures formed by wax crystallization on polymeric templates: a combined study in real and reciprocal space by microscopy and small-angle neutron scattering techniques
A.Radulescu, D. Schwahn, J. Stellbrink, E. Kentzinger, M. Heiderich, L.J. Fetters, and D. Richter

Non-flexible coils in solution: A neutron spin-echo investigation of alkyl substituted polynorbornens in tetrahydrofuran
M. Monkenbusch, J. Allgaier, J. Stellbrink, L.J. Fetters, and A. Greiner

Structure of fetuin-A stabilized calciprotein particles determined by neutron scattering - implications for calcification biology and material science
A.Heiss, D. Schwahn, H. Endo, W. Jahnen-Dechent

Star-Like Micelles wich Star-Like Interactions: A tunable Model System for Ultra-Soft Colloids
M. Laurati, J. Stellbrink, R. Lund, L. Willner, and D. Richter

Logarithmic Chain Exchange Kinetics of Polymeric Micelles
R. Lund, L. Willner, and D. Richter

The influence of constraint release on the reptation process: NSE study and comparison to simulation
M. Zamponi, A. Wischnewski, M. Monkenbusch, L. Willner, and D. Richter

Electrolyte friction in dispersions of charged colloids and micelles
M.G. McPhie and G. Nägele

Phase behaviour of charged colloidal sphere dispersions with added polymer chains
R. Tuinier, A. Fortini, M. Dijkstra

Protein crystallization using polymers: influence of chain flexibility
R. Tuinier

Synthesis of Poly(ethylene glycol)(PEG)-grafted colloidal silica particles with improved stability in aqueous environments
J. Buitenhuis and Z. Zhang

Self-diffusion of rod-like viruses in the nematic phase
M.P. Lettinga, E. Barry, and Z. Dogic

The electrostatic potential of alternating polyelectrolyte multilayers as investigated by TIRM
J. E. Wong, R. von Klitzing, P.R. Lang

Soret Coefficient of Poly(N-isopropylacrylamide)/Water in the Vicinity of Coil-Globule Transition Temperature
S. Wiegand and R. Kita

Unusual thermal diffusion in aqueous polymer solutions
S. Wiegand, R. Kita, and J. Luettmer-Strathmann

Anisotropy of Brownian Motion Close to a Wall
P. Holmqvist and P.R. Lang

Proton Pathways in a Biological Proton Pump

S. Grudinin[a,b,c] G. Büldt[b], V. Gordeliy[b,c], and A. Baumgaertner[a]
[a] *Institut für Festkörperforschung (IFF), FZJ;* [b] *Institute for Structural Biology (IBI-2), FZJ;* [c] *Center for Biophysics and Physical Chemistry of Supramolecular Structures, MIPT, Moscow, Russia*

Protein crystallography provides the structure of a protein, averaged over all elementary cells during data collection time. Thus, it has only a limited access to dynamical processes. This study demonstrates how molecular dynamics simulations can supplement experimental information in order to elucidate the structure-function relationship for a specific protein, the proton pump "bacteriorhodopsin (bR)". Results reveal the distribution of water molecules and the related hydrogen-bonded network inside bR which is essential for proton transport across this membrane protein.

I. INTRODUCTION

The protein bacteriorhodopsin (bR) resides in the membrane of the archaebacterium Halobacterium salinarum and uses photonic energy for the transmembrane proton pumping. The protein incorporates a retinal chromophore bound to a lysine residue via a protonated Schiff base linkage and absorbs light at a certain wavelength. Fig.1 shows an overall view of bacteriorhodopsin. Photoabsorption triggers an isomerization of the retinal, inducing a sequence of conformational transitions accompanied by a vectorial transfer of a proton across the membrane, leading to the release of a proton at the extracellular side and an uptake from the cytoplasmic side [1]. The numbers in Fig.1 refer to the sequential order in

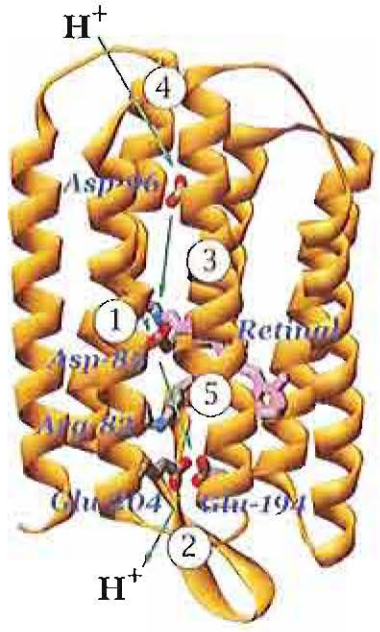

FIG. 1: Overall view of bacteriorhodopsin, shown with the retinal (purple) and residues (blue) directly involved in proton transport. The top is the cytoplasmic side. Arrows indicate proton transfer steps during the photochemical cycle. Numbers refer to the sequential order of the photocycle (see text).

the photocycle : (1) deprotonation of the Schiff base, protonation of Asp85; (2) proton release to the extracellular surface; (3) reprotonation of the Schiff base, deprotonation of Asp96; (4) reprotonation of Asp96 from the cytoplasmic surface; and (5) deprotonation of Asp85, reprotonation of the proton release site.

The details of the photocycle are still highly controversial. One problem is related to the gradual release of stored energy, an inherently nonequilibrium phenomena : to understand why the photocycle follows a productive (i.e., pumping), rather than some unproductive, relaxation pathway, it is necessary to know the relative energy barriers of individual conformational steps. The barrier may arise from breaking and forming of hydrogen bonds involving the retinal, various charged residues, internal water molecules, and long-range interactions among protein groups that respond to charge rearrangements. Another problem, which is still unclear, is the number of buried (i.e., internal) water molecules in bR, which are assumed to play a critical role in providing proton pathways and to be involved in the molecular mechanism leading to proton translocation.

X-ray crystallographical studies have provided structures of bR at various intermediate steps [1, 2], which have revealed important details of the pumping cycle. However, even at highest resolution, x-ray crystallography cannot capture all details, in particular dynamical processes during the coupling of conformational transitions and proton translocation. Therefore molecular dynamics simulations have proven to provide valuable insights to, among others, conformational fluctuations [3, 4] and water mobility inside bR [5–7].

In the following we summarize results of molecular dynamics simulations on bR trimer [7]. We argue that crystal structures are often discussed without looking at different timescales. We have shown [7] that structures on a picosecond timescale differ considerably from time-averaged x-ray structures.

II. RESULTS AND IMPLICATIONS

Studies on the ground (G) and the late M states have been performed [7], where the latter has been chosen as the key state for understanding the mechanism of proton transfer. We predict new details of the amount and the distribution of internal water molecules in bR. Comparing water distribution and hydrogen-bonded networks in two different states of bR, we suggest possible pathways for proton hopping and water movement inside bR.

Distribution of Water Molecules. The simulations reveal a much higher average number of internal water molecules per monomer than observed in crystal

structures. With respect to the distribution of water molecules, bR is divided into extracellular and cytoplasmic parts separated by an impermeable structural boundary both for the G and the M states. This is demonstrated in Fig. 2 for one bR molecule of the G-trimer (left) and the M-trimer (right), respectively. The volume occupied by one bR molecule is represented by the gray surface. Superimposed on the gray surface as depicted by blue and yellow triangulated nets are the surfaces of the volumes accessible to diffusive and trapped water molecules, respectively. The red balls indicate the positions of water molecules as found by crystallographic studies [2]. Water-accessible volumes in the late M state are larger both for trapped and diffusive water molecules. This is explained by the structural changes in this M state, which cause a total volume increase of internal cavities. The exchange of a set of diffusive internal water

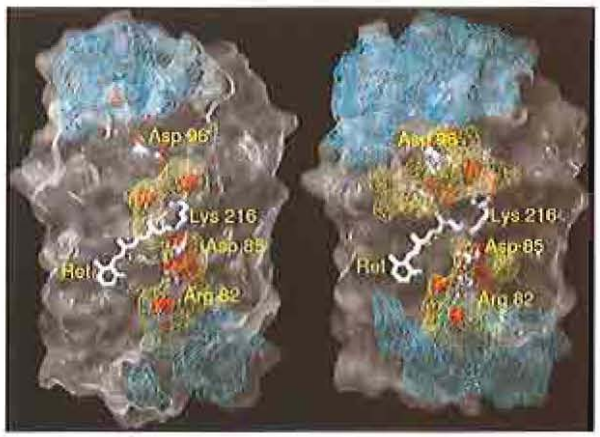

FIG. 2: Accessible volumes for internal water molecules of the G state (*left*) and the M state of bR (*right*).

molecules follows in time an exponential decay, $exp(t/\tau)$, where $\tau \approx 340$ ps for the G state and 460 ps for the M state. The average residence time of a diffusive water molecule inside the protein is 95 ps for the G state and 110 ps for the M state.

Structure of Hydrogen-Bonded Network. During the photocycle, protons are vectorially transported from the cytoplasmic side to the extracellular environment. This implies that hydrogen-bonded pathways must exist between the cytoplasmic surface of the protein and the Schiff base via the side chain Asp96 as shown by infrared spectroscopy. We have described the hydrogen-bonded pathway by the "Grotthuss relay mechanism" for proton transport [8]. There, ordered chains of water molecules are considered, where one path consists of an alternating sequence of hydrogen bonds between water molecules, H···O, separated by O–H bonds of water molecules. In this case, the protons are assumed to hop in a rate-limiting process along such a path which results in a reorientation of the participating water molecules. In our study, the Grotthuss-path model was used as a static geometrical construct rather than a dynamical one. Based on the analysis of MD trajectories, we have calculated all possible Grotthuss-pathways inside the protein.

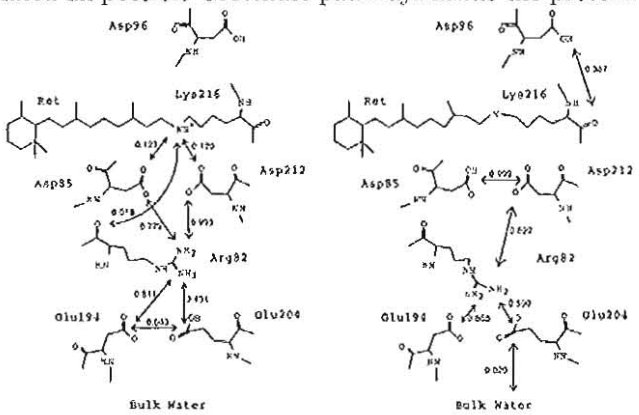

FIG. 3: Grotthuss-pathways are shown with arrows. The numbers at the arrows denote probabilities of the corresponding connections.

From these trajectories we identified the key residues involved in the pathway and have estimated the probabilities of forming different Grotthuss-pathways between polar residues and the surface of the protein for the G and M states. The probability map is presented in Fig.3. We find these pathways to be quite different for the G and M states. For instance, we see a connection between residue Glu204 and the protein surface only in the M state.

Despite the fact that several pathways can be constructed, the possible existence of such pathways is not sufficient for an actual proton translocation to take place because polarization effects are not included in the present classical model. The effect of the polarizability on the proton translocation in bR will be the subject of our future study.

[1] J. K. Lanyi, Annu. Rev. Physiol. **66**, 665 (2004).
[2] H.J. Sass, G. Büldt, R. Gessenich, D. Hehn, D. Neff, R. Schlesinger, J. Berendzen, and P. Ormos. Nature **406**, 649 (2000).
[3] O. Edholm, O. Berger and F. Jähnig J.Mol.Biol. **250**, 94 (1995).
[4] J. Baudry, E. Tajkhorshid, F. Molnar, J. Phillips and K. Schulten, J. Phys. Chem. B **105**, 905 (2001).
[5] S. Hayashi, E. Tajkhorshid and K. Schulten, Biophys. J. **83**, 1281 (2002).
[6] C. Kandt, J. Schlitter and K. Gerwert Biophys. J. **86**, 705 (2004).
[7] S. Grudinin, G.Büldt, V.Gordeliy, and A. Baumgaertner, Biophys. J. **88**, 3252.
[8] N. Agmon, Chem. Phys. Lett. **244**, 456 (1995).

Sphere Overcharging by Wrapped Polyelectrolyte

Roland G. Winkler[1] and Andrey G. Cherstvy[1,2]

[1]*Institut für Festkörperforschung, Theorie II, Forschungszentrum Jülich, D-52425 Jülich*
[2]*Max-Planck-Institut für Physik komplexer Systeme, Noethnitzerstr. 38, D-01187 Dresden*

The complexation of a polyelectrolyte bendable rod with an oppositely charged spherical macroion is investigated. We take into account the electrostatic bending of the rod and its asymmetric charge neutralization by the sphere charges. The partial neutralization of rod charges adjacent to the sphere surface leads to a spontaneous rod bending towards the sphere and a substantial overcharging of the polyelectrolyte complexe.

Nucleosome core particles (NCPs), the elementary units of the chromatin, play a fundamental role in many biological processes, e.g., in transcription and replication, DNA repair and cell division [1, 2]. Eukaryotic genomic DNA is (evolutionary) constructed to help in DNA packaging and to govern the positioning of NCPs along the DNA. It is known that particular DNA sequences have a higher affinity to the histone core, whereas, for instance, long stretches of poly(dA)•poly(dT) prevent the nucleosome formation. The structure of the NCP [3] is highly conserved in different organisms and tissues.

DNA adapts its structure to fit the highly bent state in the NCP, where the DNA radius of curvature is only twice as large as the DNA diameter. In particular, DNA is overtwisted in the NCP by 0.3-0.5bp/turn, on average, compared to DNA in solution with 10.5bp/turn. DNAs use their sequence-dependent bendability and twistability to achieve a better packaging in the NCP.

The DNA wrapped in the NCP is known to overcharge the histone core considerably. Since both the histone core and the DNA are strongly and oppositely charged objects, the electrostatic interaction between them should play an important role in their complexation (although specific DNA-histone interactions should not be overlooked). The influence of salt conditions on the NCP stability support this hypothesis: DNA is released from the NCP for salt concentration beyond the physiological range. The NCP structure also suggests that the close contacts of DNA with the histone proteins may result in neutralization of the inner-to-core DNA phosphates. Possible consequences of such neutralization have been predicted long ago and explored within a simple electrostatic model of rod bending. However, DNA interactions with the core and the DNA helical symmetry have not been included in this model, although DNA helicity was shown to be important in all-atom computer simulations of bending of asymmetrically neutralized DNA.

Various theoretical electrostatic models of complexation of polyelectrolyte chains of different flexibilities with oppositely charged spheres have been suggested as models for a DNA-histone complex (for references see [2]). The transitions between wrapped and unwrapped conformations for relatively short chains as well as the transitions between touching, bent, and completely

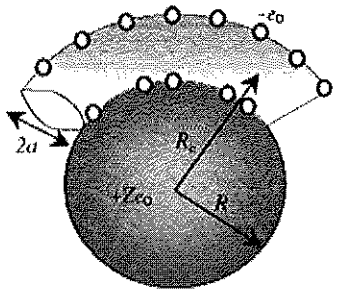

FIG. 1: Complex of a polyelectrolyte wrapped around an oppositely charged sphere.

wrapped conformations for long chains have been predicted. Rosette-like chain-sphere complexes for the chain with high bending rigidity have also been described. The complex formation has also been extensively studied by computer simulations and experimentally. However, some features of the complex formation still remain unclear. In particular, how strong is the curvature induced by an asymmetric neutralization of charges of the wrapped rod, and how does it affect the charge of the complex? How does the DNA helicity contributes to this effect?

To gain inside into the these questions, we adopt a simple model of a DNA-sphere complex. The complex consists of a bendable polyelectrolyte rod of radius a wrapped around an oppositely charged sphere of Radius R and charge Ze. The rod carries two identical arrays of charges $(-e)$, with a charge-charge separation of h, on opposite sides (see Fig. 1). When the rod is bent around the sphere, one charge array is in contact with the sphere. Thus, the charge density increases on the inner-to-sphere side of the rod and decreases on the outer-to-sphere one. If some of the inner-to-sphere rod charges are neutralized by sphere charges, the repulsion between them is diminished. The repulsion of the outer-to-sphere charges induces rod bending towards the sphere that favors rod adsorption and may result in overcharging of the sphere.

We approximate the interactions among the charges by the Debye-Hückel potential, which captures the actual screened charge-charge interaction and presume that some of the rod charges next to the sphere are neutralized

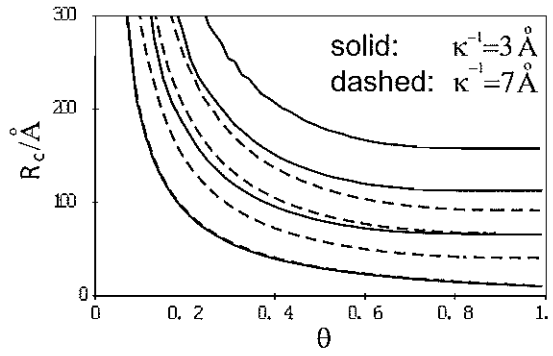

FIG. 2: Radius of spontaneous curvature of an asymmetrically neutralized rod. Parameters: $a = 10$ Å, $h = 3.4$ Å, $\kappa^{-1} = 3$ Å(solid) and $\kappa = 7$ Å(dashed), $l_p = 750$ Å, 500 Å, 250 Å, and 0 (from top to bottom).

by the mobile sphere charges. The remaining rod charges are allowed to redistribute which leads to an increase of the mean charge separation by the factor $1/(1-\theta)$, where θ is the fraction of neutralized inner rod charges. For $\kappa h \gg 1$ and for large curvature radii, the energy of the bent rod can be approximated by

$$\frac{E_{el}^{rod}}{k_BTLl_B} \approx -\frac{\ln\left[1-e^{-\kappa h_+}\right]}{hh_+} - \frac{\ln\left[1-e^{-\kappa h_-/(1-\theta)}\right]}{hh_-/(1-\theta)^2} + \frac{1}{4\kappa^2h^2}\left(\frac{h}{2(R_c+a)^2h_+} + \frac{h(1-\theta)^2}{2(R_c-a)^2h_-}\right). \quad (1)$$

Here $h_\pm = h(R_c \pm a)/R_c$ are the charge-charge separations on the inner $(-)$ and outer $(+)$ to sphere rod charge arrays. The mechanical bending energy of the bend rod is $E_{bend}^{rod}/(k_BTL) = l_p/(2R_c^2)$, where l_p is its persistence length, l_B the Bjerrum length, and R_c the radius of its centerline. We assume homogeneous rod bending, although for small R_c some modifications of the bending mechanism are possible (rod kinking etc.).

The results of minimization with respect to the radius of curvature R_c of the total energy difference between the bent and the free state are shown in Fig. 2 for a rod with parameters close to those of B-DNA. The value of the spontaneous curvature radius R_c of the rod decreases with increasing θ since less contraction of inner-to-sphere charges is required upon bending. At larger salt content (larger κ), R_c increases since the electrostatic interaction becomes weaker. The curvature radius decreases with decreasing l_p as one could expect. This spontaneous rod curvature can facilitate rod adsorption onto a sphere or another curved macroion. If the radius R of the macroion is equal to R_c, no bending energy is required to wrap a rod around the sphere. For $R > R_c$, the rod bents spontaneously, i.e., it has effectively a negative persistence length and the adsorption can continue beyond the isoelectric point of the complex.

For the calculation of the sphere-rod energy, we assume that the sphere charge is renormalized by rod adsorption

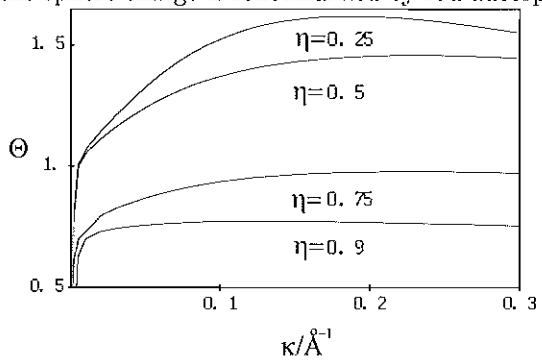

FIG. 3: Fraction of the sphere charge neutralization as a function of the inverse screening length of the solution. Parameters: $a = 10$ Å, $R = 50$ Å, $h = 3.4$ Å, $l_p = 500$ Å, and $Z = 100$.

which prevents the overcharging of the complex due to pure rod-sphere interactions. The interaction energy of a rod of length L with the sphere can be written as

$$\frac{E_{el}^{sp-rod}}{k_BTLl_B} = -\frac{(Z-2L/h)}{h(1+\kappa R)}\left[\frac{e^{-2\kappa a}}{R+2a} + \frac{1-\theta}{R}\right]. \quad (2)$$

The minimization of the energy difference between the bound and free state yields the optimal length L of the rod adsorbed on the sphere and the fraction of neutralized sphere charges $\Theta = 2L/Zh$. The fraction of compensated charges of the sphere is always smaller than unity if there is now neutralization of inner-to-sphere rod charges. Neutralization dramatically modifies the picture. As shown in Fig. 3, with decreasing fraction of immobile sphere charges, the amount of compensated sphere charges decreases. For η close to unity, there are not enough mobile charges to neutralize the inner rod charges, and the complex reveals no overcharging $(\Theta < 1)$. However, for small η the complex is substantially overcharged due to additional rod bending $(\Theta > 1)$. Figure 3 shows that for very low ionic strengths Θ drops to zero since the electrostatic persistence length $l_{el} \sim \kappa^{-2}$ rapidly grows and adsorption becomes unprofitable. For large ionic strengths, the charge of the complex also decreases since the electrostatic interactions, rod bending, and the rod-sphere attraction become weaker.

[1] W. Saenger, *Principles of Nucleic Acid Structure* (Springer Verlag, New York, 1984)
[2] A. G. Cherstvy and R. G. Winkler, J. Phys. Chem. B **109**, 2962 (2005)
[3] R. D. Kornberg and J. O. Thomas, Science **184**, 865 (1974)

Depletion interactions of anisotropic colloidal particles in polymer solutions

Erich Eisenriegler
Institut fur Festkorperforschung, Forschungszentrum Julich, D-52425 Julich, Germany

I. INTRODUCTION

The polymer depletion interaction between colloidal particles is one of the basic interactions in soft matter compound materials [1]. Free nonadsorbing polymer chains avoid the space between two particles, leading to an unbalanced pressure, which pushes them towards each other. Such depletion forces for an isolated pair of immersed particles or for a single immersed particle near a wall have been measured in recent experiments.

While the induced interaction between mesoscopic particles in a dilute or semidilute solution of long exible polymers is independent of most microscopic details it does depend on the quality of the solvent (good or theta solvent) and the size and shape of the particles.

Here we consider particles of *anisotropic* shape for which the interaction depends on both the distances between particles and their mutual orientations. Thus the entropic polymer-induced interaction provides both a force and a torque. For the dumbbell shapes of recently synthesized [2] particles consisting of two intersecting spheres, and for lens-shaped particles with spherical surfaces and ellipsoids we calculate the immersion free energy and the *orientation-dependent* depletion interaction.

We concentrate on dilute polymer solutions. Simple approximations that disregard the exibility and fractal structure of polymer chains reproduce the correct qualitative behavior only in the case of *large* particle-to-polymer size ratio. Here we consider the so called protein-limit where the mesoscopic particles are *small* compared to characteristic polymer lengths such as the end-to-end distance $\mathcal{R}$ and where the above approximations would fail.

There is an important correspondence, due to de Gennes, between the statistics of long exible polymers and critical eld theories. The perturbation of a eld theory due to an embedded small anisotropic particle can be described by a series of isotropic and anisotropic point operators. This 'small-particle expansion' is similar to a multipole expansion for a localized charge distribution or to the well known short-distance expansion of an operator product in eld theory. In the particle expansion, a given operator with scaling dimension x is multiplied by the power $(\text{size})^x$ of the particle *size* and an amplitude that depends on the *shape* of the particle.

II. SMALL-PARTICLE EXPANSION

A nonadsorbing polymer interacting with a colloidal particle corresponds to a eld theory surrounding a particle with an 'ordinary' surface which favors disorder and preserves the $O(N)$ symmetry of the order parameter. In the eld theory, the Boltzmann weight $\exp(-\delta\mathcal{H})$ of a small anisotropic particle with rotation symmetry axis $\vec{\rho}$ and re ection symmetry about its center $\mathbf{r}_{\rm P}$ can be expanded as

$$e^{-\delta\mathcal{H}} \propto 1 - \mathcal{I}\psi(\mathbf{r}_{\rm P}) - \sum_{kl} \rho_k \rho_l \left[\mathcal{A} T_{kl}(\mathbf{r}_{\rm P}) + \mathcal{A}' \partial_k \partial_l \psi(\mathbf{r}_{\rm P})\right] + \ldots \tag{1}$$

Here ψ is proportional to the energy density operator and corresponds to the density of chain-monomers and T_{kl} is the stress tensor of the eld theory. The scaling dimensions of the operators determine the size-powers $\mathcal{I} \propto (\text{size})^{d-(1/\nu)}$, $\mathcal{A} \propto (\text{size})^{x_{\rm an}}$, $\mathcal{A}' \propto (\text{size})^{x'_{\rm an}}$ of their amplitudes with

$$x_{\rm an} = d\ ,\ x'_{\rm an} = d - (1/\nu) + 2 \tag{2}$$

where d is the spatial dimension and ν the Flory exponent.

While for *ideal*, random walk like, chains $\nu = 1/2$, and the two orientation-dependent terms are of equal importance, for *self-avoiding* chains in a good solvent $\nu > 1/2$ implying $x_{\rm an} < x'_{\rm an}$, and the leading orientation-dependence comes from $\mathcal{A} T_{kl}$ while $\mathcal{A}' \partial_k \partial_l \psi$ can be neglected for small particle size.

The shape-dependent amplitudes $\mathcal{I}$, $\mathcal{A}$, $\mathcal{A}'$ for ellipsoids, dumbbells [2], and lenses in $d = 3$ have been obtained in Ref. 3 for the case of *ideal* polymers. Exact results for *self-avoiding* chains can be found in $d = 2$ spatial dimensions. For ellipses with diameters $D_\perp$ and $D_\parallel$ perpendicular and parallel to the particle axis,

$$\mathcal{A} = (D_\parallel^2 - D_\perp^2)\pi/8\ , \tag{3}$$

and for lenses and dumbbells as in Fig. 1 and 2 with particle axis in the vertical direction,

$$\mathcal{A} = \mathcal{D}^2(\pi/6)[(\pi/\ )^2 - 1]\ . \tag{4}$$

Here $0 <\ < \pi$ and $\mathcal{D} = L\sin(\ /2)$ for the dumbbells while $\pi <\ < 2\pi$ and $\equiv \pi -\ '$ for the lenses. Lenses and dumbbells are compared with their circumscribing ellipses (CE) in Figs. 1 and 2. As expected the polymers sense the lens and dumbbell as less and more anisotropic, respectively, than the circumscribing ellipses.

For a dumbbell of two touching spheres with $= 0$, the amplitude $\mathcal{A} = \mathcal{A}_{\rm id}$ for *ideal* chains,

$$\mathcal{A}_{\rm id} = (L/2)^d\, 4(\pi/4)^{d/2}(d-1)[\zeta(d)/\ (d/2)]\ , \tag{5}$$

is *reduced* to $\mathcal{A} = \mathcal{A}_{\rm id}(1 - 5\varepsilon/16)$ due to chain self-

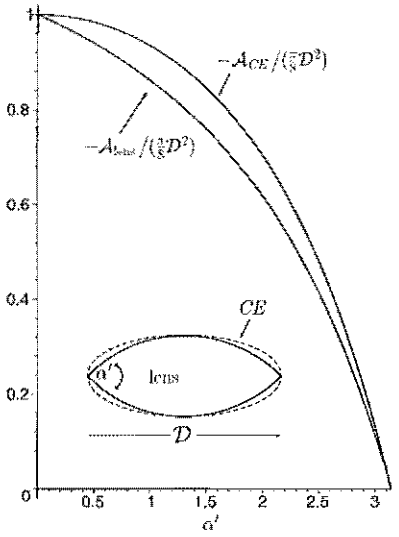

FIG. 1: Small particle amplitude $\mathcal{A}$ determining the anisotropic interaction of a lens and its circumscribed ellipse with self-avoiding polymers in $d = 2$ spatial dimensions.

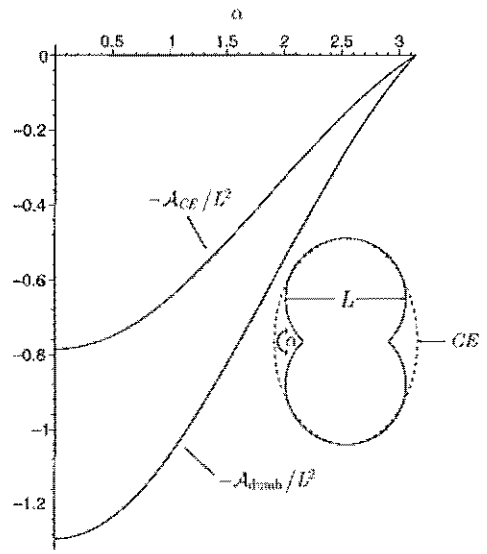

FIG. 2: $\mathcal{A}$ for a dumbbell and its circumscribed ellipse.

avoidance in $d = 4 - \varepsilon$ dimensions, while $\mathcal{A}_{\rm id}$ *coincides* with $\mathcal{A}$ for $d \to 4$ and $d \to 2$.

III. PARTICLE-WALL INTERACTION

The polymer-induced depletion interaction between the particle and a planar wall follows via the correspondence between polymers and eld theory by using the expansion (1) inside the half space. The leading contributions are given by

$$\delta F_{\rm iso}(\zeta) = p_0 \mathcal{I} \mathcal{R}^{1/\nu} (\mathcal{M}_{\rm hs} - 1) \qquad (6)$$

and

$$\delta F_{\rm aniso}(\vartheta, \zeta) = p_0 (\cos\vartheta)^2 (f + f') \qquad (7)$$

with

$$f = \frac{\mathcal{A}}{d-1} \left[d(1 - \mathcal{E}_{\rm hs}) + (\ /\nu)(\mathcal{M}_{\rm hs} - \mathcal{E}_{\rm hs}) - \zeta \frac{d}{d\zeta} \mathcal{M}_{\rm hs} \right] \qquad (8)$$

and

$$f' = \mathcal{A}' \mathcal{R}^{(1/\nu)-2} \frac{d^2}{d\zeta^2} \mathcal{M}_{\rm hs} . \qquad (9)$$

Here $\delta F_{\rm iso}(\zeta) = F_{\rm iso}(\zeta) - F_{\rm iso}(\infty)$ is the free energy change for moving the particle center from the bulk to a nite distance $z_{\rm P}$ from the wall, with ζ equal to $z_{\rm P}/\mathcal{R}$, and $\delta F_{\rm aniso}(\vartheta, \zeta) = F_{\rm aniso}(\vartheta, \zeta) - F_{\rm aniso}(\pi/2, \zeta)$ for turning at xed $z_{\rm P}$ the particle axis from an orientation parallel to the wall to an orientation that encloses an angle ϑ with the surface normal of the wall. $\mathcal{E}_{\rm hs} = \mathcal{E}_{\rm hs}(\zeta)$ and $\mathcal{M}_{\rm hs} = \mathcal{M}_{\rm hs}(\zeta)$ are the bulk-normalized density pro les of chain ends and of all chain-monomers, respectively, in the dilute polymer solution in the half space without a particle. The power-law exponent -1 appears in the length-dependence of the polymer bulk partition function.

Eqs (6)-(9) apply to particle sizes much smaller than $z_{\rm P}$ and $\mathcal{R}$. The discussion is easy for $z_{\rm P}$ $\mathcal{R}$ where for self-avoiding chains $f + f'$ tends to $\mathcal{A}d/(d-1)$. This has a smaller modulus than the corresponding value $\mathcal{A}_{\rm id}[d/(d-1)](1 +$) for ideal chains since $|\mathcal{A}_{\rm id}| > |\mathcal{A}|$, and $\equiv (f'/f)_{{\rm id},\, z_{\rm P} \ll \mathcal{R}}$ is positive.

Apart from reducing the orientation-dependent interaction at xed small particle-wall distance $z_{\rm P}$, chain self-avoidance also a ects the $z_{\rm P}$-dependence. Unlike ideal chains which induce a change in particle-orientation from parallel to perpendicular to the wall on increasing $z_{\rm P}/\mathcal{R}$, self-avoiding chains induce a parallel orientation for all distances.

[1] *Soft Matter*, G. Gompper and M. Schick (eds), Wiley-VCH 2005.

[2] P.M. Johnson, C.M. van Kats, and A. van Blaaderen, Langmuir **21**, 11510 (2005).

[3] E. Eisenriegler and A. Bringer, J. Phys.: Condens. Matter **17**, S1711 (2005).

Dynamics of Fluid Vesicles in Flows

Hiroshi Noguchi and Gerhard Gompper
Institute Theory II, IFF, Forschungszentrum Jülich, D-52425 Jülich, Germany

The deformation of vesicles in flow is studied by a mesoscopic simulation technique, which combines multi-particle collision dynamics for the solvent with a dynamically-triangulated surface model for the membrane. Shape transitions are investigated both in simple shear flows and in cylindrical-capillary flows. In simple shear flow at low membrane viscosity, the shear induces a transformation from discocyte to prolate shape with increasing shear rate, while at high membrane viscosity, the shear induces a transformation from prolate to discocyte, or tumbling motion accompanied by shape oscillations. These dynamical behaviors can be understood from a simplified model. In capillary flow, a transition to a prolate shape occurs for fluid vesicles, while vesicle with shear-elastic membranes (like red blood cells) transform into a coaxial parachute-like shape.

INTRODUCTION

Vesicles are closed lipid-bilayer membranes of usually spherical topology. They show a rich variety of morphologies depending on the lipid architecture and their environment. In thermal equilibrium, vesicle shapes have been investigated intensively using a curvature-elastic model and are now understood very well. By comparison, the behavior of vesicles in flow fields is much less explored.

The dynamical behavior of vesicles in flow is an important subject not only of fundamental research but also in medical applications. For example, in microvessels or glass capillaries, the apparent viscosity of blood depends on the tube diameter (Fåhraeus-Lindqvist effect). In diseases such as diabetes mellitus and sickle cell anemia, red blood cells have reduced deformability, which leads to an increase of the apparent blood viscosity and block microvascular flow.

The shapes of lipid vesicles and red blood cells are determined by the competition of the mechanical properties of the membrane, the constraints of constant volume V and constant surface area S, and the external hydrodynamic forces. The properties of the membrane of fluid vesicles are determined by its curvature elasticity and two-dimensional viscosity. The membrane of red blood cells has shear elasticity due to an attached spectrin network. The inside of red blood cells behaves as a Newtonian fluid.

In simple shear flow, two types of vesicle dynamics are well known, a steady state with a *tank-treading motion* of the membrane and a finite inclination angle with the flow direction, see Fig. 1, and an unsteady state with a *tumbling motion*. On the other hand, red blood cells are known to form *parachute shapes* in microvessels and glass capillaries.

The dynamics of vesicle in simple shear flow have been studied theoretically under the assumption of fixed ellipsoidal shape and for deformable shape in the absence of membrane viscosity by simulations. However, only one type of shape transition (from discocyte to prolate shape) has been reported. We have studied vesicle dynamics in the both flows using a three-dimensional mesoscopic simulation technique, which combines two methods. The solvent is treated by a particle-based hydrodynamics model, called multi-particle collision dynamics [1]. The membrane is treated by a coarse-grained, dynamically-triangulated surface model [2]. When the membrane viscosity is taken into account, several new shape transitions are discovered.

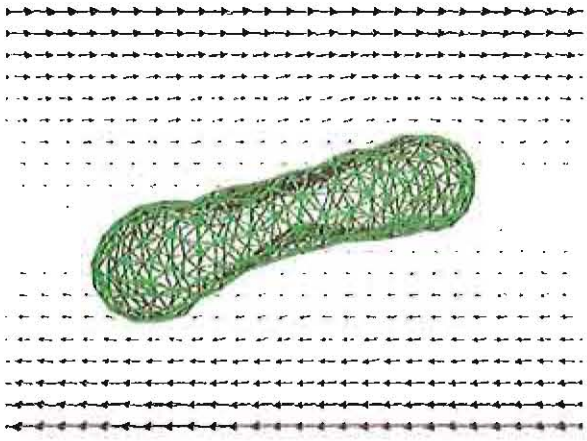

FIG. 1: Snapshot of a tank-treading discocyte vesicle under simple shear flow. The arrows represent the velocity field.

SIMPLE SHEAR FLOW

We have investigated the effect of the membrane viscosity and thermal fluctuation with several reduced volumes $V^* = 6\pi^{1/2}V/S^{3/2}$ [3, 4]. In this report, we focus on the case $V^* = 0.59$. At this reduced volume, the discocyte shape is stable and the prolate and stomatocyte shapes are metastable in the absence of shear flow. The shear flow changes this stability. A dynamical phase diagram is shown in Fig. 2.

For membrane viscosity $\eta_{\rm mb} = 0$, both discoidal and prolate vesicles exhibit tank-treading motion at all investigated shear rates, see Fig. 1. For high shear rates $\dot{\gamma}$, the discocyte vesicle transforms into a prolate, while the vesicle retains its shape for smaller shear rates. With increasing membrane viscosity $\eta_{\rm mb}$, the inclination angle θ decreases, until a transition from tank-treading to

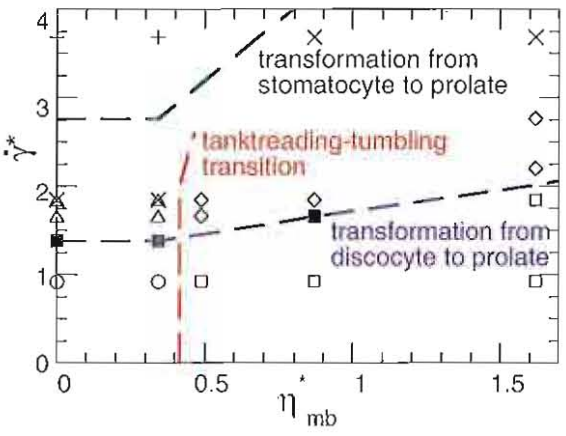

FIG. 2: Dynamical phase diagram of a vesicle in shear flow, for reduced volume $V^* = 0.59$ as a function of reduced shear rate $\dot{\gamma}^* = \dot{\gamma}\tau$ and the relative membrane viscosity $\eta^*_{mb} = \eta_{mb}/\eta_0 R_0$, where τ is the relaxation time, η_0 is the solvent viscosity, and $R_0 = \sqrt{S/4\pi}$. Symbols show simulated parameter values, and indicate tank-treading discocyte and tank-treading prolate (○), tank-treading prolate and unstable discocyte (△), tank-treading discocyte and tumbling (transient) prolate (□), tumbling with shape oscillation (◇), unstable stomatocyte (+), stable stomatocyte (×), and near transition (■). The dashed lines are guides to the eye.

tumbling motion occurs at small positive θ.

The inclination angle θ of prolates decreases faster than that of discocytes with increasing η_{mb}. At a large membrane viscosity, the prolate enters the tumbling phase, while the discocyte remains in the tank-treading phase. Remarkably, for small shear rates, the (metastable) prolate starts tumbling, but after a rotation, transforms into a tank-treading discocyte. The time dependence of the asphericity α and the inclination angle θ are shown in Fig. 3. Here, the asphericity $\alpha = (1/2)[(\lambda_1-\lambda_2)^2+(\lambda_2-\lambda_3)^2+(\lambda_3-\lambda_1)^2]/(\lambda_1+\lambda_2+\lambda_3)^2$, with the eigenvalues $\lambda_1, \lambda_2, \lambda_3$ of the moment-of-inertia tensor, is a convenient measure to distinguish oblate and prolate shapes, with $\alpha \simeq 0.2$ for the discocyte and $\alpha \simeq 0.8$ for the prolate shape (at $V^* = 0.59$). For larger shear rates, the discocyte transforms into a prolate, but the tumbling motion continues accompanied by shape oscillations between prolate and discocyte. We proposed a simple stochastic phenomenological model to describe the vesicle dynamics including morphological changes. This simple model reproduces the vesicle dynamics very well, see Fig. 3.

CAPILLARY FLOW

Both fluid and elastic (red-blood-cell model) vesicles retain their discoidal shapes in slow capillary flows. We have found that coaxial orientation with the capillary axis is unstable in slow flows [5, 6]. Instead, the vesicles align the longest axis of the moment-of-inertia tensor with the flow direction. In most previous theoretical and numerical studies, axisymmetric shapes which are coaxial with the center of the capillary were assumed and cylindrical coordinates were employed. Our results show that this assumption is justified only for high fluid velocity.

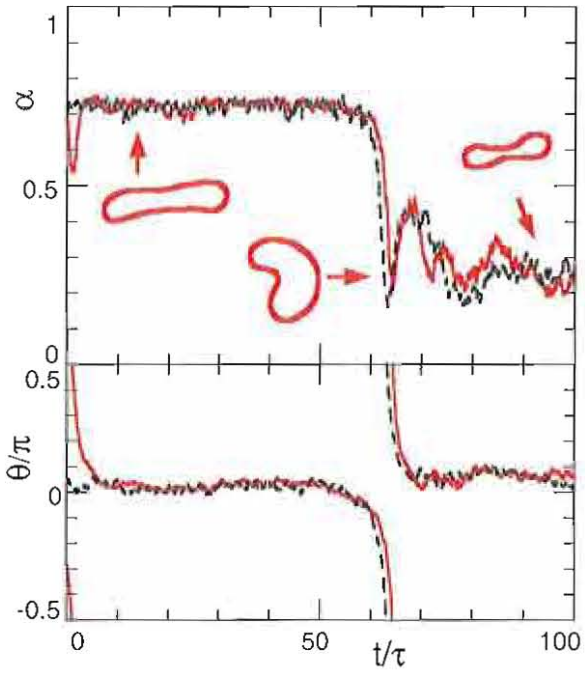

FIG. 3: Time dependence of asphericity α and inclination angle θ. The dashed lines are obtained from the simplified stochastic model. Snapshots of the vesicle cross-section are also shown.

At larger mean fluid velocity, the fluid vesicle transits into a prolate ellipsoidal shape. On the other hand, the elastic vesicle transits into a parachute shape, because the shear elasticity prevents large shear deformations. Both shape transitions reduce the flow resistance. We have found that the transition velocities are linearly dependent on the bending rigidity and on the shear modulus of the membrane.

[1] A. Malevanets and R. Kapral, J. Chem. Phys. **110**, 8605 (1999).
[2] G. Gompper and D. M. Kroll, J. Phys. Condens. Matter **9**, 8795 (1997).
[3] H. Noguchi and G. Gompper, Phys. Rev. Lett. **93**, 258102 (2004).
[4] H. Noguchi and G. Gompper, Phys. Rev. E **72**, 011901 (2005).
[5] H. Noguchi and G. Gompper, Proc. Natl. Acad. Sci. USA **102**, 14159 (2005).
[6] H. Noguchi and G. Gompper, J. Phys.: Condens. Matter **17**, S3439 (2005).

Broken ergodicity in one-dimensional systems with short-range interaction?

M. Paessens, A. Rákos, G. M. Schütz
Institute Theory II, IFF, Forschungszentrum Jülich, 52425 Jülich, Germany.

We show that one-dimensional nonequilibrium systems with local interactions may exhibit a phase with broken ergodicity. This result – obtained by high-precision dynamic Monte-Carlo simulation of a lattice gas model– is supported by a mathematical hydrodynamic description of the local coarse-grained order parameter dynamics and provides a heuristic identification of the main dynamical mode that governs the microscopic dynamics, viz. the random motion of a shock in a self-organized effective potential. This picture leads to the exact phase diagram of the system and suggests a novel mechanism for "freezing by heating".

I. INTRODUCTION

The closely related questions of phase coexistence and ergodicity breaking in noisy one-dimensional particle systems with short range interactions have been extensively investigated. In thermal equilibrium these phenomena cannot occur as there is no local mechanism that could limit the growth of islands of a minority phase inside a majority phase. In a dynamical setting this is the origin of the long-debated zero-rate conjecture which – loosely speaking – asserts that generally noisy one-dimensional systems with short-range interactions and no local dynamical constraints are ergodic.

The zero-rate conjecture has recently been disproved by constructing a rather cumbersome counterexample motivated from computer science, viz., a rather fine-tuned stochastic lattice model with approximately 10^{40} local degrees of freedom [1]. On the other hand, one has found phase separation and spontaneous symmetry breaking in models for driven diffusive systems provided that either bulk particle number conservation or vanishing local transition rates constrain the local dynamics. Such models are used in systems where low-dimensional diffusion plays an important role, such as polymer reptation, transport by molecular motors or diffusion in zeolithes. However, these results leave open the question whether broken ergodicity may arise in simple models which have no local dynamical constraints, but at the same time have a natural physical motivation.

Recently it has been shown that phase coexistence occurs in a one-dimensional driven diffusive system in the presence of Langmuir kinetics $A \rightleftharpoons 0$ which break the bulk conservation law [2]. This mechanism is inspired by the motion of motor proteins along actin filaments. The model exhibits an experimentally observed phase coexistence due to boundary conditions [3], but ergodicity is not broken. Using dynamical Monte-Carlo simulation we demonstrate the existence of broken ergodicity in a similar system with activated reaction kinetics $AAA \rightleftharpoons A0A$ and we address by an analytical approach the question whether such behaviour is generic. Since mean field theory and linear response theory are unsuitable tools for treating low-dimensional particle system far from thermal equilibrium we first derive an exact nonlinear hydrodynamic evolution equation for the coarse-grained local particle density, using to local stationarity. In a second step we employ a microscopically motivated prescription how to treat shock discontinuities and boundary layers. This not only proves broken ergodicity on macroscopic scale, but also illuminates its microscopic dynamical origin and thus shows that this phenomenon is generic [4].

II. THE MODEL AND ITS STEADY STATE

We consider the totally asymmetric exclusion process (TASEP) augmented by nonconservative reaction kinetics. Each site k from 1 to L is either empty ($n_k = 0$) or occupied by at most one particle ($n_k = 1$). Particles hop stochastically to the right neighbouring site with unit rate, provided that the target site is empty. Moreover, on a vacant site enclosed by two particles a particle may be attached with rate ω_a, and a particle enclosed by two other particles may be detached with rate ω_d. The boundaries act as fixed-density particle reservoirs where particles are injected with rate ρ_- on the left and absorbed with rate $1 - \rho_+$ on the right. In the physically interesting case

$$\omega_a = \Omega_a/L, \qquad \omega_d = \Omega_d/L \tag{1}$$

the bulk reaction rates are proportional to $1/L$ [2, 4, 5] such that the violation of particle conservation in the bulk is equal in strength with the violation at the boundaries and a competition between the two mechanisms sets in.

Numerical analysis yields a stationary phase diagram with five distinct phases (Fig. 1). In the high density phases (HD1/2) one finds an expected local density $\rho_i(t) = \langle n_i(t) \rangle > 1/2$ while in the low density phase (LD) $\rho_i < 1/2$. In HD1 the bulk density profile is dependent on ρ_+, while it is independent of both boundaries in HD2. The coexistence phase is characterized by a jump in the density profile which is localized close to a certain position in the bulk of the system. This shock connects a low density domain to its left with a high density domain to its right [2, 5]. In a different parameter regime we find a novel phase where both the LD and HD states are stable (if $L \to \infty$) for the same values of boundary densities, i.e., ergodicity is broken.

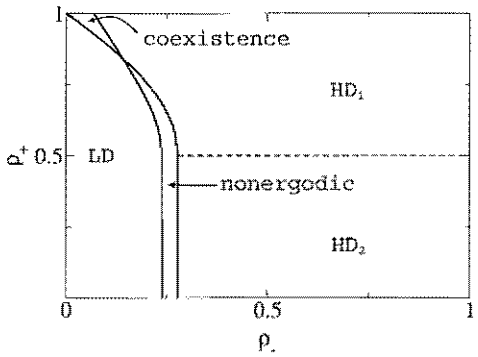

FIG. 1: Phase diagram for $\Omega_a = 0.7$ and $\Omega_d = 0.1$ with two high density phases (HD1, HD2), a low density phase (LD), a coexistence phase and the nonergodic phase.

III. DYNAMICS OF ERGODICITY BREAKING

In order to gain theoretical insight we consider the hydrodynamic limit on the Euler scale with lattice constant $a = 1/L \to 0$ and rescaled time $t = t_{\text{lattice}}/L$. Due to local stationary the hydrodynamic equation for the coarse grained density takes the form

$$\frac{\partial}{\partial t}\rho(x,t) + \frac{\partial}{\partial x}j(\rho) = S(\rho), \qquad (2)$$

with the exact current $j(\rho) = \rho(1-\rho)$ of the TASEP and the cubic source term $S(\rho) = \Omega_a\rho^2(1-\rho) - \Omega_d\rho^3$.

Since for the stationary solution of (2) two boundary conditions have to be satisfied, a density discontinuity (shock) arises which is determined by the physical requirements of current continuity and shock stability [5]. One finds a range of boundary densities which allow for three different solutions with the shock either in the bulk or at one of the two boundaries. In order to understand quantitatively the selection of the stationary shock position from a microscopic viewpoint we need to consider the effect of fluctuations. To this end we view the shock as a collective many-body excitation with single-particle random walk dynamics in an effective energy landscape $E(x)$ inside a finite box, generated by the interplay of the particle current with the reaction kinetics and leading to space-dependent hopping rates

$$w_{x\leftrightarrow x+a} = \frac{j_{R(L)}(x)}{\rho_R(x) - \rho_L(x)}. \qquad (3)$$

determined by the local current (2). In the nonergodic phase $E(x)$ has maximum of magnitude $O(L)$ in the bulk and two minima at the left and right boundary corresponding to the two stable stationary states.

This simple one-particle picture is well borne out by dynamical MC simulations. Using multispin coding rather good statistics become available for the random waiting time τ which the system spends in one of the stationary states. The numerically determined cumulative distribution function $\Phi(t) = P(\tau < t)$ is well fitted by an exponential with a mean waiting time that grows exponentially in system size.

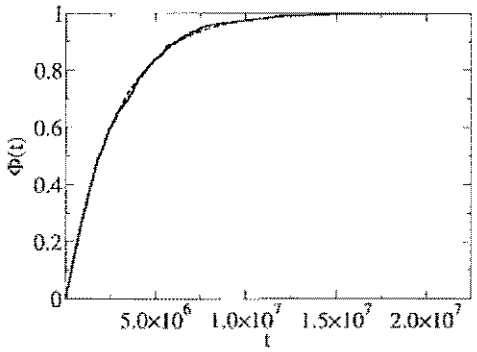

FIG. 2: Simulation data for the waiting-time distribution $\Phi(t)$ (full curve) and exponential function (broken curve).

The picture of a moving shock and integration of (2) yields the exact phase diagram presented above. For more general hopping dynamics augmented by slow reaction kinetics the structure of the hydrodynamic equation remains identical. The current and the source term have to be evaluated as expectations with respect to the invariant measure of the pure hopping dynamics.

From a physical viewpoint it is intriguing that adding noise which breaks the conservation law results in broken ergodicity through localization which is absent in the conservative system. An increase in noise strength is usually associated with heating up a system whereas localization induced by the effective potential reduces the positional entropy of the shock, corresponding to cooling. Thus we are faced with novel mechanism for "cooling by heating".

[1] P. Gacs, J. Stat. Phys. **103**, 45 (2001).
[2] A. Parmeggiani, T. Franosch and E. Frey, Phys. Rev. Lett. **90**, 086601 (2003).
[3] D. Chowdury, K. Nishinari, T. Okaada, A. Schadschneider, to appear in Phys. Rev. Lett.
[4] A. Rákos, M. Paessens and G.M. Schütz, Phys. Rev. Lett. **91**, 238302 (2003); A. Rákos and M. Paessens, to appear in Phys. Rev. E; A. Rákos, M. Paessens and G.M. Schütz, to appear in Markov Proc. and Rel. Fields.
[5] V. Popkov, A. Rákos, R.D. Willmann, A.B. Kolomeisky and G.M. Schütz, Phys. Rev. E **67**, 066117 (2003).

Shape and Motility of a Model Cell

S.V.M. Satyanarayana and A. Baumgaertner
Institut für Festkörperforschung – Theory II, Forschungszentrum Jülich, D-52425 Jülich

The shape and the motility of an adherent biolgical cell has been studied using Monte Carlo simulations. Using the simulation data we established scaling laws between the size of the cell and the enclosed size of the polymerizing actin cytoskeleton. With increasing concentration of actin molecules the cell exhibits a discontinuous transition between a motile and a static phase. It is shown that the velocity of the cell is maximal for an optimal choice of the depolymerization rate.

The migration of a biological cell [1] plays a prominent role in normal physiological processes as well as in pathology (e.g. embryogenesis, wound healing, metastasis). Basic to our understanding of migration are the physical principles of cell motility and chemotaxis, which are related to changes in cell shape due to specific rearrangements of the internal polymerizing actin cytoskeleton. Theoretical investigation of cell motility began with investigations trying to explain how the polymerization of rigid polymers (actin filaments) can push a load and have elaborated the Brownian Ratchet mechanism built on thermodynamic ideas [2–4]. Recently, we had started to extend these studies to investigations of complete cell models [5–8]. Our model represents two types of simple cells, keratocytes and cytoplast. We consider the cell to adhere strongly and reversibly to a flat substrate. The cell can approximately be modeled by a flexible ring of length L, representing the cell membrane, which encloses a certain number N of actin molecules. We use the Monte Carlo method in order to simulate the model cell. The actin monomers (type G) can polymerize and form rigid filaments (type F) by association at both ends of an existing filament. The filaments are immobile due to the strong adhesion to the substrate and hence provides the necessary force in order have a traction of the cell. Polymerization, depolymerization, nucleation and filament-branching processes require certain reaction rules and reaction probablities which were established for our simulations by extracting them from available experimental data.

SHAPES OF A MOTILE CELL.

In order to examine the shape of a cell, the effect of the F-actin filaments is of interest. The result is summarized in Fig.1 which shows the scaling behavior of the area of a cell containing G-actin and polymerized F-actin molecules, $A \sim L^2 f(N/L^2)$ with the asymptotic bahaviors $f(x) \sim const$ for $x \gg 1$, and $f(x) \sim x^{1/2}$ for $x \ll 1$, and hence

$$A \sim \begin{cases} L^2 & \text{for } \frac{N}{L} \gg 1 \\ N^{1/2}\, L & \text{for } \frac{N}{L} \ll 1\,. \end{cases} \qquad (1)$$

The cell area exhibits a discontinuous transition at a concentration $c^*=(N/L^2)^* \approx 0.020$ (Fig.1), from a "motile" phase (Fig.2), corresponding to low G-actin concentrations, to a "static" phase, where long F-actin filaments are absent. The cell assumes an ellipsoidal shape in the motile phase, which compares well with the shapes of keratocytes and cytoplasts. The reason for the discontinuity of the cell area is the elasticity-mediated protrusive mobility of the leading membrane edge. Consider the case where the length L of the membrane is fixed and the concentration of G-actin is continuously increased. During this process the number of F-actin molecules, N_F, increases linearly

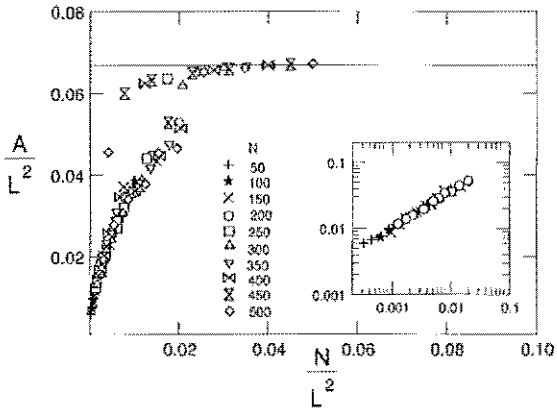

FIG. 1: Scaling of cell area as function of the number of actin monomers, N, and contour length of membrane, L.

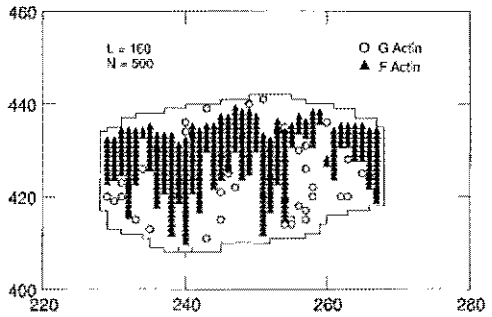

FIG. 2: Snapshot of the model cell at low concentration of G-actin. Open circles denote G-actin, full triangles represent F-actin molecules.

with N due to polymerization processes according to $N_F/N \approx 0.895$ [8], which is in agreement with experimental results[9]. With increasing amount of F-actin the shape of the cell expands, the cell membrane becomes more and more stretched which leads to a decrease of membrane fluctuations. The depressed membrane fluctuations prohibit further polymerization processes near the leading membrane edge. This allows the depolymerization processes at the rear of the cell to dominate and the shrinkage the filament network starts to take place at c^*. The scaling behavior of (1) for low concentrations can also be understood by a simple Flory-type argument[8] which leads to a radius of gyration of the cell,

$$R^2 \sim A \sim N^{\frac{2}{d+2}} L^{\frac{4}{d+2}},$$

which is in $d = 2$ identical to (1).

CELL MOTILITY

The spontaneous internal polarity, defined by the asymmetric distributions of the growing ("barbed") and shrinking ("ponted") ends of the actin cytoskeleton, determines the direction of cell motion and is maintained without external signals (e.g. chemotaxis) for a certain time (persistent random walk). It was shown theoretically and by simulations [6] that the branching process corresponds to an autocatalytic polymerization which gives rise to a persistent random walk of the cell as observed in experiments. During this type of motion the cell moves with almost constant velocity in one direction for a certain time until it spontaneously changes its direction of motion. A typical example from our simulations is shown in Fig.3. The dynamics at short and long times are governed by diffusion, whereas for intermediate times, the cell motion exhibits a drift. The spontaneous change of the direction of motion can qualitatively understood as follows. Since the branching of filaments near the leading edge of the membrane proceeds in one direction, there will be explosive growth of filaments in that direction due to the autocatalytic nature of polymerization kinetics and hence the cell moves in that direction. When the filament network is sufficiently dense, then it suppresses the membrane fluctuations at the leading edge which allows at the opposite end the depolymerization to dominate. This facilitates the filaments in the opposite sides to grow and therefore changes the direction of the cell.

Fig.4 shows the drift velocity as a function of the fraction of filamentuous F-actin. The computed drift velocities are in good agreement with experimental and other theoretical estimates[3]. This figure implies there is an optimal concentration of F-actin for rapid cell motion. One implication of this result is that some sort of regulation of the polymerization is needed. This is the topic of future research.

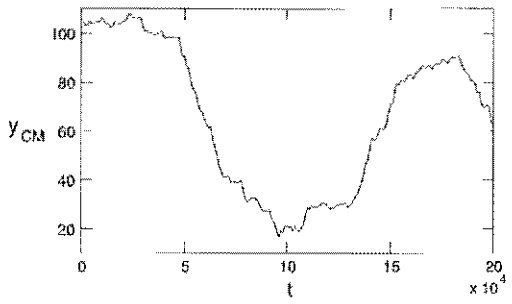

FIG. 3: Trajectory of a cell exhibiting persistent random walk.

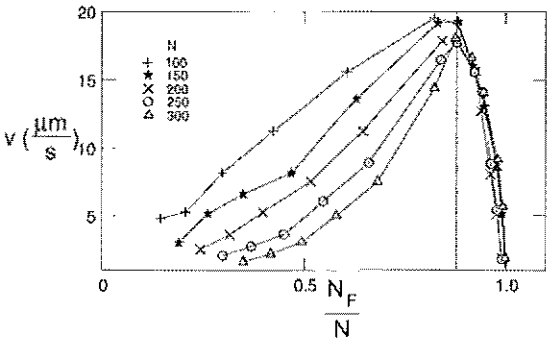

FIG. 4: Cell velocity as a function of F-actin concentration N_F/N for various N.

[1] D. Bray, *Cell Movements* (Garland Publ., New York, 1992).
[2] C. Peskin, G. Odell, and G. Oster, Biophys. J. **65**, 316 (1993).
[3] A. Mogilner and L. Edelstein-Keshet, Biophy. J. **83**, 1237 (2002).
[4] A. E. Carlsson, Biophys. J. **84**, 2907 (2003).
[5] A. Baumgaertner and R. Sambeth, J. Chem. Phys. **111**, 5223 (1999).
[6] R. Sambeth and A. Baumgaertner, Phys. Rev. Lett. **86**, 5196 (2001).
[7] R. Sambeth and A. Baumgaertner, J. Biol. Systems **9**, 201 (2001).
[8] S. V. M. Satyanarayana and A. Baumgaertner, J. Chem. Phys **121**, 4255 (2004).
[9] T. D. Pollard and G. G. Borisy, Cell **112**, 453 (2003).

Universal properties of complexes of oppositely charged polyelectrolytes

R. G. Winkler
Institut für Festkörperforschung – Theory II, Forschungszentrum Jülich, D-52425 Jülich

The aggregation of two flexible, oppositely charged polymer chains is investigated by molecular dynamics simulations. The universal properties of the complexes are studied as a function of chain length and interaction strength. For weakly interacting systems, a chain length dependent effective interaction strength is obtained, which governs the initiation of the aggregation process. At intermediate interaction strengths, the formed complexes exhibit a scaling behavior with respect to molecular weight typically for chain molecules in a bad solvent. An unusual weak dependence of the chain dimensions on the interaction strength is found in this regime. Finally, for strong interactions tightly packed globules are formed.

F&E Nr. 23.102

Aggregates between oppositely charged macromolecules play a fundamental role in technical applications and in particular in biological systems. An example is DNA which is associated with histone proteins to form the chromatin. Recently, aggregates of DNA and cationic polymers and cationic dendrimers [1] have attracted considerable attention. The reason is their potential application as DNA vectors in gene therapies. So far mostly chains with added counterions and colloids have been studied [2]. To gain insight into the structural properties of aggregates formed by flexible polyelectrolytes, we performed a series of molecular dynamic simulations of two oppositely charged linear molecules [3, 4].

The polymer chains are composed of N mass points connected by strong harmonic bonds. The finite size of the monomers is taken into account by a Lennard-Jones potential truncated at its minimum. In addition all mass points interact via Coulomb interaction. The solvent is described as a dielectric continuum and interactions with the monomers are taken into account by a stochastic and friction force. The stochastic force is assumed to be stationary, Markovian, and Gaussian.

As a consequence of the long-range nature of the Coulomb interaction, the two chains attract each other and form neutral complexes [3]. The aggregation process starts already at very low interaction strengths (λ). The reason is the large local charge density due to the presence of bonds. At very low densities, the Coulomb interaction is $\sim N^2$ for center-of-mass distances much larger than the radius of gyration of a chain. Thus, the effective interaction among the chains is chain length dependent. At small interaction strengths, the chains are free and the radii of gyration are equal to the values of chains in a good solvent (cf. Fig. 1). With increasing interaction strength, the chain extension increases slightly. Considering the scaling behavior of the radius of gyration with respect to chain length, we find the same exponent as in a good solvent, i.e., the slight chain extension does not alter the scaling properties. Beyond a certain interaction strength λ the chains form aggregates. The intramolecular Coulomb interaction is then screened and the chains shrink again.

For Coulomb energies on the order of k_BT, we expect the chains to stay close to each other with a mean distance comparable to the radius of gyration of a single chain. With the Coulomb energy $E_C \sim N^2/R_g \sim N^2/N^\nu$ the strength of the interaction is then estimated to be $\lambda_B N^\phi \approx 1$, where λ_B is the Bjerrum length. Hence, we find an effective interaction strength $\lambda^* = \lambda N^\phi$, with $\phi = 2 - \nu = 1.4$, which governs the onset of the collapse of the formed aggregate. The simulation results indeed confirm the scaling idea. The data for various chain lengths collapse approximately onto a universal curve for $\lambda^* \lesssim 10$. Systems of different chain lengths start collapsing approximately at the same value of $\lambda^* = \lambda_c^* \approx 10$ [4].

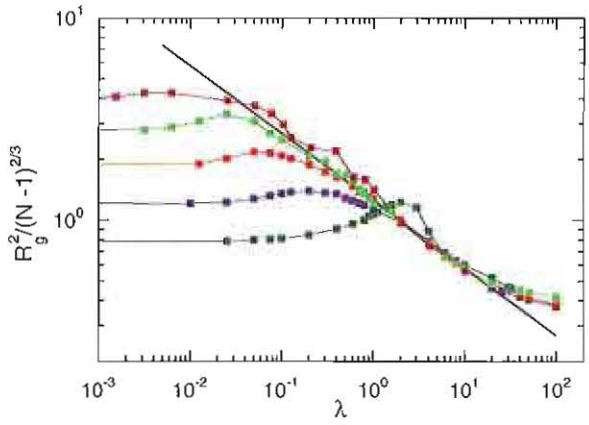

FIG. 1: Radii of gyration of one chain as a function of the interaction strength for various chain lengths. R_g^2 is scaled by $(N-1)^{2/3}$, where $(N-1)$ is the number of bonds of a chain.

A universal regime is obtained for intermediate interaction strengths. Figure 1 presents mean square radii of gyration scaled by $(N-1)^{2/3}$, corresponding to the scaling behavior of chains in a bad solvent, as a function of interaction strength. The curves for the various chain lengths nicely fall on top of each other for a broad range of interaction strengths, where the actual range depends on chain length.

Evidently, we can extract a scaling relation for the dependence of the radius of gyration on the interaction strength from Fig. 1. The data for the various chain lengths follow the relation $R_g \sim \lambda^{-1/6}$ very well in the regime of intermediate interaction strengths. This is an unusual weak λ dependence which has not been observed before.

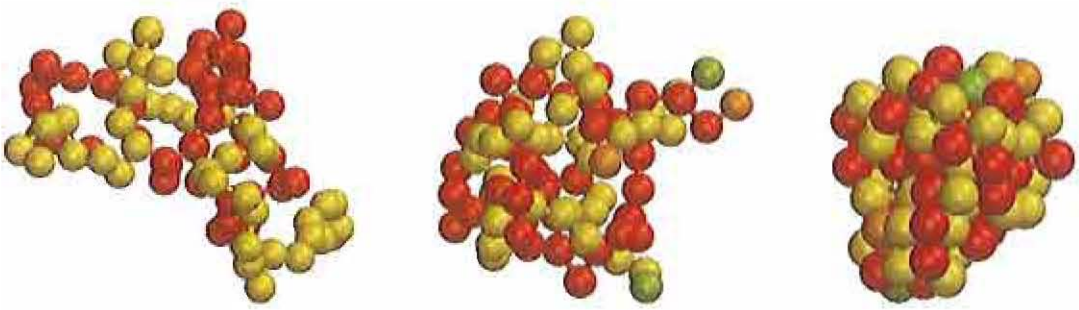

FIG. 2: Snapshots of aggregates for chains of length $N = 40$ and the interaction strengths $\lambda = 0.4$, 4, 40 (from left to right).

With increasing interaction parameter the chains ultimately form very compact, collapsed objects. The individual monomers are then closely packed and the radius of gyration is independent of the interaction strength. The chains behave in this regime like chains in a bad solvent with an almost constant density of the globule and the radius of gyration displays the dependence $R_g \sim N^{1/3}$ (cf. Fig. 2).

The change of the radius of gyration with the interaction strength is associated with a change of the density of the aggregate. For the chain lengths we have been studying, there is only a slight dependence of the density on the chain length for a given interaction strength in the regime $0.6 < \lambda < 20$. We even observe plateaus in the monomer densities for a particular interaction strength.

Applying the relation $\rho \sim N/V \sim N/R_g^3$ for the density dependence on the chain size, ρ changes with the interaction strength according to $\rho \sim \lambda^{1/2}$, when we use $R_g \sim \lambda^{-1/6}$. Hence, the density increases with the interaction strength in a non-linear manner. From the calculated density profiles the dependence $\rho \sim \lambda^{0.4}$ is obtained. The latter exponent is smaller than the one predicted by the density argument. Considering the simplicity of the used arguments and the statistical uncertainties of the simulation results, which are reflected by the fluctuations of the curves, however, the relationship supports the dependence $R_g \sim \lambda^{-1/6}$. In particular, the exponent is not larger than 1/6.

Figure 2 provides a example of aggregates formed at different interaction strengths. For the chain length $N = 40$ no compact structure is formed at $\lambda = 0.4$, although the radius of gyration of a chain is already smaller than in a good solvent (cf. Fig. 1). At $\lambda = 4.0$ there is already a pronounced peak in the pair correlation function at $r = 2\sigma$ indicating the formation of a denser structure [3]. A further increase of λ leads to an even more compact cluster. For very strong interactions, even crystalline-like structures are obtained locally [3].

The particular shape of an aggregate at a certain interaction strength is determined by the competition between an effective attractive interaction and the repulsion by the excluded volume of the monomers.

To gain insight into the aggregation mechanism, let us assume that the monomers can be redistributed such that a charge in the globule resembles a charge in a simple ionic solution. The electrostatic interactions create correlations such that any charge is surrounded by a shell of oppositely charged monomers. Thus, the Coulomb interactions are screened. As has been done for a random polyampholyte before [5], we will describe the aggregate in the same way as a systems of free charges in an ionic solution and calculate the electrostatic energy of the aggregate as if it were a small volume of a Debye-Hückel electrolyte solution. The detailed calculation [5] yields for a θ solvent the cluster size $R \sim N^{1/3}\lambda^{-1/3}$. Similarly, for the situation of a good solvent $R \sim N^{1/3}\lambda^{-2/3}$ is obtained. Using the relation $\rho \sim N/R^3$ the above cluster sizes correspond to the density dependencies $\rho \sim \lambda$ (θ solvent) or $\rho \sim \lambda^2$ (good solvent). However, none of these results agree with the scaling relations we extracted from our computer simulation data. Both, the dependence on R as well as on the density are different. One reason might be that the electrostatic screening is in the non-linear regime in the present system, whereas the predictions above are based on the linear Debye-Hückel theory. At the moment we cannot provide an explanation of the observed behavior on the basis of scaling arguments. There is either a different kind of interaction present, which governs the system behavior, or the clusters are so small that surface effects play an important role. The scaling relations outlined above might then apply to much longer chains.

[1] I. Gössl, L. Shu, A. D. Schlüter, and J. P. Rabe, *J. Am Chem. Soc.* **124**, 6860 (2002)
[2] R. Messina, C. Holm, and K. Kremer, *J. Chem. Phys.* **117** 2947 (2002)
[3] R. G. Winkler, M. O. Steinhauser, and P. Reineker, *Phys. Rev. E* **66**, 021802 (2002)
[4] R. G. Winkler, *NJP* **6**, 11 (2004)
[5] P. G. Higgs and J.-F. Joanny, *J. Chem. Phys.* **94**, 1543 (1991)

Hysteresis in one-dimensional reaction-diffusion systems

A. Rákos,[1] M. Paessens,[1] and G. M. Schütz[1,2]

[1] *Institut für Festkörperforschung, Forschungszentrum Jülich, 52425 Jülich, Germany.*
[2] *Theoretische Physik I, Universität Dortmund, 44221 Dortmund, Germany.*

We introduce a simple nonequilibrium model for a driven diffusive system with nonconservative reaction kinetics in one dimension. The steady state exhibits a phase with broken ergodicity and hysteresis which has no analog in systems investigated previously. We identify the main dynamical mode, viz. the random motion of a shock in an effective potential, which provides a unified framework for understanding phase coexistence as well as ergodicity breaking. This picture also leads to the exact phase diagram of the system and suggests a novel mechanism for "freezing by heating".

PACS numbers: 05.70.Ln, 64.60.Ht, 02.50.Ga

The closely related questions of phase coexistence, ergodicity breaking and hysteresis in noisy one-dimensional systems with short range interactions and finite local state space (such as in spin systems or vertex models) are intriguing and have received wide attention in the context of driven diffusive systems [1–5].

These phenomena are not expected to occur in one dimensional equilibrium systems. However, recently it has been demonstrated that phase coexistence occurs in a one-dimensional driven diffusive system even in the presence of Langmuir kinetics $A \rightleftharpoons 0$ which break the bulk conservation law [6]. The formation of a localized shock in this system which separates a domain of low particle density from a domain of high density has been studied subsequently [7, 8]. However, the two different domains do not represent two possible *global* steady states. The process is ergodic even in the thermodynamic limit and no hysteresis is possible.

It is the purpose of this work to demonstrate the existence of hysteresis and broken ergodicity (in the thermodynamic limit) in a driven diffusive system without bulk conservation law. Surprisingly, adding noise which is on average spatially homogeneous (a nonconservative reaction process) to a conservative spatially homogeneous nonequilibrium system with a nonvanishing particle current leads to a *space-dependent* effective potential which determines the stationary position of the shock connecting low density and high density regions. In the absence of this noise, i.e., in the usual TASEP, the shock performs an unbiased random walk in the coexistence region and hence is unlocalized, whereas suitably chosen reaction kinetics may create a variety of effective potentials which lead to broken ergodicity by localizing the shock.

We investigate the totally asymmetric exclusion process (TASEP) augmented by nonconservative reaction kinetics. The TASEP is a stochastic model of diffusing particles on a one-dimensional lattice with a hopping bias [5]. Each site from 1 to L is either empty ('$\varnothing$') or occupied by one particle ('A'). In the bulk particles hop stochastically from site i to $i+1$ with unit rate, provided that the target site is empty. The boundaries act as particle reservoirs with densities ρ_- on the left resp. ρ_+ on the right: On site 1 particles are created with rate ρ_-, provided the site is empty, which corresponds to a particle hopping from the left reservoir onto the first site. Particles on site L are annihilated with rate $1-\rho_+$, corresponding to a particle hopping into the right reservoir.

In our model particles also undergo the following reaction process: On a vacant site enclosed by two particles a particle may be attached with rate ω_a, and a particle enclosed by two other particles may be detached with rate ω_d. This process can be symbolically written as $A\varnothing A \rightleftharpoons AAA$ and may be interpreted as activated Langmuir kinetics. Without the TASEP dynamics the stationary density of this process is either $K = \omega_a/(\omega_a+\omega_d)$ or zero, with no correlations. As in previous work we consider the physically interesting case when $L \to \infty$ and these rates are proportional to $1/L$ [6–8]. Hence we define renormalized rates

$$\omega_a = \Omega_a/L, \qquad \omega_d = \Omega_d/L \tag{1}$$

where Ω_a and Ω_d are kept constant while $L \to \infty$ [9].

We find a stationary phase diagram of the model with five distinct phases (Fig. 1). The stationary density profile ρ_i is not constant as a function of lattice site i. Yet some of the phases are comparable to those of the usual TASEP with open boundaries [10, 11]: in the high density phases (HD1/2) one finds $\rho_i > 1/2$ while in the low density phase (LD) $\rho_i < 1/2$. In HD1 the bulk density profile is dependent on ρ_+, while it is independent of both boundaries in HD2 as in the maximal current phase of the TASEP. On the other hand two additional phases exist: A coexistence phase which is characterized by a stable shock position, i.e., a jump in the density profile which is localized at a certain position in the bulk of the system. The shock connects a low density domain to its left with a high density domain to its right. In a different parameter regime we find a novel phase with an unstable shock position in the bulk. In this phase both the LD and HD states are stable (if $L \to \infty$) which implies that ergodicity is broken in the thermodynamic limit. Although for finite systems a transition between the two states is possible, the mean life time of each steady state is expo-

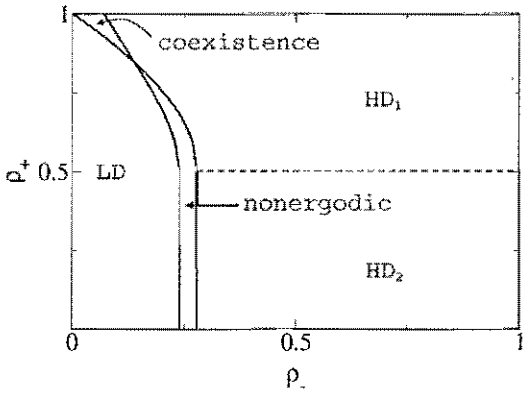

FIG. 1: Phase diagram for $\Omega_a = 0.7$ and $\Omega_d = 0.1$ with two high density phases (HD1, HD2), a low density phase (LD), a coexistence phase and the nonergodic phase.

nentially large in the system size L. This phase has no analog in the TASEP with open boundaries.

Hysteresis in this nonequilibrium setting was observed by measuring the space-averaged density $\bar{\rho}$ along the curve of constant ρ_+ while changing ρ_- in such a way that the system starting from the LD phase passed through the nonergodic phase and ended up in the HD2 phase. Then the process of changing ρ_- was reversed. A time average was not taken, $\bar{\rho}$ was measured in every k steps. On Fig. 2 one can see the resulting hysteresis loops.

To rationalize these observations we first consider the hydrodynamic limit on the Euler scale, i.e., we take $L \to \infty$ while the lattice constant is scaled by $a = 1/L$ and the time by $t = t_{\text{lattice}}/L$. Following the line of arguments of Ref. [7] we get a first order differential equation for the density profile $\rho(x)$:

$$\frac{\partial}{\partial t}\rho(x,t) + \frac{\partial}{\partial x} j(\rho) = \Omega_a \rho^2 (1-\rho) - \Omega_d \rho^3. \qquad (2)$$

As the differential equation is of first order and the boundary condition fixes the density at two positions, the differential equation does not provide a solution of the boundary problem in general. In the original lattice model this inconsistency is resolved by the appearance of a shock and/or boundary layers as described in [7].

In order to understand quantitatively the selection of the stationary shock position (which determines the phase diagram) and also to explain the phenomenon of hysteresis from a microscopic viewpoint we describe the dominant dynamical mode of the particle system in terms of the random motion of the shock. To this end we introduce space-dependent hopping rates for jumps of the shock over a lattice constant a. This furnishes us with the picture of a random walker in an effective energy landscape $E(x)$ inside a finite box. The energy landscape is generated by the interplay of the particle current with

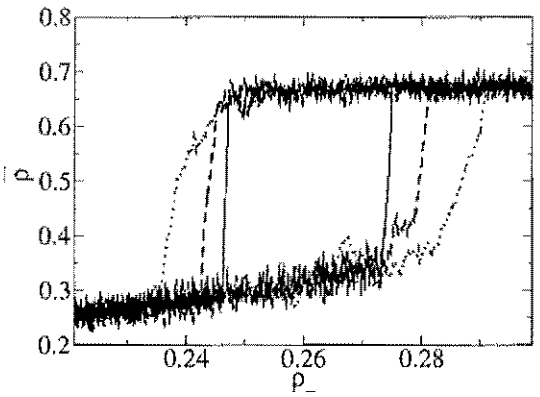

FIG. 2: Hysteresis plot for $L = 2000$, $\Omega_a = 0.7$, $\Omega_d = 0.1$, $\rho_+ = 0.45$. ρ_- was changed by 10^{-4} in every 5000 (solid line), 1500 (dashed line) and 500 (dotted line) MC steps. The hysteresis loop gets wider as the speed of changing ρ_- is increased which is reminiscent of hysteresis in usual magnetic systems.

the reaction kinetics. In this way we relate the original nonequilibrium many-particle system to an equilibrium single-particle model and obtain the phase diagram of the model.

[1] M. R. Evans, Y. Kafri, H. M. Koduvely, and D. Mukamel, *Phys. Rev. Lett.* **80**, 425 (1998).

[2] P. F. Arndt, T. Heinzel, and V. Rittenberg *J. Phys. A* **31**, L45 (1998).

[3] Y. Kafri, E. Levine, D. Mukamel, G. M. Schütz, and J. Török, *Phys. Rev. Lett.* **89**, 035702 (2002).

[4] O. M. Braun, B. Hu, A. Filippov, and A. Zeltser, *Phys. Rev. E* **58**, 1311 (1998).

[5] G. M. Schütz in *Phase transitions and Critical Phenomena* Vol 19, Eds. C. Domb and J. Lebowitz (Academic, London, 2001).

[6] R. D. Willmann, G. M. Schütz, and D. Challet, *Physica A* **316**, 430 (2002); A. Parmeggiani, T. Franosch, and E. Frey, *Phys. Rev. Lett.* **90**, 086601 (2003).

[7] V. Popkov, A. Rákos, R. D. Willmann, A. B. Kolomeisky, and G. M. Schütz, *Phys. Rev. E* **67**, 066117 (2003).

[8] M. R. Evans, R. Juhasz and L. Santen, *Phys. Rev. E* **68**, 026117 (2003).

[9] A. Rákos, M. Paessens, G.M. Schütz, *Phys. Rev. Lett.* **91**, 238302 (2003).

[10] G. Schütz and E. Domany, *J. Stat. Phys.* **72**, 277 (1993).

[11] B. Derrida, M. R. Evans, V. Hakim, and V. Pasquier, *J. Phys. A* **26**, 1493 (1993).

Single Protein dynamics in natural and denaturated state

R. Biehl[1], Z. Bu[2], B. Hoffmann[3], M. Monkenbusch[1], D.J.E. Callaway[2]

[1] *Institut für Festkörperforschung, FZJ*
[2] *Fox Chase Cancer Center, Philadelphia, USA*
[3] *Institut für Schichten und Grenzflächen, FZJ*

During operation of proteins as universal nanomachines or involved in the transmission and amplification of signals, conformational changes are omnipresent. An intriguing combination of structure and flexibility facilitates their activity. Conformational changes can be triggered by small-amplitude, nanosecond protein domain motion. Understanding how conformational changes are initiated requires the characterization of protein domain motion on these timescales and on length scales comparable to protein dimensions. We present here examinations by Neutron Spinecho Spectrometry of a multi domain protein in equilibrium and the dynamics of an unfolded smaller globular protein under thermal stress.

Protein domain motions are critical for proteins to coordinate precise biological functions. For example, coupled domain motions occur in genome regulatory proteins, motor proteins, signalling proteins, and structural proteins[1]. Structural studies have documented the conformational flexibility in proteins accompanying their activities[2]. However, the time-dependent, dynamic processes that facilitate protein domain rearrangements remain poorly understood.

The function of DNA polymerase I from Thermus aquaticus (Taq polymerase) (Fig. 1) requires coordinated domain and subdomain motions within this protein to generate a precise ligatable nick on a DNA duplex[3]. Taq has two distinct domains: a 5' nuclease (residues 1–289) for RNA primer removal and a Klenow fragment (residues 294–831, polymerase domain plus 3'-5' exonuclease catalytic centre) for nucleotide replacement in DNS repair. The Klenow fragment resembles a right hand with palm, finger, and thumb subdomains.

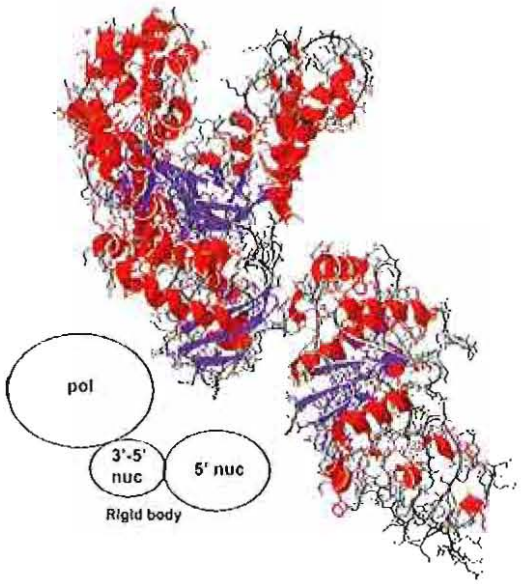

Figure 1 Structure of Taq polymerase I with the main domains. Taq polymerase possesses an extended conformation with the Klenow fragment (pol + 3'-5' nuc) and the 5' nuclease active sites separated by ≈70Å.

For NSE experiments Taq polymerase was dissolved in 99.9% D_2O per-deuterated buffer solution at pH 8.0 with a concentration of 8 mg/ml (for details see [4]). The data were collected at a wavelength of 8A in a Q range of 0.039 A^{-1} < Q < 0.260 A^{-1} at a temperature of 30°C. Within this Q range the S(Q,t)/S(Q,0) spectra obtained by NSE mainly measure coherent scattering. The spectra can be approximated by the first cumulant representation with the leading term

$$\lim_{\lim \tau \to 0} \frac{\partial}{\partial \tau} \ln\left(\frac{S(Q,\tau)}{S(q,0)}\right) = -\Gamma(Q) = -Q^2 D_{eff}(Q) \quad (1)$$

resulting in the effective Diffusion constant D_{eff} for small fourier times τ. Figure 2 compares the results to different dynamic models. The horizontal dashed line is D_{DLS} measured under same conditions. We observe clear oscillations around the mean value of the centre of mass translational diffusion at long length scales.

To examine the influence of translational and rotational diffusion of a rigid body model onto the overall Diffusion the protein was subdivided into three subdomains (see Fig. 1). The three principal-axis translational diffusion coefficients in H^T and the three principal axis rotational diffusion coefficients in H^R were obtained from the Taq polymerase crystal structure coordinates (PDB ID code 1TAQ[5])by using the program HYDROPRO[6]. D_{eff} can be calculated by

$$D_{eff}(Q) = \frac{k_B T}{Q^2} \frac{\sum_{jl} \langle b_j b_l (Q H^T Q + L(j) H^R L(l)) e^{iQ(r_j - r_l)} \rangle}{\sum_{jl} \langle b_j b_l e^{iQ(r_j - r_l)} \rangle} \quad (2)$$

where b_j and b_l are the neutron scattering lengths of effective residues j and l, respectively. $L(j) = Q \times r_j$ is the angular momentum vector. The sum was taken over effective residues j and l, with the centre of each effective residue taken as the average coordinate of the atoms in the effective residue and with the neutron scattering length b of the effective residue being the sum of neutron scattering lengths of all atoms in a residue. Results were plotted as black solid line in Figure 2. Only for longer length scales this model describes our experimental results. A purely

static model cannot describe the observed dynamics special on large Q values.

From a normal mode analysis using the program ELNEMO[7] we identify the nontrivial modes 7 and 8 as bending and torsion modes of the Klenow fragment against the 5' fragment. Higher order modes involve relative motion of the rigid domains polymerase, exonuclease and 5' nuclease against each other.

To enhance the model we include simple internal modes by allowing independent movements of single fragments at their equilibrium position, resulting in

$$D_{eff}(Q) = \sum_f D_f S_f(Q) \Big/ S_{Taq}(Q) \qquad (3)$$

with the static form factor $S_f(Q)$ and diffusion constant D_f of fragments f. $S_{Taq}(Q)$ is the static form factor of the complete protein (for details see 4).

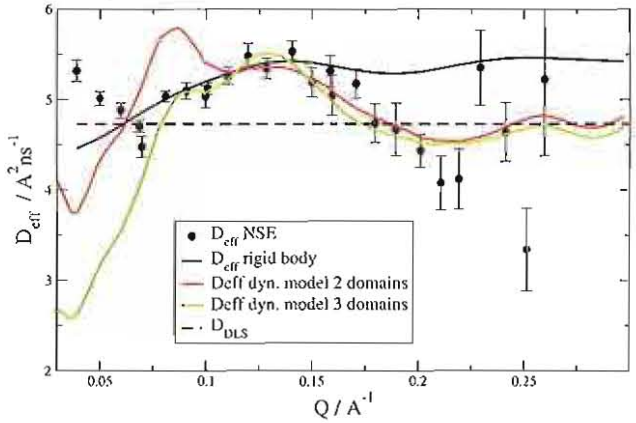

Figure 2 Comparing the experimental $D_{eff}(Q)$ of Taq polymerase by NSE (•) with those from different dynamic models.

The red line in Figure 2 is the $D_{eff}(Q)$ calculated by Eq. 3 using the dynamic model that parses Taq polymerase into two domains, the 5' nuclease and the Klenow fragment domains. The blue line is the $D_{eff}(Q)$ calculated using the dynamic model that parses Taq polymerase into three domains, the 5' nuclease, 3'–5' exonuclease, and polymerase domains. The result demonstrates that the systematic inclusion of higher normal modes consistently improves the agreement with the NSE experiment for $Q>0.05$ A^{-1}.

Although the rigid-body model calculated $D_{eff}(Q)$ using Eq. 1 has maximums and minimums the experimental $D_{eff}(Q)$ shows much more significant oscillations. Our analysis allowing simple internal modes show that NSE data reveal coupled correlated domain motion within Taq polymerase. Moreover, we show that the internal motion can be systematically analyzed by reducing the data within a normal mode framework.

Structure and flexibility of proteins can be changed by denaturation up to irreversible damage. Reversible conformational changes from biological relevant conformations e.g. by increased temperature show us possible rearrangements and allow exploration of the protein energy landscape. The NSE technique allows us to observe the dynamics in rearranged conformations.

The dynamics of the smaller protein Ribonuclease A (R≈20A) was examined in a D2O buffer solution pH 2 at different temperatures. Conditions were chosen to ensure reversible unfolding with temperatures up to 70°C. Fig. 3 shows the effective diffusion coefficients measured by NSE. We observe at 25°C a simple diffusive behaviour (black points) justifying our assumption for smaller fragments in the first section.

At a temperature of 65°C (blue) just at the maximum of the unfolding transition, revealed by Differential Scanning Calorimetry, we find a pronounced increase of D_{eff} with a small maximum at about 0.11 A^{-1}. At a temperature of 70°C when the unfolding transition is finished just an increase is found (Fig. 3 left). The increase with temperature in D_{eff} is mainly due to the change in viscosity. To eliminate effects due to temperature we calculate $6\pi\eta(T)D_{eff}/kT \approx R_H^{-1}$ (Fig. 3 right. The increase of the hydrodynamic radius R_H with increasing temperature in the low Q limit is comparable with the increase measured by DLS and SANS. From the low Q limit we observe an increase with Q of D_{eff} up to the level of the native protein. Normal mode analysis shows a strong torsion mode between two fragments separated by a gap. In the native globular state this and rotational diffusive components are invisible for NSE due to the missing contrast variation combined with an overall globular shape.

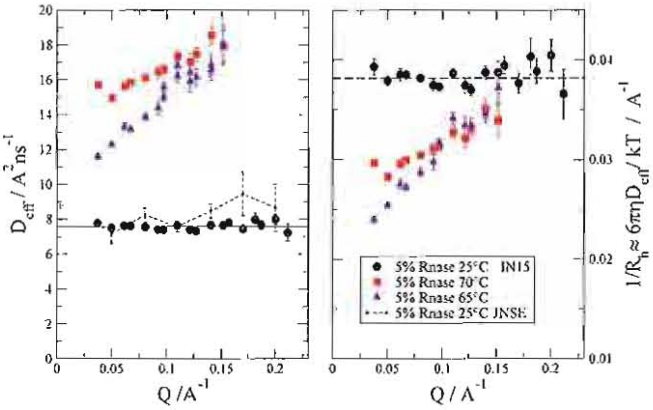

Figure 3 left: $D_{eff}(Q)$ of Ribonuclease A. right: $1/R_H$ as reduced data to emphasise non trivial temperature effects.

SANS data show also a significant increase in size with increasing temperature. Due to the unfolding the protein changes its globular shape to a more elongated shape. This makes rotational movements and internal modes visible for NSE. From this we can conclude that we also observe internal dynamics for this smaller protein in the partial unfolded state in two significant different conformations at 65 and 70°C. A detailed analysis analogous to the treatment of Taq polymerase and a molecular dynamics simulation will follow.

[1] Gai D. et al Cell 119, 47–60 (2004); Graceffa P. et al J. Biol. Chem. 278 34172 (2003); Bose-Basu B. et al Biochemistry 43, 14317 (2003); Li Y. et al EMBO J. 17, 7514 (1998)

[2] Gerstein M. et al Nucleic Acids Res. 26, 4280 (1998)

[3] Xu Y. et al J. Biol. Chem. 275, 20949 (2000)

[4] Bu Z. et al Proceedings of the National Academy of Sciences 102 17646 (2005)

[5] Kim Y. et al (1995) Nature 376, 612

[6] Garcia de la Torre J. et al Biophys. J. 78,719 (2000)

[7] Suhre K. et al Nucleic Acids Res. 32, W610–W614 (2000)

Protein diffusion in PEO networks

R. Biehl, M. Monkenbusch, A. Radulescu, J. Allgaier, D. Richter
Institut für Festkörperforschung, Forschungszentrum Jülich, Germany

G. Kali
Institut Laue-Langevin, Grenoble, France

X. Guo, R.K. Prud'homme
Department of Chemical Engineering, Princeton University, USA

Abstract

Protein diffusion of α- Lactalbumin in dense environments was examined with physically entangled polyethylene oxide networks as model system. Comparing NMR with neutron spin echo experiments results in equal diffusion like dynamics from macro- to microscopic length scales. Exponential decrease of the diffusion coefficient with PEO concentration was observed.

Introduction

The diffusion of proteins in polymer networks is examined to understand dynamic processes in dense environments like biological cells. We present measurements of the diffusant dynamics by Neutron Spin-echo Spectroscopy (NSE) at different q values together with NMR measurements at macroscopic length scales. The investigated system consists of the protein α-Lactalbumin (R_H=19.7 Å [1]) as diffusant and a network of high molecular weight polyethylene oxide. The high molecular weight ensures a long disentanglement time for the polymer in order to create a stable network.

The diffusion of macromolecules in the surrounding of a stable polymer network depends on different parameters. We focus on the ratio between the size of the diffusing macromolecules and the mesh size of the polymer network. We neglect the structure of the diffusant and assume that the time for the network to rearrange is much larger than the time for the macromolecule to diffuse over the length of a mesh size is [2].

Experimental

Network dynamics was studied at polyethylene oxide (PEO, 443000 g/mol, PDGPC: 4, Aldrich) dissolved in D2O (99.7%). The samples were centrifuged for 2h at 4500 rpm to remove insolubles. The deuterated PEO (dPEO, MW=216000 g/mol, PDGPC:1.3) is partially protonated (19.8%) to match the scattering length density of D2O. Observations of the diffusant dynamics were done with native bovine α-Lactalbumin, dissolved in D2O before dissolving dPEO. Protein concentration was about 1.3 % wt for all samples. All measurements were done at a temperature of 45°C.

Results and discussion

The radii of gyration R_g were 366Å (PEO) and 228Å (dPEO) respectively [3]. The network correlation length ξ can be estimated for good solvents by

$$\xi = R_g \left(\frac{c^*}{c} \right)^{\frac{3}{4}} \qquad (1)$$

with the overlap concentration $c^*=3M_w/4\pi N_a R_g^3$. N_a is the Avogadro constant and c the concentration. In a good solvent, we obtain with $R_g \propto M_w^{3/5}$ that the ξ is independent from molecular weight. The PEO chain correlation length can be determined by fitting an Ornstein-Zernike lineshape $\sim 1/(q^2\xi^2+1)$ onto SANS data, here measured at concentrations of 2%, 10% and 20% wt. resulting in 31A, 10A and 5A as shown in figure 1.

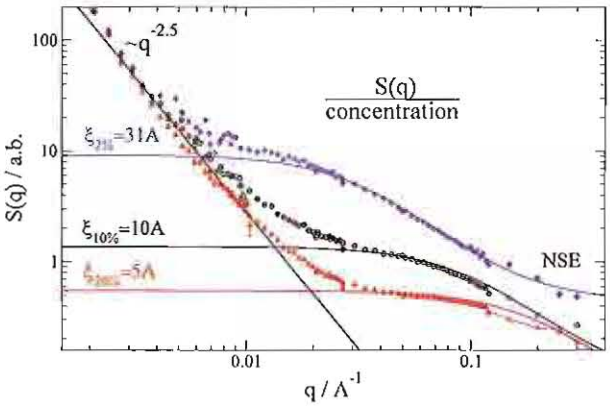

Figure 1: SANS measurements on hPEO in D_2O with concentration 2%, 10% and 20%. Fits were done by a function with Ornstein-Zernike lineshape with an additional powerlaw accounting for agglomerates. Data were scaled by the concentration.

Resulting ξ correspond to size ratios R_L/ξ of 0.63, 2 and 4 with the hydrodynamic radius of α-Lactalbumin R_L=19.7Å. The crossover from single chain relaxation to collective diffusion is predicted to occur at $q \approx 1/\xi(c)$ for a good solvent [4]. In our measurements of the PEO dynamics in D_2O by NSE we found a good agreement between the correlation length from dy-

namical NSE measurements and structural SANS measurements. ξ corresponds in both cases to the mean distance of binary contacts in the polymer solution. Assuming $c^* \approx 1/[\eta]$ with the intrinsic viscosity $[\eta]$ together with the macroscopic Mark-Houwink-Sakurada relationchip $[\eta] \approx K M_w^{\alpha}$ for PEO (K=0.0125ml/g, α=0.78) we get a mean distance 3 times larger than from our microscopic measurements of the correlation length. However, Kavassalis et al. have predicted that the critical entanglement concentration c_e is about 10 times higher than the critical overlap concentration c^* in equ. 1 [5]. From this we yield mean distances between entanglements, which can be regarded as a mesh size, bigger by a factor of 5 than the above values.

Figure 2 presents the effective diffusion coefficient of the protein in the deuterated network as result of a fitting procedure with a simple exponential decay $\sim\exp(-D_{eff}q^2\tau)$ onto the intermediate structure factor measured by NSE. We find diffusion coefficients independent from q. The average values are 13.2 Å²/ns for the 2% Protein sample respectively 6.1 Å²/ns and 2.9 Å²/ns for 10% and 20% wt. protein samples.

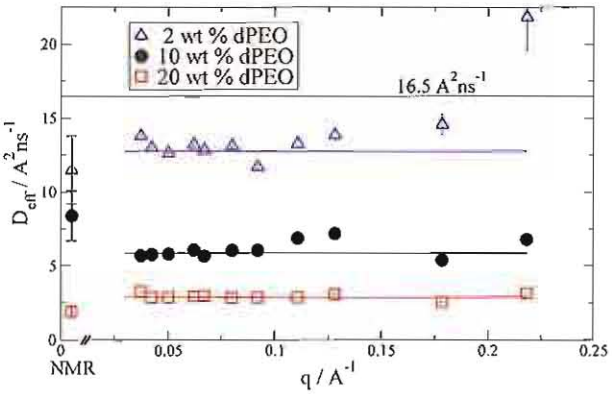

Figure 2: Effective diffusion coefficients dependent on dPEO concentration an q. At the left the results from NMR measurements is given. The straight line shows the value of free diffusion in pure D_2O

The free diffusion value is 16.5 Å²/ns in D_2O. At the left side the corresponding values from NMR measurements on macroscopic length scales were included showing similar diffusion coefficients.

In Figure 3 we compare the found concentration dependence with different models. The collective diffusion coefficients D_{coll} (■), measured by NSE in hPEO samples, show a $\sim c^{3/4}$ dependence [4]. D_{SE} assumes Stokes-Einstein diffusion of a sphere with an effective viscosity from the macroscopic Mark-Houwink relationship only valid for low concentrations (solid line) and underestimates the found diffusion coefficients. D_{SE} with η_{Zimm} assumes the same effective viscosity for the protein as measured in the hPEO gel for the polymer chain in the Zimm like regime (▽) measured by previous measurements with NSE. The protein feels a higher effective viscosity than the single chain. This additional friction should originate from the interaction with the entangled polymer network while in the effective viscosity assumptions interactions with other chains are not considered beyond the viscosity effect. Also the result of Cheng et al (dashed red line) and a corresponding fit to our data (dash-doted blue line) were given. Cheng measured diffusion coefficients of various diffusants in PEO with the macroscopic FRAP (fluorescence recovery after photobleaching) and described it by an universal function $D=D_0\exp(-\beta(R/\xi)^{\delta})$. With changed β, attributed to the change from PEO to dPEO, this functional form describes also our data very well.

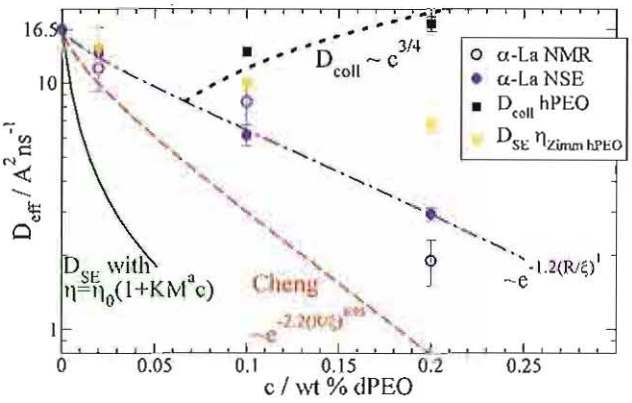

Figure 3: Comparison between different diffusion coefficients.

Finally within experimental accuracy we find on microscopic and macroscopic length scales equal diffusion coefficients and mechanisms. Between the inside of a single mesh on length scales in the order of the network correlation length and length scales much bigger than the mesh size where the diffusant has to cross the boundary of a single mesh we find no difference. With regard to the difference between binary contacts and physically entangled chains we have to think of the interior of a single mesh as being full of chain segments. These chain segments appear to be primarily responsible for the dynamics of the diffusant.

References:

[1] C. Redfield et al., Nature Structural Biology 6,10 (1999) 948

[2] Y. Cheng, R. K. Prud'homme, J.L. Thomas Macromolecules 35 (2002) 8111.

[3] M.Polvari; T.G.M. van de Ven J. Phys. Chem. 100 (1996) 13687.

[4] B. Ewen, D.Richter Advances in Polymer Science 134 (1997) 3

[5] T.A. Kavassalis, J. Noolandi Macromolecules 22, 6 2709 (1989)

Hydrophilic polymers equipped with short hydrophobic stickers as efficiency boosters for microemulsions

Ch. Frank, J. Allgaier, H. Frielinghaus
Institute for Neutron Scattering, IFF, Forschungszentrum Jülich, D-52425 Jülich

Strongly amphiphilic, symmetric block copolymers added to microemulsions increase the efficiency of surfactants dramatically (efficiency boosting). New highly unsymmetric polymers with a weaker amphiphilicity, the sticker polymers, allow for a comparable efficiency enhancement. These additives are much simpler to synthesize and commercially accessible, which favours the applicability. Experimental observations of the phase diagram, and small angle neutron scattering allow to compare microscopic parameters, namely the saddle splay modulus, the bending rigidity and the spontaneous curvature.

F&E-Nr: 23.10.2

The considered microemulsions contain equal amounts of immiscible oil and water. The non-ionic surfactant mediates between the immiscible components, which then forms domains with a surfactant layer in between. The surfactant efficiency is given by the minimum amount of surfactant needed to form a one-phase microemulsion. Using small angle neutron scattering experiments it was demonstrated that the polymer chains are attached to the surfactant layer and form mushroom conformations. The polymer decoration increases the bending rigidity of the surfactant film which in turn allows to stabilize larger domain structures or in other words to reduce the surfactant concentration.

A typical non-ionic surfactant is the linear $C_{10}E_4$ with a hydrocarbon chain of 10 carbons and a water-soluble chain of 4 ethylene oxide monomers. This surfactant is rather symmetric with equal volumes of the hydrophobic and hydrophilic ends. The initially used symmetric A-B diblock copolymers have the same chemistry, and a typical polymer used would be the $C_{350}E_{130}$. The new polymers are highly unsymmetric, one of which is the $C_{12}E_{90}$. The amphiphilicity is surely reduced, but as we will demonstrate the new polymers work equally well as efficiency boosters.

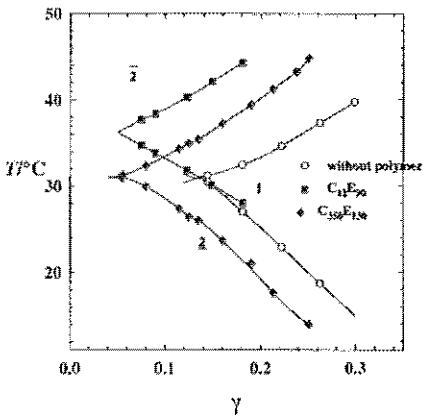

FIG. 1. Phase diagrams for microemulsions containing no additive, the conventional block copolymer $C_{350}E_{130}$, and the new sticker polymer $C_{12}E_{90}$.

However, at a first view one would expect the new additives having a very strong influence on the temperature behavior or even to destruct the formation of microemulsions because of the highly hydrophilic nature. This is not the case. Figure 1 shows phase diagrams of microemulsions containing equal amounts of water and decane, and the surfactant $C_{10}E_4$. Compared to the system without polymer, the 1-phase region is shifted to smaller surfactant concentrations γ if the conventional block copolymer $C_{350}E_{130}$ is added. The same result is obtained if the new sticker polymer $C_{12}E_{90}$ is used except that the temperature window for the 1-phase region is shifted slightly to higher temperatures. This effect is a measure for the unsymmetry of the polymer. With respect to emulsification power both additives are similar. This indicates that despite the short hydrophobic tail the new additive is quantitatively anchored at the water-oil interface.

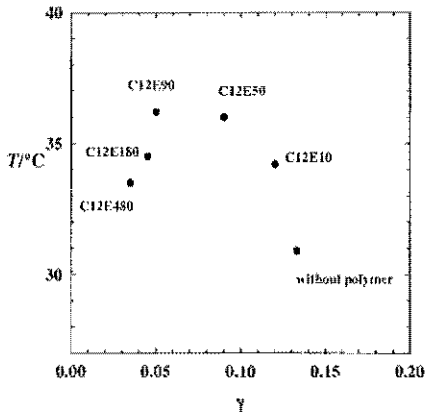

FIG. 2. Fish tail points of microemulsions with added sticker polymers varying from $C_{12}E_{10}$ to $C_{12}E_{480}$.

In a series of experiments the chain length of the hydrophilic sticker polymers was varied. In Figure 2 the lowest surfactant concentrations at which still a 1-phase microemulsion is obtained, the so called fish tail points are plotted against the temperature. All polymers contain C_{12} stickers. The chain length of the hydrophilic moiety is varied between 10 and 480 ethylene oxide monomer units. The series clearly shows that with increasing hydrophilic chain length the emulsification power is continuously boosted.

According to theoretical considerations the surfactant concentration at the fish tail point, Ψ, is correlated with the number density of polymer chains per surfactant area,

σ, and the size of the polymer chain in terms of its end-to-end distance R_{ee} in the following way [1]:

$$\ln(\Psi/\Psi_0) = -\Xi \cdot \sigma R_{ee}^2 \qquad (1)$$

with the theoretical sensitivity $\Xi = \pi/5$. Considering a constant polymer amount, δ, with respect to the total amphiphile, σ and R_{ee}^2 are correlated with the molecular weight of the polymer chain, M_W, according to $\sigma \sim M_W^{-1}$ and $R_{ee}^2 \sim M_W^{1.16}$ (for PEO [2]). Therefore, the influence of M_W on Ψ should be rather small, i.e. $\ln(\Psi/\Psi_0) \sim M_W^{0.16}$.

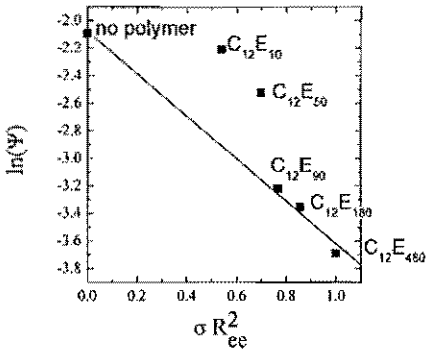

FIG. 3. Surfactant concentration dependence of the fish tail points as a function of the polymer grafting density σ scaled with the polymer size R_{ee}^2.

In Figure 3 $\ln\Psi$ is plotted against σR_{ee}^2. There is a disagreement for $C_{12}E_{10}$ and $C_{12}E_{50}$ having very short polymer chains. This is not astonishing because at those low chain lengths the polymers form much denser structures than the higher molecular weight analogs. Hence, from $C_{12}E_{90}$ on the molecular weight dependence is as theoretically predicted. The measured value for the slope of $\Xi = -1.54$ coincides exactly with the value found for the A-B block copolymers [1]. This again demonstrates that the interfacial activity of both polymer types, block copolymers and sticker polymers is identical. The small covered range of σR_{ee}^2 for the polymers $C_{12}E_{90}$ up to $C_{12}E_{480}$ reflects the weak dependency of $\ln(\Psi/\Psi_0) \sim M_W^{0.16}$.

The other important feature from Figure 2 is the temperature behavior of the fish tail points. For the shorter chain lengths there is an increase of the temperature of the fish tail point. Because of the hydrophilic nature of the sticker polymers this intuitively makes sense. The unexpected temperature decrease for the longer polymers will turn out to be the theoretically described behaviour of Lipowsky [3]. Experimentally the relation between film mean curvature $\langle H \rangle$ and temperature was examined by Sottmann and Strey [4]

$$\langle H \rangle = \mu \cdot \Delta T \qquad (2)$$

with the experimental constant $\mu = -1.4 \cdot 10^{-3}\text{Å}^{-1}\ \text{K}^{-1}$ for $C_{10}E_4$. ΔT is the temperature difference between a given temperature and the phase inversion temperature given by the fish tail point. The relation between $\langle H \rangle$ and polymer parameters is according to theoretical calculations by Lipowsky and Gompper as follows [3,5]

$$\langle H \rangle = \Upsilon \cdot \sigma R_{ee} \qquad (3)$$

with the theoretical sensitivity $\Upsilon = 0.181/(\kappa/k_BT) \approx 0.43$. The mean bending rigidity was assumed to be $\kappa = 0.42 k_BT$. If again the molecular weight is introduced into the relation, it transforms Into $\langle H \rangle \sim M_W^{0.42}$. This means that with increasing molecular weight the influence on the curvature gets smaller, which we unexpectedly saw in Figure 2 for higher molecular weights. In Figure 4 $\langle H \rangle$ is plotted against σR_{ee}. The expected dependency of Eq. 3 is obtained for the higher molecular weights with a sensitivity $\Upsilon = 0.58$. Again the shorter sticker polymers mismatch for the reasons discussed before.

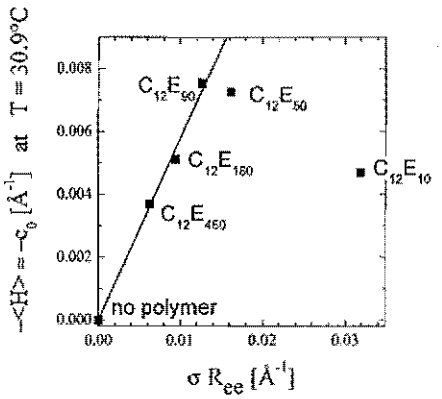

FIG. 4. Spontaneous curvature dependence as a function of the polymer density σ scaled with the polymer size R_{ee}.

Initial small angle neutron scattering experiments have been made on the simple sticker polymers as presented here, and on bifunctional sticker polymers. Using the Gaussian random field theory the structural measurement reveals the bending rigidity having a similar dependence than the membrane content Ψ (Eq. 1). First experiments find roughly the expected behaviour as predicted by Lipowsky [3]. In the future multifunctional sticker polymers are interesting since they show an enhanced polymer boosting effect [6]. The variation of the sticker anchor length is interesting since even short anchors are attracted by the membrane in a dynamical balance.

[1] H. Endo, J. Allgaier, G. Gompper, B. Jakobs, M. Monkenbusch, D. Richter, T. Sottmann, R. Strey, *Phys. Rev. Lett.* **85**, 102, 2000

[2] S. Kawaguchi, G. Imai, J. Suzuki, A. Miyahara, T. Kitano, K. Ito, *Polymer* **38**, 2885, 1997

[3] Ch. Hiergeist, R. Lipowsky, *J. Phys. II France* **6**, 1465, 1996

[4] T. Sottmann, *Dissertation* University Göttingen, Göttingen, 1997, T. Sottmann, R. Strey, *J. Chem. Phys.* **106**, 8606, 1997

[5] G. Gompper, D. Richter, R. Strey, *J. Phys. Condens. Matter*, **13**, 9055, 2001

[6] T. Auth, G. Gompper, *Phys. Rev. Lett.* **68**, 051801, 2003

Tuning the membrane properties in bicontinuous microemulsions with homopolymers and diblock copolymers probed with NSE and SANS

H. Frielinghaus, O. Holderer, D. Byelov, M. Monkenbusch, J. Allgaier, and D. Richter
Institute for Neutron Scattering, IFF, Forschungszentrum Jülich, D-52425 Jülich

The properties of bicontinuous microemulsions, consisting of water, oil and a surfactant, are modified by the addition of diblock-copolymers (boosting effect) and homopolymers (antiboosting effect). Comparison of the bending moduli that are obtained by analysis of the dynamics to those obtained from small angle neutron scattering (SANS) sheds light on the different renormalization length scales for NSE and SANS. Variation of the surfactant concentration at otherwise constant conditions of homopolymer or diblock-copolymer concentration shows that NSE results depend on the pure bending rigidity, while SANS measures the renormalized modulus. The unexpected large homopolymer effect might be explained by confinement effects.

Amphiphilic polymers are an important class of additives in microemulsions. This kind of polymer allows for an enormously increased efficiency of the surfactant, which means a decreased consumption of amphiphile.

Microemulsions are thermodynamically stable mixtures of oil and water, which are mediated by the surfactant. The surfactant forms a film separating the domains of nearly pure oil and water. While microemulsions by themselves have a whole variety of interesting phases this study focuses on polymers added by small amounts to microemulsions.

As a complementary effect we studied the influence of two homopolymers [1], which are made of the same monomers as the diblock copolymer. As an example phase diagramms with tiny amounts of the polymers PEP_5 and PEO_5 are shown in Figure 1. The more polymer is added the more surfactant is needed to form a one-phase microemulsion. This directly means an efficiency decrease by homopolymers.

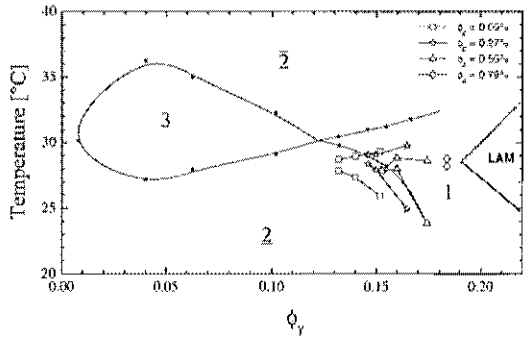

FIG. 1: Fish phase diagram (solid line) for the system H_2O–decane $C_{10}E_4$. For higher homopolymer fractions ϕ_p added to the system D_2O–decane–$C_{10}E_4$ lines with hollow symbols are used (see legend).

For a deeper understanding we performed small angle neutron scattering (SANS) and neutron spin-echo (NSE) experiments. By SANS the structural properties of the microemulsion are measured which can be connected to the bending rigidity of the surfactant membrane. The dynamics characterized by NSE measurements give also access to the bending rigidity and can be compared with the static SANS results. The presented experiments follow the changes of the phase diagram within the one-phase region.

The theory of Helfrich considers the main contribution of the free energy to arise from the elastic behavior of the surfactant film. The free energy reads:

$$F = \int dS \left[2\kappa(H - c_0)^2 + \overline{\kappa}K + ...\right] \qquad (1)$$

The first contribution considers the deviation of the mean curvature H from the spontaneous curvature c_0. The modulus is the bending rigidity κ. The second term considers the Gaussian curvature K with the elastic constant being the saddle splay modulus $\overline{\kappa}$. The theoretical prediction of the size of the polymer effects on κ are collected in the following:

$$\frac{\kappa_R}{k_BT} = \frac{\kappa_0}{k_BT} + \frac{\alpha}{4\pi}\ln(\psi) - 0.0238\frac{\phi_p(R_{hW}^3 + R_{hO}^3)}{V_p} + \frac{1}{12}\left(1 + \frac{\pi}{2}\right)\sigma(R_{dW}^2 + R_{dO}^2) \qquad (2)$$

The first term describes bare membrane properties. The second term arises from a higher membrane rigidity at length scales comparable to the membrane thickness. This renormalization effect depends on the considered length scale and therefore on the membrane volume fraction ψ. The homopolymer causes a decreased rigidity. The effect scales with the polymer content ϕ_p, the end-to-end distances of the polymers in solution R_{hW} and R_{hO}, and the average molar volume of one polymer V_p. The diblock copolymer effect is opposite and scales with the grafting density σ and the end-to-end distances of the individual blocks.

The bending rigidity κ can be measured by SANS in the following way: Describing the SANS data by the

Teubner-Strey model two structural parameters are obtained, the domain size d and the correlation length ξ. Some examples of this model fitting are depicted in Figure 2. The Gaussian random field model connects those parameters with $\kappa \sim \xi/d$ [1], which now can be compared with NSE measurements [2].

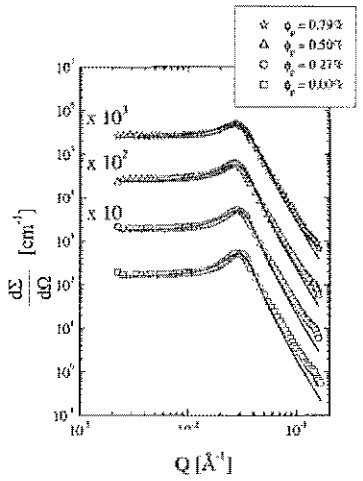

FIG. 2: Scattering cross section as a function of the scattering vector for bicontinuous microemulsions with homopolymer additions ϕ_p under bulk contrast. The membrane volume fraction ψ is fixed at 0.175. Solid lines are Teubner-Strey model fittings.

The dynamic structure factor $S(q,t)$, as measured with NSE spectroscopy is compared to a theoretical model of $S(q,t)$, giving information on parameters such as the bending constants. A model developed by Zilman and Granek describes the interface in terms of finite membrane patches in random orientation [3], with the most simple dispersion relation of the undulation modes of a free planar membrane in a viscous liquid, $\omega(k) = (\kappa/4\eta)k^3$, where η is the effective solvent viscosity. They found $S(q,t) \simeq S(q)exp(-(\Gamma_q t)^\beta)$ as an approximative expression for the dynamic structure factor for bicontinuous microemulsions at large $q(q >> q_0)$, with $\beta = 2/3$ and the q-dependent relaxation rate $\Gamma_q = 0.025\gamma_\kappa(\frac{k_BT}{\kappa})^{1/2}\frac{k_BT}{\eta}q^3$, where κ is the bending elasticity modulus, and $\gamma_\kappa \simeq 1 - 3\frac{k_BT}{4\pi\kappa}\ln(q\xi) \longrightarrow 1$ for $\kappa \gg k_BT$. While this expression explains well some features as the q-dependence of the NSE-spectra, it is essential to use an integral form of the Zilman-Granek theory in order to calculate κ [2, 4].

Results of κ as evaluated from NSE experiments with the integral expression of the Zilman-Granek theory are compared to κ obtained from SANS experiments in Figure 3. While $\kappa_{\rm NSE}$ results from an integration over all undulation mode wavevectors k and therefore is expected to yield the "bare" bending modulus without spatial renormalization effects, $\kappa_{\rm SANS}$ relies on the average structure at large scale d or ξ, therefore the resulting κ-value is the renormalized one. For reasons of comparison, the "bare" bending modulus from SANS is also shown in Figure 3 with open symbols. Both "bare" κ, i.e. the direct NSE bending rigidity and the derenormalized SANS value, do not depend on surfactant concentration, as expected from Equation 2.

While diblock copolymers yield an increase of κ, homopolymers reduce the bending modulus. The sensitivity of these effects is described by experimental coefficients (cf. Equation 2). Surprisingly, the influence of homopolymers is more than seven times larger than predicted by theory [1]. The confinement of homopolymers in the domains might be the explanation for this high sensitivity.

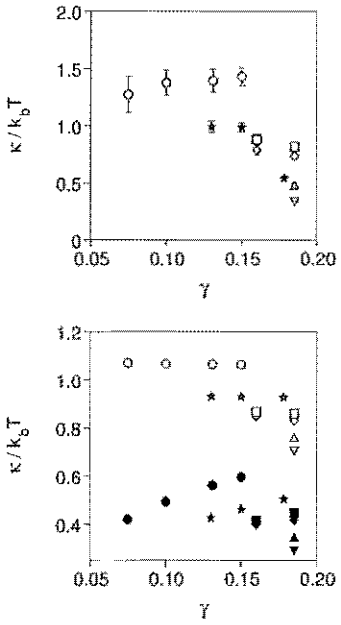

FIG. 3: Top: $\kappa_{\rm NSE}$ obtained by fitting the integral expression of the Zilman-Granek theory to the experimental data (pure microemulsion: $\star$, microemulsion with diblock polymers: $\circ$, with homopolymers: $\square$ 0.25 %, 5K; $\diamond$ 0.5 %, 5K;$\triangle$ 0.25 %, 10K;$\triangledown$ 0.4 %, 10K), as a function of the surfactant concentration γ. Bottom: $\kappa_{\rm SANS}$ before (filled symbols) and after correction for renormalization (open symbols) as a function of the surfactant concentration γ (note: $\gamma \simeq \phi_\gamma \simeq \psi$).

[1] D. Byelov, H. Frielinghaus, O. Holderer, M. Monkenbusch, J. Allgaier, and D. Richter, Langmuir **20**, 10433 (2004).
[2] O. Holderer, H. Frielinghaus, D. Byelov, M. Monkenbusch, J. Allgaier, and D. Richter, J. Chem. Phys., accepted.
[3] A. Zilman, and R. Granek, Phys. Rev. Lett. **77**, 4788 (1996).
[4] M. Mihailescu, M. Monkenbusch, H. Endo, J. Allgaier, G. Gompper, J. Stellbrink, D. Richter, B. Jakobs, T. Sottmann, and B. Farago, J. Chem. Phys.**115**, 9563, (2001).

Hierarchical structures formed by wax crystallization on polymeric templates: a combined study in real and reciprocal space by microscopy and small-angle neutron scattering techniques

A.Radulescu [1], D.Schwahn[1], J.Stellbrink[1], E.Kentzinger[1], M.Heiderich[1], L.J.Fetters[2], and D.Richter[1]

[1] *Institut für Feskörperforschung, Forschungszentrum Jülich, 52425 Jülich, Germany*
[2] *School of Chemical and biomolecular Engineering,Cornell University, Ithaca NY 14853-1301, USA*

PEB-*n* semicrystalline poly(ethylene-butene) random copolymers may become important in industrial applications because of their capability to modify the wax crystals and to improve the viscoelastic properties of crude oil and middle distillate fuels. The wax-copolymer interaction in solution is rather complex and is not yet understood. Therefore, these polymers may also be of much interest in basic research. We report here about the hierarchical morphology formed upon cooling by the mixed solutions of highly crystalline PEB-7.5 copolymer and different waxes. Multilevel structures showing characteristic sizes from 10 μm to 1 nm have been investigated in reciprocal space by three SANS techniques (classical SANS, focussing-SANS and ultra-SANS) and vizualized in real space by microscopy.

F&E-Nr: 23.55.0

Under wintry conditions, middle distillate fuels can clog the filters by precipitating large waxy crystals and thereby prevent engine operations. Polymeric additives can interact favourably with waxes (long chain C_nH_{2n+2} alkanes or simply C_n) and modify the crystal morphology to smaller units. Virtually random copolymers of ethylene and butene (designated PEB-*n* with *n* the number of ethyl side branches/100 backbone carbons) are promising candidates. Systematic small-angle neutron scattering investigations of different polymer-wax systems have shown that PEB-*n* copolymers are selective in their wax-modification capacity depending on the crystalline degree which is tuned by *n* [1,2]. Two mechanisms of polymer-wax interaction have been identified depending on which component aggregates first. Accordingly, either a co-crystallization of the wax and the copolymer into two-dimensional hairy platelets takes place, or a polymer template structure is formed first, which then acts as a nucleation center for the wax molecules. The second mechanism is still not fully understood. Therefore, we decided to investigate it in more details by performing new structural studies of the morphologies formed upon cooling in the polymer-wax mixed solutions prepared in so manner that the polymer self-assembles much earlier than the wax. We have chosen mixtures of different molecular weights (M_W) PEB-7.5 copolymers with two representative waxes, C_{24} and C_{36}. It was stated [2] that the self-assembling of this highly crystalline copolymer shows a double evolution with decreasing temperature: first, formation of large, compact aggregates and then, formation of rod-like structures with longitudinally modulated density (alternating crystalline and amorphous sequences). The aggregation features are similar for different M_W copolymers, the only difference is that they appear at different temperatures: the higher M_W, the higher the self-assembling temperature is. Thus, by combining the M_W dependence of the polymer self-assembling behaviour with the molecule length dependence of the wax cloud-point (CP, the temperature of the wax crystals appearance) [1] we found that the combinations 6K PEB-7.5/C_{24} and 30K PEB-7.5/C_{36} present the mechanism of wax crystallization on the polymeric template.

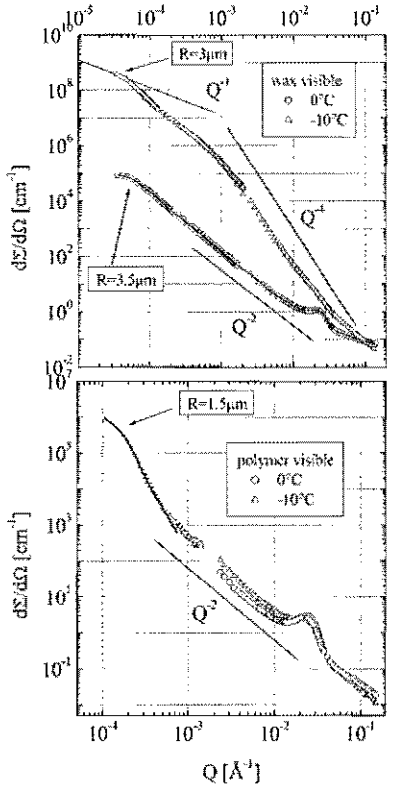

Fig.1 – Scattering patterns under wax (up) and polymer (down) contrast from a mixed solution of 6K PEB-7.5 copolymer and 4% C_{24} wax in decane at two temperatures within the common aggregation regime

By using the three SANS techniques developed at the FRJ-2 research reactor in Jülich namely, the classical pin-hole SANS, the focussing-mirror SANS (F-SANS) and the double-crystal diffractometry (U-SANS), a very wide Q

range has been investigated in the reciprocal space ($3x10^{-5}$ ÷ 0.2 $Å^{-1}$). This allowed by Fourier transformation a study of the structures developed over a very wide length scale, between 10 μm to 1 nm. The copolymer and wax conformation within the common aggregates has been separately analysed by using the contrast matching. The morphologies identified by a semiquantitative analysis of the scattering patterns in terms of power laws and the structural parameters evaluated by models have been checked in real space by complementary techniques like optical (OM) and transmission electron microscopy (TEM).

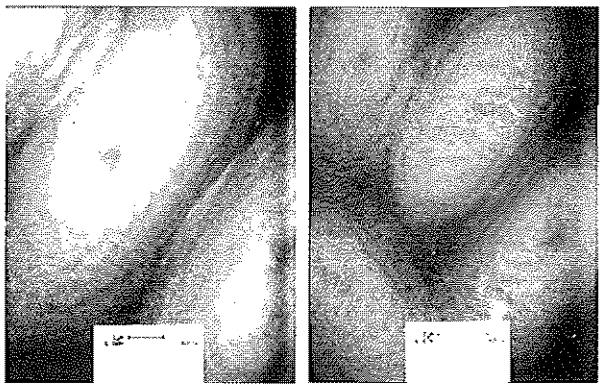

Fig.2 – TEM images of the aggregates formed in a decane solution of 30K PEB-7.5 and 4% C36 wax: top view of stacks of platelets.

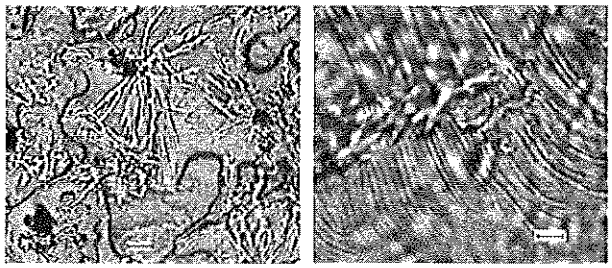

Fig.3 – Optical micrographs from solutions of 6K PEB-7.5 and 4% C_{24} wax at -10°C (left, scale bar 30μm) and 30K PEB-7.5 and 4% C_{36} wax at 25°C (left, scale bar 20μm).

Fig. 1 presents separately the polymer and wax scattering patterns from a mixed solution of low M_W PEB-7.5 copolymer and 4% C_{24} wax in decane at two temperatures within the common aggregation regime. The Q^{-2} power law behaviour at intermediate Q and the peak at around Q^*=0.025 $Å^{-1}$ revealed at 0°C by the scattering from both components indicate a cocrystallization of polymer and wax into thin, very large platelets forming a correlated arrangement [2]. The lateral size of these platelets can be evaluated from the analysis of the Guinier regime identified at low Q by USANS under the wax contrast. By modelling such a morphology in terms of the paracrystalline structure factor applied to an ensemble of finite size 2-dimensional objects [3] the structural and density parameters have been obtained. Because the correlation peak was found at the same Q value as for the polymer self-assembling scattering patterns [1] one can conclude that the primordial 1-dimensional polymer structure formed well before the occurrence of the wax crystals influences significantly the common aggregation mechanism. At -10°C the scattering patterns of both components are different to each other. The polymer still stays within 2-dimensional correlated structures as it is proved by the Q^{-2} power law behaviour at intermediate Q and the correlation peak. The low Q data measured by FSANS reveal the scattering from a secondary structure, that of the large, compact objects formed yet at very high temperatures (around 40°C) [2]. The scattering features interpreted in terms of the Beaucage unified model [4] and compared with those of the polymer self-assembling revealed that the addition of wax did not affect the morphology of these polymer aggregates which obviously have been formed and stabilized at much higher temperature than the wax CP. The wax scattering pattern at -10°C reveals that the wax surplus massively crystallizes and grows from the thin platelets into large objects with sharp interfaces (Q^{-4} power law at higher Q). From an inspection of the low Q data measured by FSANS (10^{-4}÷10^{-3} $Å^{-1}$) and USANS (below 10^{-4} $Å^{-1}$) a coexistence of two structures showing different characteristic sizes can be identified while, a 1-dimensional morphology can be tentatively attributed to the larger structure (Q^{-1} power law behaviour at very low Q). A direct visualization of the morphologies revealed by the scattering data has been possible by TEM and OM. Fig.2 shows TEM images of the aggregates formed by the high M_W PEB-7.5 copolymer and C_{36} wax as they have been isolated at room temperature from a decane solution. Stacks of platelets arranged one in top of another and resembling a top view of a shish-kebab like morphology are observed. The edges of the very large platelets are well visible while the central axis around they have grown irregularly can be guessed. Fig.3 presents two micrographs taken by OM from solutions of 6K PEB-7.5 and 4% C_{24} wax at -10°C and 30K PEB-7.5 and 4% C_{36} wax at 25°C. The images show the overall 1-dimensional morphology of the copolymer-wax aggregates formed during the later crystallization stage of the wax surplus.

One can sum up that a hierarchy of morphologies formed with decreasing temperature in solutions of random copolymers and waxes was investigated by microscopy and SANS techniques and the multilevel structure formed by a multi-stage aggregation process has been resolved. First, a polymer 1-dimensional morphology showing density modulations is formed. Then, wax crystals are formed and nucleated by the crystalline nuclei of the polymer rods. The wax is growing laterally in large platelets also involving further polymers still in solution. The primordial polymeric structure serves to template the lateral platelets in a correlated arrangement. Late aggregation stage leads to a massive crystallization of the wax surplus and formation of compact 1-dimensional structure.

[1] H.S.Ashbaugh et al., *Macromolecules*, **35**, 7044 (2002)
[2] A.Radulescu et al., *J.Polym.Sci. B, Pol.Phys.*, **42**, 3113 (2004).
[3] D.Richter et al., *Macromolecules*, **30**, 1053 (1997).
[4] G.Beaucage, D.W.Schaefer, *J.Non-Crystalline Solids*, **172-174**, 797 (1994)

Non-flexible coils in solution: A neutron spin-echo investigation of alkyl substituted polynorbornens in tetrahydrofuran

Michael Monkenbusch[1], Jürgen Allgaier[1], Jörg Stellbrink[1], Lewis J. Fetters[2] and Andreas Greiner[3]

[1] *Institut für Neutronenstreuung*
[2] *School of Chemical and Biomolecular Engineering, Cornell University, Ithaca, NY 14853-5021 USA*
[3] *Philipps-Universität Marburg, FB Chemie und Wissenschaftliches Zentrum für Materialwissenschaften, D-35032 Marburg, Germany*

The dynamics of vinyl-type poly(5-n-hexyl/propyl norbornene) (PHNB, PPNB) in dilute solution in tetrahydrofurane (THF) has been investigated by neutron spin-echo (NSE) spectroscopy. The polymer molecules have large internal rotation barriers that hinder conformational changes and thereby exhibit a dynamical stiffness that leads to a significantly retarded relaxation as compared to flexible polyisoprene chains (PI). While the latter perfectly match the prediction of the Zimm model, the polynorbornene spectra indicate a dynamical stiffness of the PH(P)NB chains, i.e. they exhibit a "frozen" coil conformation.

The vinylic polymerization [1] of norborene (bicyclo[2.2.1.]hep-2-ene) and its substituted derivatives yield polymers that display unusual properties such as good chemical resistance, dense packing in the amorphous state, large refractive indices, high glass transition temperatures and low birefringence. PNB has been characterized theoretically [2] on the molecular scale by a set of rotational potentials having low energy states separated by large energy barriers. Polymers of this type represent a new family of macromolecules where the chain energy minima of the potential are distributed along the backbone so that non-extended random 'frozen' chain [3] conformations emerge. This feature is related to large activation energies to chain segment rotation with barriers of 50-100 kJ/mol for the PNB family. Thus transitions between conformations are expected to occur only within time intervals that are large compared to those explored by typical experimental methods probing the molecular dynamics.

Dilute solutions of PHNB, fractionated PHNB (high M fraction) and PPNB in deuterated THF were investigated by neutron spin-echo (NSE) at the FRJ2-NSE spectrometer at the DIDO reactor of the FZ-Jülich. For comparison also 1% PI solutions in d-THF were measured. The asymptotic high-Q power law $S(Q) \propto Q^{1/\nu}$ could be extracted. Both linear PI solutions yield a vaule of $1/\nu = 1.61$ and the PHNB and PPNP polynorbornene solutions give $1/\nu = 1.593 \pm 0.03$ and 1.641 ± 0.03 respectively, close to $\nu = 0.6$ as expected for a self-avoiding random coil in a good solvent. To test the chain conformation on a local scale the NSE spectrometer was first used in diffraction mode with polarization analysis. A comparison of NSE data from the flexible linear reference PI and the PHNB sample both dissolved in d-THF at a concentration of 1% and 20^{0}C is shown in Fig. 1.

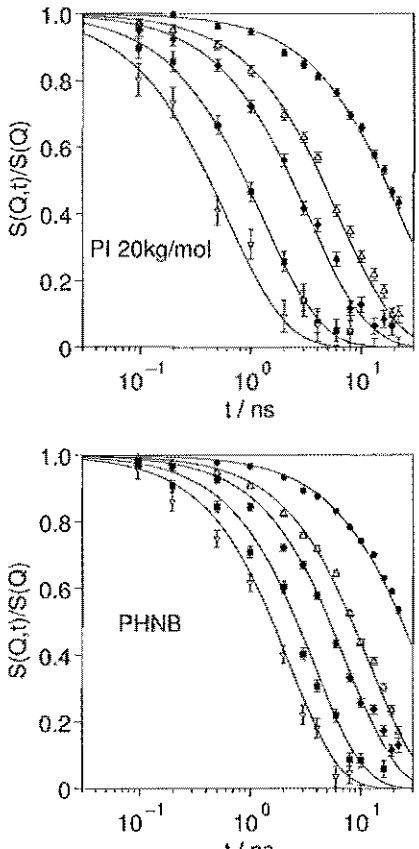

FIG. 1. Relaxation spectra of 1% dTHF-solution of PI [20kg/mol] (upper graph) compared to those from a PHNB solution (lower graph) for $Q_0 = 0.05\text{Å}^{-1}$(circles) to 0.18Å^{-1}(triangles). The lines correspond to the Zimm model prediction (see text).

It is obvious that PHNB displays a significantly retarded relaxation compared to that of PI, which virtually displays textbook [4] Zimm behavior (lines) as is discussed below. Within statistical error margins no

differences between the high M fraction and the non-fractionated PHNB neither between PHNB and PPNB is visible in the relaxation behavior. The same is true for the comparison of the 1% PHNB(fractionated) and 0.5% PHNB(fractionated) solutions, corroborating that all concentrations are well below the overlap concentration c^*. The effective diffusion constant extracted from the NSE data as function of Q is shown in Fig. 2. The $D_{\rm eff}$ data show a slight step of about 30% around $Q = 0.12\text{Å}^{-1}$. The extrapolated limiting value $D_{\rm eff}(Q = 0) \simeq 10 \cdots 12 \times 10^{-7}\text{cm}^2/\text{s}$ is a factor of $2 \cdots 3$ larger than anticipated for centre-of-mass diffusion from the unperturbed chain dimensions in accordance with dynamical light scattering (DLS) that yielded $D_{\rm DLS} = 2 \cdots 3 \times 10^{-7}\text{cm}^2/\text{s}$. In contrast PI exhibits a linear increase of $1/(\tau(Q)Q^2)$ as predicted by the standard Zimm model.

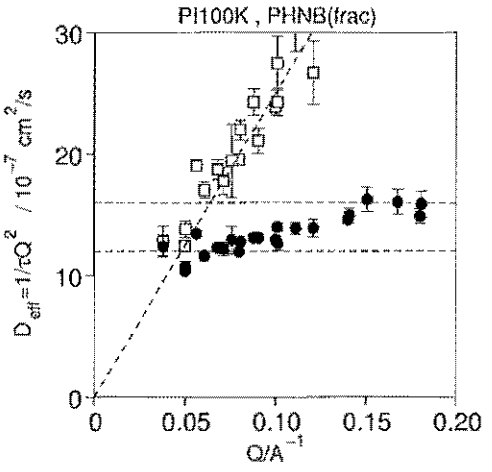

FIG. 2. Effective diffusion coefficients for fractionated PHNB (solid squares) and PPNB (solid circles) and for PI[100kg/mol](open squares). The dashed lines are guides to the eye only.

The lines in the upper part of Fig. 1 correspond to the computation of $S(Q,t)/S(Q)$ for PI with 20kg/mol by explicit summation of the Zimm model. In contrast the data from PHNB and PPNB solutions exhibit a significantly retarded relaxation compared to the reference solutions. The observed relaxation is still faster by a factor 2-3 than the expected centre-of-mass diffusion. If we consider the polynorbornenes as rigid random coils besides the centre-of-mass diffusion there should be an additional contribution to the relaxation due to rotational diffusion. Within the Zimm model the rotational diffusion is described by the first chain mode ($p = 1$). The corresponding scattering function can be computed by summation of the mode entribution from the Zimm model [4] but keeping only the first term of summation over modes (p). However, with the given coil dimensions it turns out that a few more modes up to a cut-off $p_{\rm max}$ are needed to yield a very good representation of the PHNB and PPNB data as is illustrated by the solid lines in the lower part of Fig. 1 for the high M fraction of PHNB with $p_{\rm max} = 11$ ($R_e = 450\text{Å}$).

The maximum mode number allows a straight forward determination of the size of the moving regions in the norbornene coils. Chain statistics yields $R_e = N^\nu l_{\rm eff}$ if N segments of effective length $l_{\rm eff}$ are assumed. Mapped onto the linear chain coordinate n the limiting mode $p_{\rm max}$ leads to displacements $X_{p_{\rm max}}(n) \propto \cos(\pi p_{\rm max} n/N)$, i.e. the typical extension in terms of segments is $n = N/p_{\rm max}$ which leads to an end-to-end distance of the coherently moving subcoil $r_e = n^\nu l_{\rm eff}$ i.e. $r_e = R_e p^{-\nu}$. Inserting typical numbers ($R_e = 450\text{Å}$) $\times\ 11^{-0.6} = 107\text{Å}$ within which the subcoils are virtually rigid.

The results of the NSE experiments strongly support the hypothesis that the polynorbornenes form nearly frozen coils in solution. The power law type scattering intensity $S(Q, t = 0) \propto Q^{-1/(\nu \simeq 0.6)}$ indicates that during or after synthesis the polymer is able to reach the equilibrium conformation of a flexible chain in a good solvent.

ACKNOWLEDGMENTS

We thank D.Y. Yoon for drawing our attention to the peculiar properties of polynorbornenes which lead to the presented experiment.

[1] C. Janiak and P. Lassahn, Macromol. Rapid Commun. **22**, 479 (2001).

[2] S. Krugel, F. Raubacher, and J. Wendorff, Macromol. Chem. Phys. **199**, 757 (1998).

[3] P. D. Gennes, *Scaling concepts in polymer physics* (Cornell University Press, Ithaca, N.Y, 1979).

[4] M. Doi and S. Edwards, *The Theory of Polymer Dynamics*, vol. 73 of *International Series of Monographs on Physics* (Oxford University Press, Oxford, 1994).

Structure of fetuin-A stabilized calciprotein particles determined by neutron scattering - implications for calcification biology and material science

A. Heiss[1], D. Schwahn[2], H. Endo[2], W. Jahnen-Dechent[1]

[1] *IZKF BioMAT, University Clinics, Pauwelsstrasse 30, D-52074 Aachen, Germany*

[2] *Institute for Solid State Research, Research Center Jülich, D-52425 Jülich, German*

Fetuin-A is a potent inhibitor of basic calcium phosphate (BCP) formation in the extracellular fluid of mammals. A lack of fetuin-A results in extensive calcifications in knockout mice and dialysis patients. The structural principle of this inhibition is the formation of fetuin-A - BCP particles. We applied small angle neutron scattering for the investigation of those colloidal particles.

The 50kDa serum protein fetuin-A/α_2-HS-glycoprotein (BF) is a systemic inhibitor of calcification in vivo. BF deficient mice develop severe soft tissue calcifications when backcrossed on the genetic DBA/2 background [1]. The first domain of BF exposes a highly acidic β-sheet to the aqueous solvent. This unique array of negative charges mediates the high affinity of this protein to calcium phosphates. The formation of colloidal calcium phosphate - BF composite, the so called calciprotein particles (CPP), represents the basic principle of calcium phosphate precipitation inhibition [2]. Small angle neutron scattering (SANS) and in particular the contrast variation technique was applied for a detailed structural investigation of the protein-mineral composites. A profound understanding of this inhibition mechanism, namely the mineralization in the presence of mineral binding proteins will help to understand calcification diseases and is indispensable for the development of a reliable assay to assess the risk of ectopic calcification in patients on dialysis. A comprehensive knowledge will also facilitate the development of a suitable therapy to prevent and to attenuate those uncontrolled soft tissue mineralizations.

A sufficiently large scattering contrast $\Delta\rho^2$ (being proportional to the scattered intensity according to $d\Sigma/d\Omega(Q) \propto \Delta\rho^2$) between colloidal particles and solvent is necessary for a successful scattering experiment. The symbol $\Delta\rho = (\rho - \rho_S)$ stands for the difference of the coherent scattering length densities ρ of particles such as minerals or proteins and the solvent ρ_S. In Fig.1 the relevant scattering length densities of the calcium phosphates, the protein and the solvent are depicted versus the D_2O content of the aqueous solvent. For the solvent and the protein fetuin a linear increase from -0.561 to 6.39 (solid blue line) and 1.46 to 3.41 (solid red line) in units of 10^{10} cm^{-2} is derived, respectively; ρ of water was calculated from tabulated numbers while ρ of the protein was experimentally determined. Proteins generally show a very similar scattering length density; at about 40% D_2O content the proteins are matched with water at the intersection of the two straight lines. Under these conditions proteins becomes invisible for neutrons as the scattering contrast becomes zero. The change of the protein's ρ with D_2O is ascribed by their ability to partially exchange H for D at the outer surface, i.e. at the hydrophilic part of the protein [3]. ρ for calcium phosphate is calculated from the chemical structure and mass density given in the literature, they slightly change with D_2O due to their hydrogen content.

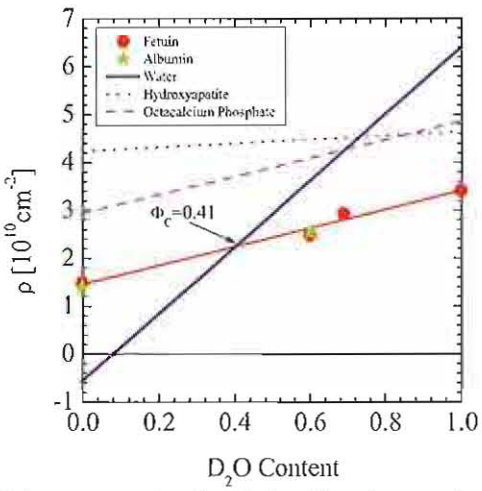

FIG.1. Coherent scattering length densities of water, the proteins fetuin and albumin, hydroxylapatide, and octacalcium phosphate with D_2O content.

In order to determine the structure of the mineral-fetuin composite the partial structure factors, namely the self-terms of the mineral (M), the protein (P), and water (W) S_{MM}, S_{PP}, S_{WW}, and the cross-term S_{MP} have to be determined separately for each Q from the scattered intensity according to

$$\mathbf{S}(Q) = [\Delta\rho^2]^{-1}\mathbf{I}(Q) \qquad (1)$$

The vectors $\mathbf{I}(Q) = \{d\Sigma/d\Omega(Q)_k\}$, $\mathbf{S}(Q) = \{S_{i,j}(Q)\}$ and the matrix $[\Delta\rho^2] = [\{\rho_i - \rho_{s,k}\}\{\rho_j - \rho_{s,k}\}]$ with $i,j = \{M,P\}$ and the number of contrasts k=1,2,..,n represent the measured intensities, the partial structure factors, and the scattering contrast, respectively. The dimension of matrix

and vectors are determined by the number of chosen contrasts n which for the present problem has to be at least three. We solved $S_{i,j}$ from an ($n = 6$) overdetermined set of equations which improves the reliability of the extracted partial scattering functions. The "water" scattering $S_{WW}(Q)$ represents the coherent superposition of S_{PP} and S_{MM} on basis of Babinet's principle when incompressibility is a good approximation. The scattering length density has to be calculated from known sample parameters

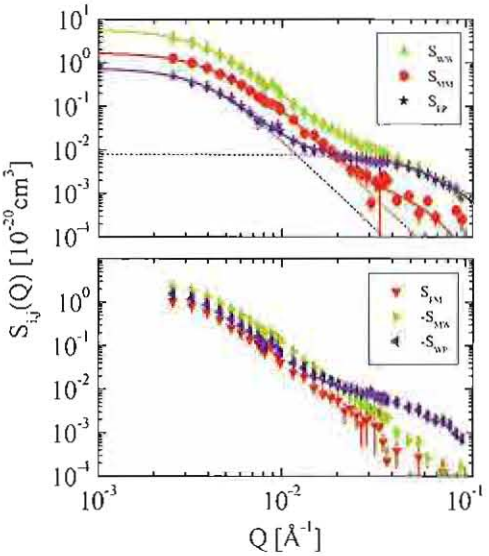

FIG. 2. Partial scattering functions. Top: The self terms allow an individual characterization of mineral and protein. Bottom: The mineral-fetuin cross term is positive, which means that the proteins are attached at the outer surface of the mineral.

The samples were prepared by mixing 2.5mg/ml fetuin, 10mM $CaCl_2$ and 6mM PO_4 in aqueous solutions of eight different D_2O/H_2O compositions between zero and 100% D_2O content. The analysis of mature / stable particles required a sample incubation for about 12 hours before starting the SANS experiment. The strongest scattering is found for the H_2O and D_2O solutions while the scattering becomes smallest at small Q for the 70% D_2O solution indicating near matching conditions for calcium phosphate but shows a relatively strong scattering resulting from the proteins at large Q. The partial scattering functions were derived from these scattering patterns on the basis of Eq. 1 as plotted in Fig.2. This analysis was a quite intricate procedure and e.g. revealed that the assumption of a hydroxyapatite polymorph leads to inconsistent results and that the octacalcium phosphate polymorph is present. A further difficulty was the variation of the coherent scattering length with D_2O content because of its large water content as well as the low volume fractions of the constituents (Fig.1).

The self terms and cross terms of $S_{i,j}$ are depicted in the upper and lower part of Fig.2, respectively. The mineral-water and protein-water cross terms S_{MW} and S_{WP} are negative while the S_{PM} protein-mineral is positive. This last term is very important for our interpretation [5]. Its positive sign gives a clear indication that mineral and fetuin proteins are locally separated. The cartoon of a model in Fig. 3 clarifies this result. The proteins are indicated as red dots the mineral is depicted as a green circle. Only a fraction of the proteins is attached at the outer surface of the mineral. For further determination of particles size and volume fraction we analyzed the self terms S_{MM} , S_{PP} , and S_{WW} of the mineral, protein, and water in terms of a form factor derived by Beaucage as indicated by the solid lines [4].

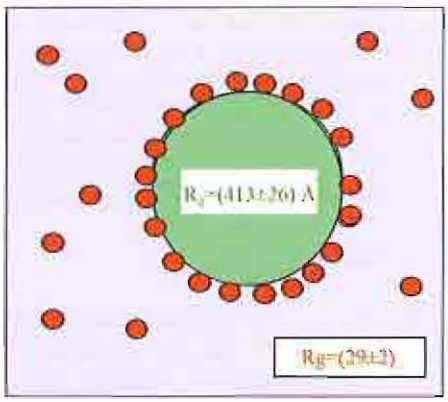

FIG. 3. Model of fetuin-mineral composite as received from contrast variation SANS experiments. The green sphere represents the mineral while the red dots the protein.

From these fits we derived the following parameters for the mineral, the attached fetuin and the free fetuin in solution. The volume fraction for the mineral is consistently determined very near 10^{-4} while for the proteins values are $7 \cdot 10^{-5}$ for the attached protein and $1.2 \cdot 10^{-3}$ for the free proteins which is slightly less than the total input value of $1.9 \cdot 10^{-3}$ (2.5mg/ml). This means that nearly 6% of the proteins are attached at the mineral surface occupying 40% volume fraction of the mineral-fetuin composite. The radius of gyration of the mineral and free protein are 413Å and 29Å, respectively.

The volume fraction of the attached proteins could be evaluated because mineral and the complex of attached proteins at a single mineral particle must have the same number density. Their volume divided by the monomer volume tells us that on the average 1830 proteins are attached at a single mineral. The mineral surface S as derived from Porod's constant divided by this number gives an average area of 36Åx36Å per particle.

We conclude that fetuin-A forms a densely packed monolayer at the outer surface resulting in a sealed surface. Hence the transformation and growth of the mineral core is drastically reduced as the ion diffusion is inhibited. Previous experiments evidenced that these particles are stable for at least 2 days.

References

[1] C. Schäfer et al, J. Clin. Invest., **112(3),** 357 (2003)
[2] A. Heiss et al, J. Biol. Chem **278,** 13333 (2003)
[3] B. Jacrot, *Rep. Prog. Phys.* **39,** 911 (1976)
[4] G. Beaucage, *J. Appl. Cryst.* **29,** 134 (1996)
[5] H. Endo, D. Schwahn, H. Cölfen, *J. Chem. Phys.* **120,** 9410 (2004)

Star-Like Micelles with Star-Like Interactions: A *tunable* Model System for *Ultra-Soft* Colloids

M. Laurati, J. Stellbrink, R. Lund, L. Willner and D. Richter
Institute Neutron Scattering

PEP-PEO block copolymer micelles are established as a *tunable* model system to investigate phase behaviour and interactions of star polymers (*ultra-soft* colloids). A star-like architecture is achieved by use of an extremely asymmetric block ratio (1:20). Micellar functionality f can be smoothly *tuned* by changing solvent composition (interfacial tension). Structure factors obtained by SANS can be quantitatively described in terms of a microscopic, effective potential developed for star polymers. The obtained experimental phase diagram reproduces to a high level of accuracy the predicted liquid/bcc-crystal transition for intermediate f. For high f the expected formation of fcc-crystal is preempted by gelation.

F&E-Nr: 23.30.0

Star polymers, *i.e.* f polymer chains tethered to a central microscopic core, can be regarded as *ultra-soft* colloids bridging the properties of linear polymer chains and hard sphere colloids. Unfortunately, the synthesis of star polymers requires considerable preparative efforts. Therefore it is of particular interest to substitute star polymers by an easy to establish model system. Ideally, this analogon should not only show the molecular architecture of star polymers, but also interact via the typical effective potential introduced by Likos et al. [1].

A few attempts to connect micellar systems to star polymers have been done, like PS-PI, PEO-PBO or hydrophobically modified PEO [2]. Similarities with star polymers have been pointed out, but a systematic attempt to quantitatively interpret experimental data of star-like micelles in terms of a microscopic, effective potential has never been performed.

In this Letter we show, that micelles formed by the amphiphilic block copolymer poly(ethylene-alt-propylene)-poly(ethylene oxide), PEP-PEO, are a *tunable* model system in the *star-like* regime that can be used to investigate phase behavior and interactions of star polymers (*ultra-soft* colloids). SANS measurements at core contrast allow a direct determination of the experimental structure factor, $S(Q)$, providing the basis for a quantitative comparison with theory. We can describe $S(Q)$ starting from the star potential with parameters directly given by experimental data. In addition, we can reproduce to a high level of accuracy the liquid-solid transition predicted in the theoretical phase diagram. This was done over a wide range of f and spanning the range from dilute to highly concentrated micellar solutions.

The asymmetric PEP-PEO block copolymer under study was synthesized by anionic polymerization [3]. The individual blocks have been selectively protonated/deuterated to achieve core contrast in our SANS experiments, *i.e.* match the scattering length density of the solvent to that of the PEO corona. This means that only the compact PEP core, which is completely unaffected by concentration, is "visible" in the SANS experiment. Single particle properties, *i.e.* functionality f, core radius R_c and overall micellar radius R_m have been determined as described in [3,4]. Here we will focus on the results obtained from concentrated solutions, where particle interactions are dominant.

SANS data were analyzed starting from the star potential, with the corona diameter σ being the only adjustable parameter.

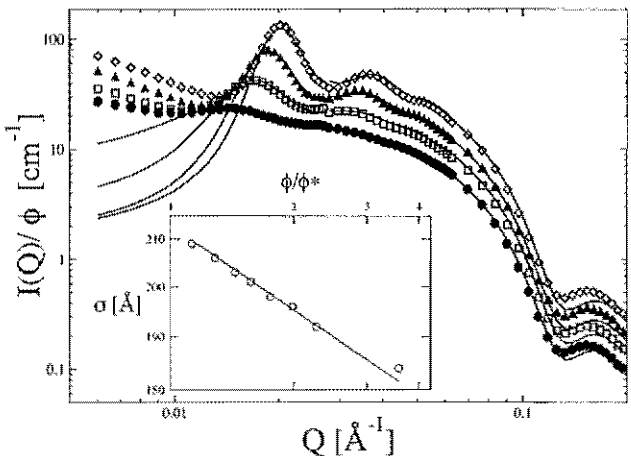

FIG. 1. Experimental intensities I(Q) for $f = 63$ at different ϕ in the fluid phase, $\phi < \phi^*$: (•) ϕ=0.017, ( ) ϕ=0.034, (▲) ϕ=0.051, (◦) ϕ=0.067 and fits (solid lines). For clarity I(Q) are divided by factors: (◦) 1, (▲) 1.5, ( ) 2, (•) 3. Insert: volume fraction dependence of σ for $f = 63$, showing the expected scaling behavior $\sigma \sim \phi^{-1/8}$ for $\phi > \phi^*$.

We directly fitted $(d\Sigma/d\Omega)(Q) = S(Q)P(Q)$ including the convolution to the experimental resolution function. We assumed a compact core model for the form factor $P(Q)$, fixing the parameters on the basis of f and R_c values obtained from the characterization of the micelles. The validity of this assumption can be rationalized from Fig. 1, where the minimum arising from the

solid core appears at $Q \approx 0.13\mathring{A}^{-1}$ independent of ϕ. The theoretical $S(Q)$ was calculated by applying the self-consistent Rogers-Young (RY) closure for the Ornstein-Zernike equation [1]. The excellent quality of the fits is shown in Fig. 1 for samples of different ϕ but same functionality $f = 63$. According to scaling theory for $\phi > \phi^*$ the stars are expected to shrink as $\propto \phi^{-1/8}$, and indeed, the fit values for $\sigma(\phi \geq \phi^*)$ show exactly this scaling behaviour as shown in the insert of Fig. 1. σ was then used to transform the given experimental number density N_s to the packing fraction $\eta = N_s\, \pi/6\, \sigma^3$.

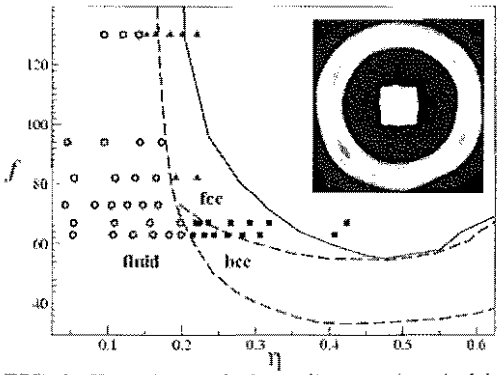

FIG. 2. Experimental phase diagram (symbols) of star-like micelles vs. theoretical phase diagram (lines) of star polymers. (○) liquid, ( ) bcc crystal and (▲) gels. Dashed line represent equilibrium phase diagram. The solid line is the RY-ideal MCT glass line. Insert: 2-dimensional SANS detector picture of $f = 63$, ϕ=0.16 evidencing Bragg reflections.

Calculating η this way for all f, we could finally compare experimental and theoretical phase diagrams, as shown in Fig. 2. The transition from the liquid to the crystalline state (body centered cubic, bcc) predicted by theory in the range of functionalities $60 < f < 70$ is perfectly reproduced in experiments for $f = 63$ and $f = 67$. Direct evidence for crystal formation comes from the presence of Bragg peaks in the 2-dimensional SANS pattern as shown in the insert of Fig. 2 for $f = 63$ and $\phi = 0.16$. Moreover crossing ϕ^* ($\eta = 0.21$) the first peak of $S(Q)$ assumes a value bigger than 2.8, which is the minimum value for freezing transition according to the *Hansen-Verlet* criterion [5]. The peak is further growing with increasing ϕ. Additionally for $\phi > \phi^*$ a third small peak is forming, and the position ratio between the three peaks is $1{:}\sqrt{2}{:}\sqrt{3}$, with an intensity at the second peak smaller than at the third (due to the smallest degeneracy), unambiguously identifying the crystal as a bcc structure.

With increasing η no evidence for the predicted transition to a fcc phase is found in our data for $f = 63$ and $f = 67$. However, we have to emphasize that for these f the difference in free energy between the two crystalline phases is only very small, $\approx kT$ [1].

With increasing f the experimentally observed liquid-solid transition is in nearly perfect agreement with the phase boundary predicted by theory, but instead of observing a crystalline fcc phase we observe gel-like structures for all $f \geq 73$. Location of the experimental gel line comes from a double evidence: First from tube inversion, which means that we tested the non-flowing behavior of the sample inverting sample holders in a bath at constant temperature. In addition, preliminary rheology experiments confirm a non-zero storage modulus. Second evidence for a gel comes from discontinuity in the first peak position and value observed in SANS measurements once we crossed ϕ^*. Structure factor peaks for $\phi > \phi^*$ are definitely smaller than 2.8, excluding formation of a crystal. The early onset of gelation at a packing fraction smaller than expected from theory, might explain also why we never observed fcc crystalline phases.

In conclusion, we have shown that star-like PEP-PEO micelles show the same interactions as star polymers, giving a significant experimental support to the picture of star polymers as *ultra-soft* colloids. We have been able to quantitatively describe micellar structure factors $S(Q)$ starting from a microscopic effective potential predicted for star polymers. The softness of the interaction potential between star-like micelles can be precisely *tuned* by adjusting the interfacial tension γ between PEP and the used solvent. In addition, we performed a detailed investigation of the phase diagram as a function of functionality f and concentration. In particular we experimentally determined the critical packing fraction for liquid-bcc crystal transition, finding excellent agreement with theory. The simple synthesis of PEP-PEO block copolymers compared to star polymers in combination with the shown analogy in terms of effective interactions make these micelles an excellent *tunable* model system for *ultra-soft* colloids.

This work was supported by the Deutsche Forschungsgemeinschaft in the framework of the Transregio-SFB TR6.

[1] C. N. Likos, M. Watzlawek , H. Löwen , B. Abbas , O. Jucknischke, J. Allgaier, and D. Richter Phys. Rev. Letters **80** 4450, (1998); M. Watzlawek, C.N. Likos, and H. Löwen, Phys. Rev. Letters **82**, 5289 (1999).

[2] T. P. Lodge *et. al*, Phys. Rev. Letters **92** 145501, (2004); I. Hamley *et. al*, Colloid Polym. Sci. **276**, 446 (1998); E. Beaudoin *et. al*, Macromolecules **35**, 7436 (2002).

[3] R. Lund, L. Willner, J. Stellbrink, A. Radulescu and D. Richter, Macromolecules, **37**, 9984 (2004).

[4] J. Stellbrink, G. Rother, M. Laurati, R. Lund, L. Willner, and D. Richter, J. Phys.: Condens. Matter **16**, S3821-S3834 (2004).

[5] J. P. Hansen and L. Verlet, Phys. Rev. **184**, 151 (1969).

Logarithmic Chain Exchange Kinetics of Polymeric Micelles

R. Lund, L. Willner, and D. Richter
Institute for Neutron Scattering

The equilibrium chain exchange kinetics in polymeric micelles has been studied by time resolved SANS on three structurally different model systems. The results show that the relaxation functions are commonly described by an ultra slow logarithmic time decay which contradicts the single exponential predicted from theory. The logarithmic dependence implies a broad distribution of expulsion rates which most likely stems from a heterogeneous release of core chains caused by topological interactions between polymer segments.

The equilibrium kinetics of polymeric micelles is not well understood. This is predominantly due to the fact that the exchange of polymeric chains between micelles cannot easily be accessed experimentally. In particular fluorescence quenching and temperature jump experiments have been used, but the drawback of these techniques is that a significant perturbation of the system is generally demanded and consequently, access to the true equilibrium behavior is not given.

In our group we have developed a time-resolved SANS technique that does not require strong physical or chemical perturbations but is rather restricted to a simple hydrogen/deuterium isotope substitution [1]. The method is based upon mixing equal amounts of deuterated and protonated micelles prepared in an isotopic solvent mixture with a scattering length density that exactly matches the average of the two constituting block copolymers. The decrease of the scattered neutron intensity due to chain exchange is then monitored in real time by SANS.

Applying this technique a comprehensive study of the exchange kinetics at equilibrium has been performed using three structurally different model systems. The first system consists of a very asymmetric poly(ethylene-*alt*-propylene)-poly(ethylene oxide) block copolymer (PEP1-PEO20, numbers denote nominal molecular weight in Kg/mol) in water/N,N-dimethylformamide (DMF) mixtures as selective solvent for PEO. The micelles formed exhibit highly extended starlike structures with strong excluded volume effects. By variation of the DMF content the interfacial tension between PEP and solvent can be effectively tuned [2] and was found to be the key control parameter for aggregation and exchange rate in this system. Thus, by the addition of 25 and 30 mol% DMF the time resolved SANS technique could be applied successfully.

The second model system was prepared from a symmetric polystyrene-polybutadiene block copolymer (PS10-PB10) in n-alkanes ($C_{10} - C_{16}$) as selective solvent for PB. A detailed SANS analysis on a partially deuterated block copolymer (h-PS10-d-PB10) revealed compact spherical micelles with weak excluded volume effects, strongly swollen cores and constant density profiles for core and corona. The kinetics in the PS10-PB10/n-alkane system can be tuned by varying the carbon chain length of the solvent. While in decane and dodecane the rate was too fast to be followed by time resolved SANS, measurements could be performed in tetradecane and hexadecane.

The third model system that has been investigated consists of the same PS10-PB10 block copolymer but DMF was used as selective solvent for PS. This combination lead to micelles with inverse morphology, i.e. PB constitutes the core and PS the corona of the micelles. The structure as obtained by SANS/contrast variation experiments is similar to the PS-PB/n-alkane micelles but without solvent in the core. The exchange rate of this system fits ideally to the applied time resolved SANS technique. A sketch of the structure of the three micellar model systems is presented in Figure 1. The results of the kinetic investigation show that the relaxation function for all three systems is commonly characterized by an ultra slow logarithmic decay. This is demonstrated in Figure 2 where the data display a linear behavior in a lin-log representation. The solid lines are fits with a logarithmic time dependence according to:

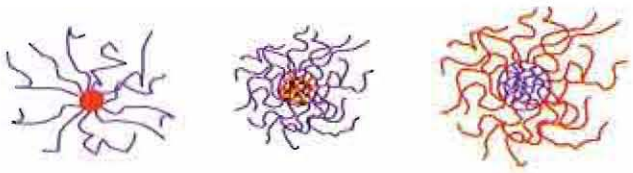

FIG. 1: Sketch of the three structurally different types of micelles used for the kinetic study: PEP1-PEO20 in water/DMF - starlike, PS10-PB10 in n-alkanes - compact with swollen core, PS10-PB10/DMF - compact with inverse morphology and fully segregated core.

$$[I(t)/I_\infty - 1]^{1/2} \sim \ln t, \qquad (1)$$

where $I(t)/I_\infty$ is the integral neutron intensity at time t normalized to the intensity at infinite time, where a completely randomized mixture of d and h block copolymer chains is obtained. This can be achieved by premixing the labelled chains prior to the micelle preparation.

The data clearly differ from the single exponential predicted from theory as shown by the dotted line in Figure 2. According to the theory of Halperin and Alexander [3] the kinetics is characterized by an insertion/expulsion mechanism of single unimers which have to diffuse over a simple potential barrier. To explain the logarithmic

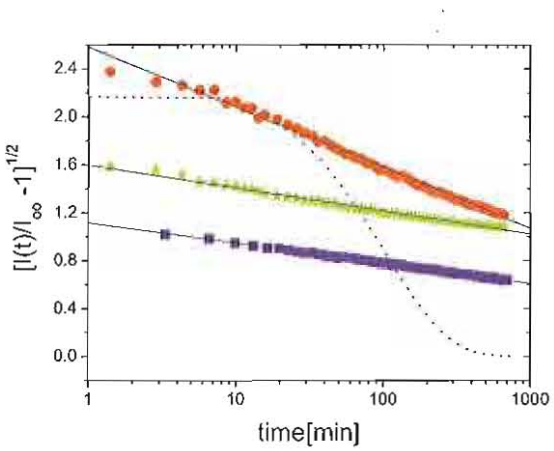

FIG. 2: Relaxation curves of three different micellar systems in a lin-log representation: PS10-PB10/DMF, PS10-PB10/hexadecane and PEP1-PEO20/water/DMF from top to bottom. The dotted line displays a fit of a single exponential.

time dependence of the relaxation function we are forced to assume an extremely broad distribution of expulsion rates. Since the corresponding block copolymers are virtually monodisperse, the distribution is an inherent property of the micelles. The origin of this broad distribution is not clear but at present the only explanation is that it stems from a heterogeneous release of chains from the core. We may speculate that this slow release of chains is caused by topological interactions between the polymer segments occupying the relatively small micellar core. It is noteworthy to mention that anomalous slow relaxations which can be accurately described by a logarithmic law have already been found in a variety of complex systems , e.g. in the relaxation in glassy systems, in the dynamics of colloids at the gel point, in friction experiments, etc.. Palmer et al. [4] have suggested a class of models based on *hierarchically constraint dynamics* to account for the anomalous slow relaxation in strongly interacting glassy materials. They argued that the path to equilibrium involves a series of correlated activation steps with increasing characteristic time. Brey and Prados [5] have derived a general kind of hierarchical model appropriate to describe the logarithmic relaxation in many complex systems. They predicted that the slope of the relaxation curves depends linearly on temperature.

Figure 3 displays kinetic measurements at different temperatures in a lin-log representation and the corresponding individual slopes of these curves versus T. Although the dependence is rather weak, within experimental error a linear behavior is obtained further justifying the existence of some kind of hierarchically constrained dynamics in the relaxation kinetics of this system. Since the ultra slow logarithmic relaxation was found independently for three different micellar model systems, this behavior can be regarded as a general phenomenon for polymeric micelles. However, the microscopic origin has yet to be identified.

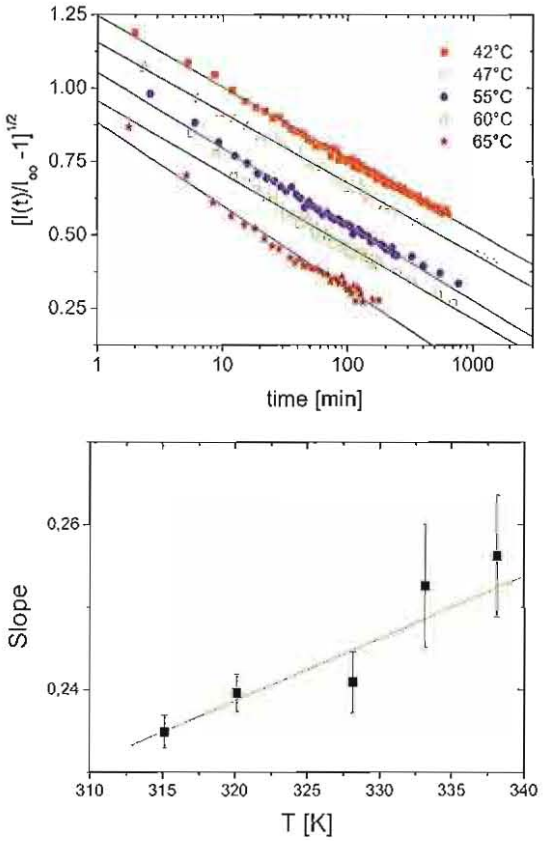

FIG. 3: Top: Relaxation curves of the PEP1-PEO20/water/DMF system at different temperatures. Bottom: Fitted slopes versus temperature.

[1] L. Willner, A. Poppe, J. Allgaier, M. Monkenbusch and D. Richter *Europhys. Lett. 55(5)*, **2001**, 667.
[2] R. Lund, L. Willner, J. Stellbrink, A. Radulescu and D. Richter, *Macromolecules, 37*, **2004**, 9984.
[3] A. Halperin and S. Alexander *Macromolecules 22*, **1989**, 2403.
[4] R. G. Palmer, D. L. Stein, E. Abrahams and P. W. Anderson *Phys. Rev. Lett. 53* **1984**, 958.
[5] J. J. Brey and A. Prados *Phys. Rev. E 63*, **2001**, 021108.

The influence of constraint release on the reptation process: NSE study and comparison to simulation

M. Zamponi, A. Wischnewski, M. Monkenbusch, L. Willner, and D. Richter
Institut für Festkörperforschung, Forschungszentrum Jülich, D-52425 Jülich, Germany

A. Likhtman
IRC, University of Leeds, Leeds LS2 9JT, Great Britain

G. Kali and B. Farago
Institut Laue-Langevin, Avenue des Martyrs, F-38042 Grenoble Cedex 9, France

By investigating the dynamics of binary polymer blends of few long labeled chains in successively shorter matrix chains by neutron spin echo spectroscopy (NSE), the effect of constraint release on the reptation process has been observed for the first time directly on a microscopic scale. Since constraint release is a many chain problem, an analytical description in the framework of the simple tube concept is not possible. Whereas a new simulation based on the slip-link model shows perfect agreement with the NSE data over the full range of matrix molecular weights.

The dynamics of linear polymer chains in the melt depends strongly on the chain length: For short, unentangled chains (and for any length at short times) the dynamics is determined by a balance of viscous and entropic forces which can be described by the Rouse model [1]. Here a given chain interacts with a heat bath, representing the neighbouring chains. For long chains topological chain-chain interactions in terms of entanglements become important and are even dominating the dynamical behaviour. In the famous reptation model these constraints are described by a virtual tube which localizes a given chain and limits its motion to an 1-dimensional Rouse motion inside the tube and a slow creep motion out of the tube (reptation) [2].
Neutron spin echo (NSE) spectroscopy is a powerful tool to explore the different dynamic regimes in polymer melts on a microscopic scale. While NSE experiments support the tube concept of topological confinement in long chain polymer systems [3], a close comparison of linear rheology data with predictions of the tube model indicates the existence of additional degrees of freedom that release the topological confinement [4]. Candidates are fluctuating chain ends escaping the tube confinement starting from both ends (contour length fluctuations, CLF) and the relaxation of the tube itself (constraint release, CR).
As was reported last year, the effect of CLF can be directly shown by NSE spectroscopy on center labeled chains, where the relaxing chain ends are masked out. While CLF is an effect of the confined chain itself, CR stems from the movement of the chains building the tube, which of course undergo the same dynamical processes as the confined chain. This leads to an additional relaxation process, which becomes more pronounced the shorter the matrix chains are. One expects a gradual loss of confinement with decreasing matrix length down to unconfined Rouse motion when the matrix chains are too short to build entanglements.
Up to now, due to the complexity of this many chain problem, there exists no quantitative description of this effect on a microscopic level in the framework of the tube concept. Whereas a new simulation model based on the slip-links model allows to simulate the dynamics of polymer melts under consideration of CLF and CR [5].

The different dynamic processes are observed as the relaxation of the coherent single chain dynamic structure factor $S(q,t)$ which is directly obtained by neutron spin echo spectroscopy on a sample which contains only few protonated chains in a deuterated matrix. To separate the effect of CR one has to consider a chain which is long enough, so that end effects like CLF do not play a role. Therefore 5% of labeled (protonated) polyethylene (PE) chains with $M_w = 36\,\mathrm{kg/mol}$ have been mixed into successively shorter matrix chains with a molecular weight ranging from 36 kg/mol to 1 kg/mol. With this low concentration of long chains it is ensured that the tube is built by the short chains only, so that the CR effect can be controlled by changing the matrix chain length.
The dynamic structure factor of these binary blends has been measured at the NSE spectrometer IN15, ILL, at a temperature of 509 K, covering a momentum transfer range of $0.3\,\mathrm{nm}^{-1} \leq q \leq 1.15\,\mathrm{nm}^{-1}$.
As expected, for the long chain in a matrix of the same molecular weight a tube confinement as for infinite long chains is observed. This is signified by the transition of the dynamic structure factor into a plateau regime. If one presents the structure factor in a Rouse scaling plot as shown in fig.1 the topological constraints lead to a splitting for different q-values. With decreasing matrix length an increasing loss of confinement becomes visible as the stronger decay of the dynamic structure factor, pointing to the onset of constraint release. Eventually for a matrix length of only one entanglement length (about 2 kg/mol) the long labeled chain displays free Rouse motion since the matrix chains are too short to confine the long chain into a tube. This is signified by the collapse of the dynamic structure factor for different q into one master curve following the Rouse scaling

(see fig.1). Hence, for the same long labeled chain one observes pure reptational behaviour in long matrix chains and pure free Rouse motion in short matrix chains.

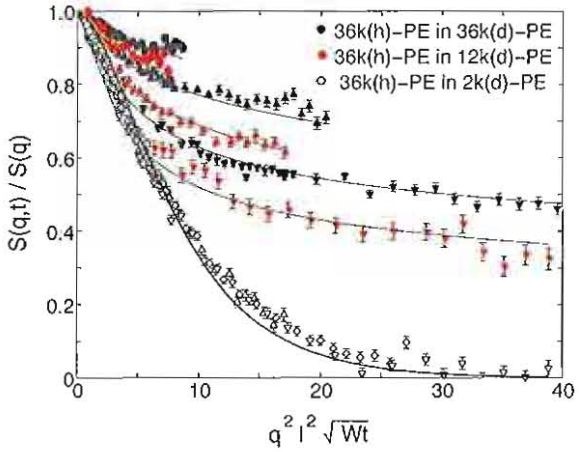

FIG. 1: Dynamic structure factor of a long labeled chain (M_w = 36 kg/mol) in different shorter matrix chains (M_w = 36, 12, 2kg/mol as indicated in the plot) in a Rouse scaling representation: if there is no topological confinement all curves for different q collapse onto one mastercurve. If topological confinement is evident, the dynamic structure factor does not fulfill the Rouse q-scaling and splits for different q-values. Lines are just a guide for the eyes.

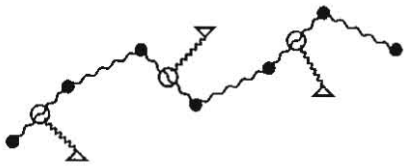

FIG. 2: Schematic view of the simulation model: the chain (bead and springs) is confined by slip-links (circles), which are connected via springs to fixed anchor points (triangles), but can slide with a friction along the chain.

This transition is well described in a new simulation based on the slip-links model. There the tube constraints are modeled by slip-links which move along a coarse grained chain and are fixed by springs attached to anchoring points (fig.2). If a slip-link reaches the end of a chain it disappears which simulates the effect of CLF. For describing CR an ensemble of chains is simulated and 2 slip-links on 2 different chains are connected, so that if one slip-link disappears the corresponding second slip-link is also removed. In this way both relaxation processes are introduced without any additional parameter. The unknown necessary parameters are number and strength of the slip-links and their friction along the chain. They are determined by simulating one homopolymer melt and comparing the result to NSE data. With the same parameter set it is possible to describe all the experimental data sets for different molecular weights and, more important, also the binary blends which display the effect of constraint release. As can be seen in fig.3 a very good agreement of simulation and NSE data for the different blends over the whole q-range is achieved.

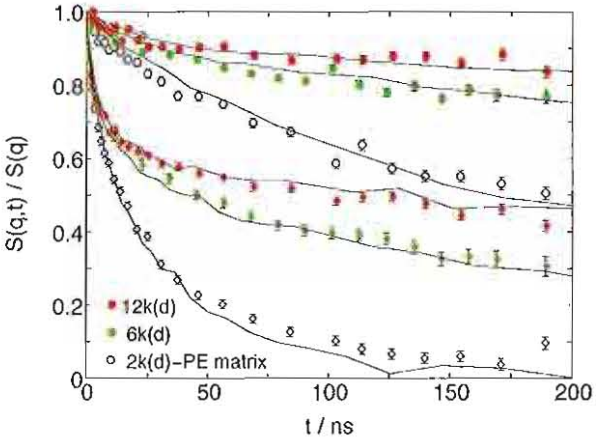

FIG. 3: Dynamic structure factor from a M_w = 36 kg/mol PE-chain in successive shorter matrix chains (M_w = 12, 6, 2kg/mol as indicated in the plot) for 2 different scattering wavevectors: q=0.5 nm^{-1} and q=0.96 nm^{-1}. Lines show the simulation results.

Summary: The effect of constraint release on the topological confinement of long polymer chains has been systematically investigated by neutron spin echo spectroscopy. The dynamic structure factor of a long chain in successive shorter matrix chains shows a clear transistion from pure reptation dynamics in long matrix chains to pure Rouse motion in short matrix chains. Therefore the effect of constraint release has been observed for the first time direct on a molecular level in space and time. The simulation model gives a consistent description of the experimental data over the whole range of matrix molecular weights. The easy selfconsistent implementation of constraint release as a destruction of entanglements, built of only 2 slip-links, gives a qualitative and quantitative agreement with the measured dynamic structure factor.

[1] P.E. Rouse, J. Chem. Phys. **21**, 1272 (1953).
[2] P. DeGennes, Journal de Physique (France) **42**, 735 (1981).
[3] P. Schleger, B. Farago, C. Lartigue, A. Kollmar, and D. Richter, Physical Review Letters **81**, 124 (1998).
[4] M. Doi and S. Edwards, *The Theory of Polymer Dynamics* (Oxford University Press, Oxford, 1986).
[5] A. Likhtman, to be published.

Electrolyte Friction in Dispersions of Charged Colloids and Micelles

M.G. McPhie[1] and G. Nägele[1]

[1]*Forschungszentrum Jülich GmbH, IFF - Weiche Materie, D-52428 Jülich, Germany*

We have developed a general mode coupling method which is capable of describing electrokinetic phenomena in dispersions of charged colloidal spheres like globular proteins or micelles (i.e. macroions), ranging from colloidal electrolyte friction to electrophoresis and linear viscoelasticity. Explicit applications of this method have been worked out for colloidal electrolyte friction with the excluded volume effects of the small electrolyte ions included, and for single-sphere electrophoresis. We show that finite size effects become relevant only for macroion-electrolyte ion size ratios typically less than five. Another important conclusion is that the experimentally observed minimum in the self-diffusion coefficient of macroions is mainly due to the hydrodynamic interactions between macroion and electrolyte ions.

The dynamics of charge-stabilized colloidal particles of globular shape (so-called macroions) dispersed in a solution of weakly charged counter- and coions forming a neutralizing and screening microion atmosphere, has attracted considerable interest, both from the experimental and theoretical point of view. The reason for the strong interest in these systems is that a large fraction of colloidal systems of biological and technological relevance are, in fact, charge-stabilized dispersions with water as the solvent. A theoretical description of the dynamics in these systems is demanding, since the transport properties are determined by a delicate interplay of electrostatic, steric and solvent-mediated hydrodynamic forces which act among all ionic species [1].

Existing theoretical work on the dynamics of charge-stabilized colloids is mostly based on an effective macrofluid model of dressed macroions which interact by an effective pair potential of spherical symmetry, the latter obtained from integrating out the microionic degrees of freedom [1]. A major drawback of the dressed macroion model is that it does not account for the kinetic influence of the microion atmosphere which can not instantaneously respond to the motion of the macroion. The retarded microion dynamics is of importance for electrokinetic phenomena like electrophoresis. An additional example is given by the electrolyte friction felt by a single charged colloidal particle diffusing through an electrolyte solution.

To understand these electrokinetic phenomena on a theoretical basis requires a more fundamental level of description where macroions and microions are treated on an equal footing as uniformly charged hard spheres imbedded in a structureless solvent of viscosity η_0, interacting by non-screened Coulombic forces. A sketch of this so-called Primitive Model of charged hard spheres is shown in Fig. 1. On the basis of the Primitive Model and the generalized Smoluchowski diffusion equation, we have developed a many-component mode coupling scheme (MCS) for quantifying the electrolyte friction effect on the tracer diffusion of a macroion. This scheme accounts for the hydrodynamic interactions (HI) between all ionic species, and for excluded volume effects arising from the small electrolyte ions [2]. We have applied this scheme to dilute aqueous dispersions of polystyrene spheres, and to

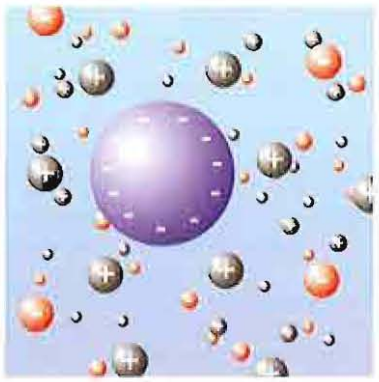

FIG. 1: Sketch of the Primitive Model of charged hard spheres.

nano-sized charged micelles. Its predictions for the long-time tracer diffusion coefficient, D_T^L, of a macroion of radius a_T, where

$$D_T^L = \frac{k_B T}{6\pi\eta_0 a_T + \Delta\zeta_T}$$

compare well with experiment.

A comparison between theoretical and experimental results for aqueous dispersions of large polystyrene spheres is displayed in Fig. 2, and for charged smaller micelles in Fig. 4. The effect of the separate microion dynamics is contained in the excess friction contribution $\Delta\zeta_T$. An important conclusion obtained in [2] is that the minimum in the macroion diffusion coefficient is mainly due to the hydrodynamic interactions between a macroion and the surrounding electrolyte ions. This minimum is essentially unaffected by the HI between the electrolyte ions themselves, and cannot be explained by the presence of direct electro-steric interactions alone, as it has been attempted in earlier statistical mechanical approaches where hydrodynamic interactions are totally ignored. Without HI, there is a charge-independent contribution to $\Delta\zeta_T$. This additional friction contribution, in turn, leads to a D_T^L which is a monotonically decreasing function of κ, in conflict with experimental observation. The charge-independent term arises from the excluded volume interaction between the colloid sphere and the electrolyte ions. With

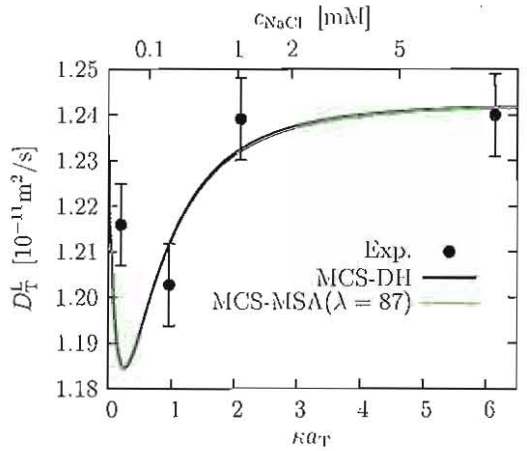

FIG. 2: Long-time macroion tracer diffusion coefficient versus reduced screening parameter κa_T and NaCl concentration, for polystyrene spheres in NaCl solution. Black solid curve: Mode coupling scheme (MCS) result for point-like microions (in Debye-Hückel limit); green curve: MCS result for size ratio $\lambda = 87$; filled circles: dynamic light scattering data from [3].

HI, the excluded volume contribution to $\Delta\zeta_T$ becomes very small, since the electrolyte ions are advected by the hydrodynamic flow field created by the moving colloidal sphere.

The results shown in Fig. 2 are for essentially point-like electrolyte ions since the polystyrene spheres are very large as compared to the microions (i.e. $\lambda = 87$). From Fig. 2 we note that the calculated diffusion coefficients are practically the same for $\lambda = 87$ (green curve) and for truly point-like electrolyte ions where $\lambda = \infty$ (black curve). In dispersions of rather small macroions like charged globular proteins and charged micelles, which are only a few nanometers in size, the finite size of the microions can play a role. We have determined the influence of the electrolyte ion's excluded volumes using known analytical results in mean spherical approximation for the partial static pair correlation functions of differently sized charged spheres. Fig. 3 includes MCS results for

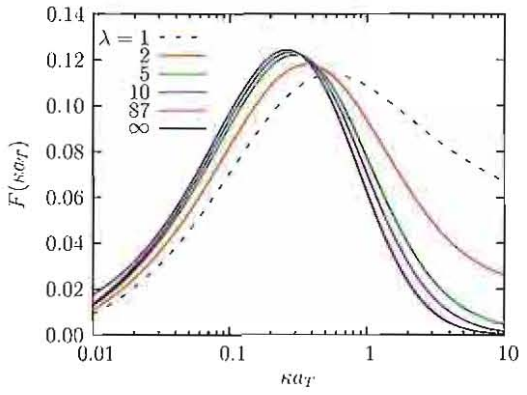

FIG. 3: MCS results for the electrical part of the reduced colloidal friction coefficient $F(\kappa a_T)$ for various macroion-microion size ratios λ as indicated. From [2].

the reduced electrostatic part, $F(\kappa a_T)$, of the electrolyte friction coefficient $\Delta\zeta_T$, with a macroion-electrolyte ion size ratio $\lambda = a_T/a_{el}$ ranging from the colloidal limit $\lambda \to \infty$ down to the pure electrolyte limit $\lambda \to 1$. As seen, the finite size of the electrolyte ions is important only for $\lambda \leq 5$, and can thus be ignored in systems with larger colloids. One can take advantage of this simplifying result in future theoretical and computer simulation studies of colloidal electrokinetic phenomena.

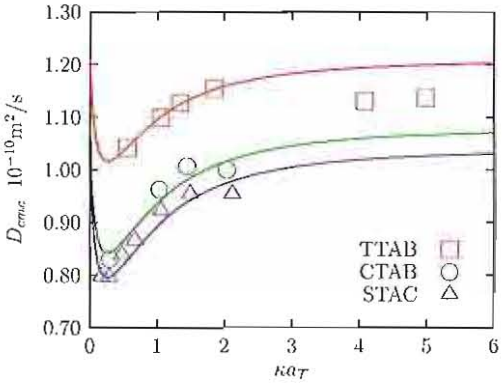

FIG. 4: Long-time tracer diffusion coefficient of aqueous solutions of globular micelles at the critical micellar concentration. The open symbols are experimental data for three different micellar systems. The lines are the mode coupling results. For details see [2].

In Fig. 4, we compare our MCS predictions, calculated using the mean spherical pair distribution functions as static input, against experimental results for the tracer diffusion coefficient of small and moderately charged micelles in aqueous solutions. The experimental data for these systems are well described by our theory. The deviations observed in system TTAB at large κa_T can be explained by a micellar shape transformation occurring at large salinity.

In extensions of the present work on colloidal electrolyte friction, we have additionally studied colloidal electrophoresis and conductivity and, in a joint theoretical-experimental paper, collective diffusion in dispersions of nano-sized charged proteins [4].

[1] G. Nägele, Lecture Notes **14** on *The Physics of Colloidal Soft Matter*, Institute of Fundamental Technological Research (Polish Academy of Sciences Publication, Warsaw, 2004).

[2] M.G. McPhie and G. Nägele, J. Phys.: Condens. Matter **16**, S4021 (2004).

[3] G.A Schumacher and T.G.M van de Ven, Faraday Discuss. Chem. Soc. **83**, 75 (1987).

[4] J. Gapinski, A. Wilk, A. Patkowski, W. Häussler, A.J. Banchio, R. Pecora and G. Nägele, submitted to The Journal of Chemical Physics (2004).

Phase behaviour of charged colloidal sphere dispersions with added polymer chains

[†]Remco Tuinier, [‡]Andrea Fortini, [‡]Marjolein Dijkstra,
[†] *Forschungszentrum Jülich, Institut für Festkörperforschung, 52425 Jülich, Teilinstitut Theorie II; Teilinstitut Weiche Materie, Germany.*
[‡] *Soft Condensed Matter, Debye Institute, Utrecht University, Princetonplein 5, 3584 CC Utrecht, The Netherlands*

We studied the stability of mixtures of highly screened repulsive charged spheres and non-adsorbing polymer chains in a common solvent using free volume theory and in Monte Carlo computer simulations. Both methods show very similar trends. We find that the screened-Coulomb repulsion counteracts the effect of the *effective* polymer-mediated attraction, showing the miscibility of dispersions containing charged colloids and neutral non-adsorbing polymers increases upon increasing the range of the screened-Coulomb repulsion, or upon lowering the salt concentration.

Adding non-adsorbing polymers to colloidal dispersions allows modifying the range and strength of attraction of the effective interactions between the colloidal particles. Adjusting the range of the attraction enables manipulating the topology of the phase diagram of a colloid-polymer mixture [1, 2]. Both the nature of the demixed phases as well as the colloid and polymer concentrations at which demixing takes place depend on the range of attraction [2]. Industrially, it is relevant to understand the phase behaviour of colloid-polymer mixtures because colloidal particles and polymer chains are often jointly present in various products, such as food dispersions [3]. Theoretically, the focus has been mainly on hard spheres dispersed in polymer solutions. In practice, many stable dispersions containing spherical colloids consist of particles that are not 'pseudo-hard' but which can be characterised by a pair potential containing an additional soft repulsive tail, such as charged colloids in an aqueous salt solution [4]. The effective pair interaction between charged colloids consists of a hard-core repulsion due to the finite size of the colloids and a screened-Coulomb (Yukawa) repulsion with the screening length given by the Debye length κ^{-1} of the solvent [4]. Adjusting the salt concentration may influence the stability of a dispersion of charged colloids mixed with a neutral depletion agent in a common aqueous salt solution. The trend found in experimental studies on mixtures of charged 'colloids' plus neutral polymers is that the miscibility is increased upon decreasing the salt concentration, i.e., increasing the range of the screened-Coulomb repulsion [3, 5, 6].

In the light of these findings we studied mixtures of colloids with a screened-Coulomb repulsion mixed with neutral polymer chains theoretically and investigated the effect of a screened-Coulomb interaction on the total effective colloid-colloid interaction and on the resulting gas-liquid and fluid-solid phase transitions in a charged colloid dispersion with added non-adsorbing polymers. From free volume theory [1] of colloids mixed with ideal polymer chains of polymer-to-colloid size ratio q, it follows that the the normalised thermodynamic potential $f \equiv \beta F v_c/V$ can be written as the sum of two terms:

$$f(N_c, V, \phi_p) = f_c(N_c, V) - \alpha \phi_p^r q^{-3} \qquad (1)$$

The first term in equation (1) is the normalised Helmholtz free energy $f(N_c, V, \phi_p^r = 0) \equiv f_c(N_c, V)$ of a 'pure colloid' fluid at a given colloid volume fraction η_c, while the second can be interpreted as a perturbation due to the presence of polymer chains with relative concentration ϕ_p^r, evaluated in a hypothetical reservoir. The free volume fraction available for the chains in the system is given by α, which is calculated from scaled particle theory (see [1, 7]). The actual polymer concentration ϕ_p follows from $\phi_p = \alpha \phi_p^r$. A concentration $\phi_p = 1$ defines the overlap concentration. Since we assume that the collection of charged spheres behave similarly as a collection of pure hard spheres plus a small perturbation, we may use the Carnahan-Starling (CS) expression [8] for the excess Helmholtz free energy to describe the thermodynamic properties of the fluid of charged spheres:

$$f_c^{\text{fluid}} = \eta_c \ln \eta_e + \frac{4\eta_e^2 - 3\eta_e^3}{m(1-\eta_e)^2}, \qquad (2)$$

where $\eta_c \equiv \pi \sigma_c^3 \rho_c/6$ with ρ_c the colloid number density and σ_c the effective diameter. The hard sphere volume fraction η_c in the classical CS expression is replaced by the effective volume fraction η_e, defined as $\eta_e = m\eta_c$, where m follows from the Barker-Henderson relation [9]:

$$(m)^{\frac{1}{3}} = 1 + \int_1^\infty (1 - \exp[-\beta U_{cc}(r/\sigma_c)])\, d(r/\sigma_c). \qquad (3)$$

The equation of state of the face-centred-cubic (fcc) crystal phase of pure hard spheres is described accurately by the expression proposed by Hall [10]. Likewise, the excess free energy for the fcc crystal phase of the charged spheres reads

$$f_c^{\text{crystal}} = \eta_c \left(2.13 + 3 \ln \left[\frac{\eta_e}{1 - \eta_e/\eta_{cp}} \right] \right), \qquad (4)$$

containing the volume fraction at close packing $\eta_{cp} = \pi\sqrt{2}/6$. These equations (2) and (4) describe the resulting osmotic pressure and fluid-fcc solid coexistence very

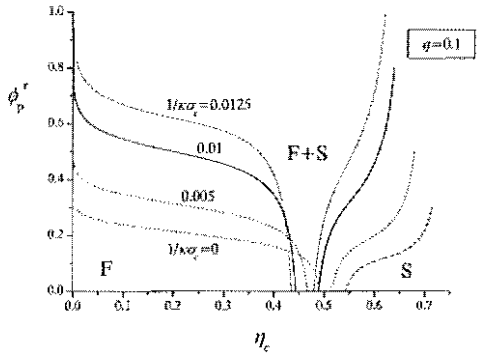

FIG. 1: Phase diagram of a mixture of charged spheres and ideal polymer as obtained from free volume theory for $q = 0.1$. The screened-Coulomb repulsion is characterised by a surface potential at contact of 20 kT and various values of $\kappa\sigma_c$ as indicated. F and S denote the stable fluid and solid fcc phase. $F + S$ indicates the fluid-solid coexistence region.

accurately for highly screened spheres [7]. We can now analyse the effect of the screened-Coulomb repulsion on the phase behaviour. The osmotic pressures and colloid chemical potentials can be found by differentiation of the Helmholtz free energy. The colloid volume fractions in each of the coexisting phases, η_c^1 and η_c^2, are obtained by equating μ_c and Π at fixed polymer reservoir concentration ϕ_p^r. The Helmholtz free energy density (4) is used for the solid phase, while the CS equation (2) is employed for the fluid. For a mixture of colloidal hard spheres and ideal polymer the free volume theory predicts a broadening of the fluid-solid transition with increasing ϕ_p^r for size ratios $q < 0.3$, while the fluid-fluid transition is metastable with respect to a broad fluid-solid transition [1, 11].

We now turn to the case of charged colloidal spheres and ideal polymer chains. In figure 1, we plot the phase diagram using the free volume theory for a size ratio $q = 0.1$ and $(\kappa\sigma_c)^{-1} = 0.0$, 0.005, 0.01, and 0.0125 in the (η_c, ϕ_p^r) plane. For $(\kappa\sigma_c)^{-1} = 0$ and $\phi_p^r = 0$, we recover the well-known pure hard sphere freezing transition at $\eta_c = 0.494$ and 0.545. In the case of charged spheres, the freezing transition at $\phi_p^r = 0$ shifts to lower colloid volume fractions η_c. The broadening of the freezing transition shifts to higher ϕ_p^r with increasing range of the screened-Coulomb repulsion $(\kappa\sigma_c)^{-1}$. This can be explained as follows. Upon increasing the range of the screened-Coulomb repulsion, $\eta_c = m\eta_c$, and hence f_c, increases. At the same time the free volume fraction α is not affected significantly ([7]) upon adding a screened-Coulomb repulsion. So, in order to attain a similar effect on f (see Eq. (18)), a higher polymer concentration is required to broaden the freezing transition. In order to assess the performance of the free volume theory, simulation results (see [7]) are shown in figure 2. The main difference is due to the fact that the results of both approaches deviate already for the mixture of hard sphere colloids plus ideal polymers, i.e., $(\kappa\sigma_c)^{-1} = 0$) [11]. The theoretical binodal is shifted with a factor of about 1.3 in ϕ_p^r as compared to the simulations. This factor between the theoretical predictions and the simulation Our results obtained from free volume theory and Monte Carlo simulations show that the additional screened-Coulomb repulsion reduces the depletion effect. For mixtures of small polymers plus relatively large charged spheres the fluid-solid transition is shifted to significantly larger polymer concentrations with increasing Debye screening length κ^{-1}. We thus recover the experimental findings.

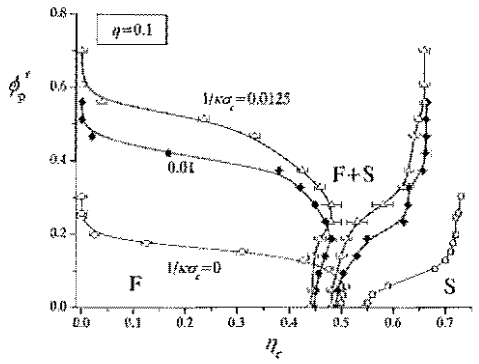

FIG. 2: Phase diagrams of a mixture of charged spheres and ideal polymer as in fig.1 as obtained from Monte Carlo simulations.

[1] H. N. W. Lekkerkerker, W. C. K. Poon, P. N. Pusey, A. Stroobants, and P. B. Warren. *Europhys. Lett.*, 20:559, 1992.

[2] S. M. Ilett, A. Orrock, W. C. K. Poon, and P. N. Pusey. *Phys. Rev. E*, 51:1344, 1995.

[3] V. Ya. Grinberg and V. B. Tolstoguzov. *Food Hydrocolloids*, 11:145, 1997.

[4] E.J.W. Verwey and J. Th. Overbeek. *Theory of the Stability of Lyophobic Colloids*. Elsevier, Amsterdam, 1948.

[5] P.D. Patel and W.B. Russel. *J. Colloid Interface Sci.*, 131:192, 1989.

[6] M. Casselyn, J. Perez, A. Tardieu, P. Vachette, J. Witz, and H. Delacroix. *Acta Cryst. D*, 57:1799, 2001.

[7] A. Fortini, M. Dijkstra, and R. Tuinier. *J. Phys: Condens. Matter*, 17:7783, 2005.

[8] N.F. Carnahan and K.E. Starling. *J. Phys. Chem.*, 51:635, 1969.

[9] J.A. Barker and D. Henderson. *J. Chem. Phys.*, 47:4714, 1967.

[10] C.K. Hall. *J. Chem. Phys.*, 52:2252, 1972.

[11] M. Dijkstra, J. M. Brader, and R. Evans. *J. Phys: Condens. Matter*, 11:10079, 1999.

Protein crystallization using polymers: influence of chain flexibility

R. Tuinier

Institut für Weiche Materie

Adding non-adsorbing polymer chains promotes protein crystallisation. Here we report the influence on the chain flexibility on the protein crystallisation efficiency. It is found that more flexible chains are more efficient in achieving 'good crystallisation' conditions, which agrees with experimental findings.

F&E-Nr: 23.102.08 (9-Punkt-Schrift)

Adding non-adsorbing polymers to protein solutions enhances crystallisation, as reported already some decades ago by Polson *et al.* [1]. Obtaining good quality crystals is needed for the determination of the protein structure using X-ray diffraction. In order to understand why the polymers help crystallization it is useful to investigate the conditions under which protein crystallization is enhanced. Helpful in that sense is the molecular dynamics computer simulation study of Ten Wolde and Frenkel [2]. They studied the crystallization of a collection of spherical particles interacting through a generalized Lennard-Jones-like pair interaction. The phase diagram of their system is qualitatively comparable to the phase diagram in Fig. 1 (upper): a fluid(F)-solid(S) coexistence with a 'hidden' gas(G)-liquid(L) coexistence curve inside the unstable region. From the simulation results it appeared that good crystals only form when a quench into the metastable gas-liquid region is made that lies near the metastable critical point.

Why do polymers help crystallisation under some conditions? Scattering studies show that adding non-adsorbing polymers to protein dispersions induces an effective attraction between the protein molecules that can be described as a depletion interaction [3,4], which is supposed to be the (additional) attraction between the proteins that enhances crystallization.

In Figure 1 (upper) a typical phase diagram is sketched for a Lennard-Jones like system that mimics the phase behaviour of a protein solution. The quantity ε is the interaction energy between the spherical particles and ϕ their volume fraction. In the lower part of Figure 1, the phase diagram for a colloid-polymer mixture is plotted (ϕ is the volume fraction of colloidal spheres and c_n is a normalized polymer concentration), following the free volume theory in ref. [5] for mixtures of hard spheres plus freely overlapping spheres that mimic the polymers with a radius equal to the polymer's radius of gyration R_g.

This analogy indicates that by adding polymers one could shift the phase diagram in the direct of optimum crystallization conditions. For instance, if the metastable gas-liquid coexistence would be located very far below the solubility curve, adding polymers would then shift the gas-liquid region much closer to the solubility curve.

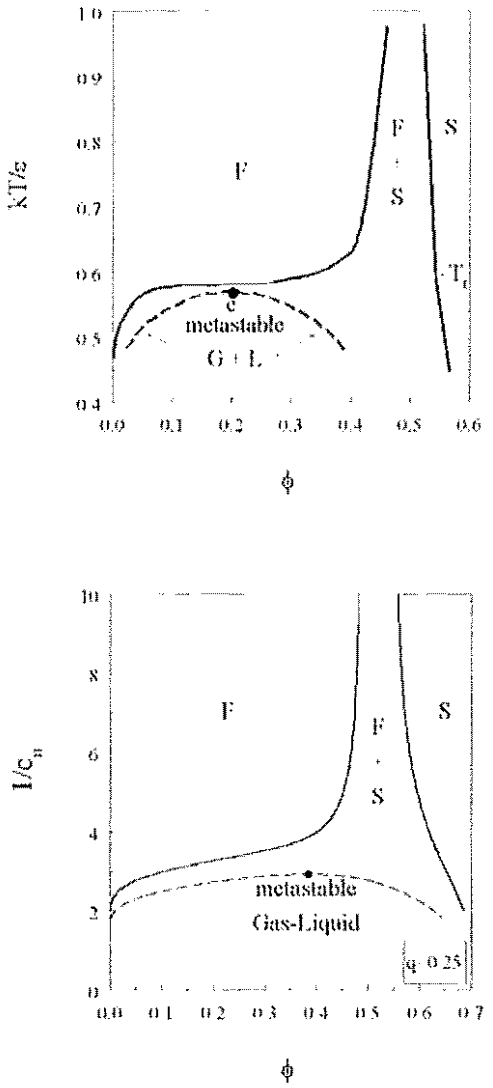

Fig.1: Sketch of the phase diagram of a Lennard-Jones fluid close to optimum crystallization conditions (upper plot) and the phase diagram of a polymer-colloid mixture with $q = R_g/R = 0.25$ where the inverse of a normalised polymer concentration c_n is plotted versus the colloid volume fraction (lower plot). Note the analogy between the diagrams.

It is remarkable that the relatively flexible polymer polyethylene glycol (PEG) is very efficient in bringing about crystallisation in protein solutions of, for instance, lysozyme [6] and leghemoglobin [7], whereas adding other polymers often only induces a liquid-liquid phase separation (e.g. the polysaccharide hydoxyethyl cellulose (HEC) mixed with lysozyme [8]). The question arises whether the segment to sphere size ratio plays a role in the ease with which crystallization occurs as induced by non-adsorbing polymer chains.

We have proposed a theory that describes the depletion interaction and resulting phase behaviour as mediated by freely jointed chains [9]. For both small and intermediate polymer-to-colloid size ratios the (respectively) gas-solid and gas-liquid coexistence curves shift to larger polymer coil volume fractions as the relative segment size A, as compared to the sphere radius R, increases. In Figure 2 we have plotted the phase diagrams that correspond to the conditions for optimal (protein) crystallisation for colloidal spheres mixed with freely jointed chains with N=∞, N=20 and N=5 segments. Here c(*) is the polymer (overlap) concentration.

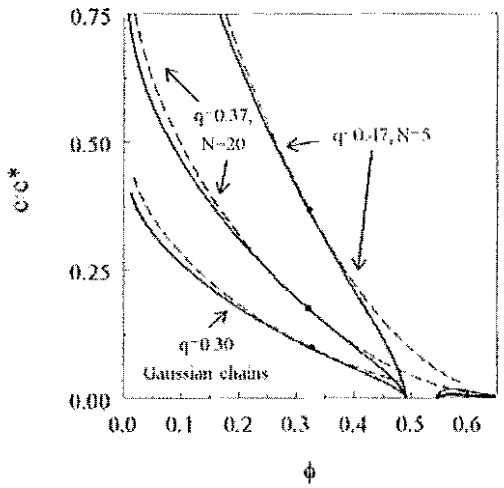

Fig.2: Phase diagrams for optimal crystallization conditions, i.e. where the metastable gas-liquid critical point is located (G-L binodals as dashed curves) near the (full) gas-solid coexistence curve. The critical points are again indicated as the filled circles.

For freely jointed chains with N=20 or 5, the optimal crystallization conditions are at larger q, and significantly larger polymer concentration as compared to the N=∞ limit. This finding may help to understand why relatively flexible polymers are better in enhancing crystallization; for less flexible chains (effectively less segments per chain) the optimum crystallization condition takes place at higher polymer concentrations. The finding that optimal crystallization conditions take place at higher polymer concentration for less flexible polymers may explain why a very flexible polymer such as PEG is so efficient in promoting good quality protein crystals and polysaccharides (reltively stiff polymer chains) are not. Since polysaccharides and proteins are often jointly present in biological systems, where crystallization is an unwanted phenomenon, there may be a biological reason for the reduced promotion of crystallization by polysaccharides.

References

[1] Polson, A., Potgieter, J.F., Largier, J.F., Mears, G.E.F., Joubert, J.F., *Biochim. Biophys. Acta* **82** (1964) 463.
[2] Ten Wolde, P.R., Frenkel, D., *Science* **277** (1997) 1975.
[3] Tuinier, R., Dhont, J.K.G., De Kruif, C.G., *Langmuir* **16** (2000) 1497.
[4] Tardieu, A., Finet, S., Bonneté, F., *J. Cryst. Growth* **232** (2001) 1.
[4] Lekkerkerker, H.N.W., Poon, W.C.K., Pusey, P.N., Stroobants, A., Warren, P.B., *Europhys.Lett.* **20** (1992) 559.
[6] Kulkarni, A.M., Chatterjee, A.P., Schweizer, K.S., Zukoski, C.F., *J. Chem. Phys.* **113** (2000) 9863.
[7] Devedzhiev, Ya. D., Kudryavtseva, N. N., Borodenko, L. I., Genina, O. S., Atanasov, B. P., *Sov. Phys. Crystallogr.* **35** (1990) 292.
[8] Hoskins, R., Robb, I.D., Williams, P.A., Warren, P.B., *J. Chem. Soc. Faraday Trans.* **92** (1996) 4515.
[9] Tuinier, R., *Europhys. J. E* **10** (2003) 123.

Synthesis of Poly(ethylene glycol)(PEG)-grafted colloidal silica particles with improved stability in aqueous environments

Johan Buitenhuis[1] and Zhenkun Zhang[1]

[1]*Forschungszentrum Jülich GmbH, IFF - Weiche Materie, D-52428 Jülich, Germany*

Colloidal dispersions of silica particles with terminally covalently grafted poly(ethylene glycol) (PEG, Mw=5000 g/mol) have been synthesized by a two-step synthesis method. Silica particles were first pre-coated with a silane coupling agent, (3-aminopropyl) triethoxysilane(APS) to incorporate active amine groups. Then the pre-coated particles were reacted with N-succinimidyl ester of monomethyl polyethylene glycol to form PEG grafted silica particles. Great effort was taken to decrease the water solubility of the pre-coated layer by applying a more stable pre-coating layer around the silica particles and binding the PEG to this layer. Characterization of the particles with light scattering shows that the colloidal dispersions can be prepared with a low degree of aggregation. The particles form stable dispersions in aqueous solutions as well as several organic solvents. Maybe the pre-coating applied in this study is also of interest to improve the water stability in some biomedical or biological applications where specific molecules are linked to a silica surface by silane coupling agents.

F&E-Nr:23.102.08

Composite colloidal particles consist of at least two types of materials, often with one material on the outside and one in the center of the particle. These composite particles combine different material properties such as specific (bio)chemical, optical, electrical, magnetic and mechanical properties. Furthermore, different stabilization layers can also be used to direct the formation of specific mesoscopic structures.

In the present paper we focus on a new synthesis procedure for colloidal dispersions of poly-(ethylene glycol) (PEG) terminally grafted on silica particles with an improved stability in water. The possibility to vary the molecular weight and the grafting density of the PEG might make the dispersions of interest for fundamental model studies on colloidal dispersions. Furthermore, the particles as well as variations of the synthesis procedure may be of some interest for biological and biomedical applications because of the decreased solubility in water of the particle surface layer as compared to the published synthesis work so far. Indeed, similar systems have been tested in applications such as drug delivery, biosensor, diagnostics, and medical imaging[1–3].

Already for about 25 years ago, Bridger and Vincent [4] reported on the synthesis of poly(ethylene oxide) (PEO) grafting on particulate silica surfaces. However, after storing the samples for about one month in aqueous solutions some aggregation was observed and evidence was found for free PEO in solution. They attributed this phenomenon to three possible reasons: hydrolysis of the link between the $(CH_3CH_2O)_3Si$- moiety and the PEO chain (urethane in their case), oxidative degradation of the PEO in aqueous solution, or slow dissolution of the surface layer of silica (to which the PEO chains are bonded). It was suggested that the third one is the main factor. The results in this work confirm this suggestion.

Since then, many publications of PEG grafting on silica surfaces have appeared. However, non of them address the stability of the coating in water, and furthermore most of them deal with the coating of macroscopic surfaces or the coating of dry silica. Here we deal with the PEG coating of colloidal dispersions of silica particles avoiding any dry states or other circumstances that lead to irreversible aggregation between the colloidal particles. Especially, the dry state generally leads to strong particle aggregation. As far as we know, four studies [1, 2, 5, 6] avoiding the dry state have been published since the work of Bridger and Vincent [4]. However, non of these studies discusses the problem of the limited water stability.

As shown in figure 1, our method can be described by two steps: Amination and PEGylation. In Amination, the hydrolysis and condensation reaction of the silane coupling agent (3-aminopropyl) triethoxysilane (APS) is used to introduce amine groups to the surface of the silica particles. In PEGylation, N-succinimidyl ester of mono-Methyl polyethylene glycol carboxylic acids (mPEG-NHS) are used to graft PEG to silica through amide bond formation by the reaction between the amine group and the N-succinimidyl group. A great effort has been devoted to form a pre-coating layer with improved stability in water in the amination step in figure 1. For this aim, bridged silane coupling agents were introduced in the amination step. Bridged silane coupling agents, when hydrolyzed, contain two or more -$Si(OH)_3$ groups. When modifying metal surfaces for corrosion protection and adhesion promotion, a more stable film can be formed with a mixture of APS and 1,2-bis-(triethoxysilyl)ethane (BTEOSE) than with pure APS [7]. Also bis[3-(trimethoxysilyl)propyl] amine(BTMOSPA) emerged as an outstanding exam-

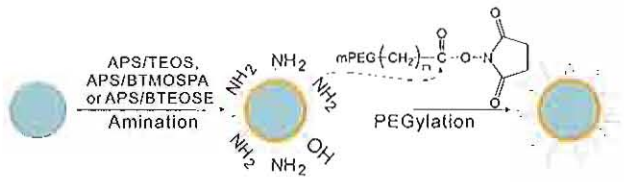

FIG. 1: Synthesis of PEG grafted colloidal silica particles by Amination and PEGylation.

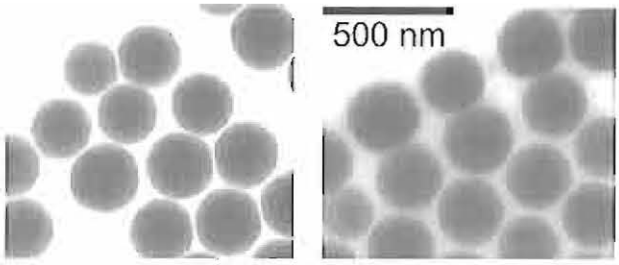

FIG. 2: TEM image of pre-coated particles (left) and PEG-coated particles (right).

ple in corrosion protection of metals in recent years[8]. These results promoted the use of BTEOSE and BTMOSPA in this work.

Figure 2 shows TEM images of a PEG coated sample and the corresponding pre-coated particle. The TEM image of the PEG coated particles shows grey zones of low density that are not shown on the image of the pre-coated particles. The same difference before and after PEG coating was also found by Joubert et al. [5], who attributed the grey zones to the PEG coating. Still, it is difficult to prove it is indeed PEG, and it should be noted that microscopy images can show misleading results, but the agreement between these results and our result is a strong indication that we see the PEG coating with TEM. In addition, elemental analysis after PEGylation of the particles shows an increase in carbon content, which is a strong indication of a PEG-coating of the particles. Furthermore, several dispersions are stable in a 5% salt solutions, contrary to bare silica particles or pre-coated particles, which in combination with the results form elemental analysis demonstrates the coating with PEG.

After washing with water buffer three times, the stability of PEG-silica with an APS/TEOS pre-coating in 5% salt solution is lost and the carbon content of an APS/TEOS pre-coated (no PEG coating yet) sample decreases from 2.5% to 0.93%, i.e. 63% of the carbon was lost. If attributed all of the lost carbon to APS moieties, 63% APS moieties in the pre-coated layer are lost. This estimate is quite comparable to the results in literature [9] where 67% aminopropylsilane on silica gel were found free in solution when dispersed in pure water for 4 hours. Here it should be noted that there are also unhydrolyzed ethoxy groups in the pre-coated layer and silica core. Hydrolysis of these unhydrolyzed ethoxy groups during washing also contributes to the above decrease of the carbon content. For instance, 1.65% carbon exists in bare silica particles dried from an ethanol/ammonia mixture as used in the synthesis of the particles, as compared to a carbon content of 0.18% after washing with water.

When BTMOSPA (or BTEOSE) was used instead of TEOS, PEG grafted particles without significant aggregation in 5% salt solution can be obtained. Most markedly, the loss rate of carbon content found for a BTMOSPA/APS sample was only 8% (from 9.06% to 8.32%) after washing with water buffer. Compared with about 60% loss rate for the APS/TEOS pre-coated particles, the pre-coated layer is almost intact after washing. Still the loss rate of carbon content of the corresponding PEG coated particles is 20% (from 11.96% to 9.44%). This higher loss rate than that of 8% for the precoated particles shows that also here a part of the PEG is lost during washing. Nevertheless, the particles are more stable in aqueous solutions than particles pre-coated with APS/TEOS.

In conclusion, a new two-step method is described to graft colloidal silica particles, avoiding any dry states or other circumstances leading to strong aggregation of the particles, using commercially available succinimidyl activated poly(ethylene glycols) (PEG). The particles obtained can be dispersed in water and several organic solvents that are a good solvent for PEG. In addition, our results confirm the suggestion by Bridger and Vincent [4] that the limited stability of PEG-grafted silica in water is probably caused by the hydrolysis of Si-O-Si bonds in the surface layer where the PEG are linked to the particle. This limited water stability of our PEG-grafted silica particles could be improved by using a mixed pre-coating.

[1] H. Xu, F. Yan, E. E. Monson, and R. Kopelman, Journal of Biomedical Materials Research Part A **66A**, 870 (2003).
[2] T. J. Yoon, J. S. Kim, B. G. Kim, K. N. Yu, M. H. Cho, and J. K. Lee, Angewandte Chemie-International Edition **44**, 1068 (2005).
[3] S. Jo and K. Park, Biomaterials **21**, 605 (2000).
[4] K. Bridger and B. Vincent, European Polymer Journal **16**, 1017 (1980).
[5] M. Joubert, C. Delaite, E. Bourgeat-Lami, and P. Dumas, Macromolecular Rapid Communications **26**, 602 (2005).
[6] C. Oh, C. D. Ki, J. Y. Chang, and S. G. Oh, Materials Letters **59**, 929 (2005).
[7] W. van Ooij, R. Edwards, and A. Sabata, U.S. Patent 5,292,549 (1994).
[8] D. Zhu and W. J. van Ooij, Progress in Organic Coatings **49**, 42 (2004).
[9] M. Etienne and A. Walcarius, Talanta **59**, 1173 (2003).

Self-diffusion of rod-like viruses in the nematic phase.

M. P. Lettinga,[1] E. Barry,[2] and Z. Dogic[2]

[1]*IFF, Institut Weiche Materie, Forschungszentrum Jülich,D-52425 Jülich, Germany*
[2]*Rowland Institute at Harvard, Harvard University, Cambridge MA 02142, USA*

The isotropic to nematic phase transition of a dispersion of rods is driven by the gain in translational entropy at the cost of orientational entropy. When the system is in the isotropic phase close to the nematic phase, rods are highly entangled which hinders the diffusion. Once the dispersion is in the nematic phase the diffusion along the local director is expected to increase, while diffusion perpendicular to the director is more strongly hindered. In this paper we quantify this behavior over a broad concentration range using video microscopy measurements on labelled *fd* viruses in a background phase of unlabelled *fd* viruses.

The pioneering work of Onsager [1] has revealed that at a critical concentration dispersion of hard rods undergo a first order phase transition from the isotropic state to the nematic state, where the rods have a long ranged orientational order. The driving force of this transition is the gain in translational entropy in the ordered state at the cost of orientational entropy. Because the ordered state is birefringent, this transition can be monitored using polarization microscopy. The direct cause of the transition, the gain in translational entropy, has however never been studied experimentally. The only data on the translational diffusion of rods in the nematic phase were taken for a system of labelled boehmite rods dispersed in a background nematic phase of unlabelled relative polydisperse boehmite rods [2]. Also simulations were performed on hard rod systems, with an aspect ratio of up to 16 [3]. In this paper we use video microscopy to monitor the translational diffusion of a mixture of labelled and unlabelled *fd* virus. The advantage of this system is that the rods are very long and stiff ($L = 880\ nm$, $D = 6.6\ nm$, $P = 3.0\ \mu m$). The phase behavior of this system can be predicted on the base of Onsager theory when a moderate flexibility and surface charge is taken into account [4].

The *fd* virus was prepared according to standard biological protocols found in Ref. [5]. The virus was purified by repetitive centrifugation (108 000 g for 5 hours) and finally re-dispersed in a 20 mM Dibasic phosphate buffer pH 7.5. The Isotropic to Nematic phase separation for *fd* in this buffer takes place at a concentration of $15.5\ mg/ml$. A small portion of the viruses was labelled with Alexa-488 (Molecular Probes) with approximately was approximately 300 molecules per *fd* virus. The final samples were prepared by adding one unit of anti-bleach solution and one unit of a dilute dispersion of labelled viruses to eight units of the concentrated *fd* virus dispersion of the desired concentration. The final ratio of labelled over unlabelled particles is 1:30000. The samples were prepared by putting 4 μl between cover slip and object glass resulting in a thin layer of around 10 μm, thus reducing the background effect of the out-of-focus tracer particles. Images were taken using a NIKON-Eclypse microscope with a mercury lamp as a light source and a 488 nm excitation 540 nm emission filter combination, using a 63× water emersion objective. The microscope was equipped with a Cool Snap Camera from Rooper scientific. The camera had an exposure time of 60 ms and was running at a rate of 16 frames per second with a 2×2 binning. The resulting pixel size was 129 nm and the field of view was 60 μm. Typically there were around hundred rods in the field of view. For each concentration ten sequences of four hundred images were recorded.

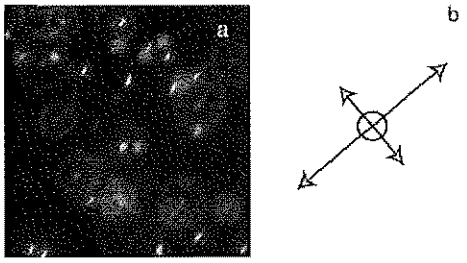

FIG. 1:
(a) Labelled rods on a background phase of unlabelled rods in the nematic phase. (b) Example of a 2-D Gaussian fit of one of the rods. The arrows indicate the long and short axis. The circle indicates the center of mass.

In Fig. 1a we show a typical example of labelled rods in a background nematic phase of unlabelled rods. Although the size of the rods is only a factor two to three more than the resolution of the microscope, still the shape of the rods is clearly anisotropic. The coordinates and orientation of the rods are obtained sequentially. First a blurred image is used to identify the rods and obtain the coordinates of its center of mass. Then, a two dimensional gaussian fit of the area around each center of the rod is performed, see Fig. 1b. From this fit we obtain for each rod the orientation. This procedure is repeated for the whole sequence of images. The coordinates are plotted in Fig. 2a for all particles and all frames using a sample in the nematic phase ($[fd] = 21\ mg/ml$). The coordinates are plotted relative to the coordinates in the first frame which is placed at the origin. The corresponding angular distribution function is plotted in Fig.

2b. Both the spacial and the angular distribution can be used to obtain the orientation of the director in the nematic phase: Fig. 2b is used to get the average angle of the long axis of the rods as obtained from; the distribution of the coordinates the director can be calculated from the eigenvectors of the momentum of inertia of the coordinates. Differences in the orientation of the director between the two independent methods are typically less than 5 degrees. The director can be "placed" along one of the two main axis by rotating the lab-frame over this angle. The diffusion coefficients of the rods parallel ($D_\parallel$) and perpendicular ($D_\perp$) to the director are then calculated from the x'- and y'-component of the mean square displacement. Note that in order to obtain $D_\perp$ one has to multiply D_x with a factor $\sqrt{2}$ since one observes only one component of the the diffusion perpendicular to the director. Here we assume that the director is oriented in the field of view. On average the mean square displacement was linear over fifty frames in the nematic phase, but only over about twenty five frames in the isotropic phase. This is due to the fact that the diffusion perpendicular to the director is slower in the nematic phase as compared to the isotropic phase. Therefore the particles stay longer in focus in the nematic phase and can be tracked for a longer time. Since the mean square displacement is linear over the first time window and displacements are up to a few times the particle length, we believe that we are monitoring the pure long-time diffusion. The mean quare displacement was measured for the whole concentration range from the isotropic phase up to the smectic phase. The results are plotted in Fig. 3. Fig. 3a shows the concentration dependence of the $D_\parallel$ and $D_\perp$. At the I-N phase transition there is a strong discontinuity in the diffusivity. $D_\parallel$ becomes a factor four faster, while $D_\perp$ becomes a factor one and a half slower than the diffusion in the isotropic phase at the phase transition. The concentration dependence of $D_\perp$ and $D_\parallel$ is very different. For $D_\parallel$ we see a initial small increase in the diffusion, which flattens and is followed by a broad region where the diffusion rate decreases monotonically. $D_\perp$, on the other hand, shows a monotonic decrease of the diffusion rate over the whole concentration region. This is in line with the simulations by Löwen. This can be seen in Fig.3b we compare our data with these simulations. To this end we used the order parameter as measure for the concentration, since the *fd* virus is a semi-flexible rod while the simulations were done on rods with a small aspect ratio. As can be seen from Fig. 3b, both the experiments and simulations show an exponential increase of ratio of $D_\parallel$ over $D_\perp$ as a function of the order parameter.

From our data and the simulations we draw the following conclusions. There are two inverse effects competing in determining the diffusion along the director: First, the stronger alignment, as manifested by an increasing nematic order parameter P_2, favors lengthwise diffusion since there are less vicinal rods to cross in moving along

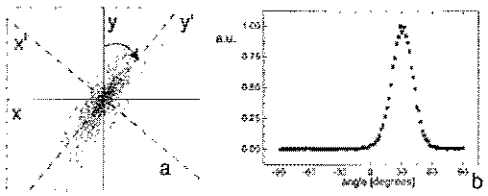

FIG. 2:
(a) Distribution of the center of mass with respect to the initial position for all traced particles in the nematic phase ($[fd] = 21\ mg/ml$). The y' and x' prime indicate the new lab-frame after rotation over the angle found from main eigen vector of the moment of inertia of the point cloud 31.2 °). (b) The orientational distribution function for the same dispersion, giving an average angle of (30.2 °).

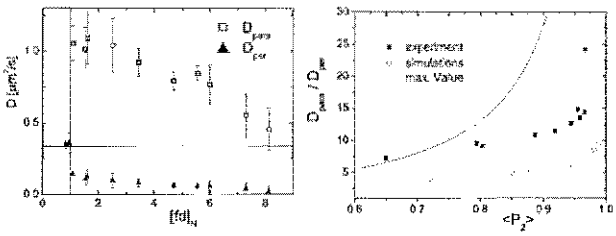

FIG. 3:
(a) The concentration dependence of the translational diffusion parallel and perpendicular to the director. The lines indicate the diffusion and concentration at the isotropic-nematic phase transition. (b) The ratio of $D_\perp$ over $D_\parallel$ as a function of the order parameter, using data of [6].

the director. Second, with increasing concentration there is less free space available, which hinders diffusion in general. It is a subtle interplay between these two effects which results in the non-monotonic behavior. Close to the isotropic-nematic transition, P_2 rapidly changes with density. Hence diffusion along the director is accelerated with increasing density. For higher densities, however, the alignment has practically saturated, and the packing constraints slow down any diffusion. In the case of diffusion perpendicular to the director both effects cause a stronger hindering and therefore a monotonic decay is observed.

[1] L. Onsager, Annals of the New York academy of science **51**, 62 (1949).
[2] M. P. B. van Bruggen, H. N. W. Lekkerkerker, G. Maret, and J. K. G. Dhont, Phys. Rev. E **58**, 7668 (1998).
[3] H. Löwen, Phys. Rev. E **59**, 1989 (1999).
[4] J. Tang and S. Fraden, Phys. Rev. Lett. **71**, 3509 (1993).
[5] J. Sambrook, E. F. Fritsch, and T. Maniatis, *Molecular Cloning: A Laboratory Manual* (Cold Spring Harbor Laboratory Press, 1989)
[6] K. R. Purdy, Z. Dogic, S. Fraden, A. Rühm, L. Lurio, and S. G. J. Mochrie, Phys. Rev. E. **67**, 031708 (2003).

The electrostatic potential of alternating polyelectrolyte multilayers as investigated by TIRM

John E. Wong[†], Regine von Klitzing[‡], Peter R. Lang,
[†] *Technische Universitat Berlin*
[‡] *Christian Albrecht Universitat Kiel*
Institut fur Festkorperforschung,
Teilinstitut Weiche Materie

Alternating layers of polycationic and polyanionic polymers were deposited on glass substrates using the dipping method introduced by Decher [1]. The interaction potential between polystyrene latex probe spheres and alternating layers of poly-(diallyldimethylammonium chloride) (PDADMAC) and poly-(styrenesulfonate) PSS were measured by total internal reflection microscopy (TIRM) [2]. Our data imply a lateral inhomogeneity of the charge sign distribution when the number of polyelectrolyte layers is larger than one.

In the mid nineties Decher has introduced a surprisingly simple method to prepare alternating multilayers of oppositely charged polyelectrolytes [1]. A negatively charged substrate, e. g. a microscope slide, is immersed into a solution of a polycation, which adsorbs onto the substrate. The adsorption is strong enough to lead to an overcharging of the substrate, i. e. a net positive charge of the newly created surface. If this system is rinsed and immersed into a solution of a polyanion, the latter adsorbs onto the positively charged surface again strong enough to cause a net sign change of the surface charge. Therefore the procedure can be repeated to eventually prepare stacks with up to several hundreds of individual layers. The structural properties of such multilayer systems have been investigated thoroughly during the last years. It is nowadays common understanding that adjacent layers are heavily interpenetrating each other [3]. It is therefore still not completely understood, how the charge inversion comes about, which is prerequisite for the further adsorption of an additional layer of the oppositely charged polyelectrolyte. To tackle this question we attempted to measure the interaction potential of PDADMAC–PSS multilayers with charged polystyrene probe spheres applying the relatively new technique of total internal re ection microscopy (TIRM).

In a TIRM experiment a colloidal sphere , with a gravitational length of less than about 100 nm is used as a probe. If the sphere and a at interface located beneath it, are equally charged, the superposition of electrostatic repulsion and gravitation will lead an e ective potential acting on the sphere of the form

$$\frac{\phi(\ z)}{k_BT} = \frac{G}{k_BT}\left[\kappa^{\ 1}(exp\{-\kappa\ \ z\} - 1) + \ \ z\right] \qquad (1)$$

where the electrostatic contribution is written in the Debey–Huckel approximation, with the screening length $\kappa^{\ 1}$. The gravitational contribution is represented by the buoyancy corrected weight $G = g4\pi R^3\ \ \rho/3$, with the sphere radius R, the density di erence between particle and solvent ρ and the acceleration constant g. z is the coordinate normal to the interface and the relative distance z is de ned such that potential minimum $\phi = 0$ is located at $z = 0$. Although this minimum represents an equilibrium state, the sphere will not remain stationary at this location, but sample elevations above and below the equilibrium separation due to Brownian motion. These separation uctuations can be monitored with the evanescent wave of a laser beam, which is scattered by the probe sphere. The spatially integrated scattered intensity is solely proportional to the smallest separation of the sphere from the interface [4]. Therefore, measuring the uctuation of the scattered intensity corresponds to monitoring separation uctuations. For a su ciently high number of events, the histogram of these uctuations converges to the probability density of separations between sphere and interface, which is related to the interaction potential by Boltzmann's equation. A typical example for the raw data in a TIRM experiments is displayed in Figure 1 together with the resulting probabilty density, $P(I)$. These data were taken from three different polystyrene latex spheres with amino-endgroups and a radius of 3 μm oating above a single PDADMAC layer on a glass substrate. The ionic strength of the solvent was controlled by addition of hydrochloric acid to $pH = 4$ to which corresponds to a screening length of $\kappa^{\ 1} = 30.4$ nm. With this value eq. 1 results the model potential displayed as full line in Figure 2, if the radius of the sphere and it's density di erence to water $\rho = 50$ kg/m^3 are applied. Without any further adjustable parameter, this calculated potential perfectly matches the experimental potentials which have been derived from the probability density curves in the bottom part of Figure 1.

The situation changes drastically, if interfaces with more than one polyelectrolyte layer are investigated. In the initial stage of the experiments there are intensity uctuations observable (see Figure 3), but they look qualitatively di erent from the data plotted in Figure 1. After about three to ve hours the uctuations atten at a high average value, represented by the red trace in Fig-

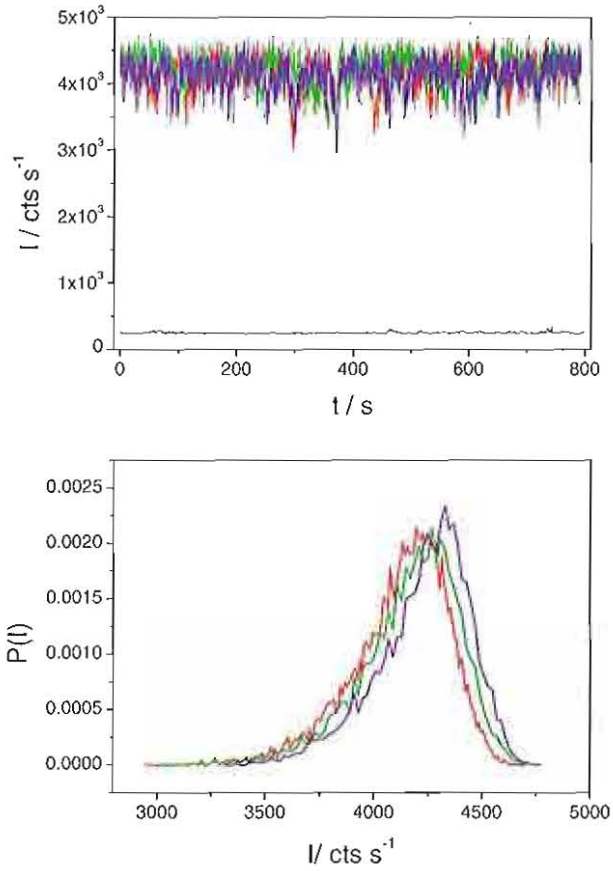

FIG. 1: Top part: TIRM data taken from three different polystyrene latex spheres with amino-endgroups and a radius of 3 μm floating above a single PDADMAC layer on a glass substrate. The screening length was set to $\kappa^{-1} = 30.4$ nm by addition of hydrochloric acid. The black trace in the bottom represent background data measured without a probe in the microscope's eld of view. Bottom part: Probability density curves of the scattered intensity calculated from the raw data shown in the top part.

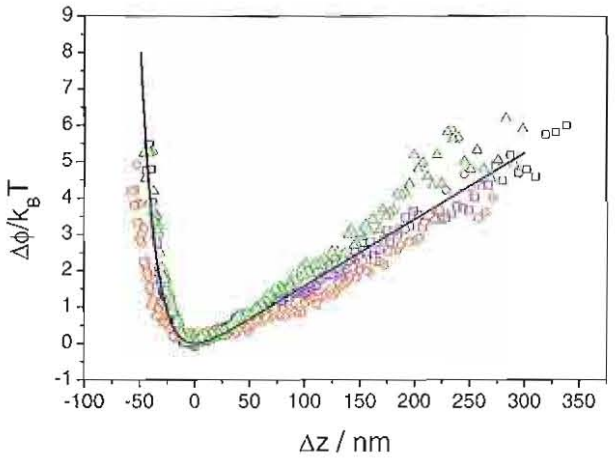

FIG. 2: Interaction potentials derived from the data shown in Figure 1. The full line is a model potential calculated according to eq. 1 without any adjustable parameter.

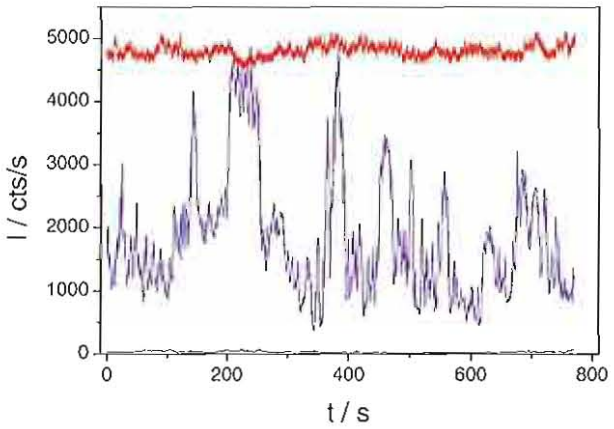

FIG. 3: TIRM data taken from a polystyrene latex spheres with sulfate endgroups and a radius of 5 μm floating above a PDADMAC–PSS double layer on a glass substrate (blue: initial stage of the experiment, red: after ve hours). The screening length was set to $\kappa^{-1} = 30.4$ nm by addition of TRIS buffer. The black line in the bottom are background data measured without any probe in the microscope's eld of view.

ure 3. This appearance is typical for a particle stuck to the interface. After this time it is not any more possibly to nd a probe sphere in the entire sample which is undergoing Brownian motion. It appears that all spheres are adsorbed to the interface, which leads us to the conclusion, that there are positively charded speckles, although we expect a net negative charge of the interface according to the preparation. The behavior we observed for the PDADMAC -PSS doublelayer does not change if the number of polyelectrolyte layers further increases. It is therefeore very likely that polyelectrolyte multilayers prepedred by the described dipping technique in general do not have a homogeneous charge sign distribution, but they rather exhibit a patchwork of negatively and positively charged speckles, no matter what the net charge according to the preparation procedure is.

[1] Decher, G. *Science* **277**, 1232 (1997).
[2] Prieve, D. *Adv. Colloid Interf. Sci.* **82**, 93 (1999).
[3] Schonhoff, M. *Current Opinion in Coll. Interf. Sci.* **8**, 86 (2003).
[4] Prieve, D. C.; Walz, J. Y. *Appl. Opt.* **32**, 1629 (1993).

Soret Coefficient of Poly(*N*-isopropylacrylamide)/Water in the Vicinity of Coil-Globule Transition Temperature

Simone Wiegand[1] and Rio Kita[2]

[1]*Forschungszentrum Jülich GmbH, IFF - Weiche Materie, D-52428 Jülich, Germany*
[2]*Max Planck Institut für Polymerforschung, Ackermannweg 10, D-55128 Mainz, Germany*

Thermal diffusion behavior of poly(*N*-isopropylacrylamide) (PNiPAM) in water was studied in the temperature range between 20 °C and 38 °C by means of thermal diffusion forced Rayleigh scattering (TDFRS). The Soret coefficient and the thermal diffusion coefficient of PNiPAM showed a strong peak at the Θ-temperature (30.6°C) where PNiPAM single chain shows a coil to globule transition by heating. Significant contributions due to interactions among segments and solvents as well as changes in the chain dimension were revealed on the thermal diffusion behavior.

F&E-Nr:23.102.08

According to thermodynamics of polymer solutions, polymers show conformational changes depending on the solvent quality. A transition of single polymer chain induced by the solvent quality change, known as a coil-globule transition, has been extensively studied because of their importance not only on polymer physics but also application aspects for the collapse of a gel network, the folding of a protein, and so on [1].

Poly(*N*-isopropylacrylamide) (PNiPAM) chain in water has a Θ temperature at 30.6 °C, where the second virial coefficient is zero, and shows the coil-globule transition by heating. Indeed, there are many reports studying PNiPAM solutions by scattering methods, [2, 3] fluorescence, [4] electronic paramagnetic resonance, [5] IR spectroscopy, [6] and calorimetry [7, 8]. However, thermal diffusion phenomena have not been studied with taking into account the coil-globule transition in the vicinity of the Θ temperature. Thermal diffusion accounts for a mass flux, J_1, in a mixture which is induced by a temperature and a concentration gradient [9].

The sign of S_T indicates whether component 1 migrates to the warm side or the cold side of the fluid. If the system is dominated by short range interactions, the thermal diffusion behavior can be attributed to single particle and collective contributions [10]. There are several detailed and systematic studies of thermal diffusion phenomena of organic polymer systems covering scaling behavior, concentration effects, and preferential solvation effects in mixed solvents [11, 12]. In contrast to those organic systems, there are only few studies for aqueous polymer solutions.

Observations of the thermal diffusion in the vicinity of coil-globule transition of PNiPAM/water will illuminate the importance of segment-segment and segment-solvent interactions. These key features can be varied experimentally according to the consequence of coil-globule transition of PNiPAM. This approach will lead to deeper understanding of thermal diffusion behavior of aqueous polymer systems as well as provide new insight to the solution properties of PNiPAM in a thermodynamically non-equilibrium state.

PNiPAM was purified by a fractionation method. One fraction was used in this study which had the weight-averaged molecular weight $M_w = 3.0 \times 10^6$ g/mol with a polydispersity M_w/M_n of 1.20. Details of sample preparation and characterizations are described elsewhere [13]. Water was deionized by a Milli-Q system. In this study 1.0 g/L PNiPAM in water was prepared with a tiny amount of the dye, Basantol Yellow [14].

The TDFRS measurements were carried out in the temperature range from 20°C to 38°C, where the temperature of the sample cell was controlled by circulating water from a thermostat with an uncertainty of 0.02 °C. The wave number in the present study was q=4600 cm^{-1}.

Figure 1 shows the temperature dependence of Soret coefficient S_T, diffusion coefficient D, and thermal diffusion coefficient D_T for 1.0 g/L PNiPAM in water. The error bar is one standard deviation. The S_T remains almost constant below 25 °C and has a maximum at 30.7 °C with a steep decrease and a plateau at higher temperatures. The diffusion coefficient turns upward at 30.7 °C with increasing temperature. These significant points agreed well with the Θ temperature (30.6 °C) reported elsewhere [15]. The diffusion coefficient shown by open circles were the results of dynamic light scattering (DLS). The sharp increase of D in the poor solvent (above the Θ temperature) corresponds to the formation of a compact conformation of polymer chains. The hydrodynamic radius (R_h) changes from 39.4 nm (21.1 °C) to 21.2 nm (37.8 °C), which is evaluated using Stokes-Einstein equation. The magnitudes of the diffusion coefficient at 20 °C is in good agreement with previous studies and shows similar temperature dependence through the coil-globule transition [15, 16]. The thermal diffusion coefficient has a shape similar to S_T, although the D_T shows an apparent increase with increasing temperature in the good solvent side and the temperature of the largest D_T was 31.2 °C. Even though the temperatures at maximum S_T and D_T differ slightly, the temperature dependence of S_T and D_T shows peaks at close to the Θ

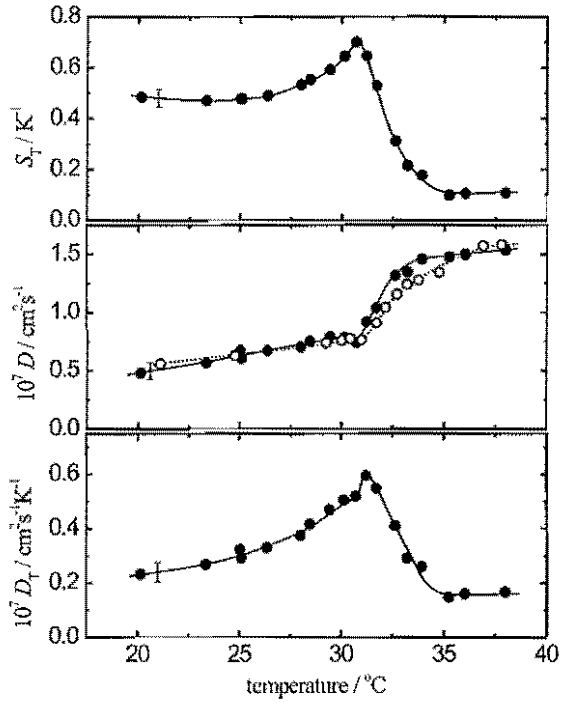

FIG. 1: Temperature dependencies of Soret coefficient S_T, translational diffusion coefficient D, and thermal diffusion coefficient D_T of 1.0 g/L PNiPAM in water obtained by TDFRS (closed circles). The diffusion coefficients shown by the open circles were the results of dynamic light scattering. Lines are drawn to guide eye.

temperature of PNiPAM *in water.*

The positive S_T *of* PNiPAM *indicates that polymers migrate to the cold side. The peak of* S_T *means that the concentration gradient is enhanced approaching the* Θ *temperature. The steep decrease of* S_T *above the* Θ *temperature could be associated with the transition to the globular state. The enhancement near the* Θ *temperature is considered with taking into account the solvent quality as follows: The direction of thermodiffusive motion of* PNiPAM *molecules in water is always towards cold side, corresponding to the positive sign of* S_T. *The polymer has a better solubility in colder water as can be judged by temperature dependence of the second virial coefficient. The thermodiffusive motion has the same direction with the better solubility side of the polymer. These facts indicate the magnitude of the concentration gradient induced by the thermal diffusion should have a tendency to be enlarged by the better solubility of polymer in the cold side. This could be origin of the enhancement of Soret coefficient and which tends to be pronounced approaching to the* Θ *temperature.*

In previous reports, we studied the ternary system of poly(ethylene oxide) in the mixed solvent water/ethanol and found a sign change of S_T *with changing the solvent compositions* [14, 17]. *A calculation of lattice chamber model for this system showed that hydrogen bonding plays a key role to describe the sign change behavior of the polymer* [17, 18]. *In a recent study of* PNiPAM/*ethanol, we found that the* S_T *and* D_T *monotonically decreased with increasing temperature, with a sign change at* 34 °C, *where ethanol is a good solvent. In this work, we observe the formation of a compact conformation together with the rapid decrease of the Soret coefficient in the poor solvent, while the sign remains positive. These results indicate the sign change behavior is relating to specific interactions between chain segments and solvent molecules.*

In conclusion, the behaviors of S_T *and* D_T *for* PNiPAM/*water are susceptible to short range associations, such as, the segment-segment and segment-solvent interactions and relating chain dimensions where the unperturbed chain showed the largest response against the field of temperature gradient. In order to clarify the effect of solvent association in detail we need to study the ternary system of* PNiPAM/*water/ethanol, where the local structures and a preferential solvation as well as a co-nonsolvency effect should be considered.*

[1] Nakata, M.; Nakagawa, T. *Phys. Rev. E* **1997, 56**, 3338-3345.
[2] Wang, X.; Wu, C. *Macromolecules* **1999, 32**, 4299-4301.
[3] Kratz, K.; Hellweg, T.; Eimer, W. *Polymer* **2001, 42**, 6631-6639.
[4] Winnik, F. M. *Macromolecules* **1990, 23**, 233-242.
[5] Winnik, F. M.; Ottaviani, M. F.; Bossmann, S. H.; Garciagaribay, M.; Turro, N. J. *Macromolecules* **1992, 25**, 6007-6017.
[6] Katsumoto, Y.; Tanaka, T.; Sato, H.; Ozaki, Y. *Journal of Physical Chemistry A* **2002, 106**, 3429-3435.
[7] Schild, H. G.; Tirrell, D. A. *J. Phys. Chem.* **1990, 94**, 4352-4356.
[8] Tiktopulo, E. I.; Bychkova, V. E.; Ricka, J.; Ptitsyn, O. B. *Macromolecules* **1994, 27**, 2879-2882.
[9] deGroot, S. R.; P., M. *Non-equilibrium Thermodynamics;* Dover: New York, 1984.
[10] Wiegand, S. *J.Phys.:Condens. Matter* **2004, 16**, R357-R379.
[11] Zhang, G. Z.; Briggs, M. E.; Gammon, R. W.; Sengers, J. V.; Douglas, J. F. *J. Chem. Phys.* **1999, 111**, 2270-2282.
[12] Rauch, J.; Köhler, W. *J. Chem. Phys.* **2003, 119**, 11977-11988.
[13] Kita, R.; Kircher, G.; Wiegand, S. *J. Chem. Phys.* **2004, 121**, 9140-9146.
[14] Kita, R.; Wiegand, S.; Luettmer-Strathmann, J. *J. Chem. Phys.* **2004, 121**, 3874-3885.
[15] Wu, C.; Wang, X. *Phys. Rev. Lett.* **1998, 80**, 4092-4094.
[16] Kubota, K.; Fujishige, S.; Ando, I. *Polymer Journal* **1990, 22**, 15-20.
[17] de Gans, B.-J.; Kita, R.; Wiegand, S.; Luettmer-Strathmann, J. *Phys. Rev. Lett.* **2003, 91**, 245501.
[18] Luettmer-Strathmann, J. *J. Chem. Phys.* **2003, 119**, 2892-2902.

Unusual thermal diffusion in aqueous polymer solutions

Simone Wiegand,[1,2] Rio Kita,[1] and Jutta Luettmer-Strathmann[3]

[1]*Max Planck Institut für Polymerforschung, Ackermannweg 10, D-55128 Mainz, Germany*
[2]*Forschungszentrum Jülich GmbH, IFF - Weiche Materie, D-52428 Jülich, Germany*
[3]*Department of Physics, University of Akron, Akron, OH 44325-4001, USA*

Thermal Diffusion Forced Rayleigh Scattering (TDFRS) results on thermal diffusion of poly(ethylene oxide) (PEO) in ethanol/water mixtures are presented. In water-rich solvent mixtures, PEO is found to migrate towards regions of lower temperature. This is typical for polymer solutions and corresponds to a positive Soret coefficient of PEO. In solvent mixtures with low water content, however, the polymer is found to migrate towards higher temperatures, corresponding to a negative Soret coefficient of PEO in ethanol-rich solutions. To our knowledge, this is the first observed sign change of the Soret coefficient of a polymer in solution. The experimental results are compared with a simple lattice model for the polymer solvent system. The calculated values in the model agree qualitatively with the experimental results.

F&E-Nr:23.102.08

The prediction of transport properties in liquid mixtures, polymer solutions and colloidal dispersions are of great technical importance [1]. Also many processes in biological systems occur under non-equilibrium conditions. While the behavior in equilibrium for many systems has been scrutinized, the understanding of processes under non-equlibrium conditions is still quite limited. In the last decade those non-equilibrium effects came into the focus of fundamental research in the field of soft matter. For instance, colloidal model systems in external fields are used to understand non-equilibrium phenomena on a microscopic level [2].

One transport property that has attracted growing interest in the last decade is thermodiffusion, also called thermal diffusion, or the Ludwig-Soret effect [3, 4]. A temperature gradient applied to a fluid mixture generally induces net mass flows which lead to the formation of concentration gradients. This effect is known as thermal diffusion or the Ludwig-Soret effect . In the stationary state where the mass flows vanish the magnitude of the effect is described by the Soret coefficients $S_{\mathrm{T},i}$

$$S_{\mathrm{T},i} = -\frac{1}{c_{i0}(1-c_{i0})}\frac{\nabla c_i}{\nabla T}, \qquad (1)$$

where c_i is the mass fraction of component i, c_{i0} is its equilibrium value, and where T is the temperature. $S_{\mathrm{T},i}$ is positive if component i moves to the low temperature region. Since the mass fractions add up to unity, $\sum_i c_i = 1$, a K-component mixture has $K-1$ independent Soret coefficients.

Typically the Soret coefficient of the heavier component of a binary liquid mixture is positive. This is not always the case, however, and the Soret coefficients in some low molecular weight liquid mixtures are known to change sign [4]. A sign change of the Soret coefficient was also observed in very recent thermophoresis experiments on protein solutions [5].

In this work we investigate systematically the Soret effect of PEO in ethanol/water mixtures. We expect interesting thermal diffusion properties for this system, since the interactions between the polymer and the two solvents are very different. Hydrogen bonding makes water an excellent solvent for PEO at room temperature while PEO is insoluble in ethanol. Due to the biocompatibility of PEO this system is also relevant for biological applications (cf. [6]).

Experiment. – We measured Soret coefficients with a holographic grating technique called thermal diffusion forced Rayleigh scattering (TDFRS) with heterodyne detection and active phase tracking [7]. The principle of TDFRS is analogous to ordinary forced Rayleigh scattering: An intensity grating is created by the interference of two laser beams. A trace amount of inert absorbing dye added to the sample converts the intensity grating within microseconds into a temperature grating, which is converted into a concentration grating within milliseconds by the effect of thermal diffusion. Both temperature and composition grating contribute to a refractive index grating read out by Bragg diffraction of a third laser beam.

The PEO in our experiments had a molecular weight of $M_{\mathrm{w}} = 2.65 \times 10^5$ gr.mol^{-1} with a polydispersity $PD = 1.1$. All samples were semidilute solutions containing 5.0±0.1 gr.L^{-1} PEO. A trace amount of dye (quinizarin, Sigma-Aldrich) was added to the samples (optical density 1-2 cm^{-1}). As for PEO in pure water basantolyellow 215 (BASF) was used. Adsorption of the dyes on PEO does not occur as their absorption spectrum remains unchanged [8, 9].

Figure 1 shows typical normalized heterodyne signals as a function of time obtained for three different solvent compositions. Analysis of the amplitude and the decay time of the fast mode leads to the same values for the Soret coefficient of water as obtained from measurements of binary ethanol/water mixtures [9]. Figure 2 shows the Soret coefficient of PEO in ethanol/water as a function

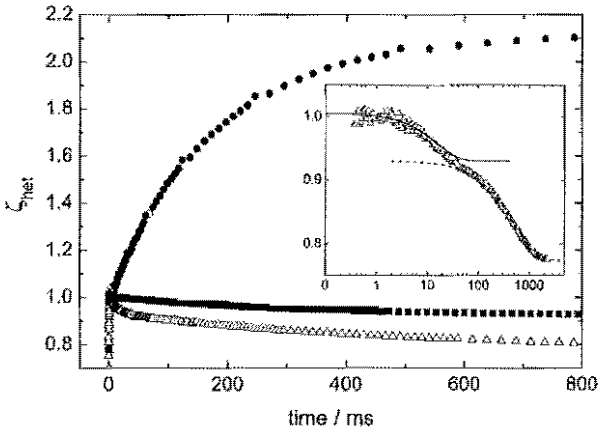

FIG. 1: Typical normalized heterodyne diffraction signal for a solution of PEO in ethanol/water (15.02 % wt H_2O (■), 50 % wt (△), 100 % wt (●)). The inset shows the two decays for 50 % wt mixture ethanol/water versus logarithm of the time.

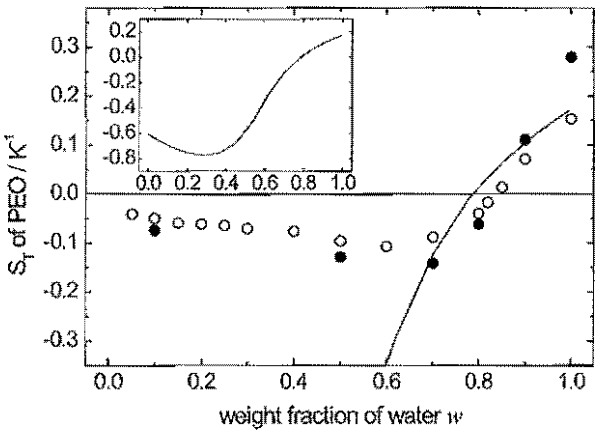

FIG. 2: Soret coefficient S_T of PEO in ethanol/water as a function of water weight fraction. The solid line represents values calculated from the two-chamber lattice model

of water weight fraction. We observe a sign change of S_T of PEO in ethanol/water mixtures at a weight fraction of 83 %. To our knowledge, this is the first observation of a sign change of the Soret coefficient of a polymer in solution.

The comparison with the theoretical line in Fig. 2 shows that a single mixed interaction energy as it has been used in the lattice model [9] is not sufficient to describe the Soret effect over the whole concentration range. In the concentration range between $w = 0.6$ and $w = 0.8$large structural changes in the liquid [10] take place. In an NMR study, it has been reported that the strength of hydrogen bonds formed among water molecules in pure water ($w = 1$) is enhanced by addition of ethanol up to $w = 0.82$, whereas the hydrogen-bond network is disrupted by further addition of ethanol and disappears around $w = 0.61$.[11] Similarly, a dielectric relaxation measurement on water/ethanol showed large structural changes in the concentration range between $w = 0.82$ and $w = 0.64$.[12]

Discussion. – Our experimental and theoretical investigation of PEO in ethanol/water mixtures gives some insight into conditions that lead to unusual thermodiffusion in polymer solutions. The experimental data presented and the calculations illustrate the role of solvent quality. Positive Soret coefficients are observed for PEO in pure water, which is an excellent solvent, while negative Soret coefficients are observed for low water content of the solution, that is under poorer solvent conditions. The sign change can be connected with the breakdown of the hydrogen bond network.

For the PEO/ethanol/water system studied here, hydrogen bonding plays a most important role. The Soret coefficient of PEO changes sign at a solvent composition, where large structural changes occur in binary mixtures of ethanol and water [13]. We are currently investigating this aspect in more detail.

[1] S. Wiegand, J. Phys.:Condens. Matt. **16**, R357 (2004).
[2] H. Löwen, J. Phys.:Condens. Matt. **13**, R415 (2001).
[3] S. deGroot and P. Mazur, *Non-equilibrium Thermodynamics* (Dover, New York, 1984).
[4] H. Tyrell, *Diffusion and Heat Flow in Liquids* (Butterworth, London, 1961).
[5] S. Iacopini and R. Piazza, Europhys. Lett. **63**, 247 (2003).
[6] E. E. Dormidontova, Macromolecules **35**, 987 (2002).
[7] W. Köhler and R. Schäfer, Adv. Polym. Sci. **151**, 1 (2000).
[8] B.-J. de Gans, R. Kita, B. Müller, and S. Wiegand, J. Chem. Phys. **118**, 8073 (2003).
[9] R. Kita, S. Wiegand, and J. Luettmer-Strathmann, J. Chem. Phys. **121**, 3874 (2004).
[10] V. Belousov and M. Panov, *Thermodynamic properties of aqueous solutions of organic substances.* (CRC Press, Boca Raton, FL, 1994).
[11] A. Coccia, P. L. Indovina, F. Podo, and V. Viti, Chem. Phys. **7**, 30 (1975).
[12] T. Sato, A. Chiba, and R. Nozaki, J. Chem. Phys. **110**, 2508 (1999).
[13] V. P. Belousov and M. Y. Panov, *Thermodynamic properties of aqueous solutions of organic substances.* (CRC Press, Boca Raton, FL, 1994).

Anisotropy of Brownian Motion Close to a Wall

Peter Holmqvist, Peter R. Lang
Institut für Festkörperforschung
Teilinstitut Weiche Materie

The diffusivity of particles suspended in a liquid is expected to slow down in the ultimate vicinity of a hard wall. Further, the diffusivity component parallel to the wall is predicted to be larger than the normal component. With our new instrumentation for evanscent wave light scattering, it was for the first time possible to proof experimentally that this predictions hold also for colloidal particles which are subject to thermal, i. e. Brownian motion.

Close to a macroscopic interface, many physical properties of soft matter systems are different from the bulk properties. For example, at the surface of long chain alkane melts the crystallization temperature of is shifted several degrees towards lower temperatures as compared to the bulk value [1]. Related effects have been reported for suspensions off colloidal particles. For instance, solutions of spherical blockcopolymer micelles exhibit surface induced ordering at solute volume fractions at which the bulk system is isotropic [2], or the isotropic to nematic phase transition of solutions of cylindrical blockcopolymer micelles is shifted to smaller volume fractions at solid interfaces [3].

While the influence of interfaces on the structure and phase behavior has been investigated in a large number of studies, there are only a few reports on the dynamics of colloidal supensions close to interfaces. Hydrodynamic calculations [4, 5] suggest that diffusivity of spherical bodies close to a wall should be smaller than in the bulk and that the component normal to the wall, $D_\perp$, is even smaller than the parallel component, $D_\parallel$, i. e.

$$\begin{aligned} D_\parallel &= D_0/\Lambda_\parallel \\ D_\perp &= D_0/\Lambda_\perp. \end{aligned} \tag{1}$$

Here D_0 is the bulk diffusion coefficient while $\Lambda_\perp$ and $\Lambda_\parallel$ are series of inverse powers of the distance to the wall, z. First experimental evidence for this prediction to hold also for colloidal particles was given by Hosoda and coworkers [6], using dynamic light scattering with evanescent illumination (EWDLS) [7]. In an EWDLS experiment a laser beam is directed to the interface between a glass body and the colloidal solution as sketched in Fig.1. If the beam is totally reflected, the electric field still leaks into the solution due to continuity requirements. This give rise to a so called evanescent wave with an exponentially decaying field strength, which can be used as the illuminating field for a dynamic light scattering experiment. Then the scattering vector is given by the wave vector difference between the scattered wave and the evanescent wave, $\mathbf{Q} = \mathbf{k}_S - \mathbf{k}_e$. In the studies published so far it was not possible to vary the scattering vector component parallel, $\mathbf{Q}_\parallel$, and normal, $\mathbf{Q}_\perp$; to the reflecting interface independently, and cosequently it was not possible to distinguish between the parallel and the normal component of the particle diffusivity. We have designed a new set up to overcome this problem and were therefore able to measure for the first time z–averaged values for the diffusivity parallel $\langle D \rangle_\parallel$ and perpendicular $\langle D \rangle_\perp$ to the interface

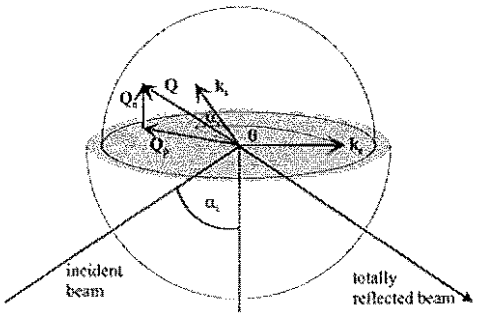

FIG. 1: Sketch of the scattering geometry in an EWDLS experiment.

In our set–up we apply a semi–spherical glass lens as the bottom part of the sample cell, which is covered by a dome containing the colloidal solution (see Fig.1). The midpoint of the glass/solution interface is placed in the center of a tripple axis diffractometer, with which we can vary the in–plane angle, θ, and the out of plane angle, α_r, independently. The magnitudes of the scattering vector components are given by $Q_\perp = 2\pi n \sin\alpha_r/\lambda_0$, $Q_\parallel = 2\pi n\sqrt{1+\cos^2\alpha_r - 2\cos\alpha_r\cos\theta}/\lambda_0$ and $Q = \sqrt{Q_\perp^2 + Q_\parallel^2}$. Here λ_0 is the vacuum wavelength of the laser and n is the refractive index of the solution. Consequently, we can record intensity auto correlation functions, $g_2(t)$, at various $Q_\perp$ while keeping $Q_\parallel$ fixed and vice versa. This is important since we could show that the short time behavior of the auto correlation function of the scattered field is given by

$$g_1(t) = \exp\left\{-\Gamma t + \mathcal{O}(t^2)\right\} \tag{2}$$

where the initial relaxation rate, Γ, is related to the diffusivity components as

$$\begin{aligned} \Gamma \;=\; & D_0[Q_\parallel^2 \int_{z>R} dz \frac{\exp\{(z-R)/\xi\}}{\Lambda_\parallel} \\ & + \left(Q_\perp^2 + \frac{1}{\xi^2}\right) \int_{z>R} dz \frac{\exp\{(z-R)/\xi\}}{\Lambda_\perp}] \end{aligned} \tag{3}$$

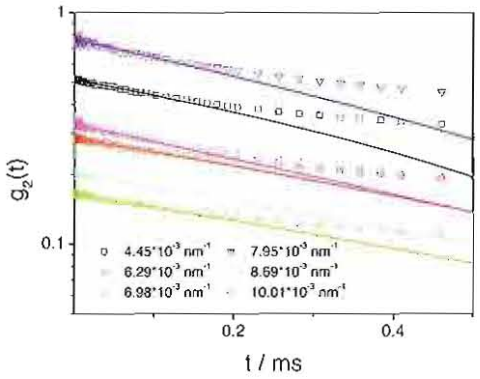

FIG. 2: Initial parts of intensity auto correlation functions recorded at constant $Q_{\|} = 0.01$ nm^{-1}. The numbers in the legend indicate different values of $Q_{\perp}$. Symbols are experimental data and full lines are non linear least squares fit wit eq. 5.

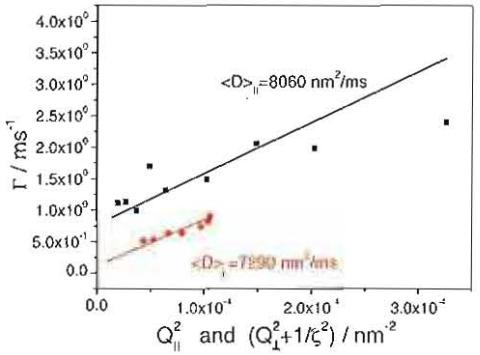

FIG. 3: Initial relaxation rates Γ as function of $Q_{\|}^2$ (black) and $(Q_{\perp}^2 + 1/\xi^2)$ (red). Symbols are results of the non linear lest squares fits of the intensity correlation functions with eq. 5. The error bars represent the uncertainties from the fitting procedure. The full line are prediction using the values indicated in the legend.

with ξ the penetration depth of the evanescent wave. The integrals on the right hand site of eq. 3 represent the experimental averaging in the direction perpendicular to the interface. We therefore define the averaged diffusivities as

$$\langle D\rangle_{\|} = D_0 \int_{z>R} \mathrm{d}z \frac{\exp\{(z-R)/\xi\}}{\Lambda_{\|}} \qquad (4)$$
$$\langle D\rangle_{\perp} = D_0 \int_{z>R} \mathrm{d}z \frac{\exp\{(z-R)/\xi\}}{\Lambda_{\perp}}$$

Thus Γ depends linearly on $Q_{\|}^2$ at constant $Q_{\perp}$ and the slope is the mean value of the diffusivity component normal to the interface, $< D >_{\|}$, and vice versa.

In the following we describe EWDLS experiments on a solution of charge stabilized silica particles with a radius $R = 27$ nm dispersed in a 10^{-2} M NaCl solution. The corresponding bulk diffusion coefficient is $D_0 = 9050$ nm^2/ms and according to eqs. 1 and 3 $< D >_{\|} = 8060$ nm^2/ms and $< D >_{\perp} = 7290$ nm^2/ms. We have recorded correlation functions at variable $Q_{\perp}$ and fixed $Q_{\|}$ and vice versa. To determine Γ, the initial part of the intensity correlation functions was nonlinear least squares fitted with the following standard expression

$$g_2(t) = 1 + 2\frac{I_S I_e}{(I_S + I_e)^2}\exp\{-\Gamma t\} + \left(\frac{I_S}{I_S + I_e}\exp\{-\Gamma t\}\right)^2, \qquad (5)$$

which relates the field auto correlation function $g_1(t)$ to the intensity auto correlation function $g_2(t)$ for the general case of mixed homodyne/heterodyne detection. Here I_S is the intensity scattered from the sample of interest and I_e is the additional uncorrelated contribution from additional sources.

The resulting Γ-values are plotted in Fig. 3 vs $Q_{\|}^2$ and $(Q_{\perp}^2 + 1/\xi^2)$ respectively. The full lines in this plot were calculated using $< D >_{\|} = 8060$ nm^2/ms and $< D >_{\perp} = 7290$ nm^2/ms, which are predicted by eq. 1. The good agreement of the experimental data shows unequivocally that also colloidal particles as small as 30 nm in radius are experiencing a wall drag effect, which slows down their mobility and makes the diffusivity anisotropic.

[1] B. M. Ocko, X. Z. Wu, E. B. Sirota, S. K. Sinha, O. Gang and M. Deutsch *Phys. Rev.* E 55, 3164 (1997).

[2] M. C. Gerstenberger and J. S.*Pedersen Phys. Rev.* E 58, 8028 (1998).

[3] *P.* Lang, L. Willner, W. *Pyckhout*-Hintzen and *R.* Krastev Langmuir 19, 7597 (2003).

[4] H. Brenner, Chem. Eng. Sci. 16, 242 (1961).

[5] A. J. Goldman, *R.* G. Cox and H. Brenner Chem. Eng. Sci. 22, 637 (1967).

[6] M. Hosoda, K. Sakai and K. Takagi *Phys. Rev.* E 58, 6275 (1998).

[7] K. H. Lan, N. Ostrowsky and D. Sornette, *Phys. Rev.* Lett. 57, 17 (1986).

Information Technology with Nanoelectronic Systems

Magnetoelectronics and Spintronics

Ab-initio calculations of interface effects in tunnelling through MgO barriers on Fe(100)
D. Wortmann, J. Enkovaara, H. Ishida, and S. Blügel

Half-metallic ferromagnets for magnetic tunnel junctions
Ph. Mavropoulos, M. Lezaic, and S. Blügel

Rashba effect in InGaAs/InP parallel quantum wires
V.A. Guzenko, A. Bringer, J. Knobbe, H. Hardtdegen, T. Schäpers

Investigation of magnetic properties of GaN thin layers implanted with Mn, Cr, or V ions
V.A. Guzenko, N. Thillosen, A. Dahmen, R. Calarco, Th. Schäpers, L. Houben, and M. Luysberg

Towards fractional flux qubits based on ferromagnetic Josephson junctions
M. Weides, H. Kohlstedt, E. Goldobin, D. Koelle, and R. Kleiner

Enhanced exchange bias due to an ultra-thin, non-magnetic insulator spacer layer
A. Paul, D.E. Bürgler, and P. Grünberg

Rotating-field magnetoresistance of spin-valves
M. Buchmeier, A. Paul, D.E. Bürgler, and P. Grünberg

Magnetic characteristics of epitaxial Ge(Mn,Fe) diluted films – a new room temperature magnetic semiconductor?
H. Braak, R.R. Gareev, D.E. Bürgler, R. Schreiber, P. Grünberg, and C.M. Schneider

Antiferromagnetic interlayer exchange coupling across epitaxial, Ge-containing spacers
R.R. Gareev, D.E. Bürgler, R. Schreiber, H. Braak, M. Buchmeier, and P.A. Grünberg

Enhanced exchange bias in ferromagnet/antiferromagnet multilayers
A. Paul, D.E. Bürgler, and P. Grünberg

Structural and magneto-transport characterization of $Co_2Cr_xFe_{1-x}Al$ Heusler alloy films
A.D. Rata, H. Braak, D.E. Bürgler, S. Cramm, and C.M. Schneider

Single-crystalline Fe nanopillars for spin-transfer measurements
H. Dassow, R. Lehndorff, D.E. Bürgler, M. Buchmeier, P.A. Grünberg, C.M. Schneider, and A. van der Hart

Epitaxial growth and characterization of Fe thin films on wurtzite GaN(0001)
R. Meijers, R. Calarco, M. Buchmeier, D.E. Bürgler, N. Kaluza, H. Hardtdegen, M.v.d. Ahe, H.L. Bay, H. Lüth

Is (Ga,Mn)N ferromagnetic?
K. Sato, H. Katayama-Yoshida, W. Schweika, and P.H. Dederichs

Ab-initio calculations of interface effects in tunneling through MgO barriers on Fe(100)

D. Wortmann,[1] J. Enkovaara,[1] H. Ishida,[2] and S. Blügel[1]

[1]*Institute "Theory I"*

[2]*College of Humanities and Sciences, Nihon University, Sakura-josui, Tokyo 156, Japan*

Electronic tunnelling through thin oxide barriers has been extensively studied in the last couple of years. It is the fundamental basis of devices employing the tunnel-magneto-resistance effect (TMR) of spin-dependent transport. While some experiments showed a strong dependence on the metal-insulator interface in theses systems, most theoretical work gave little emphasise on the complicated interplay between electronic structure, atomic structure and the tunneling process. We investigated the influence of these details on the tunneling process in a Fe/MgO/Fe(001) interfaces using the embedded Green function method and used this method to compare different formulations of single electron transport like the Landauer formula and Bardeens approach.

INTRODUCTION

Spin-polarised tunneling in a nanostructured tunneljunction is at the heart of the rapidly developing field of spintronics. While setups containing semiconducting materials have been proposed for such magnetic tunneljunctions, most successful experiments have been performed on insulating barriers between metallic contacts. In contrast to the widely used Aluminumoxid barriers which are amorphous, MgO as a barrier material offers the possibility to produce epitaxial systems with well defined atomic positions. Recent experiments on the Fe(100)/MgO/Fe tunneljunction have demonstrated high TMR ratios for such epitaxial systems. The same setup has been used in several theoretical studies which focused on the dependence of the TMR value on the thickness of the insulating MgO barrier and on the formation of a FeO interface-layer. We extend these studies by concentrating on the effects of the actual interface configuration on the spin-polarised electron transport[1].

Fe/MgO/Fe-TUNNELJUNCTION

We will present three slightly different atomic configurations of the Fe/MgO interface. The basic structure of this interface is shown in Fig. 1. The MgO layers grow 45° rotated with respect to the Fe layers. A Fe-O bond is formed at the interface with the O atom located on top of the Fe positions, the Mg is located at the four-fold hollow site of the Fe(100) layer. The first setup we are going to investigate assumes an ideal, unrelaxed structure in which the Fe-O distance equals the interlayer spacing in MgO. For the second setup, we relaxed the structure in a supercell calculation by force calculations and total energy minimisation allowing the atoms to move according to their local symmetry. Fig. 1 also gives the interlayer distances and the interface buckling obtained in this procedure. One should note, that the deviations from the ideal unrelaxed structure are practically confined to within the monolayers forming the actual interface. The most pronounced effect can be seen in the corrugation of the interface MgO layer. The reduced coordination of the small Mg ions results in a movement of these ions towards the Fe layer. As a final, more drastic modification of the interface we consider a purely hypothetical structure in which the Mg and O atomic positions are interchanged with respect to our first setup. This breaks the Fe-O bonds at the interface and puts the O atoms on-top of the hollow sites of the Fe(100) layers. In the present paper we restrict the discussion to a single barrier thickness of 3 monolayers (ML) of MgO and a ferromagnetic alignment of the two Fe electrodes.

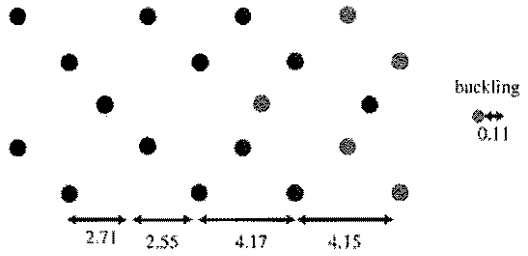

FIG. 1: Atomic structure of the Fe(100)/MgO interface. The relaxed interlayer distances and the buckling of the first MgO layer are specified in atomic units (1 a.u.=0.529 Å).

COMPUTATIONAL DETAILS

The computations have been performed within the generalised gradient approximation to the density functional theory using the full-potential augmented plane wave (FLAPW) method as implemented in the FLEUR-code[2]. The conductances were obtained within the embedded Green function method using the Landauer formula as described in Refs. [3, 4]. The structural relaxation was carried out using a set of 90 k-points in the irreducible wedge of the Brillouin-zone.

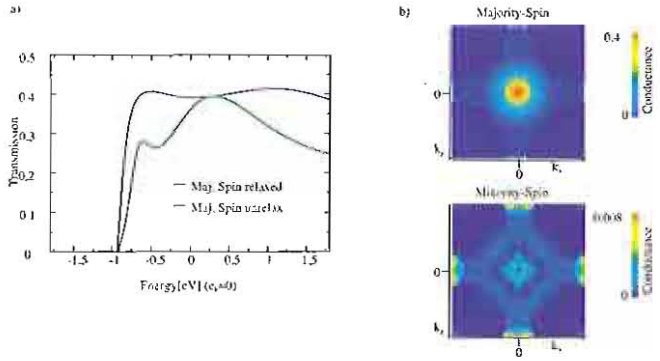

FIG. 2: Ferromagnetic Fe/MgO(3ML)/Fe junction. a) Transmission rate (in units of $\frac{e^2}{h}$). Only electrons with normal incidence are considered. The plot shows the values for the majority spin in the relaxed and the unrelaxed structure. The transmission rate of minority electrons are invisible on this scale. The Fermi energy e_F is the origin of the energy scale. b) Zero-bias Landauer-conductance (in units of $\frac{e^2}{h}$) for the relaxed tunneljunction as a function of $\vec{k}_\parallel$. $\vec{k}_\parallel = 0$ corresponds to the centre of the square Brillouin-zone. Note the difference in the scaling between the plot exhibiting the majority and minority states.

RESULTS

We will first focus on the transmission rate T (transmission probability summed over all incoming states) of electrons impinging with normal incidence ($\vec{k}_\parallel = 0$) on the barrier. Fig. 2a) shows the transmission rate for electrons of the unrelaxed and the relaxed Fe/MgO/Fe interface. Only the majority spin electrons have a significant probability of transmission through the barrier. The corresponding values for the minority spin are about two orders of magnitude smaller. A single band of propagating Bloch states in Fe is responsible for the finite transmission in the majority spin channel starting at -0.8 eV. Even though the second setup is only slightly modified by including the atomic relaxations, the small atomic displacements modify the transmission considerably.

Accidentally, at the Fermi level e_F both setups show nearly identical transmission rates $T(e_F)$ and hence the zero-bias limit of the conductance Γ given by the Landauer equation

$$\Gamma(\vec{k}_\parallel = 0) = \frac{e^2}{h} T(\vec{k}_\parallel = 0; e_F)$$

is about the same. So far, this discussion included only states of normal incidence. Fig. 2b) shows the zero-bias conductance for all $k_\parallel$ values. Only the data for the relaxed interface are shown, the unrelaxed setup shows a very similar behaviour. The total integrated conductance is clearly dominated by the majority spin by two orders of magnitude and the most significant contribution is due to the peak around $\vec{k}_\parallel \sim 0$.

In the hypothetical setup, in which the Mg and O atoms are interchanged a much more drastic effect can be seen. Fig. 3a) depicts the transmission for $\vec{k}_\parallel = 0$ for this setup. At first glance the overall shape of the transmission curve looks similar to those in Fig. 2a). However, one should note, that the values are significantly lower. This sharp decrease in the transmission probability is probably due to the decrease in coupling as a consequence of the breaking of the Fe-O bonds. However, as seen in the zero-bias conductance for the complete Brillouin zone (Fig. 2b)) at other $\vec{k}_\parallel$ values now a large contribution to the minority-spin conductance can be found. Hence, the spin-polarisation of the total conductance is strongly reduced and even changes sign in this setup.

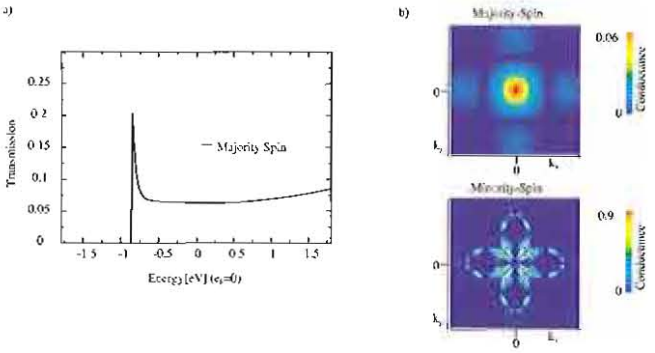

FIG. 3: Ferromagnetic Fe/MgO(3ML)/Fe junction in which the Mg and O atoms have been interchanged. For further details, see caption of Fig. 2.

SUMMARY

By investigating different atomic modifications of the Fe/MgO/Fe tunneljunctions we demonstrated that the details of the interface have in general a large effect on the conductance of the junction. This clearly demonstrates that the popular interpretation of the tunneling conductance in terms of pure bulk properties like the spin-polarisation at the Fermi-level is insufficient for a profound understanding and detailed calculations are required.

[1] D. Wortmann, G. Bihlmayer and S. Blügel 2004 *J. Phys. Cond. Mat.* **16** S5819.
[2] https://www.flapw.de
[3] D. Wortmann, H. Ishida and S. Blügel 2002 *Phys. Rev. B* **65** 165103.
[4] D. Wortmann, H. Ishida and S. Blügel 2002 *Phys. Rev. B* **66** 075113.

Half-metallic ferromagnets for magnetic tunnel junctions

Phivos Mavropoulos, Marjana Ležaić, and Stefan Blügel
Institut für Festkörperforschung, Forschungszentrum Jülich, D-52425 Jülich, Germany

Using theoretical arguments, we show that, in order to exploit half-metallic ferromagnets in tunneling magnetoresistance (TMR) junctions, it is crucial to eliminate interface states at the Fermi level within the half-metallic gap; contrary to this, no such problem arises in giant magnetoresistance elements. Moreover, based on an *a priori* understanding of the electronic structure, we propose an antiferromagnetically coupled TMR element, in which interface states are eliminated, as a paradigm of materials design from first principles. Our conclusions are supported by *ab-initio* calculations.

Half-metallic ferromagnets (HMFs) are ferromagnetic materials showing, in the ideal case, 100% spin polarization at the Fermi level E_F, due to a metallic density of states in one spin direction (usually majority spin) combined with a band gap in the other spin direction. They have drawn strong attention because of their potential applications in spintronics. In principle, HMFs under moderate voltage can carry current in only one spin direction and are thus ideal components for Giant Magnetoresistant (GMR) and Tunneling Magnetoresistant (TMR) devices. For instance, Bowen *et al.* [1] obtained in a $La_{2/3}Sr_{1/3}MnO_3/SrTiO_3/La_{2/3}Sr_{1/3}MnO_3$ junction an extreme TMR ratio higher than 1800%, attributed to the half-metallicity of $La_{2/3}Sr_{1/3}MnO_3$. In a recent work [2] we pursued a better theoretical understanding of such effects.

In TMR junctions a difficulty arises in the presence of interface states around E_F in the half-metallic gap at the metal-insulator contact. Consider, for instance, the TMR junction in Fig. 1 (A and B), where the bands are shown schematically. Panel A shows the band alignment for both spin directions for a parallel (P) alignment of the magnetzation of the half-metallic leads, while panel B shows the same for an antiparallel (AP) alignment. At the interfaces, possible localized interface states are shown for minority-spin. If interface states are present, they contribute to the tunneling current j. The current is controlled by two sequential processes: (i) by the tunneling itself, characterized by a rate $1/\tau_{\rm tunn}$, and (ii) by re-filling the interface states after an electron has tunneled out of them, with a characteristic rate of $1/\tau_{\rm fill}$ (or by emptying these states after an electron has tunneled into them, with a rate of $1/\tau_{\rm empty}$). Since these processes take place sequentially, the characteristic times $\tau_{\rm tunn}$ and $\tau_{\rm fill(empty)}$ must be additive. Then, in the AP alignment the current $j_{\rm AP}$ has a non-zero value, and expression for $j_{\rm AP}$ has the form (see also Fig. 1B)

$$j_{\rm AP} \sim 1/(\tau_{\rm fill} + \tau^{\downarrow\downarrow}_{\rm tunn}) + 1/(\tau^{\downarrow\uparrow}_{\rm tunn} + \tau_{\rm empty}). \qquad (1)$$

The first term refers to filling a spin-down interface state at the left lead in Fig. 1B (up) and tunneling to the right lead, while the second term refers to tunneling from the spin-up continuum of the left lead in Fig. 1B (down) into the interface state of the right lead, and then emptying

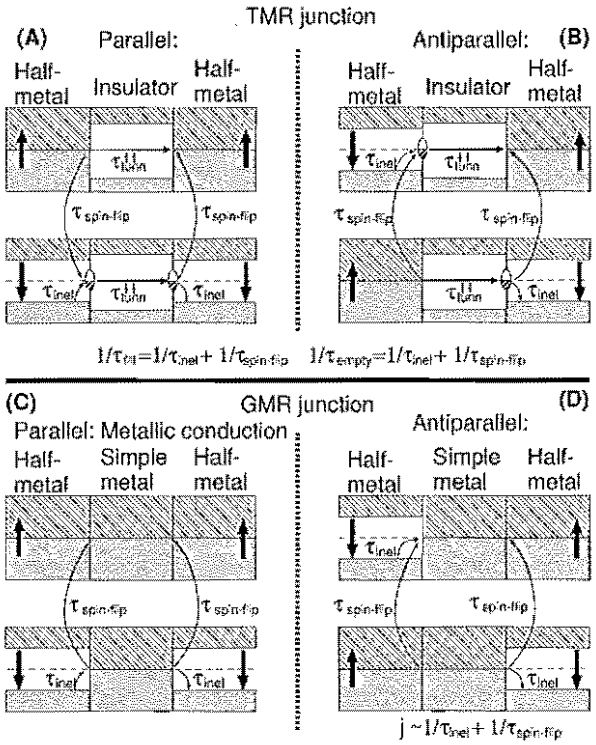

FIG. 1: Schematic band profile in TMR (A and B) and GMR (C and D) junctions using half-metallic leads. In the middle of the gaps, E_F is shown as a dashed line. Filled bands are shown as dark shaded regions, empty bands are lightly shaded; unshaded regions correspond to the band gaps. In A and C, the parallel magnetic alignment of the leads is shown for both spin directions; in B and D the antiparallel one. In the TMR case interface states appear within the half-metallic gap. Then $\tau_{\rm tunn}$ determines the current, and the half-metallic property is irrelevant. In GMR (C and D) no such problem appears, since there is metallic conduction in the parallel magnetic alignment.

it. We distinguish among four different tunneling times, for the four different cases of tunneling between majority and minority states as shown in Fig. 1 A and B. We we name these $\tau^{\uparrow\uparrow}_{\rm tunn}$, $\tau^{\downarrow\downarrow}_{\rm tunn}$, $\tau^{\downarrow\uparrow}_{\rm tunn}$, and $\tau^{\uparrow\downarrow}_{\rm tunn}$. The slowest of the two processes (i) and (ii) determines the current. If, in comparison to the slow tunneling rate, the states

are immediately refilled (or emptied) after a tunneling event, then $\tau_{\mathrm{fill(empty)}} \ll \tau_{\mathrm{tunn}}$ and j_{AP} is determined by the tunneling rate alone, irrespectively of the half-metallic band gap. Similar considerations hold for the minority-spin current in the P case.

The characteristic times τ_{fill} and τ_{empty} are determined by inelastic processes contributing with a rate $1/\tau_{\mathrm{inel}}$, and, more importantly, by the spin-orbit coupling [3] with a rate of $1/\tau_{\mathrm{spin-flip}}$. This acts in parallel with the inelastic processes, and thus

$$1/\tau_{\mathrm{fill(empty)}} = 1/\tau_{\mathrm{inel}} + 1/\tau_{\mathrm{spin-flip}} \qquad (2)$$

Additional factors can come into this equation in the presence of defects or impurities. Although the rate $1/\tau_{\mathrm{fill(empty)}}$ is low, that tunneling can be a much slower process (τ_{tunn} is long, growing exponentially with insulator thickness and barrier height). Therefore, for thick or high insulating barriers the interface states are immediately re-filled (or re-emptied) after each tunneling event, and they act as a reservoir of electrons. In this case, Eqs. (1) and (2) lead to

$$j_{\mathrm{AP}} \sim 1/\tau^{\uparrow\downarrow}_{\mathrm{tunn}} + 1/\tau^{\uparrow\downarrow}_{\mathrm{tunn}}, \quad j_{\mathrm{P}} \sim 1/\tau^{\uparrow\uparrow}_{\mathrm{tunn}} + 1/\tau^{\downarrow\downarrow}_{\mathrm{tunn}} \qquad (3)$$

This means, that the current depends only on the tunneling rates for the two spin directions and not at all on the half-metallic property of the lead. Thus some TMR ratio can appear, but no extraordinary effect can be guaranteed by the half-metallic property, unless one can eliminate the interface states.

In GMR *junctions*, on the other hand, the interface states play no significant role, as demonstrated in Fig. 1 C and D. In the P case the conduction is metallic, while in the AP case it is confined at most to the value of the spin polarization at E_F in the bulk of the half-metallic leads.

The most studied half-metallic ferromagnets are probably Heusler alloys. Unfortunately, calculations of Heusler alloy / semiconductor interfaces are conclusive on the appearance of interface states at E_F in almost all cases. On the other hand, the class of half-metallic zinc-blende pnictides and chalcogenides shows no interface states at E_F when brought in contact with zinc-blende (zb) semiconductors [4]. Therefore, we consider this class of compounds well suited for TMR *junctions*.

The zinc-blende structure, along the ⟨001⟩ direction, can be viewed as an epitaxial structure of chemically alternating atomic layers. For example, CrTe has the form $\cdots$CrTeCrTe$\cdots$. We introduce semiconducting CdTe layers which decouple two CrTe leads. The structure will have the form $\cdots$CrTeCrTeCdTeCrTeCrTe$\cdots$. This structure is still ferromagnetic and half-metallic with no interface states at E_F. But now we introduce one layer of Mn at the CrTe/CdTe interface to cause an AP coupling of the leads. The layer-by-layer structure will be $\cdots$CrTeCrTe|Mn|TeCdTe|Mn|TeCrTeCr$\cdots$ The AP coupling is expected because of the Mn-Mn interaction, by the same mechanism which brings MnTe to an antiferromagnetic state. The idea of this interface engineering is to introduce an element with higher number of valence electrons at the interface (here Mn in the place of Cr), so that the double exchange mechanism is not any more present, because the bands are filled.

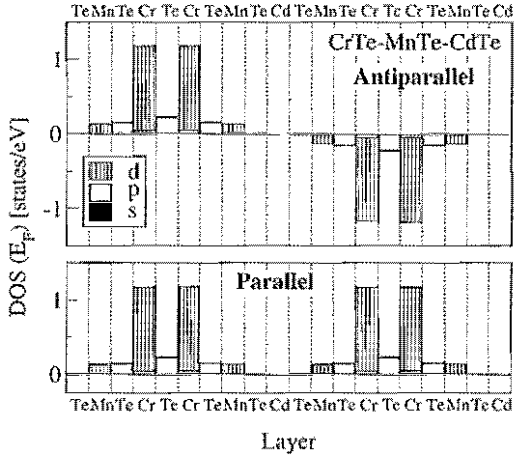

FIG. 2: Layer-resolved density of states at E_F for the junction in the ground state (top) (AP alignment) and also in the P alignment (bottom).

We verified these predictions by density-functional calculations, using used the full-potential linearized augmented plane-wave method as implemented in the FLEUR code. In the ground state, the leads are AP coupled. In addition, the Mn atoms are antiferromagnetically coupled to the Cr atoms. Each lead is by itself half-metallic, so that the whole system is non-conducting (see Fig. 2). Spin-down electrons are blocked in the first half of the *junction*, whereas spin-up electrons are blocked in the second part. The P state is half-metallic throughout the *junction* and conducting by tunneling of spin-up electrons, as can be seen in Fig. 2 (bottom). The switching energy from the AP to the P state can be tuned by introducing more CdTe layers. To show this, we compare the case without a CdTe layer, where $\Delta E = 124$ meV, to the case of Mn-CdTe-Mn ($\Delta E = 15$ meV), and then to the case of Mn-CdTeCdTe-Mn ($\Delta E = 3.6$ meV). Each additional CdTe layer lowers the energy difference by an order of magnitude. One or two more CdTe layers should decouple the layers sufficiently.

[1] M. Bowen *et al.*, Appl. Phys. Lett. **82**, 233 (2003).
[2] Ph. Mavropoulos, M. Ležaić, and S. Blügel, Phys. Rev. B **71** (2005).
[3] Ph. Mavropoulos *et al.*, Phys. Rev. B **69**, 054424 (2004);
[4] Ph. Mavropoulos, I. Galanakis, and P. H. Dederichs, J. Phys.: Condens. Matter **16**, 4261 (2004);

Rashba Effect in InGaAs/InP Parallel Quantum Wires

V. A. Guzenko[1], A. Bringer[2], J. Knobbe[1], H. Hardtdegen[1], T. Schäpers[1]
CNI – Center of Nanoelectronic Systems for Information Technology ([1]ISG, [2]IFF)

We report on the Rashba effect in InGaAs/InP quantum wires with an effective width ranging from 1.18 µm down to 210 nm. By measuring 160 wires in parallel universal conductance fluctuations could be suppressed so that the characteristic beating effect in the magnetoresistance was observable down to very low magnetic fields. A characteristic shift of the nodes in the beating pattern was found for decreasing wire width. By assuming a realistic soft-wall potential, the experimentally observed node positions could be reproduced.

The concept of many recently proposed spin electronic devices relies on one-dimensional semiconductor structures in conjunction with the Rashba effect. Here, the basic idea is the control of the spin orientation by utilizing the Rashba spin-orbit coupling [1]. In these structures the inversion asymmetry imposed by an asymmetric macroscopic potential profile of a semiconductor quantum well results in lifting of the spin-degeneracy. The Rashba spin-orbit coupling leads to a spin precession for propagating electrons. By means of a gate electrode on top of the quantum well the shape of the potential profile and thus the degree of spin-precession can be controlled [2, 3]. This mechanism opens up the possibility to design electronic devices, where the switching process is realized by changing the spin orientation in the semiconductor. Indeed, this scheme is the basis for the well-known spin-transistor proposed by by Datta and Das [4]. It was already pointed out in their proposal that the performance of the device can be considerably improved if a one-dimensional semiconductor channel a "quantum wire" between the ferromagnetic drain and source contacts is used.

We report here on a concise experimental and theoretical investigation of the Rashba effect in InGaAs/InP quantum wires. In contrast to previous experiments, a large number of wires have been measured in parallel. This allowed us to suppress universal conductance fluctuations, which are usually superimposed on the Shubnikov-de-Haas (SdH) oscillations. Consequently, the beating pattern in the magnetoresistance which indicates the presence of the Rashba effect could be resolved down to very low magnetic fields. In order to explain the measured results, detailed simulations of the energy spectrum were performed taking a realistic potential profile into account.

As can be seen in Figure 1, a pronounced beating pattern is observed in the magnetoresistance R_{xx} for all sets of quantum wires, except for the set of very narrow wires (340 nm). For the following analysis of the transport properties the relevant width of the wires is the effective electrical width W_{eff}. Information on this parameter can be obtained from the position B_{max} of the broad resistance maximum observed at low magnetic fields (Figure 1.) The peak at B_{max} originates from diffusive boundary scattering. Owing to carrier depletion at the boundary of the quantum wires, the effective width is smaller than the geometrical width.

A closer look on the beating pattern for the different sets of wires (Figure 1) reveals that the position of the first order node does not change with decreasing wire width. In

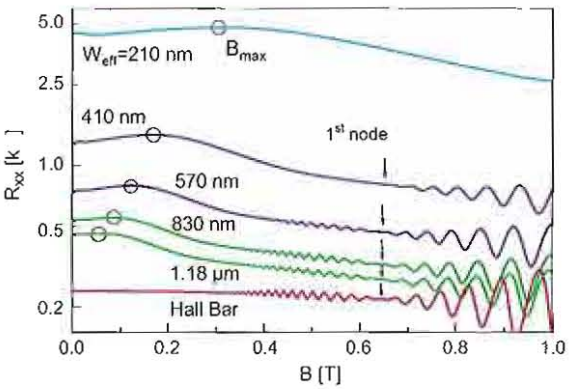

Figure 1: Shubnikov-de-Haas-oscillations of quantum wires of different effective widths (log-scale) at 0.6 K. The first order node of the beating pattern is indicated by an arrow.

contrast, the second-order node initially located at 0.3 T for the Hall bar structure shifts to higher magnetic fields for narrower wires. The Shubnikov-de-Haas-oscillations of the narrowest wires (W_{eff} = 210 nm) do not show any oscillations below 1 T. This can be attributed to the strong effect of diffusive boundary scattering resulting in a significant reduction of the electron mobility. The node positions of the beating patterns for all wire widths can be found in Figure 2.

The beating pattern in the magnetoresistance results from an interplay of an external magnetic field B and spin-orbit interaction. Without spin-orbit coupling B organizes the spectrum of the electrons in a set of degenerate Landau levels. Their energies increase linearly with B. The spin-orbit interaction mixes the Landau levels and leads to an inhomogeneous level density, responsible for the beating pattern. For a two-dimensional electron gas the energy levels are known analytically. That leads to an analytical formula for the magnetoresistance depending on B, α_R, E_F the Fermi energy, m^* the effective mass, the g-factor of the electron spins and the level broadening Γ, due to impurity scattering [5]. The material parameters m^*, g, E_F, α_R, Γ for our two-dimensional electron gas had been determined by a least mean square fit of the theoretical formula to the experimentally measured magnetoresistance (see Figure 3(a)).

With increasing B the Landau levels cross the Fermienergy. Spin-orbit coupling strongly effects the rate by which this crossing takes place. This allows a direct determination of the node position in the SdH-oscillations, as illustrated in

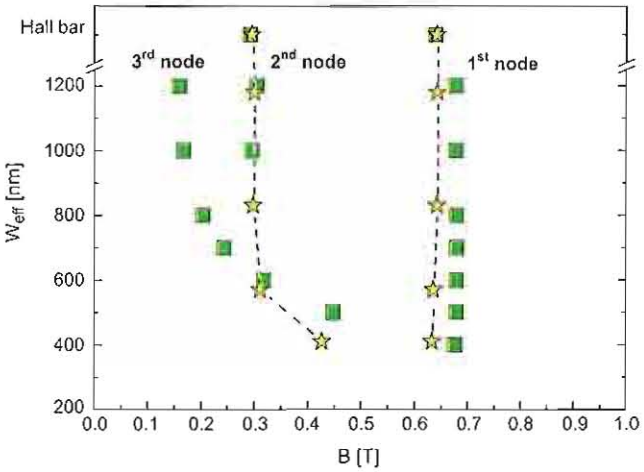

Figure 2: Positions of the first and second order nodes of the beating pattern experimental observed in the magnetoresistance (⋆). The node positions obtained from the simulation are marked by (□).

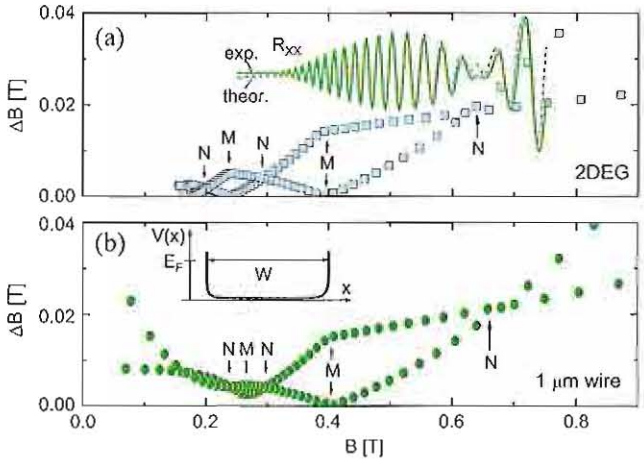

Figure 3: Spacing of neighboring Landau levels crossing E_F at different magnetic fields for a 2DEG (a) and a 1 µm wide wire (b). Position of nodes (N) and maxima (M) in the beating pattern of SdH-oscillations. The experimental and theoretical curve of R_{xx} of the 2DEG is added in (a) for comparison. A schematic illustration of the wire potential is shown in (b) as an inset.

Figure 3. When plotting the B-positions at which the energy of a Landau-level equals E_F versus their spacing one finds positions M with neighboring levels almost degenerate and positions N with equal spacing between levels. As can be seen by direct comparison to the experimental curve shown in Figure 3(a)), at M the SdH-oscillations have a large amplitude, while N are positions of nodes.

The spectrum for electrons in a wire transforms gradually from degenerate Landau-levels to quasi one-dimensional subbands, when the diameter of the Landau-orbit gets comparable to W with decreasing B. When W decreases more and more of nodes in the beating-pattern disappear and below a critical W there is no node anymore. For our structure with an assumed soft-wall potential this critical width is roughly 400 nm, as can be seen in Figure 2. Up to 600 nm two nodes can be detected. For $W > 600$ nm three nodes can clearly be identified.

We determined the nodal positions with the material parameters found for the 2 dimensional electron gas (2DEG) and they agree well with the experimentally observed positions, as can be seen in Figure 2. However, the third order node expected from the simulation could not be resolved experimentally, due to level broadening by scattering processes. We checked further the dependence on the form of the potentials. The positions of the nodes depend on W much stronger for parabolic confinement so that no reasonable agreement with experiment could be achieved [6]. Furthermore, variation of α_R in the simulation led to a large deviation of the nodes from the experimentally observed ones. Thus, our simulations confirm that α_R does not change at least down to the wire width, where no beating pattern could be observed anymore.

[1] E. I. Rashba, Fiz. Tverd. Tela (Leningrad) [Sov. Phys. Solid State **2**, 1109 (1960)] 2, 1224 (1960).
[2] J. Nitta, T. Akazaki, H. Takayanagi, and T. Enoki, Phys. Rev. Lett. **78**, 1335 (1997).
[3] G. Engels, J. Lange, Th. Schäpers, and H. Lüth, Phys. Rev. B **55**, R1958 (1997).
[4] S. Datta and B. Das, Appl. Phys. Lett. **56**, 665 (1990).
[5] J. Luo, H. Munekata, F. F. Fang, and P. J. Stiles, Phys. Rev. B **38**, 10142 (1988).
[6] J. Knobbe and Th. Schäpers, Phys. Rev. B

Investigation of magnetic properties of GaN thin layers implanted with Mn, Cr, or V ions

V.A. Guzenko,[1] N. Thillosen,[1] A. Dahmen,[1] R. Calarco,[1] Th. Schäpers,[1] L. Houben,[2] and M. Luysberg[2]

[1] *Institute of Thin Films and Interfaces (ISG1) and CNI - Center of Nanoelectronic Systems for Information Technology, Research Centre Jülich GmbH, 52425 Jülich, Germany*

[2] *Institute of Solid State Research (IFF) and CNI - Center of Nanoelectronic Systems for Information Technology, Research Centre Jülich GmbH, 52425 Jülich, Germany*

In this article we present the investigation of magnetic and structural properties of n- and p-type GaN layers implanted with Mn, Cr, or V. After implantation the samples were annealed in a N_2 atmosphere at a constant temperature in the range between 700°C and 1050°C. Measurements of the magnetization depending on magnetic field as well as on the temperature reveal typical paramagnetic behavior. Additionally, a weak antiferromagnetic coupling between the implanted ions was observed. 3d-metal rich precipitates of crystalline nature are revealed by high resolution transmission electron microscopy.

An improved spin injection efficiency [1] and local electrostatic control of magnetic moments make diluted magnetic semiconductors (DMS) of great interest for designing spintronic devices [2, 3]. DMS based on GaN attracted attention due to prediction of room temperature ferromagnetism, firstly in GaN:Mn [4] and later in GaN:Cr and GaN:V [5, 6]. It has been proposed that the ferromagnetic state in GaN:Mn with Mn content up to 10%, in GaN:Cr and GaN:V with even higher impurity concentration should be achieved. According to the band structure calculations by Sato *et al.* [5, 6], ferromagnetic ordering, pertaining to the partial filling of the anti-bonding impurity states, seems to be possible in n-type GaN:V. The choice of material with n-type conductivity would allow to avoid the technological difficulties during the preparation of the ohmic contacts.

Many techniques were employed for the fabrication of GaN-based DMS. Various groups reported on either ferromagnetic [7–11] or paramagnetic [12, 13], antiferromagnetic [14] or spin-glass [15] behavior. The origin of the ferromagnetism in GaN-based DMS is thus far from being understood. Hence, the question whether it is possible to fabricate homogeneous ferromagnetic layers without precipitation is of particular importance and still open.

The GaN layers were grown by MOCVD on a (0001) sapphire substrate. The overview of the samples used is given in Table I. Mn^+, Cr^+ or V^+ ions were implanted along [0001] direction with an energy of 200 keV and a dose of 5×10^{16} cm^{-2}. During the implantation the samples were held at a temperature of 350°C, to prevent amorphization. Implanted samples were cut in pieces, cleaned in HCl to remove residual unintentional ferromagnetic contaminations and, subsequently, each piece was annealed at 700°C for 5 min in flowing N_2 atmosphere. The magnetization of the samples was measured by a SQUID magnetometer Quantum Design MPMS7. Particular attention has been paid to enhance the sensitivity of the experimental setup and to reduce the systematic error due to the background signal from the sample holder (for details refer to [13]).

TABLE I: Sample overview.

Sample	Implant	Thickness (μm)		Dopant	
		undoped	doped	Element	Content(cm^{-3})
nMn	Mn	3.0	1.5	Si	2×10^{17}
nCr	Cr	3.0	1.5	Si	2×10^{17}
nV	V	3.0	1.5	Si	2×10^{17}
pMn	Mn	1.0	1.0	Mg	2×10^{17}

In Fig. 1a the magnetization as a function of the magnetic field for samples nMn and pMn, measured at 2, 10 and 100 K, is shown. The data are presented in units of Bohr magnetons per atom, calculated as $m/(\mu_B AD)$, where m is the measured magnetic moment, A the sample area, D the implantation dose, and μ_B the one Bohr magneton. Because of the inhomogeneous ion depth distribution, this gives only a rough estimate of the polarization degree of the spins of the 3d-ions. The data show a typical paramagnetic behavior and can be fitted well by the Brillouin function $B_S(B,T)$ for temperatures of 3, 10 and 100 K, and spin $S = 5/2$. The diamagnetic background signal was subtracted by measuring the magnetization curve of the corresponding as grown samples. No considerable difference between p- and n-doped samples could be observed. A reasonable fit for 2 K could be only achieved for an effective temperature T_{eff} slightly higher than the experimental one T_{exp}. At 10 and 100 K the difference between T_{eff} and T_{exp} is negligible. The magnetization saturates much slower than for the ferromagnetic GaMnAs [2], and a discrepancy between the measured and calculated saturation magnetization was observed. The experimentally determined magnetization M at 2 K is lower by a factor of 0.22 in respect to the theoretically expected one M_{calc}. We denominate this factor by $x_{\text{eff}} \equiv M/M_{\text{calc}}$. The evaluation of the magnetization curves of the samples nMn, nCr and nV at 2 K and 10 K reveals a similar behavior for the Cr ($S = 2$) and V ($S = 3/2$) implanted samples (Fig. 1b). $x_{\text{eff}} \approx 0.28$ for sample nV and 0.23 for sample nCr at 2 K were evaluated.

Similar effect was observed by Graf *et al.* [12] and

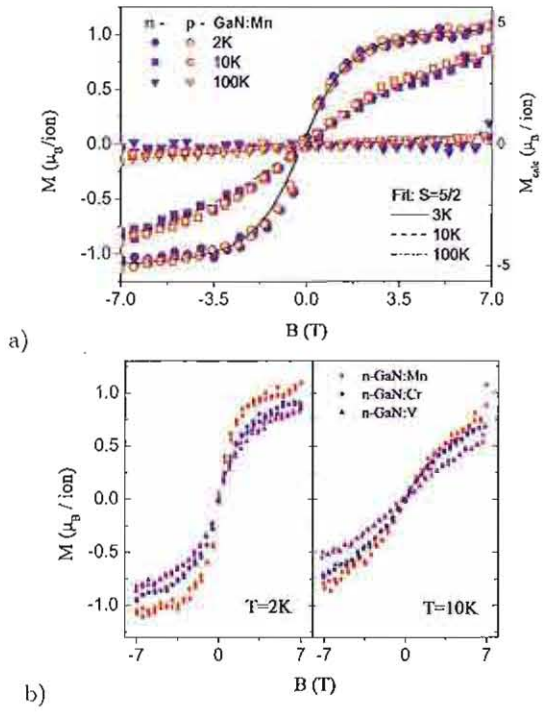

FIG. 1: a) Magnetization curves of the samples nMn and pMn. The lines display fits by the Brillouin function. b) Magnetization curves of n-type GaN:X (X = Mn, Cr or V).

Zając *et al.* [14]. Magnetization of highly diluted GaN:Mn could be described by Brillouin function B_S. With increasing 3d-impurity content the formation of pairs and larger clusters of antiferromagnetically ordered spins takes place, which respond to the applied magnetic field less effectively then single ions. For such samples an effective temperature $T_{\text{eff}} > T_{\text{exp}}$ and an effective impurity content Nx_{eff} with $x_{\text{eff}} < 1$ can be introduced. Thus $M = Nx_{\text{eff}} g\mu_B S B_S(B, T_{\text{eff}})$, with N the total ion number, $g \approx 2$ the Landé factor and μ_B the Bohr magneton.

An indication of the paramagnetic behavior can also be found in the temperature dependency of all samples, shown in Fig. 2. All data can be fitted by the Curie-Weiss law $1/(T - \Theta)$, with the Curie-Weiss temperatures Θ having negative values, which is an indication of the antiferromagnetic coupling between implanted ions.

All samples became almost insulating after ion implantation. This can be attributed to deep electron traps, related to the complexes between the implanted ions and native defects as well as to radiation damage defects [16]. The low concentration of free carriers is a possible reason of an antiferromagnetic, rather than a ferromagnetic coupling between implanted ions. Furthermore, the presence of the precipitates of the Cr-rich secondary phase (possibly antiferromagnetic) was demonstrated by the high-resolution TEM [13].

In conclusion, studies of magnetic properties of GaN:X (X = Mn, Cr or V) layers, prepared by ion implantation, reveal paramagnetic behavior with an antiferromagnetic coupling between the 3d-metal ions. This behavior can be explained by the low concentration of the free carriers mediating the ferromagnetism and formation of precipitates of antiferromagnetic secondary phase. No indications of a ferromagnetic ordering was found.

We thank Dr. A. Kaluza and Dr. B. Schineller for supplying the doped GaN wafers.

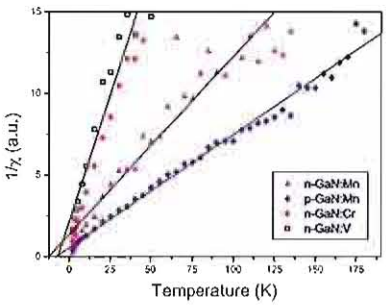

FIG. 2: Temperature dependence of the magnetization of all samples (nMn-nV, pMn) measured at a field of 50 mT.

[1] G. Schmidt, D. Ferrand, L. W. Molenkamp, A. T. Filip, and B. J. van Wees, Phys. Rev. B **62**, R4790 (2000).
[2] H. Ohno, Science **281**, 951 (1998).
[3] T. Figielski and T. Wosinski, Physica E **9**, 295 (2001).
[4] T. Dietl, H. Ohno, F. Matsukura, J. Cibert, and D. Ferrand, Science **287**, 1019 (2000).
[5] K. Sato and H. Katayama-Yoshida, Jap. J. Appl. Phys. **40**, L485 (2001).
[6] K. Sato, H. Katayama-Yoshida, and P. H. Dederichs, J. Supercond. **16**, 31 (2003).
[7] M. L. Reed et al., Appl. Phys. Lett. **79**, 3473 (2001).
[8] M. L. Reed et al., Mat. Lett. **51**, 500 (2001).
[9] N. Theodoropoulou et al., Appl. Phys. Lett. **78**, 3475 (2001).
[10] J. S. Lee et al., J. Appl. Phys. **93**, 4512 (2003).
[11] J. M. Baik et al., Phys. Stat. Sol. B **234**, 943 (2002).
[12] T. Graf et al., J. Appl. Phys. **93**, 9697 (2003).
[13] V. Guzenko et al., Journal of Applied Physics **96**, 5663 (2004).
[14] M. Zając et al., Appl. Phys. Lett. **79**, 2432 (2001).
[15] S. Dhar et al., Appl. Phys. Lett. **82**, 2077 (2003).
[16] A. Y. Polyakov et al., J. Appl. Phys. **93**, 5388 (2003).

Towards fractional flux qubits based on ferromagnetic Josephson junctions

M. Weides[1], H. Kohlstedt[1], E. Goldobin[2], D. Koelle[2] and R. Kleiner[2]

[1]*CNI - Center of Nanoelectronic Systems for Information Technology*
Institute for Electronic Materials, Research Centre Juelich, D-52425 Juelich, Germany
[2]*Physikalisches Institut - Experimentalphysik II, Universität Tübingen*

We present ferromagnetic Nb/Al_2O_3/$Ni_{60}Cu_{40}$/Nb Josephson junctions (SIFS) with an ultrathin Al_2O_3 tunnel barrier. The junction fabrication was optimized regarding junction insulation and homogeneity of current transport. Using ion-beam-etching and anodic oxidation we defined and insulated the junction mesas. The additional 2 nm thin Cu layer below the ferromagnetic NiCu (SINFS) lowered interface roughness and ensured very homogeneous current transport. A high yield of junctional devices with j_c spreads less than 2% was obtained. Our fabrication procedure may offer a solution for the strict uniformity requirements for flux based qubits.

The realization of qubits for quantum computation attracts considerable interest. One approach is to use low Tc Niobium Josephson junctions (JJ) which utilize an ultrathin ferromagnetic layer to change the coupling of the two superconducting electrodes [1]. Whether the junction is in the 0 or π coupled state depends on the properties of ferromagnetic layer and especially its thickness d_F .

The first step to realize a qubit is the formation of a so called semifluxon. Recent theoretical considerations predict fractional flux-quanta in SIFS junctions with a step-like ferromagnetic layer [2]. Exploiting such semifluxons for qubits systems [3] (Fig. 1) demands low spread of extrinsic and intrinsic parameters, e.g. junction area and current density.

The fabrication of SIFS multi-layers was performed in-situ by a computer-controlled Leybold Univex 450B magnetron sputtering system. Thermally oxidized 4-inch Si wafer served as substrates. The wafers were clamped onto a water cooled Cu-block. First a 120 nm Nb bottom electrode and an 5 nm thick Al overlayer were deposited. Subsequently the aluminium was oxidized for 30 min in a separate chamber at an oxygen partial pressure ranging from 0.015 to 0.45 mbar. As ferromagnetic layer we deposited the diluted $Ni_{60}Cu_{40}$ alloy (T_C = 225K), followed by a 40 nm Nb cap-layer. For realization of "wedge" shaped NiCu-layer, the substrate and sputter target are shifted about half the substrate length. This facilitates the preparation of SIFS (and SINFS, N: normal metal) junctions with different F-layer thicknesses to avoid the inevitable run to run variations. In this way we prepared F-layers ranging between 1 and 15 nm. The background pressure was 5*10 7 mbar.

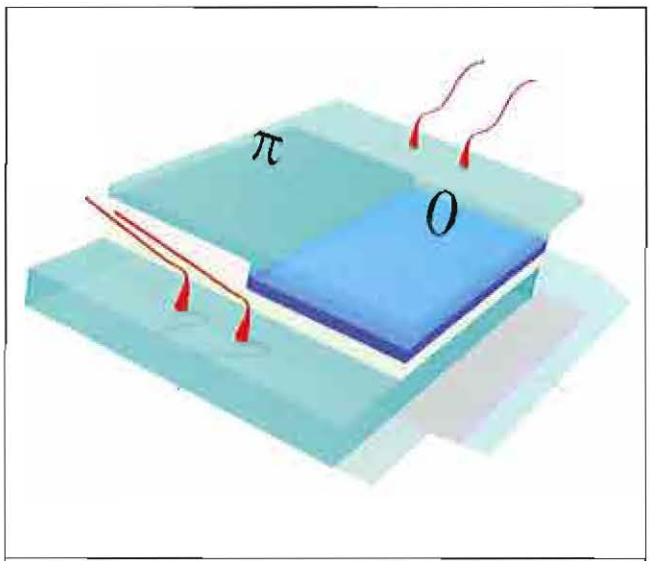

Figure 1 Josephson junction with step in ferromagnetic interlayer and 0-π phase discontinuity. Fractional flux $\Phi_0/2$ (Semifluxon) appears along 0-π phase step.

Tunnel junctions with a crossbar geometry were patterned using optical lithography and Ar ion beam milling. A three level photo mask procedure was applied. First the bottom SIFS-layer areas were defined by a lift-off process. After the lift-off various kinds of tunnel junctions were defined by applying the second photo mask step followed by reactive ion beam etching for the Nb layer and Ar for the NiCu and Al layers. The etching was controlled by a mass spectrometer and the procedure was stopped by reaching the Al_2O_3 tunnel barrier. During etching the substrate was tilted by 70 and rotated to avoid etch fences at the edges of the mesas. The mesas were isolated by SNEAP (Selective Niobium Anodization Process). It is interesting to note that the anodization was successful in the presence of NiCu layer. We obtained no problems with parallel currents through the NiCu layer during anodization. Probably the ferromagnetic layer is so thin that it is immediately overgrown by Nb_2O_5 and Al_2O_3 shortly after starting the anodization procedure. At a rate about 1 V/s we anodized the junction up to a voltage of 60 V (corresponding to 51 nm of anodized Niobium)

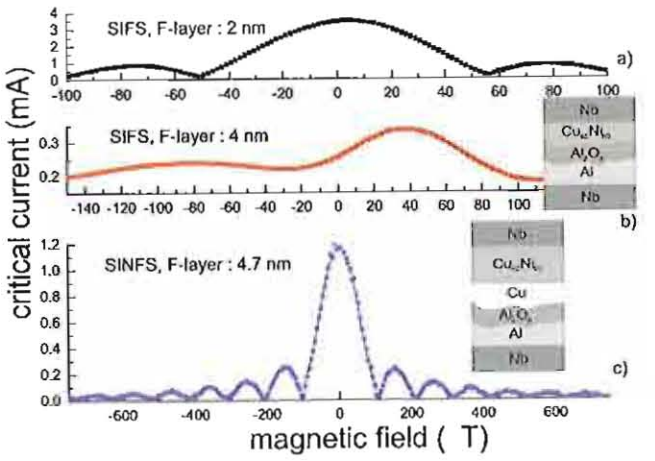

Figure 2: Ic(H) of (a) SIFS (2 nm NiCu), (b) SIFS (4 nm NiCu) and (c) SINFS (Cu 2 nm, NiCu 4.7 nm) stack. Oxygen pressure is 0.45 mbar for SIFS and 0.015 mbar for SINFS type.

was reached. The form factor of 2.3 for Niob corresponds to 120 nm of formed Nb_2O_5, providing a com plete side coverage of the barrier and the ferromagnetic layer.

In the last photo mask step the wiring layer was defined. After a slight ion beam etching to achieve low contact resistance, a 300 nm thick Nb wiring was deposited.

For the ferromagnetic SIFS and SINFS junctions the areas were 10.000 μm^2 large. More details can be found in [4].

The Fraunhofer modulation of I_c is seen in Fig. 2 for SIFS junctions with 2 nm (a) and 4 nm (b) NiCu layers and a SINFS junction with 2 nm Cu and 4.7 nm NiCu (c). All the ferromagnetic junction investigated in this work are still in 0 coupled regime [5]. In general the interface barrier roughness leads to inhomogeneous current transport, which can cancel out the coherent Josephson coupling and leads to disturbed Fraunhofer pattern. The conditions for non-uniform supercurrent are given by the ratio of NiCu interface roughness over the decay length ξ_{F1} and oscillation length ξ_{F2} of the supercurrent. In $Ni_{60}Cu_{40}$ these values are about 1 3 nm, to be published in [5]. For thin (below 3 nm) NiCu layers we see a clean Fraunhofer modulation (Fig. 2 (a)). However for thicker NiCu layers the $I_c(H)$ deviated considerably (Fig. 2 (b)). Although electrical measurements on SIS junctions suggested a high quality barrier this suggests some finite roughness of the Al_2O_3 tunnel barrier and/or of the NiCu layer.

As AFM-measurements indicated the 2 nm NiCu layer on-top the Al_2O_3 forms similar roughness contours, so effective thickness of NiCu is constant and supercurrent transport remains homogeneous as seen in Fig. 1(a). When doubling the thickness of NiCu to 4.7 nm its top roughness is about 0.9 nm and the effective NiCu layer thickness is not uniform. This is supported by transport measurements seen in Fig. 1(b). By including a 2 nm Cu layer under the NiCu the $I_c(H)$ we recovered the clean Fraunhofern pattern. We

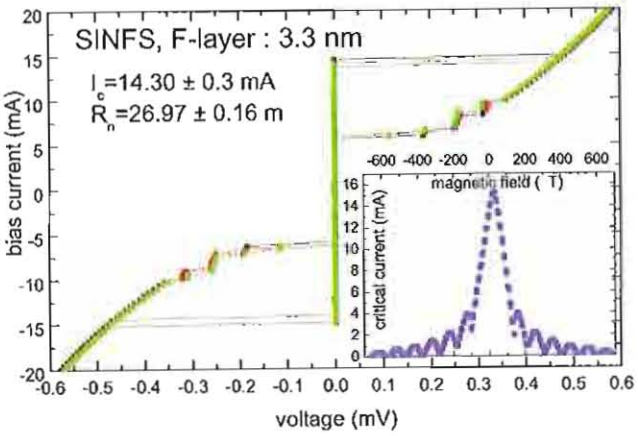

Figure 3: IVs of three SINFS junction, O2 oxidation pressure is 0.015 mbar. $\delta I_c = 2\%$, $\delta R_n = 0.5\%$.

could even use the thinner Al_2O_3 barrier for SINFS, although this should increase the Al_2O_3 roughness slightly. The Cu-layer between Al_2O_3 and NiCu smoothes the lower NiCu-interface and provides an uniform effective ferromagnetic layer. Even for thicker (up to 8.5 nm) NiCu- layers we see uniform supercurrents through such SINFS junctions (Fig. 2(c)). For NiCu thicker than 8.5 nm we can not measure any supercurrent due to the strong Cooper pair breaking. This will be reported elsewhere [5].The strong proximity effect of Cu leads to weak pair breaking of the super-current in the N-layer. SIFS and SINFS samples (N: 2 nm Cu layer) showed identical critical current densities, so junction properties are determined by the ferromagnetic layer. For all NiCu thicknesses we obtained a low junction to junction deviation. In Fig. 3 the characteristics of three underdamped SINFS junctions with a 3.3 nm NiCu layer are shown. The parameter spread of critical current and normal resistance (and therefore β_c) is below 2% (I_c = 14, 3 mA, R_n = 26.97 mΩ and β_c = 5.0). Even the very sensitive subgap characteristics are nearly identical for all junctions as seen in Fig. 3. These junction exhibit a high-quality $I_c(H)$ pattern (inset of Fig. 3), just like the Fraunhofern pattern of SINFS with 4.7 nm NiCu layer in Fig. 1 (c).

Motivated by the demand for ferromagnetic JJ with low parameter spread, we have developed an alternative fabrication process. Transport measurements on SINFS junction showed that the quality of junctions was considerable improved using Nb_2O_5 as insulator and planarization of the ferromagnetic interlayer by an additional Cu layer. Our fabrication procedure may offer a solution for the strict uniformity requirements for the formation of qubits.

[1] A. Buzdin, JETP Lett. 78 (2003) 583–586.

[2] E. Goldobin, D. Koelle, R. Kleiner, Phys. Rev. B 66 (2002)

[3] E. Goldobin, K. Vogel, O. Crasser, R. Walser, W. Schleich, D. Koelle, R. Kleiner, Phys. Rev. B 72 (2005)

[4] M. Weides et al., cond-mat/0511546, to published in Physica C

[5] M. Weides, H. Kohlstedt et al., paper in preparation

Enhanced exchange bias due to an ultra-thin, non-magnetic insulator spacer layer

A. Paul, D. E. Bürgler, and P. Grünberg
Institute "Electronic Properties"

The exchange bias effect of Co/CoO bilayers is found to significantly increase when an ultra-thin, non-magnetic insulating AlO_x spacer is added at the ferromagnet/antiferromagnet interface. The dependence on the spacer thickness is non-monotonic with a maximum two-fold enhancement of the exchange bias field H_{EB} at a spacer thickness of 1.0 nm. These observations are explained in terms of a discontinuous layer structure of the spacer and its thickness evolution. There is no indication of an intrinsic magnetic interaction across the AlO_x spacer layer.

When a ferromagnet/antiferromagnet (FM/AF) bilayer is cooled in an external magnetic field below the blocking temperature of the AF, a direct exchange coupling between the FM and AF layers gives rise to a shift of the magnetization loop of the FM layer along the field axis. This shift of the loop center away from zero external field is termed *exchange bias field*, H_{EB}. Although the microscopic origin is not yet fully understood, exchange-bias has attracted much interest due to the application in magnetoresistive sensors [1].

A basic question concerns the range of the exchange bias interaction: Whether exchange bias results from nearest-neighbor coupling at the FM/AF interface only is a matter of ongoing debate, because long-range contributions to exchange bias have been claimed [2] as well as negated [3] in earlier work. Here, we study the effect of an insulting spacer layer, namely AlO_x, on the exchange bias effect [4].

$CoO/AlO_x/Co$ samples are prepared in a dc magnetron sputtering system with a base pressure of 1×10^{-7} mbar. Pieces of an oxidized Si(100) wafer with a size of about 1 cm^2 serve as substrates. The deposition starts by growing a Co layer, which is subsequently oxidized *in-situ* to obtain the antiferromagnetic CoO layer. Next, an Al layer is grown and also oxidized *in-situ* to form the insulating AlO_x spacer layer before depositing the top Co layer and a capping layer. The thickness of the top Co layer is kept constant at 5 nm, while the bottom Co and the Al thicknesses are varied. Magnetization loops are measured by means of a superconducting quantum interference device (SQUID) at 10 K after field cooling in an external field $H_{FC} = 4$ kOe from room temperature to 10 K, *i.e.* well below the blocking temperature $T_B \approx 180$ K of CoO. We employ our standardized ultra-violet light (UV) assisted oxidation procedure developed for TMR structures for oxidizing both Co and Al: The O_2 pressure is increased to 200 or 20 mbar for Co or Al, respectively, and the samples are kept at 50°C while irradiated by UV light for one hour. In order to choose a suitable thickness t_0 of the bottom Co layer prior to the oxidation procedure, we measure magnetization loops for different initial thicknesses $t = 18$, 7, and 4.5 nm (Fig. 1). H_{EB} and the coercivity decrease with t and vanish at $t_0 \approx 7.0$ nm. The magnetization signal does not completely vanish, even for $t = 4.5$ nm a small signal is visible. We attribute it to ferromagnetic material (*i.e.* non-oxidized Co) which is not in contact with CoO and to a background signal from the sample holder.

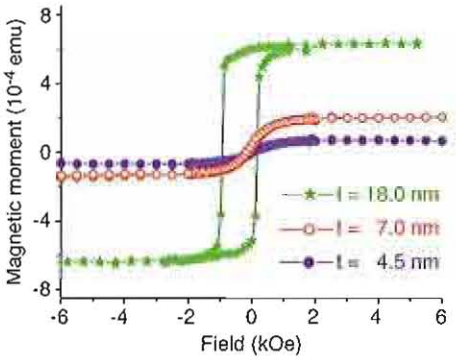

FIG. 1: SQUID magnetization loops of Co layers with different thicknesses t after oxidation: H_{EB} and the coercive field vanish for $t < t_0 \approx 7$ nm.

The dependence of H_{EB} on the thickness of the AlO_x spacer is shown in Fig. 2, where the bottom Co thickness is fixed at $t = t_0 = 7.0$ nm and the Al thickness t_{Al} is varied from 0.5 to 2.0 nm. All loops except that for $t_{Al} = 0.5$ nm are sheared and indicate a distribution of exchange bias fields. The averaged exchange bias field H_{EB} is determined using the following definition,

$$\int_{-\infty}^{-H_{EB}} \{M_{\searrow}(H) - M_{\nearrow}(H)\}dH = \int_{-H_{EB}}^{\infty} \{M_{\searrow}(H) - M_{\nearrow}(H)\}dH, \quad (1)$$

where $M_{\searrow(\nearrow)}(H)$ are the magnetization branches for decreasing (increasing) field. Thus, $-H_{EB}$ is the field, that bisects the area enclosed by the magnetization loop. This definition is well suited for sheared loops and minimizes the influence of the background signals discussed in the context of Fig. 1. The extracted averaged H_{EB} values are marked in Figs. 2(a)-(f) by dashed, red lines and plotted in Fig. 2(g). First, H_{EB} is lower compared to the sample without AlO_x spacer (black symbol), but then significantly increases and reaches a value more than twice as high than for $t_{Al} = 1.0$ nm. For a further increase of the spacer thickness the exchange bias fields decrease and become negligible for $t_{Al} \geq 2.0$ nm. The blue dotted line in Fig. 2(g) is a fit to the data for $t_{Al} \geq 1.0$ nm using the expression $H_{EB} \propto \exp(-t_{Al}/T)$. The decay length $T = 0.3$ nm is smaller than previously found for metallic spacers ($T \approx 1$–5 nm [2, 5]) and does not support a long-range interaction through the insulator spacer.

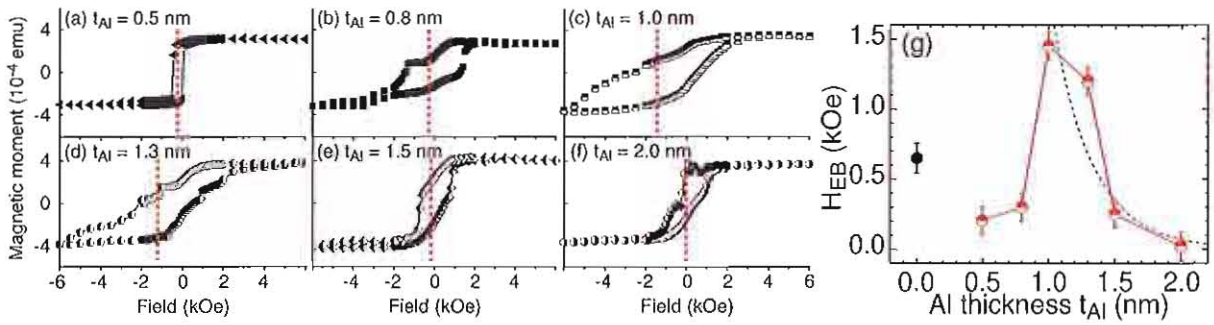

FIG. 2: SQUID magnetization loops of $CoO/AlO_x(t_{Al})/Co(5\ nm)$ structures with different initial Al thicknesses t_{Al}. The initial bottom Co thickness is fixed at $t = t_0 = 7.0$ nm. Dashed, vertical lines indicate the H_{EB} values determined according to Eq. (1) and plotted in (g). The black symbol represents a sample without AlO_x spacer. The dotted blue line is an exponential fit yielding a decay length $T \approx 0.3$ nm.

Our observations differ from previous reports dealing with metallic spacers in two aspects: (i) We observe an *enhancement* of $|H_{EB}|$ compared to the situation without spacer and (ii) the dependence of H_{EB} on the spacer thickness is *strongly non-monotonic*. For metallic spacers the exchange bias fields decrease exponentially with thickness. We relate both observations to the growth and structure of the AlO_x spacer layer on CoO. From cross-sectional TEM images it is evident that the spacers are discontinuous up to thicknesses of almost 2 nm. The increase of H_{EB} at $t_{Al} = 1.0$ nm by more than a factor of two compared to the situation without an AlO_x spacer can then be understood in the framework of the model put forward and numerically simulated by Ernult *et al.* [6]: These authors considered the influence of non-magnetic impurities in the form of Au islands inserted at the AF/FM interface and found an enhancement of the exchange bias effect. In their model, bubble-like domain walls are formed in the AF between the edges of neighboring Au islands when the FM film is magnetized in the direction opposite to H_{FC}, because the AF spins in direct contact with the FM film are dragged along with the FM magnetization. In the areas underneath the islands, however, the AF spins are not reversed. They can keep the memory of their initial (field-cooled) state and enhance the exchange bias effect by exerting via the bubble-like domain walls a restoring torque on the reversed AF spins and the FM magnetization.

The initial decrease of H_{EB} from about 650 Oe without spacer to 200 and 300 Oe at $t_{Al} = 0.5$ and 0.8 nm, respectively [Fig. 2(g)], cannot be explained by a further oxidation of the uncovered CoO in the holes of the spacer during the formation of AlO_x, because H_{EB} is decreasing instead of increasing. A degradation of the AF order right at the CoO interface towards the FM layer due to the additional oxidation (in contrast to the defect formation at a distance from the interface) could explain the decreasing H_{EB} for small t_{Al}. However, there is no mechanism that recovers the AF order at the CoO interface when t_{Al} approaches 1.0 nm. In particular, the formation of bubble-like domains discussed above relies on an non-degraded interface between the islands, otherwise the bubble-like domains would not form. Therefore we dismiss a direct influence of the Al oxidation process. We rather suggest that the formation of the bubble-like domain walls strongly depends on the AlO_x island density which is not varied experimentally nor theoretically in Ref. [6]: For low island coverage and thus large separation of the islands, the formation of the bubble-like domain walls is unfavorable due to the large domain wall areas. In this case, the AlO_x islands just reduce the contact area between CoO and the top Co layer, and thus H_{EB} is also reduced. On the other hand, for $t_{Al} > 1.0$ nm, the AlO_x islands coalesce, the interaction area diminishes, and H_{EB} gradually vanishes [Fig. 2(g)]. Therefore, there exists an optimum AlO_x islands density, for which the enhancement of H_{EB} due to the bubble-like domain walls is maximized. At $t_{Al} = 2.0$ nm, the spacer layer is continuous and, accordingly, the exchange bias effect is negligible. Therefore, the decay of H_{EB} in Fig. 2(g) depends on the evolution of the AlO_x island density and does not reflect the characteristic lengthscale of an intrinsic magnetic interaction across the spacer.

In conclusion, we have observed a significant enhancement in the exchange bias field due to an ultrathin (≈ 1.0 nm), non-magnetic insulator spacer at the AF/FM interface of exchange-biased CoO/Co bilayers which is explained in terms of the discontinuous structure of the spacer layer. The experiments do not indicate an intrinsic magnetic interaction through AlO_x or a long-range contribution to the exchange bias effect. The proposed mechanism based on the model of Ernult *et al.* [6] could be optimized by employing micro-engineered or self-organized structured spacer layers to significantly enhance the exchange bias effect for future spintronic devices.

[1] B. Dieny, J. Magn. Magn. Mater. **136**, 335 (1994).
[2] N. J. Gökemeijer, T. Ambrose, and C. L. Chien, Phys. Rev. Lett. **79**, 4270 (1997).
[3] L. Thomas, A. J. Kellock, and S. S. P. Parkin, J. Appl. Phys. **87**, 5061 (2000).
[4] A. Paul, D. E. Bürgler, M. Luysberg, and P. Grünberg, Europhys. Lett. **68**, 233 (2004).
[5] M. Gryters, M. Cierlings, and D. Riegel, Phys. Rev. Lett. **64**, 132401 (2001).
[6] F. Ernult *et al.*, J. Appl. Phys. **94**, 6678 (2003).

Rotating-field magnetoresistance of spin-valves

Matthias Buchmeier, Amitesh Paul, Daniel E. Bürgler, and Peter Grünberg
Institute of Solid State Research, Electronic Properties (IFF6) and
CNI – Center of Nanoelectronic Systems for Information Technology

We investigate the magnetoresistance of spin-valves by rotating the magnetic field with different fixed strengths. The data reflect in general a mixture of giant and anisotropic magnetoresistance (GMR and AMR). We present an experimental procedure to suppress all AMR contributions without disturbing the GMR response. The angular MR curves are fitted with a single-domain model to determine with high precision the exchange bias field, the uniaxial anisotropies, the GMR ratio, and the interlayer coupling field.

A standard spin-valve structure consists of two ferromagnetic (FM) layers separated by a non-magnetic (noble) metal spacer. The fixed FM layer is pinned by an antiferromagnetic (AF) layer [1] due to the exchange bias field $|H_{\mathrm{EB}}|$. The other FM layer can freely follow the external field. Magnetic sensors based the giant magnetoresistance (GMR) in spin-valves require a low coercive field of the free layer and a large H_{EB} of the pinned layer.

We prepare our spin-valves by dc magnetron sputtering. The layer sequence grown on oxidized Si substrates is Ta(5.0 nm)/NiFe(3.0 nm)/FeMn (15.5 nm)/NiFe(3.0 nm)/Co(2.0 nm)/Cu(3.5 nm)/Co(2.0 nm)/NiFe(7.0 nm). The NiFe film on top of the AF FeMn layer together with a thin Co polarizing layer represent the fixed layer. The free layer also consists of a Co polarizing layer and NiFe. Polarizing Co layers on both sides of the spacer enhance the GMR ratio due to the higher degree of spin polarization of Co. Samples are first annealed in an inert atmosphere of N_2 gas for 10 minutes at 473 K, *i.e.* above the FeMn Néel temperature $T_{\mathrm{N}} = 458$ K, and subsequently field-cooled to RT in a field of 130 Oe.

We employ a conventional four-probe dc technique with the applied constant current flowing parallel to the exchange bias direction (EBD) of the pinned layer, *i.e.* the direction of magnetic field during field-cooling. The external field is rotated in the sample plane with different, but fixed magnitudes [2, 3]. Unpatterned square or rectangular samples with typical linear dimensions of the order of 10 mm are contacted by needles or wire-bonding. We used different contact geometries defined in Fig. 1. The contact geometry has a strong influence on the current distribution in the sample. The GMR effect depends on the relative angle $\theta_{\mathrm{f}} - \theta_{\mathrm{p}}$ between the free and pinned layer and is for isotropic polycrystalline samples independent of the in-plane current direction. Therefore, the measured GMR ratio is not affected by the contact geometry. On the other hand, the macroscopically measured AMR ratio is strongly dependent on the current distribution, because AMR depends on the angle between the local magnetization and the current direction. The AMR ratio measured for a homogeneous current distribution reflects in good approximation the microscopic AMR ratio. For current distribution where the current predominantly flows along circular trajectories, local AMR contributions average out, and the macroscopically measured AMR ratio is strongly reduced. We confirm these expectations by finite-element simulations. In Fig. 1 we show the results for two contact geometries. The green parts labeled "current" are the left and upper part of the current distribution in a rectangular sample in L- and T-geometry, respectively. The other halves of the sample follow from mirroring at the right and bottom edge, respectively. The red parts labeled "AMR" show the macroscopically measurable AMR ratio when the current contact is fixed at the the position marked by a cross and the voltage contact is moved across the sample. The color levels render the macroscopically measured AMR ratio normalized to the microscopic AMR ratio (note the different scale bars). In Fig. 1(a) the current distribution is more homogeneous and accordingly the variations of the measured AMR are small. In the L-geometry –the second contact lies on a horizontal line with the fixed contact– the macroscopic AMR approximately equals the microscopic. In Fig. 1(b) the current distribution is largely inhomogeneous, and the measured AMR ratio is almost completely suppressed in some regions or strongly enhanced in others. In the T-geometry with both contact lying on vertical line, the measured AMR ratio is only a few percent of the microscopic AMR ratio.

We model the magnetic state of the system in a single-domain approach assuming rigid in-plane magnetizations [4]. The equilibrium magnetization angles of the free, pinned, and possible additional FM layers at a given external field $\vec{H}$ are calculated numerically from the total minima of the free energy. In our case, the NiFe textur-

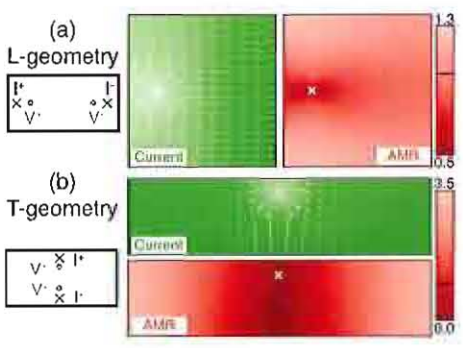

FIG. 1: Finite-element simulation for a rectangular sample contacted in (a) L-geometry and (b) T-geometry.

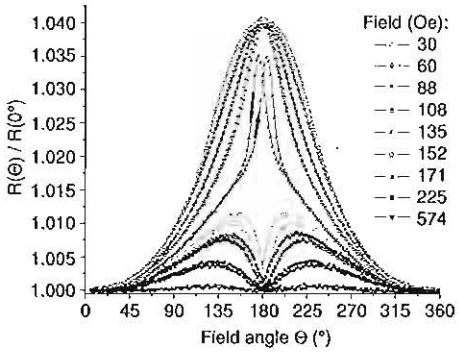

FIG. 2: Angular dependence of the resistance R normalized to the value for the EBD (corresponding to 0°) measured in T-geometry at different external field strengths as indicated.

ing layer is an additional FM that also contributes via AMR to the total MR response. We take into account the Zeeman energies and the uniaxial anisotropies of all FM layers, bilinear interlayer coupling between the free and pinned layer, and the unidirectional anisotropy of the pinned layer given by H_{EB}. The total MR due to both GMR and AMR is then calculated from the equilibrium magnetization angles and the field and current directions. The AMR and GMR amplitudes are fit parameters.

Figure 2 shows the angular dependence of resistance R at different field strengths measured in the T-geometry in order to experimentally suppress the AMR contributions. The external field is rotated starting from the EBD (corresponding to 0°) by 360° in clockwise (cw) direction and then back in counterclockwise (ccw) direction. The curves are dominated by the GMR. At low fields (30-108 Oe) the magnetization of the pinned layer is approximately fixed in the EBD, while the free layer rotates with the field. As the external field gets closer to the $|H_{\mathrm{EB}}|$ of about 150 Oe the deviation from the sinusoidal GMR behavior increases, and a difference between the cw and ccw rotation direction appears. As the field is increased above $|H_{\mathrm{EB}}|$, the alignment between the magnetizations of the pinned and free layer at the field direction opposite to the EBD (180°) switches from antiparallel to parallel corresponding to a MR maximum and minimum, respectively. A further increase of the field strength leads to a gradually decreasing MR. Above 200 Oe, where the curves are dominated by the AMR effect, they become almost flat, because the impact of AMR on the angular MR is intentionally suppressed in the T-geometry (AMR< 0.07%). We find rotational hysteresis in all examined samples in the field range around $|H_{\mathrm{EB}}|$, where we also observe hysteresis in conventional field-sweep MR curves [5].

Figure 3 shows representative examples of fits for some experimental curves from Fig. 2. The deviations of the model from the data in Figs. 3(b) and (c) are due to hysteresis and domain nucleation. By simultaneously fitting the angular dependence of the MR at different field strengths to our model, we are able to extract the strength H_{EB} and the direction of the exchange-bias field, the uniaxial anisotropy fields of the free and pinned

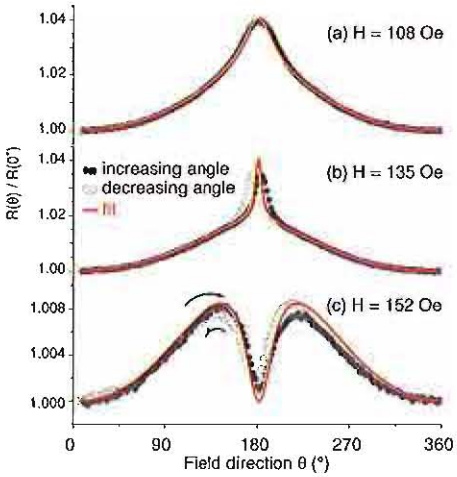

FIG. 3: Angular dependence of the resistance R in T-geometry normalized to the value at 0° at different external field strengths. Filled and open circles are for the increasing (clockwise) and decreasing (counterclockwise) angular sweeps, respectively. The red lines show the fitted curves.

layer, and the interlayer coupling field. We find uniaxial anisotropy fields of 0.6-3% of H_{EB} and weak ferromagnetic interlayer coupling fields (about 4% of H_{EB}). The collinearity of the uniaxial anisotropy axes and the EBD suggests that the uniaxial anisotropies are induced during the field-cooling. Ferromagnetic coupling across thin spacers is quite common and can be attributed to "orange peel" coupling due to finite interface roughness or to magnetic bridges. See Ref. [5] for detailed fit result.

We have described in detailed angular MR measurements of exchange-biased spin-valves. We showed experimentally and by finite-element simulations that AMR contributions can be suppressed by choosing an appropriate contact geometry. The advantage of varying the field direction over standard magnetization and MR loop measurements with fixed field direction is the higher accuracy in determining the GMR ratio, the uniaxial anisotropies of the free and pinned FM layers, and the interlayer coupling between them. The higher precision results from (i) the intrinsically larger data set (variation of field magnitude *and* direction), and (ii) –in particular for H_{EB}– from the fact that the measurements can be performed at external fields smaller or larger than H_{EB}, where no hysteresis and domains are involved. The described procedures allow for a quick and precise characterization of unpatterned spin-valve multilayer stacks.

[1] B. Dieny, J. Magn. Magn. Mater. **136**, 335 (1994).
[2] Th. G. S. M. Rijks, R. Coehoorn, M. J. M. de Jong, and W. J. M. de Jonge, Phys. Rev. B **51**, 283 (1995).
[3] B. H. Miller, E. Y. Chen, and E. D. Dahlberg, J. Appl. Phys. **73**, 6384 (1993).
[4] M. Buchmeier, B. K. Kuanr, R. R. Gareev, D.E. Bürgler, and P. Grünberg, Phys. Rev. B **67**, 184404 (2003).
[5] A. Paul, M. Buchmeier, D. E. Bürgler, and P. Grünberg, J. Appl. Phys. **97**, 023910 (2005).

Magnetic characteristics of epitaxial Ge(Mn,Fe) diluted films – a new room temperature magnetic semiconductor ?

H. Braak, R. R. Gareev, D. E. Bürgler, R. Schreiber, P. Grünberg, and C. M. Schneider
Institute "Electronic Properties"

We prepare 100 nm-thick, epitaxial $Ge_{100-(x+y)}(Mn_x,Fe_y)$ diluted films with Mn and Fe concentrations of several at. % using a layer-by-layer deposition scheme at elevated temperature. We measure saturation magnetization m_S *versus* temperature curves for a variety of (x,y) combinations and find for fixed temperatures a non-trivial dependence of m_S on x and y. Within a certain window in the (x,y) parameter space $Ge_{100-(x+y)}(Mn_x,Fe_y)$ exhibits a Curie temperature of 350 K and $m_S \approx 10$ emu/cm^2 at room temperature.

Electronics based on spin transport, the so-called spintronics, will be the seminal technology for future information processing devices. A key problem to be solved is the injection of a spin-polarized current into semiconductors. One pathway to circumvent the problem of the conductivity mismatch [1] between conventional ferromagnetic metallic electrodes and semiconductors is to employ magnetic semiconductors [2] as spin sources. Ge-based magnetic semiconductors are promising materials to achieve sizable spin injection into Ge [3]. New Ge-based Ge(Co,Mn) diluted magnetic semiconductors have recently attracted special attention due to their high Curie temperature and the potential of a straight-forward integration into common semiconductor technology [4].

Here we report on $Ge_{100-(x+y)}(Mn_x,Fe_y)$ films. They are grown on GaAs(001) surfaces after desorbing the native oxide layer by annealing the wafers at 880 K for one hour. The sample size is 4×10 mm^2. All three materials Ge, Mn, and Fe are deposited by thermal evaporation at growth rates of about 0.1 Å/s while keeping the substrate temperature constant at 530 K. Ge, Mn, and Fe are grown as 100 Å-thick trilayers with the sublayer thicknesses corresponding to the desired composition. The final 100 nm-thick films are composed of ten such trilayers. In detail, a 100 nm-thick film of $Ge_{100-(x+y)}(Mn_x,Fe_y)$ is a tenfold repetition of $[100-(x/\alpha+y/\beta)]$ Å Ge, $[x/\alpha]$ Å Mn, and $[y/\beta]$ Å Fe, where the coefficients $\alpha, \beta \approx 1.9$ arise from the different volumes per atom in bulk Ge, Mn, and Fe. After deposition the samples are *in-situ* annealed at a temperature of 730 K for one hour. The structural characterization by reflection high-energy electron diffraction (RHEED) and low-energy electron diffraction (LEED) confirms that all samples grow epitaxially up to our standard thickness of 100 nm. Several samples with different Mn and Fe concentrations are prepared under otherwise identical conditions (see Table I). For one composition ($x = 4$ and $y = 2$) we additionally vary the substrate temperature during deposition and also study the influence of the annealing. The magnetic properties are measured with a SQUID magnetometer in the temperature range from $2-400$ K with the magnetic field applied in the plane of the film. First, the sample is cooled in zero field to 5 K, and then we start measuring the magnetic moment in a saturating field of 1 T while warming up the sample.

TABLE I: Compositions of the $Ge_{100-(x+y)}(Mn_x,Fe_y)$ samples in at. %, the corresponding saturation magnetizations m_S measured at 5 K, and the Curie temperatures T_C.

$100-(x+y)$ (at. %)	x (at. %)	y (at. %)	m_S at 5 K (emu/cm^3)	T_C (K)	x/y
96	4	0	-	-	∞
94	4	2	29	350	2
92	4	4	29	350	1
88	4	8	6	270	0.5
94	2	4	12	250	0.5
90	8	2	72	350	4

No ferromagnetic ordering is observed for the two-component $Ge_{96}(Mn_4)$ sample without any Fe. We merely measure the parasitic diamagnetic signal. When we add a small amount of Fe for the $Ge_{94}(Mn_4,Fe_2)$ specimen, the magnetization at 5 K augments to 29 emu/cm^3. As shown by the red circles in Fig. 1, the m_S–T curve shows a negative curvature, and the phase transition occurs at about $T_C = 350$ K. In contrast to Ge(Co,Mn) films reported in Ref. [4], we observe for our epitaxial Ge(Mn,Fe) film a definite magnetization of 7 emu/cm^3 at room temperature (RT). The inset in Fig. 1 displays the hysteresis loop taken at 2 K after subtracting the diamagnetic background signal. Saturation is achieved at $H_S \approx 0.25$ T, and the coercive force H_C is larger than 25 mT, but its value decreases to below 1 mT close to RT. If we raise the Fe content to 4 at. %, *i.e.* $x/y \approx 1$, m_S and T_C remain unchanged (Table I). For $y = 8$ at. %Fe [$Ge_{88}(Mn_4Fe_8)$] m_S at 5 K is strongly reduced to about 6 emu/cm^3, and T_C decreases to 270 K. The shape of

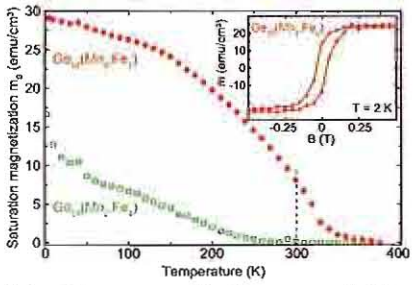

FIG. 1: Saturation magnetization m_S of $Ge_{94}(Mn_4,Fe_2)$ (red) and $Ge_{94}(Mn_2,Fe_4)$ (green) *versus* temperature. T_C of $Ge_{94}(Mn_4,Fe_2)$ is 350 K, *i.e.* above RT marked by the dashed line. The inset shows the hysteresis loop of $Ge_{94}(Mn_4,Fe_2)$ measured at 2 K.

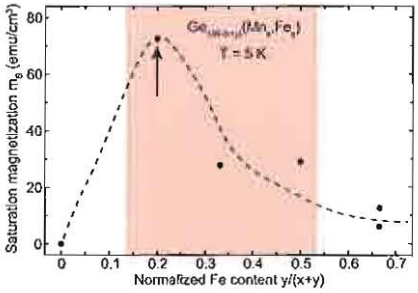

FIG. 2: Saturation magnetization m_S at 5 K of samples with different Mn and Fe concentrations x and y, respectively, plotted as a function of $y/(x+y)$. The colored area marks the range in which we find ferromagnetic ordering at RT, and the arrow marks the sample with the highest magnetization at RT. The dashed line is a guide to the eyes.

the m_S–T curve in this case is different compared to those of the samples with high T_C. The magnetization decreases linearly with temperature to zero. For the $Ge_{94}(Mn_2,Fe_4)$ sample we reduce the total amount of Mn and Fe, but keep the ratio $x/y \approx 0.5$ constant (Table I). We obtain a T_C of about 250 K and a m_S of approximately 12 emu/cm^3. The shape of the m_S–T curve is again rather linear and is displayed by the green squares in Fig. 1. Note the completely different magnetic behavior of the two samples in Fig. 1, although they contain the same amount of magnetic atoms ($x + y = 6$ at. %). The highest m_S at 5 K of approximately 72 emu/cm^3 is achieved in this study for the $Ge_{90}(Mn_8,Fe_2)$ sample, which reveals the phase transition at 350 K. The value of m_S at 5 K corresponds to an average magnetic moment per Mn or Fe atom of about 1.9 μ_B. If we attribute the full magnetization to only one of the magnetic species, we obtain 9.5 μ_B per Fe atom or 2.3 μ_B per Mn atom, respectively. Therefore, the observed magnetism cannot originate solely from the magnetic moment of the Fe. Preliminary X-ray absorption magnetic circular dichroism experiments confirm that in our samples both Fe and Mn have residual magnetic moments with parallel alignment.

Figure 2 shows m_S at 5 K *versus* the Fe concentration normalized to the total concentration of magnetic atoms $y/(x+y)$ for all samples discussed so far. The colored area indicates the range of $y/(x+y)$, where we observe a non-zero magnetization at RT. Obviously, a certain amount of Fe is needed to stabilize ferromagnetic ordering at low temperature as well as at RT. A similar statement holds for Mn as discussed for the samples $Ge_{94}(Mn_4,Fe_2)$ and $Ge_{94}(Mn_2,Fe_4)$ in the context of Fig. 1. Additionally, the concentration ratio of Mn and Fe x/y must be unity or larger (Table I). Thus, ferromagnetism at RT exists only in a small window of relative and absolute Mn and Fe concentrations. Resistivity measurements in a four-point geometry of the $Ge_{94}(Mn_4,Fe_2)$ and $Ge_{90}(Mn_8,Fe_2)$ films reveal a monotone decreasing resistance with increasing temperature. This typical non-metallic behavior indicates the formation of a semiconducting material with ferromagnetic ordering at RT.

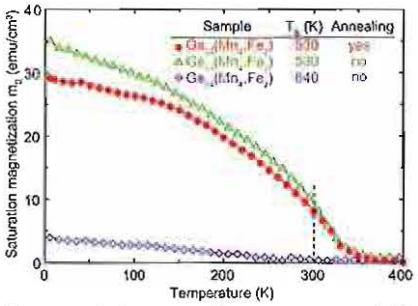

FIG. 3: Influence of the annealing process and the substrate temperature T_S on the magnetic properties of $Ge_{94}(Mn_4,Fe_2)$ samples. The dashed line indicates RT.

In order to optimize the growth procedure, we study the influence of the annealing step after deposition. Figure 3 shows the comparison of the m_S–T behaviors of similarly prepared $Ge_{94}(Mn_4,Fe_2)$ samples with (red curve) and without (green curve) annealing. The non-annealed sample shows a slightly higher m_S for all temperatures below T_C. Thus, the films are thermally stable up to at least 730 K. However, an increase of the substrate temperature T_S during deposition from 530 to 640 K (blue curve in Fig. 3) drastically changes the magnetic properties. The m_S magnetization drops significantly, T_C is reduced by 80 K to about 270 K, and the curve shape changes from curved to linear. Variations of the effective Fe and Mn concentrations due to different temperature dependences of the sticking coefficients –in particular for Mn with a clearly higher vapor pressure than Fe and Ge - may contribute to the strong reduction of m_S and T_C. However, these variations are not likely to be the only reason, because a reduction of the Mn concentration by more than 50% would be required (Table I). On the other hand, the system is much more sensitive to the temperature during deposition than during the final annealing step, because the sample grown at $T_S = 640$ K reveals worse magnetism than that annealed at 730 K. This difference indicates that atomic exchange processes occurring during the deposition are important.

Regarding the question raised in the title, we conclude that the ferromagnetism of the films is not simply related to the formation of ferromagnetic inclusions in the Ge host material, because for increasing Fe concentration the saturation magnetization and T_C decrease. The dependences on the temperature during growth and annealing indicate that subtle atomic ordering processes play a role for the development of ferromagnetism at RT.

[1] G. Schmidt, D. Ferrand, L. W. Molenkamp, A. T. Filip, and B. J. van Wees, Phys. Rev. B **62**, R4790 (2000).
[2] H. Ohno, Science **281**, 951 (1998).
[3] Y. D. Park, A. T. Hanbicki, S. C. Erwin, C. S. Hellberg, J. M. Sullivan, J. E. Mattson, T. F. Ambrose, A. Wilson, G. Spanos, and B. T. Jonker, Science **295**, 651 (2002).
[4] F. Tsui, L. He, L. Ma, A. Tkachuk, Y. S Chu, K. Nakajima, and T. Chikyow, Phys. Rev. Lett. **91**, 177203 (2003).

Antiferromagnetic interlayer exchange coupling across epitaxial, Ge-containing spacers

R. R. Gareev, D. E. Bürgler, R. Schreiber, H. Braak, M. Buchmeier, and P. A. Grünberg
Institute "Electronic Properties"

We give experimental evidence for antiferromagnetic interlayer exchange coupling of Fe(001) layers across epitaxial, Ge-containing spacers consisting of either Ge-wedges embedded between two Si boundary layers or Si-Ge-multilayers. The coupling strengths are of the order of 1 mJ/m^2 and decay on a length scale below 2 Å as determined from magneto-optic Kerr effect and Brillouin light scattering. The coupling evolves with spacer thickness from ferromagnetic to prevailing 90° or antiferromagnetic for Ge-wedges and Si-Ge-multilayers, respectively. The bilinear coupling is comparable in both cases, but the biquadratic contribution is suppressed for Si-Ge-multilayer spacers. Thus, Si-Ge-multilayer spacers give rise to perfect antiparallel alignment of the Fe magnetizations.

Our recent observations of antiferromagnetic interlayer exchange coupling (AFC) across non-conducting epitaxial spacers of nominally pure Si [1] focus particular interest on highly resistive structures exhibiting non-oscillatory AFC. For nominally pure, highly resistive Si spacers the total coupling strength exceeds 5 mJ/m^2 and thus is significantly larger than for metallic spacers [1]. Furthermore, current-perpendicular-to-plane transport measurements demonstrate that AFC coexists with transport via tunneling [2]. The reason to study Ge-containing spacers is to investigate the existence and the properties of AFC across another semiconductor than Si. As reported previously [3] epitaxial Fe/Ge/Fe structures reveal no evidence of AFC. Therefore, we use AFC-mediating, epitaxial Si boundary layers (BL) at the interfaces towards the Fe layers in order to avoid the formation of magnetic Fe-Ge compounds that prevent AFC [3]. The lattice mismatch of about 4% between Ge (a_{Ge} = 5.66 Å) and Si (a_{Ge} = 5.43 Å) gives rise to the Stransky-Krastanov (SK) growth mode: several monolayers of strained Ge grow epitaxially on Si, and Ge hillocks form for larger Ge thickness [4]. In order to avoid SK growth we also try to stabilize the strain in the spacer by piling up thin layers of Ge and Si [5].

We grow our Fe/spacer/Fe(001) structures in a molecular-beam epitaxy system using a 150 nm-thick Ag(001) buffer system on GaAs(001). The spacer layers are deposited at low rates (< 0.1 Å/s). Three types of spacers are prepared: (i) Ge-wedges, (ii) Ge-wedges embedded between two 4 Å-thick Si BL at both the bottom and top interfaces towards the Fe layers, and (iii) multilayers consisting of N alternating 2 Å-thick Si and Ge sublayers. The nominal thickness of the Ge-wedges ranges from zero to 15 Å. The in-plane crystalline structure of all layers is characterized by means of low-energy electron diffraction (LEED). Magnetic properties are measured by magneto-optical Kerr effect (MOKE) and Brillouin light scattering (BLS). Bilinear and biquadratic coupling constants, J_1 and J_2, are determined by fitting the field dependence of MOKE and BLS data using the usual phenomenological areal energy density expression for interlayer exchange coupling,

$$E_{ex} = -J_1 \cos(\vartheta) - J_2 \cos^2(\vartheta), \qquad (1)$$

where ϑ is the angle between the two Fe film magnetizations. The external magnetic field is applied along an easy-axis of Fe(001).

First, we prepare Fe/Ge-wedge/Fe trilayers without BL or with only one BL at the bottom or top interface. In all these cases the MOKE hysteresis curves reveal 100% remanent magnetization characteristic for zero or FM coupling in agreement with Ref. [3]. In order to prevent Fe-Ge interdiffusion we deposit Si BL at both interfaces. Figure 1 shows typical LEED patterns for all five layers. The bottom Si BL grows at RT with a similar in-plane lattice constant as Fe(001). The nominally pure Ge spacers start to grow epitaxially on Si with an in-plane cubic structure and a lattice parameter of about 2.9 Å (a_{Fe} = 2.87 Å). For Ge thicknesses < 6 Å we observe LEED patterns for the Ge spacer, the top BL, and the top Fe layer. Thus, we obtain epitaxial growth of the whole structure.

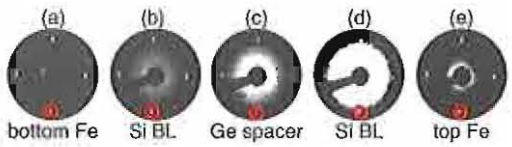

FIG. 1: LEED patterns taken at 55 eV for (a) 50 Å bottom Fe layer, (b) 4 Å Si bottom BL, (c) 5 Å Ge spacer, (d) 4 Å Si top BL, and (e) 30 Å top Fe layer. Si BL, Ge spacer, and top Fe layer are grown at RT. Red circles mark the position of the (01) spot of bcc-Fe(001) corresponding to an in-plane lattice constant of 2.9 Å.

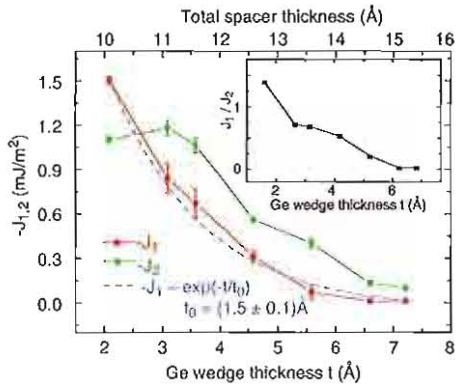

FIG. 2: Bilinear (J_1, red) and biquadratic (J_2, green) coupling constants versus nominal Ge thickness t for a wedge-type Fe(50 Å)/Si/Ge(t)/Si/Fe(30 Å) structure with 4 Å-thick Si BL. The blue, dashed line is an exponential fit and yields a decay length of about 1.5 Å. The upper abscissa gives the total spacer thickness including the Si BL. The inset shows the ratio J_1/J_2 versus t.

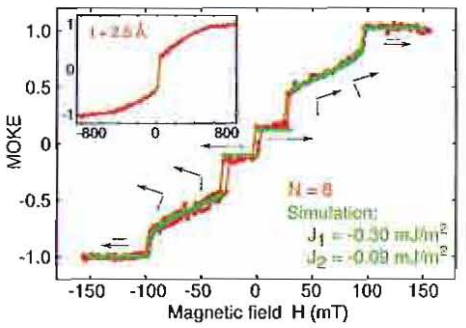

FIG. 3: Experimental (red) and fitted (green) MOKE hysteresis loop of a sample with an $N = 6$ Si-Ge-multilayer spacer: Fe(50 Å)/Si/Ge/Si/Ge/Si/Ge/Fe(30 Å). All Si and Ge layers are 2 Å thick. Arrows indicate the magnetization alignment obtained from the fitting. Inset: Hysteresis loop of a wedge-type Fe(50 Å)/Si/Ge(t)/Si/Fe(30 Å) sample at $t = 2.5$ Å.

Figure 2 shows the dependence of J_1 and J_2 on the thickness of the Ge spacer t for a sample with two BL. J_1 quickly drops with t and can be described by an exponential decay with a decay length of about $t_o = 1.5$ Å (blue, dashed line in Fig. 2). $|J_2|$ is smaller than $|J_1|$ only for $t < 3$ Å. However, the biquadratic coupling is dominating for all Ge thicknesses because $|J_1| < 2|J_2|$ (see inset of Fig. 2), and the layer magnetizations are canted in the remanent state, even for smallest t. The decay of J_1 is very similar to the case of nominally pure Si-wedges ($t_o = 1.7$ Å), whereas the J_2 behavior is opposite to the Si case [1]: the J_1/J_2 ratio decreases for Ge-wedges, but it increases for Si-wedges. The similar behavior of the bilinear coupling indicates its intrinsic origin. The likely reason for the observed strong biquadratic coupling is the competition between bilinear coupling and FM coupling due to magnetic bridges [6]. The onset of SK hillock growth at Ge thicknesses $t > 6$ Å reduces the efficiency of the FM bridge annihilation upon further Ge deposition. Note that the vanishing of J_1 and the prevalence of J_2 coincide with the disappearance of the LEED spots.

In a next step we prepare samples of the form Fe/Si/Ge.../Fe with N alternating Si and Ge sublayers as spacers. We observe LEED patterns similar in quality to Fig. 1, even for larger spacer thicknesses than for the Ge-wedge. Figure 3 depicts as an example the MOKE hysteresis loop of a sample with $N = 6$. The green line is a fit yielding J_1 and J_2 as indicated. J_1 is dominating ($|J_1| > 2|J_2|$), and thus the hysteresis loop exhibits a plateau for $|H| < 30$ mT due to perfect antiparallel alignment (arrows in Fig. 3). The step at $H = 0$ arises from the different Fe thicknesses. Such a plateau is not observed for the samples with Ge embedded between BL (inset of Fig. 3). Fig. 4 shows the dependence of the coupling constants on N. The coupling is FM for smallest spacer thicknesses ($N < 4$) and becomes due to FM bridges prevailing 90°-coupling for $N = 4$, where $J_2 \approx 6J_1$. For $N = 5$, J_1 and J_2 are comparable. The increase of J_1 from $N = 4$ to 6 and the simultaneous steep decrease of J_2 is due to the transition from FM coupling first to competing FM and antiferromagnetic interactions giving rise to 90°-coupling [6] and further to dominant AFC for $N = 6$ to 8. Finally, for $N = 9$ AFC

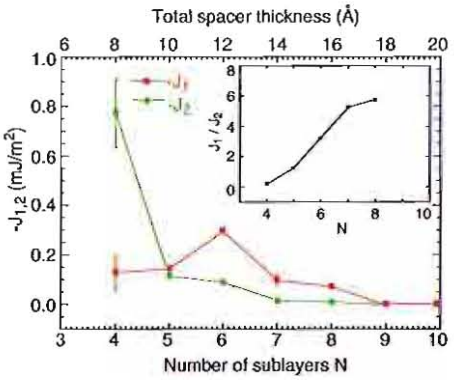

FIG. 4: Bilinear (J_1, red) and biquadratic (J_2, green) coupling constants versus the number N of 2 Å-thick Si and Ge sublayers in the multilayer spacer for structures of the form Fe(50 Å)/Si/Ge.../Fe(30 Å). The upper abscissa gives the total spacer thickness in Å. The inset shows the ratio J_1/J_2 versus t.

is negligible, and both FM layers are aligned parallel to the field H. The maximum of $|J_1|$ of about 0.3 mJ/m^2 is reached for $N = 6$ corresponding to a total spacer thickness of 12 Å. Taking for the Ge-wedge samples the thickness of the BL into account, a total spacer thickness of 12 Å corresponds to $t = 4$ Å. Thus, J_1 across Si-Ge-multilayers is comparable to that across embedded Ge-wedges of similar total thickness (Fig. 2). The bilinear coupling extends to about the same total spacer thicknesses: 16 Å ($N = 8$) for the multilayer spacers and 15 Å ($t = 7$ Å) for the embedded Ge-wedges (Fig. 2). However, the evolution of J_2 is completely different: for multilayer spacers it is very strong for small N due to strong intermixing, but drops rapidly and becomes secondary for larger N. This different behavior is best recognized by comparing the dependence of the J_1/J_2 ratios in the insets of Figs. 2 and 4. We relate these observations to the well-established mechanism of strain stabilization in Si/Ge multilayers [7] that shifts the transition to the SK hillock growth to larger thicknesses, as indicated by our LEED data. Thus, the multilayer spacers show improved growth compared to the Ge-wedge samples, once they are thick enough ($N > 5$) to sufficiently suppress the formation of FM bridges.

Our results indicate that relatively strong AFC is a common feature of well-ordered, epitaxial spacer layers consisting of semiconducting elements.

[1] R.R. Gareev, D.E. Bürgler, M. Buchmeier, R. Schreiber, and P. Grünberg, J. Magn. Magn. Mater. **240**, 235 (2002).
[2] R.R. Gareev, L.L. Pohlmann, S. Stein, D.E. Bürgler, P.A. Grünberg, and M. Siegel, J. Appl. Phys. **93**, 8038 (2003).
[3] J.J. de Vries, J. Kohlhepp, F.J.A. den Broeder, P.A. Verhaegh, R. Jungblut, A. Reinders, and W.J.M. de Jonge, J. Magn. Magn. Mater. **165**, 435 (1997).
[4] Y.-W. Mo, D.E. Savage, B.S. Swartzentruber, and M.G. Lagally, Phys. Rev. Lett. **65**, 1020 (1990).
[5] R.R. Gareev, D.E. Bürgler, R. Schreiber, H. Braak, M. Buchmeier, and P. A. Grünberg, Appl. Phys. Lett. **83**, 1806 (2003).
[6] J.C. Slonczewski, J. Appl. Phys. **75**, 6474 (1994).
[7] S.C. Jain and W. Hayes, Semicond. Sci. Technol. **6**, 547 (1991).

Enhanced exchange bias in ferromagnet/antiferromagnet multilayers

A. Paul, D. E. Bürgler, and P. Grünberg
Institute "Electronic Properties"

We study a series of NiFe(10.0 nm)/[$Ir_{20}Mn_{80}$(6.0 nm)/$Co_{80}Fe_{20}$(3.0 nm)]$_N$ multilayers with different numbers N of bilayers grown by dc magnetron sputtering. After field-cooling, SQUID and MOKE measurements show a sizable increase of the exchange bias field with N. X-ray specular and diffuse scattering data reveal no significant variation of the lateral correlation length and only a weak dependence of the vertical rms interface roughness on N. Atomic and magnetic force microscopy, however, show a strong reduction of the grain size accompanied by distinct changes of the magnetic domain structure. We conclude that the enhancement of the exchange bias effect is related to the shrinking of the domain size in the antiferromagnet due to the structural evolution in the multilayers.

Magnetic field sensors based on giant magnetoresistance (GMR) in spin-valve structures [1] rely on the exchange bias effect [2] which is employed to fix the magnetization direction of the ferromagnetic reference layer. In spite of its widespread application, exchange bias is not yet fully understood.

We study exchange bias in [$Ir_{20}Mn_{80}$(6.0 nm)/$Co_{80}Fe_{20}$(3.0 nm)]$_N$ multilayers (MLs) with varying number N of ferromagnet/antiferromagnet (FM/AF) bilayers prepared by dc magnetron sputtering. We employ a 10 nm-thick NiFe buffer layer grown on oxidized Si wafers in order to improve the texture of the MLs. All specimens are first annealed at 533 K, i.e. above the Néel temperature T_N = 520 K of IrMn, for 60 minutes in Ar gas and then cooled to room temperature (RT) in an external field of 130 Oe in order to induce the unidirectional anisotropy.

The microstructure and the layer quality are investigated by low angle x-ray reflectivity (XRR) and x-ray diffuse scattering (XDS) measurements [3] employing a Bruker-axs D8 diffractometer with Cu-K_α radiation. We measured in specular geometry with the angle of incidence θ_i equal to the exit angle θ_f as well as in off-specular geometry with an offset of $\Delta\omega = 0.13°$ between θ_i and θ_f. True specular reflectivity is obtained by subtracting the off-specularly reflected intensity from the specular one. Diffuse scattering as a function of the in-plane component of the momentum transfer vector is measured by keeping the scattering angle 2θ fixed and rocking the specimen around $\theta_i = \theta_f$. The diffuse scattering measurement provides information about the structure of the interfaces in the film plane. Magnetization loops are recorded by means of a superconducting quantum interference device (SQUID) as well as the magneto-optic Kerr effect (MOKE). Atomic and magnetic force microscopy (AFM/MFM) measurements in tapping mode are performed with a multimode SPM from Digital Instruments using Co-based magnetic tips.

Figure 1 shows SQUID magnetization loops for different N. There are always two hysteresis loops, one corresponding to the magnetically soft NiFe buffer layer and the other to the pinned CoFe layer(s) in the ML. The relative contributions to the sample's total moment confirm this assignment. The averaging over an increasing number of CoFe layers results in slanted loops for larger N. The exchange bias field H_{EB} clearly increases from 330 Oe for N = 1 to about 900 Oe for N = 10, and it tends to saturate [Fig. 3(c)]. This is even more evident in the MOKE data, where the limited penetration depth of the laser light (about 20 nm) enhances the relative weight of the topmost CoFe layers.

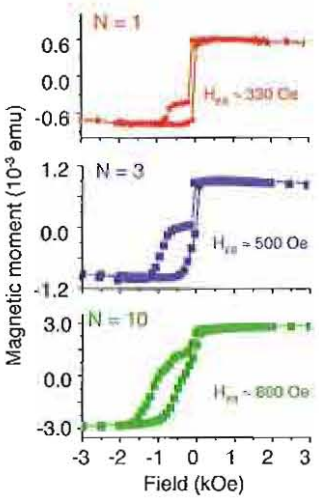

FIG. 1: SQUID magnetization loops of SiO_2/NiFe(10.0 nm)/[IrMn(6.0 nm)/CoFe(3.0 nm)]$_N$ MLs with different numbers of bilayers N. The relative contribution of the FM NiFe buffer decreases and H_{EB} increases with N.

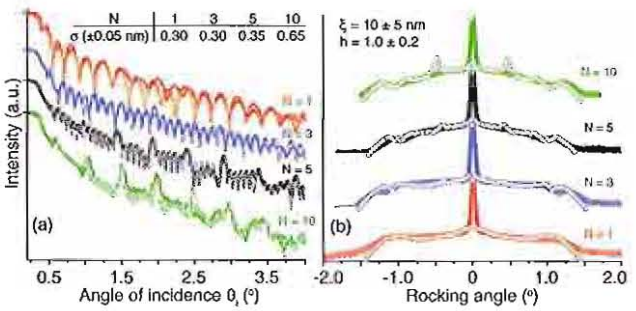

FIG. 2: (a) True specular XRR and (b) XDS at θ_i = 1.5° of SiO_2/NiFe(10.0 nm)/[IrMn(6.0 nm)/CoFe(3.0 nm)]$_N$ MLs: The fits (open symbols) yield in (a) σ's as indicated and in (b) no significant dependence of ξ and h on N.

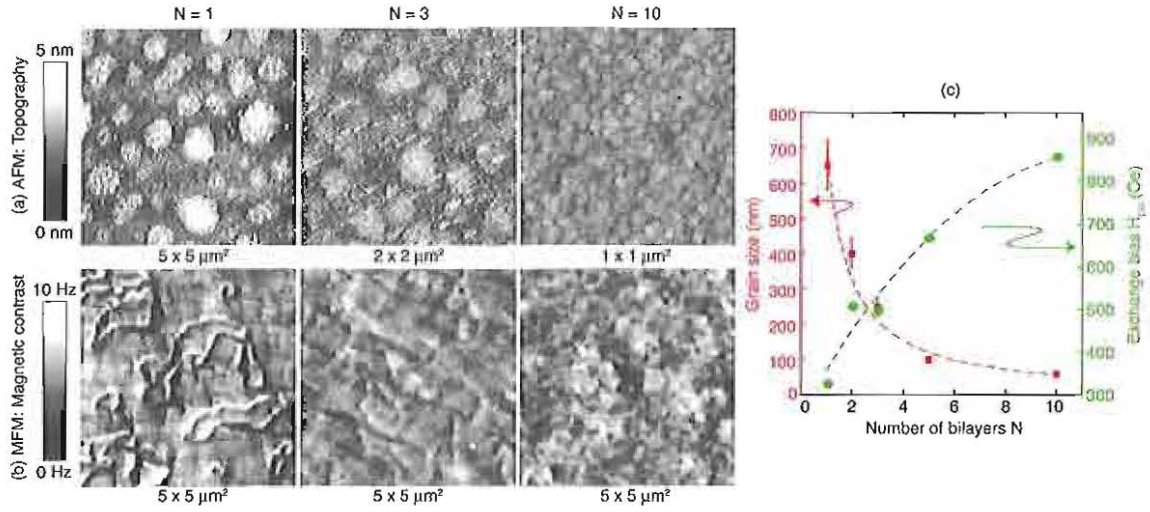

FIG. 3: (a) AFM and (b) MFM micrographs of SiO_2/NiFe(10.0 nm)/[IrMn(6.0 nm)/CoFe(3.0 nm)]$_N$ MLs. MFM images are recorded at zero field after saturating the specimens in the field-cooling direction. Note the different image sizes in (a). (c) Correlation of the dependences of the grain size and H_{EB} on N. Dashed lines are guides to the eyes.

Figure 2(a) shows true specular reflectivity scans and fits based on procedures described in Refs. [4, 5]. The roughness of all IrMn/CoFe interfaces is assumed to be equal and is represented by a single fitting variable σ, and the individual layer thicknesses are fitting parameters. The top CoFe layer is expected to be oxidized, and hence its electron density as well as its thickness are separate fitting parameters. We do not consider any intermixed layer due to the positive heat of mixing for IrMn and CoFe. The fits yield a rather weak increase of σ from 0.3 to 0.6 nm as N increases from 1 to 10. The presence of Bragg peaks and total thickness oscillations (Kiessig fringes) in the off-specular reflectivities signifies a high degree of vertical correlation from layer to layer with a vertical correlation length larger than the total ML thickness [6].

Rocking curves and their fits are plotted in Fig. 2(b). Several basic models for the roughness cross-correlation within a ML have been reported in the literature and are discussed in detail in Ref. [3]. We found the best agreement with the model of Holý and Baumbach [6]. It takes into account that interfaces are formed successively from the substrate to the surface and assumes complete correlation. Each interface adds some statistically independent roughness, which is assumed to be completely transferred to all subsequent interfaces. Thus, roughness is accumulated, and σ increases with N. The fitting parameters are σ, the fractal dimension h, and the lateral correlation length ξ. The vertical correlation length κ is found to be larger than the total ML thickness. We observe no significant dependence of h and ξ on N. Moreover, the texture of the MLs as investigated by x-ray diffraction is similar for all N. AFM images shown in Fig. 3(a), however, reveal a strong variation of the grain size from 650 nm for $N = 1$ to 60 nm for $N = 10$ [Fig. 3(c)]. Moreover, the MFM micrographs [Fig. 3(b)] indicate a significant change of the magnetic domain structure with N: The extended domains for $N = 1$ gradually form structures of about 500 nm in diameter for $N = 10$.

We attribute the enhanced H_{EB} to the 10-fold shrinking of the grain size, rather than to the small increase of σ by only 0.3 nm. Due to the absence of long-range dipolar interactions in an AF, domains are stabilized by defects such as grain boundaries. Thus, the smaller grain size at larger N gives rise to smaller AF domains and, thus, a higher density of uncompensated spins, which are aligned during field-cooling and then couple to the FM layer [7, 8]. The shrinking of the FM domains with increasing N confirms a link between the grain size and the magnetic ordering. However, we cannot directly correlate AF domains with the observed FM domains as in Ref. [9], because our samples are field-cooled. Nevertheless, it is likely that the domain state of the AF also changes with grain size, because grain boundaries are energetically preferred sites for AF domain walls.

In conclusion, the structural evolution in [FM/AF]$_N$ MLs leads for increasing N to smaller grains and presumably smaller AF domains, which – as expected in the framework of the domain state model [7] – significantly enhance the exchange bias effect.

[1] B. Dieny, J. Magn. Magn. Mater. **136**, 335 (1994).
[2] W. H. Meiklejohn, C. P. Bean, Phys. Rev. **105**, 904 (1957).
[3] A. Paul, G. S. Lodha, Phys. Rev. B **65**, 245416 (2002).
[4] L. G. Parratt, Phys. Rev. **95**, 359 (1954).
[5] L. Nevot, P. Croce, Rev. Phys. Appl. **15**, 761 (1980).
[6] V. Holý, T. Baumbach, Phys. Rev. B **49**, 10668 (1994).
[7] U. Nowak, K. D. Usadel, J. Keller, P. Miltényi, B. Beschoten, G. Güntherodt, Phys. Rev. B **66**, 14430 (2002).
[8] J. Keller, P. Miltényi, B. Beschoten, G. Güntherodt, U. Nowak, K. D. Usadel, Phys. Rev. B **66**, 14431 (2002).
[9] F. Nolting, A. Scholl, J. Stöhr, J. W. Seo, J. Fompeyrine, H. Siegwart, J.-P. Locquet, S. Anders, J. Lüning, E. E. Fullerton, M. F. Toney, M. R. Scheinfein, H. A. Padmore, Nature **405**, 767 (2000).

Structural and magneto-transport characterization of $Co_2Cr_xFe_{1-x}Al$ Heusler alloy films

A. D. Rata, H. Braak, D. E. Bürgler, S. Cramm, and C. M. Schneider
Institute of Solid State Research, Electronic Properties (IFF6) and
CNI - Center of Nanoelectronic Systems for Information Technology

Heusler alloys are predicted to be half-metallic by first-principles theoretical calculations, making them interesting materials for future spintronic applications. Recent studies revealed for the full-Heusler compound $Co_2Cr_{0.6}Fe_{0.4}Al$ in the bulk a magnetoresistance of 30% and when used as ferromagnetic electrode up to 16% tunneling magnetoresistance (TMR). Here, we report on the growth of $Co_2Cr_{0.6}Fe_{0.4}Al$ thin films by magnetron sputtering at room temperature. The films are characterized by x-ray diffraction and SQUID magnetometry. Tunneling junctions with the layer sequence $Co_2Cr_{0.6}Fe_{0.4}Al$/MgO/CoFe yield a TMR ratio of 37% at room temperature. Our results are very encouraging for further studies involving epitaxial $Co_2Cr_{0.6}Fe_{0.4}Al$ electrodes in combination with epitaxial MgO barriers.

The efficient injection of spin currents into non-magnetic materials, which is a prerequisite for many future spintronic concepts [1] to work, requires materials with high spin polarization of the conduction electrons. Promising candidates are the so-called Heusler alloys [2]. Many Heusler compounds are predicted to show half-metallic properties from first-principles calculations [3]. They are characterized by the presence of a band gap only for one spin direction and metallic properties for the other resulting in 100% spin polarization of the charge carriers. However, there has not yet been an experimental report on half-metallicity at room temperature (RT).

The Co-based full-Heusler compounds (*e.g.*, $Co_2Cr_xFe_{1-x}Al$, Co_2MnSi, and Co_2MnGe) are intensively investigated due to their high Curie temperatures and the absence of empty lattice sites, which makes them less susceptible for site disorder. Site disorder is widely accepted to destroy the half-metallicity. Miura *et al.* [4] have predicted that for the Co_2CrAl Heusler compound in the $B2$ structure site disorder between Cr and Al is not so critical and allows for 84% spin polarization. Experimentally, Block *et al.* [5] have reported that $Co_2Cr_{0.6}Fe_{0.4}Al$ bulk material in the ordered $L2_1$ structure exhibits 30% magnetoresistance at RT in a magnetic field of 1 kOe. Shortly thereafter, Inomata *et al.* [6] have found 16% tunneling magnetoresistance (TMR) at RT in structures containing $Co_2Cr_{0.6}Fe_{0.4}Al$ as one ferromagnetic electrode.

Here, we investigate the structure and magnetic properties of $Co_2Cr_{0.6}Fe_{0.4}Al$ (CCFA) thin films grown by magnetron sputtering. First attempts to integrate these films as electrodes in TMR junctions yield up to 37% TMR.

CCFA thin films with various thicknesses are grown by magnetron sputtering on SiO_2 substrates. The base pressure in our chamber is below 1×10^{-7} mbar and the sputtering Ar pressure is varied between 1×10^{-3} and 3×10^{-3} mbar. CCFA is DC sputtered from a stoichiometric $Co_2Cr_xFe_{1-x}Al$ target with $x = 0.6$. The sputtering rate, measured with a quartz balance, is set to 0.7 Å/s. The tunneling barriers are RF sputtered from a MgO target, and the SiO_2 substrates are kept at RT. After deposition, the Heusler films can be annealed *in-situ* up to 600°C. The film stoichiometry is checked *ex-situ* by secondary ions mass spectroscopy (SIMS). The composition of our films is similar to the target composition. The structure of the Heusler films is identified *ex-situ* by x-ray diffraction (XRD). For the magnetic characterization, we employ SQUID magnetometry.

Figure 1 shows a wide θ–2θ XRD scan from a 100 nm-thick CCFA film. Despite the low deposition temperature and the absence of any seed layer, which normally promotes textured growth, clear diffraction peaks are identified. They indicate a polycrystalline structure of the film. Ideally, for the characteristic $L2_1$ structure of a Heusler compound, one should be able to distinguish besides the fundamental reflections, *e.g.* (220), two types of superlattice reflections, *e.g.* (111) and (200). Our CCFA films grown on amorphous oxidized SiO_2 substrates take the so-called $B2$ (CsCl type) structure, where the absence of the (111) peak indicates complete disorder between Al and (Cr, Fe) atoms, while the Co atoms occupy the correct sublattice. The same type of disordered structure

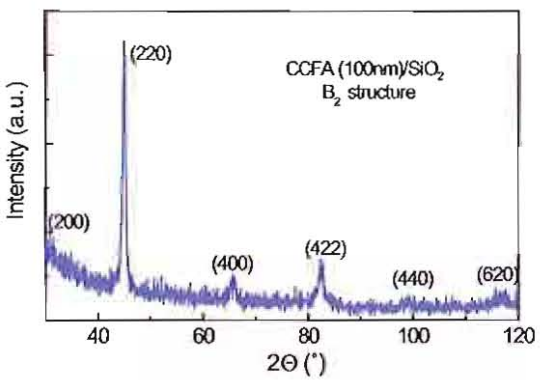

FIG. 1: $\theta - 2\theta$ XRD measurement of a 100 nm-thick CCFA film deposited at RT on SiO_2.

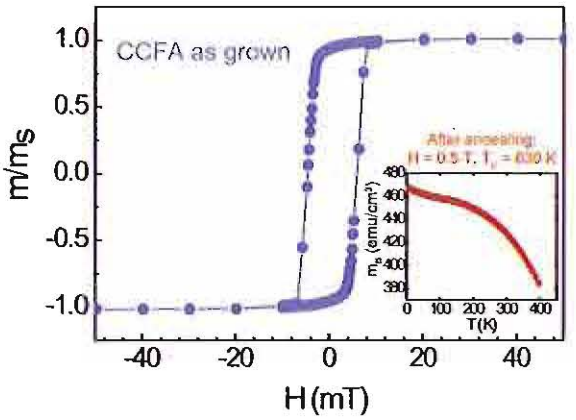

FIG. 2: Magnetic hysteresis curve measured by SQUID at RT of an as-grown 100 nm-thick CCFA film. The inset shows the temperature dependence of the saturation magnetization of the same film after annealing in vacuum at 500°C for 1 hour. The Curie temperature is about 630 K.

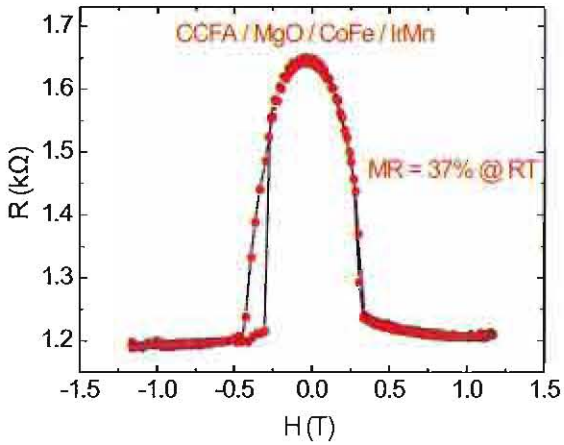

FIG. 3: Magnetoresistance curve of a CCFA(25 nm)/ MgO(3 nm)/CoFe(5 nm)/IrMn(15 nm) structure deposited on SiO_2 and measured at RT.

has previously been observed in CCFA films by Inomata *et al.* [6].

Our CCFA Heusler films display a soft ferromagnetic behavior as shown by the M–H loop in Fig. 2. The coercive field is approximately 5 mT. Our films are magnetically softer compared to the recently reported results about CCFA films deposited on Al_2O_3 substrates, which have a coercive field of 10 mT. The Curie temperature of a as-grown film is estimated to be about 540 K from the extrapolation of the magnetization *versus* temperature curve. After annealing in vacuum at 500°C for one hour, the Curie temperature is increased to 630 K (inset of Fig. 2). The total magnetic moment obtained from the saturation magnetization at 5 K is 2.0 μ_B per formula unit (f.u.) for as-grown films and 2.4 μ_B/f.u. after annealing in vacuum. These values are small compared to the theoretical value 3.8 μ_B/f.u. for ordered CCFA with $L2_1$ structure [3]. On the other hand, our values are comparable to the data reported from films grown at elevated temperatures [7]. Moreover, even the magnetic moment measured in bulk samples is smaller than the calculated one [8].

Finally, we deposit TMR structures with the following layer sequence: SiO_2/ CCFA(25 nm)/MgO(3 nm)/CoFe(5 nm)/IrMn(15 nm). The completed stack is annealed in vacuum for 1 hour at 250°C. Although an IrMn antiferromagnet is employed to pin the magnetization of the upper CoFe electrode, the two ferromagnetic layers do not switch separately, as observed in SQUID measurements. We mention at this point that no further treatment (annealing above the Néel temperature of the antiferromagnet and field cooling) has been applied to this structure. Junctions with areas from 3×3 up to 15×15 μm^2 are patterned for magnetotransport measurements by standard optical lithography.

In Fig. 3 we show the magnetoresistance curve measured at RT. The TMR ratio defined as TMR $= (R_{AP} - R_P)/R_P$, where R_{AP} and R_P are the resistances for the antiparallel and parallel magnetization configurations, respectively, reaches 37%. This value is among the largest reported so far for TMR structures comprising a ferromagnetic Heusler electrode.

Further investigations of the magnetotransport properties of TMR structures grown with optimized parameters are in progress. The main focus will be on using suitable seed layers in order to achieve highly textured or even epitaxial CCFA thin films. The combination of epitaxial CCFA electrodes with epitaxial MgO barriers promises much higher TMR ratios and insight into the half-metallic properties at the interface.

[1] S. A. Wolf, D. D. Awschalom, R. A. Buhrman, J. M. Daughton, S. von Molnár, M. L. Roukes, A. Y. Chtchelkanova, and D. M. Treger, Science **294**, 1488 (2001).
[2] F. Heusler, Verh. Dtsch. Phys. Ges. **5**, 219 (1903).
[3] I. Galanakis, P. H. Dederichs, and N. Papanikolaou, Phys. Rev. B **66**, 174429 (2002).
[4] Y. Miura, K. Nagao, and M. Shirai, Phys. Rev. B **69**, 144413 (2004).
[5] T. Block, C. Felser, G. Jakob, and J. Ensling, J. Solid State Chem. **176**, 646 (2003).
[6] K. Inomata, S. Okamura, R. Goto, and N. Tezuka, Jpn. J. Appl. Phys. **42**, L419, (2003).
[7] R. Kelekar and B. M. Clemens, J. App. Phys. **96**, 540 (2004).
[8] H. J. Elmers, G. H. Fecher, D. Valdaitsev, S. A. Nepijko, A. Gloskovskii, G. Jakob, G. Schönhense, S. Wurmehl, T. Block, C. Felser, P.-C. Hsu, W.-L. Tsai, and S. Cramm, Phys. Rev. B **67**, 104412 (2003).

Single-crystalline Fe nanopillars for spin-transfer measurements

H. Dassow[1,3], R. Lehndorff[1,3], D. E. Bürgler[1,3], M. Buchmeier[1,3], P. A. Grünberg[1,3], C. M. Schneider[1,3], and A. van der Hart[2,3]
[1] *Institute of Solid State Research - Electronic Properties (IFF6)*
[2] *Institute of Thin Films and Interfaces - Process Technology (ISG-PT)*
[3] *CNI – Center of Nanoelectronic Systems for Information Technology*

Current-induced magnetization switching (CIMS) due to spin-transfer torques is an advanced switching concept for magnetic nanostructures in spintronic devices. Most previous studies employed sputtered, polycrystalline samples. Here, we report on the first measurements of CIMS in single-crystalline Fe(14 nm)/Cr(0.9 nm)/Fe(10 nm)/Ag(6 nm)/Fe(2 nm) nanopillars. The central Fe layer is coupled to the thick one by interlayer exchange coupling over the Cr spacer. Nanopillars with diameter $d \approx 150$ nm are prepared by optical and e-beam lithography. By applying a DC current at small magnetic fields, we observe CIMS at both polarities of the current. We assign this behavior to the opposite spin scattering asymmetries of the Fe/Cr and Fe/Ag interfaces. At high magnetic fields, a step-like resistance change most likely due to magnetic excitations is measured at positive bias current. The critical current density is $j_c \approx 10^8$ A/cm^2.

In a magnetic multilayer an electric current perpendicular to the layers (CPP) gets spin polarized by the ferromagnetic layers, leading to the giant magneto resistance effect (GMR). Thus, spin currents sense the magnetization state of the magnetic system. Slonczewski [1] and Berger [2] first predicted that these spin currents can also directly influence the magnetizations without applying an external magnetic field. At low fields, the so-called spin-transfer effect leads to current-induced magnetic switching [3, 4] making it a promising effect for an advanced switching concept [5]. At fields exceeding the coercivity, the spin-transfer effect excites large angle precessional motions of the magnetization and generates microwave signals [6].

We deposit the magnetic multilayer with a standard MBE system. A 150 nm-thick Ag(001) buffer layer on a GaAs(001) substrate improves growth quality and serves as a bottom lead for the resistance measurements. The following layers are deposited at room temperature: Fe(14)/Cr(0.9)/Fe(10)/Ag(6)/Fe(2) [thicknesses in nm]. They all grow epitaxially with (001) orientation. The two bottom layers [Fe(14) and Fe(10)] are coupled by interlayer exchange coupling over the Cr interlayer. The Fe(10) layer is therefore magnetically harder than the top Fe(2) layer. In order to prevent sample oxidation we use a 50 nm-thick Au capping layer, which also protects the layers in the subsequent etching steps.

In order to measure the spin-torque effects in the CPP-geometry we have developed a combined process of optical and e-beam lithography. A scheme of the junction geometry is presented in Fig. 1(a). We use HSQ (Hydrogen Silsesquioxane) as negative e-beam sensitive resist to define small nanopillars and ion-beam etching (IBE) to transfer the pattern to the sample [see Fig. 1(b)]. The pillar is then planarized by spin-coating HSQ and opened by IBE to have access to the top of the nanopillar. The top electrode for the 4-point resistance measurements is prepared by lift-off of 300 nm Au.

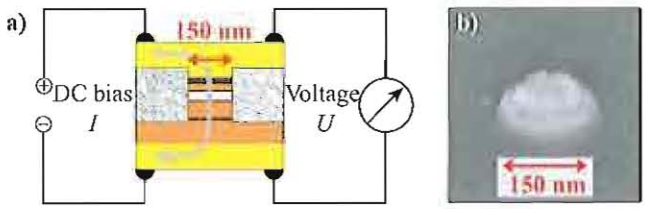

FIG. 1: (a) Scheme of the junction geometry. The DC current is confined to a diameter of $d \approx 150$ nm by the nanopillar. The voltage drop is measured across the pillar in 4-point geometry. (b) SEM micrograph of a nanopillar after ion-beam etching showing typical redeposition effects at the edges.

The DC voltage drop of a constant current I applied to the junction is measured, and by dividing with I we calculate the absolute resistance R. The differential resistance dU/dI is recorded with lock-on technique by mixing a constant current with a small modulated voltage (≈ 300 μV and ≈ 12 kHz).

The CPP magnetoresistance loop of a junction without applying a DC bias current is shown in Fig. 2. The solid blue (dashed green) line represents the data with magnetic field along the easy (hard) axis of Fe(001). The curves show a completely different behavior for the two directions, but are the same along the second pair of easy and hard axes. Thus, the structure is still single-crystalline and exhibits 4-fold magnetocrystalline in-plane anisotropy. The saturation field of the structured sample is 190 mT, which is more than twice the value of the extended layers. Another difference is obvious in the minor GMR loop (inset of Fig 2). Coming from large positive magnetic field, the resistance drops to a smaller value and jumps back to the high resistance state at larger negative fields. On the way back, the resistance stays at the maximum value. The drop on the first half of the cycle does not occur in every measurement.

Thus, the patterning has changed the magnetic config-

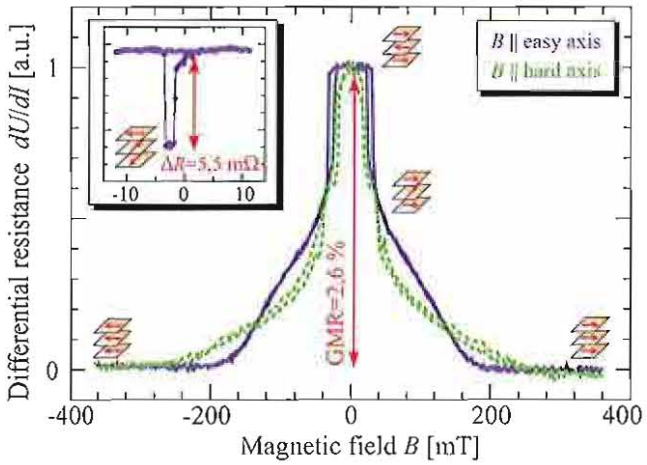

FIG. 2: Magnetoresistance loop with magnetic field parallel to an easy axis (blue solid) and a hard axis (green dashed). Inset: Minor magnetoresistance loop. Only in the first half of the loop ($+B \rightarrow -B$) the resistance drops to a smaller value corresponding to a canted magnetization state. In the second half the resistance stays at the maximum value.

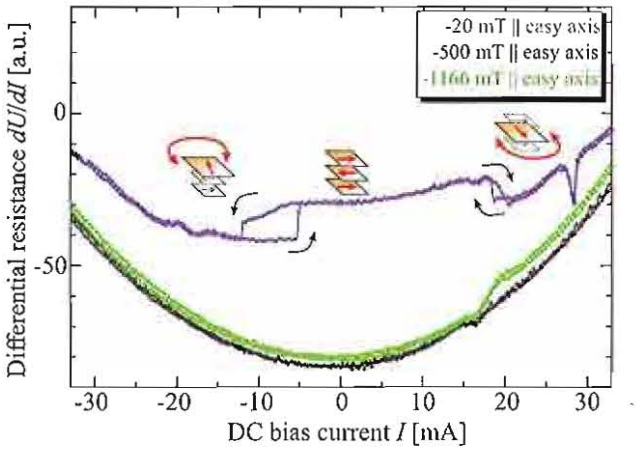

FIG. 3: DC current loops with magnetic field parallel to an easy axis. At high magnetic fields of -1166 mT a single step occurs at positive bias currents. At smaller magnetic fields (-500 mT) this step is less pronounced. At -20 m, we observe hysteretic CIMS at both polarities of the current and relate it to the opposite spin scattering asymmetries of the Fe/Cr and Fe/Ag interface, respectively.

uration by introducing dipolar stray fields over the edges of the nanomagnet, and we cannot separate the contributions of both subsystems to the GMR. The dramatic increase in the saturation field can also be explained by the competition between the interlayer exchange coupling, external, and dipolar fields.

The overall GMR ratio defined as $(R_{\mathrm{AP}} - R_{\mathrm{P}})/R_{\mathrm{P}} = 2.6\%$@RT and 5.6%@4 K, where R_{AP} is the highest resistance value in the antiparallel configuration and R_{P} denotes the smallest resistance in the saturated state.

A DC current influences the resistance R and, at some critical values, the magnetization state of the junction (see Fig. 3). Positive current corresponds to an electron flow from the "free" Fe(2) to "fixed" Fe(10) layer. We observe a parabolic background which is usually explained by Joule heating of the junction. On top of that, we measure field dependent resistance changes, which can be attributed to spin-torque effects. For instance, at -20 mT, the resistance drops at $I_C^+ = +18.2$ mA from a high-resistive to an intermediate state. After reducing the current again, the resistance jumps back to the large value. But also at negative bias the resistance changes at $I_C^- = -12.1$ mA from large to small resistance. With an estimated junction diameter of $d = 150$ nm the corresponding critical current densities are $j_c^+ = 1 \cdot 10^8$ A/cm^2 and $j_c^- = -7 \cdot 10^7$ A/cm^2.

The occurrence of jumps at both polarities of the current is at first glance surprising, but it can be explained by taking into account that Fe/Cr and Fe/Ag interfaces have spin scattering asymmetries with opposite signs, leading to inverted spin-transfer torques and, thus, inverse CIMS – similar to inverse GMR [7, 8]. For $I < 0$, the torque induced by the Fe/Ag/Fe subsystem switches the top Fe(2) layer, whereas for $I > 0$ the torque generated by the Fe/Cr/Fe subsystem remagnetizes the central Fe(10) layer.

At large magnetic fields exceeding the saturation field, the two thick bottom layers [Fe(14) and Fe(10)] are stronger stabilized by the Zeeman energy than the Fe(2) layer, and therefore only one step-like resistance change at $I > 0$ due to the magnetic excitation of Fe(2) is observed under these conditions.

In summary, we have prepared single crystalline Fe nanopillars by molecular beam epitaxy and a combined process of optical and e-beam lithography. After the structuring process the magnetic properties change so that the "free" Fe(2) layer is now coupled to the rest of the system by dipolar stray fields. Under the influence of a DC current we are able to measure distinct resistance changes, which give clear evidence of spin-transfer torque effects, in particular hysteretic CIMS, at current densities $j_c \approx 10^8$ A/cm^2.

[1] J. C. Slonczewski, J. Mag. Mag. Mater. **159**, L1 (1996).
[2] L. Berger, Phys. Rev. B **54**, 9353 (1996).
[3] E. B. Myers *et al.*, Science **285**, 867 (1999).
[4] J. Grollier *et al.*, Appl. Phys. Lett. **78**, 3663 (2001).
[5] D. E. Bürgler, in *Magnetism goes Nano* (Forschungszentrum Jülich GmbH, 2005).
[6] S. I. Kiselev *et al.*, Nature **425**, 380 (2003).
[7] M. Buchmeier, R. Schreiber, D. E. Bürgler, and P. Grünberg, Europhys. Lett. **63**, 874 (2003).
[8] M. AlHajDarwish *et al.*, Phys. Rev. Lett. **93**, 157203 (2004).

Epitaxial growth and characterization of Fe thin films on wurtzite GaN(0001)

R. Meijers[1], R. Calarco[1], M. Buchmeier[2], D.E. Buergler[2], N. Kaluza[1], H. Hardtdegen[1], M.v.d. Ahe[1], H.L. Bay[1], H. Lueth[1]

[1]*Institute of Thin Films and Interfaces (ISG1) and cni - Center of Nanoelectronic Systems for Information Technology, Research Centre Juelich, 52425 Juelich, Germany*

[2]*Institute of Solid State Research (IFF) and cni - Center of Nanoelectronic Systems for Information Technology, Research Centre Juelich, 52425 Juelich, Germany*

Fe films of different thicknesses were deposited on wurtzite GaN(0001) layers by electron beam evaporation. They were studied by a number of characterization techniques such as low-energy electron diffraction (LEED), X-ray diffraction (XRD), atomic force microscopy (AFM), and ferromagnetic resonance (FMR). Despite the large lattice mismatch between Fe and wurtzite GaN a clear epitaxial relation was determined. Three distinct Fe domain orientations were found rotated by 120° relative to each other. Due to the formation of crystalline domains a hexagonal in-plane magnetic anisotropy was observed.

In recent years physical processes governing spin-dependent phenomena in semiconductors have been studied intensively, in particular with the aim of quantum information processing. An essential ingredient is the achievement of an efficient injection of a spin-polarized current from a ferromagnet (FM) into a semiconductor (SC). Advantageous is a good crystalline quality of the FM and an abrupt interface FM/SC. Spin injection efficiencies up to 5% have been achieved at room temperature for Fe layers grown epitaxially on GaAs [1]. Another interesting heterostructure might be Fe/GaN, because recent theoretical calculations predict a long spin relaxation lifetime in pure GaN, about three orders of magnitude longer than in GaAs [2]. Spin coherence lifetimes of 20 ns at T = 5K were observed experimentally in bulk GaN [3], despite dislocation densities of ~$5x10^{8}$ cm^{2}. Although Fe has a cubic symmetry in contrast to the hexagonal wurtzite structure of GaN it could still be an interesting heterostructure, because Fe layers grown on other hexagonal surfaces showed good ferromagnetic properties.

We deposited a series of Fe layers with different thicknesses in ultra high vacuum on (0001) GaN layers grown by metal organic vapour-phase epitaxy. Details of the growth conditions are discussed in [4]. The crystalline structure and a possible epitaxial relation to the GaN substrate of the Fe layers was determined by low energy electron diffraction (LEED) and x-ray diffraction (XRD).

θ-2θ scans revealed only peaks corresponding to a (110) bcc Fe surface and thus we conclude that the Fe layers grow epitaxially with (110) planes parallel to the (0001) GaN surface. However, the relative orientation of the (110) Fe plane to the (0001) GaN plane can not be determined from these measurements so there is still a rotational degree of freedom around the (0001) surface normal.

To investigate the epitaxial relation between both layers LEED images and pole figures measured by XRD were studied and compared with theoretical images from simulations. Examples of the experimental data are shown in Fig.1 a,b.

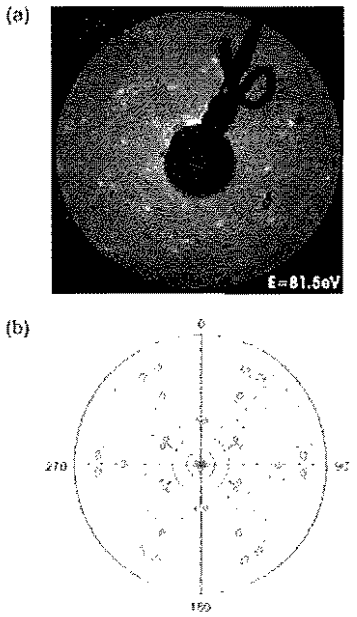

Figure 1 (a) Photograph of complex LEED pattern of a 70 nm Fe layer deposited on GaN(0001) taken with an electron beam energy of E = 81.5 eV after annealing at 500 °C for 60 min. (b) Measured pole figure for a 70 nm Fe(110) / GaN(0001) / Al_2O_3(0001) structure.

Theoretical calculations for cubic layers on hexagonal ones suggest two preferred orientations between both layers, which are the so-called Nishiyama-Wassermann (NW) and Kurdjumov-Sachs (KS) orientations. Taking into account the hexagonal symmetry of one of the layers, three distinct orientations are actually equivalent under a symmetry operation, due the equivalence of the three hexagon diagonals, and are thus equally likely. Therefore one would expect to find three different domain types in the grown layers, which is indeed observed experimentally. The groups of points in Fig.1 a,b already indicated this. The experimental results in these figures fit perfectly to simulations for three equivalent NW domains rotated by 120° relative to each other.

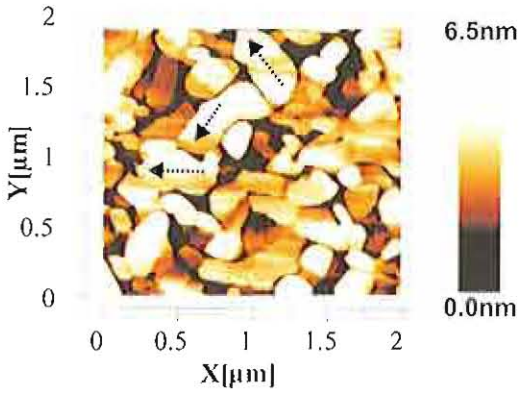

Figure 2 AFM image showing the surface morphology of a 70nm Fe layer deposited at room temperature. For thicker layers at higher growth rate, the island-like structureThe arrows indicate the different orientation of the islands.

The three domain types can also be observed in some AFM images, depending on the growth parameters of the layer. As indicated by the arrows in Fig.2 islands are present which seem to have a certain preferential direction and the relative angle between them is again 120°. The formation of islands is to be expected for the relatively large lattice mismatch between Fe(110) and GaN(0001), but the average roughness of a single island is below 0.5 nm as determined by a cross-section of the AFM image in Fig.2.

Magnetic properties of thin Fe layers varying in thickness between 5 and 50 nm were investigated with the magneto optic Kerr effect (MOKE) and FMR. The MOKE experiments, at RT, show a thickness-dependent easy axis coercive field between 1 mT (5 nm) and 2 mT (40 nm). To investigate the magnetic anisotropy, the angle dependence of the FMR signal was measured with a cylindrical resonator with the magnetic field applied in-plane. The resulting diagram for a 20 nm Fe layer is shown in Fig.3 where the colour coding indicates the reflected microwave-radiation. The graph clearly shows a hexagonal anisotropy in contrast to a cubic one for bulk Fe, i.e. the easy axes are 60° apart from each other and the same holds for the hard axes. This can be explained by the formation of three types of crystalline Fe domains rotated by 120° relative to each other as described above; so these magnetic measurements support our structural results. By comparing the FMR spectrum with XRD measurements, we conclude that the easy axis is parallel to a [001]Fe axis, which is also the case in bulk α-Fe. The hexagonal anisotropy with a strength of 8mT (cf. Fe(001)/Ag: ~55 mT) is independent of the layer thickness and surprisingly large, since for hexagonal symmetry the first-order cubic anisotropy contributions should cancel out and second-order terms are expected to be much smaller.

We conclude that despite the formation of differently oriented crystalline domains, the Fe layers show good ferromagnetic properties, which are the topic of a forthcoming paper [5].

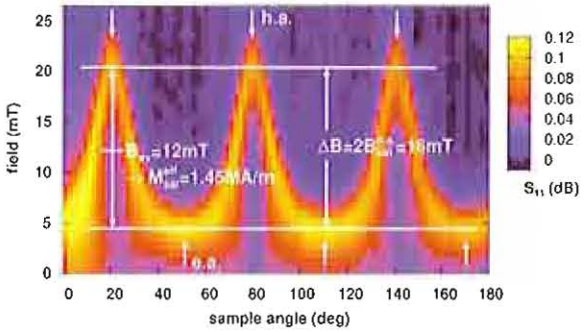

Figure 3 Angle-dependence of FMR signal of a 20 nm Fe layer measured at RT with the field applied in-plane. Microwaves with a frequency of 4.37GHz were used. The reflected microwave intensity (colour code) is plotted against the applied magnetic field (y-axis) and the angle between the magnetic field and the sample(x-axis). The easy axes (e.a.) as well as the hard axes (h.a.) are marked by white arrows.

In summary, bcc Fe(110) films were grown epitaxially on wurtzite GaN(0001). Due to the hexagonal symmetry of the GaN(0001) surface, the formation of three crystalline domain orientations was observed. The epitaxial relation was determined to be of the Nishiyama–Wassermann type. Despite the formation of crystalline domains, the layers show ferromagnetism at RT and an effective hexagonal in-plane magnetic anisotropy as a result of the three crystalline domain types in contrast to the cubic anisotropy expected for bulk bcc Fe.

Further investigations into the behaviour of Fe on $Al_xGa_{1-x}N$ and $In_xGa_{1-x}N$ for $0<x<1$ as well as the determination of the Schottky barrier between Fe and the respective nitride substrate are planned.

[1] M. Ramsteiner, Microelectron. Eng. 63 (2002) 3.

[2] S. Krishnamurthy, M. van Schilfgaarde, N. Newman, Appl. Phys. Lett. 83 (2003) 1761.

[3] B. Beschoten, E. Johnston-Halperin, D.K. Young, M. Poggio, J.E. Grimaldi, S. Keller, S.P. DenBaars, U.K. Mishra, E.L. Hu, D.D. Awschalom, Phys. Rev. B 63 (2001) 121202.

[4] R. Meijers, R. Calarco, N. Kaluza, H. Hardtdegen, M.v.d. Ahe, H.L. Bay, H. Lueth, M. Buchmeier, D.E. Buergler J. Crystal Growth 283 (2005) 500.

[5] M. Buchmeier, D.E. Buergler, et al., submitted to physica status solidi.

Is (Ga,Mn)N ferromagnetic?

K. Sato[1,2], H. Katayama-Yoshida[2], W. Schweika[3] and P. H. Dederichs[1]
[1]*IFF-Theorie III;* [2]*University of Osaka, Japan;* [3]*IFF-Streumethoden*

The magnetic properties and the Curie temperatures of dilute magnetic semiconductors (DMS) are calculated from first-principles by mapping *ab initio* results on a Heisenberg model. Basically two classes of DMS are found. The first class includes systems like (Ga, Mn)Sb and (Ga, Mn)As, where the Mn d-states are nearly localised. Here the ferromagnetism is induced by $p-d$ exchange, being relatively weak, but long ranged. The second class consists of systems like (Ga, Mn)N and (Zn, Cr)Te, where the impurity d-levels lie in the gap, exhibiting impurity bands for sufficiently large concentrations. Here the ferromagnetism is induced by double exchange within the impurity band, leading to strong, but short-ranged exchange interactions. In such dilute systems magnetic percolation is difficult to achieve, so that, in particular in (Ga, Mn)N, the Curie temperatures are very small.

Dilute magnetic semiconductors (DMSs), such as (In, Mn)As and (Ga, Mn)As have been well investigated as hopeful materials for spintronics. Curie temperatures (T_C's) of these DMSs are well established and some prototypes of spintronics devices have been produced based on these DMSs. The magnetism in these DMSs have been theoretically investigated and it is known that the ferromagnetism in these systems as well as in (Ga, Mn)Sb can be well described by Zener's p-d exchange interaction, due to the fact that the majority d-states lies energetically in the lower part of the valence band.

While these p-d exchange systems, in which the majority d-states of Mn impurities are practically localized, are well understood, there exist an even larger class of systems where the d-levels lie in the gap exhibiting impurity bands for sufficiently large concentrations. To these impurity band systems belong (Ga, Mn)N, (Ga, Cr)N, (Ga, Cr)As, (Zn, Cr)Te, (Zn, Cr)Sc and many others as shown by first-principles calculations. Most of these systems are controversially discussed in the literature. This concerns in especially (Ga, Mn)N, which according to predictions by Dietl based on the p – d model is a candidate for high temperature ferromagnetism. However the experimentally reported Curie temperatures scatter between 20-940 K and even spin-glass behaviour has been observed.

In this paper, we will show that a general obstacle for ferromagnetism exists in these dilute systems, in particular in (Ga, Mn)N [1]. Due to the large band gap the wave function of the impurity state in the gap is well localized, leading to a strong, but short ranged exchange interaction, being dominated by the nearest neighbors. Therefore, for low concentrations, the percolation of a ferromagnetic cluster through the whole crystal cannot be achieved, so that a ferromagnetic alignment of the impurity moments cannot occur. Thus a paramagnetic or disordered, spin-glass like, state is observed, in particular for low concentrations.

The electronic structure of DMS is calculated based on the local density approximation (LDA) by using the Korringa-Kohn-Rostoker (KKR) method. We focus on (Ga, Mn)N and (Ga, Mn)As as typical examples for the double exchange and the p-d exchange systems, respectively. In these systems, Mn impurities distribute randomly on Ga sites in the host semiconductor being described as $(Ga_{1-c}, Mn_c)X$, where c is the Mn concentration and X refers to N or As. To describe the substitutional disorder, we use the coherent potential approximation (CPA). While the CPA describes the electronic structure in the mean field approximation, we go beyond this approximation and explicitly calculate the exchange interaction J_{ij} between two impurities at sites i and j, which are embedded in the ferromagnetic CPA medium. For the evaluation of J_{ij} we use the frozen potential approximation and apply a formula by Liechtenstein et al.

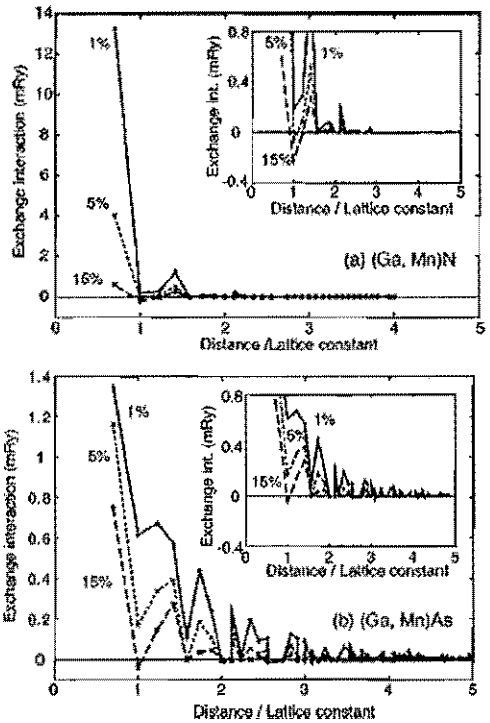

FIG. 1. Calculated exchange interaction J_{ij} in (a) (Ga, Mn)N and (b) (Ga, Mn)As as a function of distance.

According to this formula, the total energy change due to infinitesimal rotations of the two magnetic moments at site i and j is calculated using the magnetic force theorem, and the total energy change is mapped on the (classical) Heisenberg model $H = -\Sigma_{i=j} J_{ij} \vec{e}_i \vec{e}_j$, where $\vec{e}_i$ is a unit vector parallel to the magnetic moment at site i, thus resulting in the effective exchange coupling constant J_{ij}.

Figure 1 shows the calculated exchange interactions J_{ij} in (Ga, Mn)N and (Ga, Mn)As. As shown in the fig. 1-(a), in (Ga, Mn)N the interaction strength is strong, but the interaction range is short, so that the exchange coupling between nearest neighbors dominates. For example, the nearest neighbor interaction J_{01} in 1% Mn-doped GaN is about 13.5 mRy, while the other interactions are almost 2 orders of magnitude smaller than J_{01} except for J_{04}. Therefore, in this case the very large mean field value of T_C is mostly determined by J_{01}.

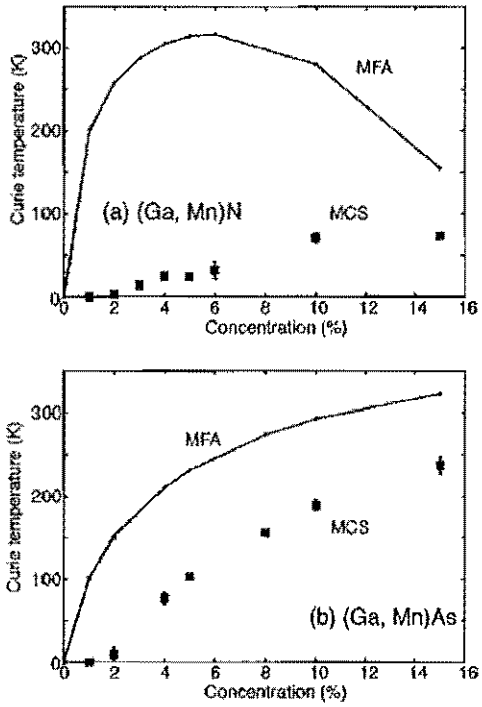

FIG. 2. Curie temperatures of (a) (Ga, Mn)N and (b) (Ga, Mn)As calculated by the mean field approximation (MFA, solid lines) and by Monte Carlo simulations (MCS, filled squares). Interactions up to 15 shells are included.

The interaction arises from the double exchange mechanism between the impurity gap states. Since these are exponentially localised, the interaction is short ranged being dominated by the nearest neighbours. In contrast to (Ga, Mn)N, the interaction is long ranged in (Ga, Mn)As, in particular at small concentrations, as is shown in Fig. 1(b). Here the p−d exchange mechanism is dominant, as shown in Ref. 2. In fact, the interaction extends further then 3-4 lattice constants and is mediated by the extended hole state. Only at higher concentrations the interaction range is reduced by screening.

The Curie temperatures T_c are firstly calculated in the mean field approximation, leading to $k_B T_c^{MFA} = \frac{2}{3} c \sum_{i=0} J_{oi}$, where k_B is the Boltzmann constant. Already at small concentrations c, this leads to very high Curie temperatures, especially for (Ga, Mn)N. These high values are dominated in the sum overall neighbours i by the strong interaction of the nearest neighbours. Unfortunately the calculated trend is wrong. The reason for this is that at small concentrations the strong nearest neighbour interaction becomes ineffective, since the small concentrations do not allow a cluster of nearest neighbours to percolate through the whole system. In fact, for the considered fcc sublattice the percolation threshold for nn interaction is 20 %, so that below this threshold ferromagnetism can only exist if the longer ranged interactions are sufficiently strong.

For these reasons we have calculated the Curie temperatures numerically exact by Monte Carlo simulations using the cumulant crossing method of Binder. Three different cell sizes are used and the results are averaged over 30 random configurations of Mn atoms. For (Ga, Mn)N the resulting Curie temperatures are for small concentrations reduced by one to two orders of magnitudes and even for 5, 10 or 15 % Mn the Curie temperatures are far below room temperature. In contrast to this, for (Ga, Mn)As the reductions are due to the longer ranged interactions not so large, but still significant. In fact, here the calculated T_c-values are in good agreement with recent measurements for thin films of (Ga, Mn)As, being free of Mn interstitials.

Thus we have shown that in the usual concentration range below 10 % strong ferromagnetism cannot occur in (Ga, Mn)N. Due to the large band gap of GaN the Mn-Mn interaction is short ranged which due to percolation problems strongly reduces the Curie temperatures. Higher Curie temperatures naturally require larger impurity concentrations. This is achievable in II-VI semiconductor, e.g. in $Zn_{1-c}Cr_cTe$. Here our calculations yield for 20 % Cr a Curie temperature of 300 K [3], being in good agreement with experiments by Ando et al. [4].

[1] K. Sato et al., Phys, Rev. **B70**, 201202(R) (2004).
[2] K. Sato et al., Physica **B340-342**, 863 (2003).
[3] T. Fukushima et al., Jap. J. Appl. Phys. **43**, L1416 (2004).
[4] H. Saito et al., Phys. Rev. Lett. **90**, 207202 (2003).

Information Technology with Nanoelectronic Systems

Terahertz-Electronics

Meandering of the grain boundary in high-T_c bicrystal Josephson junctions
M. I. Faley, C. L. Jia, L. Houben, D. Meertens, U. Poppe and K. Urban

Josephson and Classical Detection of Terahertz Radiation Using [100]-Tilt $YBa_2Cu_3O_{7-x}$ Bicrystal Junctions.
Y.Y. Divin, D.A. Tkachev, V.V. Pavlovskii, M. Liatti, U. Poppe, V. N.Gubankov, K. Urban

Applications of a High Temperature Superconductor SQUID Microscope with soft-magnetic Flux Guide
U. Poppe, M. I. Faley, R. R. Gareev, M.Weides, E. Zimmermann, W. Glaas, K. Urban

Meandering of the grain boundary in high-T_c bicrystal Josephson junctions

M. I. Faley, C. L. Jia, L. Houben, D. Meertens, U. Poppe and K. Urban
Institut für Festkörperforschung, Forschungszentrum Jülich GmbH, Jülich, Germany

We have produced submicrometer wide bicrystal Josephson junctions on the basis of $YBa_2Cu_3O_{7-\delta}$ (YBCO) films and investigated their microstructure and superconducting properties. A 300 nm thick homoepitaxial buffer layer of $SrTiO_3$ on the $SrTiO_3$ bicrystal substrates has helped to improve the quality and reproducibility of the junctions. The observed spread of the angles of the deviation of the GB in the film from the direction of the GB in the substrate on the slot- and other defect-free parts of the GB was below 10°. Due to the d-wave symmetry of the order parameter in YBCO the reduction of the curvature of the GB leads to an improvement of the homogeneity of the current flow and a doubling of the critical current I_c of the junction. The observed I_cR_n product of symmetric 20° bicrystal junctions was ~ 400 μV at 77.4 K and ~ 1 mV at 63 K. Integration of such junctions in SQUIDs with a square 16-mm multilayer flux transformer has allowed, for the first time, to reach a field resolution for the high-T_c magnetometers of ~ 3.5 fT/√Hz at 77.4 K [1].

For the applications of sensitive THz detectors and low noise superconducting quantum interference devices (SQUIDs) it is important to have the highest possible values of the characteristic voltages $V_c = I_cR_n$ of the Josephson junctions. Low noise SQUIDs serve, e.g., as a preamplifier in the signal multiplexer for the bolometer arrays used for radioastronomy at THz frequencies [2]. The use of the [100] tilted high-T_c bicrystal junctions (see, e.g., [3] and references therein) is problematic for SQUIDs because tilted at angles above 5° $YBa_2Cu_3O_{7-x}$ (YBCO) films demonstrate a reduced critical current density (see, e.g., [4]), which can lead to an increased magnetic flux motion and noise in the SQUID applications of such junctions. In this work we report on a possible way to improve reproducibility and V_c of bicrystal Josephson junctions with in-plane misorientation.

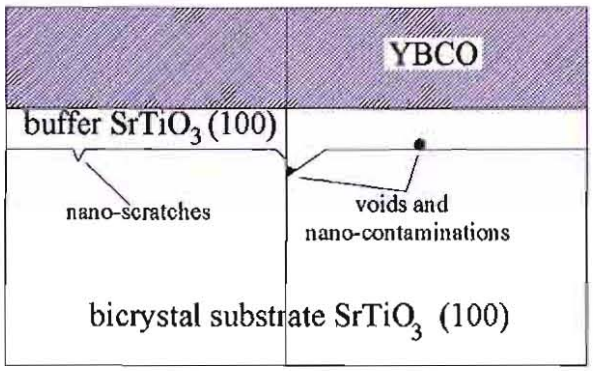

Figure 1 Schematic view of the bicrystal $SrTiO_3$ (100) substrate with a $SrTiO_3$ (100) buffer layer and a YBCO film.

One of the main obstacles limiting the reproducibility of the bicrystal junctions is the quality of the bicrystal grain boundary (GB) in the substrates. Voids are often present in the GB and prevent electrical contact between the electrodes in some parts of the GB in the superconducting film. To reduce the number of these and other defects in the GB and on other parts of the bicrystal substrate we have deposited a $SrTiO_3$ buffer layer ~ 300 nm thick prior to the deposition of the YBCO film (see Fig.1). The films were deposited by sputtering at 2 mbar ($SrTiO_3$) or 3.3 mbar (YBCO) in 99.999% pure oxygen. HRTEM and AFM studies have shown that the microstructure of the $SrTiO_3$ films is better compared to the microstructural properties of the pristine substrates. This buffer layer has covered the nanometer size defects on the GB and led to a significant reduction of meandering and density of slots in the GB of the YBCO film (see Fig.2).

Figure 2 HRSEM images of a bicrystal GB in a YBCO film: (a) GB with a slot and (b) GB without slots.

A significant effect on the superconducting current density can be expected from the local deviations of the GB from a symmetric one, because this can lead to a more than

one order of magnitude change in the critical current density J_c, normal state resistance R_n, and characteristic voltage V_c of the bicrystal Josephson junction due to the d-wave symmetry of the order parameter in YBCO and the anisotropy of the tunnelling matrix elements [5]. For the symmetric GB the local critical Josephson current density can be described by the Sigrist-Rise expression [6]:

$$J_c \sim f_1(n_1)f_2(n_2) = [\sin^2(\alpha+\beta)-\cos^2(\alpha+\beta)][\sin^2(\alpha-\beta)-\cos^2(\alpha-\beta)] = (\cos 4\alpha+\cos 4\beta)/2 \quad , \quad (1)$$

where 2α is the in-plane misorientation angle in the bicrystal substrate and β is the local angle between GBs in the YBCO film and in the substrate. In defect-free parts of the GB like one shown in the Fig.2b the spreads of the angle β is below 10°. According to the expression (1) this should lead to an improvement of the homogeneity of the current flow and a doubling of the total critical current I_c of the junction (see Fig.3).

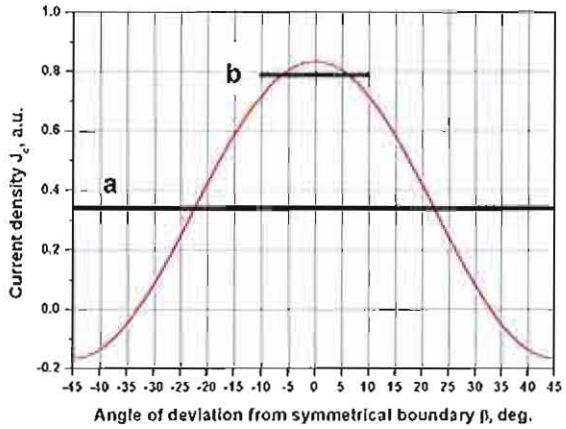

Figure 3 Local critical current density J_c vs angle β of deviation from symmetrical GB for 24° bicrystal Josephson junction estimated (red line) according to the expression (1) and average values of J_c for large-angle (a) and 10° (b) spreads of β.

The junctions were integrated in SQUID magnetometers and gradiometers with multilayer flux transformers similar to ones described in [7]. The magnetometers were vacuum-tight encapsulated and surrounded by a grounded conductive non-magnetic microwave absorber. Low-pass filters ($\tau \sim 1$ μs) were installed on the electrical inputs for the heater and the modulation-feedback coil. The estimated Nyquist noise of the microwave absorber was ~ 1 fT/√Hz and the cut-off frequency was ~ 10 GHz at 77.4 K.

The SQUID magnetometers with a square 16-mm multilayer flux transformer ($\partial B/\partial \Phi \sim 0.5$ nT/Φ_0) have, for the first time, reached a field resolution of ~ 3.5 fT/√Hz at the white noise frequencies above 10 Hz and ~ 7 fT/√Hz at 1 Hz and operation temperature 77.4 K (see Fig.4). The measurements of the intrinsic noise of the magnetometers were performed inside a 3-layer μ-metal shield and a YBCO superconducting shield.

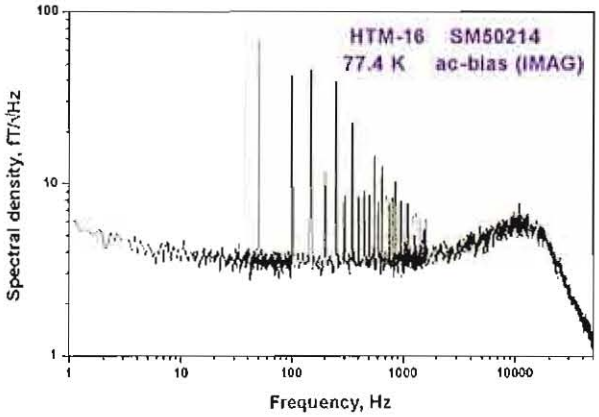

Figure 4 Spectral density of field noise of a dc-SQUID magnetometer with the described Josephson junctions and a 16-mm multilayer flux transformer.

The SQUIDs with a gradiometric flux transformer (base length $L \sim 10$ mm) have achieved gradient resolutions ~ 15 fT/cm√Hz at frequencies above 10 Hz and ~ 30 fT/cm√Hz at 1 Hz and an operation temperature of 77.4 K. A decrease of the operation temperature down to the melting nitrogen temperature ~ 63 K has sometimes resulted in about 2 times increase of the SQUID voltage modulation and some further reduction of the noise.

Thus the modifications of the Josephson junction technology has helped to improve the resolution of the high-T_c SQUID sensors at 77.4 K operation temperature to the typical resolution of the commercially available low-T_c SQUID sensors operating at 4.2 K. The performed integration of the modified junctions in the DC-SQUID magnetometers has demonstrated the effects of the changes in the junction technology.

[1] M. I. Faley, C. L. Jia, L. Houben, D. Meertens, U. Poppe and K. Urban, Supercond. Sci. Technol. **19,** S1 (2006).

[2] J. E. Ruhl et al., The South Pole Telescope, arXiv:astro-ph/0411122 v1 4 Nov 2004

[3] Divin Y Y, Poppe U, Jia C L, Shadrin P M, and Urban K Physica C **372-376** 115 (2002). E. Sarnelli, G. Testa, D. Crimaldi, A. Monaco, and M. A. Navacerrada, Supercond. Sci. Technol. **18,** L35 (2005).

[4] T. Nurgaliev, E. Mateev, T. Donchev, S. Miteva, P. B. Mozhaev, I. V. Borisenko, G. A. Ovsyannikov, and I. M. Kotelyanski, Vacuum **76,** 245 (2004).

[5] Z. G. Ivanov, E. A. Stepantsov, T. Claeson, F. Wenger, S. Y. Lin, N. Khare, and P. Chaudhari, Phys. Rev. B **57** 602 (1998).

[6] M. Sigrist and T. M. Rice, J. Low Temp. Phys. **95,** 389 (1994).

[7] M. I. Faley, U. Poppe, K. Urban, V. Yu. Slobodchikov, Yu. V. Maslennikov, A. Gapelyuk, B. Sawitzki , and A. Schirdewan, Appl. Phys. Lett. **81,** 2406 (2002).

Josephson and Classical Detection of Terahertz Radiation Using [100]-Tilt $YBa_2Cu_3O_{7-x}$ Bicrystal Junctions.

Y.Y. Divin[1], D.A. Tkachev[1], V.V. Pavlovskii[2], M. Liatti[1,2], U. Poppe[1], V. N.Gubankov[2], K. Urban[1]

[1]*CNI-Center of Nanoelectronic Systems for Information Technology and Institute of Solid State Research, Research Center Juelich, Juelich, Germany*

[2]*Institue of Radio Engineering and Electronics of Russian Academy of Sciences, Moscow 101999, Russia*

Detection of THz radiation by [100]-tilt $YBa_2Cu_3O_{7-x}$ bicrystal junctions with high I_cR_n- product has been studied. For low-resistance junctions, Josephson frequency-selective detection was found up to a frequency of 5.3 THz, which is above the optical phonon frequency (f_0 = 4.6 THz) in $YBa_2Cu_3O_{7-x}$. For high-resistance junctions, classical broadband detection was observed up to 0.4 THz. It is shown by computer simulations that a broadband detector, based on optimized [100]-tilt Josephson junctions with R_n =100 Ohm, might reach the values of noise equivalent power NEP <2· 10^{-14} W/Hz$^{1/2}$ up to 2 THz. Low-resistance [100]-tilt junctions are suggested for applications in THz Hilbert spectroscopy and high-resistance junctions – in THz imaging.

A spectral range of the ac Josephson effect and, correspondingly, a frequency-selective detection mechanism in [001]-tilt high-T_c bicrystal junctions were found to scale with characteristic voltages I_cR_n of the junctions [1,2]. Due to an island growth of the c-axis high-T_c thin films, the [001]-tilt junctions demonstrate a faceted meandering of high-T_c bicrystal boundary around a substrate boundary, inhomogeneous current transport and low characteristic voltages I_cR_n. Recently, the [100]-tilt high-T_c Josephson bicrystal junctions with a three-fold increase of the I_cR_n–values have been reported [3] and the spectral range of the ac Josephson effect might be extended to higher frequencies. Here, we report on the detection of THz radiation by [100]-tilt high-T_c bicrystal Josephson junctions.

The *I-V* curves of a 1μm-wide 2×14° [100]-tilt $YBa_2Cu_3O_{7-x}$ bicrystal junction at temperatures from 7 to 75K are shown in Fig. 1, being in good agreement with the RSJ model in the temperature range of 45–75 K [4].

The inset shows an AFM image, indicating that meandering of the $YBa_2Cu_3O_{7-x}$ grain boundary is less than 20 nm.

The normalized response curves $\Delta I(V)/\Delta I_c$ of low-resistance [100]-tilt $YBa_2Cu_3O_{7-x}$ Josephson junction to THz laser radiation are shown in Fig. 2. The curves demonstrate odd-symmetric resonances at voltages $V = hf/2e$, due to a frequency pulling of Josephson oscillations by the THz radiation. A high-frequency fall-down of the resonance amplitudes with exponential behaviour $\propto exp(-(hf/2e)^2/R_nP_0)$ was observed for low-resistance junctions. The P_0–values of the order of 10^{-5} W obtained for [100]-tilt junctions are close to those of the [001]-tilt junctions [2]. The amplitudes of the response curves were several times higher than for [001]-tilt junctions with similar R_n-values [1], due to higher I_cR_n-values. We succeeded in measurements of a response to laser radiation with the frequency of 5.2 THz (inset in Fig.2), which is above the frequency of the strongest optical phonon (4.6 THz) in $YBa_2Cu_3O_{7-x}$.

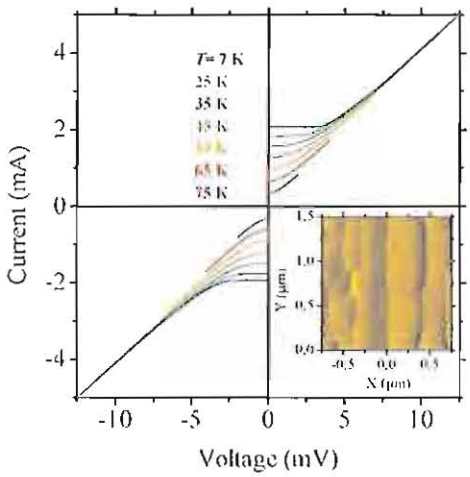

Figure 1 Current-voltage characteristics of a 1μm-wide 2×14° [100]-tilt $YBa_2Cu_3O_{7-x}$ bicrystal junction at temperatures from 7 to 75K. Inset: AFM image of unpatterned [100]-tilt $YBa_2Cu_3O_{7-x}$ grain boundary.

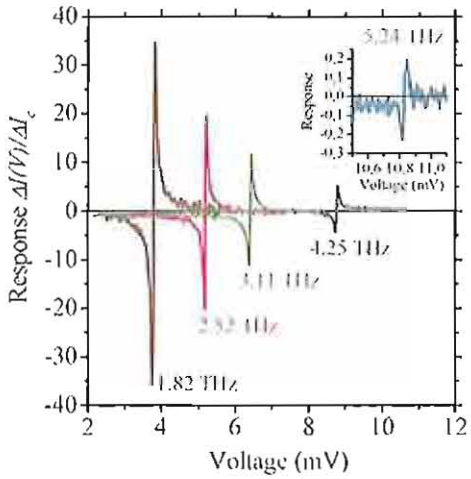

Figure 2 Normalized responses $\Delta I(V)/\Delta I_c$ of low-resistance [100]-tilt $YBa_2Cu_3O_{7-x}$ Josephson junctions to THz radiation. Main graph :R_n = 6 Ω, I_cR_n = 4.8 mV, T = 30 K. Inset: R_n = 1 Ω, I_cR_n = 6 mV, T = 10 K.

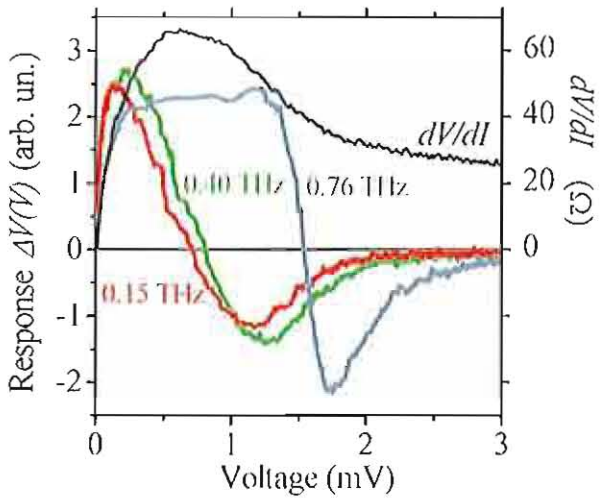

Figure 3 Voltage responses $\Delta V(V)$ of a high-resistance [100]-tilt $YBa_2Cu_3O_{7-x}$ Josephson junction to THz radiation and differential resistance $R_d(V)$. $I_cR_n = 2.8$ mV, $T = 40$ K.

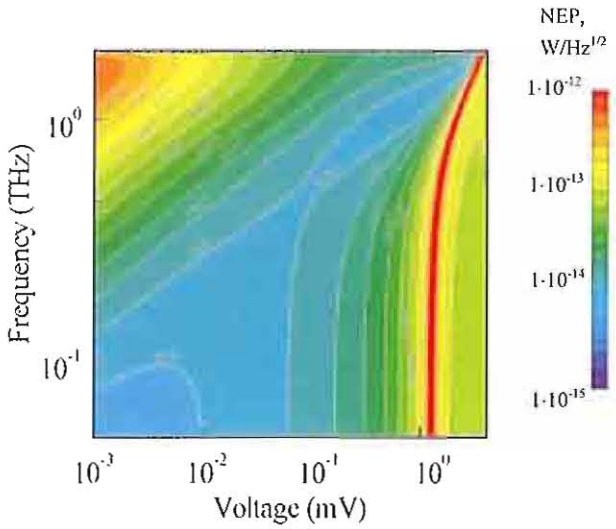

Figure 4 Noise-equlivalent power *NEP* of Josephson detector vs. frequency and voltage. $R_n = 100\ \Omega$, $I_cR_n = 4.4$ mV, $T = 40$ K.

The low-frequency limit f_l of the ac Josephson effect is reached, when separate Josephson spectral lines at $f_n = n2eV/h$ with thermally-broadened linewidths $\delta f_n = n^2\delta f_l$ start to overlap. We got a simple estimate of $f_l = (3\delta f_0 f_c^2/2)^{1/3}$, where $\delta f_0 = 4\pi(2e/h)^2 kTR_n$ and $f_c = 2eI_cR_n/h$ [2]. At lower frequencies, the spectrum of Josephson oscillations is continuous, such that the detection process for low frequencies up to f_l will not be of frequency-selective type. We have studied this type of detection in our high-resistive [100]-tilted junctions with high I_cR_n- values. The experimental results are presented in Fig. 3. The voltage response curves $\Delta V(V)$ of the [100]-tilt junction to radiation with frequencies f up to 0.40 THz are practically frequency independent and proportional to the voltage dependence of the second derivative d^2V/dI^2 of the I-V curve. This behaviour is an essential feature of classical detection. Only the response curve measured at 0.76 THz starts to follow the Josephson frequency-selective mechanism. The estimated f_l-value was around 0.45 THz. This value might be increased for optimised junctions.

We have performed a numerical simulation of radiation detection by high-resistive Josephson junctions with high I_cR_n-values, using the RSJ model. The voltage response ΔV, the impedance $Z(\omega)$ and the noise voltage were calculated from solutions of the Fokker-Plank equation for the Fourier-coefficients of the probability distribution of the Josephson phase and, from this, the responsivity η and noise-equivalent power *NEP* were derived. Results of a computer simulation for *NEP* are shown in Fig. 4. The parameters of Josephson detector are close to those of our best [100]-tilt junctions. It follows from Fig. 5, that this Josephson detector, when biased at a voltage $V = 0.3$ mV, might have values of *NEP* better than $2\cdot10^{-14}$ W/Hz$^{1/2}$ in the frequency range from 0 to 1.8 THz. The estimated value of f_l is around 0.9 THz for this case. Indeed, numerical simulations gave us more optimistic values of the spectral range of broadband detection by Josephson junctions This classical THz Josephson detector requires a working temperature of 30-40 K, which can be easily realized by cryocoolers.

The [100]-tilt $YBa_2Cu_3O_{7-x}$ bicrystal Josephson junctions show excellent perspectives for applications in terahertz Hilbert spectroscopy, where optimized low-resistance junctions with high I_cR_n will improve signal/noise ratio, and in terahertz imaging for medical and security screening, where high-resistance junctions will significantly increase the spectral bandwidth of classical detection [5,6].

[1] Y.Y. Divin, O.Y. Volkov, V.V. Pavlovskii, U. Poppe, K. Urban, IEEE Trans. Appl. Supercond. **11**, 582 (2001).

[2] Y.Y. Divin, O.Y. Volkov, M.V. Liatti, V.N. Gubankov, IEEE Trans. Appl. Supercond. **13**, 676 (2003).

[3] Y.Y. Divin, I.M. Kotelyanskii, P.M. Shadrin, C.L. Jia, U. Poppe, K. Urban, *Proc. 6th European Conf. Appl. Superconductuivity (IOP Conf. Series N 181)* ed. A Andreone et al. (Bristol: IOP Publishing) p.3112-3118 (2004)

[4] M.V. Liatti, U. Poppe, Y.Y. Divin."Low-frequency noise and electrical transport in [100]-tilt $YBa_2Cu_3O_{7-x}$ bicrystal junctions (submitted, 2005)

[5] Y.Y. Divin, D.A. Tkachev, V.V. Pavlovskii, O.Y. Volkov, M.V. Liatti, V.N. Gubankov, K. Urban. "Classical and Josephson detection of THz radiation using $YBa_2Cu_3O_{7-x}$ [100]-tilt bicrystal junctions" (submitted, 2005)

[6] Y.Y. Divin, M.V. Liatti, D.A. Tkachev, V.V. Pavlovskii, V.V. Shirotov, O.Y. Volkov, U. Poppe, C.L. Jia, V.N. Gubankov, K. Urban. ICECom2005 Conf. Proceedings of 18th Int. Conf. on Appl. Electromagnetics and Communications (Ed. D. Bonefacic, KoREMA, Zagreb, Croatia) pp.277-278 (2005).

Applications of a high temperature superconductor SQUID microscope with soft-magnetic flux guide

U. Poppe[1], M. I. Faley[1], R. R. Gareev[1], M.Weides[1], E. Zimmermann[2], W. Glaas[2], K. Urban[1]
[1]*Institute of Solid State Reseacrh,* [2]*Zentrallabor für Elektronik*
and CNI – Center of Nanoelectronic System for Information Technology, Research Center Juelich, Germany

A scanning SQUID microscope based on High-Temperature Superconductor (HTS) dc-SQUIDs was developed. A soft magnetic amorphous foil was used to guide the flux from room temperature samples to the liquid nitrogen cooled SQUID-sensor and back. The flux guide passes through the pick-up loop of the HTS SQUID providing an improved coupling of magnetic flux of the object to the SQUID. The device was used to measure of the magnetic field of current carrying wires and for the investigation of the stray fields of magnetic tunnel junction device structures. A lateral resolution of better than 10 µm was achieved.

As SQUIDS are the most sensitive magnetic flux sensors providing an unsurpassed product of field sensitivity and spatial resolution. The scanning SQUID-microscope (SSM) is a powerful tool for fundamental and applied research in order to image stray fields above magnetic samples [1]. The spatial resolution is usually limited by the sensor area or by the distance between sensor and sample. By using a specially designed flux guide geometry we have developed a scanning SQUID microscope based on HTS dc-SQUIDs and a soft magnetic amorphous foil to guide the flux from room temperature samples efficiently to the liquid nitrogen cooled SQUID-sensor and back to the sample [2]. The flux guide passes through the pick-up loop of the HTS SQUID improving the coupling of magnetic flux of the object to the SQUID. The SQUID magnetometer consisted of an elongated SQUID loop (100 µm × 10 µm) with about 1 µm wide Josephson junctions together with a directly coupled pick-up loop with a dimension of about 1 mm × 2.5 mm. The SQUID sensors [3] were produced with superconducting $YBa_2Cu_3O_{7-x}$ films. The high-oxygen-pressure dc-sputtering technique was used for the deposition of the films on 24° bicrystal $SrTiO_3$ substrates.

The sample is moved by a precision x–y scanning stage and a z-translation stage driven by micro-step stepper motors providing a positional resolution better than 1 µm. For a microscope head with an aperture of 70 µm in the magnetic shielding and a tip diameter of about 10 µm the sensitivity was determined to about 0.6 nT/√Hz. The spatial resolution of such an instrument was around 10 µm.

An example of a measurement of the magnetic field z-component above a current-carrying meander is shown in Figure 1. The current in neighbouring lines produces magnetic fields with opposite sign. The structure consists of 4 pairs of 10 µm wide wires with different length. For the structuring of the test film a lithography mask with defect leading to an electrical short between the second and the third line of the meander was used. Fields of wires carrying currents less than 1 µA could be detected with a time constant of 1 sec. In all figures the z-component $B_z(x,y)$ is false color coded where blue are magnetic fields directed into the scanning plane and red shows areas where the field is directed out of the plane.

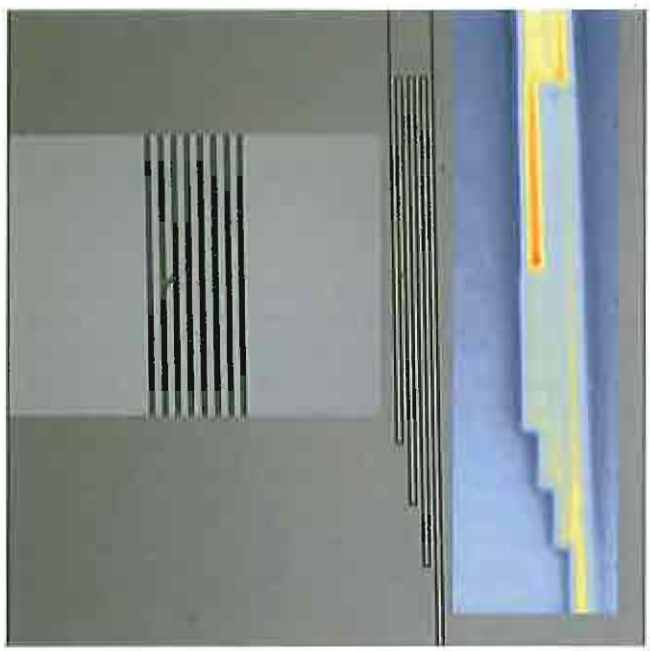

Figure 1: 2D-distribution of the magnetic field $B_z(x,y)$ above an ac-current carrying (90 µA, 1.6 kHz) thin-film with eight 10 µm wide lines separated at 10 µm distance from each other (right). A photo of the meander is shown on the left. Between the second and the third wire an electrical short can be recognized.

Furthermore we performed measurements on magnetic thin film samples as they are used for recording media or heterostructures for magneto-electronic devices. In contrast to the magnetic force microscope, which has a much better spatial resolution, the SSM with an extremely soft magnetic flux antenna does not significantly disturb the sample magnetization during image recording.

Figure 2 shows an example of magnetic stray fields of a $Co/Al_2O_3/Co$-tunnel junction device (TMR). Different magnetic domain structure distributions before and after demagnetization can be recognized.

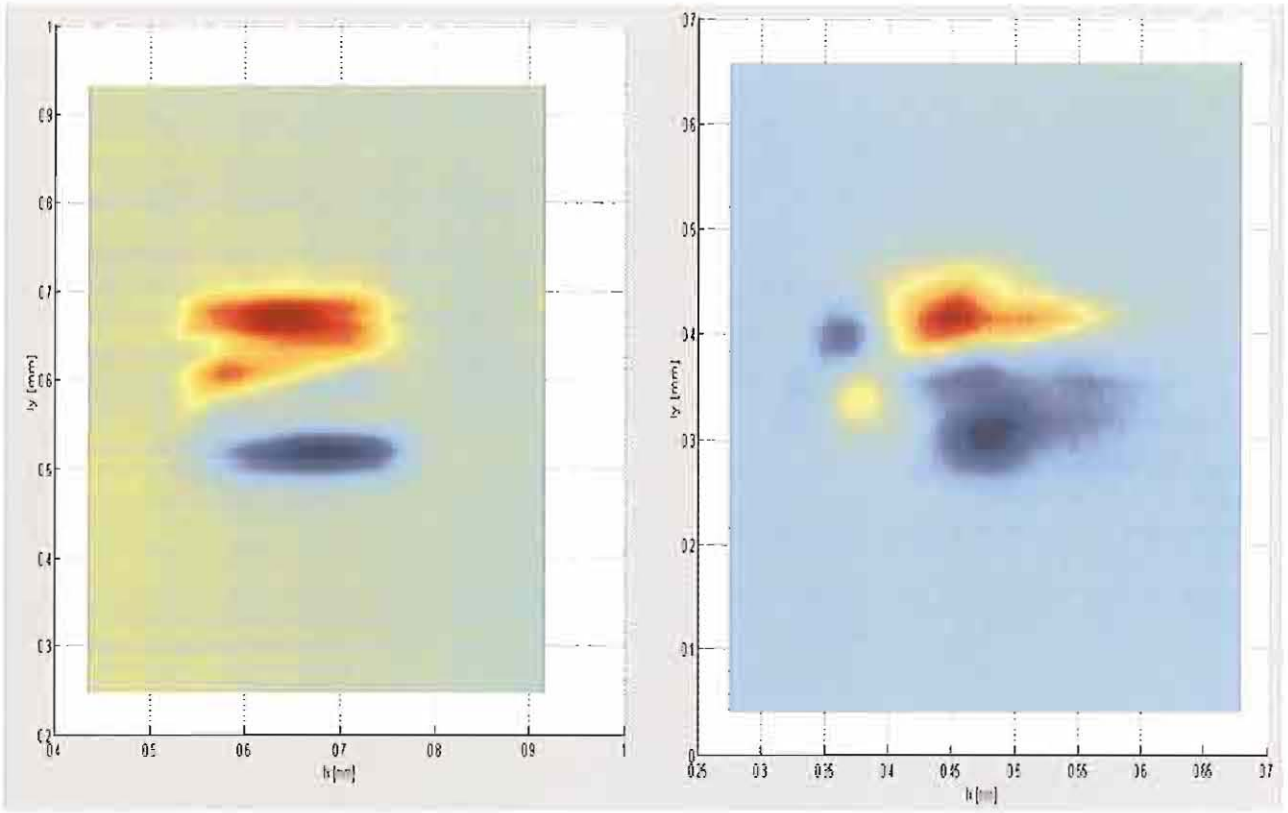

Figure 2: Magnetic stray fields of a TMR-Co/Al_2O_3/Co-tunnel junction device, which was: (a) magnetized or (b) demagnetized. Junction area: 180 µm × 200 µm.

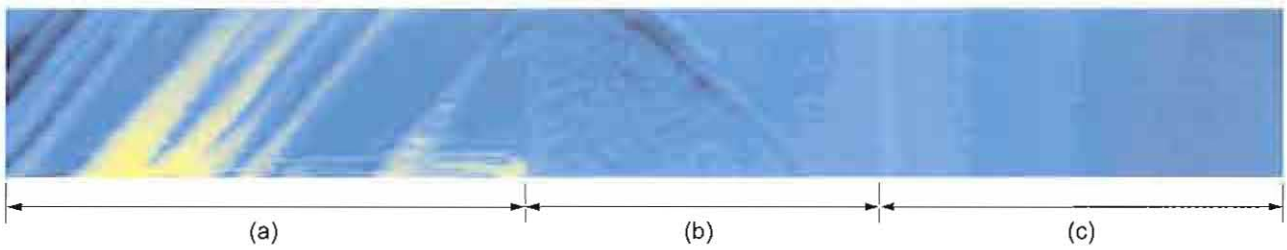

Figure 3: Stray fields of a Fe/barrier/Fe multilayer with SiGeSi barriers of different thickness:
(a) Fe/SiGeSi/Fe, 0.6 nm barrier; (b) Fe/SiGeSiGeSi/Fe 1 nm barrier; (c) Fe/SiGeSiGeSiGeSi/Fe, 1.6 nm barrier. Scan area: 0.7 × 7 mm.

Stray fields of a Fe/barrier/Fe multilayer test structure with SiGeSi barriers [4] of different thickness are shown in Figure 3. Such measurements can help to investigate the magnetic coupling through different barriers or the influence of possible pinholes in tunnel junctions or other spintronic devices.

A further development of the scanning SQUID-microscope with a finer tip of the soft magnetic flux guide leading to a submicron spatial resolution is planned for the future.

[1] J. R. Kirtley et al., Annual Review of Material Science Vol.29, 117 (1999).

[2] U. Poppe et al., Supercond. Sci. Technol. Vol.17, 191 (2004).

[3] M. I. Faley et al., Applied Physics Letters Vol.81, 2406 (2002).

[4] R. R. Gareev et al., Applied Physics Letters, Vol.83, 1806 (2003).

Information Technology with Nanoelectronic Systems

Hysteretic Oxide-Based Memories

On a Novel Low Resistive Nonvolatile Random Access Memory Concept
R. Meyer

Size effects in ultra-thin epitaxial ferroelectric heterostructures
V. Nagarajan, R. Ramesh, C.L. Jia, H. Kohlstedt, R. Waser

Electrical characterization of MIS- and ferroelectric MFMIS-diodes for FeFET memory applications
A. Gerber, H. Kohlstedt, T. Heeg, J. Schubert, M. Fitzilis, P. Meuffels, T. Schneller, R. Waser

Integration of registered ferroelectric nanostructures
S. Clemens, T. Schneller, A. Rüdiger, F. Peter, Th. Schmitz, S. Tiedke, R. Waser

Shallow and deep donor and acceptor defects in high permittivity perovskites: Their influence on the leakage current of MIM capacitors
H. Schroeder

Enhancement of Ferroelectricity in Strained $BaTiO_3$ Thin Films
J. Schubert, K.J. Choi, M. Biegalski, Y.L. Li, A. Sharan, L.-Q. Chen, D.G. Schlom, C.B. Eom

Impact of the top-electrode material on the permittivity of single-crystalline $Ba_{0.7}Sr_{0.3}TiO_3$ thin films
R. Plonka, R. Dittmann, N.A. Pertsev, E. Vasco, R. Waser

Scaling of the Ferroelectric Field Effect Transistor and a new FeFET programming concept
M. Fitsilis, H. Kohlstedt, A. Gerber, Y. Mustafa, R. Waser

Chemical Mechanical Polishing for Integrated Ferroelectric Nanostructures
S. Clemens, A. Rüdiger, S. Röhrig, T. Schneller, R. Waser

Simulation of Quantum Dead-Layers in Nanoscale Ferroelectric Tunnel Junctions
K. M. Indlekofer, H. Kohlstedt

Impedance Spectroscopy Study of TiO_2 Having Bistable Resistance States
D. S. Jeong, H. Schroeder, R. Waser

Resistive Switching and Data Reliability of Epitaxial (Ba, Sr)TiO_3 Thin Films
R. Oligschlaeger, R. Waser, R. Meyer, S. Karthäuser, R. Dittmann

Hysteretic Current-Voltage Characteristics of Ferroelectric Tunnel Junctions
N. A. Pertsev, H. Kohlstedt, R. Waser

Extrinsic Influences on Piezoresponse Force Microscopy
F. Peter, B. Reichenberg, A. Rüdiger, K. Szot

Studies on the Ion Migration in Lateral Structures for Future Electrochemical Bridging Memory Devices
C. Rohde, R. Waser

A Model for a Resistive Switch Memory Cell with Rechargeable Space Charge
H. Schroeder

"Ab-Initio" Band Structure Calculations for $SrTiO_3$ and the Thermionic Emission Current in Metal-$SrTiO_3$ Contacts
H. Schroeder, Ph. Mavropoulos

Atomic Layer Deposition of $PbTiO_x$ Thin Films Using Liquid Delivery Source Injection
T. Watanabe, S. Hoffmann-Eifert, C. S. Hwang, S. Mi, C. Jia, R. Waser

Grow Mode Evolution and Strain Relaxation in $BaxSr_{1-x}TiO_3$ Pulsed Laser Deposited on $SrRuO_3/SrTiO_3$
J. Q. He, E. Vasco, C. L. Jia, R. Dittmann, R. H. Wang

On a Novel Low Resistive Nonvolatile Random Access Memory Concept

René Meyer
Institute of Solid State Research, and CNI – Center of Nanoelectronic Systems for Information Technology, Research Center Jülich, Germany

A novel nonvolatile Ferroresistive Random Access Memory concept is presented. The proposed memory element consists of a planar capacitor-like 2-layer structure formed by a highly conductive ferroelectric/ non-ferroelectric thin film stack in intimate contact with low ohmic electrodes. Depending on the orientation of the polarization in the ferroelectric layer, the stack resistance can be toggled between a high and a low conductive state. By variation of the doping concentration, an R_{on}/R_{off} ratio up to several orders of magnitude is realized in the simulation. The memory window is found to be adjustable by the doping level as well.

Over the past 15 years, non-volatile random access memories based on ferroelectrics have been studied in view of its potential for a future universal memory, which unifies fast read/ write cycles and random access of DRAM and SRAM with non-volatile information storage of Flash [1,2]. Although the functionality of non-volatile memories utilizing the ferroelectric effect have been demonstrated and 64 Mbit FeRAM engineering samples are already available [3], the capacitive sensing scheme leads to a serious bottleneck regarding scalability issues by limiting the use of simple planar capacitor structures in future FeRAM generations.

This contribution reports on a novel ferroelectric memory device, which, in contrast to ferroelectric capacitors, allows the storage of digital information via a high and a low conductive state [4]. The particular memory element consists of a 2-layer system formed by a semi-conductive ferroelectric and a semiconductor between metal electrodes (MFSM). The device will further be referred to as Ferro Resistive Random Access Memory or FRRAM. It can be regarded as a generalized concept of a ferroelectric diode [5], which only consists of one conductive ferroelectric layer and where a semiconductor is used as electrode (MFS structure). The hysteresis in the *I-V* relation of the FRRAM originates from the formation of a potential barrier or a potential well inside the structure, which can be addressed by a polarization reversal in the ferroelectric.

The simplified operation principle, whereby ferroelectric and non-ferroelectric layer are assumed to be insulators, is shown in Fig. 1. Derived from the device structure (Fig. 1a), the schematic illustrates the space charge distribution (Fig. 1b), the inner electric field (Fig. 1c) and the inner potential (Fig. 1d and 1e) as a function of the orientation of the polarization under short circuit conditions.

Caused by a separation layer between the electrode and the ferroelectric layer on one side, the polarization charge at the ferroelectric/ insulator interface remains unscreened. In case of a negative polarization charge, a potential barrier is formed. This may hinder residual electrons from passing through the structure. In case of positive polarization charges at the interface, a potential well is formed and unhindered electron transport across the interface is expected.

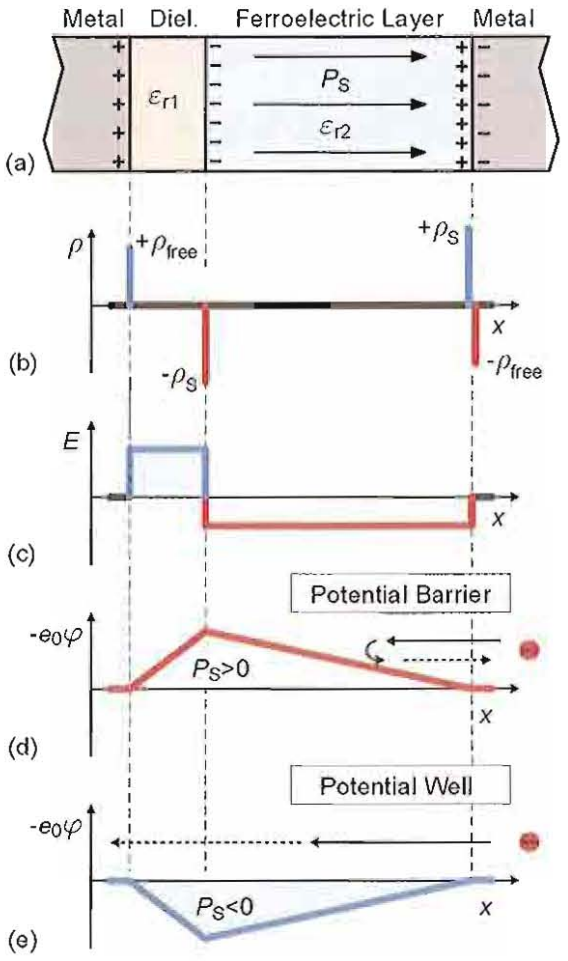

Fig. 1: Simplified operation principle of the proposed memory device: (a) ideal ferroelectric/ insulator stack, (b) respective space charge distribution, (c) the inner electric field and the potential distribution in the layered system. Depending of the orientation of P_S in the ferroelectric film, a potential barrier (d) or a potential well (c) for electrons is formed.

Numerical simulation studies prove the simplified operation principle to hold even in case of highly conductive thin films, at which the polarization charge is internally screened by mobile charge carriers. A drift-diffusion approach for electrons [6] is used to estimate the *I-V* relation for a polarization parallel and anti-parallel to an external field as a function of an applied voltage. High electronic conductivity of both layers is introduced by donor-doping the thin films in combination with low ohmic contacts. The obtained electron profiles are illustrated as a function of an applied bias voltage in Fig. 2 for the case of charge carrier depletion (upper graph) and charge carrier enrichment (lower graph). A switching of the polarization is neglected for simplicity. Due to the high concentration of electrons, no inversion occurs and electrons remain the majority charge carrier even in case of depletion.

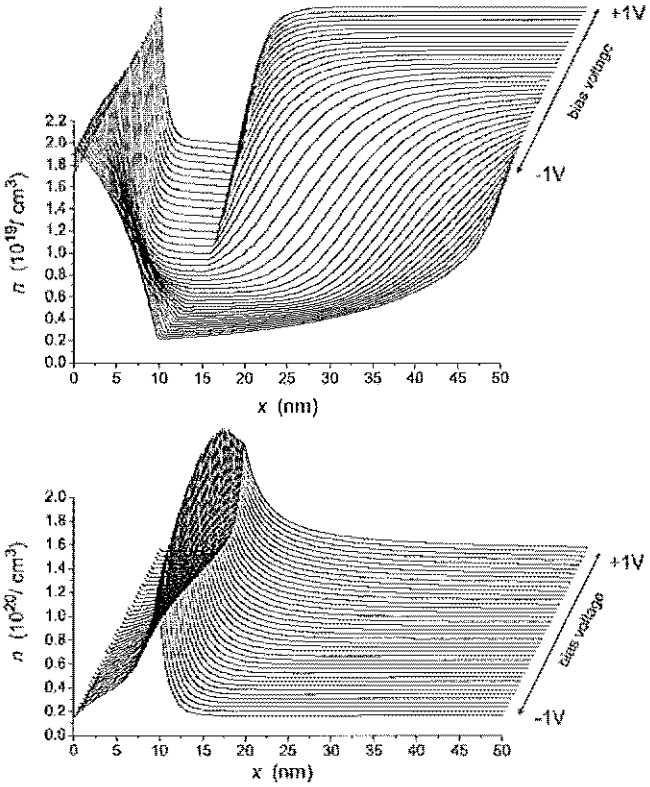

Fig. 2: Electron density distribution of highly conductive films as a function of the applied voltage: (upper graph) case of depletion and formation of a potential barrier; (lower graph) case of enrichment due to formation of a potential well.

Simulations of the hysteretic *I-V* curve of the memory device with respect to switching as well as an estimation of the influence of the donor content on the R_{on}/R_{off} ratio are given in Fig. 3. Further parameters such as film thicknesses, spontaneous polarization, material permittivities and contact properties, which may also have a strong impact on the *I-V* curve and may allow a tailoring of the device properties, are currently under investigation. Thin non-ferroelectric interface layers, so called dead layers, are found not to deteriorate the performance of the proposed device.

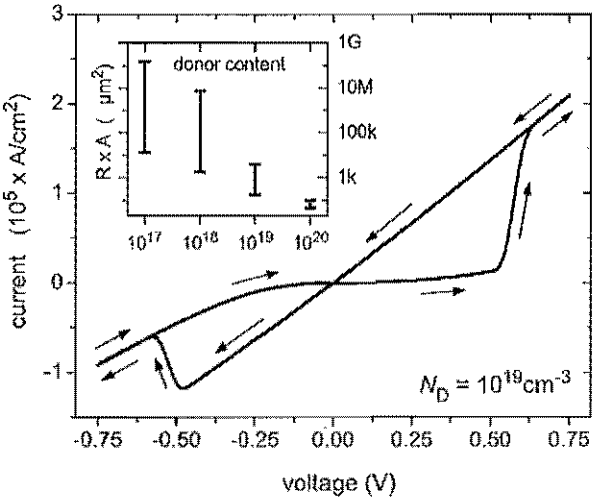

Suitable material systems for this memory concept are complex oxides, II-VI mixed crystals, but also conductive ferroelectric polymers. Due to the broad scalability of the resistance, even materials with a low remnant polarization $< 1\mu C/cm^2$ are applicable. In case of complex oxides, it is expected that the processing technology required for a realization of the FRRAM might be very similar to those already developed for FRAMs.

Acknowledgement

The author likes to thank H. Kohlstedt for discussions.

[1] J. F. Scott, Ferroelectric Memories, Springer, Berlin 2000.

[2] R. Waser, ed., 'Nanoelectronics and Information Technology', Wiley-VCH 2003.

[3] Texas Instruments, press release.

[4] R. Meyer, H. Kohlstedt, arXiv:cond-mat/0312609

[5] V. M. Fridkin, *Ferroelectric Semiconductors*, New York, USA: Consultants Bureau, 1980.

[6] M. Okano and Y. Watanabe, *Appl. Phys. Lett.* **76** pp. 233, 2000.

Size effects in ultra-thin epitaxial ferroelectric heterostructures

V. Nagarajan[1], R. Ramesh[2], C.L. Jia[3], H. Kohlstedt[3], R. Waser[3]
[1]*School of Materials Science, University of New South Wales, Sydney NSW 2052*
[2]*Department of Materials Science and Engineering, University of California, Berkeley.*
[3]*Institute of Solid State Research and CNI – Center of Nanoelectronic Systems for Information Technology, Research Center Jülich, Germany*

We report on the effect of thickness scaling in model $PbZr_{0.2}Ti_{0.8}O_3$ (PZT)/$SrRuO_3$ heterostructures. Although theoretical models for thickness scaling have been widely reported, direct quantitative experimental data for ultrathin perovskite (<10 nm) films in the presence of real electrodes have still not been reported. In this paper we show a systematic quantitative experimental study of the thickness dependence of switched polarization in (001) epitaxial PZT films, 4 to 80 nm thick. A preliminary model based on a modified Landau Ginzburg approach suggests that the nature of the electrostatics at the ferroelectric-electrode interface plays a significant role in the scaling of ferroelectric thin films.

The effect of thickness scaling in ferroelectrics has recently been of immense interest [1-5]. As the dimensions (both lateral and vertical direction) of the perovskite layer decreases, the fundamental question of size dependence becomes crucial. From a theoretical point of view, two models have been traditionally used to describe size effects, namely an "intrinsic effect" and a "depoling" field effec. Experimentally Tybell et al.[5] qualitatively showed that even a 4 nm thick epitaxial $PbZr_{0.2}Ti_{0.8}O_3$ (PZT) film grown on Nb doped STO is ferroelectric. However a direct experimental quantification of the ferroelectric polarization, particularly for films in the sub-10nm thickness range has not been reported. Fur such ultra-thin films direct experimental quantification of size effects are complicated by extrinsic effects such as leakage and therefore methods other than the traditional P-E hysteresis loop have been reported to characterize the stability of the polar state [4]. In this paper we present experimental measurements of the switched polarization in PZT films of thickness down to 4nm, in the presence of real electrodes.

A 70 nm thick SRO layer was grown on STO at 650°C followed by the PZT layer via pulsed laser deposition (PLD). The deposition was carried out at 100 mTorr of oxygen and the sample was cooled down from growth temperature in 1 Atmosphere of oxygen. In order to avoid complications from 90° domain formation the PZT films were grown in a thickness range from 4nm to 80nm, for which they are entirely c-axis oriented. The switchable polarization was measured using a Radiant Technologies Precision Premier system at 16kHz (hysteresis loops) and a novel AFM based pulsed probing technique with conductive Pt-Ir tips was employed to measure the pulsed polarization.

We focused on the PZT (0/20/80) composition, since it has an in-plane lattice parameter of 3.94Å which is closely lattice matched to SRO(3.93Å). Fig 1(a) is a set of hysteresis loops measured at 16 kHz for 15, 50 and 160nm (for comparison) thick films. The loops are sharp, square, and well-saturated. The $2P_r$ value obtained from the loop for the 15nm thick film is ~150μC/cm^2 which is in agreement with theoretically predicted values for this composition of PZT with an in-plane compressive strain.

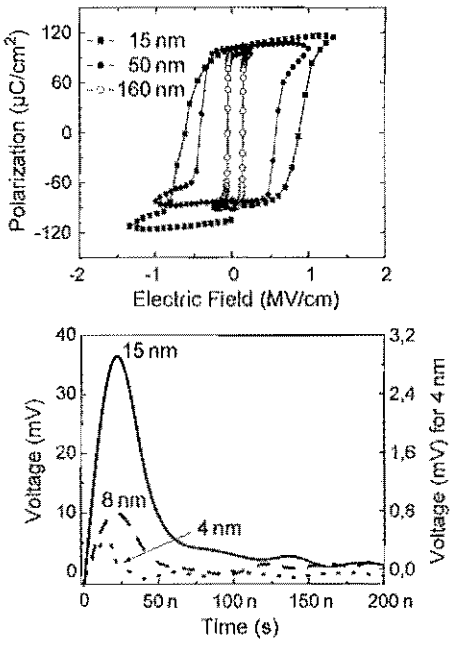

Fig. 1: (a) Hysteresis loops, (b) Current transients

Additionally a systematic increase in the coercive field is observed as the thickness is scaled down to 15 nm, in agreement with previous reports [6]. We measured the polarization under pulsed probing conditions using a AFM based test set-up. In order to reduce short circuit paths and to allow fast rise times, capacitors with sub-micron lateral dimensions were fabricated using a modified lift-off technique in which the photoresist was deliberately underdeveloped. By making contact to 0.4 by 0.4 μm^2 pads, we recorded the switched (P*) and non-switched polarization (P^) to obtain the switchable polarization (ΔP). Figures 1(b) plots the switching transients of the 15 and 8 nm at an applied field of 2750 kV/cm and transients of the measured 4 nm film at 3250 kV/cm, respectively. The switched charge (i.e. area under the transient) for the 15 and 8nm film were calculated to be 145 and 70 ± 5 μC/cm^2 respectively. A higher field was necessary for the 4 nm film to obtain a fully switched transient. Integration of the ΔP transient,

yielded a switched charge of 11 ± 3 μC/cm^2. This is also evident in the change of the vertical scale in the signal response recorded by the oscilloscope. For the 15 nm film it is approximately 40 mV (left axis) while for the 4nm film it has dropped to 0.5 mV(right axis). The inset to fig 2(b) is a plot of the P* and P^ transients for the 4nm film. The difference between the P* and P^ is minute, indicative of a very low magnitude of the switched charge. These results demonstrate that down to 15nm there is no observable drop in the switched polarization. Below 15 nm, it progressively decreases to approximately 11μC/cm^2 for the 4 nm film.

We now compare the experimentally measured thickness dependence with that predicted from theory. In Fig. 2 we show the normalized polarization (termed as the order parameter) as a function of film thickness normalized to the correlation length, ξ (d/ξ). The value of ξ for this particular composition was calculated to be 2.4 nm using parameters from Li[6] and Zembilgotov [7]. We also plot the predicted thickness dependence, from an intrinsic size effect model (solid plot), from the macroscopic depoling field model [8-10] (dashed plot) and ab-initio calculations for SRO/$BaTiO_3$/SRO (dotted plot).

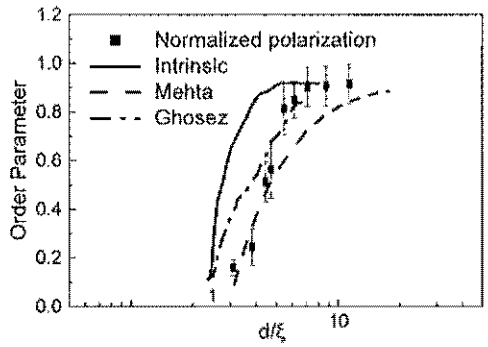

Fig. 2 Comparison of the order parameters from theory and experiments.

The plot shows that the sub-10 nm thick films lie more closely to the depoling model. However in order to clearly differentiate between the intrinsic size effect and depoling field effect, we need to explore the nature of the critical exponent *(or scaling law)*. Using the approach of Kretschmer and Binder [8] the Curie temperature of the thin film, T_c^{film}, is related to the expected theoretical transition temperature for a film of the same thickness (but without any polarization suppression T_c) as:

$$\frac{T_c^{film} - T_c}{T_c} \propto d^{-\zeta}$$

where d is the thickness of the film and ξ is the shift exponent, equal to 1 for the case where the expression is dominated by depolarizing field and ξ =2 for the case where the suppression is dominated by intrinsic effects.[13] Our preliminary calculations show a linear fit with a slope of ~1, suggesting the governing role of depoling fields at the electrode-ferroelectric interface in determining the stability of ferroelectricity, in agreement with the theoretical predictions of Ghosez [1]. However to conclusively verify this, accurate experimental determination of T_c for a ferroelectric heterostructure with top and bottom electrodes, coupled with a more complex model which takes into account the surface and/or depolarization effects [6] is needed.

We wish to point out that the results shown in this work are very depended on the misfit strain. The lattice mismatch of PZT (0/20/80) is very close to that of the substrate and the $SrRuO_3$.

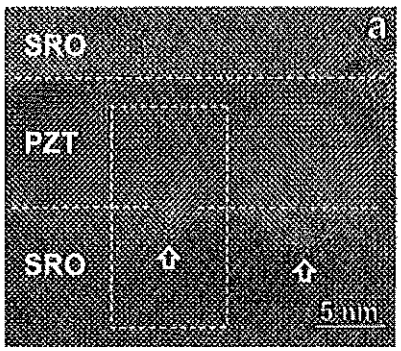

Fig. 3 High Resolution Transmission Electron Micrographs: (a) HRTEM image of a 8nm SRO/PZT (52/48)/SRO heterostructure. The arrows point towards misfit dislocations.

The HRTEM (High Resolution Transmission Electron Micrograph) image (Fig. 3) shows a misfit dislocation which alters the strain and polarization on a nano-meter scale. Therefore only a careful analysis of the microstructure data and the electrical data results in reliable results.

[1] P. Ghosez and K. M. Rabe, Appl. Phys. Lett. **76,** 2767-69 (2000).
[2] J. Junquera and P. Ghosez, Nature **422,** 506-509 (2003).
[3] T. M. Shaw, S.-T. McKinstry, and P. C. McIntyre, Ann. Rev. Mat. Sci **30,** 263-298 (2000).
[4] S. K. Streiffer, et al., Phys. Rev. Lett. **89,** 67601-604 (2002).
[5] T. Tybell, C. H. Ahn, and J.-M. Triscone, Appl. Phys. Lett. **75,** 856-858 (1999).
[6] S. Li etal., Jpn. J. Appl. Phys. 36, 5169 (1997).
[7] A. G. Zembilgotov, N. A. Pertsev, H. Kohlstedt, and R. Waser, J. App. Phys. **91,** 2247-2254 (2002).
[8] R. Kretschmer and K. Binder, Phys. Rev. B **20,** 1065-1076 (1979).
[9] I. P. Batra, P. Wurfel, and B. D. Silverman, J. Vac. Sci Technol **10,** 687-692 (1973).
[10] R. R. Mehta, B. D. Silverman, and J. T. Jacobs,J. App. Phys. **44,** 3379-3385 (1973).

Electrical characterization of MIS- and ferroelectric MFMIS-diodes for FeFET memory applications

A. Gerber[1], H. Kohlstedt[1], T. Heeg[2], J. Schubert [2], M. Fitzilis[1],
P. Meuffels[1], T. Schneller[3], R. Waser[1,3]
[1]*Institute of Solid State Research,* [2]*Institute of Thin Films and Interfaces and CNI – Center of Nanoelectronic Systems for Information Technology*
[3]*Institute of Electronic Materials IWE II, RWTH Aachen*

State-of-the-art integrated devices combine the classical semiconductors with electro ceramic materials in order to further increase the degree of miniaturization and to show up new functional properties like for example non-volatility in ferroelectric memories (FeRAMs). A challenging approach is the ferroelectric field effect transistor (FeFET). Here the gate oxide of a conventional MOSFET is replaced by a ferroelectric material. Sever interface problems hinder so far the commerlization of this advanced non-volatile memory device. We report on the successful of CeO_2 and $DyScO_3$ as dielectric buffer layer between on Si. Retention times up to 1000s have been achieved for Pt/PZT/Pt/CeO_2/Si stacks.

Ferroelectric materials are characterised by a spontaneous polarization which is switchable by an external electric field. On the basis of this fundamental property, non-volatile ferroelectric memories have been developed. The individual elements are ferroelectric capacitors with a metal-ferroelectric metal structure. Another interesting approach is the so-called "ferroelectric field effect transistor" (FeFET) [1]-[4]. The principle layout of an FeFET is rather similar to that of a conventional MOSFET. The dielectric gate oxide is replaced by a ferroelectric gate oxide. The reversal polarization of the ferroelectric layer is used to alter the resistance of the

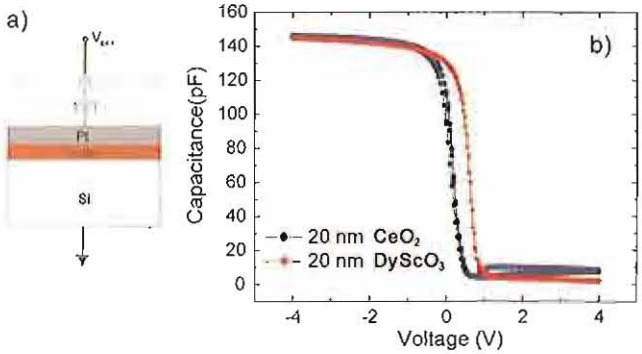

Fig. 1: a) Sketch of a MIS diode as a part of an MFMIS structure. The top electrode and the PZT has been removed using IBE. This procedure allows the characterization of the buffer layer after the sample processing. b) C(V) measurement of a MIS diode at 100 kHz, using 20 nm $DyScO_3$ and 20 nm CeO_2 with platinum top contacts. Both materials show no hysteretic effects

semiconducting source-drain which defines the computational "0" and "1. The compact device structure (1-T cell) makes the FeFET a promising candidate for future non-volatile memories including low power consumption, a fast read access time and low writing times. On the other hand, the integration of ferroelectric materials into a CMOS technology is a task with many obstacles. Typical ferroelectric materials as, e.g., $PbZr_xTi_{1-x}O_3$ (PZT), $BaTiO_3$ (BTO) and $SrBi_2Ta_5O_9$ (SBT) react with silicon at higher temperatures creating an interlayer with crucial properties, and therefore cannot be used without a buffer layer to avoid interdiffusion or chemical reactions [2].

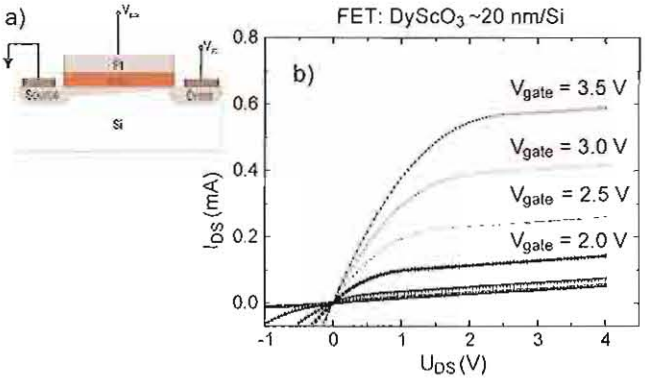

Fig. 2: a) Cross section of a plane transistor. We used ultra-large transistors, from 25*25 μm^2 to 100*100 μm^2 channel area. b) Transistor characteristics of a transistor with 20 nm $DyScO_3$ as gate oxide with a channel size of 25*100 μm^2 (L*W).

Since the oxide-silicon interface is known as the critical part of such a device, one should first focus on the electrical properties of the bufferlayer-silicon interface. Due to the high dielectric constant of 20-25, we concentrate on $DyScO_3$ and CeO_2 [4], optimized the deposition process (PLD) for these materials and measured the electrical properties of patterned MIS-diodes (metal-insulator-semiconductor). **Fig. 1a** shows a sketch of such a MIS diode with a platinum top electrode. **Fig. 1b** displays capacitive measurements, performed on $DyScO_3$ and CeO_2 samples with improved process parameters and a thickness of 20 nm each. Both materials show very low leakage currents, are stable to voltage cycling and moreover show no significant hysteresis, which is often a problem of high-k dielectrics above a few nm thickness. **Fig. 2a** shows a schematic cross section of a plane field-effect-transistor

(FET), which we used to test the gate oxides. In **Fig. 2b**, a I_{SD} versus V_{SD} plot of a 20 nm $DyScO_3$-FET is presented.

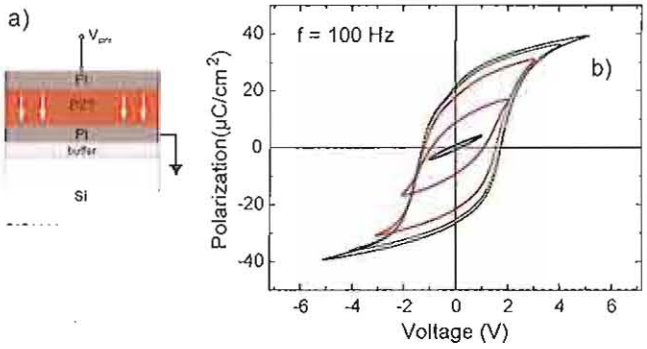

Fig. 3: a) Sketch of an MFM structure using the "floating" electrode as bottom electrode. This MFM diode is always a part of an MFMIS sample to measure the properties of the ferroelectric layer. b) Plot of the polarization versus applied voltage of a 150 nm PZT film. The remanent polarization is for well saturated hysteresis ~23 $\mu C/cm^2$.

Based on our results of the MIS structures, we turned towards the fabrication of MFMIS structures (metal-ferroelectric-MIS), in which the inner metal electrode has no electrical contact to the environment (floating condition). This procures several advantages. The textured platinum (111) electrode for example, can act as template layer for PZT growth and the metal interlayer opens the possibility to measure the properties of the ferroelectric layer directly on one sample [2], [5] The optimized growth condition of PZT on Pt are well known from ferroelectric capacitors. In **Fig. 3a** such the MFM-teststructure can be seen. Here the "floating" electrode serves as bottom electrode. **Fig. 3b** shows the properties of a 150nm thick PZT(30/70) MFM diode grown with the CSD method. The hysteresis loops are well saturated at higher voltages and so called subloops at lower voltages (< 4 V) are visible. The ferroelectric has a very low leakage current, a good retention and fatigue properties. A measurement of the capacitance over the complete MFMIS stack using 150 nm PZT and a 20 nm CeO_2 buffer layer, is shown in **Fig. 4b**. There the response of the remanent polarization is visible, leading to a hysteresis with clockwise direction. The hysteresis which is often called memory window is of the order of 0.5 V. Thinner buffer layers and ferroelectric materials with a lower dielectric constant lead to a larger memory window and more stable polarization states. This is one of our further goals. **Fig. 3c** depicts a retention measurement using the same sample. The breakdown for the "on" state appears after some minutes, due to unstable minor loops of the ferroelectric layer. These results are quite encouraging and demand further investigations to improve the performance of Fe-FETs.

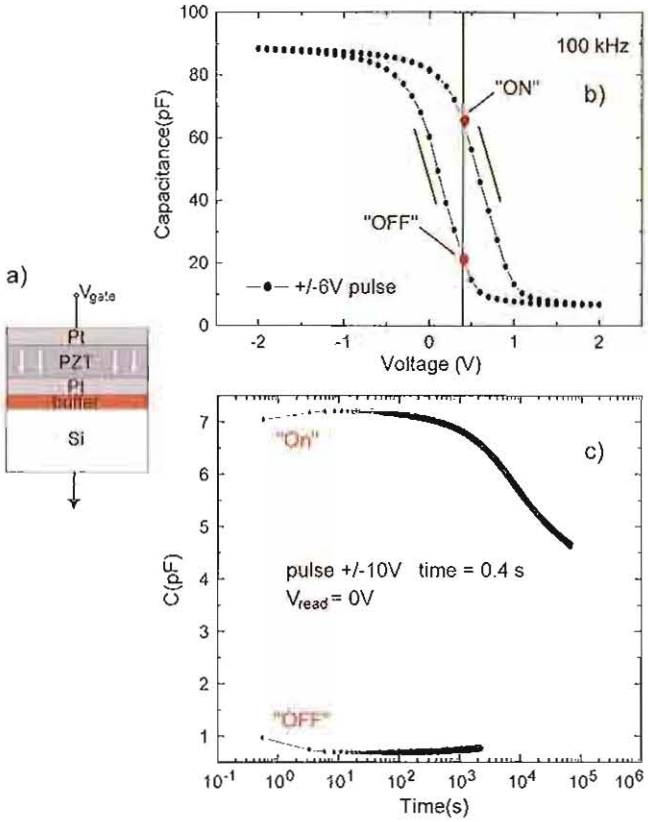

Fig.4: a) Sketch of a MFMIS diode. The inner metal electrode is floating. b) CV measurement of an MFMIS diode using 150nm PZT and 20 nm CeO_2 . The hysteresis is caused by the polarization of the ferroelectric layer. From the flatband voltage shift one can calculate the memory window to ~0.5 V, which is enough to separate an "on" and an "off" state. c) Retention measurement of a capacitor of the same sample, measured at V_{read}=0 V.

Acknowledgement

The authors thank B. Hermanns and H. Haselier for technical support. In addition we thank René Meyer for helpful discussions.

[1] K. Sugibuchi, Y. Kurogi, and N. Endo *J. Appl Phys. Vol* **46**, No. 7 (1975).

[2] R. Waser, ed., 'Nanoelectronics and Information Technology', Wiley-VCH 2003.

[3] B. E Park, H. Ishiwara *Appl. Phys.Lett Vol* **79**, 806 (2001).

[4] H. W. Song, C. S. Lee, D. G. Kim, K. No ***Thin Solid Films 368*, 61-66 (2000).**

[5] E.Tokumitsu, T. Isobe, T. Kijima, H.Ishiwara *Jpn. J. Appl. Phys. Vol.* **40** (2001)

Integration of registered ferroelectric nanostructures

S. Clemens[1,2], T. Schneller[1,2], A. Rüdiger[2], F. Peter[2], Th. Schmitz[3], S. Tiedke[3], R.Waser[1,2]
[1]*Institute of Electronic Materials IWE II, RWTH Aachen,*
[2]*Institute of Solid State Research and CNI - Center of Nanoelectronic Systems for Information Technology, Research Center Jülich, Germany*
[3] *aixACCT Systems GmbH, Dennewartstr. 25-27, D-52068 Aachen, Germany*

Nanoscale ferroelectric materials pave the way for high-density non-volatile storage media devices. For their implementation a regular patterning of the nanostructures is mandatory. We present a combined approach of a top-down written TiO_2 template and a subsequent bottom-up chemical solution deposition (CSD) of lead titanate. This way we obtain a regular pattern over large areas with the ease of chemical solution deposition for the individual grains. In a subsequent step these structures will be embedded into a low-*k* dielectric to enable the necessary processing steps for integration. To demonstrate the feasibility of this approach we embedded standard CSD nanograins and determined their piezoelectric activity. A common metal electrode deposited on top of this polished surface enables the electrical characterization of large numbers of grains simultaneously.

Top-down fabricated ferroelectric nanostructures provide long-range ordering but often suffer from degradation during the post-deposition processing e.g. introduction of surface defects from etching. Samples produced by CSD are not exposed to any post-fabrication treatment but clearly not registered. To take advantage of both techniques we suggested a combined approach of e-beam structured TiO_2 seeds and $PbTiO_3$ nanograins [1] as illustrated in Fig. 1. These grains are produced by a modified 2-butoxyethanol based CSD technique [2]

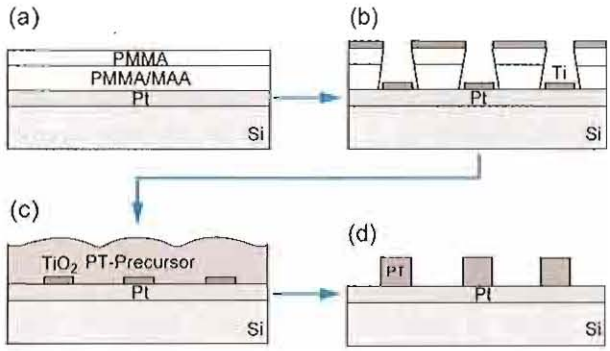

Figure 1: (a) a two-layer resist system is spin-coated onto the platinized substrate (b) the resist is exposed by e-beam, developed and a thin titanium layer is evaporated on top (c) lift-off in N-methyl pyrollidone and a $PbTiO_3$-precursor solution is spin-coated onto the pre-annealed TiO_2-structures (d) the precursor film is pyrolized and crystallized.

The TiO_2 dots have a diameter as small as 30 nm. Consequently lead titanate grains down to lateral dimensions of 50 nm and a separation distance of 75 nm were grown onto 50 nm wide nucleation sites [3] , where nucleation of the PT grains almost exclusively took place on the TiO_2 nanoseed structures (Fig. 2) [4] . Ferroelectricity in these grains was proven by switching experiments using an AFM cantilever.

Figure 2: AFM topography scan of a 1 by 1 μm^2 area of lead titanate nanograins. The triangular shape of most grains indicates a (111)-oriented growth induced by the (111) platinum electrode.

To demonstrate the feasibility of the embedding procedure, a dielectric layer of low-*k* hydrogen silsesquioxane (HSQ) is spin-coated onto non-registered samples, embedding and insulating the perovskite nanostructures. To enable electrical contact, the HSQ-layer is polished down to the top of the $PbTiO_3$ grains employing a chemical mechanical polishing step (Fig.3).

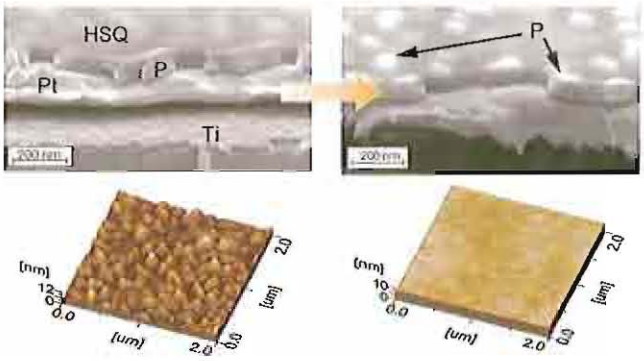

Figure.3: $PbTiO_3$ grains embedded in a dielectric layer of HSQ. The SEM images on top show the sample cross-section before (left) and after polishing (right). On the right, the $PbTiO_3$ grains are exposed. The AFM-images illustrate the surface roughness before and after the polishing step.

We obtain an excellent surface roughness of less than half a nanometer as compared to a roughness of about 2 nm prior to polishing. After proving piezoelectric activity in most of the accessible $PbTiO_3$ grains (Fig. 4) the samples are coated with collective gold top-electrodes of about 75 µm in diameter.

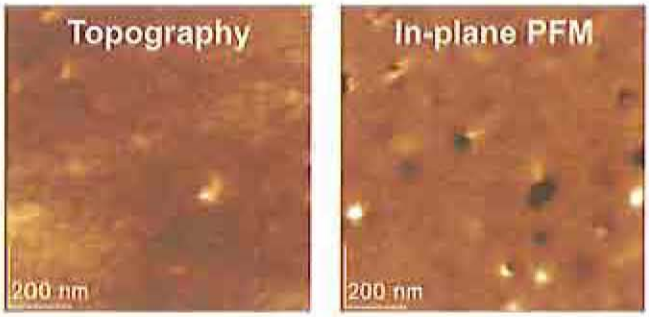

Figure. 4: Topography (left) and in-plane piezoelectric response (right) of lead titanate grains in a HSQ-layer after polishing. Depending on the polishing parameters a thinner layer and larger ferroelectric surface fraction can be achieved.

An initial result of experiments with a large number of ferroelectric grains embedded into a low-*k* dielectric layer is illustrated in Fig. 5. With a surface fraction of about 10% of ferroelectric material the remaining 90% of dielectric layer have to be considered with respect to

a) the dielectric permittivity and the resulting contribution to the overall capacity
b) the leakage contribution of the dielectric material and
c) effects of different thermal expansion for the dielectric layer and the ferroelectric nanostructures causing the risk of gaps between both materials.

In addition to these contributions *in parallel,* the polishing agent affects the surface of the ferroelectric grains thus creating another slightly different layer *in series* that is situated directly underneath the metal electrode. The effects mentioned in a) and b) are experimentally taken care of in a dedicated compensation for leakage currents and parasitic capacities [5]. Respective circuit models to take into account the other effects are in progress. In the next step the registered grains will be embedded and polished. As their dimensions show less statistical fluctuations, the exposed (i.e. available electrode) area of each grain for a given thickness of the layer will be similar.

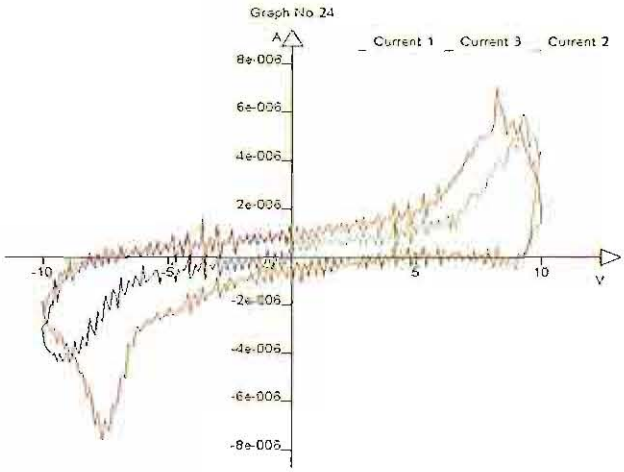

Figure.5: Current response of embedded $PbTiO_3$ grains with a common gold top-electrode of 75µm in diameter. The coercive voltage of about 8V can be explained by a modification of the $PbTiO_3$ grain surface due to the polishing step.

As the quality of the dielectric layer immediately changes the performance of the integrated ferroelectric capacitor, a set of experiments to minimize its leakage and to optimize the deposition and polishing process are on the way.

We have shown that ferroelectric structures can be grown in a registered way without need for a detrimentous post-deposition treatment. The ability to embed those structures into a low-*k* dielectric opens a way to further integrate them into circuits and makes a large number of very small samples in parallel accessible to experiments on their size dependence, the impact of electrode materials and long-term effects such as fatigue and retention.

[1] T. Schneller, R. Waser, *Ferroelectrics*, 267, 293 (2002)
[2] R.W. Schwartz, T. Schneller, and R. Waser, *C. R. Chimie, 7, 433 (2004)*
[3] S. Clemens, T. Schneller, A. v.d.Hart and R. Waser, submitted
[4] S.Bühlmann, P. Muralt, S. von Allmen, *Appl. Phys. Lett.*, 84, 2614 (2004)
[5] T. Schmitz, K. Prume, B. Reichenberg, S. Tiedke, A. Roelofs, R. Waser, J. Eur. Cer. Soc., 24 ,1145 (2004)

Shallow and deep donor and acceptor defects in high permittivity perovskites: Their influence on the leakage current of MIM capacitors

Herbert Schroeder

Institute of Electronic Materials and CNI – Center of Nanoelectronic Systems for Information Technology, Research Center Jülich, Germany

High-permittivity mixed-oxides with perovskite-type structure (e.g.,(Ba,Sr)TiO_3) are candidates for replacing SiO_2- and SiN_x-dielectrics in capacitors of DRAM memory cells as these traditionally used dielectrics suffer from increasing leakage currents with decreasing thickness due to higher integration. In general, leakage currents are not very well understood yet and hardly predictable in the wide band-gap perovskites, but may be a serious problem, too. Usually, they are modelled exclusively as interface injection or bulk limited currents in the literature. Recently, a new model combining these two mechanisms was able to successfully describe the leakage current dependencies on electric field, temperature and dielectric thickness in BST between platinum electrodes. In this paper we present simulation calculations of this model in dependence on defect properties such as concentration, in-band defect energies and type (donor, acceptor) which are usually difficult to define experimentally. The results show a large dependence of the leakage current on these properties and are compared to experimental data.

Leakage currents mechanisms for insulators or wide band gap semiconductors such as (Ba,Sr)TiO_3 (BST) usually fall into two classes: Interface injection limited or bulk conduction limited. Recently, a new model was offered combining these two classes, interface injection (thermionic emission or tunnel injection) with electronic band conduction [1,2]. With this model and related simulation calculations it was possible to describe leakage current data in BST successfully (field, temperature and thickness dependence [3]). Up to now the model considered only shallow donors (lying close to the conduction band edge such as oxygen vacancies; see Fig. 1) leading to Schottky contacts at the interface for many electrodes and n-type bulk conduction. In a next step the model was modified for arbitrary defects and contacts and the results of this generalization is reported [4].

In Fig. 1 the conditions for the model are sketched in a schematic band diagram for BST (band gap 3.3 eV) limited by the bottom edge of the conduction band (E_C=0) and the top edge of the valence band (E_V). The experimental in-gap energy levels of some common defects or doping materials (E_D for donors and E_A for acceptors) are shown as symbols. Also shown are some of the defect energy levels used as input for the simulation calculations (full lines) and the corresponding equilibrium Fermi levels (dotted lines) assuming a defect concentration of 10^{19} cm^{-3} and electronic compensation. Except for the defect levels lying close to the band edges the Fermi levels always are between the defect level and the corresponding band edge (E_C for donors, E_V for acceptors) indicating that for these deep levels only a small portion of the defects are ionized and compensated by electronic carriers (electrons and holes; respectively) keeping fair to good insulating properties. E_D and E_A were varied between 0.15 and 2 eV measured from the respective band edges.

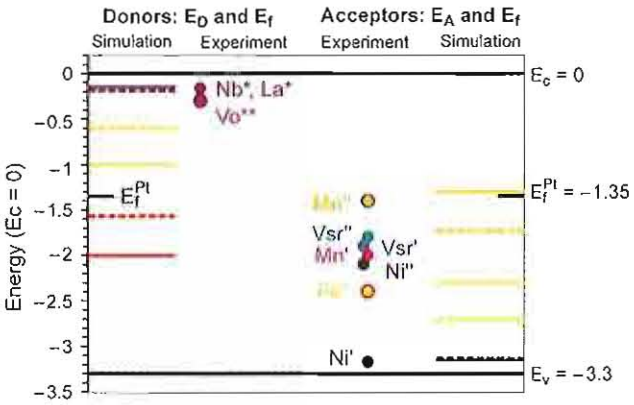

Fig. 1: Schematic band diagram showing in-band gap energies of different donor- and acceptor-type defects (full lines and symbols) and the corresponding equilibrium Fermi energies (dotted lines) for defect concentrations of 10^{19} cm^{-3} as well as Fermi level of Pt-electrodes.

Adding electrodes to the system – in the simulations Pt was used - results in large changes: The Fermi levels of the electrodes (–1.35 eV for Pt) and the BST thin film equilibrate at the interfaces by exchanging charge. In the vicinity of the interfaces the Fermi level of BST is "pinned" at the electrode level resulting in a transition of nearly all the defect levels from formerly deep to shallow, i.e. the defect level is lying between the Fermi level and the respective band edge and the defects are completely ionized. Although this results in large space charge concentrations (10^{19} cm^{-3}) and thus bending of the bands the screening (i.e. to shield the bulk insulator with the thermal equilibrium from the electrode effect) is usually incomplete in thin films (thickness < 100 nm) due to the high permittivity, which makes a large difference compared to e.g. low permittivity Si.

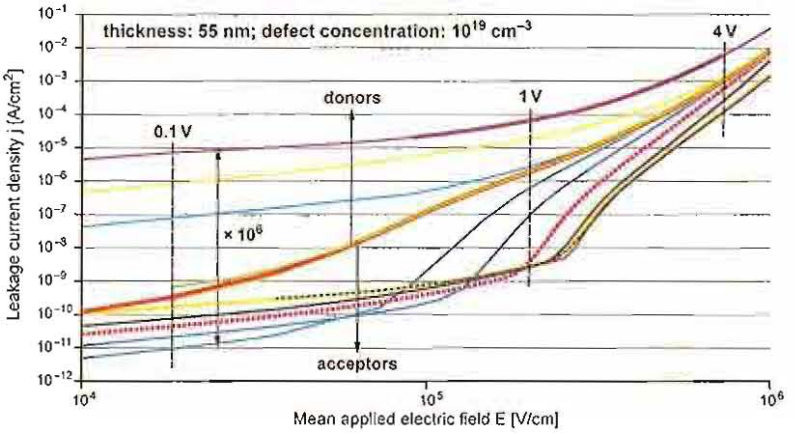

Fig. 2: Leakage current density j vs. applied electrical field E for a 55 nm thick high-permittivity (ε_r=550) BST thin film between Pt electrodes with 2 nm wide "dead layers" (ε_r=22) in dependence on different defect type and energy (measured from E_C), indicated on the right. "deep" and "shallow" characterize the defect in the "undisturbed" BST bulk.

Figure 2 shows the results of the simulation calculations for the different defect energy levels for a constant defect concentration of 10^{19} cm^{-3} for a 55 nm thick BST film between Pt electrodes. The log-log-plot shows the leakage current density vs. the mean applied electrical field. Dramatic changes can be observed in both, the shape of the curves and the absolute value of the leakage: While at large applied fields (E> 0.8 MV/cm) the range is less than a factor of 30, at small fields (E< 50 kV/cm) it is six orders of magnitude! Below that field all curves approach zero current in a linear fashion. The red curve in the middle separates the curves with donor defects (above) from the acceptor ones (below). It is identical for the largest donor and acceptor levels which stay "deep" with electrodes, i.e. the defects are not very effective. This curve is also identical to the one without any defects!

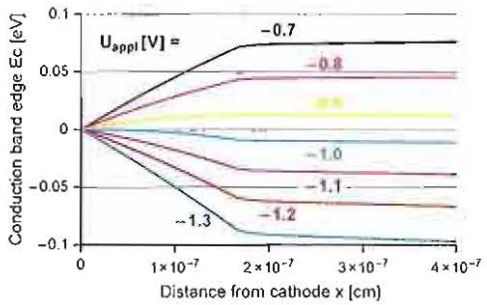

Fig. 3: Conduction band edge energy in the vicinity of the cathode of an acceptor doped sample (E_A=-2.0 eV in Fig. 1) showing a transition from a Schottky contact (slope<0 for U_{appl}>1 V) to an ohmic contact (slope>0 for U_{appl}<1 V).

The curves for the donors show a very similar, smooth behaviour, but for deeper energy level the turnover to the linear slope is shifted to lower fields. Due to the positive space charge of the donors these specimen have Schottky contacts (electric field at cathode < 0; also defined as $E_F^M < E_F^{BST,\,equi}$) for electrons at the cathode for all fields.

The curves for the acceptor defects have two distinctive regimes: A very steep at high fields followed by a (sharp) bend at medium fields (100 – 200 kV/cm). This bend is shifted to lower fields with increasing defect energy (measured from E_V). This bend can be associated with the transition from a Schottky contact to an ohmic contact for electrons at the cathode (see Fig. 3) making the Schottky reduction ineffective and thus leveling off the electron injection current. On the other hand, the hole injection at the similar anode (the other electrode) is strongly increased but due to the fact that the Pt Fermi level (- 1.35 eV) is still on the electronic side the electronic current is usually larger than the hole current. But this is changing with acceptor defect level and is the reason for the crossover of these curves at fields around 100 kV/cm in Fig. 2.

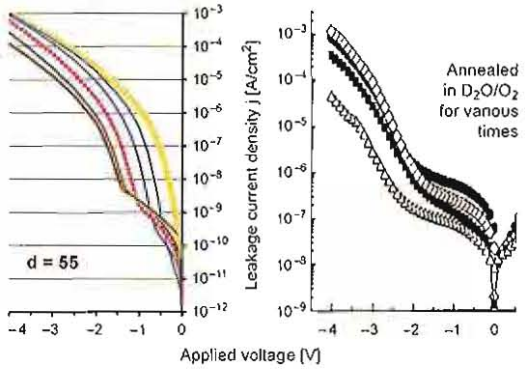

Fig. 4:BST thin film between Pt electrodes: Comparison between simulation (left, d=55 nm) and experiment (right, d=200 nm)(ref. 5).

Fig. 4 presents a comparison between simulation for acceptor doped specimen and experiment with BST specimens annealed in D_2O/O_2 gas removing donor-type oxygen vacancies and thus enhancing the effective acceptors [5]. The results are reasonably well comparable.

In conclusion the new model combining carrier injection and bulk conduction can describe experimental results semi-quantitatively.

Acknowledgement

The author would like to thank P. Meuffels (IEM) for helpful discussions.

[1] H. Schroeder, S. Schmitz and P. Meuffels, *Appl. Phys. Letters* **82**, 781 (2003).
[2] J.D. Baniecki et al., *J. Appl. Phys.* **94**, 6741 (2003).
[3] H. Schroeder and S. Schmitz, *Appl. Phys. Letters* **83**, 4381 (2003).
[4] H. Schroeder, to be published in *Appl. Phys. Letters*, 2005.
[5] J.H. Ahn et al., *Appl. Phys. Letters* 77, 1378 (2000).

Enhancement of Ferroelectricity in Strained $BaTiO_3$ Thin Films

J. Schubert[3], K. J. Choi[1], M. Biegalski[2], Y. L. Li[2], A. Sharan[2], L.-Q. Chen[2], D. G. Schlom[2], C. B. Eom[1]

[1]*Department of Materials Science and Engineering, University of Wisconsin-Madison, Madison, Wisconsin 53706*

[2]*Department of Materials Science and Engineering, Penn State University, University Park, Pennsylvania 16802*

[3]*Institute of Thin Films and Interfaces and CNI - Center of Nanoelectronic Systems for Information Technology, Research Center Juelich, Germany*

Biaxial compressive strain has been used to dramatically enhance the ferroelectric properties of $BaTiO_3$ thin films. This strain, imposed by coherent epitaxy, can result in a ferroelectric transition temperature nearly 500 °C higher and a remanent polarization at least 250% higher than bulk $BaTiO_3$ single crystals.

Enormous strains can exist in thin films when one material is deposited on another [1] due to differences in crystal lattice parameters and thermal expansion behavior between the film and the underlying substrate or arising from defects formed during film deposition [2, 3]. As a result, the properties of thin films can be dramatically different than the intrinsic properties of the corresponding unstrained bulk materials. While such strain often leads to degraded film properties, if judicious use is made of substrates and growth parameters, strain offers the opportunity to enhance particular properties of a chosen material in thin film form, namely strain engineering. Large shifts in the transition temperature (T_c) and remanent polarization (P_r) are expected [4,5] and have been observed [6] in ferroelectrics.

To predict the T_c enhancement and the temperature dependence of the lattice parameters of $BaTiO_3$ thin films under large biaxial strains using Landau thermodynamic theories [4], we determined a new set of phenomenological coefficients, since existing ones are only applicable to small compressive strains (<~0.4%) [5].

Figure 1 shows the T_c enhancement predicted from thermodynamic analysis for a $BaTiO_3$ thin film under biaxial strain. The green region shows the range in predicted T_c due to the range of reported property coefficients for $BaTiO_3$ that enter into the thermodynamic analysis [7]. Figure 1 implies that a biaxial compressive strain of only ~1% should be sufficient to produce strained (001) $BaTiO_3$ films with a T_c comparable to or higher than unstrained $Pb(Zr,Ti)O_3$ films. Although Fig. 1 might seem to imply that T_c can be enhanced without bound, there are limits to strain engineering. The driving force for film relaxation increases with strain and film thickness. When films are grown to thicknesses greatly exceeding their critical values, relaxation toward a zero-strain state by the introduction of dislocations begins. Thus, for strain engineering to be effective it is important to grow films below, or at least close to, their critical thickness for relaxation. As the critical thickness at which dislocations begin to form varies approximately inversely with lattice mismatch [1], lower mismatch is desired to allow strained $BaTiO_3$ films to grow that are thick enough to allow their ferroelectric properties to be conveniently probed or utilized in devices. We also note that Fig. 1 only applies to thick strained ferroelectrics; as ferroelectrics get thin (<~100 Å), their ferroelectric properties can be drastically diminished by finite-size effects [6-8]. Optimizing the trade off between strain and film thickness depends on the particular application. Based on the equilibrium critical thickness [1] for $BaTiO_3$, this would constrain ε_s to be less than about 0.5%, however, we experimentally find that it is possible to grow 500 Å thick coherent $BaTiO_3$ films at $\varepsilon_s = -1.7\%$.

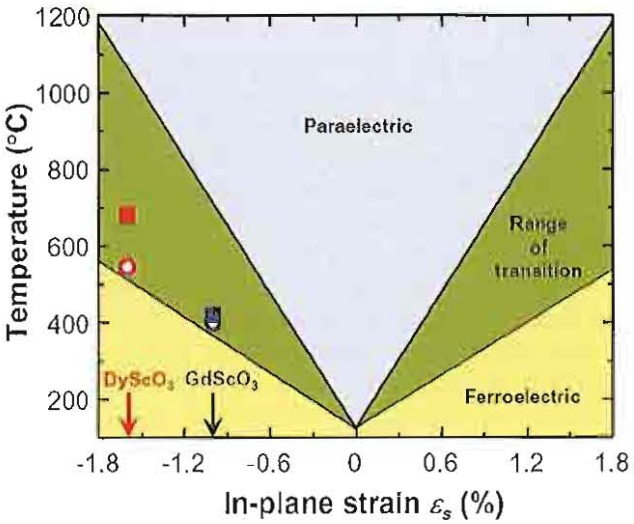

Fig.1. Expected T_c of (001) $BaTiO_3$ under biaxial in-plane strain ε_s, based on thermodynamic analysis[4]. The green region represents the range (error bars) in the predicted T_c due to the spread in reported property coefficients [7] for $BaTiO_3$ that enter into the thermodynamic analysis. The data points show the observed ε_s and T_c values of coherent $BaTiO_3$ films grown by MBE (circles) on $GdScO_3$ and $DyScO_3$ substrates and by PLD (squares) on $GdScO_3$ and $DyScO_3$ substrates.

We used the single crystal substrates $GdScO_3$ and $DyScO_3$ because they are structurally [9], chemically [9], and thermally compatible with $BaTiO_3$, and they have appropriate lattice constants to impart ε_s of about –1.0% and –1.7%, respectively, on coherent (001) $BaTiO_3$ films. Epitaxial $BaTiO_3$ thin films were grown on (110) $GdScO_3$ and

(110) $DyScO_3$ substrates by reactive molecular beam epitaxy (MBE) and by pulsed laser deposition (PLD). These films are epitaxial, purely *c*-axis oriented (the *c*-axis of all $BaTiO_3$ domains is perpendicular to the wafer surface), and, with the exception of the 2000 Å thick $BaTiO_3$ film on $DyScO_3$, are fully coherent with the substrates, without any resolvable lattice relaxation. To identify the ferroelectric phase transition, the temperature dependence of the in-plane and out-of-plane lattice parameters of the films and substrates was measured using a variable temperature four-circle x-ray diffractometer. Unstrained $BaTiO_3$ undergoes a ferroelectric transition at about 130 °C from the high-temperature cubic (*Pm3m*) to the low-temperature tetragonal (*P4mm*) phase [7]. Figure 2 shows the temperature dependence of the lattice parameters of $BaTiO_3$ grown on $DyScO_3$ and $GdScO_3$. The green line corresponds to the theoretical expected transition temperature. An enhanced transition temperature for the $BaTiO_3$ is clearly observed.

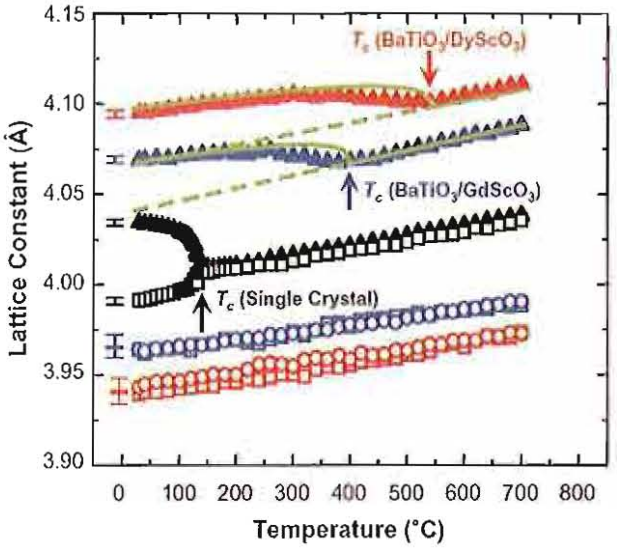

Fig.2. Temperature dependence of the lattice parameters of single crystal $BaTiO_3$ and strained $BaTiO_3$ thin films grown by MBE

Figure 3 shows the ferroelectric hysteresis loops measured on ferroelectric stacks grown on $GdScO_3$ and $DyScO_3$ substrates with 2000 Å thick $BaTiO_3$ layers, together with results from a $BaTiO_3$ single crystal [10]. The hysteresis loops are shifted in the positive voltage direction. This imprint effect is probably due to the asymmetric interfacial properties of the top and bottom electrodes to the $BaTiO_3$ films. Even though we used $SrRuO_3$ for both electrodes, the growth temperature (350 °C) of the top electrode was much lower than that of the bottom electrode(680 C), which might lead to poor crystallinity of the top electrode and asymmetric interfaces. The P_r and coercive field (E_r) were determined to be ~50 μC/cm^2 and 80 kV/cm for the fully coherent $BaTiO_3$/$GdScO_3$ sample and ~70 μC/cm^2 and 25

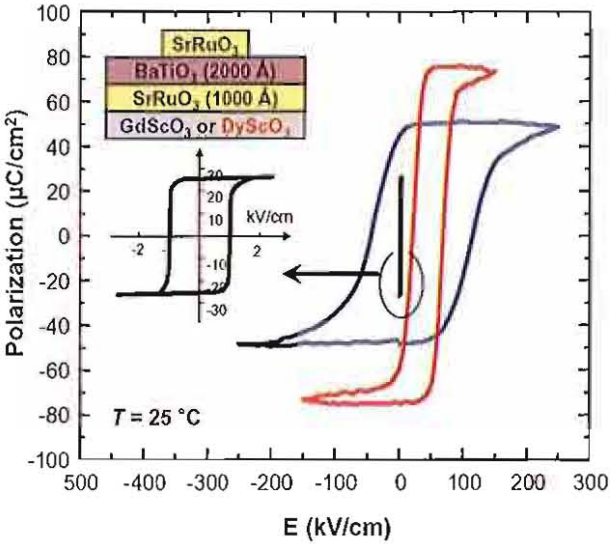

Fig.3. Polarization–electric field hysteresis loops of $BaTiO_3$ thin film capacitors (2000 Å) grown by PLD with $SrRuO_3$ top and bottom electrodes. The inset shows the hyseresis loop of an unstrained bulk BaTiO3 single crystal for comparison [10]

kV/cm for the partially relaxed $BaTiO_3$/$DyScO_3$ sample, respectively. This P_r value is almost 270% of the 26 μC/cm^2 [10] of single crystal $BaTiO_3$, and comparable to the P_r of unstrained $Pb(Zr,Ti)O_3$ films . As this P_r of ~70 μC/cm^2 was observed in a partially relaxed sample with ε_s of −1.3%, a coherently strained $BaTiO_3$/$DyScO_3$ sample with ε_s of −1.7%, could have an even higher P_r.

[1] W.D. Nix, *Metall. Trans. A* **20**, 2217 (1989).
[2] J. S. Speck, A. C. Daykin, A. Seifert, A. E. Romanov, W. Pompe, *J. Appl. Phys.* **78**, 1696 (1995).
[3] W. D. Nix, B. M. Clemens, *J. Mater. Res.* **14**, 3467 (1999).
[4] A. F. Devonshire, *Philos. Mag.* **42**, 1065 (1951).
[5] N. A. Pertsev, A. G. Zembilgotov, A. K. Tagantsev, *Phys. Rev. Lett.* **80**, 1988 (1998).
[6] S. K. Streiffer *et al.*, *Phys. Rev. Lett.* **89**, 067601 (2002).
[7] K.-H. Hellwege, A. M. Hellwege, Eds., *Landolt-Börnstein: Numerical Data and Functional Relationships in Science and Technology* (Springer, Berlin, 1981), New Series, Group III, vol. 16a, pp. 67, 73, 74.
[8] C. H. Ahn, K. M. Rabe, J.-M. Triscone, *Science* **303**, 488 (2004).
[9] J. Schubert *et al.*, *Appl. Phys. Lett.* **82**, 3460 (2003).
[10] B. Jaffe, W. R. Cook Jr., H. Jaffe, *Piezoelectric Ceramics* (Academic Press, London, 1971), p. 78.

Full paper see: Science, **306** (2004), 1005 - 100

Impact of the top-electrode material on the permittivity of single-crystalline $Ba_{0.7}Sr_{0.3}TiO_3$ thin films

R. Plonka[1], R. Dittmann[2], N. A. Pertsev[3], E. Vasco[2], R. Waser[1,2]
[1]*Institute of Electronic Materials IWE II, RWTH Aachen,*
[2]*Institut of Solid State Research and CNI - Center of Nanoelectronic Systems for Information Technology, Research Center Jülich, Germany*
[3]*A. F. Ioffe Physico-Technical Institute, Russian Academy of Sciences, St. Petersburg*

We observed significant influence of the top-electrode material on the thickness and temperature dependences of the dielectric response of single-crystalline $Ba_{0.7}Sr_{0.3}TiO_3$ thin-film capacitors. For $SrRuO_3/Ba_{0.7}Sr_{0.3}TiO_3/SrRuO_3$ samples, the position of dielectric maximum shifts to lower temperatures with decreasing film thickness, whereas the samples with Pt top electrodes exhibit an opposite trend. Moreover, the apparent "interfacial" capacitance, extracted from the film-thickness dependence of dielectric response, is very different for these two types of samples and strongly depends on temperature. Experimental results are analyzed theoretically in the light of the depolarizing-field and strain effects on the transition temperature and permittivity of ferroelectric films.

The collapse of the dielectric constant with decreasing thickness, observed in perovskite ferroelectric thin films, like $Ba_xSr_{1-x}TiO_3$ (BST), is an issue of fundamental importance and essential for the successful integration of these materials as high-permittivity layer in future dynamic random access memories or for their use in non-volatile ferroelectric memories. [1][2] The interface between BST and the electrode material plays a crucial role in terms of the dielectric collapse and the degradation of the ferroelectric properties with decreasing film thickness.

Therefore, we investigated the influence of different electrode materials on the thickness dependence of the properties of BST thin-film capacitors, fabricated by pulsed laser deposition. We compared fully epitaxial capacitors with conducting $SrRuO_3$ (SRO) top- and bottom-electrodes (SRO samples) to SRO/BST capacitors with metallic Pt top electrode (Pt samples).

X-ray analysis of the BST film out-of-plane lattice parameter a_3 prove that both types of samples (Fig.1, left axis) are in the same strain state at a given film-thickness t (see also [3]).

Room-temperature dielectric measurements revealed a significant influence of the top-electrode material on the thickness-dependence of the dielectric response: While from the slope of the linear fit of the reciprocal capacitance density c_{eff}^{-1} vs. film thickness t (Fig. 1, right vertical axis) similar thick-film permittivities 1 can be derived ($\varepsilon_\infty^{SRO} \approx 6700$ versus $\varepsilon_\infty^{Pt} \approx 5700$), the y-intercept of this linear fit yields an apparent "interfacial" capacitance density, which in the case of the *SRO samples* ($c_i^{SRO} = 1030$ fF/μm^2) is about five times higher than the value associated with *Pt samples* ($c_i^{Pt} = 200$ fF/μm^2).

Since both types of samples are in the same strain state, the differences in the dielectric properties originate from other mechanisms connected with the top-electrode interface. A possible mechanism may be the different screening length of the electrodes, connected with an SRO lattice dielectric constant one order of magnitude higher than for Pt.

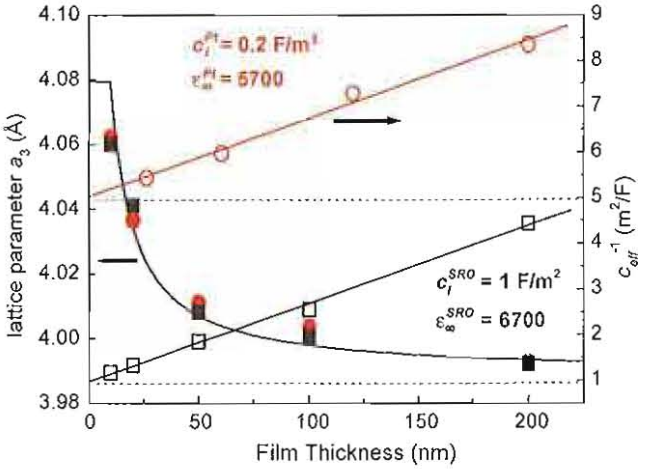

Fig. 1 Thickness dependence of the out-of-plane lattice parameter $a_3(t)$ (closed symbols referred to left vertical axis) and the inverse of the capacitance density at room temperature (open symbols referred to right vertical axis) for samples with SRO (squares) or Pt (circles) top-electrodes. The solid curve shows the theoretical dependence c(t) determined in Ref. 7, whereas the solid lines correspond to linear fits for the experimentally achieved data.

Dielectric measurements were performed at a wide temperature range (Fig. 2). In general, peaks of the dielectric constant can be observed for all samples, while the dielectric peak broadens and its height decreases with decreasing film thickness t. However, the position $T_m(t)$ of the peak shifts with decreasing film thickness to *higher* temperatures for the Pt samples, whereas for the SRO ones it shifts to *lower* temperatures. Furthermore, the dielectric response ε_{eff} of the latter increases with decreasing thickness at temperatures below 260 K [see Fig. 2 (b)]. The insets in Fig. 2 show the temperature dependence of the "apparent" interface capacitance density, which for both systems show a very different behavior, with even negative values c_i^{SRO} for low temperatures.

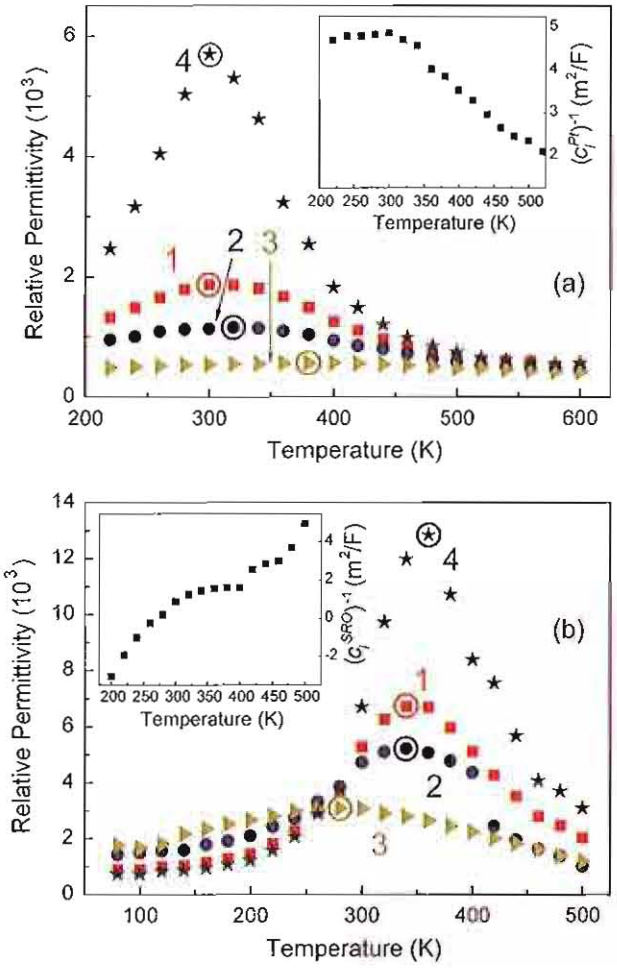

Fig. 2: Temperature dependence of the relative permittivity measured in samples with Pt (a) or SRO (b) top-electrodes. The numbers correspond to different BST layer thicknesses [(a): 120 nm (1); 60 nm (2); 26 nm (3); assuming an infinitely-thick BST layer (from linear slope of the thickness series) (4); (b): 200 nm (1); 100 nm (2); 50 nm (3); and an infinitely-thick BST layer (4)]. Circles mark the position of the maximum of each curve.

Insets show the temperature dependence of the inverse interface capacitance density (from y – intercept of the thickness series).

We modeled the ferroelectric film/electrode interfaces by a thin low-permittivity layers with characteristics independent of the film thickness t. In the case of a short-circuited capacitor, a depolarizing field $E_{dep} \cong -P_3/(c_i t)$ exists inside the film, where P_3 is the film out-of-plane polarization, and c_i is the total interfacial capacitance per unit area. The influence of E_{dep} on the transition temperature T_c can be described with the aid of the nonlinear thermodynamic theory of epitaxial ferroelectric films. [4] The calculation shows that the depolarizing field affects only the second-order polarization term $a_3^* P_3^2$ in the expression for the film thermodynamic potential G derived in Ref. [4]. The renormalized coefficient a_3^{**} is given by $a_3^{**} \cong a_3^* + 1/(2c_i t)$. Since the phase transition in BST films must be of the second order,[15] T_c can be found from the condition $a_3^{**} = 0$, which yields

$$T_c(t) = \theta - \frac{\varepsilon_0 C}{c_i t} + 4\,\frac{\varepsilon_0 C Q_{12}}{s_{11}+s_{12}} S_m(t),$$

where θ and C are the Curie-Weiss temperature and constant of the bulk material, s_{ln} *are the film elastic compliances,* Q_{12} *is the electrostrictive constant,* and S_m is the misfit strain.

It shows that the depolarizing-field effect leads to a decrease of T_c in thinner films, which is inversely proportional to the film thickness t and to the interfacial capacitance c_i. Similar thickness dependence is displayed by the temperature T_m corresponding to the dielectric maximum in our SRO samples.

At the same time, the misfit-strain effect, described by the last term of the equation, leads to an increase of the transition temperature T_c with decreasing thickness in case of BST films grown on SRO/STO, because S_m is negative here and its magnitude increases in thinner films as can be seen from the thickness dependence of a_3 (Fig. 1). This trend is similar to the thickness dependence of the dielectric-peak position T_m observed in our Pt samples.

Since the influence of electrode material on the film permittivity is likely to result from the superposition of several different effects, the dielectric behavior of SRO/BST/SRO and Pt/BST/SRO capacitors cannot be consistently described by our model in a wide temperature range. Nevertheless, one of the most remarkable experimental results, namely, the increase of dielectric response with decreasing thickness observed for SRO/BST/SRO samples at low temperatures, can be explained by the decrease of ferroelectric transition temperature due to the depolarizing-field effect.

[1] D. E. Kotecki, J. D. Baniecki, H. Shen, R. B. Laibowitz, K. L. Saenger, J. J. Lian, T. M. Shaw, S. D. Athavale, C. Cabral, Jr., P. R. Duncombe, M. Gutsche, G. Kunkel, Y.-J. Park, Y.-Y. Wang, and R. Wise, IBM J. Res. Develop. 43, 151 (2000).

[2] N. Setter and R. Waser, Acta Mater. 48, 151 (2000).

[3] R. Dittmann, R. Plonka, E. Vasco, N. A. Pertsev, J. Q. He, C. L. Jia, S. Hoffmann-Eifert, and R. Waser, Appl. Phys. Lett. 83, 5011 (2003)

[4] N. A. Pertsev, A. G. Zembilgotov, and A. K. Tagantsev, Phys. Rev. Lett. 80, 1998 (1999); Ferroelectrics 223, 79 (1999).

Scaling of the Ferroelectric Field Effect Transistor and a new FeFET programming concept

M. Fitsilis[1], H. Kohlstedt[1], A. Gerber[1], Y. Mustafa[2], R. Waser[1,2]
[1]*Institute of Solid State Research and CNI - Center of nanoelectronic Systems for Information Technology, Research Center Jülich, Germany*
[2]*Institute of Electronic Materials IWE II, RWTH Aachen*

The scaling of the ferroelectric field effect transistor (FeFET) is studied by utilizing transistor model simulation (BSIM3v3). Two scaling approaches are discussed – "variable gate stack scaling", that requires changing the gate stack, and "constant gate stack scaling", that leaves the gate stack unchanged. The material parameters were assumed fixed throughout the scaling procedure. Also, a new FeFET programming concept is proposed that eliminates a separate erase cycle and simplifies memory design.

The importance of non-volatile memory for storage of digital information is without question. Compared to other memory types, the ferroelectric field effect transistor (FeFET) presents a promising alternative for a future generation memory device that combines high speed operation with non-volatility. Using a FeFET in a memory application necessitates the investigation of new programming methods to take advantage of the unique characteristics of the device. Also, the scaling potential of the FeFET must be investigated, because it is important to have a long term view in order to be competitive.

New Programming Concept

First, a new programming concept is proposed that eliminates the need for a separate erase operation. Instead it incorporates both a "write" and an "erase" in one programming cycle (Fig. 1) [1]. The pulse applied to the cells that are to be programmed is V in the first half and goes to zero in the second half. The V/2 voltage that is applied to some of the cells in Fig. 1 does not change their state (polarization remains unchanged).

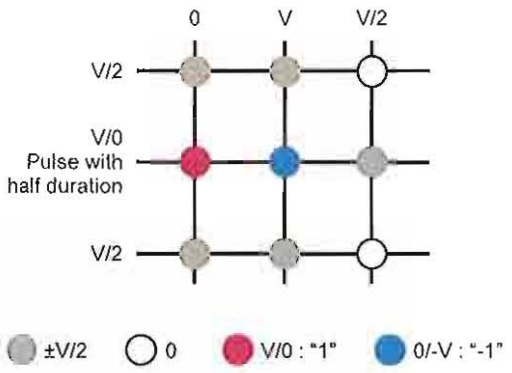

Fig. 1: Programming that incorporates a write and an erase operation in one single operation.

This is enabled by a low doping concentration in the FeFET substrate (10^{14} cm^{-3}) that makes it possible to reverse the polarization if e.g. *5 V* are applied to both source and drain and both gate and bulk are grounded as seen in the simulation of Fig. 2. The applied voltage in combination with the low doping concentration leads to accumulation of holes in the channel region, so that the Si surface is at a positive potential. This programming method is termed "positive voltage erase".

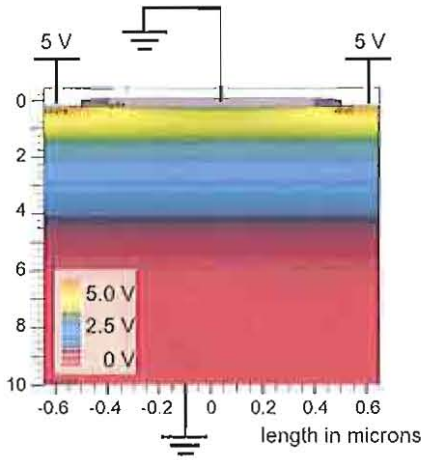

Fig. 2: Potential distribution in substrate during "positive voltage erase".

FeFET Scaling

Next, the scaling of the FeFET is studied. The parameters that were considered are shown in Fig. 3.

X_D is the maximum depletion length and depends on the substrate doping concentration. The two proposed scaling methods [2] are pictured in Fig. 4. *Variable gate stack scaling* has three freedom factors (t_{Fe}, t_{Ox}, N_{SUB}), while *constant gate stack scaling* has only one (N_{SUB}).

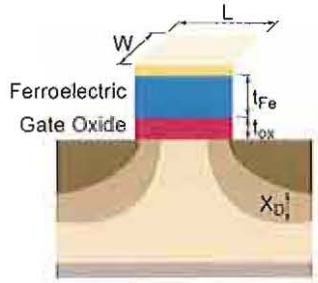

Fig. 3: FeFET parameters modified with scaling.

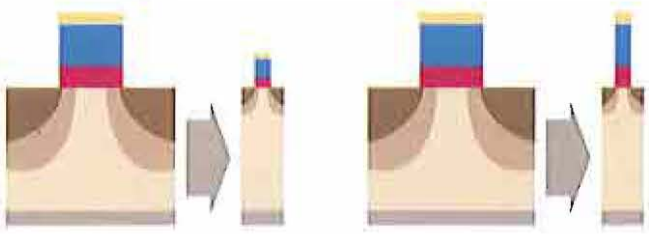

Fig. 4: Variable (left) and constant (right) gate stack scaling.

With *variable gate stack scaling* the write voltage is scaled to be compatible with CMOS. This leads to smaller hysteresis sub-loops with each scaling step (Fig. 5 left). The *I-V* curves in Fig. 5 (right) show how the I_{On}/I_{Off} ratio diminishes as a result of the smaller polarization.

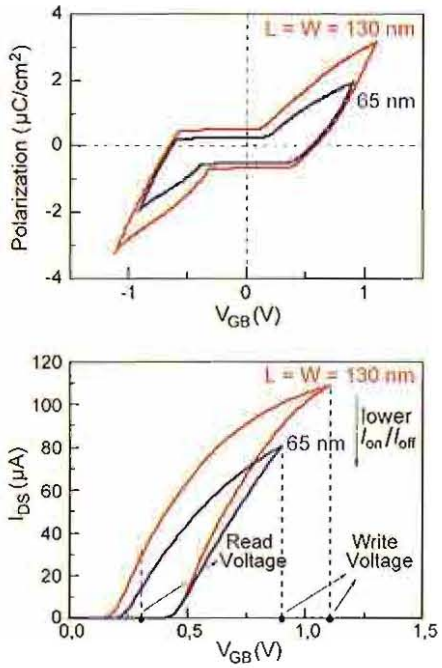

Fig. 5: P-V_{GB} (left) and I_{DS}-V_{GB} (right) for the FeFETs scaled with variable gate stack scaling.

In *constant gate stack scaling* the write voltage is kept constant and only the substrate doping is adjusted for a maximal I_{On}/I_{Off} ratio. The *I-V* curves of the scaled devices are shown in Fig. 6. Both read voltage and V_{DS} are kept constant during scaling in both cases.

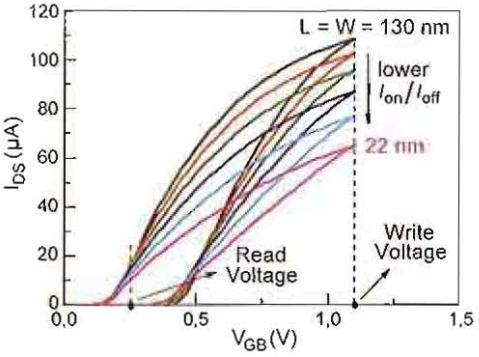

Fig. 6: I_{DS}-V_{GB} curves for the FeFETs scaled with constant gate stack scaling.

Fig. 7 summarizes the simulated results. In both case the I_{On}/I_{Off} ratio diminishes with scaling. *Constant gate stack scaling*, however, can scale to much smaller sizes. In *variable gate stack scaling* the smaller write voltage is the limiting factor for further scaling. This however, makes this scaling method voltage-compatible to CMOS.

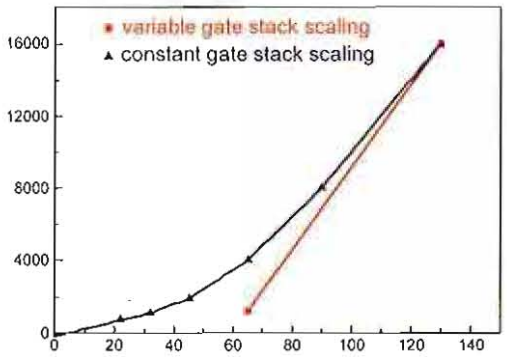

Fig. 7: FeFET scaling roadmap based on I_{on}/I_{off} ratio.

Throughout scaling the specifications were I_{on} > 10 μA and an I_{on}/I_{off} >1000.

[1] M. Fitsilis et. Al, New Concept for using Ferroelectric Transistors in Nonvolatile Memories, Integrated Ferroelectrics, **60**, pp. 45-58, (2004).

[2] M. Fitsilis et. Al, Scaling the Ferroelectric Field Effect Transistor, Integrated Ferroelectric, to be published.

Chemical Mechanical Polishing for Integrated Ferroelectric Nanostructures

S. Clemens[1, 2], A. Rüdiger[2], S. Röhrig[2], T. Schneller[1, 2], R. Waser[1, 2]
[1]*Institute of Electronic Materials IWE II, RWTH Aachen*
[2]*CNI – Center of Nanoelectronic Systems for Information Technology (IFF)*

In order to evaluate the feasibility of integrating nanoscale ferroelectric materials into next generation high-density memory devices, basic questions regarding the ever shrinking structure sizes are under discussion. The physical properties of ferroelectrics that reach the nanoscale regime are intensively studied [1]. Extrinsic and intrinsic influences are known to strongly affect the properties of the functional ferroelectrics. Regarding integration, new fabrication methods emerge, allowing the production of large-area, high-density ferroelectric structure arrays in effective manners. Our group presents a technique based on chemical mechanical polishing to improve the insight into the electrical properties of nanoscaled ferroelectrics by enabling direct electrical hysteresis measurements [2]. At the same time it highlights a possible way of integrating nanosized ferroelectric grains into future memory devices. Furthermore we show, that manipulation of shape and aspect ratio of these grains is also an option using chemical mechanical polishing [3].

Ferroelectric $PbTiO_3$ nanograins are grown on 1"-square platinized substrates by a 2-butoxyethanol based chemical solution deposition technique [4]. The grains are embedded in a layer of low-k flowable oxide (hydrogen silsesquioxane – HSQ) as an insulating matrix. The final sample setup is schematically shown in Figure 1.

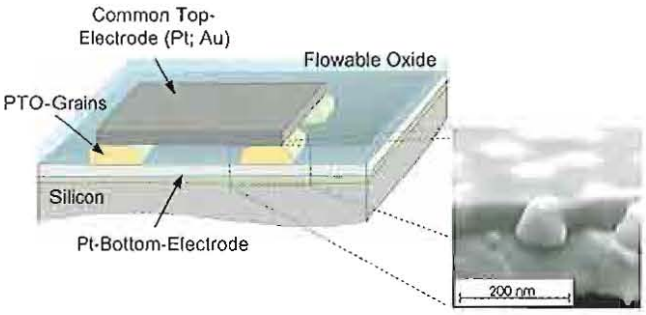

Figure 1: Sample setup enabling direct hysteresis measurements (left). Insert on the right: SEM-image of an embedded $PbTiO_3$ grain. Here, the HSQ-layer is polished down to the grain top.

In order to provide electrical contact to the grains we developed a dedicated chemical mechanical polishing (CMP) step. For this, a commercial available PM4-tabletop polisher is used. The about 20 nm thick residual HSQ-layer on top of the grains is removed using Syton-SF1 as polishing slurry and very soft, chemical resistant polishing pads (ChemoMet). Uniform material removal rates between 7 and 15 nm/min are achieved resulting in extremely smooth surfaces down to 0.4 nm rms. Macroscopic top electrodes (Pt, Au) with diameters between 75 µm and 200 µm provide contact to several $PbTiO_3$ grains in parallel. Figure 2 presents an equivalent circuit model for this setup. Direct electrical characterization measurements are carried out on an Aix-ACCT TFAnalyzer 2000 ferroelectric test system. A triangular voltage signal is applied between collective top- and bottom-electrode and the current response is measured.

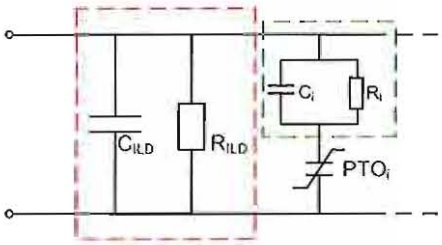

Figure 2: Equivalent circuit diagram for the embedded ferroelectric grains.

C_{ILD} and R_{ILD} represent capacitance and resistance of the HSQ-layer in parallel to the ferroelectric grains (red dashed box in Figure 2). Both, capacitive and leakage current through the dielectric layer are superimposed to the ferroelectric signal but can be compensated. Even in uncompensated measurements switching currents (peaks) appear, to some extent indicating very high coercive fields up to 1.5 MV/cm (see Figure 5).

As the embedded $PbTiO_3$ grains are grown by a self-assembly method, their size distribution is wide, resulting in a maximum grain height of about 50 nm. Most of the grains are smaller and therefore covered with HSQ even after the polishing step, resulting in a distinct in series capacitance C_i and resistance R_i for every single grain (green dashed box, Figure 2). These in-series elements explain the high coercive fields encountered.

In order to decrease the height distribution of the $PbTiO_3$ grains, it is an option to grow them on dedicated TiO_2 nucleation site templates as presented earlier [5]. The controlled deposition ob $PbTiO_3$ grains leads towards further integration, but the reduced grain heights to about 20 nm hamper integration at this point.

The formation of a chemically / mechanically modified interface layer on top of the polished grains during CMP seems to be negligible for the increased coercive field. Polishing experiments on non-embedded $PbTiO_3$ grains show, that even after abrasion of half their initial heights their functionality remains unchanged [3]. Figure 3 compares cross sectional SEM images of $PbTiO_3$ grains before and after CMP.

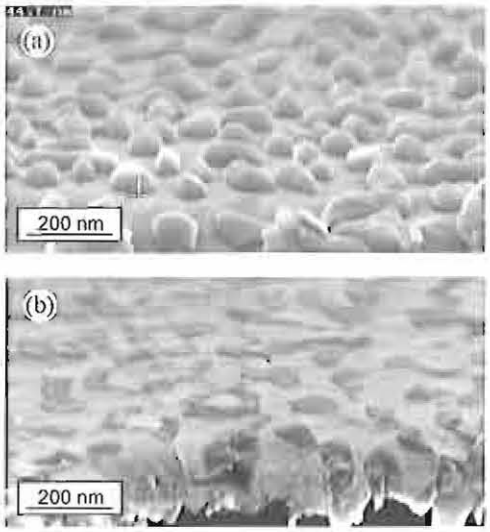

Figure 3: SEM images of (a) an unpolished sample and (b) a sample that was polished for 30 seconds. Only a few nanometer of the original grain height is left after the polishing step.

For the non-embedded $PbTiO_3$ grains the same polishing parameters are used as for the HSQ-layers. Only the polishing time is reduced to less than 30 seconds. Loss of piezoelectric activity is not detected as verified by piezo-response force microscopy (PFM) measurements. It seems that domain structures indicating ferroelectricity are even intensified after polishing. Figure 4 shows PFM images that demonstrate ferroelectric switching of a polished grain.

Besides proving that neither the chemical agents nor the mechanical abrasion during polishing are significantly affecting the ferroelectric performance, our results show the feasibility of using CMP to nano-manipulate shape and aspect ratio of thermodynamically grown ferroelectric grains. Especially for the studies on size effects this feature is of major interest.

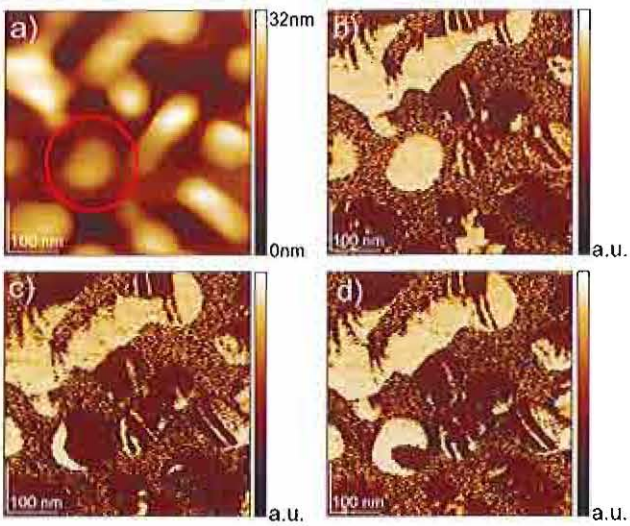

Figure 4: Bi-directional switching of a $PbTiO_3$ grain (highlighted) that was polished for 15 seconds. The fairly round grain is about 15 nm in height and 100 nm in diameter. The single images depict: a) topographic information, (b) inplane phase information and (c) - (d) inplane phase information after applying dc voltages of -5 V and 5 V to the grain, respectively.

Acting on the assumption, that it is primary a residual HSQ-layer on top of the $PbTiO_3$ grains that boosts the coercive field, the field should drop for samples that are polished further. Figure 5 shows the I-V-curves of two samples that were polished to different extends.

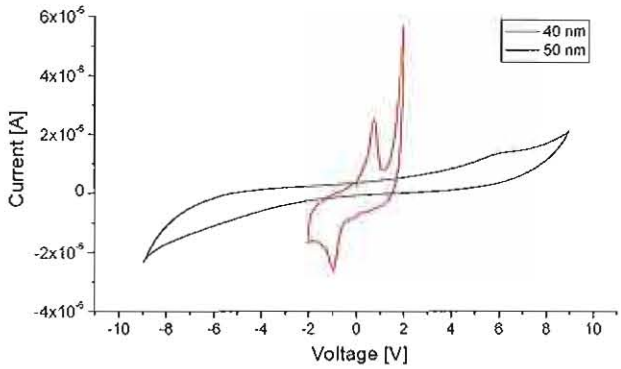

Figure 5: Current response of embedded $PbTiO_3$ grains at 100 Hz. Black curve: only highest grain-tops polished (about 50 nm thick layer, 75 µm diameter Au pad on top). Red curve: polished slightly further (about 40 nm thick, 200 µm Pt pad).

As expected, the thinner sample (red curve) with the larger top-electrode shows increased leakage current and capacitance, as evidenced in Figure 5 by the widening of the curve. The risk of obtaining short circuits increases dramatically, here. At the same time the switching peaks move towards a lower coercive field and are not as smeared out as peaks that appear when the sample is only slightly polished. While for the black curve the coercive field can be calculated to 1.2 MV/cm, it decreases to 250 kV/cm in case of the red curve, approaching literature values for $PbTiO_3$ thin films.

In conclusion we showed the value of chemical mechanical polishing for the integration and characterization of nanosized ferroelectric structures. On the one hand it enables direct electrical characterization of ferroelectrics by uncovering structures that are embedded in a dielectric matrix. In addition, modification in shape and aspect ratio of nanoscaled ferroelectrics is possible, providing new information on ferroelectric size effects.

[1] A. Rüdiger, T. Schneller, A. Roelofs, S. Tiedke, T. Schmitz, R. Waser, Appl. Phys. A **80**, 1247 (2005).
[2] S. Clemens, T. Schneller, R. Waser, A. Rüdiger, F. Peter, S. Kronholz, T. Schmitz, S. Tiedke, Appl. Phys. Lett. **87**, 142904 (2005).
[3] S. Clemens, S. Röhrig, A. Rüdiger, T. Schneller, and R. Waser, accepted for publication in Small.
[4] R.W. Schwartz, T. Schneller, and R. Waser, C. R. Chimie **7**, 433 (2004)
[5] S. Clemens, T. Schneller, A. van der Hart, F. Peter, R. Waser, Adv. Mater. **17**, 1357 (2005).

Simulation of Quantum Dead-Layers in Nanoscale Ferroelectric Tunnel Junctions

K. M. Indlekofer[1], H. Kohlstedt[2]
CNI – Center of Nanoelectronic Systems for Information Technology ([1]ISG, [2]IFF)

We simulate the current-voltage characteristics of a metal-ferroelectric-metal tunnel junction by use of a nonequilibrium Green's function approach. Quantum effects such as Friedel oscillations lead to deviations from the conventional semiclassical description of contacts in such a tunneling structure. As a consequence, we predict a well-pronounced bistable resistive switching effect, depending on the polarization state of the ferroelectric tunnel barrier.

Recently, the concept of a ferroelectric tunnel junction (FTJ) based on a metal-ferroelectric-metal (MFM) layer sequence has been presented [1], consisting of two (semi-) metals separated by an ultrathin ferroelectric layer as visualized in the inset of Figure 1(a). Theoretical and experimental results clearly indicate that FTJs may be realized experimentally. For application-relevant metal-ferroelectric interfaces, the charge distribution and field penetration inside the metal electrodes is commonly described semi-classically on the basis of the Thomas-Fermi screening length. On a nanometer length scale of FTJ device systems, however, a quantum mechanical description of the electronic states and their nonlinear self-consistent charging becomes essential.

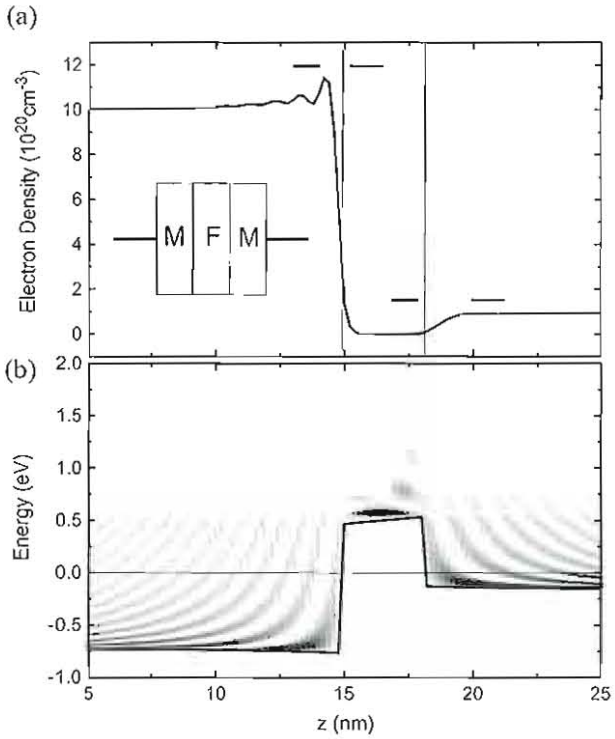

Figure 1: Simulated electron density distribution (a) and potential energy profile (b) (with LDOS grayscale plot) for zero bias. In the shown polarization state of the ferroelectric tunnel barrier, the positive polarization charge is located at the left interface. The Fermi energy corresponds to the dash-dotted line. The inset shows a schematic sketch of the tunnel junction.

In this article, we show that quantum interference effects such as Friedel oscillations lead to deviations from the semiclassical Fermi-Thomas screening within a metal-insulator-metal tunnel junction, resulting in a considerable field penetration inside the metallic contacts [2]. A Green's function based quantum kinetic transport theory, which is well-estabilished in the context of transport simulation of semiconducting tunnel devices, provides the basis of our calculations. Considering an idealized protype FTJ system in the clean-limit, we obtain a bistable device behavior.

In order to simulate the I-V characteristics of the FTJ, a non-equilibrium Green's function approach has been used. The employed empirical tight-binding one-band formulation constitutes a good approximation for the description of conduction band electrons inside the ferroelectric tunnel barrier and the electrodes. Within this framework, nonlinear Coulomb charging effects are accounted for in terms of a self-consistent Hartree-potential. Polarization charges at the two interfaces of the ferroelectric material are implemented as charged mono-layers. (For simplicity, we assume a mono-domain polarization state with a polarization vector perpendicular to the junction plane. The device structure is translationally invariant within the grown layers.) An applied bias voltage is implemented as a difference in the local Fermi-energies of the two reservoirs.

In the following, we will discuss an idealized case of an MFM structure in the clean-limit, assuming an effective electron mass of $m^* = 0.5\, m_e$ and a dielectric constant of $\varepsilon_r = 300$ throughout the device. The ferroelectric tunnel barrier of 3.2 nm and 0.5 eV height (with interface polarization charges of $\sigma = \pm 5 \times 10^{13}$ cm^{-2}) is surrounded by two (semi-) metallic contact regions with electron concentrations of 10^{21} cm^{-3} and 10^{20} cm^{-3}, respectively. These parameters have been chosen in order to clearly visualize quantum effects in nanoscale tunnel systems. (Since the tunneling time of an electron through a ferroelectric barrier is unknown, the chosen parameters – especially for ε_r – should be considered as rough estimations.) Of course, they have to be adjusted to match the individual experimental device structure.

Figure 1(a) shows the simulated electron contration under zero bias conditions (short circuit case). Due to the wave-nature of the electron, Friedel oscillations arise within the electrode regions in the vicinity of the tunnel barrier (clearly pronounced in the left contact). The oscillation period is given by the Fermi wavelength divided by two ($\lambda_F/2 \approx 1.0$ nm in

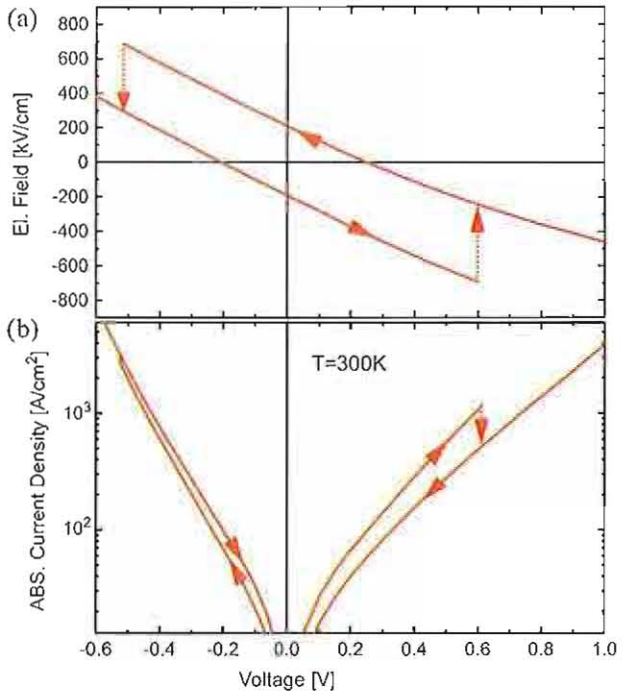

Figure 2: Simulated electric field (a) and current-density (b) characteristics. The assumed intrinsic coercitive field is 700 kV/cm.

the l.h.s. reservoir). As an important consequence, quantum mechanically determined partially depleted regions close to the tunnel barrier arise (see arrows in Figure 1(a): 1.0 nm and 2.2 nm), in contrast to the abrupt electron concentration drop in the classical case. We refer to this phenomenon as a "quantum dead-layer" (analogous to a conventional dead-layer which also introduces a non-screening and non-ferroelectric region at the metal-insulator interface). Within the semi-metallic electrode on the r.h.s., the depleted region is further extended due to band-bending, varying with the applied voltage. In Figure 1(b), the corresponding self-consistent potential energy profile for the electrons is shown (solid line) with a grayscale plot for the local density of states (LDOS). In the shown grayscale mapping, a darker color in the LDOS plot corresponds to a higher density of states. Note that the applied voltage corresponds to the difference in the local Fermi-energies at the outer ends of the contacts. One can clearly identify the polarization charge at the interfaces of the ferroelectric tunnel barrier in terms of a kink in the continuous part of the potential energy and a tilted barrier potential due to the resulting depolarization field of ≈ 200 kV/cm. The LDOS plot reveals the wave-properties of the electron: Firstly, standing wave patterns result from reflections at the tunnel barrier, giving rise to the Friedel oscillations with a quantum dead-layer. Secondly, multiple reflections within the barrier region yield resonances in the higher energy region. Latter may become relevant for hot-carrier injection conditions. Furthermore, within the reservoir on the l.h.s., a shallow triangular quantum well arises, which is responsible for the screening charge.

The local electric field within the ferroelectric barrier as a function of the applied voltage is shown in Figure 2(a). (A positive voltage corresponds to an energy lowering of the right reservoir in Figure 1(b).) Here, an intrinsic coercitive field of 700 kV/cm has been assumed, resulting in transition voltages of approximately +0.6 V and -0.5 V. The asymmetry stems from the assumed electron concentration asymmetry within the electrodes. Since there is a significant voltage drop within the electrode regions close to the barrier (depleted regions), the external voltage necessary to induce a polarization flip in the ferroelectric material is significantly higher than the intrinsic voltage drop across the barrier. Additionally, in Figure 2(b), the corresponding current-density vs. voltage characteristics is plotted in a log-scale, revealinge an exponential behavior of the current density which is determined by the tunnel barrier. Depending on the the polarization state and the sign of the applied voltage, the slope in the log-scale varies due to different potential profiles.

The bistable I-V characteristics could make such an MFM device a possible candidate for a non-volatile memory element. Obviously, the total capacitance of the considered device structure will also be affected by the quantum dead-layer and depletion effects discussed above. In general, the influence of polarization charges due to a ferroelectric layer inside such a nanodevice on the I-V characteristics will certainly depend on the screening properties of the adjacent contact regions. Here, quantum mechanically determined charge distributions and accompanying depletion regions play an important role.

In conclusion, we have considered quantum interference effects in ultrathin metal-ferroelectric-metal tunnel junctions. The current-voltage charateristics of an exemplary tunnel structure in the clean-limit has been simulated with the help of a nonequilibrium Green's function formalism. As a result, a bistable resistive switching behavior was predicted. Although the simulations were performed for a specific set of parameters, ferroelectric tunnel junctions in general might be a first step into a new class of tunnel systems. Here we can think of junctions which consist of magnetic or superconducting electrodes and ferroelectric barriers. For a theoretical description of electronic transport in such nanosystems, a quantum kinetic approach as discussed in this letter offers a consistent treatment of quantum interference und tunnel effects under the influence of polarization charges.

[1] J. R. Contreras, H. Kohlstedt, U. Poppe, R. Waser, C. Buchal, and N. A. Pertsev, Appl. Phys. Lett. 83, 4595 (2003).

[2] K. M. Indlekofer and H. Kohlstedt, Europhys. Lett. 72, 282 (2005).

Impedance Spectroscopy Study of TiO_2 Having Bistable Resistance States

D. S. Jeong, H. Schroeder, R. Waser
CNI – Center of Nanoelectronic Systems for Information Technology (IFF)

The impedance of 27-nm-thick amorphous TiO_2 films showing bistable resistive switching was investigated in the frequency domain (100 Hz – 10 MHz). The impedance spectra were characterized for the various resistance states, a fresh state (before electroforming, FS), a high resistance state (HRS), and a low resistance state (LRS). The impedance spectrum of the FS shows the usual law of dielectric response. The impedance spectra of the HRS and the LRS suggest the existence of dc conductance in TiO_2 with the value corresponding to the HRS and the LRS, respectively, and show almost the same capacitances independent on the resistance state. For a better understanding, numerical calculations, based on the finite element analysis (FEA), of impedance spectra were performed for both, a local filament and an interface related model. The simulation data for the filament model agree much better with the experimental results.

Resistive switching behavior of transition metal oxide (TMO) materials, including TiO_2 and NiO [1, 2] as well as perovskite-type oxides such as $SrZrO_2$ and $Pb(Zr_x, Ti_{1-x})O_3$ [3, 4], is a very attractive subject of technical and scientific research. Recently, TMOs having bistable resistance states, a high resistive state (HRS) and a low resistive state (LRS), were evaluated for their use in resistive switching random access memory (ReRAM) devices because of the expected advantages of the ReRAM for future integration architectures [5]. Another, more scientific motivation for these vigorous efforts is to clarify the mechanism of the resistive switching which is under debate for several decades.

We investigated the impedance of sputter grown TiO_2 films at the various resistance states (FS, HRS, and LRS) in the frequency domain (100 Hz – 10 MHz). The resistive switching measurements were performed by applying dc bias voltage on the top-electrodes of $Pt/TiO_2/Pt$ capacitors. The impedance spectra were measured at 0 V with an oscillation voltage of 0.05 V. The details of sample preparation and measurements can be found elsewhere [6].

Figure 1 shows the typical current vs. dc bias voltage curves of TiO_2. It represents a unipolar resistive switching behavior, where the polarity of applied voltage hardly affects the switching unlike the bipolar switching of perovskite-type oxides. To prevent permanent dielectric breakdowns of the film at the switching to the LRS, we set the current compliance to 7 mA. The reset current for the switching from LRS to the HRS is around 30 mA.

The measured impedances Z for TiO_2 were inverted to the corresponding admittances, $Y = 1/Z$, which are shown in Figure 2 vs. applied frequency. The spectrum of the FS is in good agreement with the universal law of dielectric response[7], i.e. constant ratio $Re(Y_F)/Im(Y_F)$, and there is no indication of a dc conductance in the FS.

In contrast, the real parts $Re(Y_{L,H})$ for the LRS and the HRS suggest the existence of constant dc conductances in TiO_2 in these states, which is in parallel connection with ac conductance. The dc conductances obtained from the figure are consistent with the resistances recognized by dc voltage measurements. Unlike the $Re(Y_{L,H})$, the imaginary parts, $Im(Y_{L,H})$ of the admittance are hardly influenced by the resistance state. Therefore, we can conclude that the resistive switching is due to some very localized changes.

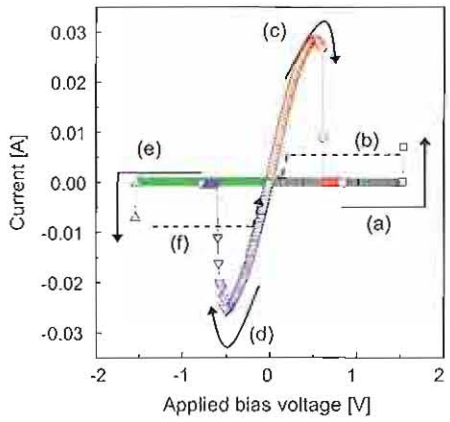

Figure 1: Typical current vs. dc voltage curves for 27-nm-thick TiO_2 between Pt electrodes showing switching. Assuming HRS as initial state of TiO_2, the current increases along the line (a) with increasing positive dc bias. After the switching to the LRS the current limited by the current compliance, decreases to zero along the dashed line (b). Then, increasing the positive dc voltage again, the current follows line (c) in the LRS until switching back to the HRS. As the behavior is completely symmetric the sequence for negative bias is (e), (f), (d).

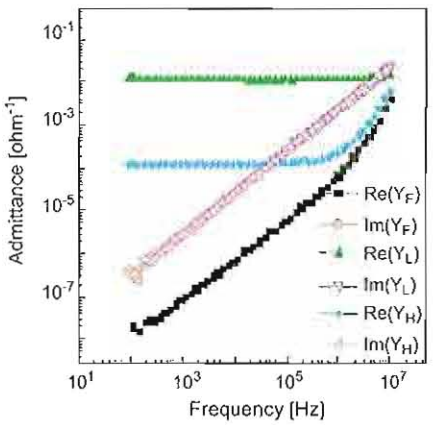

Figure 2: The admittance (Y) of TiO_2 at the various resistance states (FS, HRS, and LRS) in log-log plot. The closed and open symbols denote the real and imaginary parts of Y, respectively. Y_F, Y_H, and Y_L are of the FS, the HRS, and the LRS, respectively.

For further insight into the resistive switching mechanism, impedance spectra were simulated for two models, the filament model and an interface related model, using the finite element analysis (FEA) method. Some results on the voltage distribution are presented in Figure 3 for an applied voltage of 1 V from bottom to top. The homogeneous FS is characterized by a constant voltage drop similar to the voltage distribution at the outside edges of Figure 3(a). The filament model explains the resistive switching by the rupture and formation of localized highly conductive pathways (filaments). The voltage distribution of this model is shown in Figure 3(a) for which the volume of transformation of the resistive state during forming is much smaller than in the more homogeneous interface related model. In this model (Figure 3(b)), the resistance state is determined by the location of a virtual cathode (dashed line) which is parallel with the interface between dielectric and anode and created during electroforming of the dielectric. In the shown HRS most of the dielectric volume has already transformed to a low resistance state. When the virtual cathode reaches the anode, the resistance state is determined to be the LRS. Unfortunately, the microscopic details of the resistive changes are still not clear.

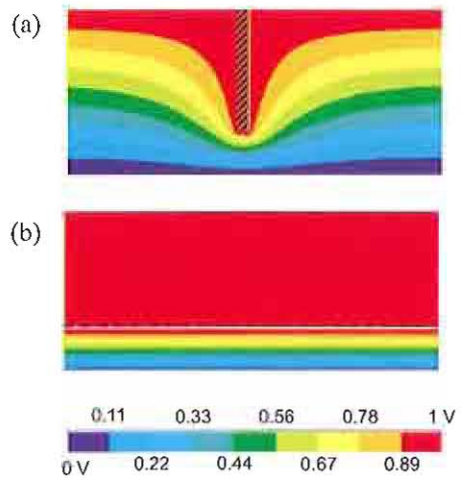

Figure 3: Voltage distributions in dielectric film in the HRS obtained by the FEA for application of 1 V bias on top-electrode for (a) the filament model and (b) the interface related model. The hatched area in (a) designates a highly conductive filament with 20 nm length and 2 nm width penetrating part of 27 nm thick dielectric. The resistivities of the highly conducting and insulating phases are assumed as 0.02 Ωcm and 2×10^8 Ωcm, respectively. The dashed line in (b) designates a virtual cathode created during eletroforming and serving as the boundary between conducting (upper part) and insulating (lower part) phases. The thickness and resistivity of the conducting phase/insulating phase are 20 nm/7 nm and 10^3 Ωcm/2×10^8 Ωcm), respectively.

The simulated impedance spectra of the two models are shown in Figure 4 together with the simulated spectrum of the FS having no conductive phase. The spectrum of the filament model is in much better agreement with the experimental data than the interface related one. In particular, there is nearly no deviation of the imaginary parts $\mathrm{Im}(Y_{CF})$ and $\mathrm{Im}(Y_{CFL})$ and an overlapping of the constant dc conductance with the ac conductance similar as in Figure 2. However, it can be noted that the calculated dc conductance of the filament model is much lower than that of the experimental spectrum. On the other hand, the spectrum of the interface related model shows great deviations from the experimental data for both the $\mathrm{Re}(Y_{CG})$ and $\mathrm{Im}(Y_{CG})$.

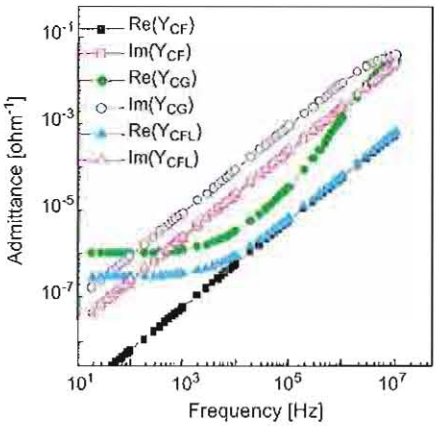

Figure 4: The calculated impedance spectra described in terms of the complex admittance (Y) of the FS (Y_{CF}), the interface related model (Y_{CG}), and the filament model (Y_{CFL}), respectively. The parameters taken for the calculations are identical to those for the calculations of the voltage distributions in Figure 4(a) and (b). Additionally, for the calculation of Y_{CFL} the density of filaments is assumed to be 2.5×10^{11} cm^{-2}, i.e. 1 filament in a square of 20×20 nm^2.

Therefore, we conclude that the filament model is a much better explanation for the impedance spectra of TiO_2 showing the bistable resistive switching behavior.

[1] F. Argall, Solid-State Electron. **11**, 535 (1968).
[2] B.J. Choi et al., J. Appl. Phys. **98**, 033715 (2005).
[3] A. Beck, J.G. Bednorz, Ch. Gerber, C. Rossel, and D. Widmer, Appl. Phys. Lett. **77**, 139 (2000).
[4] J. R. Contreras, H. Kohlstedt, U. Poppe, R. Waser, C. Buchal, and N. A. Pertsev, Appl. Phys. Lett. **83**, 4595 (2003).
[5] R. Waser (ed.), *Nanoelectronics and Information Technology* (Wiley-VCH Verlag GmbH & Co. KGaA, Weinheim, 2003), p. 526.
[6] D. S. Jeong, H. Schroeder, and R. Waser, submitted to Appl. Phys. Lett.
[7] A. K. Jonscher, J. Phys. D **32**, R57 (1999).

Resistive Switching and Data Reliability of Epitaxial (Ba, Sr)TiO_3 Thin Films

R. Oligschlaeger[1, 2], R. Waser[1, 2], R. Meyer[2], S. Karthäuser[2], R. Dittmann[2]
[1]*Institut für Werkstoffe der Elektrotechnik II*
[2]*CNI – Center of Nanoelectronic Systems for Information Technology (IFF)*

We report on resistive switching of capacitor-like $SrRuO_3/Ba_{0.7}Sr_{0.3}TiO_3/Pt$ thin films epitaxially grown on $SrTiO_3$ substrates. We observe a weak but stable hysteresis in the current-voltage curve. By applying short voltage pulses, a high or low resistive state as well as intermediate states can be addressed even at room temperature. We demonstrate a multiple-branch hysteresis curve corresponding to multilevel switching modus revealing different sub-loops for different write voltages. Furthermore reliability issues such as cycling endurance and data retention are presented. Read-write operations over 10,000 cycles show a fatigue-like drift of both resistance states. No data loss is found upon continuous readout

Many different material systems such as oxides, organic materials, semi-conductors show bistable switching of resistivity. This effect is of a great interest for future non-volatile memories. For scalability reasons, resistive information storage concepts have the higher potential compared to charge based storage concepts. Recently, dielectric perovskite type oxides (ABO_3) have attracted increasing attention as candidates for resistive information storage [1]. Multilevel storage was demonstrated for Cr-doped $SrZrO_3$ structures [1]. Here, different resistance levels could be addressed by a variation of length and amplitude of the programming voltage pulse. There is still some debate about the physical mechanisms of the resistance change and about the key experimental parameters. Mechanisms under discussion are (i) trapping/detrapping effects and charge transfer processes via donor and acceptor levels (Cr^{3+}/ Cr^{4+}), (ii) a Mott metal-insulator transition, (iii) formation of local current domains, (iv) redox processes of extended defects and (v) conductivity changes due to a reversal of a local spontaneous polarization. Polarization changes might not be stringently of ferroelectric nature, but might also be due to defect dipoles e.g. formed by acceptor/oxygen vacancy defect associates. In our present work, we investigate resistive switching of 0.2% chromium-doped $Ba_{0.7}Sr_{0.3}TiO_3$ (BST) capacitor-like thin films of around 40 nm thickness deposited by PLD.

Figure 1(a) displays the quasi-static measurement of the hysteretic *I(V)*-characteristic between +6.0 V and -6.0 V obtained at room temperature for 10 subsequent cycles with a frequency of 25 mHz. The current compliance is set to 10 mA corresponding to an effective current density of 25 A/cm^2 for a pad size of 0.04 mm^2. The sample starts in the low resistance state when sweeping the voltage from zero to positive values (1). In the subsequent voltage sweep from positive to negative voltages (2–3), the sample shows an increased resistance. At negative voltage the sample resistance switches back from a high to a low resistive state (4). In the branch from zero to positive values (1) the virgin sample shows a slightly higher resistance than obtained in the subsequent cycles. The high and low current curves cross at zero voltage. The maximum resistance change (R_{High}/R_{Low}) is about 5. In contrast to hysteretic *I(V)* curves with abrupt resistance changes, reported in Ref. [1], a less distinctive resistance change is observed here. On samples with stable *I(V)* characteristic, switching in pulse mode is studied to demonstrate two level and multilevel data storage at RT. Results are illustrated in Figure 1(b) (one bit) and Figure 2(a) (two bit). Employing a positive voltage pulse of +6.0 V for 0.2 s switches the system into a high impedance state. After applying a negative pulse of -6.0 V for 0.2 s the low impedance state is recovered. Between these write and erase pulses the state is readout with 0.5 V continuously over 10 s.

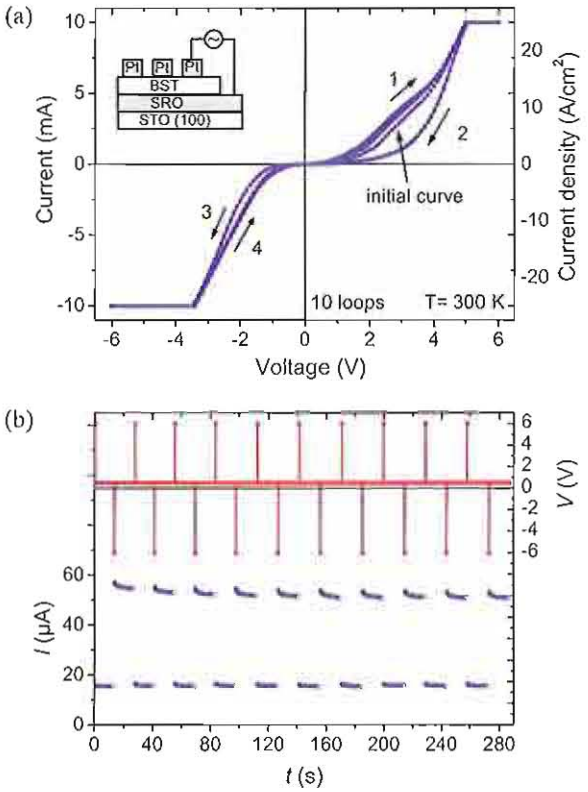

Figure 1: (a) *I(V)*-characteristics of a Pt/BST/SRO/STO (001) structure. 10 voltage sweeps with an amplitude of 6 V and 0.1 V/s at RT. Arrows show the sweep direction of the applied voltage. **(b)** Two state switching performance at RT. Applied voltage vs time (upper curve); readout current vs time (lower curve).

Employing write pulses of intermediate amplitudes allow to address different low impedance states. Different impedance states can only be set, if the programming voltage is in the window corresponding to the hysteresis in the *I(V)*-curve. Four stable equidistant impedance levels are ob-

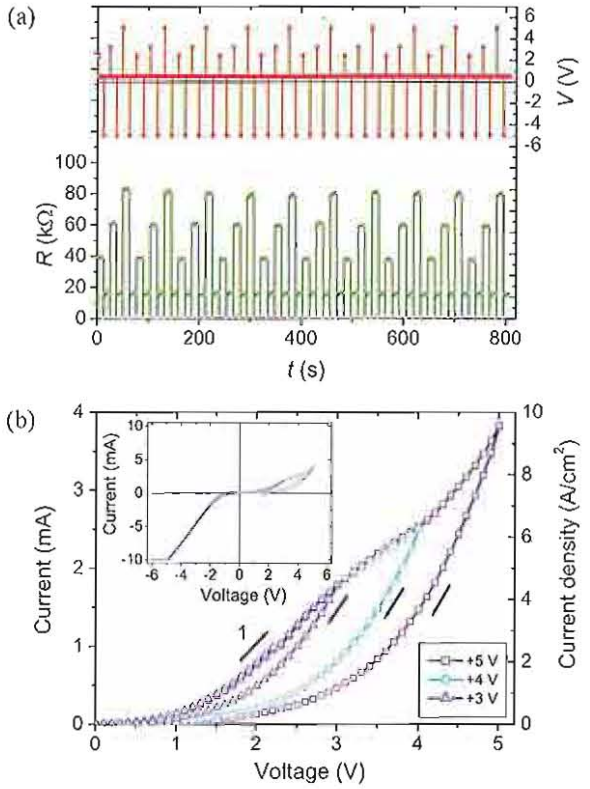

Figure 2: (a) 2-bit multi state resistive information storage of a Pt/BST/SRO/STO (001) structure at RT. Programming voltages for multilevel switching: 2.4 V, 3.3 V, 5.0 V; erase voltage: -5.0 V. (b) *I(V)* characteristics showing different sub-loops for different write voltages.

tained by applying 0.2 s long voltage write pulses of 2.4 V, 3.3 V, and 5.0 V and an erase pulse of -5.0 V, respectively. If the programming voltage is further increased (e.g. from 5.0 V to 6.0 V), no additional resistance change is found. In Figure 2(b) the *I(V)*-curves corresponding to multilevel switching modus are shown. Starting from negative erase voltages the voltage is raised to different write voltages resulting in different sub-loops. Even though for other materials different types of *I(V)*-curves have been reported [1], in our case no threshold voltage V_{th} had to be reached to switch from R_{on} to a higher impedance state. Reliability of the stored resistance state is studied for once write-erase/ continuous readout and for cyclic write/ erase operation.

Figure 3 displays the time dependence of the current corresponding to the high and the low resistive states, which show an exponential decrease especially after switching to the high resistance state. The relaxation time of several hours, suggests a participation of slow solid state electrochemical processes. Measurements show that both states are stable for at least 10^4 at RT. Write/erase endurance measurements demonstrate switching over 10^4 cycles. Figure 4 shows a typical decrease of the resistance in both states. In order to determine the charge transport mechanism the temperature dependence of the current in both impedance states was measured. The current in both states (R_{on} and R_{off}) is found to be thermally activated with activation energies of

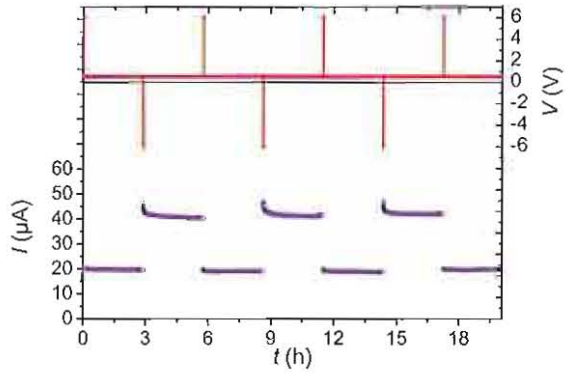

Figure 3: Demonstration of non-volatile data readout in a write once/continuous read and a erase once/continuous read operation. Write/erase pulse time: 0.2 s. Readout time: 10^4 s

0.19 eV and 0.22 eV, respectively. These findings together with the nonlinear *I(V)*-curves indicate a thermally activated hopping between isolated states as the dominating mechanism for conduction in both states. No metallic behavior is seen analogous to Cr-doped $SrZrO_3$ reported in Ref.[1]. The question remains, whether one cause of resistive switching could be the existence of ferroelectricity in BST epitaxially grown on SRO/STO substrates. A tetragonal distortion of

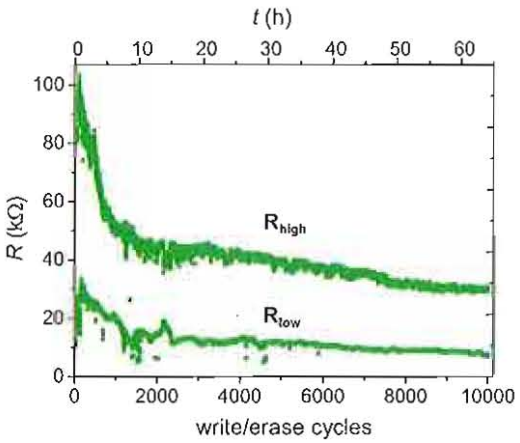

Figure 4: Switching reliability of a Pt/BST/SRO/STO (001) device for a "write-read-erase-read" sequence of 10000 cycles. write/erase voltage: 6 V/-6 V.

the unit cell even at RT originates from the lattice mismatch between substrate and film resulting in a compressive strain of the BST film. To examine the influence of ferroelectricity on the resistive switching we investigated the temperature dependence of switching behavior up to 180 °C. Resistive switching is observed in BST thin layers (40 nm) below and above the ferroelectric-to-paraelectric transition assumed to be at 60 °C, indicating a switching behavior independent from any ferroelectric lattice transition.

[1] A. Beck, J. G. Bednorz, Ch. Gerber, C. Rossel and D. Widmer, Appl. Phys. Lett. **77**, 139 (2000).

Hysteretic Current-Voltage Characteristics of Ferroelectric Tunnel Junctions

N. A. Pertsev[1, 2], H. Kohlstedt[1], R. Waser[1, 3]
[1]*CNI – Center of Nanoelectronic Systems for Information Technology (IFF)*
[2]*A. F. Ioffe Physico-Technical Institute, Russian Academy of Sciences, St. Petersburg, Russia*
[3]*Institute of Materials in Electrical Engineering and Information Technology 2 (IWE2), RWTH Aachen University, Aachen, Germany*

The current-voltage (*I-V*) characteristics of ferroelectric tunnel junctions (FTJs) are calculated for direct electron tunneling. First, the role of converse piezoelectric effect is analyzed. It is shown that the lattice strains of piezoelectric origin modify the *I-V* relationship owing to strain-induced changes of the barrier thickness, electron effective mass, and position of the conduction-band edge. Since the polarization reversal in a ferroelectric barrier alters the sign of piezoelectric coefficient, the *I-V* curve displays resistive switching at the coercive voltage and a hysteretic behavior. Second, the effect of internal electric field caused by incomplete screening of polarization charges is analyzed. For asymmetric FTJs, this depolarizing-field effect also leads to a considerable change of the barrier resistance after the polarization reversal. However, the symmetry of resulting hysteretic *I-V* curve is different from that characteristic of strain-related resistive switching. Crossover between two types of hysteretic behavior is described taking into account both the strain and depolarizing-field effects.

Tunnel junctions of several different types are currently studied from the fundamental point of view and used in microelectronics. Famous examples are the superconducting Nb/Al-Al_2O_3/Nb tunnel junctions for high-frequency digital electronics [1] and magnetic CoFe/Al_2O_3/CoFe tunnel junctions for nonvolatile memory applications [2]. Another interesting possibility is to employ a ferroelectric material as a tunnel barrier separating two conductors [3]. Since ferroelectrics possess several specific physical properties, the current-voltage characteristics of such ferroelectric tunnel junctions (FTJs) are expected to be different from those of conventional metal-insulator-metal junctions. In particular, the electric-field-induced polarization reversal in a ferroelectric barrier may have a pronounced effect on the conductance of a FTJ. Indeed, the polarization switching alters the sign of polarization charges existing at a given barrier/electrode interface, changes positions of ions in ferroelectric unit cells, and modifies lattice strains inside a ferroelectric barrier. Motivated by these considerations, we carried out the theoretical analysis of current-voltage relationships that characterize the direct quantum mechanical electron tunneling across a few-nanometer-thick ferroelectric barrier.

To calculate the tunnel current through an ultrathin ferroelectric barrier, we used the Wenzel-Kramer-Brillouin approximation and the one-band model. Owing to the converse piezoelectric effect inherent in ferroelectrics, the barrier thickness t, position of the conduction-band edge E_c, and the electron effective mass m^* depend on the voltage V applied between the electrodes. These dependences may be written as $t = t_0 + d^*V$, $E_c = E_{c0} + \kappa\, d^*V/t_0$, $m^* = m_0^*(1 + \mu\, d^*V/t_0)$, where d^* is the effective longitudinal piezoelectric coefficient of the ferroelectric layer, κ is the deformation potential of the conduction band, and $\mu = \partial \ln m^*/\partial S$ characterizes the sensitivity of the effective mass to the out-of-plane film strain S [4]. Using the above relations, the tunneling probability D can be calculated as a function of the total electron energy E in the direction perpendicular to the barrier. The calculation gives

$$D(E) = \exp\left\{-\frac{4(2m_0^*)^{1/2}}{3\hbar e}\frac{t_0}{V}\left(1+\frac{d^*V}{t_0}\right)\left(1+\mu\frac{d^*V}{t_0}\right)^{1/2}\right.$$
$$\left.\times\left[\left(E_{c0}+\kappa\frac{d^*V}{t_0}-E\right)^{3/2}-\left(E_{c0}-eV+\kappa\frac{d^*V}{t_0}-E\right)^{3/2}\right]\right\}$$

where e is the electron charge and $\hbar$ is the Planck constant. It can be seen that the voltage dependence of D differs considerably from the case of nonpiezoelectric barriers [5].

The tunnel current was evaluated at zero absolute temperature in the approximation developed by Simmons [6]. Restricting our analysis to the range of small voltages, we represented the current density J in the form of a series expansion $J(V) = C_1V + C_2V^2 + C_3V^3 + \ldots$ and calculated coefficients of the linear, quadratic, and cubic terms analytically [4]. Remarkably, the quadratic term, which is negligible for a symmetric nonpiezoelectric barrier [6], becomes significant for FTJs. Since the coefficient C_2 appears to be directly proportional to the piezoelectric constant d^*, the current density is sensitive to the orientation of ferroelectric polarization with respect to the applied electric field. This orientation, which determines the sign of d^*, changes after polarization reversal in the barrier at the coercive voltage V_c. Therefore, a resistive switching takes place at $V = V_c$ so that the current-voltage curve becomes hysteretic. Figure 1 shows such hysteretic curve calculated numerically for a representative set of the junction parameters. It is seen that two branches of this curve just touch each other at zero voltage. Here an "inversion" of the junction resistance takes place because the direction of applied field reverses at $V = 0$. For the employed set of parameters, the low-resistance state transforms into the high-resistance one at both the positive and negative coercive voltages.

Since the polarization charges $\rho = -\operatorname{div}\mathbf{P}$ at the barrier surfaces are not perfectly compensated for by free charge carriers even in the presence of metallic electrodes (due to the finite electronic screening length in metals), a depolarizing field should exist in FTJs. Evidently, this internal elec-

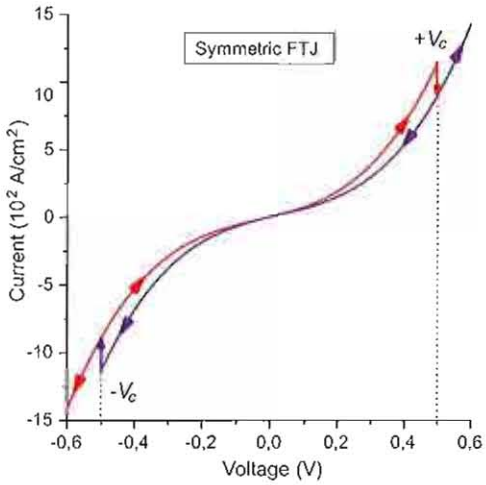

Figure 1: Influence of converse piezoelectric effect on the current-voltage characteristic of a symmetric ferroelectric tunnel junction. The current density was calculated using the following values of the junction parameters: barrier height at zero voltage $\Phi_0 = 0.5$ eV, $t_0 = 2$ nm, $m^* = m_e$ (m_e is the free electron mass), $d^* = 50$ pm/V, $\kappa = -4.6$ eV, and $\mu = 10$.

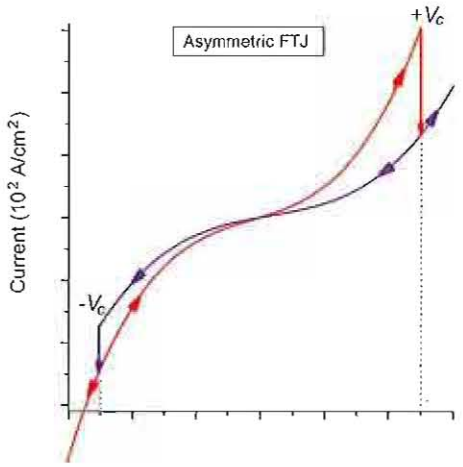

Figure 2: Combined effect of piezoelectric strain and depolarizing field on the current-voltage characteristic of asymmetric FTJ. The current density was calculated for the following values of the junction parameters: $\Phi_0 = 0.5$ eV, $\Delta\Phi = 0.02$ eV, $t_0 = 2$ nm, $m^* = m_e$, $d^* = 50$ pm/V, $\kappa = -4.6$ eV, and $\mu = 10$.

tric field modifies the potential barrier in the junction and so influences the tunnel current. The analysis shows, however, that in symmetric junctions (with identical electrodes) the depolarizing field cannot induce significant resistive switching. The situation changes dramatically in asymmetric FTJs, which involve dissimilar top and bottom electrodes. In this case the mean value of the electrostatic potential in the barrier differs from zero even in a junction with short-circuited electrodes, and, moreover, this mean value changes sign after the polarization reversal. Accordingly, the depolarizing field creates a jump $2\Delta\Phi$ of the mean barrier height at the coercive voltage. Since the tunnel current exponentially depends on the mean barrier height [6], the resistive switching caused by depolarizing-field effect is expected to be pronounced in asymmetric FTJs.

The ratio of conductances, which characterize the low- and high-resistance states in asymmetric FTJs, is determined at zero voltage by the depolarizing-field effect only. Numerical estimates show that this ratio may be several times larger than unity. The whole current-voltage curve of an asymmetric FTJ can be calculated by taking into account both the strain and depolarizing-field effects. Figure 2 demonstrates the theoretical curve obtained for a representative junction, where the asymmetry is significant. It can be seen that the symmetry of the current-voltage curve changes when the depolarizing-field effect overrides the strain-related one. In particular, the current jumps occurring at the positive and negative coercive voltages are opposite in sign in this case. A crossover between the first (Figure 1) and second (Figure 2) type of the hysteretic curve takes place as the degree of junction asymmetry increases [4].

Thus, the theoretical calculations strongly support the idea that the polarization reversal in a nanoscale ferroelectric barrier may result in a pronounced resistive switching. They also indicate that asymmetric FTJs with dissimilar top and bottom electrodes are preferable for nonvolatile memory applications because of a larger resistance on/off ratio.

[1] K. K. Likharev and V. K. Semenov, IEEE Trans. Appl. Supercond. **1**, 3 (1991).

[2] J.-M. Slaughter, M. DeHerrera, and H. Dürr, in *Nanoelectronics and Information Technology, Advanced Electronic Materials and Novel Devices*, edited by R. Waser (Wiley-VCH, New York, 2003), Chap. 23, p. 591.

[3] L. Esaki, R. B. Laibowitz, and P. J. Stiles, IBM Tech. Discl. Bull. **13**, 2161 (1971); L. L. Chang and L. Esaki, *ibid.* **14**, 1250 (1971).

[4] H. Kohlstedt, N. A. Pertsev, J. Rodríguez Contreras, R. Waser, Phys. Rev. B **72**, 125341 (2005).

[5] E. L. Wolf, *Principles of Tunneling Spectroscopy* (Plenum, New York, 1985).

[6] J. G. Simmons, J. Appl. Phys. **34**, 1793 (1963).

Extrinsic Influences on Piezoresponse Force Microscopy

F. Peter[1], B. Reichenberg[2], A. Rüdiger[1], K. Szot[1,3]
[1]*CNI – Center of Nanoelectronic Systems for Information Technology (IFF)*
[2]*aixACCT Systems GmbH, Aachen,*
[3]*Institute of Physics, University of Silesia, Katowice, Poland*

Piezoresponse force microscopy (PFM) is the method of choice to investigate piezoactivity on a nanometer scale. In order to use it as a tool in the quest for the superparaelectric limit, extrinsic effects on the measurement have to be taken into account. We studied different influences from the sample, the experimental setup as well as the physical principle of the measuring method with the aim of giving a quantitative impact on the result.

PFM is a powerful tool to analyse local piezoelectric activity and to study the ferroelectric domain structure. In this method a conducting tip is brought into contact with the sample and an AC voltage is applied to the tip. The piezoresponse parallel to the surface ("in-plane") as well as perpendicular to the surface ("out-of-plane") is optically detected as a deflection of the cantilever. In the quest of experimentally determining the superparaelectric limit [1] the intrinsic piezoeffect has to be analysed. But extrinsic effects are superimposed to the sample response. When theses effects are quantitatively known they can be accounted for in the interpretation of the measurement data.

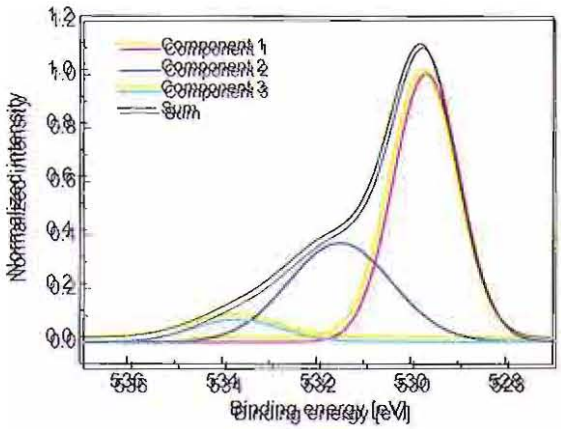

Figure 1: O 1s core line with additional components of the (covered) surface of a $BaTiO_3$ single crystal

Under ambient conditions perovskites like $BaTiO_3$ and $PbTiO_3$ are covered by an adsorbate layer. An X-Ray Photoelectron microscopy (XPS) measurement at room temperature of the O 1s core line is shown in Figure 1.
Three different components can be detected:

- Component 1: Oxygen in Lattice (529.8eV)
- Component 2: Chemisorbed CO or CO_2 (531.5eV)
- Component 3: Physisorbed OH or H_2O (533.8eV)

In situ XPS measurements under ultrahigh vacuum conditions show that above 350 °C H_2O and OH are completely removed whereas the chemisorbed layer cannot be totally eliminated up to 800 °C. Measurements of different angles at room temperature show that under grazing incidence component 3 is not reduced indicating that this peak comes from the layer on top of the crystal. From this we deduced that the top adsorbate layer is physisorbed OH or H_2O [2].

This adsorbate layer causes a considerable field reduction below the tip. The influence of the additional layer was quantitatively determined. The average piezoresponse of a $BaTiO_3$ single crystal was determined by PFM under the following four different conditions:

- ambient conditions
- high vacuum
- high vacuum after heating to 350 °C with subsequent cooling and
- after exposing the sample to ambient conditions.

These steps were done consecutively, always scanning the same area. The result is shown in Figure 2.

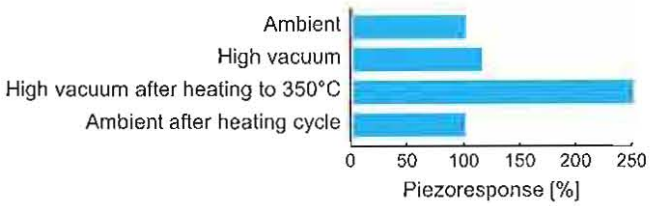

Figure 2: O 1s core line with additional components of the (covered) surface of a $BaTiO_3$ single crystal

In many PFM measurements the in-plane signal is substantially larger than the out-of-plane signal. An example of the difference is given in Figure 3 where the in-plane and out-of-plane piezoresponse of nanograins prepared by chemical solution deposition is shown.

Geometrical considerations show that for standard AFM tips the in-plane optical amplification is a factor of about 20 larger than the out-of-plane amplification. In a dedicated experiment a factor of approximately 18 is measured [3].

Due to the larger in-plane optical amplification these PFM images show more detail and less noise. However, in-plane PFM measurements show a large dependency on the shape of the piezoelectric material. This effect is important when studying the piezoresponse of grains as opposed to relatively flat films.

We simulated the piezoresponse of a 64 nm wide and 12 nm high $BaTiO_3$ grain with and without a 2 nm adsorbate layer. Instead of placing the AFM tip only in the centre of the grain, we moved it from the centre to the perimeter. The

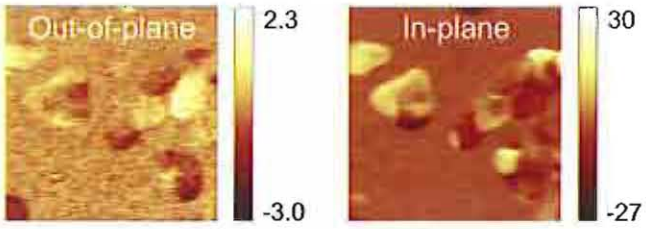

Figure 3: 450 nm × 450 nm Out-of-plane (left) and in-plane (right) PFM measurement of $PbTiO_3$ nanograins. The signal-to-noise ratio is a factor of 3.5 better in the in-plane image

simulation results are shown in Figure 4. In the case without adsorbates the out-of-plane piezoresponse is almost constant whereas the in-plane response is zero in the centre and increases dramatically towards the perimeter of the grain. With adsorbates the out-of-plane response decreases near the edge. This is a consequence of the potential divider created by the additional adsorbates; the voltage actually applied to the perovskite decreases as the grain becomes thinner near the perimeter. But even with a smaller voltage applied, the in-plane signal shows a similar increase as the adsorbate-free case. Examining the electric field at different positions shows that the component parallel to the surface increases. This in turn results in an increased shear deformation which is detected as an in-plane signal. In-plane piezoresponse thus can only be detected in an unsymmetrical setup.

Measuring these effects (constant piezoresponse in the out-of-plane direction and enhancement in the in-plane direction) is challenging as the assumptions used in the simulation are difficult to control. The polarisation of the ferroelectric material has to be uniform in the direction perpendicular to the surface. Furthermore the stoichiometry of the complete grain has to be constant; if it changes so as to create a non-piezoelectric phase at the perimeter the superelevation could be cancelled. Figure 5 shows the topography and piezoresponse of a $BaTiO_3$ grain prepared by pulsed laser deposition on a $SrRuO_3$ covered $SrTiO_3$ single crystal [4].

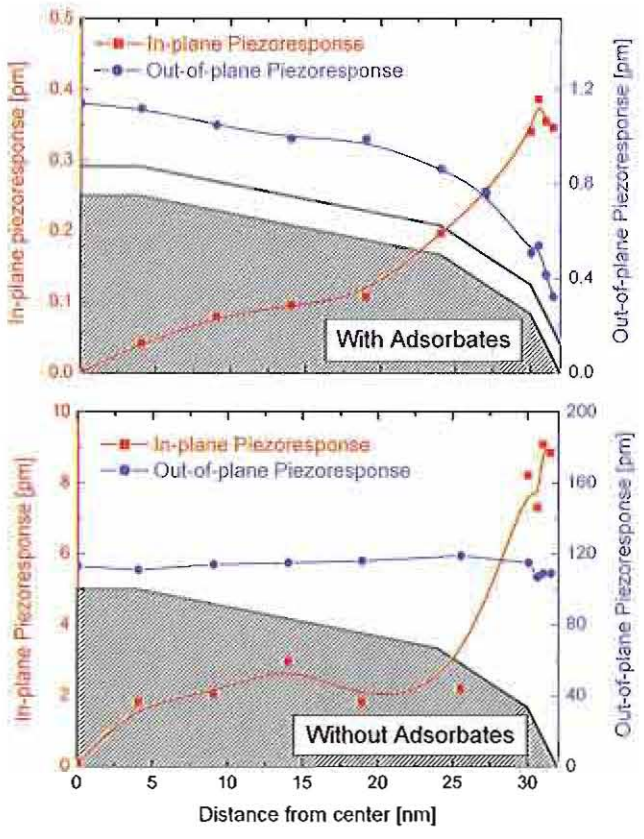

Figure 4: Simulated in-plane and out-of-plane piezoresponse (absolute values) as a function of the distance from the centre of the nanograin. The shape of the grain is indicated in the background.

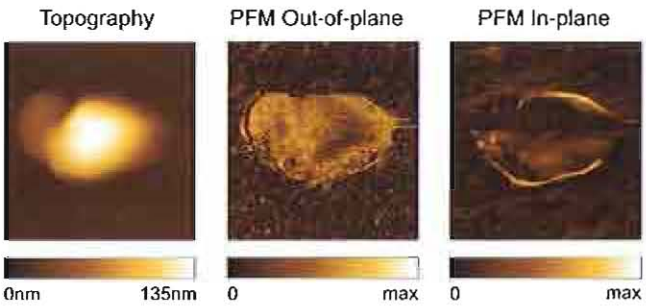

Figure 5: Topography (500 nm × 500 nm), out-of-plane and in-plane piezoresponse of a $BaTiO_3$ grain. The out-of-plane response is relatively constant over the total grain whereas the in-plane response is very small in the middle and high at the perimeter.

In summary we have shown three different extrinsic influences on PFM:

- With XPS-measurements we have shown the existence of an adsorbate layer on top of $BaTiO_3$ under ambient conditions. This layer, which can be partly removed by heating under vacuum, results in a reduced voltage applied to the piezoelectric material and a reduction of the piezoresponse.
- For similar deformations the measured in-plane piezoresponse is generally one order of magnitude larger than the out-of-plane response.
- In asymmetric arrangements an apparent enhancement of the in-plane piezoresponse can be a shape-effect.

[1] A. Roelofs, T. Schneller, K. Szot, and R. Waser, *Applied Physics Letters* **81**, 5231 (2002)
[2] F. Peter, K. Szot, and R. Waser, B. Reichenberg, S. Tiedke, and J. Szade, *Applied Physics Letters* **85**, 2896 (2004)
[3] F. Peter, A. Rüdiger, R. Waser, K. Szot and B. Reichenberg, *Review of Scientific Instruments*, 76, 046101 (2005)
[4] F. Peter, A. Rüdiger, R. Dittmann, R. Waser, K. Szot, B. Reichenberg, and K. Prume, *Applied Physics Letters* **87**, 082901 (2005)

Studies on the Ion Migration in Lateral Structures for Future Electrochemical Bridging Memory Devices

C. Rohde[1], R. Waser[2]
[1]*CNI – Center of Nanoelectronic Systems for Information Technology (IFF)*
[1, 2]*Institut für Werkstoffe der Elektrotechnik II*

In search of new memory device concepts the focus is put on technologies which offer low power consumption, non-volatility reasonably high switching speed as well as high scalability, and a stable long term behaviour. Preferably, new memory devices should also enable a non-destructive read-out operation. That is why electrochemical bridging memory cells are investigated. Depending on the bias polarity metallic paths are formed or erased in a solid electrolyte. Typically, chalcogenide glasses are used as host material because of the high mobility of silver or copper ions through them. In this study, silver sulphide is used as electrolyte between silver/platinum electrodes. Lateral structures are fabricated to investigate the metallic path between the electrodes and the reactions at the interface between electrode and solid electrolyte.

Established technologies such as Dynamic Random Access Memory (DRAM) or Static Random Access Memory (SRAM) show partly unfavourable behaviour. While the state of DRAM cells has to be refreshed periodically, SRAM requires much die area. That is why electrochemical bridging devices are investigated as an alternative [1][2]. Depending on the bias polarity metallic paths are formed or dissolved in a solid electrolyte which is placed between an inert and an oxidizable electrode (Figure 1).

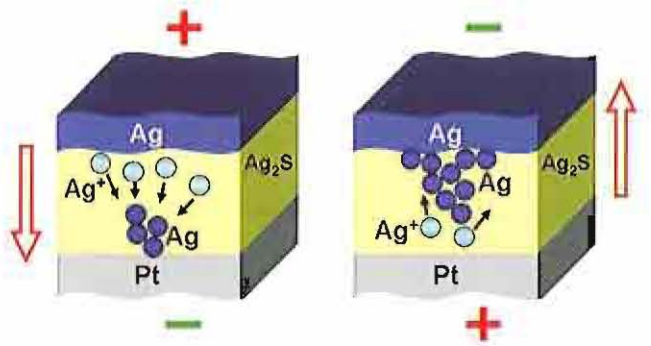

Figure 1: Switching mechanism of an electrochemical cell. A silver sulphide layer lies between a platinum and an Ag electrode. By applying a positive bias to the silver electrode, silver ions start migrating through the thin film, get discharged at the cathode and build an Ag filament as a conductive path. Reversing the bias polarity dissolves the path: silver ions migrate back to the silver electrode.

For investigating the details of the switching mechanism, we fabricated *lateral* structures by optical lithography and lift-off processes on a silicon substrate. An Ag layer is deposited by e-beam evaporation on a titanium oxide adhesion layer (Figure 2(a)). Subsequently, Pt electrodes are sputtered. The sample is used as anode in a sodium sulphide bath while a gilded Cu plate serves as cathode. By applying a constant current the free Ag area is converted into silver sulphide [3][4]. Both electrodes consist of a Ag/Pt stack. During the conversion to silver sulphide the silver below the platinum top layer is partly converted as well. That is why the electrode width has to be broader than 10 µm in this lateral design.

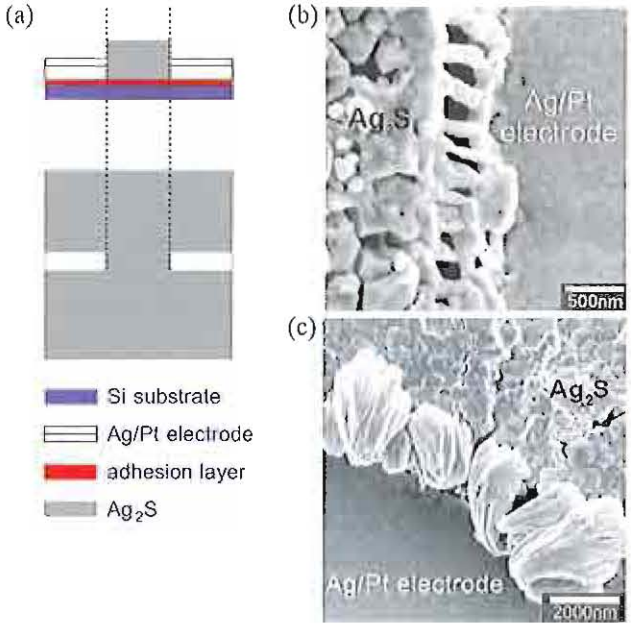

Figure 2: Reactions at the interface of electrode and electrolyte. (a) Schematic of the lateral sample structure (b) SEM image of the anodic reaction: silver migrates from the electrode into the electrolyte thereby forming dendrites. (c) SEM image of the cathodic reaction: silver deposits at the electrode.

A second set of samples is fabricated with one electrode consisting of only Pt and the counter electrode of a Ag/Pt stack, and the electrodes of a third set of samples are only made out of Pt. The electrode shapes vary between opposite finger structures and electrodes that end on edges or tips to investigate the metal path growth. Electrode distances of 100, 30, 10, and 3 µm are chosen.

Electrical measurements are performed with a Keithley 617 electrometer. Initially, the cell is in a high resistive state. Before switching to a low resistive state can be observed, a forming step has to be applied. If a symmetrical system with Ag/Pt electrodes is used, forming can be executed with a positive or negative voltage. For the setup consisting of one Pt and one Ag/Pt electrode, a positive forming voltage has

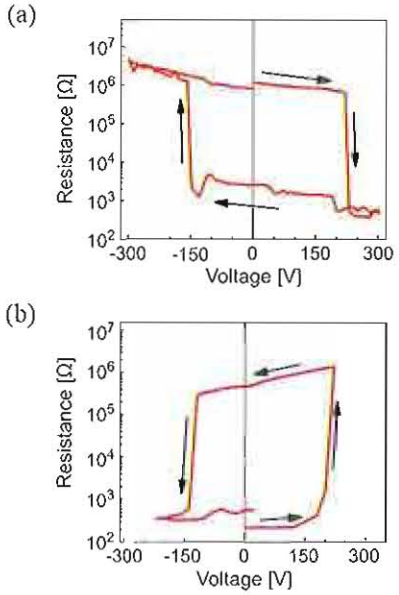

Figure 3: Switching cycles for different forming voltages. The voltage is increased step-wise with a rate of 20 mV/2 s. (a) Forming with -100 mV and (b) forming with +100 mV in a symmetrical system with an electrode distance of 10 µm.

to be applied to the Ag/Pt stack. The smaller the electrode distance and the higher the forming voltage is, the lower is the forming time. For an electrode distance of 3 µm the forming time varies between 900 s and 10 s for voltages between 100 mV and 400 mV. For the same voltages but an electrode distance of 10 µm the forming time varies between 1300 s and 25 s. During this time, an asymmetrical metallic path forms between the electrodes which can be closed by reversing the voltage. In the following the cell is switched between the high and low resistive state by changing the bias polarity (Figure 3). The forming step obviously leads to an asymmetrical path as switching can also be observed if both electrodes consist of a Ag/Pt stack. Samples with only Pt electrodes do not show any low resistive state which suggests that the conductive path developed during forming must consist of Ag clusters.

The sample surface is investigated by scanning electron microscopy (SEM). No difference in the surface structure between the low and high resistive state can be observed, yet after forming the electrode reactions are visible (Figure 2(b) and (c)). At the interface between anode and electrolyte silver dendrites are formed. Rohnke et al. [5] have observed a similar dendritic growth in a AgBr/Ag system. The transfer process at the electrode includes three steps: (a) formation and relaxation of a vacancy at the electrode (here Ag), (b) jump of the ionized metal atom into the electrolyte lattice, and (c) the relaxation of the new ion in the electrolyte lattice [6]. For low voltages (<300 mV) the electrolyte does not tend to track back from the electrode so that Ag dendrites are not visible. During the cathodic reaction Ag ions are reduced and Ag deposits at the electrode/electrolyte interface.

The resistive state can be changed by voltages as small as 150 mV (Figure 3) and a resistance ratio between high and low resistive state of ~ 1000 can be achieved. Due to the large electrode distance the switching times of a few seconds are still high. Both states are stable and can be read out non-destructively by a voltage smaller than the switching voltage, e.g. 10 mV. Repetitive voltage sweeps between 0 V and the level of the switching voltage do not change the resistive state. Nonetheless, the more sweeps are performed in the low resistive state, the more decreases the resistance. This suggests that the conductive path is further strengthened, hence more Ag migrates from the electrode into the solid electrolyte. An HP 4284A LCR meter is used to measure the frequency dependence of the resistance in the two states (Figure 4). While the high resistive state shows a strong frequency dependence, the resistance in the low resistive state is frequency-independent. This further supports the model of a metallic path between the electrodes.

The resistance ratio of ~ 1000 between the low and high resistive state is very promising for future memory application. As the electrode distances of more than 3 µm are quite large, the switching times are still high. In future experiments it will be focused on structures with smaller electrode distance achieved by electron-beam writing and/or a vertical setup.

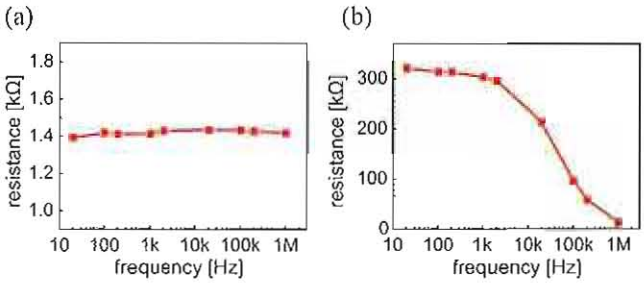

Figure 4: Frequency dependence of the low and high resistive state. (a) Low resistive state; (b) High resistive state.

[1] M.N. Kozicki, M. Mitkova, M. Park, M. Balakrishnan, C. Gopalan, Superlattices and Microstructures **34** (2003) 459–465

[2] K. Terabe, T. Hasegawa, T. Nakayama, M. Aono, Nature, **433** (2005) 47–50

[3] C. Wagner, J. Chem. Phys., **21** 1819–1827

[4] D.W. Hatchett, X. Gao, S.W. Catron, H.S. White, J. Phys. Chem. **100** (1996) 331–338

[5] M. Rohnke, T. Best, J. Janek, J. Solid State Electrochem. **9** (2005) 239–243

[6] J. Janek, Solid State Ionics, **131** (2000) 129–142

A Model for a Resistive Switch Memory Cell with Rechargeable Space Charge

H. Schroeder

CNI – Center of Nanoelectronic Systems for Information Technology (IFF)

For future ultra-large scale-integrated memory chips in cross-bar architecture simple non-volatile memory cells are desirable such as switchable resistors. Among a large variety of candidates such as magnetic RAM, phase change materials, molecules are also polymers and other organic insulating materials as well as ferroelectric and paraelectric oxides. Some resistive switch memory cells using organic thin films between electrodes rely on some charge storage component within the insulator, e.g. rechargeable metal ions or defects dispersed in the matrix but locally centered in the thin insulating film. To describe the experimental I-V-curves an advanced leakage current model combining interface injection current with the drift-diffusion current in the film bulk has been applied. The simulated I-V-curves of this model show features very similar to the experimental data. Parameter variations were performed to evaluate the extension of this type of memory cell to other dielectric material such as perovskite oxides.

Cross-bar architectures of simple non-volatile memory cells such as switchable resistors are favored for solving the expected geometric problems currently used dynamic random access memory (DRAM) architectures will face in future ultra-large scale-integrated memory chips [1]. Therefore, materials showing the long-known resistive switching phenomenon [2] experience a revival and are evaluated for their possible use in an advanced memory cell. Among a large variety of candidates are materials for magnetic RAM, phase change materials, molecules and also polymers and other organic insulating materials as well as ferroelectric and paraelectric oxides. Although the switching effect is clearly documented in numerous experiments the mechanisms are still under discussion.

In Figure 1 an example for resistive switching in an organic insulator (AIDCN) between Al electrodes and some rechargeable metal ions or complexes in the center of the organic dielectric is demonstrated by I-V-curves: Curve (a) starting at very low current (representing the high resistive OFF-state) switches at a certain applied voltage (≈ 2 V) to a high current (representing the low resistive ON-state) and stays in that state, curve (a) at > 2 V and curve (b). The OFF-state can be recovered by applying a short pulse with negative voltage (or current) so that curve (c) is measured reproducing (a). Such a behavior can be used as a memory cell by reading the different resistances at voltages lower than the switching voltage. The stack for the case in Figure 1 has been read and switched more than 10^6 times with switching times less than 10 ns [3].

The geometry of the used stack and the centered rechargeable space charge is sketched in Figure 2. The nominally 20 nm thick centered Al electrode was found to be dispersed in non-connected Al clusters within the dielectric matrix, but still locally concentrated in the center. Without the centered Al metal the resistive switching behavior could not be observed [3].

To describe the measured leakage currents an advanced leakage current model was applied. This new model was developed to successfully explain the field, temperature and thickness dependence of the leakage currents in thin films

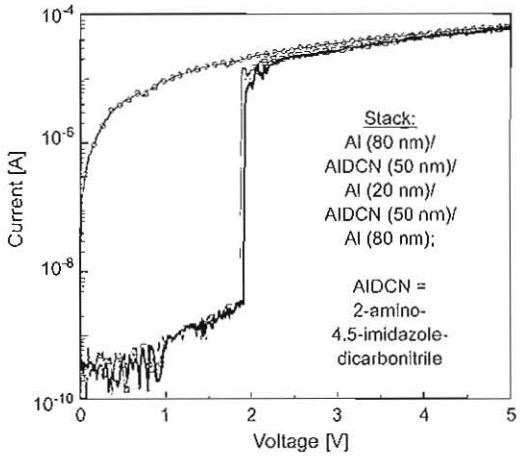

Figure 1: Resistive switching in a bi-stable organic insulator (AIDCN) between Al electrodes (after Ma et al. [3]).

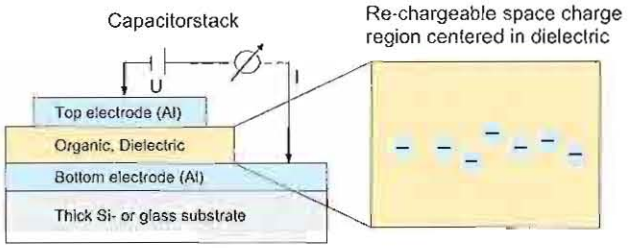

Figure 2: Schematic sketch of stack and space charge geometry

of high-permittivity mixed oxide dielectrics such as $SrTiO_3$ (STO) and (Ba, Sr)TiO_3 (BST) between platinum electrodes [4]. It combines the interface injection/ejection currents from the electrodes into the dielectric (electrons at the cathode/anode, holes at the anode/cathode) modeled by thermionic emission with the drift-diffusion conduction in the film bulk modeled as a wide band-gap semiconductor.

For the description of the experimental data with centered rechargeable space charge as shown in Figure 2 such a layer was implemented into the model, as it is sketched in Figure 3. The space charge was distributed homogeneously

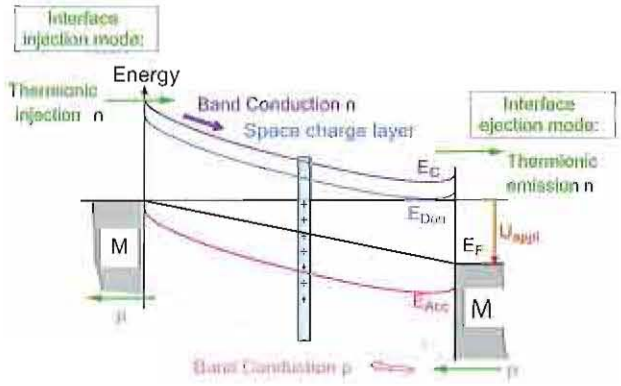

Figure 3: Schematic outline of the combined leakage current model used for the simulation calculations. [4, 5]).

in the centered 2 nm of a 55 nm thick dielectric between Pt electrodes. In Figure 3 are also shown possible additional defects, donors and acceptors, assumed to be homogeneously distributed in the dielectric film at constant defect energy levels within the gap, E_{Don} and E_{Acc}, respectively.

Simulation calculations have been performed with this model. As many of the needed input parameters are not known for the organic dielectrics parameter variations have been performed in order to show the trends [5]:

a) Centered space charge density
   $C = (\pm 0.3,\ 1,\ 3,\ 10)\ \mu C/cm^2$ distributed over 2 nm;
   the resulting densities
   $N_{charged\ defects} = (\pm 0.096, 0.32, 0.96, 3.2) \times 10^{20}\ cm^{-3}$.
b) Dielectric constant $\varepsilon_r = 10, 30, 100, 200, 550$.
c) Homogeneous "background" defect density of donors and acceptors: $N_{Don}, N_{Acc} = 10^{16}, \ldots, 10^{19}$ at defect energy levels $E_{Don} = -0.15$ eV; $E_{Acc} = -2$ eV (below E_C).

Other parameters were kept constant such as dielectric thickness d = 55 nm, temperature T = 425 K, carrier mobilities (about 0.6 cm^2/Vs) and effective densities of states in conduction and valence band (about $6 \cdot 10^{20}\ cm^{-3}$).

In Figure 4 examples for the simulation results are shown in a "Schottky-plot" for the parameter set C = (0, ± 0.3) $\mu C/cm^2$, $\varepsilon_r = 10$ (characteristic for organic insulators) and no effective background defect density. While at high fields (voltages) the difference in leakage currents is not so large (about a factor of 10 for different polarity of the centered charge), at low fields the current decrease for the curve with positive space charge C^+ is very steep. Assuming switching at some intermediate field (as indicated by the arrow) a rather similar behavior as for the measured curve in Figure 1 is achieved. By increasing the space charge density C the difference of the curves with ±C will increase. The reason for this behavior is due to the poisson equation for both, the increased change of the interface fields influencing the injection current and the changes of the internal fields and carrier concentrations in the film bulk changing the conductivity.

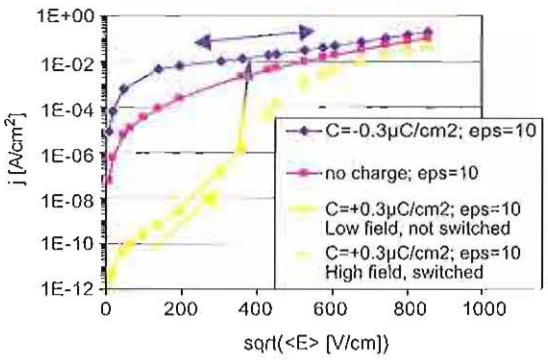

Figure 4: Schottky plot of 55 nm thick dielectric with indicated centered space charge, no effective background defects and $\varepsilon_r(eps) = 10$, characteristic for organic dielectrics; the bi-colored arrow indicates assumed switching [5].

On the other hand the differences decrease by increasing the background defect density because the fields are then increasingly determined by these defect charges instead of the centered rechargeable space charge C. For the case shown in Figure 4(a) background defect density of $5 \times 10^{18}\ cm^{-3}$ reduces the current difference for ±C to less than an order of magnitude at all fields.

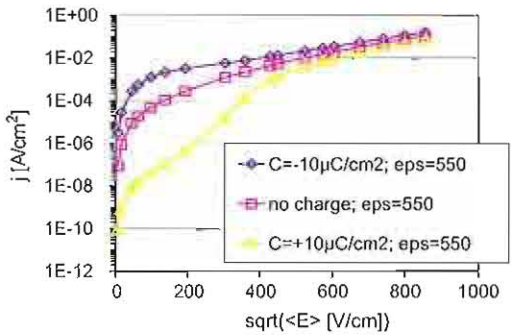

Figure 5: Schottky plot of 55 nm thick dielectric with indicated centered space charge, no effective background defects and $\varepsilon_r(eps) = 550$, characteristic for high-permittivity oxide dielectrics [5].

A similar dependence as in Figure 4 show the simulations for $\varepsilon_r = 550$, characteristic for high-permittivity dielectrics such as STO or BST, but C has to be enlarged about the same factor as demonstrated in Figure 5 for $C = \pm 10\ \mu C/cm^2$. This is explained by the fact that the internal fields are determined by the ratio $S = C/\varepsilon_r$ in the poisson equation. As C is much larger in the last case, the effect of the background defect density is greatly reduced.

In conclusion, the applied model can describe the observed resistive switching qualitatively. An optimization of the fitting by the model calculations may be achieved by using more appropriate parameters of the organic dielectric.

[1] G. Snider, P. Kuekes, T. Hoog, and R. Stanley Williams, Appl. Phys. **A80**, 1183 (2005).
[2] G. Dearnaly, A.M Stoncham, and D.V. Morgan, Reports Prog. Phys. **33**, 1129 (1970).
[3] L.P. Ma et al., Appl. Phys. Letters **80**, 2997 (2002); Appl. Phys. Letters **82**, 1419 (2003)
[4] H. Schroeder and S. Schmitz, Appl. Phys. Letters **83**, 4381 (2003).
[5] H. Schroeder, Mat. Res. Soc. Proc. **889**, W-8.4 (2005).

"Ab-Initio" Band Structure Calculations for $SrTiO_3$ and the Thermionic Emission Current in Metal-$SrTiO_3$ Contacts

H. Schroeder, P. Mavropoulos

CNI – Center of Nanoelectronic Systems for Information Technology (IFF)

Leakage currents through metal/insulator/metal (MIM) thin film capacitor structures with high-permittivity or ferroelectric thin insulating films of perovskite-type mixed-oxides are an important issue because such materials are candidates as capacitor dielectrics in advanced DRAM cells and as new gate materials in FETs, or may be used in switchable resistive memories (ReRAM). The injection of electronic carriers at the metal electrode/insulator (MI) interface is often described by thermionic emission over a (Schottky) barrier. For both, the injection and the band conduction, materials parameters dependent on band structure properties such as the effective electron mass, m*, are entering the corresponding equations. From "ab-initio" band structure calculations for $SrTiO_3$ these numbers were determined, showing significant deviations from literature values. Using the new numbers as input for simulation calculations of an advanced leakage current model the calculated currents and thus the extracted parameters from fits to experimental data (e.g. barrier height) are changed, too.

Leakage currents through metal/insulator/metal (MIM) thin film capacitor structures with high-permittivity or ferroelectric thin insulating films of perovskite-type mixed-oxides such as $SrTiO_3$ (STO) or (Ba, Sr)TiO_3 are an important issue because such materials are candidates for replacing the traditional low-k materials in CMOS integrated circuits, SiO_2 and SiN_x, as capacitor dielectrics in advanced DRAM cells and as new gate materials in FETs, or may be used in switchable resistive memories (ReRAM). Important for the modeling and quantitative description of experimental leakage current data is – besides the conduction inside the wide band-gap semiconductor – the carrier injection at the electrodes. Most commonly, thermionic emission over the interface (Schottky) barrier is used as injection mechanism. The corresponding equation is also known as Richardson-equation for the case of injection into the vacuum. For the application to the injection into a dielectric an effective electron mass, m*, is introduced the value of which is often rather uncertain.

For the model material STO the electronic band structure was calculated from first principles using the full-potential linearized augmented plane-wave method within the generalized gradient approximation of density functional theory (FLAPW-GGA-DFT). The dispersion of the conduction band is presented in Figure 1 showing large anisotropy with light and heavy electrons [1].

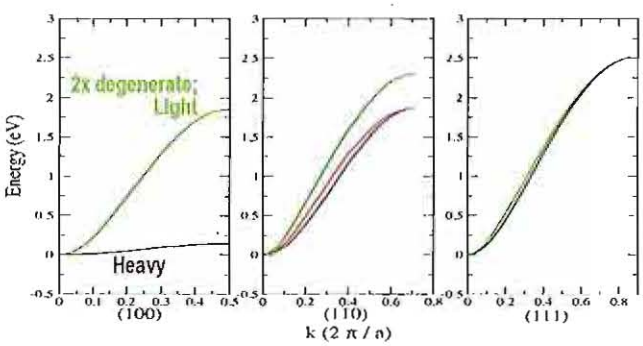

Figure 1: Conduction bands for $SrTiO_3$ showing large anisotropy with light and heavy electrons.

Using the usual approach of anisotropic, but parabolic bands the temperature dependence of the total density of occupied states in the conduction band was calculated for all 3 bands and for both spins with the position of the Fermi level E_F as parameter (Figure 2, top) and from this the effective density of states at the bottom of the conduction band, N_C (Figure 2, middle) which is nearly independent on E_F. Separation of the factor $(kT)^{3/2}$ results in a temperature "independent" pre-factor with an effective mass for the density of states, m^*_{DOS} (Figure 2, bottom). The extracted number for the limit of low temperatures is $m^*_{DOS}(STO) = 0.95\ m_0$ (m_0 is the free electron mass) [1], rather different from values used in the literature of 4 to 4.5 [2].

A current equation similar to the Richardson-equation for the vacuum using also the same band structure from "first principles" with the full anisotropy of both, bands and

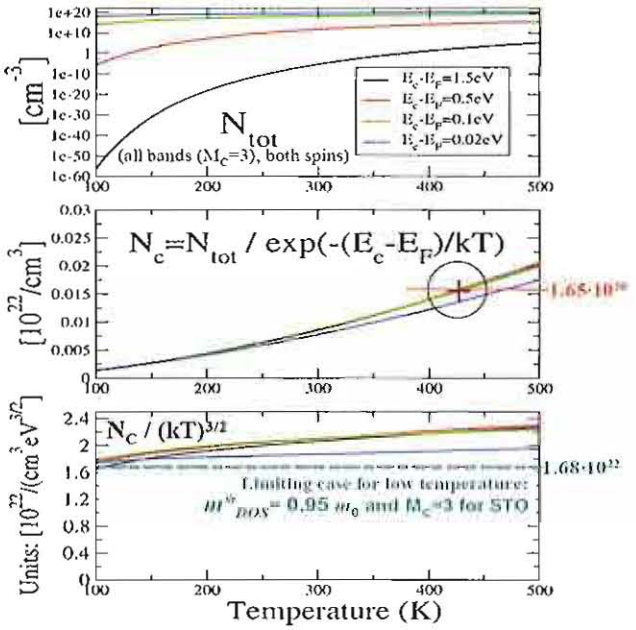

Figure 2: Temperature dependence of total density of states in the conduction band for different Fermi levels (top), effective density of states at the bottom of conduction band (middle), and the prefactor containing m^*_{DOS} (bottom).

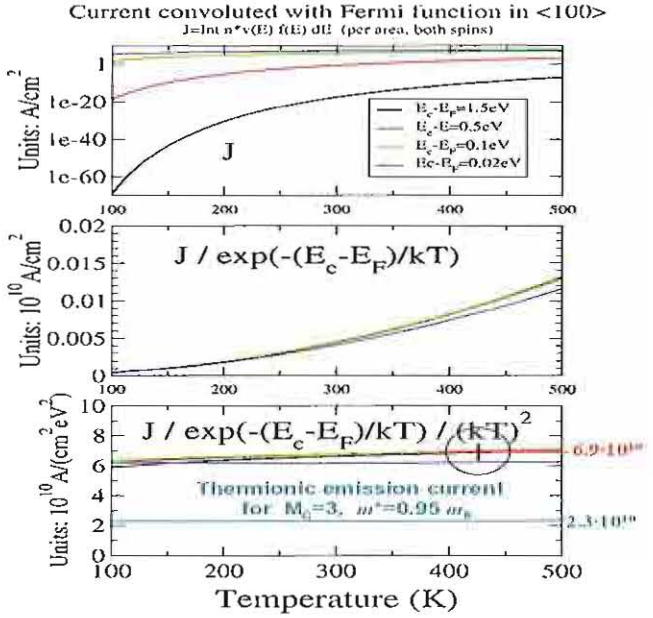

Figure 3: Temperature dependence of thermionic emission current density for different Fermi levels (top), dto. normalized to the Boltzmann factor (middle), and temperature independent pre-factor containing $A^*(m^*_R)$ (bottom) [1].

the group velocity vector (instead of the spherical surfaces of constant energy in the free electron approximation) was deduced resulting in currents and corresponding effective masses m^*_R depending on STO crystal orientation. In Figure 3 the result for the <100>-direction is plotted (top) vs. temperature for different Fermi levels. Again, the separation of a Boltzmann factor (middle) and of the characteristic T^2-dependence results in a constant pre-factor called effective Richardson constant A* (bottom) because it contains the corresponding effective mass m^*_R. Using m^*_{DOS} from Figure 2 in the Richardson constant A for the vacuum as it is usually done [2, 3] the resulting A* is a factor 3 lower than the calculated one in Figure 3 bottom. Therefore, the extracted number from Figure 3 is $m^*_R<100> = 3 \times m^*_{DOS} = 2.84\ m_0$ for the <100>-direction. The corresponding value for the <111>-direction is $m^*_R<111> = 1.61 \times m^*_{DOS} = 1.54\ m_0$ [1].

These numbers calculated from first principles as well as literature data and those for free electrons were used as input for simulation calculations of an advanced leakage current model for MIM thin film capacitor stacks. This model combines carrier injection/ejection at the MI interfaces, modeled by thermionic emission, with the drift-diffusion current in the insulating wide band-gap semiconductor [3]. The simulations were done for T = 425 K.

The results are compared in a so-called Schottky-plot (i.e. log(current j) vs. sqrt(applied electrical field E)) in Figure 4 and show significant differences, more than one order of magnitude at all fields between the largest, corresponding to literature data, and the smallest for the free electron values. The current densities of the cases using the calculated numbers from first principles are in between. At low fields the current density is determined by N_C, and thus by m^*_{DOS}, while at high fields the curves approach the Schottky limit of thermionic emission, for which the current density is determined by the effective Richardson constant A* und thus by m^*_R. This is nicely shown by the enlargements for small and high fields and the additional curves with "Highest N_C, lowest A*" and "Lowest N_C, highest A*" which cross at intermediate fields.

In conclusion, effective electronic masses m*, deduced from "ab-initio" band structure calculations for the model material STO, are different for the density of states in the conduction band and for the current equation of thermionic emission into STO similar to the Richardson equation for vacuum. In addition, for the current they dependent on the direction. The deduced numbers are also significantly different from numbers found in the literature for STO or BST so far. Using all the different effective masses as input for model calculations the resulting leakage current densities vary by more than a factor of 10.

[1] H. Schroeder, P. Mavropoulos, and G. Bihlmayer, submitted to Journal Appl. Phys.
[2] J.D. Baniecki et al., J. Appl. Phys. **89**, 2873 (2001); J. Appl. Phys. **97**, 114101 (2005).
[3] H. Schroeder et al., Appl. Phys. Letters **82**, 781 (2003); Appl. Phys. Letters **83**, 4381 (2003).

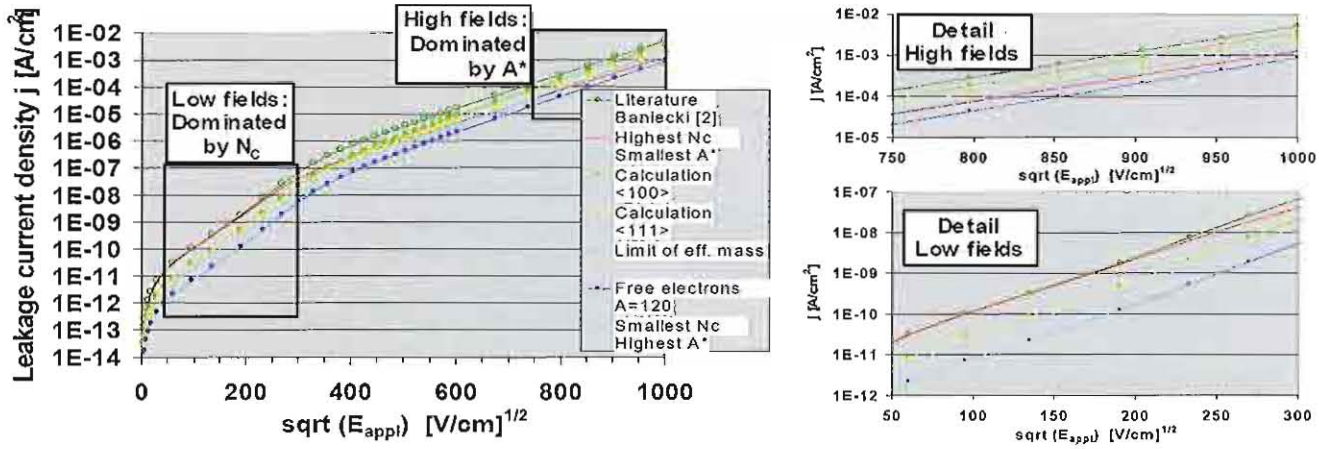

Figure 4: Schottky plot of simulated leakage current density of 55 nm thick STO dielectric between Pt electrodes using different numbers for N_C (m^*_{DOS}) and A* (m^*_R) from literature, "ab-initio" calculations and free electron approximation as indicated [1].

Atomic Layer Deposition of $PbTiO_x$ Thin Films Using Liquid Delivery Source Injection

T. Watanabe[1], S. Hoffmann-Eifert[1], C. S. Hwang[2], S. Mi[1], C. Jia[1], R. Waser[1]
[1]*CNI – Center of Nanoelectronic Systems for Information Technology (IFF)*
[2]*School of Materials Science and Engineering, Seoul National University, Seoul*

Titanium and lead β-diketonate based precursors dissolved in ethylcyclohexane were evaluated as precursors for future atomic layer deposition (ALD) of Pb(Zr, Ti)O_3 films. TiO_x and PbO films were deposited by a liquid injection atomic layer deposition at various precursor volumes per cycle. Against increasing precursor injection volume, a self-regulated deposition rate of PbO and TiO_x films were confirmed at the deposition temperatures under the thermal decomposition temperatures of the precursors. Subsequently, $PbTiO_x$ films were prepared by mixing the binary ALD processes. The $PbTiO_x$ film deposited on 3D structure showed a uniform film thickness and cation composition over the complex structure.

One major challenge in the integration of dielectric thin films like Pb(Zr, Ti)O_3 [PZT] and (Ba, Sr)TiO_3 into high-density memory devices is the reduction of the film thickness below 50 nm combined with the necessity for homogeneous, stoichiometric films on complex three dimensional (3D) structures. Metalorganic chemical vapor deposition (MOCVD) was used for covering 3D structures with ferroelectric thin films because of the high ability to achieve good step coverage [1, 2]. However, recent studies indicated that the films deposited over 3D structures by MOCVD have a gradient in the cation composition, even if the film thickness appeared to be uniform over the complex structure [3].

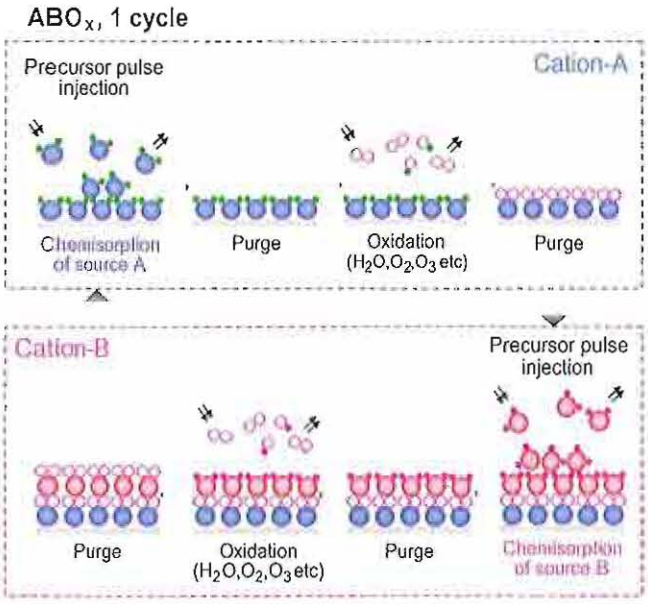

Figure 1: Schematic of atomic layer deposition of ternary ABO_x film. The small sequences for cation-A and -B may be repeated several times in one ABO_x cycle to adjust the final film composition to stoichiometric.

Atomic layer deposition (ALD) is a surface reaction controlled process and by this gives the possibility to achieve homogenicity on complex structures. The ALD process utilizes chemisorption on a pre-deposited layer. It typically consists of sequential precursor and reactant supply, and inert gas purge in between. At the purge turn, extra precursors and reactants that do not contribute to the chemisorption will be removed from the film's surface and pumped out of the reactor. Hence, with enough precursor supply, conformal film coverage and a high controllability of the film thickness can be expected even for non-planar substrates. We applied ALD to multi-component oxides on a noble metal electrode layer for pre-studies on future high-density capacitors with 3-D structure [4, 5]. The gas supply sequence of multi-component ALD was schematically shown in Figure 1. The separate precursor supply can prevent gas phase reaction of precursors. The film composition of a multi-component oxide is adjusted by repeating a binary oxide process in one cycle.

An ALD system equipped with an pulsed injection system of four independent liquid sources was designed for this study. The precursors dissolved in solvent are kept at room temperature until being supplied to the vaporizer. Hence, the liquid injection system is free from long-term thermal degradation of precursors so that the operating lifetime of the precursors can be elongated.

In this study, we focused on $PbTiO_3$ aiming in final process development of ALD-PZT films. Establishing a technique to cover 3D structure with PZT thin film uniformly is an urgent task to promote further integration of ferroelectric random access memory. We evaluated various Ti and Pb precursors. After optimizing the binary PbO and TiO_x ALD, the two processes were combined to prepare $PbTiO_x$ films. Figures 2(a) and 2(b) show the PbO and TiO_x film thickness deposited in one cycle with respect to volume of injected precursor pre cycle. $Pb(DPM)_2$ [DPM: $(C_{11}H_{19}O_2)_2$, dipivaloylmethanato] and $Ti(Oi\text{-}Pr)_2(DPM)_2$ dissolved in ethycyclohexane with concentration of 0.1 M were used. For oxidation, water vapor was supplied into the reactor. The deposition rate of PbO film saturated against precursor supply above 10 µl/cycle at deposition temperature of 240°C, while it kept increasing at 300°C. This is because the $Pb(DPM)_2$ is thermally decomposed at 300°C. From an Arrhenius plot, the thermal decomposition temperature of $Pb(DPM)_2$ was estimated to be around 260°C. In turn, the estimated thermal decomposition temperature for

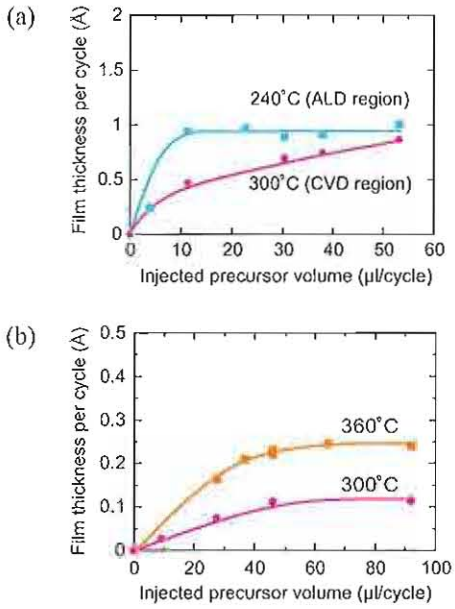

Figure 2: Film thickness deposited per cycle (a) PbO and (b) TiO_x films on $Pt/ZrO_x/SiO_x/Si$ substrates using $Pb(DPM)_2$ and $Ti(Oi\text{-}Pr)_2(DPM)_2$ as a function of injected precursor volume in one cycle. The film thickness was estimated by XRF.

$Ti(Oi\text{-}Pr)_2(DPM)_2$ was about 400°C. As expected, TiO_x films revealed a saturated deposition rate below the thermal decomposition temperature, both at 360 and 300°C as can be seen in Figure 2(b). PbO films were already crystallized under present experimental condition, but all TiO_x films were amorphous.

In case of a multi component oxide ALD with separate precursor supply, the lowest thermal decomposition temperature of precursors will determine the process temperature. Hence, the process temperature of subsequent $PbTiO_x$ films was set to 240°C. Interestingly, Ti layer immediately covered Pb layer, while long incubation time existed for depositing Pb layer onto Ti layer. The incubation time, which can be shortened by increasing Pb precursor volume supplied in one cycle, was considered to be responsible for the non-saturated deposition rate of Pb in the $PbTiO_x$ process. In case of multi-component ALD, the interactions of precursors with pre-deposited cation layers have significant impact on successful layer-by-layer growth. Figure 3 shows a cross sectional TEM picture of a $PbTiO_x$ film deposited on a 3D structure pre-covered with Ir bottom electrode layer. The $PbTiO_x$ film was amorphous in accordance with

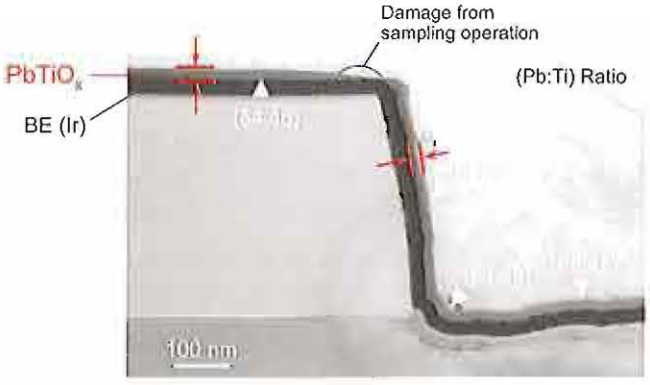

Figure 3: Crosse sectional TEM of $PbTiO_x$ film deposited on 3D structure pre-covered with Ir bottom electrode later. The numbers in brackets indicate the local molar ratio of Pb to Ti measured by TEM-EDS. These values were averaged for 3–8 measurements.

XRD analysis. We prepared Pb-rich $PbTiO_x$ film to compensate for Pb evaporation in the subsequent annealing step for crystallization. Although the process was not an ideally self-regulated one, the film thickness appears to be homogeneous and there was less deviation in the cation composition over the structure. We conclude that the present set of precursors is promising for development of a future ALD-PZT process.

One of the authors (TW) is grateful for receiving research fellowship from Alexander von Humboldt Stiftung.

[1] M. Shimizu, S. Hyodo, H. Fujisawa, H. Niu, and T. Shiosaki, *Jpn. J. Appl. Phys.* **36**, 5808 (1997).

[2] H. Fujisawa, K. Kita, M. Shimizu, and H. Niu, *Jpn. J. Appl. Phys.* **40**, 5551 (2001).

[3] C. S. Hwang, S. Y. No, J. Park, H. J. Kim, H. J. Cho, Y. K. Han, and K. Y. Oh, *J. Electrochem. Soc.* **149**, G185 (2002).

[4] T. Watanabe, S. Hoffmann-Eifert, C.S. Hwang, and R. Waser, Materials Research Society Symposium Proceedings, Ferroelectric Thin Films XIII **902E** (2006). (accepted)

[5] T. Watanabe, S. Hoffmann-Eifert, C.S. Hwang, and R. Waser, *J. Electrochem. Soc.* (submitted)

Grow Mode Evolution and Strain Relaxation in $Ba_xSr_{1-x}TiO_3$ Pulsed Laser Deposited on $SrRuO_3/SrTiO_3$

J. Q. He[1], E. Vasco[1], C. L. Jia[1], R. Dittmann[1] R. H. Wang[2]
[1]*CNI -- Center of Nanoelectronic Systems for Information Technology (IFF)*
[2]*Department of Physics and Center for Electron Microscopy, Wuhan University, China*

The thickness evolution of the microstructure of epitaxial $Ba_{0.7}Sr_{0.3}TiO_3$ (BST) thin films grown on $SrRuO_3$ (SRO)/$SrTiO_3$ (STO) was investigated by means of transmission electron microscopy (TEM). Within the BST layer, a layered structure (three sub-layers) is distinguished according to the configuration of lattice strain and defects. The first sub-layer extends for 3 nm from the lattice-coherent BST/SRO interface. The second 13 nm thick sub-layer forms a semicoherent interface with the first sub-layer due to the existance of a misfit dislocation network. The third sublayer extends beyond the second sub-layer exhibiting a structure characterized by compact columnar features. Planar defects are formed at the boundaries between such features. The formation of a layered structure within the BST films is discussed in the light of the growth of films on lattice-mismatched substrates.

$Ba_xSr_{1-x}TiO_3$ (BST) has attracted a lot of attention in recent years as high-permittivity material for high-density dynamic random access memory capacitors as well as as ferroelectric model system for ferroelectric random access memory [1]. Furthermore, BST shows resistive switching [2] and is therefore a candidate for future resistive switching memory devices.

Elastic strain directly influences the ferroelectric phase transition [3] and the inhomogeneous stress field associated with dislocations has been discussed as possible mechanism for the suppression of ferroelectricity on the nanometer scale [4]. Since extended defects play a crucial role for the resistive switching mechanisms as well [5], the evolution of the microstructure with increasing thickness is an issue of fundamental importance for the engineering of all above mentioned BST thin film-based devices. In this work, we present a detailed analysis of the microstructure of BST/$SrRuO_3$ (SRO) heterostructures investigated by cross-sectional high-resolution TEM (HRTEM).

The BST/SRO heterostructures were grown in-situ by pulsed laser deposition (PLD), on commercial single-crystalline (001) STO substrates. The BST film thicknesses were in the range of 4–210 nm. HRTEM investigations were performed with a JEOL 4000EX microscope. More details about the preparation of thin films and TEM specimen can be extracted from references [6].

Figure 1(a) shows a cross-sectional image of a 4 nm thick BST film stacked between two SRO layers. This film is strained by the SRO layers through the coherent BST/SRO interfaces. No misfit dislocations were observed in the 4 nm thick BST film. As the BST film thickness increases (>9 nm), misfit dislocations are observed and their density rises. Figures 1(b) and (c) show the lattice images of 9 and 30 nm thick BST films in the [110] BST direction, respectively.

The lateral arrows denote the BST/SRO interfaces whereas the dot lines mark the inner interface between BST sub-layers and indicate a layered structure. The first sub-layer extends for 3 nm from the lattice-coherent BST/SRO interface. The morphology and thickness of this first sub-

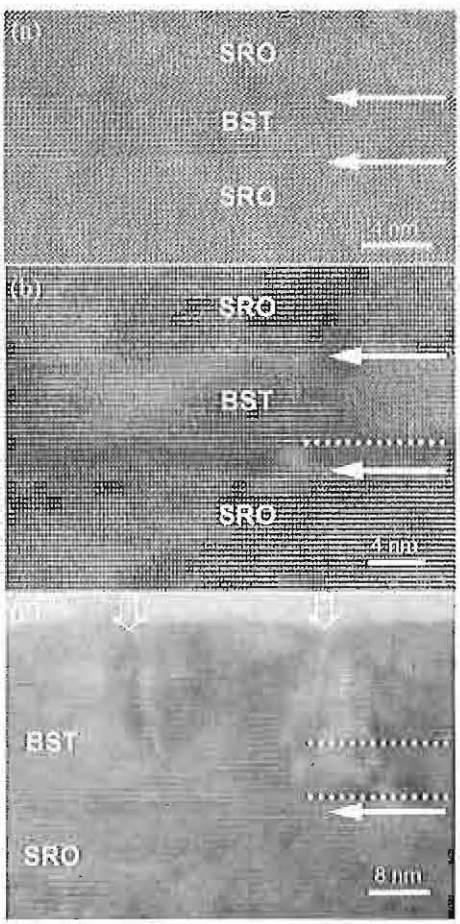

Figure 1: Low-magnification lattice fringe images of 4 nm (a), 9 nm (b) and 30 nm (c) thick BST films stacked between 30 nm (top) and 100 nm (bottom) thick SRO layers. The solid arrows denote the SRO/BST and BST/SRO interfaces, the dot lines mark the sub-layer interfaces and the open arrows point to planar defects between columnar features.

layer are independent of the thicknesses of the subsequent sub-layers. The second sub-layer is separated from the first one by a network of misfit dislocations and has a thickness of about 13 nm. The third sub-layer exhibits a columnar structure characterized by the presence of planar defects (as marked by red vertical arrows in Figure 1(c)), which rise from the interface between the third and the second sub-layer. These defects are mostly formed at the boundary of columnar features, and few of them propagate into the second sub-layer.

The results above can be understood in terms of a change of the growth mode during the film deposition. In the lattice-mismatched BST/SRO system, the BST thin film grows coherently on the SRO surface starting from a 2D nucleation process taking place at early growth stages. Once the thickness exceeds the critical value of 9 nm at which the strain-associated energy becomes higher than that required for the formation of misfit dislocations the film relaxes partially by the creation of such dislocations.

During this growth stage, the number of the created dislocations is still insufficient for a full relaxation of the mismatch strain. Thus, the film regions seated directly above the dislocations are more relaxed than those between dislocations. The inhomogeneity of the strain field within the film favors the heterogeneous nucleation and coarsening of 3D islands on the relaxed areas, where the nucleation energy is lower and induces a crossover to the columnar growth regime. The defects accumulated in the coalescence regions of the islands can easily induce the planar defects observed by TEM.

Figure 2(a) shows the map of lattice distortion of a 17 nm thick BST film along the out-of-plane axis investigated by geometric phase analysis. The difference of contrast corresponds to different distortion levels. Figure 2(b) plots the profile of the relative lattice distortion (with respect to the SRO lattice) in a dislocation-free area and indicates that the lattice strain in the first sub-layer (1L) is higher than that in the second sub-layer (2L).

The nature of the factors that hinder the propagation of the misfit dislocations into 1L, stabilizing the lattice distortion in this region, remains to be elucidated. In the absence of structural defects and/or stoichiometric defects of the cations, as shown by TEM, such factors can be plausibly connected with a nonuniform stoichiometry of the oxygen along the BST film thickness with an oxygen deficiency in the distinctive layer. This deficiency would appear during the growth of the coherent film (early stages of the growth) as a complementary strain relaxation mechanism and would act as kinetic barrier preventing the propagation of dislocations beyond the inner BST interface [7].

The observed inhomogeneous strain distribution in the thin films may be an explanation for the broadening of the ferroelectric–to-paraelectric phase transition observed in BST thin films, which becomes even more pronounced with decreasing film thickness. Furthermore, a discontinuous change of the ferroelectric and resistive switching properties is expected for thicknesses in the range of 15 nm where the transition from 2D to 3D growth occurs.

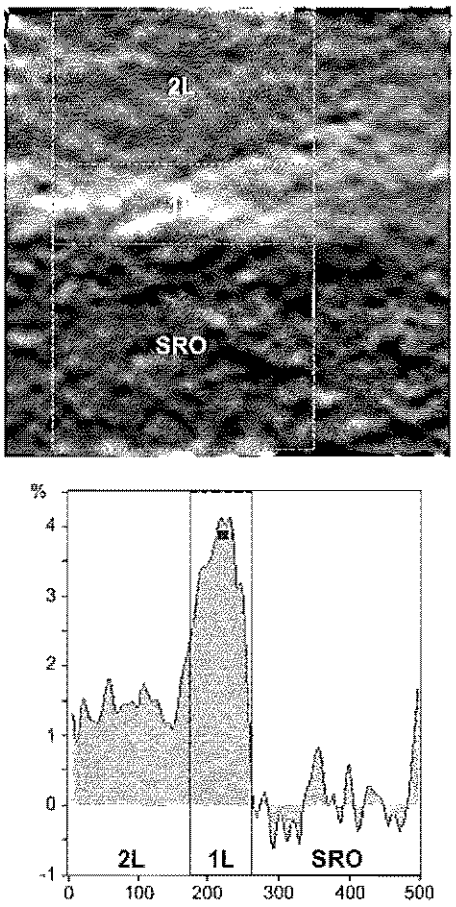

Figure 2: (a) Power spectrum of the high–magnification lattice image of a 210 nm thick BST film with $g1_{SRO} = 101$ as reference lattice, (b) shows the strain field map {profile} along the out-of-plane direction.

[1] S N. Setter and R. Waser, Acta Mater. 48, 151 (2000).
[2] R. Oligschlaeger, R. Meyer, S. Karthäuser, R. Dittmann and R. Waser, accepted for publication in Appl. Phys. Lett.
[3] N. A. Pertsev, A. G. Zembilgotov, and A. K. Tagantsev, Ferroelectrics 223, 79 (1999)
[4] M. Chu, I. Szafraniak, R. Scholz, C. Harnega, D. Hesse, M. Alexe and U. Gösele, Nature Materials 3, 87 (2004)
[5] K. Szot, G. Bihlmeyer, W. Speier, R. Waser, submitted to Nature Materials
[6] J. Q. He, E. Vasco, C. L. Jia, R. Dittmann and R. H. Wang, J. Appl. Phys. 97, 104907 (2005)
[7] J. Q. He, E. Vasco, R. Dittmann and R. H. Wang, submitted to Phys. Rev. Lett.

Large Scale Facilities for Research with Photons, Neutrons and Ions

Development of thin films spin turners
A. Ioffe, Th. Brückel, V. Bodnarchuk, A. Belushkin

Neutron scattering with vector polarisation analysis on $U_{14}Au_{51}$
W. Schweika, S. Easton, and K.-U. Neumann

A new thermal neutron spectrometer/diffractometer (SV30) with polarizsation analysis at the research reactor FRJ-2
H. Conrad, T. Brückel, A. Budwig, K. Bussmann, L.-J. Chang, R. Engels, V. Fracassi, J. Heinen, R. Heinrichs, M. Heinzler, H. Heybutzki, A. Ioffe, E. Küssel, T. Kulessa, F. Lexis, R. Müller, M. Pap, M. Paulzen, B. Schmitz, J. Schmitz, G. Schaffrath, A. Sparbrodt, G. Stollwerk, F. Suxdorf

Development and Test of the first 2D-CASCADE-Detector
W. Hinderer, G. Kemmerling, M. Klein, C. Schmidt, H. Conrad

Larmor labelling by spin flippers with rotating magnetic field
A. Ioffe

The new very small angle neutron scattering instrument KWS-3
E. Kentzinger, A. Radulescu, J. Stellbrink, D. Richter and Th. Brückel

Development of thin films spin turners

Alexander Ioffe [1], Thomas Brückel [1], V. Bodnarchuk[2], A. Belushkin[2]

[1] *Forschungszentrum Jülich GmbH, Institut für Festkörperforschung, 52425 Jülich, Germany*
[2] *Joint Institute of Nuclear Research, Frank Laboratory of Neutron Physics, 141980 Moscow region, Russia*

The energy resolution of the present day neutron spectrometers of inelastic scattering can be significantly improved by the use of neutron spin-echo (NSE) technique. We are developing a new approach that is to use rotating magnetic fields to provide the NSE effect. Such fields can be created, for example, in thin spin turners based upon magnetic foils by a proper combination of external high-frequency magnetic fields. In clear contrast to the coil-type RF flippers which are currently used in the NSE technique, the flexibility of such foils will allow for an easy shaping of the magnetic field area according to the axial geometry of a neutron scattering experiment and, indeed, will open the possibility for a spin echo set up, where the simultaneous collection of data corresponding to different momentum transfers will take place. Experiments with thin films of different metallic glassy alloys carried out at the polarimeter LAP-ND at FZ Juelich show that metallic glassy alloy $Co_{66}Si_{15}B_{14}Fe_4Ni$ provides very small depolarization of neutron beam at the zero field and shows minimal depolarization in small external fields. In the same time magnetic saturation field in the film amounts to 5.4 kG, thus satisfying the π-flip conditions for 4 Å neutrons for thin, 25 μm, foils.

1. Introduction

The energy resolution of the present day neutron spectrometers of inelastic scattering is typically about 0.5 - 2%. However, the studies of many problems of solid state physics, e.g. crystal fields in rear earth compounds, high-T_c superconductors e.t.c., require a tenfold increase in the accuracy of the determination of the energy transfer, ω. The above –mentioned limit in the ω-resolution is a consequence of the determination of ω as the difference of the well-defined energies of the incident, E_i, and scattered, E_f, neutrons. Indeed, a high monochromatization of the incident beam is required and mostly limits the neutron intensity. Neutron spin-echo technique (NSE) [1] allows for direct measurements of the intermediate scattering function $S(Q, t)$, which is the Fourier transform of the intermediate scattering law $S(Q, \omega)$, as a function of the energy transfer $\omega = E_i - E_f$. Indeed, a monochromatization of the incident beam is not required, however, a rather wide spread in the wavelength of the incident beam results in a low Q-resolution. Therefore, it is natural to improve the ω-resolution of triple-axis (TAS) or time-of-flight (TOF) spectroscopy joining them with NSE technique [2].

2. Thin magnetic films spin turners

We are developing a new approach that is to use rotating magnetic fields to provide the NSE effect. Such fields can be created, for example, in thin spin turners [3] based upon magnetic foils by a proper combination of external high-frequency magnetic fields. The suggested spin turners are essentially non-adiabatic, i.e. the neutron spin direction does not change during the transition through the border of magnetic film and just precesses around the magnetic field direction in the film. In clear contrast to the coil-type RF flippers which are currently used in the NSE technique, the flexibility of such foils will allow for an easy shaping of the magnetic field area according to the axial geometry of a neutron scattering experiment and, indeed, will open the possibility for a spin echo set up, where the simultaneous collection of data corresponding to different momentum transfers will take place. They can also be accommodated for the use

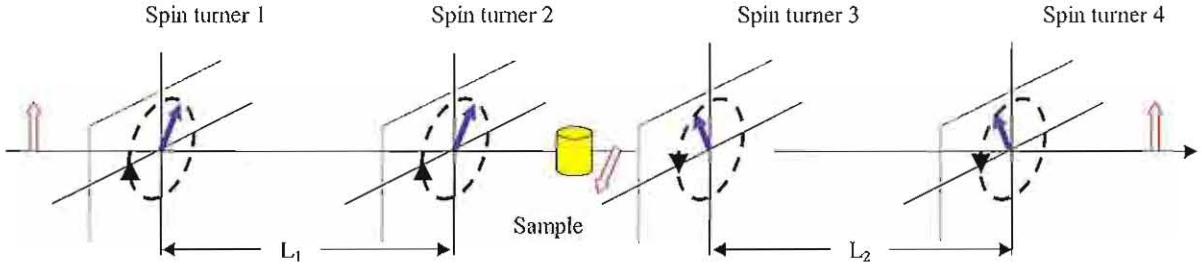

Fig. 1. Neutron spin-echo spectrometer with rotating magnetic fields

with pulsed neutron sources and by the tilt of foils one can also realize the dispersive ($\omega = \omega(q)$) NSE arrangement that allows for the so-called phonon focusing [2, 4].

For a practical realization of the spin turners we propose to use thin magnetic films with rotating magnetic field that is and driven by two sinusoidal signals shifted by 90° (Fig.2). We are presently considering the use of

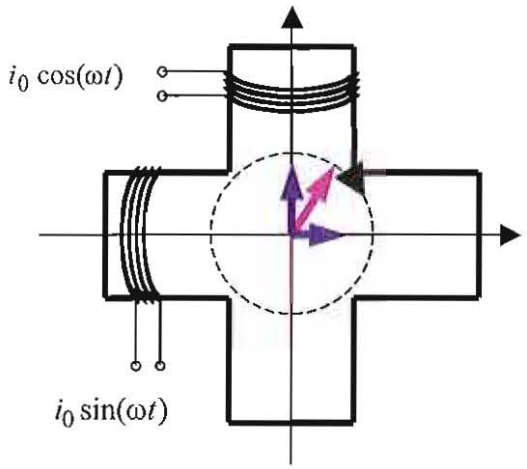

Fig.2 Spin turner with rotating magnetic field.

films of metallic glassy alloys that feature a high frequency susceptibility (300-500 kHz), the extreme magnetic softness (coercitive field of about 50 mG) and rather high saturation magnetic field up to 0.8 T.

However, such spin turner is a dispersive device: the precession angle of neutron spin in magnetic field depends on the propagation time through the foil, i.e. from the neutron wavelength. Indeed, the spin turner shows a good performance only for wavelength bands centred around wavelengths λ_n, for which the condition of the π-flip is fulfilled. To exploit the full power of pulsed sources the magnetic field B_c should be continuously tuned in time satisfying the condition $B_c\lambda_n = const$. This can be achieved by the time ramping the field B_c. In ferromagnetics, a strong and unaccepted depolarization of the neutron beam appears for the field below the saturation field B_c. However, the magnitude of this effect for metallic glasses (produced by the process of an extremely quick cooling of melted alloys, so that no crystallization takes place) can be much less.

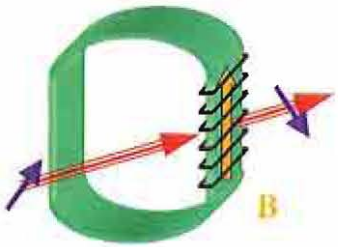

Fig.3. Sample arrangement for neutron depolarization experiment.

To check this we have carried out an experiment with thin films of five different types of metallic glassy alloys at the polarimeter LAP-ND at FZ Juelich. The neutron polarization P_i of the incoming beam is perpendicular to the foil induction B; at the exit all three components of the outgoing polarization P_f are analyzed and the rotation angle φ of the Larmor precession inside the film is determined. These values allowed us to determine the depolarization rate and magnetic induction of TMF. In the Fig.3 the studied foil is shown as a closed loop ribbon, but in real experiments we also additionally studied unclosed ribbon. The closing should close magnetic field lines, thus increasing the value of magnetic induction in TMF and consequently suppress scattered fields around TMF. Indeed, the parasitic rotation of the polarization by scattered fields is also suppressed, thus allowing for more precise determination of the induction. These experiments show that metallic glassy alloy $Co_{66}Si_{15}B_{14}Fe_4Ni$ (Good Fellow) is the most appropriate sample for our purposes (see Table 1): it practically does not depolarize the neutron beam at the zero field and shows minimal depolarization in small external fields. In the same time magnetic saturation field in the film amounts to 5.4 kG, thus satisfying the π-flip conditions for 4 Å neutrons for thin, 25 μm, foils.

Table 1.

Sample	Current, mA	P_i	P_fx	P_fy	P_fz	$\lvert P_f \rvert$	φ,°	B_{exp}, kG
Empty current coil	0	(0;1;0)	0	0.86	0	0.86	0	
	291,7	(0;1;0)	-0.35	0.82	0.02	0.8	23	
$Co_{66}Si_{15}B_{14}Fe_4Ni$	0	(0;1;0)	0.03	0.85	0	0.85	0	
	291,7	(0;1;0)	0.64	0.39	0.03	0.75	215	5.4

References

1. F.Mezei, Z.Phyzik **255**, 146, 1972.
2. F.Mezei, in Neutron Inelastic Scattering 1977, IAEA Vienna, 1978, p.125.
3. A.Ioffe, Physica B **335** (2003) 169.
4. Th.Keller, R. Golub, F. Mezei and R. Gähler, Physica B, 234-236, p.1126.

Neutron Scattering with Vector Polarisation Analysis on $U_{14}Au_{51}$

Werner Schweika,[1] S. Easton,[1,2] and K.-U. Neumann[2]

[1] *Institut für Festkörperforschung, Forschungszentrum Jülich, D-52425 Jülich, Germany*
[2] *Loughborough University, Great Britain*

(Dated: January 19, 2006)

We have developed a new technique of vector polarisation analysis for neutron scattering experiments using an initially precessing neutron polarisation.[1] Different to existing zero-field techniques this method has a much larger potential for applications, since it can be used also on multi-detector and time-of-flight instruments, typical instruments at the new neutron spallation sources. We compare results on the complex magnetic structure of $U_{14}Au_{51}$, with previous findings.[2]

In addition to nuclear coherent scattering, one distinguishes two further scattering cross-sections that are related to the spin properties of the neutron probe. First, the scattering amplitude depends on the spins of the nuclei in a sample, which leads to the so-called spin-incoherent scattering and hydrogen serves as a well-known important example. Second, the neutron's magnetic moment is an ideal probe to study magnetic structures and excitations in condensed matter physics.

Using polarised neutrons and polarisation analysis one can separate experimentally all three distinct contributions. The simplest version of polarisation analysis has an important potential for studies of soft matter.[3] The ability to discern spin-flip (sf) scattering from non-spin flip (nsf) scattering, independent of the direction of the polarisation of the incident beam, allows one to separate coherent from incoherent scattering, *i. e.* to separate self- and pair-correlation functions.

The directional dependence of sf and nsf scattering is of interest for studies of magnetic structures and correlations. In general, scattering cross-sections for magnetic scattering depend on the direction of the polarisation of the incident neutron beam with respect to (i) the scattering vector **Q** and (ii) the direction of the magnetic moments in the sample. Two simple rules can be established: First, only the component of the magnetic moments which is perpendicular to **Q** contributes to scattering of neutrons. Second, the component of the initial neutron polarization, which is perpendicular to the magnetic moments in the sample, changes sign upon scattering. The most common and conventional approach is based on the classical work of Moon, Riste and Koehler[4], where one applies a guide field to turn the polarisation parallel and perpendicular to **Q** for the measurements. This will enable to separate and to analyse the magnetic scattering for many cases: in general this applies for paramagnetic samples, and in case of ordered magnetic structures with collinear spins.

There are many interesting materials, for instance multi-ferroics, with complex magnetic structures which cannot be unambiguously examined by such a conventional technique of polarisation analysis. Another topic is in in the field of highly correlated electrons with unresolved questions concerning possible static and dynamic spin-lattice couplings; these may cause unique non-trivial rotations of the neutron polarisation upon scattering. For solving all these problems it is of high interest to unravel all possible arbitrary rotations of the neutron polarisation.

All previously existing methods for vector polarisation analysis need a zero magnetic field around the sample. The principle to prepare an incident polarisation and measure an arbitrary rotated final polarisation can be realised only for a single specific momentum and energy transfer.

Our method is based on the idea to include and work with precessing neutron polarisation as known from spin-echo techniques.

In the conventional set-up of the DNS instrument at the Jülich research reactor, see Fig. 1, the monochromatic beam will be polarised by the initial polariser, (optionally for inelastic studies the beam will be chopped), then the neutron polarisation may be switched with respect to the guide field by a pi-rotation inside the flipper coil, next the polarisation will enter the field around the sample that can turn the polarisation in x,y,z (or any) direction.

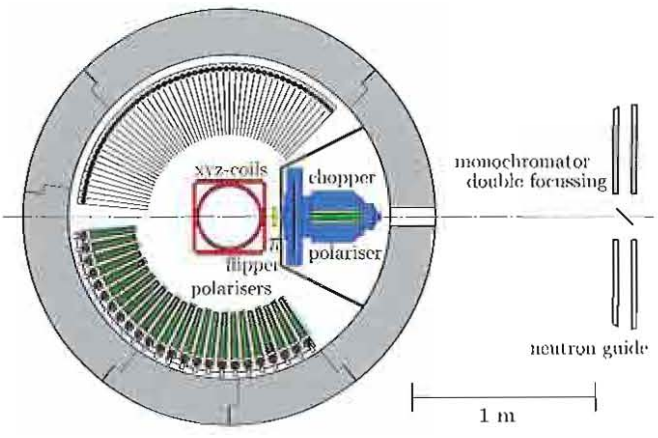

FIG. 1: Scheme of the DNS instrument.

This allows one to measure sf or nsf scattering for all directions, *i. e.* the trace of the polarisation matrix of the initial and final polarisation vector. For polarisation

changes other than 0 oder 180 degrees, which contribute to off-diagonal elements of the polarisation matrix, the final polarisation will start to precess in the applied field and appear as a reduced polarisation in the analyser system.

Instead of attempting to realign the precessing scattered neutrons to determine the changes by the sample, thinking of time reversal gives us an elegant key to a simple solution: We may start with an precessing polarisation in the initial path and we may tune the precession angle for a desired polarisation at the sample. Scattering with polarisation changes from a precessing into a non-precessing state will provide us with the off-diagonal elements of the polarisation matrix.

Surprisingly, we do not need any additional sophisticated equipment for full vector polarisation analysis. We only need to induce a $\pi/2$ rotation (instead of 0 or π) by the flipper and to control the precessing phase by a variation of the applied magnetic field.

Previous vector polarisation studies (polarimetry) on $U_{14}Au_{51}$ using the Cryopad device at the ILL revealed a complex chiral magnetic structure, a so-called q=0 structure, for which AF-magnetic Bragg peaks coincide with nuclear structural Bragg peaks.[5] As an example a measured polarisation stereogram for the (201) peak is shown.

We repeated the experiment on DNS with the new precession technique for VPA. Part of the results are shown in Fig. 3, for the (201) Bragg peak. The crystal is oriented with its b-axis parallel to the vertical z-axis. The spins are ordered within the a-b plane with a hexagonal star-like structure. The nuclear scattering is confirmed by a measurement above the Neel temperature at 30K and remains independent of the polarisation. At lower temperatures two oscillating curves are measured by turning the flipper in $+\pi/2$ and $-\pi/2$ mode. Maxima are found for a rotation of the polarisation from the z to the y direction. For an initial polarisation along x (which is set parallel to the scattering vector) only spin-flip scattering is observed for the magnetic scattering, excluding a rotation to y or z. For all cases, and taking nuclear scattering into account, an effective depolarisation is observed. These results are in excellent agreement with the pol-figures 6b of Ref.5.

In principle this new precession technique is possible on any neutron scattering instrument which allows for conventional polarisation analysis a la Moon, Riste and Koehler[4]. Different to existing zero-field techniques this method has a unique property which gives a much larger potential for applications, since it can be used also on multi-detector and time-of-flight instruments, typical instruments at the new neutron spallation sources.

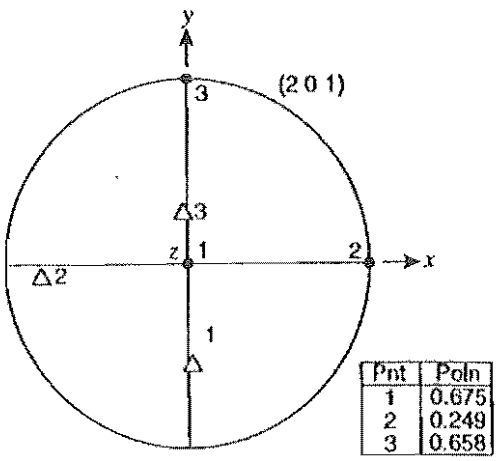

FIG. 2: Stereogram for (201) of $U_{14}Au_{51}$ at 15 K. Full (open) symbols indicate the direction of initial (final) polarisation taken from Brown *et al.*[5]

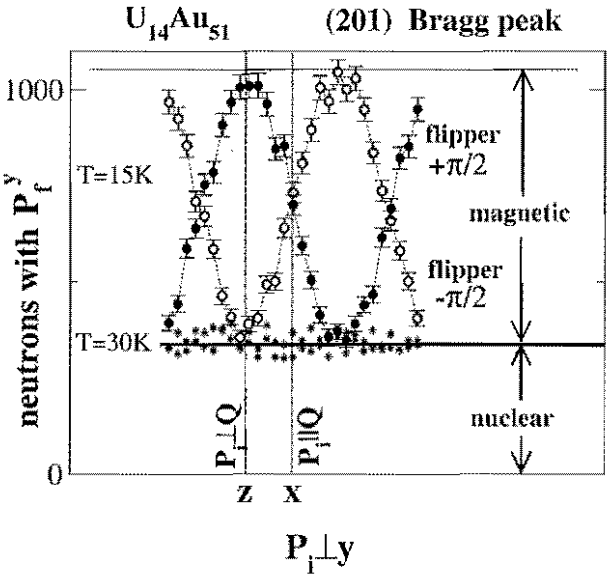

FIG. 3: Vector polarisation analysis on the (201) Bragg peak of $U_{14}Au_{51}$. Initially the polarisation is perpendicular to the applied field in y-direction. At lower temperatures, T=15K, there is an additional magnetic contribution for which the neutron polarisation changes from $P_i \parallel z$ to $P_f \parallel y$. At 30K there is only a nuclear Bragg component which continues to precess after the scattering event.

[1] W. Schweika, Physica B **335** (1-4), pp.157-163 (2003).
[2] W. Schweika, S. Easton, K.-U. Neumann, Neutron News **16** (2), 14-17 (2005).
[3] A. Narros, A. Arbe, F. Alvarez, J. Colmenero, R. Zorn, W. Schweika, D. Richter Macromolecules **38**, 9847 (2005).
[4] R.M. Moon, T. Riste, W.C. Koehler, Phys. Rev. **181**, 920 (1969).
[5] P. J. Brown et al. J. Phys.: Cond. Matter 1997.

A new thermal neutron spectrometer/diffractometer (SV30) with polarization analysis at the research reactor FRJ-2

H. Conrad[1], T. Brückel[1], A. Budwig[5], K. Bussmann[1], L.-J. Chang[1], R. Engels[4], V. Fracassi[5], J. Heinen[1], R. Heinrichs[3], M. Heinzler, H. Heybutzki[5], A. Ioffe[1], E. Küssel[1], T. Kulessa[5], F. Lexis[2], R. Mueller[1], M.Pap[5], M. Paulzen[2], B. Schmitz[1], J. Schmitz[2], G. Schaffrath[2], A. Sparbrodt[2], G. Stollwerk[3], F. Suxdorf[4]

[1] Institut für Festkörperforschung - Institut für Streumethoden –
[2] Betriebsdirektion
[3] Zentralabteilung Forschungsreaktoren
[4] Zentrallabor für Elektronik
[5] Zentralabteilung Technologie

The new instrument at the 4H6 thermal neutron beam channel of the FRJ-2 reactor is a high intensity multi-purpose installation commissioned recently. It will be used both as a diffractometer for crystallographic investigations and as a triple-axis spectrometer with polarization analysis for measurements of magnetic and nuclear inelastic scattering. The instrument features two exchangeable monochromators (Cu [200] and PG [002]), which enable focusing of the in-pile beam cross section of 90×100 mm² both horizontally and vertically down to a smallest spot of about 10×25 mm² at the sample position. High monochromatic neutron current densities at the sample position of up to 4×10^7 cm^{-2}s^{-1} (for pyrolytic graphite at 34 meV) and energies of up to 117 meV (with copper) have been achieved. The utilization of ^{3}He filters both as polarizer and analyzer enables polarization analysis for high energy neutrons over a large solid angle of 60°×60°. The spectrometer is equipped with a detector module that carries an analyzer unit with a single detector. In its diffractometer mode it will be equipped with a pixelated image plate neutron detector.

The instrument SV30 replaces the old triple axis spectrometer SV4 and is designed for maximum neutron current densities at the sample position and polarization analysis employing ^{3}He filters. In order to achieve the intensity optimization, the entire available in-pile beam port cross section of 90 cm² of the 4H6 channel is exploited in contrast to only 40 cm² as compared to the old instrument. Moreover, the double-monochromator has been substituted by two focusing single-monochromators (copper and pyrolytic graphite), which can be exchanged by remote control. As to the ^{3}He filters, spin exchange optical pumping (SEOP) as well as metastable exchange optical pumping (MEOP) is being developed in our institute. Together with remotely exchangeable collimators and filters (erbium and pyrolytic graphite), the two monochromators are installed in a helium filled vessel in the center of the primary shielding. This shielding is equipped with three separate beam channels at monochromator-2θ-angles of 26.8°, 41.4° and 74.3°, respectively. The corresponding neutron energies are 34 meV, 14 meV and 5 meV for graphite [002] and 117 meV, 50 meV and 17 meV for copper [200], respectively. The spectrometer is shown in Figure 1.

Both monochromators are built as a matrix of 7 columns and 15 rows of separate 2×2 cm² single crystals. Both the columns and rows can be independently and remotely rotated so as to enable independent horizontal and vertical focusing. The copper monochromator is shown in Figure 2. An example of focusing recorded with a position sensitive detector is shown in Figure 3.

Figure 1. The new spectrometer/diffractometer SV30 at the FRJ-2 reactor. The three beam ports of the monochromator shielding (magenta) can be easily recognized. Sample table and analyzer/detector tower are moved on air cushions across a polished glass floor.

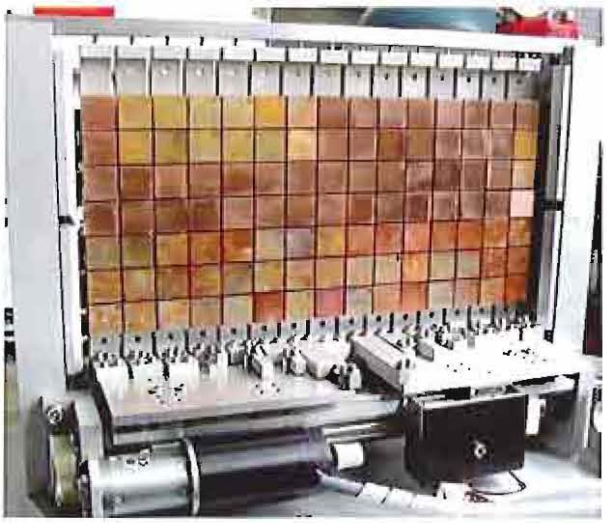

Figure 2. Double-focusing copper monochromator composed of a matrix of 7 by 15 individual single-crystals with an area of 2×2 cm² each. The columns and rows can be independently rotated in order to enable separate horizontal and vertical focusing.

Figure 3. Focus of the PG-monochromator at a neutron energy of 34 meV recorded with a position sensitive detector. The dark blue elliptical area is about 10 mm by 25 mm.

Gold foil activation measurements of the six different monochromatic neutron current densities at the sample position yielded the results compiled in Table 1.

As an example of a first inelastic measurement a transverse [200] phonon off the (220)-reflection of a small aluminum single crystal with $q = 0.31$ Å^{-1} is shown in Figure 4. The data were taken with an incoming neutron energy of 34 meV and in energy loss. Vertical focusing only has been applied and a reduced neutron current on sample of only 20% due to the then still missing shielding around the secondary spectrometer.

Table 1. Gold foil activation results. The numbers for the neutron current density j are average values over a 1×3 cm² area centered at the respective foci.

Copper [200]

2θ [°]	λ_0 [Å]	E [meV]	j [10^7 cm^{-2} s^{-1}]
26.8	0.84	117	0.51
41.4	1.28	50	2.00
74.3	2.18	17	0.48

Pyrolytic graphite [002]

2θ [°]	λ_0 [Å]	E [meV]	j [10^7 cm^{-2} s^{-1}]
26.8	1.54	34	4.00
41.4	2.37	14	1.70
74.3	4.05	5	0.31

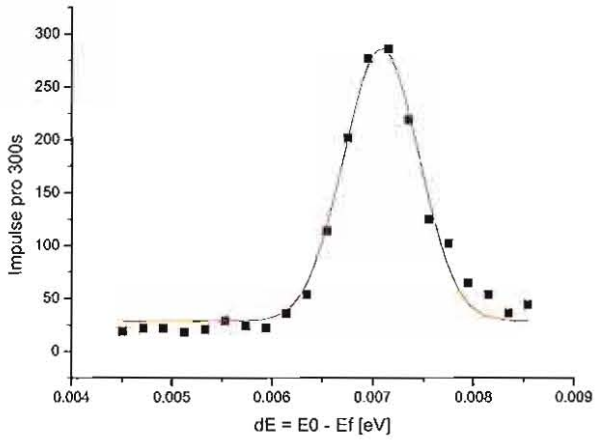

Figure 4. Phonon near (220) with $\mathbf{q} = 0.31$ Å^{-1} parallel [100] measured with a small aluminium single crystal of 16 mm in diameter and a height of 4 cm. Vertical focusing only and reduced incoming intensity of 20% applied.

Development and Test of the first 2D-CASCADE-Detector

W. Hinderer[1], G. Kemmerling[1], M. Klein[2], C. Schmidt[2], H. Conrad[3]

[1]Zentralinstitut für Elektronik, Forschungzentrum Jülich
[2]Physikalisches Institut der Universität Heidelberg
[3]Institut für Festkörperforschung - Streumethoden, Forschungszentrum Jülich

The principle of the Cascade neutron detector is a hybrid GEM based gas detector which uses a ^{10}B coating as neutron converter and a mixture of Argon/CO_2 as the counting gas. Several 1D-Cascade detectors have already been tested at ILL and PSI with great success. The latest prototype with an active area of 20x20 cm^2 features for the first time a 2D-Readout. The successful operation of the complete detector system has been shown during the operation of the research reactor FRJ-2 at the experimental test site EKN.

The 2D-CASCADE-Detector under investigation is equipped with a double-sided readout structure which is sandwiched between two GEM-foils on either side. The readout structure is a simple flexible printed circuit board. It essentially consists of 128 stripes in x- and 128-stripes in y-direction. The entire stack is sealed with a ^{10}B-coated drift electrode on either side. The two GEM-foils which are closest to the readout structure are operated in amplification mode at a gain of about 60. These GEM-foils are termed Gain-GEMs. All the other GEM-foils are operated in transparent mode, i.e. at a gain of 1. They are called Transfer-GEMs. The Gain-GEMs as well as the Transfer-GEMs are coated with Boron on one side only. This setup is depicted in Figure 1.

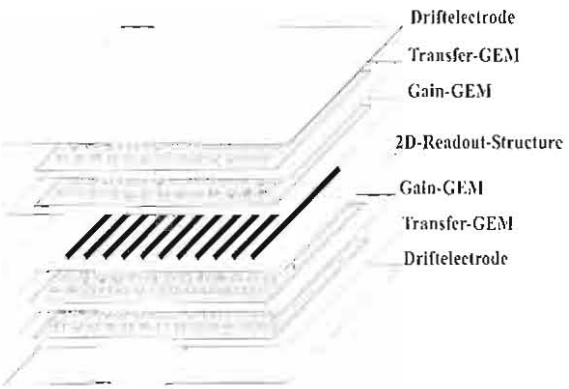

Figure 1. Design of the first 2D-CASCADE prototype.

The construction of the CASCADE detector is based on a modular concept. The GEM-foils, the readout structure and the drift electrodes are glued onto steel frames. The resulting modules are stacked one upon another to form a detector stack. This stack is held in place and pressed together by screws. Between every two frames a thin Teflon foil of the same shape as the frame is placed for electrical isolation and to prevent gas leakage. The detector is operated with Ar/CO_2

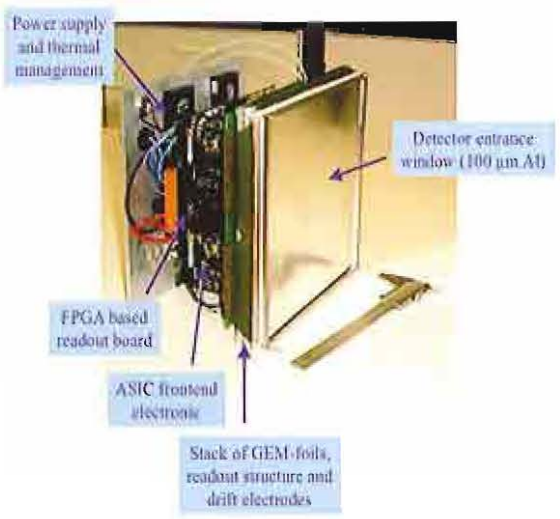

Figure 2. Prototype tested at EKN at the research reactor FRJ-2.

The detector and its readout electronics is designed to cope with a count rate of 2.5 MHz on the whole active area of 20x20 cm^2. In the worst case this count rate can be even on one single pixel. To satisfy these challenging demands a new readout system, based on modern ASIC and FPGA technology, was designed. Figure 3 shows a photo of the readout system.

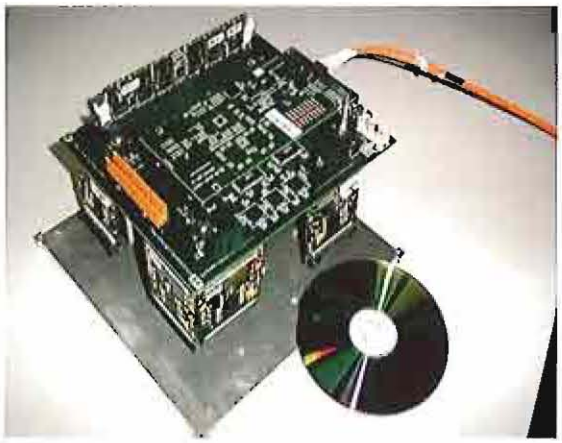

Figure 3. The readout electronics with the FPGA board on the top and edgewise four front end boards with the CIPix-Chip.

The primary processing of the 256 detector channels are done by four CIPix-Chips which were developed for the H1 experiment at DESY. This ASIC integrates 64 readout channels, each of which consists of a low-noise preamplifier, a shaper, a buffer and a discriminator. The digital discriminator signals are generated synchronously to a clock of 10 MHz. The digital data are processed by a FPGA board which has an optical link to a host computer. The bandwidth of the optical link of 80 Mbyte/s allows for fast data transfer to the host computer. There are large amounts of SRAM and DRAM memories on the FPGA board for storing and histogramming the data which may drastically reduce the necessary bandwidth to the host computer.

The complete detector system was characterized at the experimental test site EKN at the research reactor FRJ-2. Three examples of the acquired results are shown in the following figures.

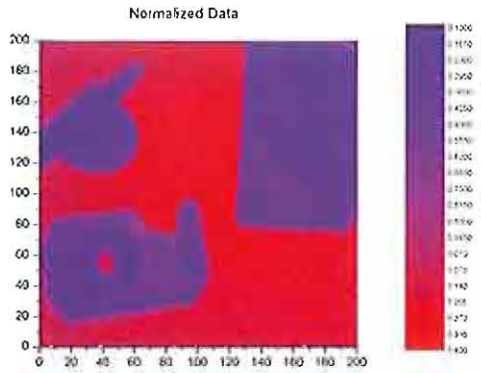

Figure 4. Radiographic picture of a tape dispenser, a gas flow controller and a computer mouse.

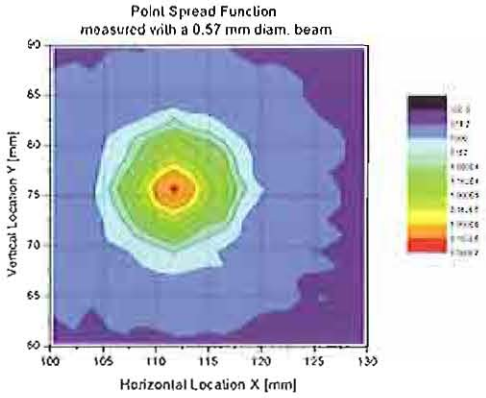

Figure 5. Point Spread Function

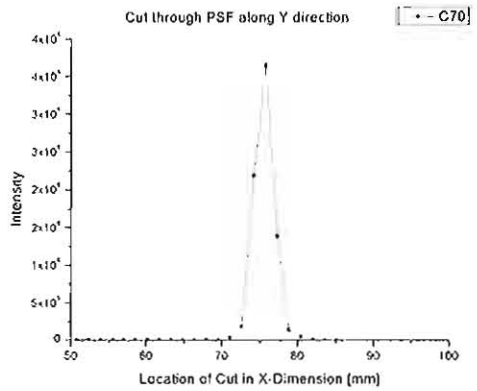

Figure 6. Cut through the Point Spread Function along the Y direction.

Finally, in Figure 7 you can see several Time of Flight Spectra. The Bi-filter in the neutron guide leads to many characteristic dips in the spectra. The dip at $\lambda = 4.52$ Å is due to the reflectometer HADAS which is in the same beam line.

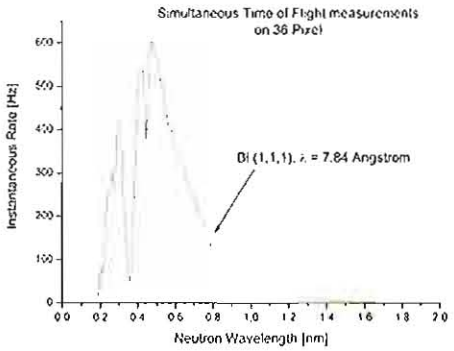

Figure 7. Time of Flight spectra.

Larmor labelling by spin flippers with rotating magnetic field

A. Ioffe
Forschungszentrum Jülich GmbH, Institut für Festkörperforschung, 52425 Jülich, Germany

The neutron spin-echo (NSE) method, which is the most powerful tool of high-resolution neutron spectroscopy, is known in two versions: either with the long solenoids or short alternating fields. Here we consider an alternative version that makes use of spin flippers with an in-plane rotating magnetic field vector. Some possible applications of such technique are discussed. This approach can be considered as an alternative to the present-day NSE techniques.

Neutron inelastic scattering provides extremely valuable information about the atomic collective motions with the microscopic length scale from the nearest neighbor distances to a few nanometers and the time scale that ranges from characteristic microscopic times as picoseconds up to microseconds in the case of slow motions as e.g. critical fluctuations in phase transitions, dynamic behavior of disordered systems (structural and spin glasses), etc. The change in neutron energy, ΔE, corresponding to these slow motions is extremely small (in the order of 1 neV) and requires extremely high energy resolution methods. Conventional methods of inelastic spectroscopy, time-of-flight or triple-axis, are relying on a differential approach, when the energy exchange is determined as the difference of two well-defined energies of incident and scattered neutrons. Therefore, any attempt to reach a very high, better than $\Delta E/E=10^{-4}$, energy resolution by conventional neutron spectroscopy methods will require extremely high monochromatization of the incident beam thus resulting in intolerable intensity losses. Indeed, the studies of slow dynamical process required a new non-traditional approach, the so-called neutron spin-echo (NSE) technique [1]. It provides few orders of magnitude higher energy resolution than any other technique of inelastic (quasielastic) neutron scattering.

The NSE technique is based on the phenomenon of Larmor precession of the neutron spin in a transverse magnetic field. When the neutron propagates across a region of magnetic field of strength B, the neutron spin undergoes a precession with the Larmor frequency $\omega_L = \gamma_n B$ (γ_n - the gyromagnetic ratio). The total precession angle φ_L, is defined by this frequency and the time τ of propagation of the neutron through the magnetic field region of length L:

$$\varphi_L = \omega_L \tau = \frac{\gamma_n}{v_n \cdot \cos(\psi)} \int_L B dl \qquad (1)$$

where ψ is the inclination of the neutron trajectory and v_n is the neutron velocity along it.

In this case, the orientation of the neutron spin can be considered as the arrow of a "Larmor clock" that is attached to every neutron. Indeed, the "time" shown by the clock is defined by the field integral (Eq. (1) seen by each neutron. Such a Larmor labelling opens the unique possibility for the development of "unusual" neutron scattering techniques, where the energy (momentum) resolution does not require the initial and final states to be well selected.

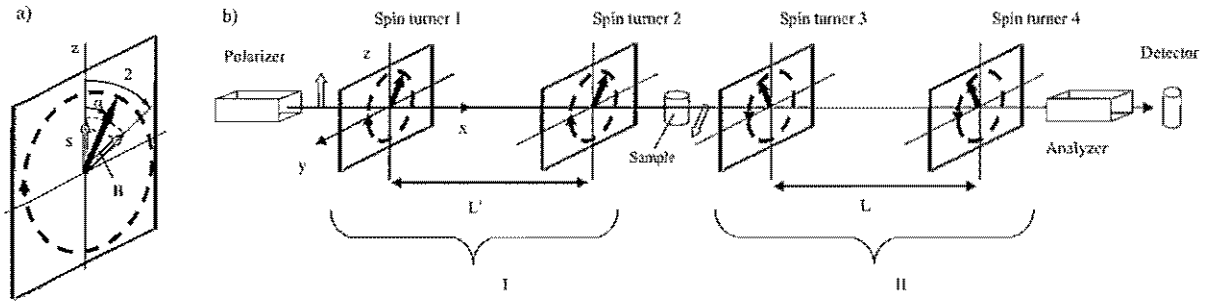

Figure 1. a) The spin flipper with rotating magnetic field (RMF). In-plane rotation of the neutron spin vector is achieved by the Larmor precession of neutron spin by angle π around the magnetic field vector **B**. b) Layout of the NSE spectrometer built by two pairs of the RMF flippers

At present there are two well developed practical realizations of NSE principle: generic NSE technique [1] and neutron resonance spin echo technique (NRSE) [2].

Recently, we proposed a new kind of NSE technique, which is based upon the use of thin magnetic spin flippers with an in-plane rotating magnetic field vector (RFNSE) [3]. The main element of such a NSE spectrometer is the spin turner that provides the in-plane rotation of the neutron spin vector with a constant angular velocity ω, so that the angle of neutron spin rotation will be proportional to time t (Fig. 1a). Practically it is achieved by the Larmor preces-

sion of neutron spin around the magnetic field vector B that rotates in the plane *yz* with the angular velocity ω_B. If the Larmor precession angle is π, then the neutron spin will be mirror- reflected relative to the field vector, thus rotating in the plane *yz* with the angular velocity $\omega = 2\omega_B$.

A pair of such spin turners separated by a field-free area of length L (cascade I in Fig. 1b) is acting like a Larmor clock that shows the time $\alpha = 2\omega_B T = 2\omega_B L'/V_n$ of propagation of neutron with velocity V_n between the turners. This time depends both on the neutron velocity V_n and the length L' of its trajectory between flippers, but not on the arrival time. Indeed, the neutron velocity is coded by the angle α, so that the beam polarization at the sample spectrometer is a sinusoidal function of the neutron wavelength λ, $P_z = \cos(2\omega h\lambda L/m_n)$ (here h is the Plank constant and m_n is the neutron mass). For a wide spectrum neutron illumination, the neutron beam at the sample is an overlap of such functions with different periods and is completely depolarized.

The NSE principle is to apply a decoding operation to such beam. This decoding operation is essentially the time inversion and is practically achieved either by the change of the field direction (generic NSE) or the change of the sense of the RF-fields rotation (NRSE). The suggested NSE spectrometer is in a way analogue to NRSE spectrometer, so that it contains cascade II (Fig. 1b) with the opposite sense of magnetic field vector rotation. Then the final orientation of the spin vector relative to z-axis is

$$\beta = 2\omega\left[\frac{L_1}{v_n} - \frac{L_2}{v_n + \Delta v_n}\right] \qquad (2)$$

where Δv_n is the change of the neutron velocity at the sample. As it follows from Eq. (2), changing the distance between foils in the cascade II, one can change β in rather wide range, thus providing a sinusoidal modulation of the outgoing neutron beam, the so-called NSE signal.

This novel RFNSE technique can be applied in all cases, when the use of Larmor precession devices may result in an improvement either in energy or momentum resolution of neutron scattering instruments, particularly for an improvement in the resolution of triple-axis spectrometers [4] In this case, the momentum resolution is defined by the triple-axis spectrometer, while the energy resolution is defined by the NSE setup and may be increased up to 1 μeV without significant intensity loss.

Another application of the RFNSE technique is high resolution measurements of the neutron momentum transfer in small-angle scattering, diffraction and reflectometry [5]. In this case the Larmor precession is used to label the angle ψ rather than wavelength as in NSE spectroscopy (Eq. (1)) and, in complete analogy with the abovementioned, a high angular resolution can be obtained when using practically uncollimated incident neutron beams. If a sample is placed in the RFNSE spectrometer with tilted spin turners (Fig. 2), then scattering at the sample results in different path lengths between turners 3 and 4. The NSE signal is recorded by the change of distance L_2. Recalling that the effective field integral is $2\omega_B L'$, one may conclude that the recorded signal is a superposition of NSE signals of different frequencies resulting from different effective field integrals over the neutron trajectories. The scattering profile can be restored by the Fourier transform of the recorded intensity.

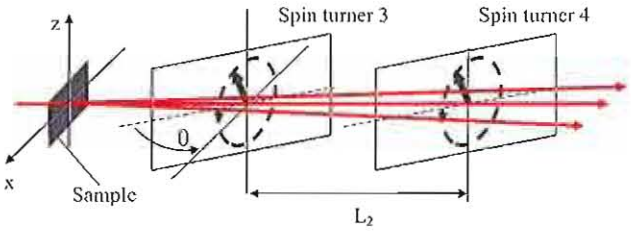

Figure 3. SERGIS configuration. F1- F4 are RMF flippers. Sample is scattering in *xy* plane, where there is no incident beam collimation

The result of Monte-Carlo simulations of a corresponding experiment is shown in Fig. 3. NSE signals corresponding to small beam deviations ψ in the plane *ZX* are well resolved in spite of the use of an only weakly collimated, ± 1°, incident neutron beam [6].

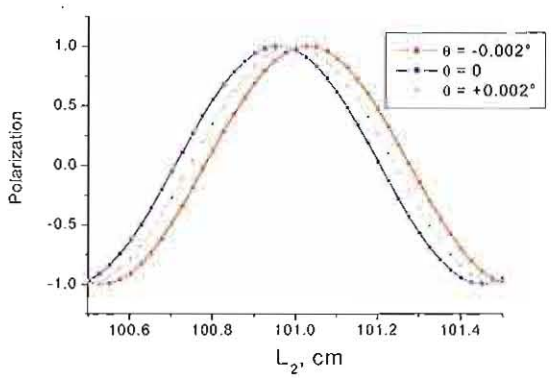

Figure 3. Shift of the NSE signal caused by the deviation of a practically uncollimated (±1°) neutron beam in ZX plane. RMF spin turners driving frequency of 50 kHz, L_1 = 1 m and θ_0= 45°.

It is a pleasure to thank the VITESS team - S. Manoshin, K.Lieutenant and G. Zgismond for their permanent support.

[1]. F. Mezei, Z.Phyzik 255, 146, 1972.
[2]. R. Gähler, R. Golub, J. de Physique, C3-229, 45, 1984.
[3]. A. Ioffe, Physica B 335 (2003) 169; A. Ioffe, Nucl. Instrum. Meth. A529, 2004, p. 39.
[4]. Th.Keller et al. *Physica B*, 241-243 (1997) 101.
[5]. M.Th. Rekveldt, *Physica B*, 234-236 (1997) 1135; J.Major et al., *Physica B*:336,(2003), 8.
[6]. A. Ioffe, S. Manoshin. Nucl. Instrum. Meth. A529, 2004, p. 45.

The New Very Small Angle Neutron Scattering Instrument KWS-3

E. Kentzinger, A. Radulescu, J. Stellbrink, D. Richter and Th. Brückel
Institut für Festkörperforschung, Forschungszentrum Jülich

The newly built very small angle neutron scattering instrument KWS3 is the worldwide unique SANS instrument running on the focusing mirror principle. It allows performing scattering experiments with a wave vector transfer resolution between 10^{-4} and 10^{-3} Å^{-1}, bridging a gap between Bonse-Hart and pinhole cameras. This instrument will be transferred to FRMII, which should lead to an increase in wave vector transfer resolution by one order of magnitude and to an increase in flux by two orders of magnitude.

Ultra-small angle (U-SANS) and small angle neutron scattering (SANS) experiments are performed by two different types of instruments to cover a combined Q-range from $\approx 10^{-5}$Å^{-1} up to ≈ 1Å^{-1}. Bonse-Hart cameras (Double Crystal diffractometers) are used for U-SANS experiments, whereas the "standard" SANS experiment is performed using a pinhole camera. In principle, the Q-range of both instrument classes overlaps. Typical U-SANS instruments like S18 (ILL), PCD (NIST) or DKD (FZJ) may reach maximum Q-vectors of $\approx 5\times10^{-3}$Å^{-1}. The disadvantage of these instruments is that they do not allow taking a full area image on a 2D position sensitive detector. On the other hand, the well-known pinhole instrument D11 at Institut Laue-Langevin (France) reaches a minimum Q-vector of 5×10^{-4} Å^{-1} by use of large wavelengths and sample-to-detector distances ($\approx$40m). But the required instrumental setting pushes both types of instruments to its limits, mainly due to signal-to-noise level and the reduced flux at sample position.

Recently the use of neutron lenses as additional elements of a pinhole SANS instrument has been tested to overcome this intensity problem [1]. The design and concept of the KWS3 instrument at FZ Jülich (Germany) is even more advanced [2]. The principle of this instrument is a one-to-one image of an entrance aperture on a 2D position-sensitive detector by neutron reflection from a double-focusing elliptical mirror. To date, KWS-3 is the worldwide unique SANS instrument running on this principle. It permits to perform SANS studies with a scattering wave vector resolution between 10^{-4} and 10^{-3} Å^{-1} with considerable intensity advantages over conventional pinhole-SANS instruments. Therefore it perfectly bridges the "Q-gap" between U-SANS and SANS: Very Small Angle Scattering (V-SANS). The increasing need for these intermediate Q-vectors arises from the growing interest in biological and colloidal samples, which typically have characteristic length scales in the µm range. In this report we will give a short survey on the instrument concept and its actual realization and present some first results obtained from "real" samples. We will then detail the expected improvements related to the move of KWS-3 to FRMII.

A detailed description of the instrument has already been given in Ref. [2]. Figure 1 shows a sketch of the instrument. The main innovation and challenge in building this instrument was to build a large mirror having a shape as close as possible to an ellipsoid and with a surface roughness less than 5 Å (rms). The mirror is a 1.2 m long, 0.1 m wide and 0.05 m thick toroidal double focusing Zerodur mirror of 11 m focal length, and coated with 1000 Å ^{65}Cu and 100 Å Al as a protection layer. At such a short mirror length with respect to the focal length, the toroidal shape is a good enough approximation to an elliptical shape. The reflection plane has been chosen to be horizontal, reducing the deterioration of the image due to gravity. The entrance pinhole is at one focus of the mirror, the other focus is in the detection plane of a 2D position-sensitive detector. The contrast ratio of the image on the detector was determined to be 10^{-4}.

Very recently a new elliptical mirror, built using the replica technology [3] has been installed concentrically to the toroidal mirror (Fig. 1). First tests with neutrons were performed which indicate that further improvements of the setup are required.

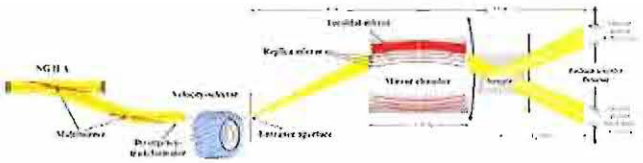

Figure 1 KWS3 experimental setup

At KWS3 the effect of multiple scattering requires special attention. An example of how this effect influences the evaluation of the geometrical and density parameters is presented in Figure 2. There the scattering patterns from a mixed solution of 1% PEB-7.5 random copolymer (M_W=30K) and 4% hexatriacontane paraffin in d-22 are shown for different sample thickness in polymer contrast. The inset of the figure shows the raw data together with the empty beam measurement. Comparison of the intensity in forward direction for the sample and empty beam provided a sample transmission of 10%, 20% and 70% in case of 2mm, 1mm and 0.2mm sample thickness, respectively. Multiple scattering is dominant in the case of the thickest sample while for the 0.2 mm sample thickness it is a minor contribution. Data analysis in terms of Beaucage model [4] revealed a significant variation of the power law behaviour and R_g with sample thickness. We can conclude that in order to have a reasonable sample transmission and to avoid

contribution from multiple scattering very thin samples are required. Recently we developed cells with large radius and variable thickness, covering the full cross section of the incoming beam. This allows to perform a systematic investigation of the multiple scattering effect as a function of cell thickness and thus to avoid misinterpretations. Another way to get the same result is to vary the sample contrast but, for certain samples, this is a much more difficult approach.

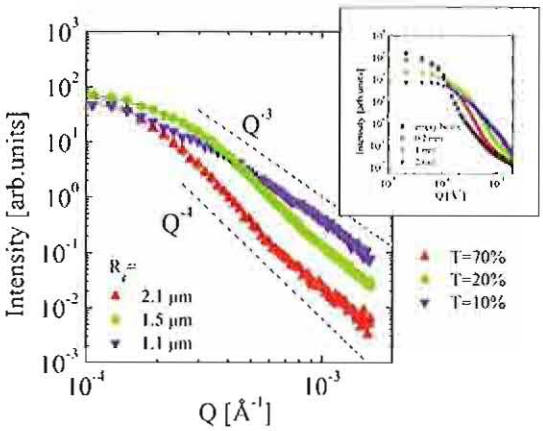

Figure 2 Scattering patterns from a mixed solution of 1% PEB-7.5 random copolymer (MW=30K) and 4% hexatriacontane paraffin in d-22 in polymer contrast. Results obtained for different sample thickness (as denoted by symbols explained within the inset together with the empty beam measurement) reveal how the multiple scattering influences the interpretation of the data.

We present in figure 3 the scattering pattern from a crystalline-amorphous poly(co-olefins) diblock copolymer in dilute solution over the whole Q range accessed by combining all three kinds of small-angle neutron scattering instruments in Jülich: The classical pin-hole instrument KWS2, the focusing-mirror KWS3 instrument and the double crystal diffractometer DKD [5]. The data allow a semi quantitative evaluation of structures of size scales between 10Å and 10 μm and reveal the multilevel morphology of copolymer aggregates, being consistent with the microscope observations (up-right inset of figure 4). By the aggregating *s*PP and amorphous P(E-*co*-P) blocks at small scale a 2-d structure seems to be formed (Q^{-2} power law at larger Q). This structure evolves at intermediate scale into a rod-like structure (Q^{-1} power law at intermediate Q). The rods associate in bundles and the correlation effects between them result in the "shoulder"-like structure at around $Q^* \cong 3.5\text{-}4 \times 10^{-3}$ Å^{-1} (bottom-left inset of figure 3). At much larger scale (micrometer order) the rod bundles form network-like structures with mass fractal aspects (Q^{-3} power law) which associate in very large aggregates resembling snowflakes. The sharp intensity drop at around 7×10^{-5} Å^{-1} may reveal an additional contribution from the correlations between lateral branches of these aggregates over a characteristic length of about 10 μm.

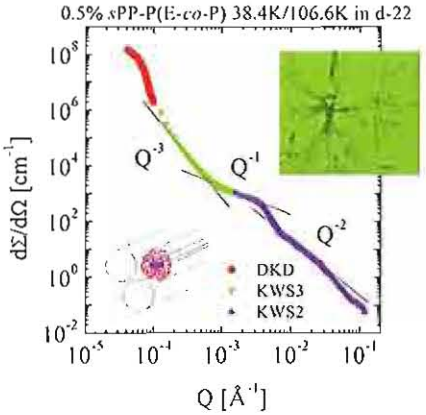

Figure 3 Scattering from a crystalline-amorphous diblock copolymer [4]. The lines indicate power law behaviour in different Q ranges. KWS2: conventional pinhole SANS; KWS3: VSANS; DKD: Double Crystal diffractometer ("U-SANS").

In 2006, KWS3 will be transferred to the new FRMII reactor. A special cold neutron guide will be built, permitting an access to larger wavelengths, leading to an increase in the range of Q-resolutions down to 10^{-5}Å^{-1}. Also, this transfer will result in an increase of the neutron flux at sample position by two orders of magnitudes, permitting the use of small material amounts, which is often the case with biological substances. This dramatic increase in flux will permit to optimally use the reflectometry mode of KWS-3. In this mode, performing SANS on thin film systems under grazing incidence (GISANS) will permit the access to in-plane correlation lengths around the μm, a length scale hardly accessible to off-specular scattering at a reflectometer or to GISANS at a pinhole camera. Also, the implementation of polarized neutrons and a polarization analysis covering the whole detector area will permit the investigation of magnetic correlations.

[1] M.R. Eskilden et al., Nature, **391**, 563, 2000; S.-M. Choi et al., J. Appl. Cryst., **33**, 793 (2000)

[2] B. Alefeld et al., Physica B, **283** 330 (2000), E. Kentzinger et al., Physica B **350** e779–e781 (2004)

[3] http://wave.xray.mpe.mpg.de/rosat/

[4] G. Beaucage and D.W. Schaefer, J.Non-Cryst.Solids 172-**174**, 797 (1994)

[5] A. Radulescu et al., Neutron News, **16-2**, 18 (2005)

Publications

2004

Abbas, B.; Schwahn, D.; Willner, L.
Phase behavior of the polybutadiene / polystyrene diblock copolymer with additions of the non-selective solvent dichlorobencene in temperature and pressure fields
Journal of Polymer Science B - Polymer Physics, **42** (2004), 3179 - 3190

Allahyarov, E.; Gompper, G.; Löwen, H.
Attraction between DNA molecules mediated by multivalent ions
Physical Review E, **69** (2004), 041904

Allahyarov, E.; Löwen, H.; Gompper, G.
DNA condensation, redissolution and mesocrystals induced by tetravalent counterions
Europhysics Letters, **68** (2004), 894 - 900

Asteriadi, A.; Sigel, R.; Vlassopoulos, D.; Meier, G.; Dorgan, J. R.; Knauss, D. M.
Molecular Control of the Viscosity of Model Dendritically Branched Polystyrene Solutions: from Polymeric to Colloidal Behavior
Macromolecules, **37** (2004), 1016 - 1022

Avramescu, M. E.; Sager, W. F. C.; Borneman, Z.; Wessling, M.
Adsorptive membranes for billirubin removal
Journal of Chromatography B, **803** (2004), 215 - 223

Balanetskyy, S.; Grushko, B.; Kowalska-Strzeciwilk, E.; Velikanova, T. Ya.; Urban, K.
An investigation of the Al-Pd-Fe phase diagram between 50 and 100at.% Al: Phase equilibria at 900-1020°C
Journal of Alloys and Compounds, **364** (2004), 164 - 170

Balanetskyy, S.; Grushko, B.; Urban, K.; Velikanova, T. Ya.
Ternary cubic phases in the Al-Pd-Fe system
Powder Metallurgy and Metal Ceramics, **43** (2004), 396 - 405

Balanetskyy, S.; Grushko, B.; Velikanova, T. Y.
Orthorhombic epsilon-phases and structures in Al-Pd-(Fe)
Zeitschrift für Kristallographie, **219** (2004), 548 - 553

Balanetskyy, S.; Grushko, B.; Velikanova, T. Ya.
Decagonal quasicrystals of a new structural type
Zeitschrift für Kristallographie, **219** (2004), 12, 779 - 781

Balanetskyy, S.; Grushko, B.; Velikanova, T. Ya.
Monoclinic Al_2Fe phase, its equilibrium and nonequilibrium formation
Metallofizika I Noveishie Tekhnologii, **26** (2004), 407 - 417

Balanetskyy, S.; Grushko, B.; Velikanova, T. Ya.; Urban, K.
An investigation of the Al-Pd-Fe phase diagram between 50 and 100at% Al:phase equilibria at 750°C
Journal of Alloys and Compounds, **376** (2004), 158 - 164

Balanetskyy, S.; Grushko, B.; Velikanova, T. Ya.; Urban, K.
Investigation of the Al-Pd-Fe phase diagram between 50 and 100 at.% Al:ternary phases
Journal of Alloys and Compounds, **368** (2004), 169 -174

Baldus, O.; Waser, R.
Laser crystallization studies of barium strontium titanate thin films
Journal of the European Ceramic Society, **24** (2004), 3013

Ballone, P.; Jones, G. J.
A reactive force field simulation of liquid-liquid phase transitions in phosphorus
Journal of Chemical Physics, **121** (2004), 8147 - 8157

Barbi, M.; Place, C.; Popkov, V.; Salerno, M.
A Model of Sequence-Dependent Protein Diffusion along DNA
Journal of Biological Physics, **30** (2004), 203 - 226

Barbi, M.; Place, C.; Popkov, V.; Salerno, M.
Base-sequence-dependent sliding of proteins on DNA
Physical Review E, **70** (2004), 041901

Baud, S.; Ramseyer, C.; Bihlmayer, G.; Blügel, S.; Barreteau, B. R.; Desjonquères, M. C.; Spanjaard, D.; Bernstein, N.
Comparative study of ab initio and tight-binding electronic structure calculations applied to platinum surfaces
Physical Review B, **70** (2004), 235423

Baunemann, A.; Becker, R.; Winter, M.; Fischer, R. A.; Thomas, R.; Ehrhart, P.; Waser, R.; Devi, A.
Mononuclear precursor for MOCVD of HfO_2 thin films
Chemical Communications, (2004), **14**, 1610 - 1611

Bedanta, S.; Chen, X.; Sahoo, S.; Kleemann, W.; Kentzinger, E.; Nordblad, P.; Cardoso, S.; Freitas, P. P.
Collective magnetic states of ferromagnetic nanoparticles in the superspin limit
Physica Status Solidi C, 1 (2004), **12**, 3288 - 3296

Belin-Ferrè, E. (Ed.); Feuerbacher, M. (Ed.); Ishii, Y. (Ed.); Sordelet, D. (Ed.)
Quasicrystals 2003 - Preparation, Properties and Applications
Warrendale, PA, Materials Research Society, 2004
Materials Research Society Proceedings Vol. **805** (1-55899-743-1)

Bhakta, R.; Thomas, R.; Hipler, F.; Bettinger, H.; Müller, J.; Ehrhart, P.; Devi, A.
Precursor engineering and evaluation: Studies on the nature of molecular mechanisms involved in the MOCVD of TiO_2 thin films
Journal of Materials Chemistry, **14** (2004), 3231 - 3238

Biehl, R.; Guo, X.; Prud'homme, R. K.; Monkenbusch, M.; Allgaier, J.; Richter, D.
Diffusion of compact macromolecules through polymer meshes: mesh dynamics and probe dynamics
Physica B: Condensed Matter, **350** (2004), 1/3, 76 - 78

Bolten, D.; Böttger, U.; Waser, R.
Effect of interfaces in Monte Carlo computer simulations of ferroelectric materials
Applied Physics Letters, **84** (2004), 2379

Bolten, D.; Böttger, U.; Waser, R.
Reversible and irreversible piezoelectric and ferroelectric response in ferroelectric ceramics and thin films
Journal of the European Ceramic Society, **24** (2004), 725 - 732

Borisenko, S. V.; Kordyuk, A. A.; Legner, S.; Kim, T. K.; Knupfer, M.; Schneider, C. M.; Funk, J.; Golden, M. S.; Sing, M.; Claessen, P. M.; Yaresko, A.; Berger, H.; Grazioli, C.; Turchini, S.
Circular dichroism and bilayer splitting in the normal state of underdoped $(Pb,Bi)_2Sr_2(Ca_xY_{1-x})Cu_2O_{8+\delta}$ and overdoped $(Pb,Bi)_2Sr_2CaCu_2O_{8+\delta}$
Physical Review B, **69** (2004), 224509

Brener, E. A.; Iordanskii, S. V.; Saptsov, R. B.
Condensate Formation and Vortex Generation in Bose Gas upon Cooling
JETP Letters, **79** (2004), 410 - 415

Bronstein, L.; Goerigk, G.; Kostylev, M.; Pink, M.; Khotina, I.; Valetsky, P.; Matveeva, V.; Sulman, E.; Sulman, M.; Bykov, A.; Lakina, N.; Spontak, R.
Structure and Catalytic Properties of Pt-Modified Hyper-Cross-Linked Polystyrene Exhibiting Hierarchical Porosity
Journal of Physical Chemistry B, **108** (2004), 18234 - 18242

Brzank, A.; Schütz, G. M.; Bräuer, P.; Kärger, J.
Molecular traffic control in single-file networks with fast catalysts
Physical Review E, **69** (2004), 031102

Bräuer, P.; Fritzsche, S.; Kärger, J.; Schütz, G.; Vasenkov, S.
Diffusion in Channels and Channel Networks
Molecules in interaction with surfaces and interfaces / eds.: R. Haberlandt, D. Michel, A. Pöppl, R. Stannarius. - Berlin, Springer, 2004. - Lecture Notes in Physics ; 634). - 3-540-20539-X. - S. 89 - 125

Brückner, W.; Thomas, J.; Hertel, Y. Y.; Schäfer, R.; Schneider, C. M.
Magnetic domains in a textured Co nano-pillar
Journal of Magnetism and Magnetic Materials, **283** (2004), 82

Buca, D.; Mörschbächer, M. J.; Holländer, B.; Luysberg, M.; Loo, R.; Caymax, M. (Ed.); Mantl, S.
The use of ion implantation and annealing for the fabrication of strained silicon on thin SiGe virtual substrates
High-Mobility Group-IV Materials and Devices / ed.: M. Caymax ... - Warrendale, PA, 2004. - (Materials Research Society Symposium proceedings ; 809). - 1-55899-759-8. - S. B1.6.1

Buchenau, U.; Wischnewski, A.
Fragility and compressibility at the glass transition
Physical Review B, **70** (2004), 092201

Byelov, D.; Frielinghaus, H.; Allgaier, J.; Gompper, G.; Richter, D.
SANS studies of polymer efficiency boosting in microemulsions - diblock copolymers versus homopolymers
Physica B: Condensed Matter, **350** (2004), 1/3, Suppl. 1, e931 - e933

Byelov, D.; Frielinghaus, H.; Holderer, O.; Allgaier, J.; Richter, D.
Microemulsion efficiency boosting and the complementary effect . 1 . Structural properties
Langmuir, **20** (2004), 10433 - 10443

Bürgler, D. E.; Gareev, R. R.; Buchmeier, M.; Pohlmann, L. L.; Braak, H.; Schreiber, R.; Grünberg, P.
Interlayer exchange coupling of ferromagnetic films across semiconducting interlayers
Nanostructured magnetic materials and their applications / ed.: B. Aktas ... - Kluwer, Dordrecht, 2004. - 1-402-02004-X. - S. 71 - 77

Bürgler, D. E.; Gareev, R. R.; Buchmeier, M.; Pohlmann, L. L.; Braak, H.; Schreiber, R.; Grünberg, P.
Interlayer exchange coupling of ferromagnetic films across semiconducting interlayers
Functional micro- and nanosystems / ed.: K.-H. Hoffmann. -Berlin, Springer, 2004. - 3-540-21612-X. - S. 9 - 12

Bürgler, D. E.; Gareev, R. R.; Pohlmann, L. L.; Braak, H.; Buchmeier, M.; Luysberg, M.; Schreiber, R.; Grünberg, P. A.
Interlayer exchange coupling across epitaxial Si spacers
Molecular Physics Reports, **40** (2004), 13 - 22

Carbone, G.; Persson, B. N. J.
Dewetting at soft viscoelastic interfaces
Journal of Chemical Physics, **121** (2004), 5, 2246 - 2252

Cecco, C.; Barth, C.; Gille, P.; Feuerbacher, M.; Krausch, G.; Reichling, M.
Cleaved surfaces of δ-AlNiCo and ξ'-AlPdMn
Journal of Non-Crystalline Solids, **334-335** (2004), 491 - 494

Chatterji, T.; Liß, K. D.; Tschentscher, T.; Janossy, B.; Strempfer, J.; Brückel, Th.
High-energy non-resonant X-ray magnetic scattering from $EuAs_3$
Solid State Communications, **131** (2004), 713 - 717

Chatterji, T.; Siemensmeyer, K.; Welzel, S.; Caliebe, W.
Temperature and field dependence of the magnetic properties of $Nd_{2-x}Ce_xCuO_4$
European Physical Journal B, **42** (2004), 205 - 217

Cherstvy, A. G.; Kornyshev, A. A.; Leikin, S.
Torsional Deformation of Double Helix in Interaction and Aggregation of DNA
Journal of Physical Chemistry B, **108** (2004), 6508 - 6518

Cherstvy, A. G.; Winkler, R. G.
Complexation of semiflexible chains with oppositely charged cylinder
Journal of Chemical Physics, **120** (2004), 19, 9394 - 9400

Cichocki, B.; Ekiel-Jezewska, M. L.; Nägele, G.; Wajnryb, E.
Hydrodynamic interactions between widely separated particles at a free surface
Europhysics Letters, **67** (2004), 3, 383 - 389

Cichocki, B.; Ekiel-Jezewska, M. L.; Nägele, G.; Wajnryb, E.
Motion of spheres along a fluid-gas interface
Journal of Chemical Physics, **121** (2004), 5, 2305 - 2316

Colmenero, J.; Alvarez, F.; Narros, A.; Arbe, A.; Monkenbusch, M.; Richter, D.; Farago, B.
Self-atomic motions in glass-forming polymers: neutron scattering and molecular dynamics simulations results
Slow Dynamics in Complex Systems, 02.-09.11.2003 : 3rd International Symposium on Slow Dynamics in Complex Systems / eds.: M. Tokuyama, I. Oppenheim. - 2004. - (AIP Conference Proceedings ; 708). - 0-7354-0183-7. - S. 655 - 658

Conrad, H. (Ed.)
Advanced Cold Moderators : ACoM-6 ; proceedings of the 6th International Workshop on Advanced Cold Moderators held at Forschungszentrum Jülich from 11 - 13 September 2002
Jülich, Forschungszentrum, Zentralbibliothek, 2004
Schriften des Forschungszentrums Jülich . Reihe Materie und Material/Matter and Materials ; 20. - 3-89336-363-7

Conrad, H.; Kuhs, W. F.; Nünighoff, K.; Pohl, C.; Prager, M.; Schweika, W.
Inelastic scattering and spectral measurements of advanced cold moderator media
Physica B: Condensed Matter, **350** (2004), 1/3, Suppl. 1, e647 - e650

Conrad, H.; Nünighoff, K.; Pohl, C.; Prager, M.; Kuhs, W. F.
Inelastic neutron scattering and spectral measurements of advanced cold moderator materials
Advanced Cold Moderators : ACoM-6 ; proceedings of the 6th International Workshop on Advanced Cold Moderators held at Forschungszentrum Jülich from 11 - 13 September 2002 / ed.: H. Conrad. - Jülich, 2004. - (Schriften des Forschungszentrums Jülich . Reihe Materie und Material/Matter and Material ; 20). - 3-89336-363-7. - S. 113 - 121

Da Silva, J. L. F.; Schroeder, K.; Blügel, S.
Trend for the multilayer relaxation sequence of stepped Cu surfaces
Physical Review B, **70** (2004), 245432

da Silva, J. L.; Schroeder, K.; Blügel, S.
First-principles investigation of the multilayer relaxation of stepped Cu surfaces
Physical Review B, **69** (2004), 245411

Dhont, J. K. G.
Thermodiffusion of interacting colloids.I. A statistical thermodynamics approach
Journal of Chemical Physics, **120** (2004), 3, 1632 - 1641

Dhont, J. K. G.
Thermodiffusion of interacting colloids.II. A microscopic approach
Journal of Chemical Physics, **120** (2004), 3, 1642 - 1653

Dhont, J. K. G.
Translational Brownian Motion
Physics meets Biology : From Soft matter to Cell biology ; Lecture notes of the 35th Spring School of the Institut für Festkörperforschung / ed.: G. Gompper ... - Jülich, Forschungszentrum, 2004. - (Schriften des Forschungszentrums Jülich - Reihe Materie und Material / Matter and Material ; 19). - 3-89336-348-3. - S. A2.1 - A2.43

Di Cola, E.; Plucktaveesak, N.; Waigh, T. A.; Colby, R. H.; Tan, J.; Pyckhout-Hintzen, W.; Heenan, R.
Structure and dynamics in aqueous solutions of amphiphilic sodium maleate-containing alternating copolymers
Macromolecules, **37** (2004), 8457 - 8465

di Napoli, S.; Bihlmayer, G.; Blügel, S.; Alouani, M.; Dreyssé, H.; Llois, A. M.
Band contribution to the electronic transport in noncollinear magnetic materials: application to $LaMn_2Ge_2$
Physica B: Condensed Matter, **354** (2004), 154 - 157

di Napoli, S.; Bihlmayer, G.; Blügel, S.; Alouani, M.; Dreyssé, H.; Llois, A. M.
Noncollinear magnetism in $LaMn_2Ge_2$ and $LaMn_2Si_2$ compounds
Journal of Magnetism and Magnetic Materials, **272-276** (2004), Suppl. 1, e265 - e266

Di Napoli, S.; Llois, A. M.; Bihlmayer, G.; Blügel, S.; Alouani, M.; Dreyssé, H.
Magnetic structure and transport properties of noncollinear $LaMn_2X_2$ (X=Ge,Si) systems
Physical Review B, **70** (2004), 174418

Divin, Y. Y.; Liatti, M.; Shirotov, V.; Poppe, U.; Gabankov, V. N.; Urban, K.
Terahertz Josephson Detectors and Hilbert Spectroscopy
Conference Digest of 2004 Joint 29th International Conference on Infrared and Millimeter Waves and 12th International Conference on Terahertz Electronics. - IEEE, 2004. - 0-7803-8490-3. - S. 227 - 278

Divin, Y. Y.; Volkov, O. Y.; Liatti, M.; Gubankov, V. N.
Terahertz Josephson effect in (001)-and (100)-tilt $YBa_2Cu_3O_{7-x}$ grain-boundary junctions
6th European Conference on Applied Superconductivity, Sorrento, Italy / ed.: A. Andreone, G. P. Pepe, R. Christiano, G. Masullo. - 2004. - 0-7503-0981-4. - (IoP Conference series ; 181). - S. 2970 - 2977

Divin, Y.; Kotelyanskii, I. M.; Shadrin, P.; Jia, C. L.; Poppe, U.; Urban, K.
(100)-tilt $YBa_2Cu_3O_{7-x}$ grain boundary Josephson junctions with high I_cR_n-product on $NdGaO_3$ bicrystal substrates
6th European Conference on Applied Superconductivity, Sorrento, Italy / ed.: A. Andreone, G. P. Pepe, R. Christiano, G. Masullo. - 2004. - 0-7503-0981-4. - (IoP Conference series ; 181). - S. 3112 - 3118

Dobnikar, J.; Halozan, D.; Brumen, M.; von Grünberg, H.-H.; Rzehak, R.
Poisson-Boltzmann Brownian dynamics of charged colloids in suspension
Computer Physics Communications, **159** (2004), 73 - 92

Ebert, Ph.
Imaging and Characterizing Nanoscale Fluctuations in the Distribution of Dopant Atoms by Scanning Tunneling Microscopy. Defects and Diffusion in Semiconductors-Annual Retrospective
Defect and Diffusion Forum, **230-232** (2004), 111 - 124

Ebert, Ph.
Importance of bulk properties in the structure and evolution of surfaces of quasicrystals
Progress in Surface Science, **75** (2004), 109 - 130

Ebert, Ph.; Jäger, N. D.; Urban, K.; Weber, E. R.
Nanoscale Fluctuations in the Distribution of Dopant Atoms: Dopant-Induced Dots and Roughness of Electronic Interfaces
Journal of Vacuum Science and Technology B, **22** (2004), 4, 2018 - 2025

Eckold, G.; Caspary, D.; Elter, P.; Güthoff, F.; Hoser, A.; Schmidt, W.
Time-resolved phonons as a microscopic probe for demixing processes
Physica B: Condensed Matter, **350** (2004), 83 - 86

Eckold, G.; Caspary, D.; Gibhardt, H.; Schmidt, W.; Hoser, A.
Kinetics of decomposition in ionic solids: III. Time evolution of phonons during spinodal decomposition in AgCl-NaCl
Journal of Physics: Condensed Matter, **16** (2004), 5945

Eisenriegler, E.
Anisotropic colloidal particles in critical fluids
Journal of Chemical Physics, **121** (2004), 3299

Ellerkmann, U.; Liedtke, R.; Böttger, U.; Waser, R.
Interface related thickness dependence of the tunability in $BaSrTiO_3$ thin films
Applied Physics Letters, **85** (2004), 4708 - 4710

Elsebrock, R.; Makovicka, C.
A laboratory scale moulding technique to fabricate high precision 2D columnar and honeycomb structures
Materials Letters, **58** (2004), 3945 - 3947

Elsebrock, R.; Makovicka, C.; Meuffels, P.; Waser, R.
Structured oxide ceramics by a sodium chloride moulding technique
Materials Letters, **58** (2004), 26, 3348 - 3349

Endo, H.; Schwahn, D.; Cölfen, H.
An analysis of calcium carbonate / polymer hybrid crystals applying contrast variation SANS
Physica B: Condensed Matter, **350** (2004), 1/3, Suppl. 1, e943 - e945

Endo, H.; Schwahn, D.; Cölfen, H.
On the Role of Block Copolymer Additives for Calcium Carbonate Crystallization - neutron scattering investigation by applying contrast variation
Journal of Chemical Physics, **120** (2004), 9410 - 9423

Faley, M. I.; Pratt, K.; Reinemann, R.; Schurig, D.; Gott, S.; Sarwinski, R. E.; Paulson, D. N.; Starr, T. N.; Fagaly, R. L.
High Temperature Superconductor dc-SQUID Micro-Susceptometer for Room Temperature Objects
Superconductor Science and Technology, **17** (2004), s324 - s327

Faley, M.; Poppe, U.; Slobodchikov, V.; Maslenikov, Yu. V.; Urban, K.
A high temperature superconductor dc SQUID planar gradiometer measurement system for routine inspections
Superconductor Science and Technology, **17** (2004), s301 - s304

Fendt, R. E. F.; Sprung, M.; Gutt, C.; Seeck, O. H.; Tolan, M.
X-ray reflectivity study of the influence of temperature fluctuations on the density profile of thin liquid films
Zeitschrift für Kristallographie, **219** (2004), 4, 205 - 209

Feuerbacher, M.; Caillard, D.
[0 1 0] dislocations in the complex metallic alloy ksi'-Al-Pd-Mn
Acta Materialia, **52** (2004), 1297 - 1304

Feuerbacher, M.; Heggen, M.; Urban, K.
Defects in complex intermetallics and quasicrystals
Materials Science and Engineering A, **375-377** (2004), 84 - 89

Feygenson, M.; Toperverg, B. P.; Rücker, U.; Kentzinger, E.; Brückel, Th.
Neutron quantum well states in Fe/Co/Fe trilayers
Physica B: Condensed Matter, **350** (2004), 1/3, Suppl. 1, e233 - e235

Fitsilis, M.; Kohlstedt, H.; Waser, R.; Ullmann, M.
A new concept for using ferroelectric transistors in nonvolatile memories
Integrated Ferroelectrics, **60** (2004), 45 - 58

Frielinghaus, H.; Byelov, D.; Allgaier, J.; Gompper, G.; Richter, D.
Efficiency boosting and optional viscosity tuning in microemulsions studied by SANS
Physica B: Condensed Matter, **350** (2004), 1/3, 186 - 192

Fujihara, S.; Schneller, T.; Waser, R.
Interfacial reactions and microstructure of BaTiO3 films prepared using fluorideprecursor method
Applied Surface Science, **221** (2004), 178 - 183

Fukushima, T.; Sato, K.; Katayama-Yoshida, H.; Dederichs, P.H.
Theoretical prediction of Curie temperatures in (Zn,Cr)S, (Zn,Cr)Se and (Zn,Cr)Te
Japanese Journal of Applied Physics Part 2: Letters, **43** (2004), 11A, L1416 - L1418

Fütterer, T.; Vliegenthart, G. A.; Lang, P.
Particle Scattering Factor of Janus Micelles
Macromolecules, **37** (2004), 22, 8407 - 8413

Gerber, P.; Kügeler, C.; Böttger, U.; Waser, R.
Effects of ferroelectric switching on the piezoelectric small-signal response (d_{33}) and electrostriction (M_{33}) of lead zirconate titanate thin films
Journal of Applied Physics, **95** (2004), 9, 4976 - 4980

Gerber, P.; Roelofs, A.; Kugeler, C.; Bottger, U.; Waser, R.; Prume, K.
Effects of the top-electrode size on the piezoelectric properties (d_{33} and S) of lead zirconate titanate thin films
Journal of Applied Physics, **96** (2004), 2800

Gerber, P.; Roelofs, A.; Kügeler, C.; Böttger, U.; Waser, R.; Prume, K.
Effects of the top-electode size on the piezoelectric properties (d_{33} and S) of lead zirconate titanate thin films
Journal of Applied Physics, **96** (2004), 2800 - 2804

Goad, M.; Pyckhout-Hintzen, W.; Kahle, S.; Allgaier, J.; Richter, D.; Fetters, L. J.
Rheological properties of 1,4-polyisoprene over a large molecular weight range
Macromolecules, **37** (2004), 8135 - 8144

Goerigk, G.; Schweins, T. C.; Huber, K.; Ballauff, M.
The distribution of Sr^{2+} counterions around polyacrylate chains analyzed by anomalous small-angle X-ray scattering
Europhysics Letters, **66** (2004), 3, 331 - 337

Gompper, G.; Kaupp, U. B.
Introduction: Physics meets Biology
Physics meets biology : from soft matter to cell biology ; lecture notes of the 35th Spring School of the Institut für Festkörperforschung / ed.: G. Gompper ... - Jülich, Forschungszentrum, 2004. - (Schriften des Forschungszentrums Jülich - Reihe Materie und Material / Matter and Material ; 19). - 3-89336-348-3. - S. 11.1 - 11.24

Gompper, G.; Kroll, D. M.
Triangulated-Surface Models of Fluctuating Membranes
Statistical Mechanics of Membranes and Surfaces : the 5th Jerusalem Winter School for Theoretical Physics / ed.: D. R. Nelson, T. Piran, S. Weinberg. - Singapore, World Scientific, 2004. - 981-238-760-9. - S. 359 - 426

Groudeva-Zotova, S.; Elefant, D.; Kaltofen, R.; Thomas, J.; Schneider, C. M.
NiMn/FeNi exchange biasing systems - magnetic and structural characteristics after short annealing close to the phase transition point of the AFM layer
Journal of Magnetism and Magnetic Materials, **278** (2004), 379

Grushko, B.; Döblinger, M.
Decagonal quasicrystals in Al-Ni-Co: generality and particulars
Zeitschrift für Kristallographie, **219** (2004), 447 - 455

Grushko, B.; Velikanova, T. Ya.
Formation of Quasicrystals and Related Structures in Systems of Aluminum with Transition Metals. 2. Binary Systems Formed by Aluminum with 4d and 5d Metals
Powder Metallurgy and Metal Ceramics, **43** (2004), 5/6, 311 - 322

Grushko, B.; Velikanova, T. Ya.
Stable and metastable quasicrystals in Al-based alloy systems with transition metals
Journal of Alloys and Compounds, **367** (2004), 58 - 63

Guo, X.
Property degradation of tetragonal zirconia induced by low-temperature defect reaction with water molecules
Chemistry of Materials, **16** (2004), 3988 - 3994

Guo, X.; Ding, Y.
Grain boundary space charge effect in Zirconia
Journal of the Electrochemical Society, **151** (2004), 1, J1 - J7

Guo, X.; Schober, T.
Water Incorporation in Tetragonal Zirconia
Journal of the American Ceramic Society, **87** (2004), 746 - 748

Guo, X.; Waser, R.
Space charge concept for acceptor-doped zirconia and ceria and experimental evidences
Solid State Ionics, **173** (2004), 63 - 67

Guzenko, V. A.; Thillosen, N.; Dahmen, A.; Calarco, R.; Schäpers, Th.; Houben, L.; Luysberg, M.; Schineller, B.; Heuken, M.; Kaluza, A.
Magnetic and structural properties of GaN thin layers implanted with Mn, Cr, or V ions
Journal of Applied Physics, **96** (2004), 10, 5663 - 5667

Halder, S.; Schneller, T.; Waser, R.
Microstructural and electrical characterization of (Ba,Sr)TiO3 thin films prepared by a new carboxylate free chemical solution deposition (CSD) route
Ferroelectric thin films XII / ed.: S. Hoffmann-Eifert ... - Warrendale, PA, 2004. - (Materials Research Society Symposium Proceedings ; 784). - 1-55899-722-9. - S. 387 - 391

Hauer, B.; Hempelmann, R.; Udovic, T. J.; Rush, J. J.; Kockelmann, W.; Schäfer, W.; Jansen, E.
Neutron scattering studies on the vibrational excitations and the structure of ordered niobium hydrides: The lambda phases
Journal of Physics: Condensed Matter, **16** (2004), 5205 - 5228

He, J. Q.; Teren, A.; Jia, C. L.; Erhart, P.; Urban, K.; Waser, R.; Wang, R. H.
Microstructure and interfaces of HfO_2 thin films grown on silicon substrates
Journal of Crystal Growth, **262** (2004), 295 - 303

He, J. Q.; Jia, C. L.; Schubert, J.; Wang, R. H.
Microstructures of epitaxial $La_{0.7}Ca_{0.3}MnO_3$ thin films grown on $SrTiO_3$ and $NdGaO_3$ substrates
Journal of Crystal Growth, **265** (2004), 241

Hecker, M.; Mattern, N.; Brückner, W.; Schneider, C. M.
Effect of annealing on structural properties of Co thin films and Co/Cu multilayers
Materials Science Forum, **443-444** (2004), 193 - 196

Hecker, M.; Schneider, C. M.; Oppeneer, P. M.; Mertins, H.-Ch.
Layer-selective magnetization reversal in GMR layer systems
Physica B: Condensed Matter, **345** (2004), 173

Heggen, M.; Feuerbacher, M.
Constitutive model of quasicrystal plasticity: Strain-rate and temperature dependence
Quasicrystals 2003 - Preparation, Properties and Applications. - Warrendale, PA, MRS, 2004. - (Materials Research Society Symposium proceedings ; 805). - 1-55899-743-1. - S. LL 5.1.1.

Heggen, M.; Spaepen, F.; Feuerbacher, M.
Evolution of the Free Volume during Homogeneous Flow of a Metallic Glass
Quasicrystals 2003 - Preparation, Properties and Applications. - Warrendale, PA, MRS, 2004. - (Materials Research Society Symposium proceedings ; 805). - 1-55899-743-1. - S. MM 7.2.1.

Heggen, M; Spaepen, F.; Feuerbacher, M.
Plastic deformation of $Pd_{41}Ni_{10}Cu_{29}P_{20}$ bulk metallic glass
Materials Science and Engineering A, **375-377** (2004), 1186 - 1190

Heinrich, M.; Pyckhout-Hintzen, W.; Allgaier, J.; Richter, D.; Straube, E.; McLeish, T. C. B.; Wiedenmann, A.; Blackwell, R. J.; Read, D. J.
Small-angle neutron scattering study of the relaxation of a melt of polybutadiene H-polymers following a large step strain
Macromolecules, **37** (2004), 5054 - 5064

Henkel, M.; Paessens, M.; Pleimling, M.
Scaling of the linear response in simple ageing systems without disorder
Physical Review E, **69** (2004), 056109

Henkel, M.; Schütz, G. M.
On the universality of the fluctuation-dissipation ratio in non-equilibrium critical dynamics
Journal of Physics A - Mathematical and General, **37** (2004), 591 - 604

Hofer, C.; Ellerkmann, U.; Halder, S.; Meyer, R.; Waser, R.
Scaling effect on the dielectric constant in $Ba(Ti_xZr_{1-x})O_3$ thin films
Journal of Electroceramics, **13** (2004), 1/3, 101 - 104

Hofer, C.; Meyer, R.; Böttger, U.; Waser, R.
Characterization of $Ba(Ti,Zr)O_3$ ceramics sintered under reducing conditions
Journal of the European Ceramic Society, **24** (2004), 1473 - 1477

Hoffmann-Eifert, S. (Ed.); Funakubo, H. (Ed.); Joshi, J. L. (Ed.); Kingon, A. I. (Ed.); Koutsaroff, I.P. (Ed.)
Ferroelectric Thin Films XII
Warrendale, PA, Materials Resesarch Society, 2004
Materials Research Society Symposium Proceedings ; 784

Holm, C.; Hofmann, T.; Joanny, J. F.; Kremer, K.; Netz, R. R.; Reineker, P.; Seidel, C.; Vilgis, L. S.; Winkler, R. G.
Polyelectrolyte Theory
Polyelectrolytes with Defined Molecular Architecture II / ed.: M Schmidt. - Berlin, 2004. - (Advances in Polymer Science ; 166). - 3-540-00556-0. - S. 244

Hoshino, T.; Asato, M.; Nakamura, T.; Zeller, R.; Dederichs, P. N.
Screened Full-Potential KKR Calculations for Iron Compounds, based on the Generalized-Gradient Approximation
Journal of Magnetism and Magnetic Materials, **272-276** (2004), Suppl. 1, e231 - e232

Hoshino, T.; Asato, M.; Nakamura, T.; Zeller, R.; Dederichs, P. N.
Screened Full-Potential KKR Calculations for Transition Metals, based on the Generalized-Gradient Approximation
Journal of Magnetism and Magnetic Materials, **272-276** (2004), Suppl. 1, e229 - e239

Hoshino, T.; Asato, M.; Zeller, R.; Dederichs, P. N.
Full-Potential KKR Calculations for Vacancies in Al: Screening Effect and Many-Body Interactions
Physical Review B, **70** (2004), 094118

Houben, L.; Jia, C.; Tillmann, R. G. E.; Urban, K.
Quantitative aberration-corrected transmission electron microscopy
Microscopy and Microanalysis, **10** (2004), Suppl. 3, 38 - 40

Houben, L.; Luysberg, M.; Brammer, T.
Electron beam illumination effects on electronstatic potential mapping in holographic imaging of semiconductors in TEM
Microscopy of Semiconducting Materials / ed.: Cullis ... - IoP, 2004. - (Institute of Physics Conference Series ; 180). - 0-7503-0979-2. - S. 49

Houben, L.; Luysberg, M.; Brammer, T.
Illumination effects in holographic imaging of the electrostatic potential of defects and pn-junctions in transmission electron microscopy
Physical Review B, **70** (2004), 165313

Houben, L.; Thust, A.; Urban, K.
Analysis of aberration corrected grain boundary phase images from focal series reconstruction in $YBa_2Cu_3O_7$
Proceedings of the 13th European Microscopy Congress, Antwerpen, 22.08.04-27.08.04. - 1 (2004). - S. 137

Hu, X. S.; Biehl, R.; Prud'homme, R. K.; Monkenbusch, M.; Lal, J.
Fluctuations of bare membranes and their modification on incorporation of polymers having equally spaced anchors
Physica B: Condensed Matter, **350** (2004), 1/3, 217 - 219

Hueging, N.; Tillmann, R. G. E.; Luysberg, M.; Trinkaus, H.; Urban, K.
Quantitative TEM analysis of structural defects in helium implanted silicon
Microscopy of Semiconducting Materials / ed.: Cullis ... - IoP, 2004. - (Institute of Physics Conference Series ; 180). - 0-7503-0979-2. - S. 373 - 378

Hueging, N.; Tillmann, R. G. E.; Luysberg, M.; Trinkaus, H.; Urban, K.
Quantitative diffraction contrast analysis on the pressure of helium filled nanocracks in implanted silicon
Materials Science : proceedings of EMC 2004, 22.08.-27.08.2004, Antwerpen / ed.: G. van Tendeloo. - Belgian Society for Microscopy. - 2 (2004). - S. 379, CD-ROM, Beitrag MS07.05

Höhler, H.; Atodiresei, N.; Schroeder, K.; Zeller, R.; Dederichs, P. N.
Cd-vacancy and Cd-interstitial complexes in Si and Ge
Physical Review B, **70** (2004), 155313

Ioffe, A.
Larmor labelling, polarisation analysis and its applications
Nuclear Instruments and Methods in Physics Research Section A, **529** (2004), 1/3, 39 - 44

Ioffe, A.
Neutron speed echo add-on to TAS: an increase in energy resolution without the use of polarized neutrons
Journal of Magnetism and Magnetic Materials, **272-276** (2004), 2136 - 2137

Ioffe, A.; Brückel, Th.; Bodnarchuk, V.; Yaradajkin, S.; Belushkin, A.
Development of NSE-based methods of medium-resolution neutron spectroscopy at IBR-2
Proceedings of the Germany-JINR User Meeting 'Condensed Matter Physics with Neutrons at the IBR-2 Pulsed Reactor', Dubna, Russia, 12. - 16.06.2004. - 2004. - S. 12 - 18

Ioffe, A.; Bussmann, K.; Dohmen, L.; Axelrod, L.; Gordeev, I. L.; Brückel, Th.
LAP-ND: a new instrument for vector polarisation analysis and neutron depolarisation measurements at FRJ-2
Physica B: Condensed Matter, **350** (2004), 1/3, Suppl. 1, e815 - e818

Ioffe, A.; Manoshin, S.
A neutron spin-echo spectrometer based upon thin magnetic film flippers: the simulation of performance
Physica B: Condensed Matter, **345** (2004), 235 - 238

Ioffe, A.; Manoshin, S.
Larmor labelling by thin spin flippers with rotating magnetic field: simulations of performance of neutron scattering instruments
Nuclear Instruments and Methods in Physics Research Section A, **529** (2004), 1/3, 45 - 49

Janotta, A.; Dikce, Y.; Schmidt, M.; Eisele, C.; Stutzmann, M.; Luysberg, M.; Houben, L.
Light-induced modification of a-SiO_x (II): Laser crystallisation
Journal of Applied Physics, **95** (2004), 4060

Jia, C. L.; Lentzen, M.; Urban, K.
High-resolution Transmission Electron Microcopy Using Negative Spherical Aberration.
Microscopy and Microanalysis, **10** (2004), 174 - 184

Jia, C. L.; Urban, K.
Atomic-Resolution Measurement of Oxygen Concentration in Oxide Materials
Science, **303** (2004), 2001 - 2004

Jiang, C. S.; Li, S. C.; Yu, H. B.; Eom, D.; Wang, X. D.; Ebert, Ph.; Jia, C. L.; Xue, Q. K.; Shih, C. K.
Building Pb nanomesas with atomic layer precision
Physical Review Letters, **92** (2004), 106104-1 - 106104-4

Jones, G. J.
Material Science
NIC Symposium 2004 : Symposium, 17. - 18. February 2004, Forschungszentrum Jülich, Proceedings / ed.: D. Wolf ... - Jülich, NIC, 2004. - (NIC series ; 20). - 3-00-012372-5. - S. 169

Kahle, A.; Winkler, B.; Radulescu, A.; Schreuer, J.
Small-angle neutron scattering study of volcanic rocks
European Journal of Mineralogy, **16** (2004), 407 - 417

Kahle, A.; Winkler, B.; Radulescu, A.; Schreuer, J.
Small-angle neutron scattering study of volcanic rocks (abstract)
Lithos : an International Journal of Mineralogy, Petrology and Geochemistry, **73** (2004), 1/2, Suppl. 1, s54

Kang, K.; Gapinski, J.; Lettinga, M. P.; Buitenhuis, J.; Meier, G.; Dhont, J. K. G.; Patkowski, A.
DLS and FCS on Tracer Spheres in Concentrated Rod Dispersions
Proceedings of the 2004 Photon Correlation and Scattering Conference cosponsored by ESA, OSA, NASA Glenn Research Center, NCMR, the University of Amsterdam, and the Van der Waals-Zeemann Institute Amsterdam, The Netherlands, August 16-18, 2004. - S. 15 - 17

Karthäuser, S.; Vasco Matias, E.; Dittmann, R.; Waser, R.
Fabrication of arrays of $SrZrO_3$ nanowires by pulsed laser deposition
Nanotechnology, **15** (2004), s122 - s125

Kawabata, Y.; Nagao, M.; Seto, H.; Komura, S.; Taheda, T.; Schwahn, D.; Yamada, N.; Nobuto, H.
Temperature and pressure effects on the bending modulus of monolayers in a ternary microemulsion
Physical Review Letters, **92** (2004), 056103

Keiper, J. S.; Behles, J. A.; Bucholz, T. L.; Simhan, R.; de Simone, J. M.; Lynn, G. W.; Wignall, G. D.; Melnichenko, Y. B.; Frielinghaus, H.
Self-assembly of phosphate fluorosurfactants in carbon dioxide
Langmuir, **20** (2004), 1065 - 1072

Kemmerling, G.; Clemens, U.; Engels, R.; Heiderich, M.; Rongen, H.; Schelten, J.; Schwahn, D.; Zwoll, K.; Pyckhout-Hintzen, W.
Performance measurements of a new large area neutron scintillation detector system
IEEE Transactions on Nuclear Science, **51** (2004), 3, 1098 - 1102

Kentzinger, E.; Dohmen, L.; Alefeld, B.; Rücker, U.; Stellbrink, J.; Ioffe, A.; Richter, D.; Brückel, Th.
KWS-3, the new focusing-mirror ultra small-angle neutron scattering instrument and reflectometer at Jülich
Physica B: Condensed Matter, **350** (2004), 1/3, Suppl. 1, e779 - e781

Kita, R.; Kircher, G.; Wiegand, S.
Thermally induced sign change of Soret coefficient for dilute and semidilute solutions of poly(N-isopropylacrylamide) in ethanol
Journal of Chemical Physics, **121** (2004), 18, 9140 - 9146

Kita, R.; Wiegand, S.; Luettmer-Strathmann, J.
Sign change of the Soret coefficient of poly(ethylene oxide) in water/ethanol mixtures observed by thermal diffusion forced Rayleigh scattering
Journal of Chemical Physics, **121** (2004), 8, 3874 - 3885

Klingeler, R.; Breuer, C.; Wirth, I.; Blanchard, A.; Bechthold, P. S.; Neeb, A. V.; Eberhardt, W.
Scanning tunneling spectroscopy of small Ce-doped endohedral fullerenes on HOPG
Surface Science, **553** (2004), 95 - 104

Kluge, M.; Schober, H. R.
Diffusion and jump-length distribution in liquid and amorphous $Cu_{33}Zr_{67}$
Physical Review B, **70** (2004), 224209

Kluthe, C.; Al-Kassab, T.; Barker, J.; Pyckhout-Hintzen, W.; Kircheim, R.
Segregation of hydrogen at internal Ag/MgO (metal/oxide)-interfaces as observed by small angle neutron scattering
Acta Materialia, **52** (2004), 2701 - 2710

Knaapila, M.; Kisko, K.; Lyons, B. P.; Stepanyan, R.; Foreman, J. P.; Seeck, O. H.; Vainio, U.; Pålsson, L.-O.; Serimaa, R.; Torkkeli, M.; Monkman, A. P.
Influence of Molecular Weight on Self-Organisation, Uniaxial Alignment, and Surface Morphology of Hairy-Rodlike Polyfluorene in Thin Films
Journal of Physical Chemistry B, **108** (2004), 30, 10711 - 10720

Koch, E.; Zeyher, R.
Renormalization of the electron-phonon coupling in the one-band Hubbard model
Physical Review B, **70** (2004), 094510

Koizumi, S.; Monkenbusch, M.; Richter, D.; Schwahn, D.; Farago, B.
Concentration fluctuations in polymer gel investigated by neutron scattering: Static inhomogeneity in swollen gel
Journal of Chemical Physics, **121** (2004), 12721 - 12731

Koroteev, Yu. M.; Bihlmayer, G.; Gayone, J. E.; Chulkov, E. V.; Blügel, S.; Echenique, P. M.; Hofmann, Ph.
Strong Spin-Orbit Splitting on Bi Surfaces
Physical Review Letters, **93** (2004), 046403

Kozhuharova, R.; Ritschel, M.; Elefant, D.; Graff, A.; Leonhardt, A.; Mönch, I.; Mühl, T.; Groudeva-Zotova, S.; Schneider, C. M.
Well-aligned Co-filled carbon nanotubes: Preparation and magnetic properties
Applied Surface Science, **238** (2004), 355

Krasyuk, A.; Oelsner, A.; Nepijko, S. A.; Kuksov, A.; Celinski, Z.; Schneider, C. M.; Schönhense, G.
Dynamics of magnetic stray fields during magnetization reversal of Co dots
Applied Physics A, **79** (2004), 1925

Krause, B.; Dürr, A. C.; Schreiber, F.; Dosch, H.; Seeck, O. H.
Late growth stages and post-growth diffusion in organic epitaxy. PTCDA on Ag(111)
Surface Science, **572** (2004), 385 - 395

Krause, B.; Schreiber, F.; Dosch, H.; Pimpinelli, A.; Seeck, O. H.
Temperature dependence of the 2D-3D transition in the growth of PTCDA on Ag(111): A real-time X-ray and kinetic Monte-Carlo study
Europhysics Letters, **65** (2004), 3, 372 - 378

Kriegs, H.; Steffen, W.; Fytas, G.; Monaco, G.; Dreyfus, C.; Fragouli, P.; Pitsikalis, M.; Hadjichristidis, F. H.
High frequency acoustic excitations in ordered diblock copolymer studied by inelastic x-ray scattering
Journal of Chemical Physics, **121** (2004), 5, 2376 - 2380

Kuksov, A.; Schneider, C. M.; Oelsner, A.; Krasyuk, A.; Neeb, D.; Schönhense, G.; De Nadai, F. C.; Brookes, N. B.
Investigating magnetization dynamics in permalloy microstructures using time-resolved X-PEEM
Journal of Applied Physics, **95** (2004), 6530

Kunes, J.; Oppeneer, P. M.; Valencia, S.; Abramsohn, D.; Mertins, H.-Ch.; Schneider, C. M.
Understanding the XMLD and its magnetocrystalline anisotropy at the $L_{2,3}$-edges of 3d transition metals
Journal of Magnetism and Magnetic Materials, **272-276** (2004), 2146

Kurz, Ph.; Förster, F.; Nordström, D. A.; Bihlmayer, G.; Blügel, S.
Ab initio treatment of noncollinear magnets with the full-potential linearized augmented plane wave method
Physical Review B, **69** (2004), 024415

Kwon, S.; Schütz, G. M.
Generalized scaling relations for unidirectionally coupled nonequilibrium systems
Physica A, **341** (2004), 136 - 144

Köbler, U.; Hoser, A.
Universal temperature dependence of the magnetic excitations
Journal of Magnetism and Magnetic Materials, **272-276** (2004), 342 - 343

Kügeler, C.; Böttger, U.; Waser, R.
Piezoelectric MEMS actuators fabricated by chemical solution deposition and surface micromachining technologies
Microfabricated Systems and MEMS VII / ed.: J. L. Davidson ... - Pennington, NJ, 2004. - (Electrochemical Society proceedings ; 9/2004). - 1-56677-422-5. - S. 278 - 287

Lamura, A.; Burkhardt, T. W.; Gompper, G.
Helical polymer in cylindrical confining geometries
Physical Review E, **70** (2004), 051804

Lang, P.
Surface induced ordering effects in soft condensed matter systems
Journal of Physics: Condensed Matter, **16** (2004), R699 - R720

Lentzen, M.
The tuning of a Zernike phase plate with defocus and variable spherical aberration and its use in HRTEM imaging
Ultramicroscopy, **99** (2004), 211 - 220

Lentzen, M.; Thust, A.; Urban, K.
Accuracy of Aberration Measurements forHRTEM Using Zemlin Tableaus
Proceedings of EMC, 2004, Antwerpen. - S. IM01.P04

Lentzen, M.; Thust, A.; Urban, K.
The Error of Aberration Measurements in HRTEM Using Zemlin Tableaus
Microscopy and Microanalysis, **10** (2004), 980 - 981

Lettinga, M. P.; Dhont, J. K. G.
Non-equilibrium phase behaviour of rod-like viruses under shear flow
Journal of Physics: Condensed Matter, **16** (2004), 38, s3929 - s3939

Lettinga, M. P.; Koenderink, G. H.; Kuipers, B. W. M.; Bessels, E.; Philipse, R. H.
Rotational dynamics of colloidal spheresprobed with fluorescence recovery after photobleaching
Journal of Chemical Physics, **120** (2004), 9, 4517 - 4529

Lettinga, M. P.; Wang, H.; Dhont, J. K. G.
Microstructural response of a near-critical colloid-polymer mixture to shear flow
Physical Review E, **70** (2004), 061405-1 - 061405-14

Lettinga, P. M.
Viruses as Colloidal Model Systems
Physics meets biology : from soft matter to cell biology ; lecture notes of the 35th Spring School of the Institut für Festkörperforschung / ed.: G. Gompper ... - Jülich, Forschungszentrum, 2004. - (Schriften des Forschungszentrums Jülich - Reihe Materie und Material / Matter and Material ; 19). - 3-89336-348-3. - S. C11.1 - C11.39

Levine, E.; Willmann, R. D.
Spontaneous symmetry breaking in a non-conserving two-species driven model
Journal of Physics A - Mathematical and General, **37** (2004), 3333 - 3352

Liatti, M.; Divin, Y.; Gubankov, V. N.; Urban, K.
Low - frequency noise in (001)-tilt $YBa_2Cu_3O_{7-x}$ grain - boundary Josephson junctions
6th European Conference on Applied Superconductivity, Sorrento, Italy / ed.: A. Andreone, G. P. Pepe, R. Christiano, G. Masullo. - 2004. - 0-7503-0981-4. - (IoP Conference series ; 181). - S. 3106 - 3111

Liebsch, A.
Single Mott transition in the multi-orbital Hubbard Model
Physical Review B, **70** (2004), 165103

Liu, C.; Klein, H.; Jung, P.
Embrittlement of RAFM EUROFER97 by Implanted Hydrogen
Journal of Nuclear Materials, **335** (2004), 77 - 82

Lookman, I. V.; Bowman, R. M.; Gregg, J. M.; Kut, J.; Rios, S.; Dawber, M.; Rüdiger, A.; Scott, J. F.
Thickness dependence of true phase transition temperatures in barium strontium titanate films
Journal of Applied Physics, **96** (2004), 555 - 562

Lookman, I. V.; Bowman, R. M.; Gregg, J. M.; Kut, J.; Rios, S.; Dawber, M.; Rüdiger, A.; Scott, J. F.
Thickness independence of true phase transition temperatures in barium strontium titanate films
Journal of Applied Physics, **96** (2004), 555

Lopez-Cabarcos, E.; Rubio-Retama, B. J.; Lopez-Ruiz, B.; Heinrich, M.; Fernandez-Barbero, A.
Small angle neutron scattering study of the structural modifications induced by the entrapped glucose oxidase in polyacrylamide microgels
Physica A, **344** (2004), 417

Lott, D.; Solina, D.; Almokhtar, M.; Mibu, K.; Schmidt, W.; Schreyer, A.
Modifications of the spin density wave of Cr in Fe/Cr multilayers by insertion of Sn studied by neutron diffraction
Physica B: Condensed Matter, **350** (2004), 1/3, Suppl. 1, E245 - E248

Lund, R.; Willner, L.; Stellbrink, J.; Radulescu, A.; Richter, D.
Role of interfacial tension for the structure of PEP-PEO polymeric micelles. A combined SANS and pendant drop tensiometry investigation
Macromolecules, **37** (2004), 9984 - 9993

Lund, R.; Willner, L.; Stellbrink, J.; Radulescu, A.; Richter, D.
Tuning of structure and kinetics of chain exchange in star-like PEP-PEO block copolymer micelles
Physica B: Condensed Matter, **350** (2004), 1/3, Suppl. 1, e909 - e912

Luysberg, M.; Houben, L.; Guzenko, V.; Calarco, R.
Aberration corrected microscopy on Cr implantation induced in GaN
Proceedings of the 13th European Microcopy Congress / ed.:G. van Tendeloo. - Belgian Society for Microscopy. - 2 (2004). - S. 423

Luysberg, M.; Hueging, N.; Urban, K.; Buca, D.; Holländer, B.; Mantl, S.; Mörschbächer, M.; Fichtner, P. F. P.; Loo, R.; Caymax, M.
In-situ TEM on He implantation induced defects in SiGe/Si
Proceedings of the 13th European Microscopy Congress / ed.: G. van Tendeloo. - Belgian Society for Microscopy. - 2 (2004). - S. 377

Magrez, A.; Schober, T.
Preparation, sintering, and water incorporation of proton conducting Ba0.99Zr0.8Y0.2O3-delta: comparison between three different synthesis techniques
Solid State Ionics, **175** (2004), 585 - 588

Mahajan, S.; Cho, B.-K.; Allgaier, J.; Fetters, L. J.; Coates, G. W.; Wiesner, U.
Synthesis of amphiphilic ABC triblock copolymers with PEO as the middle block
Macromolecular Rapid Communications, **25** (2004), 1889 - 1894

Malkinski, L.; Zhou, W. L.; He, J.; Celinski, Z.; Camley, R.; O'Keevan, T.; Yano, J.; Pivoda, T.; Vovk, A.; Hecker, M.; Schneider, C. M.; Szade, J.; Skrzypek, D.
Microstructure and magnetic properties of $Fe/KCoF_3$ thin films
Journal of Magnetism and Magnetic Materials, **272-276** (2004), Suppl. 1, e901 - e903

Mangiapia, G.; Accardo, A.; Locelso, F.; Tesauro, D.; Morelli, G.; Radulescu, A.; Paduano, L.
Mixed micelles composed of Peptides and Gadolinium complexes as tumor-specific contrast agents in MRI: a SANS study
Journal of Physical Chemistry B, **108** (2004), 17611 - 17617

Matthes, F.; Tong, L.; Schneider, C. M.
Spin-polarized photoemission spectroscopy of the MgO/Fe interface on GaAs(100)
Journal of Applied Physics, **95** (2004), 7240

Mavropoulos, P.; Galanakis, I.; Dederichs, P. N.
Multilayers of zinc-blende half-metals with semiconductors
Journal of Physics: Condensed Matter, **16** (2004), 4261 - 4272

Mavropoulos, P.; Papanikolaou, N.; Dederichs, P. N.
Korringa-Kohn-Rostoker Green-function formalism for ballistic transport
Physical Review B, **69** (2004), 125104

Mavropoulos, P.; Sato, K.; Zeller, R.; Dederichs, P. N.; Popescu, V.; Ebert, H.
Effect of the spin-orbit interaction on the band gap of half metals
Physical Review B, **69** (2004), 054424

Mavropoulos, Ph.; Galanakis, I.; Popescu, V.; Dederichs, P. N.
Influence of spin-orbit coupling on the band gap of Heusler alloys
Journal of Physics: Condensed Matter, **16** (2004), s5759 - s5762

McPhie, M. G.; Nägele, G.
Colloidal electrolyte friction: the effect of finite-sized electrolyte ions
Journal of Physics: Condensed Matter, **16** (2004), s4021 - s4038

Mehaddene, T.; Kentzinger, E.; Hennion, B.; Tanaka, K.; Numakura, H.; Marty, A.; Parasote, V.; Cadeville, M. C.; Zemirli, M.; Pierron-Bohnes, V.
Lattice dynamics and migration enthalpies in $CoPt_3$ and FePd
Physical Review B, **69** (2004), 024304-1 - 024304-13

Meinnel, J.; Grimm, H.; Hernandez, O.; Jansen, E.
Assignment of three methyl tunneling lines in a trichloromesitylene single crystal
Physica B: Condensed Matter, **350** (2004), 1/3, Suppl. 1, e459 - e462

Melnichenko, Y. B.; Wignall, G. D.; Cole, D. R.; Frielinghaus, H.
Density fluctuations near the liquid-gas critical point of a confined fluid
Physical Review E, **69** (2004), 057102

Meyer, R.; Waser, R.
Resistive donor-doped $SrTiO_3$ sensors: I, basic model for a fast sensor response
Sensors and Actuators B, **101** (2004), 335

Mezei, F.; Eccleston, R. S.; Tietze-Jaensch, H.
Instruments and User Support
The ESS Project Update / eds.: G. S. Bauer, K. Clausen, R. S. Eccleston, I. A. K. Gardner, F. Mezei, H. Tietze-Jaensch. - Bad Honnef, 2004. - Chapter 5, S. 5.1 - 5.22

Mi, S.; Grushko, B.
Investigation of the high-Al region of Al-Cu-Ru
Intermetallics, **12** (2004), 425 - 435

Mi, S.; Grushko, B.; Dong, C.; Urban, K.
Phase equilibrium in the vicinity of the Al-Ni-Ru decagonal phase
Journal of Non-Crystalline Solids, **334-335** (2004), 214 - 217

Mompiou, F.; Caillard, D.; Feuerbacher, M.
In-situ observation of dislocation motion in icosahedral Al-Pd-Mn quasicrystals
Philosophical Magazine, **84** (2004), 2777

Monkenbusch, M.; Wischnewski, A.; Willner, L.; Richter, D.
Direct observation of the transition from free to constrained single segment motion in entangled polymer melts
Physica B: Condensed Matter, **350** (2004), 214

Mörschbächer, M. J.; da Silva, D. L.; Fichtner, P. F. P.; Oliviera, E.; Behar, M.; Zawislak, F. C.; Holländer, B.; Luysberg, M.; Mantl, S.; Loo, R.; Caymax, M.
Microstructure evolution effects of helium redistribution in as-implanted silicon and $Si_{0.8}Ge_{0.2}$/Si heterostructures
Nuclear Instruments and Methods in Physics Research Section B, **219-220** (2004), 703 - 707

Nagarajan, V.; Prasertchoung, S.; Zhao, T.; Zheng, H.; Ouyang, J.; Ramesh, R.; Tian, W.; Pan, X. Q.; Kim, D. M.; Eom, C. B.; Kohlstedt, H.; Waser, R.
Size effects in ultrathin epitaxial ferroelectric heterostructures
Applied Physics Letters, **84** (2004) 5225

Narros, A.; Alvarez, F.; Arbe, A.; Colmenero, J.; Richter, D.; Farago, B.
Hydrogen motions in the alpha relaxation regime of poly(vinyl ethylene): A molecular dynamics simulation and neutron scattering study
Journal of Chemical Physics, **121** (2004), 3282 - 3294

Narros, A.; Alvarez, F.; Arbe, A.; Colmenero, J.; Richter, D.; Farago, B.
Self-motion of protons in the α-relaxation of poly(vinylethylene):a neutron scattering and MD-simulation study
Physica B: Condensed Matter, **350** (2004), 1/3, Suppl. 1, e1091 - e1093

Nepijko, S. A.; Oelsner, A.; Krasyuk, A.; Gloskovskii, A.; Sedov, N. N.; Schneider, C. M.; Schönhense, G.
Lateral resolving power of a time-of-flight photoemission electron microscope
Applied Physics A, **78** (2004), 47

Niu, A. Z.; Stellbrink, J.; Allgaier, J.; Willner, L.; Richter, D.; Koenig, B. W.; Gondorf, M.; Willbold, S.; Fetters, L. J.; May, R. P.
A New View of the Anionic Diene Polymerization Mechanism
Macromolecular Symposia, **215** (2004), 1 - 15

Niu, A. Z.; Stellbrink, J.; Allgaier, J.; Willner, L.; Richter, D.; Radulescu, A.; Koenig, B. W.; Gondorf, M.; Willbold, S.; Fetters, L. J.; May, R. P.
Real-time SANS and 1H-NMR studies during 'living' anionic polymerization of butadiene in hydrocarbon media
Physica B: Condensed Matter, **350** (2004), 1/3, Suppl. 1, e921 - e925

Noguchi, H.; Gompper, G.
Fluid Vesicles with Viscous Membranes in Shear Flow
Physical Review Letters, **93** (2004), 258102

Nägele, G.
The Physics of Colloidal Soft Matter
Warsaw, Polish Academy of Sciences Publishing, 2004
Institute of Fundamental Technological Research . Lecture Notes ; 14

Nünighoff, K.; Conrad, H.; Filges, D.; Goldenbaum, F.; Neef, R.-D.; Pohl, Ch.; Schaal, H.; Stelzer, H.; Tietze-Jaensch, H.; Paul, N.; Wohlmuther, W.; Ninaus, W.; Smirnov, A.
The JESSICA Experiment - Part 1: Improvements of the JESSICA-Experiment
Advanced Cold Moderators : ACoM-6 ; proceedings of the 6th International Workshop on Advanced Cold Moderators held at Forschungszentrum Jülich from 11 - 13 September 2002 / ed.: H. Conrad. - Jülich, 2004. - (Schriften des Forschungszentrums Jülich . Reihe Materie und Material/Matter and Materials ; 20). - 3-89336-363-7. - S. 155 - 160

Nünighoff, K.; Pohl, Ch.; Bollini, V.; Bubak, A.; Conrad, H.; Filges, D.; Glückler, H.; Goldenbaum, F.; Hansen, G.; Lensing, B.; Neef, R. D.; Paul, N.; Prasuhn, D.; Pysz, K.; Schaal, H.; Soltner, H.; Stelzer, H.; Tietze-Jaensch, H.; Bernnat, W.; Keinert, J.; Mattes, M.; Ninaus, W.; Koulikov, S.; Smirnov, A.; Wohlmuther, M.
Ice moderator experiments at very low temperatures
European Physical Journal A, **22** (2004), 519 - 528

Oelsner, A.; Krasyuk, A.; Fecher, G. H.; Schneider, C. M.; Schönhense, G.
Image enhancement in photoemission electron microscopy by means of imaging time-of-flight analysis
Journal of Electron Spectroscopy and Related Phenomena, **137-140** (2004), 757

Oelsner, A.; Krasyuk, A.; Neeb, D.; Nepijko, S.; Kuksov, A.; Schneider, C. M.; Schönhense, G.
Magnetization changes visualized using photoemission electron microscopy
Journal of Electron Spectroscopy and Related Phenomena, **137-140** (2004), 751

Ohl, M.; Monkenbusch, M.; Richter, D.; Pappas, C.; Lieutenant, K.; Krist, T.; Zsigmond, G.; Mezei, F.
The high-resolution neutron spin-echo spectrometer for the SNS with $\tau \geq 1$ μs
Physica B: Condensed Matter, **350** (2004), 1/3, 147 - 150

Ohly, C.; Hoffmann-Eifert, S.; Waser, R.
Nanocrystalline alkaline earth titanate and their conductivity characteristics under changing oxygen ambients
Journal of Electroceramics, **13** (2004), 599 - 603

Oppeneer, P.; Liebsch, A.
Ultra-fast demagnetization in Ni: Theory of magneto-optics for non-equilibrium electron distributions
Journal of Physics: Condensed Matter, **16** (2004), 5519

Paessens, M.; Schütz, G. M.
Phase transitions and correlations in the bosonic pair contact process with diffusion: Exact results
Journal of Physics A - Mathematical and General, **37** (2004), 4709 - 4722

Paessens, M.; Schütz, G. M.
Reaction fronts in stochastic exclusion models with three-site interactions
New Journal of Physics, **6** (2004), 120

Pascual, J. I.; Bihlmayer, G.; Koroteev, Yu. M.; Rust, H. P.; Ceballos, G.; Hansmann, M.; Horn, K.; Chulkov, E. V.; Blügel, S.; Echenique, P. M.; Hofmann, Ph.
Role of Spin in Quasiparticle Interference
Physical Review Letters, **93** (2004), 196802

Patkowski, A.; Gapinski, J.; Meier, G.
Dynamics of supercooled van der Waals liquid under pressure. A dynamic light scattering study
Colloid and Polymer Science, **282** (2004), 874 - 881

Paul, A.; Bürgler, D. E.; Luysberg, M.; Grünberg, P.
Enhanced exchange bias due to an ultra-thin, non-magnetic insulator spacer layer
Europhysics Letters, **68** (2004), 233 - 239

Paul, A.; Kentzinger, E.; Rücker, U.; Bürgler, D. E.; Grünberg, P.
Sequence, symmetry, and magnetic fluctuations of the magnetization reversal in exchange-biased multilayers
Physical Review B, **70** (2004), 224410-1 - 224410-5

Pebler, J.; Frommen, Ch.; Mangold, M.; Stief, R.; Krimmel, A.; van de Kamp, R.; Ohl, M.; Regnault, L.-P.
Comparison of the non-linear spin dynamics in antiferromagnetic chain compounds Na_2MnF_5 and $(ND_4)_2MnF_5$
Zeitschrift für Anorganische und Allgemeine Chemie, **630** (2004), 829 - 840

Persson, B. N. J.; Albohr, O.; Creton, C.; Peveri, V.
Contact area between a viscoelastic solid and a hard, randomly rough, substrate
Journal of Chemical Physics, **120** (2004), 18, 8779 - 8793

Persson, B. N. J.; Mugele, F.
Squeeze-out and wear: fundamental principles and applications
Journal of Physics: Condensed Matter, **16** (2004), 10, R295 - R356

Persson, B. N. J.; Tartaglino, U.; Tosatti, E.; Albohr, O.
Rubber Friction on Wet Rough Substrates at Low Sliding Velocity: The Sealing Effect
Kautschuk Gummi Kunststoffe, **57** (2004), 10, 532 - 537

Persson, B. N. J.; Tartaglino, U.; Tosatti, E.; Ueba, H.
Electronic friction and liquid-flow-induced voltage in nanotubes
Physical Review B, **69** (2004) 23, 235410

Peter, F.; Szot, K.; Waser, R.; Reichenberg, B.; Tiedke, S.; Szade, J.
Piezoresponse in the light of surface adsorbates: Relevance of defined surface conditions for perovskite materials
Applied Physics Letters, **85** (2004), 2896

Pipich, V.; Schwahn, D.; Willner, L.
The Lifshitz line of the disordered and microemulsion phase in an A/B/A-B three component homopolymer/diblock copolymer mixture
Physica B: Condensed Matter, **350** (2004), 1/3, Suppl. 1, e897 - e900

Pithan, C.; Shiratori, Y.; Magrez, A.; Dornseiffer, J.; Haegel, F.-H.
Nanocrystalline lead free piezoceramic $(K_x, Na_{1-x})NbO_3$ derived from microemulsion mediated synthesis
Ceramic Transactions, **167** (2004), 41

Pohl, Ch.; Conrad, H.; Filges, D.; Goldenbaum, F.; Neef, R.-D.; Nünighoff, K.; Schaal, H.; Stelzer, H.; Tietze-Jaensch, H.; Paul, N.; Wohlmuther, W.; Ninaus, W.; Smirnov, A.
The JESSICA Experiment - Part II: Results from the JESSICA-Experiment
Advanced Cold Moderators : ACoM-6 ; proceedings of the 6th International Workshop on Advanced Cold Moderators held at Forschungszentrum Jülich from 11 - 13 September 2002 / ed.: H. Conrad. - Jülich, 2004. - (Schriften des Forschungszentrums Jülich . Reihe Materie und Material/Matter and Materials ; 20). - 3-89336-363-7. - S. 175 - 181

Pohlmeier, A.; Lustfeld, H.
Reaction rates of heavy metal ions at geoethite: relaxation experiments and modeling
Journal of Colloid and Interface Science, **269** (2004), 131 - 142

Popescu, V.; Ebert, H.; Papanikolaou, N.; Zeller, R.; Dederichs, P. N.
Spin-dependent Transport in Ferromagnet/Semiconductor/Ferromagnet Junctions: a Fully Relativistic Approach
Journal of Physics: Condensed Matter, **16** (2004), 48, s5579 - s5586

Popkov, V.
Infinite reflections of shock fronts in driven diffusive systems with two species
Journal of Physics A - Mathematical and General, **37** (2004), 1545 - 1557

Popkov, V.; Schütz, G. M.
Why spontaneous symmetry breaking disappears in a bridge system with PDE-friendly boundaries
Journal of Statistical Mechanics : Theory and Experiment, (2004), P12004

Poppe, U.; Faley, M.; Zimmermann, E.; Glaas, W.; Breunig, I.; Speen, J. R.; Jungbluth, B.; Soltner, H.; Halling, H.; Urban, K.
High temperature superconductor dc-SQUID microscope with a soft magnetic flux guide
Superconductor Science and Technology, **17** (2004), s191 - s195

Postnikov, A. V.; Chiuzbaian, S. G.; Neumann, M.; Blügel, S.
Electron spectroscopy and density-functional study of 'ferric wheel' molecules
Journal of Physics and Chemistry of Solids, **65** (2004), 4, 813 - 817

Prager, M.
Probing lattice distortions in mixed CH_3I_{1-c} Br_c by methyl rotational tunneling
Journal of Chemical Physics, **120** (2004), 1881 - 1885

Prager, M.; Kirstein, O.
The lattice and rotational dynamics of the methyl halides described by pair potentials based on universal force fields
Journal of Chemical Physics, **120** (2004), 5199 - 5207

Prager, M.; Pieper, J.; Buchsteiner, A.; Desmedt, A. V.
Methyl rotational potentials as a probe of the cage potential surface in methyl iodide clathrate
Physica B: Condensed Matter, **350** (2004), 1/3, Suppl., 1, e399 - e402

Prager, M.; Pieper, J.; Buchsteiner, A.; Desmedt, A. V.
Probing adsorption sites in a cubic II water clathrate cage by methyl group rotation of CH_3J guest molecules
Journal of Physics: Condensed Matter, **16** (2004), 7045

Prinz, D.; Pyckhout-Hintzen, W.; Littke, R.
Development of the meso- and macroscopic structure of coals with rank as analyzed with small
Fuel, **83** (2004), 547 - 556

Progrebnyakov, A. V.; Xi, X. X.; Redwing, J. M.; Vaithyanathan, V.; Schlom, D. G.; Soukiassian, A.; Mi, E. A.; Jia, C. L.; Giencke, J. E.; Eom, C. B.; Chen, J.; Hu, Y. F.; Cui, Y.; Qi, L.
Properties of MgB_2 thin films with carbon doping
Applied Physics Letters, **85** (2004), 2017 - 2019

Radulescu, A.; Mathers, R. T.; Coates, G. W.; Richter, D.; Fetters, L. J.
A SANS study of the self-assembly in solution of syndiotactic polypropylene homopolymers, syndiotactic polypropylene-block-poly(ethylene-co-propylene) diblock copolymers, and an alternating atactic-isotactic multisegment polypropylene
Macromolecules, **37** (2004), 6962 - 6971

Radulescu, A.; Schwahn, D.; Monkenbusch, M.; Fetters, L. J.; Richter, D.
Structural study of the influence of partially crystalline poly(ethylene-butene) random copolymers on paraffin crystallization in dilute solutions
Journal of Polymer Science B - Polymer Physics, **42** (2004), 3113 - 3132

Radulescu, A.; Schwahn, D.; Monkenbusch, M.; Richter, D.; Fetters, L. J.
The interaction mechanism of triacontane praffin with semi-crystalline poly(ethylene-butene) random copolymers in dilute solution studied with SANS
Physica B: Condensed Matter, **350** (2004), 1/3, Suppl. 1, e927 - e930

Rakos, A.; Schütz, G. M.
Exact shock measures and steady state selection in a driven diffusive system with two conserved densities
Journal of Statistical Physics, **117** (2004), 55 - 76

Rathgeber, S.; Pakula, T.; Urban, V.
Structure of star-burst dendrimers: A comparison between small angle x-ray scattering and computer simulation results
Journal of Chemical Physics, **121** (2004), 8, 3840 - 3853

Regnery, S.; Ehrhart, P.; Fitsilis, F.; Waser, R.; Ding, Y.; Jia, C. L.; Schumacher, M.; Schienle, F.
(Ba,Sr)TiO_3 thin film growth in a batch processing MOCVD reactor
Journal of the European Ceramic Society, **24** (2003), 2, 271-276

Regnery, S.; Thomas, R.; Haselier, H.; Ehrhart, P.; Waser, R.; Lehnen, P.; Miedl, S.; Schumacher, M.
Nucleation and growth of thin (Ba, Sr) TiO_3 films in a MOCVD reactor
Integration of advanced micro- and nanoelectronic devices : critical issues and solutions / ed.: J. Morais ... - Warrendale, PA, 2004. - (Materials Research Society Symposium proceedings ; 811). - 1-55899-761-X. - S. D9.7.1 - D9.7.6

Reichenberg, B.; Szot, K.; Schneller, T.; Breuer, U.; Tiedke, S.; Waser, R.
Inhomogeneous Local Conductivity Induced by Thermal Reduction in $BaTiO_3$ Thin Films and Single Crystals
Integrated Ferroelectrics, **61** (2004), 43 - 49

Richter, D.; Monkenbusch, M.; Willner, L.; Arbe, A.; Colmenero, J.
Direct observation of the crossover from glassy alpha-relaxation to Rouse dynamics in a polymer melt
Europhysics Letters, **66** (2004), 239 - 245

Ripoll, M.; Mussawisade, K.; Winkler, R. G.; Gompper, G.
Low-Reynolds-number hydrodynamics of complex fluids by multi-particle-collision dynamics
Europhysics Letters, **68** (2004), 106 - 112

Roelofs, A.; Szot, K.; Waser, R.
Domain switching and self-polarization in perovskite thin films
Nanoscale phenomena in ferroelectrics thin films / ed.: S. Hong. - Dordrecht, Kluwer Academic Publishers, 2004. - 1-4020-7630-4 . - S. 135 - 155

Rottländer, P.; Kozielewski, T.; Prager, M.; Richter, D.
Backscattering spectrometer RSSM for the FRM-II reactor in Munich
Physica B: Condensed Matter, **350** (2004), 1/3, Suppl. 1, e823 - e825

Ruskov, T.; Asenov, S.; Spirov, I.; Garcia, C.; Mönch, I.; Graff, A.; Kozhuharova, R.; Leonhardt, A.; Mühl, T.; Ritschel, M.; Schneider, C. M.; Groudeva-Zotova, S.
Mössbauer transmission and back-scattered conversion electron study of Fe nanowires encapsulated in multi-walled carbon nanotubes
Journal of Applied Physics, **96** (2004), 7514

Russina, A. I.; Triolo, A.; Aihara, Y.; Telling, M. T. F.; Grimm, H.
Quasi-elastic neutron scattering investigation of dynamics in polymer electrolytes
Macromolecules, **37** (2004), 8653 - 8660

Rytkönen, K.; Akola, J.; Manninen, M.
Sodium atoms and clusters on graphite: a density functional study
Physical Review B, **69** (2004), 205404

Rücker, U.; Demokritov, S. O.; Nassar, J.; Grünberg, P.
Magnetic interlayer coupling across semiconducting EuS layers
Europhysics Letters, **66** (2004), 5, 736 - 742

Rüdiger, A.
Lateral scaling in ferroelectric nanostructures
Nanofair 2004 : New Ideas for Industry -International Symposium Karlsruhe, 23./24.11.2004. - Düsseldorf, 2004. - (VDI-Berichte ; 1839). - 3-18-091839-X. - S. 43 - 46

Sacharow, L.; Morgenstern, M.; Bihlmayer, G.; Blügel, S.
High spin polarization at the interface between a Fe monolayer and InAs(110)
Physical Review B, **69** (2004), 085317

Sager, W.; Blokhuis, E. M.
Self-Assembly
Physics meets biology : from soft matter to cell biology ; lecture notes of the 35th Spring School of the Institut für Festkörperforschung / ed.: G. Gompper ... - Jülich, Forschungszentrum, 2004. - (Schriften des Forschungszentrums Jülich - Reihe Materie und Material / Matter and Material ; 19). - 3-89336-348-3. - S. A3.1 - A3.29

Samoilov, V. N.; Persson, B. N. J.
Squeezing wetting and nonwetting liquids
Journal of Chemical Physics, **120** (2004), 4, 1997 - 2004

Samoilov, V. N.; Sivebaek, I. M.; Persson, B. N. J.
The effect of surface roughness on the adhesion of solid surfaces for systems with and without liquid lubricant
Journal of Chemical Physics, **121** (2004), 19, 9639 - 9647

Sato, K.; Schweika, W.; Dederichs, P. N.; Katayama-Yoshida, H.
Low-temperature ferromagnetism in (Ga, Mn)N: Ab initio calculations
Physical Review B, **70** (2004), 201202-1 - 201202-4

Sato, K.; Dederichs, P. N.; Katayama-Yoshida, H.; Kudrnovsky, J.
Exchange interactions and Curie temperatures in diluted magnetic semiconductor
Journal of Magnetism and Magnetic Materials, **272-276** (2004), 1983 - 1984

Satyanarayana, S. V. M.; Baumgaertner, A.
Shape and motility of a model cell: a computational study
Journal of Chemical Physics, **121** (2004), 4255 - 4265

Schall, P.; Feuerbacher, M.; Urban, K.
Plasticity of decagonal Al73Ni10Co17 quasicrystals
Quasicrystals 2003 - Preparation, Properties and Applications. - Warrendale, PA, MRS, 2004. - (Materials Research Society Symposium proceedings ; 805). - 1-55899-743-1. - S. LL 5.5.1.

Schall, P.; Feuerbacher, M.; Urban, K.
Dislocation in basic-nickel Al-Ni-Co single quasicrystals
Philosophical Magazine Letters, **84** (2004), 471

Schall, P.; Feuerbacher, M.; Urban, K.
Dislocations and dislocation reactions in decagonal Al-Ni-Co quasicrystals
Physical Review B, **69** (2004), 134105

Schall, P.; Feuerbacher, M.; Urban, K.
Plastic deformation of decagonal $Al_{73}Ni_{10}Co_{17}$ single quasicrystals
Philosophical Magazine, **84** (2004), 7, 705 - 718

Schlapp, M.; Hoelzel, M.; Gilles, C. G.; Ioffe, A.; Brückel, T.; Fuess, H.; von Seggern, H.
Novel type of neutron image plates based on KCl:Eu^{2+} - LiF
Physica B: Condensed Matter, **350** (2004), Suppl. 1, e861 - e864

Schlapp, M.; Conrad, H.; von Seggern, H.
Pixelated Neutron Image Plates
Journal of Physics D - Applied Physics, **37** (2004), 2607 - 2612

Schmidt, W.; Rheinstädter, M.; Raymond, S.; Ohl, M.
UFO - a multianalyser option for IN_{12}
Physica B: Condensed Matter, **350** (2004), 1/3, Suppl. 1, E849 - E851

Schmitz, T.; Prume, K.; Reichenberg, B.; Roelofs, A.; Waser, R.; Tiedke, S.
In-situ compensation of the parasitic capacitance for nanoscale hysteresis measurements
Journal of the European Ceramic Society, **24** (2004), 1145

Schneider, C. M.; Kozhuharova, R.; Groudevazotova, S.; Zhao, B.; Mühl, T.; Mönch, I.; Vinzelberg, H.; Ritschel, M.; Leonhardt, A.; Fink, J.
Nanotube spintronics: Magnetic systems based on carbon nanotubes
Frontiers of multifunctional integrated nanosystems / eds.: E. Buzaneva, P. Scharff. - Kluwer Acad. Publ., 2004. - (NATO science series ; 152). - 1-402-02171-2. - S. 359 - 378

Schneider, C. M.; Kuksov, A.; Krasyuk, A.; Oelsner, A.; Neeb, D.; Nepijko, S. A.; Schönhense, G.; Mönch, I.; Kaltofen, R.; Morais, J.; de Nadai, C.; Brookes, N. B.
Incoherent magnetization rotation observed in subnanosecond time-resolving x-ray photoemission electron microscopy
Applied Physics Letters, **85** (2004), 13, 2562 - 2564

Schneider, C. M.; Zhao, B.; Kozhuharova, R.; Groudeva-Zotova, S.; Mühl, T.; Ritschel, M.; Mönch, I.; Vinzelberg, H.; Elefant, D.; Graff, A.; Leonhardt, A.; Fink, J.
Towards molecular spintronics: magnetotransport and magnetism in carbon nanotube-based systems
Diamond and Related Materials, **13** (2004), 215 - 220

Schneider, St.; Jolly, T. W.; Kohlstedt, H.; Waser, R.
Use of reactive gases with broad-beam radio frequency ion sources for industrial applications
Journal of Vacuum Science and Technology A, **22** (2004), 1493 - 1499

Schober, H. R.
Diffusion in a model metallic glass: Heterogeneity and ageing
Physical Chemistry Chemical Physics, **6** (2004), 3654 - 3658

Schober, H. R.
Vibrations and relaxations in a soft sphere glass: boson peak and structure factors
Journal of Physics: Condensed Matter, **16** (2004), s2659 - s2670

Schober, H. R.; Ruocco, G.
Size effects and quasilocalized vibrations
Philosophical Magazine, **84** (2004), 13/16, 1361 - 1372

Schober, T.; Magrez, A.
Sol-gel Preparation of Selected High Temperature Proton Conductors
Ionics, **10** (2004), 17

Schober, T.; Ringel, H.
Proton Conducting Ceramics: Recent Advances
Ionics, **10** (2004), 391 - 395

Schwahn, D.; Balz, M.; Tremel, W.
Crystallization of the $CaCO_3$ mineral in the presence of the protein ovalbumin
Physica B: Condensed Matter, **350** (2004), 1/3, Suppl. 1, e947 - e949

Schwartz, R. W.; Schneller, T.; Waser, R.
Chemical solution deposition of electronic oxide films
Comptes Rendus Chimie, **7** (2004), 433

Schweika, W.
Scattering Experiments
Physics meets biology : from soft matter to cell biology ; lecture notes of the 35th Spring School of the Institut für Festkörperforschung / ed.: G. Gompper ... - Jülich, Forschungszentrum, 2004. - (Schriften des Forschungszentrums Jülich - Reihe Materie und Material / Matter and Material ; 19). - 3-89336-348-3. - S. B1.1 - B1.29

Schweika, W.; Reichert, H.; Babik, W.; Klein, O.; Engemann, S.
Strain-induced incomplete wetting at CuAu (001)-surfaces
Physical Review B, **70** (2004), 041401-1 - 041401-4

Schönhals, A.; Goering, H.; Schick, Ch.; Frick, B.; Zorn, R.
Glass transition of polymers confined to nanoporous glasses
Colloid and Polymer Science, **282** (2004), 882 - 891

Schönhals, A.; Goering, H.; Schick, Ch.; Frick, B.; Zorn, R.
Poly(methyl phenyl siloxane) in Random Nanoporous Glasses: Molecular Dynamics and Structure
Dynamics in small confining systems : Materials Research Society Fall Meeting, Boston, Mass., 30.11. - 05.12.2003. - Warrendale, PA, 2004. - (Materials Research Society Symposium proceedings ; 790). - 1-55899-728-8. - S. 9.3.1-6

Schönherr, G.; Schütz, G. M.
Exclusion process for particles of arbitrary extension: Hydrodynamic limit and algebraic properties
Journal of Physics A - Mathematical and General, **37** (2004), 8215 - 8231

Schütz, G.
Statistical Mechanics
Physics meets biology : from soft matter to cell biology ; lecture notes of the 35th Spring School of the Institut für Festkörperforschung / ed.: G. Gompper ... - Jülich, Forschungszentrum, 2004. - (Schriften des Forschungszentrums Jülich - Reihe Materie und Material / Matter and Material ; 19). - 3-89336-348-3. - S. A1.1 - A1.37

Schütz, G. M.; Trimper, S.
Elephants can always remember: Exact long-range memory effects in a non-Markovian random walk
Physical Review E, **70** (2004), 045101(R)

Schütz, G. M.; Willmann, R. D.; Grosskinsky, S.
Spontaneous symmetry breaking in a driven two-species lattice gas
Workshop: Large Scale Stochastic Dynamics, Oberwolfach, 29.8. - 4.9. 2004. - Oberwolfach, Mathematisches Forschungsinstitut, 2004. - (Oberwolfach Report ; 43/2004). - S. 33 - 35

Shadrin, P.; Jia, C. L.; Divin, Y.
Faceting of Grain Boundary and Critical Current in (001)-tilt $YBa_2Cu_3O_{7-x}$ Bicrystal Junctions
6th European Conference on Applied Superconductivity, Sorrento, Italy / ed.: A. Andreone, G. P. Pepe, R. Christiano, G. Masullo. - 2004. - 0-7503-0981-4. - (IoP Conference series ; 181). - S. 3053 - 3058

Shiratori, Y.; Magrez, A.; Pithan, C.
Phase transformation of $KNaNb_2O_6$ induced by size effect
Chemical Physics Letters, **391** (2004), 288

Shirotov, V. V.; Divin, Y. Y.
A Frequency-Selective Josephson Detector of Pulsed Subterahertz Radiation
Journal of Communications Technology and Electronics, **49** (2004), 9, 1066 - 1069

Stellbrink, J.; Rother, G.; Laurati, M.; Lund, R.; Willner, L.; Richter, D.
Poly(ethylene-alt-propylene)-poly(ethylene oxide) diblock copolymer micelles: a colloidal model system with tunable softness
Journal of Physics: Condensed Matter, **16** (2004), s3821 - s3834

Steriotis, Th. A.; Stefanopoulos, K. L.; Kanellopoulos, N. K.; Mitropoulos, A. Ch.; Hoser, A.
The structure of adsorbed CO2 in carbon nanopores: a neutron diffraction study
Colloids and Surfaces A:Physicochemical and Engineering Aspects, **241** (2004), 239 - 244

Strempfer, J.; Rütt, U.; Bayrakci, S. P.; Brückel, Th.; Jauch, W.
Magnetic properties of transition metal fluorides MF_2 (M = Mn, Fe, Co, Ni) via high-energy photon diffraction
Physical Review B, 69 (2004), 014417-1 - 014417-9

Su, Y.; Istomin, K.; Wermeille, D.; Fattah, A.; Foucart, P.; Meuffels, P.; Hupfeld, D.; Brückel, Th.
Re-examination of charge and orbital ordering in lightly doped La1-xSrxMnO3 by X-ray scattering
Journal of Magnetism and Magnetic Materials, **272-276** (2004), Suppl. 1, e291 - e292

Tappe, S.; Bottger, U.; Waser, R.
Electrostrictive resonances in $(Ba_{0.7}Sr_{0.3})TiO_3$ thin films at microwave frequencies
Applied Physics Letters, **85** (2004), 624

Tillmann, R. G. E.; Hüging, N.; Trinkaus, H.; Luysberg, M.; Urban, K.
Quantitative Transmission Electron Microscopy Analysis of the Pressure of Helium-Filled Nano-Cracks in Implanted Silicon
Microscopy and Microanalysis, **10** (2004), 199 - 214

Tillmann, R. G. E.; Thust, A.; Urban, K.
Spherical Aberration Correction in Tandem with Exit-Plane Wave Function Reconstruction: Interlocking Tools for the Atomic Scale Imaging of Lattice Defects in GaAs
Microscopy and Microanalysis, **10** (2004), 185 - 198

Tuinier, R.
Protein-Polymer Mixtures
Physics meets biology : from soft matter to cell biology ; lecture notes of the 35th Spring School of the Institut für Festkörperforschung / ed.: G. Gompper ... - Jülich, Forschungszentrum, 2004. - (Schriften des Forschungszentrums Jülich - Reihe Materie und Material / Matter and Material ; 19). - 3-89336-348-3. - S. C4.1 - C4.32

Tuinier, R.; Fleer, G. J.
Concentration and Solvency Effects on the Excess Amount and Surface Free Energy of a Colloidal Particle in a Solution of Nonadsorbing Polymer
Macromolecules, **37** (2004), 8754 - 8763

Tuinier, R.; Fleer, G. J.
Concentration and Solvency Effects on the Pair Interaction between Colloidal Particles in a Solution of Nonadsorbing Polymer
Macromolecules, **37** (2004), 8764 - 8772

Urban, K.; Feuerbacher, M.
Structurally complex alloy phases
Journal of Non-Crystalline Solids, **143** (2004), 334 - 335

Urban, K.; Feuerbacher, M.
Structurally complex alloy phases
Science, **334-335** (2004), 143 - 150

Vangeyte, P.; Leyh, B.; Heinrich, M.; Grandjean, J.; Bourgaux, C.; Jerome, R.
Self-assembly of poly(ethylene oxide)-b-poly(e-caprolactone) copolymers in aqueous solution
Langmuir, **20** (2004), 8442 - 8451

Vasco, E.; Dittmann, R.; Karthäuser, S.; Waser, R.
Fabrication of stress-induced $SrRuO_3$ nanostructures by pulsed laser deposition
Applied Physics A, **79** (2004), 1461

Voigt, J.; Kentzinger, E.; Rücker, U.; Wermeille, D.; Hupfeld, D.; Schweika, W.; Schmidt, W.; Brückel, Th.
Direct observation of the interlayer exchange coupling mechanism in a magnetic [Er/Tb] multilayer
Europhysics Letters, **65** (2004), 4, 560 - 566

Volokitin, A. I.; Persson, B. N. J.
Resonant photon tunneling enhancement of the radiative heat transfer
Physical Review B, **69** (2004) 4, 045417

von Bergmann, K.; Bode, M.; Kubetzka, A.; Heide, M.; Blügel, S.; Wiesendanger, R.
Spin-Polarized Electron Scattering at Single Oxygen Adsorbates on a Magnetic Surface
Physical Review Letters, **92** (2004), 4, 046801

Walter, G.; Hoppe, U.; Vogel, J.; Hartmann, P.; Goerigk, G.
A structural study of anomalous phosphate glasses
Proceedings of the XX International Conference on Glass, Kyoto, Japan. - 2004. - S. 1 - 6

Wang, H.; Elsebrock, R.; Schneller, T.; Waser, R.; Yao, X.
Bismuth zinc niobate ($Bi_{1.5}ZnNb_{1.5}O_7$) ceramics derived from metallo-organic decomposition precursor solution
Solid State Communications, **132** (2004), 481

Waser, R.; Böttger, U.; Grossmann, M.
Static and dynamic properties of domains
Ferroelectric Random Access Memories / ed.: , H. Ishiwara ... - Springer, Berlin, 2004. - (Topics in Applied Physics ; 93). - 3-540-40718-9. - S. 31 - 45

Waser, R.; Rüdiger, A.
Pushing towards the digital storage limit
Nature Materials, **3** (2004), 81 - 82

Wedler, G.; Schneider, C. M.; Trampert, A.; Koch, R.
Strain relief of heteroepitaxial bcc-Fe(001) films
Physical Review Letters, **93** (2004), 236101

Wiebe, J.; Sacharow, L.; Wachowiak, A.; Bihlmayer, G.; Heinze, S.; Blügel, S.; Morgenstern, M.; Wiesendanger, R.
Scanning tunneling spectroscopy on Co(0001):Spectroscopic signature of stacking faults and dislocation lines
Physical Review B, **70** (2004), 035404

Wiegand, S.
Thermal diffusion in liquid mixtures and polymer solutions
Journal of Physics: Condensed Matter, **16** (2004), R357 - R379

Winkler, R. G.
Structure of Polyelectrolyte Solutions: Influence of Salt and Chain Flexibility
9th Dresden Polymer Discussion : Polyelectrolytes / ed.: U. Scheler. - Weinheim, Wiley-VCH, 2004. - 3-527-31044-4. - S. 55 - 70

Winkler, R. G.
Universal properties of complexes formed by two oppositely charged flexible polyelectrolytes
New Journal of Physics, **6** (2004), 11

Winkler, R. G.; Mussawisade, K.; Ripoll, M.; Gompper, G.
Rod-like Colloids and Polymers in Shear Flow: A Multi-Particle-Collision Dynamics Study
Journal of Physics: Condensed Matter, **16** (2004), s3941 - s3954

Wischnewski, A.; Zamponi, M.; Monkenbusch, M.; Willner, L.; Pyckhout-Hintzen, W.; Richter, D.; Likhtman, A. E.; McLeish, T. C. B.; Farago, B.
Molecular observation of contour length fluctuations in polymer melts
Physica B: Condensed Matter, **350** (2004), 193

Wortmann, D.; Bihlmayer, G.; Blügel, S.
Ab initio calculations of interface effects in tunnelling through MgO barriers on Fe(100)
Journal of Physics: Condensed Matter, **16** (2004), 5819 - 5822

Woudenberg, F. C. M.; Sager, W. F. C.; ten Elshof, J. E.; Verweij, H.
Nanostructured Dense ZrO_2 Thin Films from Nanoparticles Obtained by Emulsion Precipitation
Journal of the American Ceramic Society, **87** (2004), 8, 1430 - 1435

Wu, C. H.; Jones, G. J.
Stability and structure of Li_nH molecules (n=3-6): Experimental and density functional study
Journal of Chemical Physics, **120** (2004), 5128 - 5132

Wunnicke, O.; Mavropoulos, P.; Zeller, R.; Dederichs, P. N.
Ballistic spin injection from Fe into ZnSe(001), (111), and (110), and into GaAs(001)
Journal of Physics: Condensed Matter, **16** (2004), 4643 - 4659

Yurechko, M.; Grushko, B.; Velikanova, T. Ya.; Urban, K.
A comparative study of the Al-Co-Pd and Al-Co-Ni alloy systems
Journal of Alloys and Compounds, **367** (2004), 20 - 24

Yurechko, M.; Grushko, B.; Velikanova, T. Ya.; Urban, K.
Ternary Extensions in Al-Pd-Mn (Fe,Co)
Phase Diagrams in Materials Science : proceedings of the 6th Internatioal School-Conference PDMS VI 2001, 14.10.-20.10.01 / ed.: T. Ya. Velikanova. - 2004. - 3-932120-45-0. S. 92 - 97

Zeller, R.
An elementary derivation of Lloyd's formula valid for full-potential multiple-scattering theory
Journal of Physics: Condensed Matter, **16** (2004), 36, 6453 - 6468

Zhao, X.; Liu, Y.; Inoue, S.; Suzuki, T.; Jones, G. J.; Ando, Y.
Smallest carbon nanotube is 3 Å in diameter
Physical Review Letters, **92** (2004), 125502

Zheng, J. C.; Huan, C. H. A.; Wee, A. T. S.; van Hove, M. A.; Fadley, C. S.; Shi, F. J.; Rotenberg, E.; Barman, S. R.; Paggel, J. J.; Horn, K.; Ebert, Ph.; Urban, K.
Atomic-scale structure of the fivefold surface of AlPdMn quasictystals: A quantitative x-ray photoelectron diffraction analysis
Physical Review B, **69** (2004), 134107-1 - 134107-10

Zorn, R.; Frick, B.; Hartmann, L.; Kremer, F.; Schönhals, A.; Richter, D.
Dynamics of confined glass-forming systems observed by neutron scattering
Physica B: Condensed Matter, **350** (2004), 1/3, Suppl. 1, e1115 - e1118

2005

Allahyarov, E.; Gompper, G.; Löwen, H.
DNA condensation and redissolution: interaction between overcharged DNA molecules
Journal of Physics: Condensed Matter, **17** (2005), s1827 - s1840

Antons, A; Neaton, J.B.; Rabe, K. M.; Vanderbilt, D.
Tunability of the dielectric response of epitaxially strained SrTiO3 from first principles
Physical Review B, **71** (2005), 024102

Ashbaugh, H. S.; Guo, X.; Schwahn, D.; Prud'homme, R. K.; Richter, D.; Fetters, L. J.
Interaction of paraffin wax gels with ethylene/vinyl acetate copolymers
Energy & Fuels, **19** (2005), 138 - 144

Auth, T.; Gompper, G.
Fluctuation Spectrum of Membranes with Anchored Linear and Star Polymers
Physical Review E, **72** (2005), 031904

Balanetskyy, S.; Grushko, B.; Velikanova, T. Ya.; Urban, K.
Decagonal quasicrystals in Al-Pd-Fe
Intermetallics, **13** (2005), 649 - 654

Balanetskyy, S.; Grushko, B.; Velikanova, T. Ya.; Urban, K.
Study of phase equilibria in the Al-Pd-Re system
Powder Metallurgy and Metal Ceramics, **43** (2004), 480 - 483

Baldus, O.; Waser, R.
Experimental and numerical investigations of heat transport and crystallization kinetics in laser-induced modification of barium strontium titanate thin films
Applied Physics A, **80** (2005), 1553

Bauer, G.
Accelerator driven neutron sources - then and now
Development opportunities for small and medium scale accelerator driven neutron sources. - Vienna, 2005. - (IAEA-TECDOC ; 1439). - S. 31 - 39

Bedanta, S.; Petracic, O.; Kentzinger, E.; Kleemann, W.; Rücker, U.; Paul, A.; Brückel, Th.; Cardoso, S.; Freitas, P. P.
Superferromagnetic domain state of a discontinuous metal insulator multilayer
Physical Review B, **72** (2005), 024419-1 - 024419 -7

Bethke, C.; Kisker, E.; Weber, N.B.; Hillebrecht, F. U.
Core-valence interactions in Cr and Fe 2p photoemission
Physical Review B, **71** (2005), 024413

Blanchard, A.; Graham, R.S.; Heinrich, M.; Pyckhout-Hintzen, W.; Richter, D.; Likhtman, A. E.; McLeish, T. C. B.; Read, D. J.; Straube, E.; Kohlbrecher, J.
SANS observation of chain retraction after a large step deformation
Physical Review Letters, **95** (2005), 166001

Blügel, S. (Ed.); Brückel, Th. (Ed.); Schneider, C. M. (Ed.)
Magnetism goes nano : electron correlations, spin transport, molecular magnetism ; lecture manuscripts of the 36th Spring School of the Institute of Solid State Research ...
Jülich, Forschungszentrum, Zentralbibliothek, 2005
Schriften des Forschungszentrums Jülich . Reihe Materie und Materal / Matter and Material ; 26. - 3-89336-381-5

Braak, H.; Gareev, R. R.; Bürgler, D. E.; Grünberg, P.; Schreiber, R.; Schneider, C. M.
Magnetic characteristics of epitaxial Ge(Mn,Fe) diluted films - a new room temperature magnetic semiconductor?
Journal of Magnetism and Magnetic Materials, **286** (2005), 46

Brener, E. A.; Malinin, S. V.; Marchenko, V. I.
Fracture and friction: Stick-slip motion
European Physical Journal E, **17** (2005), 1, 101 - 113

Brener, E. A.; Temkin, D. E.
Velocity-selection problem for combined motion of melting and solidification fronts
Physical Review Letters, **94** (2005), 184501

Brzank, A.; Schütz, G.
Molecular Traffic Control in Porous Nanoparticles
Diffusion Fundamentals : Leipzig 2005 / ed.: J. Kärger, F. Grinberg, P. Heitjans. - Leipzig, Universitätsverl., 2005. - 3-86583-073-0. - S. 120 - 121

Brzank, A.; Schütz, G. M.
Molecular traffic control in porous nanoparticles
Applied Catalysis A-General, **288** (2005), 194 - 202

Brückel, Th.
Elastic Scattering from Many-Body Systems
Neutron scattering : lectures of the laboratory course held at the Forschungszentrum Jülich / ed.: T. Brückel ... - Jülich, Forschungszentrum, 2005. - (Schriften des Forschungszentrums Jülich, Reihe Material und Materie ; 28). - 3-89336-395-5. - S. 3-1 - 3-28

Brückel, Th.
Magnetism
Neutron scattering : lectures of the laboratory course held at the Forschungszentrum Jülich / ed.: T. Brückel ... - Jülich, Forschungszentrum, 2005. - (Schriften des Forschungszentrums Jülich, Reihe Material und Materie ; 28). - 3-89336-395-5. - S. 16-1 - 16-19

Brückel, Th. (Ed.)
Scattering Techniques II: Magnetic X-Ray Scattering
Magnetism goes nano : electron correlations, spin transport, molecular magnetism ; lecture manuscripts of the 36th Spring School of the Institute of Solid State Research ... / eds.: S. Blügel, T. Brückel, C. M. Schneider. - Jülich, 2005. - (Schriften des Forschungszentrums Jülich . Reihe Materie und Material / Matter and Material ; 26). - 3-89336-381-5. - S. B5.1 - B5-34

Brückel, Th. (Ed.)
Forschung mit Neutronen in Deutschland - Status und Perspektiven
Jülich, Forschungszentrum Jülich, Institut für Festkörperforschung, 2005

Brückel, Th. (Ed.); Heger, G. (Ed.); Richter, D. (Ed.); Zorn, R. (Ed.)
Neutron scattering : lectures of the laboratory course held at the Forschungszentrum Jülich Jülich, Forschungszentrum, Zentralbibliothek, 2005
Schriften des Forschungszentrums Jülich . Reihe Materie und Material / Matter and Materials; 28. - 3-89336-395-5

Bu, Z.; Biehl, R.; Monkenbusch, M.; Richter, D.; Callaway, D.J.E.
Coupled protein domain motion in Taq polymerase revealed by neutron spin-echo spectroscopy
Proceedings of the National Academy of Sciences of the United States of America, **102** (2005), 49, 17646 - 17651

Bürgler, D. E.
Advanced magnetic switching concepts
Magnetism goes nano : electron correlations, spin transport, molecular magnetism ; lecture manuscripts of the 36th Spring School of the Institute of Solid State Research ... / eds.: S. Blügel, T. Brückel, C. M. Schneider. - Jülich, 2005. - (Schriften des Forschungszentrums Jülich . Reihe Materie und Material / Matter and Material ; 26). - 3-89336-381-5. - S. 6.1 - 6.19

Bürgler, D. E.
Spin-transport in layered systems
Magnetism goes nano : electron correlations, spin transport, molecular magnetism ; lecture manuscripts of the 36th Spring School of the Institute of Solid State Research ... / eds.: S. Blügel, T. Brückel, C. M. Schneider. - Jülich, 2005. - (Schriften des Forschungszentrums Jülich . Reihe Materie und Material / Matter and Material ; 26). - 3-89336-381-5. - S. 5.1 - 5.18

Caciuc, V.; Blügel, S.; Hölscher, H.
Ab initio investigation of NC-AFM image contrast on InAs(110) surface
Physical Review B, **72** (2005), 035423

Carbone, G.; Persson, B. N. J.
Crack motion in viscoelastic solids: role of the flash temperature
European Physical Journal E, **17** (2005), 261

Carbone, G.; Persson, B. N. J.
Temperature induced crack motion instabilities in viscoelastic solids
Physical Review Letters, **95** (2005), 124301

Chen, J.; Jung, P.; Rödig, M.; Ullmaier, H.; Bauer, G. S.
Ductility recovery in structural materials for spallation targets by post-irradiation annealing
Journal of Nuclear Materials, **343** (2005), 227 - 235

Chen, J.; Jung, P.; Ullmaier, H.
Stresses, strains and cracks in a helium-implanted SiC/C composite
Journal of Nuclear Materials, **336** (2005), 194 - 200

Cherifi, S.; Hertel, Y. Y.; Kirschner, J.; Wang, H.; Belkhou, R.; Locatelli, A.; Heun, S.; Pavlovska, A.; Bauer, E.
Virgin domain structures in mesoscopic Co patterns: Comparison between simulation and experiment
Journal of Applied Physics, **98** (2005), 043901

Cherstvy, A. G.
Effect on DNA charge helicity on B-Z DNA transition
Journal of Chemical Physics, **123** (2005), 116101

Cherstvy, A. G.
Structure of DNA toroids and electrostatic attraction of DNA duplexes
Journal of Physics: Condensed Matter, **17** (2005), 8, 1363 - 1374

Cherstvy, A. G.; Kornyshev, A. A.
DNA Melting in Aggregates: Impeded or Facilitated?
Journal of Physical Chemistry B, **109** (2005), 13024 - 13029

Cherstvy, A. G.; Winkler, R. G.
Simple Model for Overcharging of a Sphere by a Wrapped Oppositely Charged Asymmetrically Neutralized Polyelectrolyte: Possible Effects of Helical Charge Distribution
Journal of Physical Chemistry B, **109** (2005), 2962 - 2969

Choi, B.J.; Jeong, D.S.; Kim, S.K.; Rohde, C.; Choi, S.; Oh, J.H.; Kim, H. J.; Hwang, C.S.; Waser, R.; Reichenberg, B.; Tiedke, S.
Resistive switching mechanism of TiO2 thin films grown by atomic-layer deposition
Journal of Applied Physics, **98** (2005), 33715

Clemens, S.; Schneller, T.; van der Hart, A.; Peter, F.; Waser, R.
Registered deposition of nanoscale ferroelectric grains by template-controlled growth
Advanced Materials, **17** (2005), 11, 1357 - 1361

Clemens, S.; Schneller, T.; Waser, R.; Rüdiger, A.; Peter, F.; Kronholz, S.; Schmitz, T.; Tiedke, T.
Integration of ferroelectric lead titanate nanoislands for direct hysteresis measurements
Applied Physics Letters, **87** (2005), 142904

Conrad, H.
Neutron Sources
Neutron scattering : lectures of the laboratory course held at the Forschungszentrum Jülich / ed.: T. Brückel ... - Jülich, Forschungszentrum, 2005. - (Schriften des Forschungszentrums Jülich, Reihe Material und Materie ; 28). - 3-89336-395-5. - S. 1-1 - 1-22

Conrad, H.
Spectroscopy: 1. The Triple-axis Spectrometer
Neutron scattering : lectures of the laboratory course held at the Forschungszentrum Jülich / ed.: T. Brückel ... - Jülich, Forschungszentrum, 2005. - (Schriften des Forschungszentrums Jülich, Reihe Material und Materie ; 28). - 3-89336-395-5. - S. 9.1-1 - 9.1-17

Conrad, H.
Spectroscopy: 2. The back-scattering spectrometer
Neutron scattering : lectures of the laboratory course held at the Forschungszentrum Jülich / ed.: T. Brückel ... - Jülich, Forschungszentrum, 2005. - (Schriften des Forschungszentrums Jülich, Reihe Material und Materie ; 28). - 3-89336-395-5. - S. 9.2-1 - 9.2-7

Da Silva, J. L. F.; Schroeder, K.; Blügel, S.
First-principles investigation of the role of registry relaxations on stepped Cu(100) surfaces
Physical Review B, **72** (2005), 033405

Darlinski, G.; Bottger, U.; Waser, R.; Klauk, H.; Halik, M.; Zschieschang, U.; Schmid, G.; Dehm, C.
Mechanical force sensors using organic thin-film transistors
Journal of Applied Physics, **97** (2005), 93708

de Luca, E.; Waigh, T. A.; Kim, J.S.; Jeon, H.S.; Pyckhout-Hintzen, W.
Phase separation in randomly charged polystyrene sulphonate ionomer solutions
Polymer, **46** (2005), 7109 - 7117

Dederichs, P. H.
Dilute Magnetic Semiconductors
Magnetism goes nano : electron correlations, spin transport, molecular magnetism ; lecture manuscripts of the 36th Spring School of the Institute of Solid State Research ... / eds.: S. Blügel, T. Brückel, C. M. Schneider. - Jülich, 2005. - (Schriften des Forschungszentrums Jülich . Reihe Materie und Material / Matter and Material ; 26). - 3-89336-381-5. - S. E4.1 - E4.17

Dederichs, P. H.
Interlayer Exchange Coupling
Magnetism goes nano : electron correlations, spin transport, molecular magnetism ; lecture manuscripts of the 36th Spring School of the Institute of Solid State Research ... / eds.: S. Blügel, T. Brückel, C. M. Schneider. - Jülich, 2005. - (Schriften des Forschungszentrums Jülich . Reihe Materie und Material / Matter and Material ; 26). - 3-89336-381-5. - S. C3.1 - C3.21

Dederichs, P. H.; Galanakis, I.; Mavropoulos, Ph.
Half-metallic Alloys: Electronic Structure, Magnetism and Spin Polarisation
Journal of Electron Microscopy, **54** (2005), Suppl. 1, i53 - i56

Dederichs, P. H.; Sato, K.; Katayama-Yoshida, H.
Dilute Magnetic Semiconductors
Phase Transitions, **78** (2005), 851

Di Cola, E.; Waigh, T. A.; Trinick, J.; Tskhovrebova, A.H.; Pyckhout-Hintzen, W.; Dewhurst, C.
Persistence length of titin from rabbit skeletal muscles measured with scattering and microrheology techniques
Biophysical Journal, **88** (2005), 6, 4095 - 4106

Divin, Y. Y.; Liatti, M. V.; Tkachev, D.A.; Pavlovskii, V. V.; Shirotov, V. V.; Volkov, O. Y.; Poppe, U.; Jia, C. L.; Gubankov, V. N.; Urban, K.
Terahertz Detection and Spectroscopy Based on High-Tc Josephson Junctions
Proceedings of 18th International Conference on Applied Electromagnetics and Communications, 12.10.-14.10.2005, Dubrovnik, Croatia / ed.: D. Bonefacic. - Zagreb, KoREMA, 2005. - 953-6037-44-0. - S. 277 - 278

Divin, Y. Y.; Liatti, M.; Shirotov, V. V.; Volkov, O. Y.; Poppe, U.; Jia, C. L.; Gubankov, V. N.; Urban, K.
Terahertz Detection and Spectrosopy with Nanoscale Bicrystal High-Tc Junctions
Proceedings of the Workshop on Nanoelectronics Days, Forschungszentrum Jülich, 09.02.2005 - 11.02.2005. - 2005. - S. 168 - 169

Dror, Y.; Pyckhout-Hintzen, W.; Cohen, Y.
The conformation of polymers dispersing single-walled carbon nanotubes in water: a small angle neutron scattering study
Macromolecules, **38** (2005), 7828 - 7836

Dror, Y.; Salalha, Z. A.; Pyckhout-Hintzen, W.; Yarin, A.; Zussman, E.; Cohen, Y.
From carbon nanotube dispersion to composite nanofibers
Progress in Colloid and Polymer Science, **130** (2005), 64 - 69

Ebert, H.; Bornemann, S.; Minar, B. Q.; Kosuth, M.; Sipr, O.; Dederichs, P. N.; Zeller, R.; Cabria, I.
Electronic and Magnetic Properties of Free and Supported Transition Metal Clusters
Phase Transitions, **78** (2005), 71

Ebert, Ph.
Spin-polarized Scanning Tunneling Microscopy
Magnetism goes nano : electron correlations, spin transport, molecular magnetism ; lecture manuscripts of the 36th Spring School of the Institute of Solid State Research ... / eds.: S. Blügel, T. Brückel, C. M. Schneider. - Jülich, 2005. - (Schriften des Forschungszentrums Jülich . Reihe Materie und Material / Matter and Material ; 26). - 3-89336-381-5. - S. E 3.1-E 3.23

Eisenriegler, E.
Field theory of polymer-colloid interactions
Complex Colloidal Suspensions / ed.: G. Gompper, M. Schick. - Weinheim, Wiley-VCH, 2005. - (Soft Matter ; 2). - 3-527-31369-9. - S. 87 - 146

Eisenriegler, E.; Bringer, A.
Depletion interactions of non-spherical colloidal particles in polymer solutions
Journal of Physics: Condensed Matter, **17** (2005), s1711 - s1729

Faley, M.
SQUID Magnetometers and Gradiometers based on a High-Tc Oxide Heterostructure
Journal of Communications Technology and Electronics, **50** (2005), 4, 461 - 467

Faley, M.; Jia, C. L.; Poppe, U.; Urban, K.
Bicrystal Josephson junctions on the basis of YBa2Cu3O7-d thin films
Proceedings of the Workshop on Nanoelectronics Days, Forschungszentrum Jülich, 09.02.2005-11.02.2005. - 2005. - S. 122 - 123

Faley, M.I.; Maslennikov, Yu.V.
Superconducting measuring system fror detection of magnetic impurities in construction materials
Journal of Communications Technology and Electronics, **50** (2005), 6, 694 - 699

Ferriani, P.; Heinze, S.; Bihlmayer, G.; Blügel, S.
Unexpected trend of magnetic order of 3d transition-metal monolayers on W(001)
Physical Review B, **72** (2005), 024452

Feuerbacher, M.
On the nature of phason planes in the complex metallic alloy ksi-Al-Pd-Mn
Acta Materialia, **53** (2005), 3833 - 3840

Fortini, A.; Dijkstra, M.; Tuinier, R.
Phase behaviour of charged colloidal sphere dispersions with added polymer chains
Journal of Physics: Condensed Matter, **17** (2005), 7783 - 7803

Frank, C.; Sottmann, T.; Stubenrauch, C.; Allgaier, J.; Strey, R.
Influence of amphiphilic block copolymers on lyotropic liquid crystals in water-oil-surfactant systems
Langmuir, **21** (2005), 9058 - 9067

Frick, B.; Alba-Simionesco, C.; Dosseh, G.; Le Quellec, C.; Moreno, A.; Colmenero, J.; Schönhals, A.; Zorn, R.; Chrissopoulou, K.; Anastasiadis, S.; Dalnoki-Verres, K.; Higgins, A.
Inelastic neutron scattering for investigating the dynamics of confined glass forming liquids
Journal of Non-Crystalline Solids, **351** (2005), 2657 - 2667

Fröhlich-Schlapp, M.; Ioffe, A.; Conrad, H.; Brückel, Th.; Fueß, H.; von Seggern, H.
Novel materials and concepts for neutron image plates
Nuclear Instruments and Methods in Physics Research Section A, **551** (2005), 1, 46 - 51

Galanakis, I.; Lezaic, M.; Bihlmayer, G.; Blügel, S.
Interface properties of NiMnSb/InP and NiMnSb/GaAs contacts
Physical Review B, **71** (2005), 214431

Gapinski, J.; Wilk, A.; Patkowski, A.; Häußler, W.; Banchio, A. J.; Pecora, R.; Nägele, G.
Diffusion and Microstructural Properties of Dispersions of Charged Nano-sized Proteins: Experiment vs. Theory
Journal of Chemical Physics, **123** (2005), 054708

Gardner, J. S.; Cornelius, A. L.; Chang, L.-J.; Prager, M.; Brückel, Th.; Ehlers, G.
Spin dynamics in $Ho_2Ru_2O_7$
Journal of Physics: Condensed Matter, **17** (2005), 7089 - 7095

Genix, A.-C.; Arbe, A.; Alvarez, F.; Colmenero, J.; Willner, L.; Richter, D.
Dynamics of poly(ethylene oxide) in a blend with poly(methyl methacrylate): A quasielastic neutron scattering and molecular dynamics simulation study
Physical Review E, **72** (2005), 031808

Gerber, P.; Kügeler, C.; Ellerkmann, U.; Schorn, P.; Böttger, U.; Waser, R.
Effects of ferroelectric fatigue on the piezoelectric properties (d33) of tetragonal lead zirconate titanate thin films
Applied Physics Letters, **86** (2005), 112908

Gobert, D.; Kollath, C.; Schollwöck, U.; Schütz, G.
Real-time dynamics in spin-1/2 chains with adaptive time-dependent density matrix renormalization group
Physical Review E, **71** (2005), 036102

Gompper, G. (Ed.); Schick, M. (Ed.)
Complex Colloidal Dispersions
Weinheim, Wiley-VCH, 2005
Soft Matter ; 2; - 3-527-31369-9

Gompper, G. (Ed.); Schick, M. (Ed.)
Polymer Melts and Mixtures
Weinheim, Wiley-VCH, 2005
Soft Matter ; 1; - 3-527-30500-9

Gompper, G.; Noguchi, H.
Vesicle dynamics in shear and capillary flows
Journal of Physics: Condensed Matter, **17** (2005), s3439 - s3444

Gompper, G.; Schick, M.
An Introduction to Soft Matter
Polymer Melts and Mixtures / ed.: G. Gompper, M. Schick. - Weinheim, Wiley-VCH, 2005. - (Soft Matter ; 1). - 3-527-30500-9. - S. 1 - 16

Grudinin, S.; Büldt, G.; Gordeliy, I. L.; Baumgaertner, A.
Water Molecules and Hydrogen-Bonded Networks in Bacteriorhodopsin-Molecular Dynamics Simulations of the Ground State and the M-Intermediate
Biophysical Journal, **88** (2005), 3252 - 3261

Grushko, B.; Kowalska-Strzeciwilk, E.; Przepiorzynski, B.; Surowiec, M.
Investigation of the Al-Cr Gamma-range
Journal of Alloys and Compounds, **402** (2005), 98 - 104

Guo, X.; Mi, S.; Waser, R.
Nonlinear electrical properties of grain boundaries in oxygen ion conductors: case of acceptor doped ceria
Electrochemical and Solid State Letters, **8** (2005), 1, J1 - J3

Guo, X.; Pithan, C.; Ohly, C.; Jia, C.-L.; Dornseiffer, J.; Haegel, F.-H.; Waser, R.
Enhancement of p-type conductivity in nanocrystalline $BaTiO_3$ Ceramics
Applied Physics Letters, **86** (2005), 082110

Guo, X.; Vasco, E.; Mi, S.; Szot, K.; Wachsman, E.; Waser, R.
Ionic conduction in zirconia films on nanometer thickness
Acta Materialia, **53** (2005), 5161

Guo, X.; Zhang, Z.; Sigle, W.; Waser, R.
Schottky barrier formed by network of screw dislocations in $SrTiO_3$
Applied Physics Letters, **87** (2005), 162105

Gurevich, V. L.; Parshin, D. A.; Schober, H. R.
Pressure dependence of the boson peak in glasses
Physical Review B, **71** (2005), 014209

Gömann, K.; Borchardt, G.; Schulz, M.; Gömann, A.; Maus-Friedrichs, W.; Lesage, B.; Kaitasov, O.; Hoffmann-Eifert, S.; Schneller, T.
Sr diffusion in undoped and La-doped $SrTiO_3$ single crystals under oxidizing conditions
Physical Chemistry Chemical Physics, **7** (2005), 2053 - 2060

Halder, S.; Gerber, P.; Schneller, T.; Waser, R.
Electromechanical properties of $Ba(Ti_{1-x}Zr_x)O_3$ thin films
Applied Physics A, **81** (2005), 11 - 13

Halder, S.; Schneller, T.; Böttger, U.; Waser, R.
Fabrication and electrical characterization of Zr-substituted $BaTiO_3$ thin films
Applied Physics A, **81** (2005), 25 - 29

Halder, S.; Schneller, T.; Meyer, R.; Waser, R.
Effect of ozone treatment on the electrical properties of $(Ba_{0.7}Sr_{0.3})TiO_3$ thin films
Journal of Applied Physics, **97** (2005), 114904

Halder, S.; Schneller, T.; Waser, R.
Crystallization temperature limit of $(Ba,Sr)TiO_3$ thin films prepared by a non oxocarbonate phase forming CSD route
Journal of Sol-Gel Science and Technology, **33** (2005), 3, 299 - 306

Hauck, J.; Mika, K.
Characteristic Lattice Complexes
Zeitschrift für physikalische Chemie, **219** (2005), 439 - 454

Hauck, J.; Mika, K.
Structure types with different properties
Progress in Solid State Chemistry, **33** (2005), 1 - 56

Hauck, J.; Mika, K.; Sager, W.
Morphological lattice complexes
Crystal Research and Technology, **9** (2005), 917 - 923

He, J. Q.; Jia, C. L.; Vaithyanathan, V.; Schlom, D. G.; Schubert, J.; Gerber, A.; Kohlstedt, H. H.; Wang, R. H.
Interfacial reaction in the growth of epitaxial $SrTiO_3$ thin films on (001) Si substrates
Journal of Applied Physics, **97** (2005), 104921

He, J. Q.; Vasco, E.; Jia, C. L.; Dittmann, R.
Microstructure of epitaxial BST/SRO bilayer films on $SrTiO_3$ substrates
Journal of Applied Physics, **97** (2005), 104907

Hecker, M.; Schneider, C. M.; Mertins, H.-Ch.; Rücker, U.; Kentzinger, E.
Magnetic order in Co/Cu multilayers studied by polarized soft X-rays and neutrons
Journal of Magnetism and Magnetic Materials, **286** (2005), 416 - 419

Heggen, M.; Feuerbacher, M.
Metadislocation reactions and metadislocation networks in the complex metallic alloy ξ'-Al-Pd-Mn
Materials Science and Engineering A, **400-401** (2005), 89 - 92

Heggen, M.; Spaepen, F.; Feuerbacher, M.
Creation and annihilation of free volume during homogeneous flow of a metallic glass
Journal of Applied Physics, **97** (2005), 033506

Hermann, M. A.; Schweika, W.; Leupold, O.; Rüffer, R.; Nolas, G. S.; Grandjean, F.; Long, G. J.
Neutron and nuclear inelastic scattering study of the Einstein oscillators in Ba, Sr, and Eu-filled germanium clathrates
Physical Review B, **72** (2005), 174301

Herms, M.; Irmer, G.; Verma, P.; Goerigk, G.
Nondestructive characterization of nanoparticles in solids by Raman spectroscopy and small angle X-ray scattering
Testing, Reliability, and Application of Micro- and Nano-Material Systems III / ed.: R. E. Geer ... - 2005. - (Proceedings of the SPIE ; 5766). - 0-8194-5747-7. - S. 32 - 39

Hertel, R.
High-density nickel nanowire arrays
Ordered Porous Nanostructures and Applications / ed.: R. B. Wehrspon. - New York, NY, Springer, 2005. - 0-387-23541-8. - S. 165 - 184

Hertel, R.; Fruchart, O.; Cherifi, S.; Jubert, P.-O.; Heun, S.; Locatelli, A.; Kirschner, J.
Three-dimensional magnetic-flux-closure patterns in mesososcopic Fe islands
Physical Review B, **72** (2005), 214409

Hillebrecht, F. U.; Morozov, A.; Kirschner, J.
Direct observation of electronic correlation in C_{60} by double photoemission
Physical Review B, **71** (2005), 125406

Hirsch, S.; Klein, H.; Jung, P.
Dimensional changes of silica-, borosilicate- and germania-glasses and quartz under irradiation
Journal of Non-Crystalline Solids, **351** (2005), 40/42, 3279 - 3288

Hoffmann-Eifert, S.; Puchalla, J.; Cattaneo, L.; Carella, S.; Waser, R.
Ferroelectric (Pb, Ba)(Zr, Ti)O_3 thin films grown by MOCVD
15th European Conference on Chemical Vapor Deposition / ed.: A. Devi ... - 2005. - (Proceedings of the Electrochemical Society ; 2005-09). - 1-56677-427-6. - S. 982 - 989

Hofmann, Ph.; Gayone, J. E.; Bihlmayer, G.; Koroteev, Y.M.; Chulkov, E. V.
Electronic structure and Fermi surface of Bi(100)
Physical Review B, **71** (2005), 195413

Holderer, O.; Frielinghaus, H.; Byelov, D.; Monkenbusch, M.; Allgaier, J.; Richter, D.
Dynamic properties of microemulsions modified with homopolymers and diblock copolymers: The determination of bending moduli and renormalization effects
Journal of Chemical Physics, **122** (2005), 094908

Hueging, N.; Luysberg, M.; Urban, K.; Buca, D.; Mantl, S.
Evolution of the defect structure in helium implanted SiGe/Si heterostructures investigated by in-situ annealing in a transmission electron microscope
Applied Physics Letters, **86** (2005), 042112

Höhler, H.; Atodiresei, N.; Schroeder, K.; Zeller, R.; Dederichs, P. N.
Vacancy-complexes with oversized impurities in Si and Ge
Physical Review B, **71** (2005), 035212

Indris, S.; Heitjans, P.; Behrens, H.; Zorn, R.; Frick, B.
Fast Dynamics of H_2O in Hydrous Aluminosilicate Glasses Studied with Quasielastic Neutron Scattering
Physical Review B, **71** (2005), 064205

Ishida, H.; Johannes, M.; Liebsch, A.
Effect of dynamical Coulomb correlations on the Fermi surface of $Na_{0.3}CoO_2$
Physical Review Letters, **94** (2005), 196401

Jones, G. J.; Akola, J.; Ballone, P.
A density functional/Monte Carlo study
Advances in Polycarbonates / ed.: D. J. Brunelle, M. R. Korn. - ACS, 2005. - (ACS Symposium Series ; 898). - 0-8412-3887-1. - S. 200 - 213

Jones, G. J.; Akola, J.; Ballone, P.
Ring-opening polymerization and branching in polycarbonates: a density functional/Monte Carlo study
Advances in Polycarbonates / ed.: D. J. Brunelle, M. R. Korn. - Oxford University Press, 2005. - (ACS Symposium Series). - 0-8412-3887-1. - S. 200 - 215

Jung, P.
Radiation damage in general : reports on summary session
Journal of Nuclear Materials, **343** (2005), 368 - 369

Jung, P.; Henry, J.; Chen, J.
Tensile properties of candidate structural materials for high power spallation sources at high helium contents
Journal of Nuclear Materials, **343** (2005), 275 - 284

Kahle, S.; Gapinski, J.; Hinze, G.; Patkowski, A.; Meier, G.
A comparison of relaxation processes in structurally related van der Waals glass formers: The role of internal degrees of freedom
Journal of Chemical Physics, **122** (2005), 074506

Kanaya, T.; Monkenbusch, M.; Watanabe, H.; Nagao, M.; Richter, D.
Dynamics of deuterated polystyrene-protonated butadiene diblock copolymer micelles by neutron spin echo
Journal of Chemical Physics, **122** (2005), 144905

Kang, K.; Gapinski, J.; Lettinga, M. P.; Buitenhuis, J.; Meier, G.; Ratajczyk, M.; Dhont, J. K. G.; Patkowski, A.
Diffusion of spheres in crowded suspensions of rods
Journal of Chemical Physics, **122** (2005), 044905-1 - 044905-13

Kaupuzs, J.; Mahnke, R.; Harris, R. J.
Zero-range model of traffic flow
Physical Review E, **72** (2005), 056125

Kehr, K. W.; Mussawisade, K.; Schütz, G. M.; Wichmann, T.
Diffusion of particles on lattices
Diffusion in Condensed Matter / eds.: P. Heitjans, J. Kärger. - Berlin, Springer, 2005. - 2. Aufl. - 3-540-20043-6. - S. 745 - 792

Kirstein, O.; Prager, M.; Dimeo, R.M.; Desmedt, A.
Rotational dynamics of methyl groups in m-xylene
Journal of Chemical Physics, **122** (2005), 014502

Kita, R.; Wiegand, S.
Soret Coefficient of Poly(N-isopropylacrylamide)/Water in the Vicinity of Coil-Globule Transition Temperature
Macromolecules, **38** (2005), 4554 - 4556

Kohlstedt, H.; Pertsev, N. A.; Contreras, J.R.; Waser, R.
Theoretical current-voltage characteristics of ferroelectric tunnel junctions
Physical Review B, **72** (2005), 125341

Koppitz, T.; Jung, P.; Müller, G.; Weisenburger, A.; Futakawa, M.; Ikeda, Y.
Improved cavitation resistance of structural materials in pulsed liquid metal targets by surface hardening
Journal of Nuclear Materials, **343** (2005), 1/3, 92 - 100

Krasyuk, A.; Wegelin, F.; Nepijko, S. A.; Elmers, H. J.; Schönhense, G.; Bolte, M.; Schneider, C. M.
Self-trapping of magnetic oscillation modes in Landau flux-closure structures
Physical Review Letters, **95** (2005), 207201

Kravtsov, E.; Brucas, R.; Hjörvarsson, B.; Hoser, A.; McIntyre, G.; Nefedov, A. G.; Radu, F.; Remhof, A.; Zabel, H.
Proximity effect of vanadium on strain and spin-density waves in thin Cr films
Journal of Magnetism and Magnetic Materials, **286** (2005), 425 - 431

Krupin, O.; Bihlmayer, G.; Starke, K.; Gorovikov, S.; Prieto, K. C.; Döbrich, K.; Blügel, S.; Kaindl, G.
Rashba effect at magnetic metal surfaces
Physical Review B, **71** (2005), 201403,

Kubetzka, A.; Ferriani, P.; Bode, M.; Heinze, S.; Bihlmayer, G.; von Bergmann, K.; Pietzsch, O.; Blügel, S.; Wiesendanger, R.
Revealing Antiferromagnetic Order of the Fe Monolayer on W(001): Spin-Polarized Scanning Tunneling Microscopy and First-Principles Calculations
Physical Review Letters, **94** (2005), 087204

Kuepper, K.; Kadiroglu, M.; Postnikov, A. V.; Prince, K.C.; Matteucci, M.; Galakhov, V.R.; Hesse, H.; Borstel, G.; Neumann, M.
Electronic structure of highly ordered Sr_2FeMoO_6: XPS and XES studies
Journal of Physics: Condensed Matter, **17** (2005), 4309

Kwon, S.; Schütz, G. M.
Absorbing phase transitions of unidirectionally coupled nonequilibrium systems
Physical Review E, **71** (2005), 046122

Köbler, U.; Hoser, A.
Stable magnetic universality classes for $T \Rightarrow 0$
Physica B: Condensed Matter, **362** (2005), 295 - 305

Köbler, U.; Hoser, A.; Bos, J.; Schäfer, W.; Pohlmann, L.
Weak ferromagnets with integer and half-integer spin quantum numbers
Physica B: Condensed Matter, **355** (2005), 90 - 99

Köbler, U.; Hoser, A.; Schäfer, W.
On the temperature dependence of the magnetic excitations
Physica B: Condensed Matter, **364** (2005), 55 - 70

Köbler, U.; Kawakami, M.; Schnelle, W.
Universal behaviour of the magnetic heat capacity for $T \rightarrow 0$
Physica B: Condensed Matter, **367** (2005), 255 - 266

Laurati, M.; Stellbrink, J.; Lund, R.; Willner, L.; Richter, D.; Zaccarelli, E.
Star-like micelles with star-like interactions: a quantitative evaluation of structure factors and phase diagram
Physical Review Letters, **94** (2005), 195504

Lettinga, M. P.; Barry, E.; Dogic, Z.
Self-diffusion of rod-like viruses in the nematic phase
Europhysics Letters, **71** (2005), 692 - 698

Lettinga, M. P.; Dogic, Z.; Wang, H.; Vermant, J.
Flow Behavior of Colloidal Rodlike Viruses in Nematic Phase
Langmuir, **21** (2005), 17, 8048 - 8057

Lettinga, M. P.; Kang, K.; Imhof, A.; Derks, D.; Dhont, J. K. G.
Kinetic pathways of the nematic-isotropic phase transition as studied by confocal microscopy on rod-like viruses
Journal of Physics: Condensed Matter, **17** (2005), s3609 - s3618

Levine, E.; Mukamel, D.; Schütz, G. M.
Long-range attraction between probe particles mediated by a driven fluid
Europhysics Letters, **70** (2005), 565 - 571

Levine, E.; Mukamel, D.; Schütz, G. M.
Zero-range process with open boundaries
Journal of Statistical Physics, **120** (2005), 759 - 778

Lezaic, M.; Galanakis, I.; Bihlmayer, G.; Blügel, S.
Structural and magnetic properties of the (001) and (111) surfaces of the half-metal NiMnSb
Journal of Physics: Condensed Matter, **17** (2005), 3121 - 3136

Liebsch, A.
Novel Mott transitions in a nonisotropic two-band Hubbard model
Physical Review Letters, **95** (2005), 116402

Liebsch, A.; Ishida, H.; Bihlmayer, G.
Coulomb correlations and orbital polarization in the metal-insulator transition of VO2
Physical Review B, **71** (2005), 085109

Loppinet, B.; Fytas, G.; Vlassopoulos, D.; Likos, C. N.; Meier, G.; Liu, G. J.
Dynamic of Dense Suspensions of Star-Like Micelles with Responsive Fixed Cores
Macromolecular Chemistry and Physics, **206** (2005), 163 - 172

Lounis, S.; Mavropoulos, Ph.; Dederichs, P. N.; Blügel, S.
Noncollinear Korringa-Kohn-Rostoker Green function method: Application to 3d nanostructures on Ni(001)
Physical Review B, **72** (2005), 224437

Lüssem, B.; Karthäuser, S.; Haselier, H.; Waser, R.
The origin of faceting of ultrafast gold films epitaxially grown on Mica
Applied Surface Science, **249** (2005), 197 - 200

Lüssem, B.; Müller-Meskamp, L.; Karthäuser, S.; Waser, R.
A new phase of the c(4x2) superstructure of alkanethiols grown by vapour phase deposition on gold
Langmuir, **21** (2005), 5256 - 5258

Manoharan, S.S.; Singh, B.; Discroll, J.; Brandford, W.; Cohen, L.; Besmehn, A.
Magnetism and electronic transport in $Sr_{4-x}La_xRu_{2-x}Mn_xO_9$: Interplay of Mn and Ru redox chemistry
Journal of Applied Physics, **97** (2005), 10A304-1 - 10A304-3

Masalovich, S.; Ioffe, A.; Schlapp, M.; von Seggern, H.; Küssel, E.; Brückel, Th.
Optimization of a neutron image plate detector with low gamma-sensitivity
Nuclear Instruments and Methods in Physics Research Section A, **539** (2005), 1/2, 236 - 249

Mavropoulos, P.; Lezaic, M.; Blügel, S.
Half-metallic ferromagnets for magnetic tunnel junctions by ab initio calculations
Physical Review B, **72** (2005), 174428

Meijers, R.; Calarco, R.; Kaluza, N.; Hardtdegen, H.; von der Ahe, M.; Bay, H. L.; Lüth, H.; Buchmeier, M.; Bürgler, D. E.
Epitaxial growth and characterization of Fe thin films on wurtzite GaN(0001)
Journal of Crystal Growth, **283** (2005), 500

Melnichenko, Y. B.; Wignall, G. D.; Cole, D. R.; Frielinghaus, H.; Bulavin, L.A.
Liquid-gas critical phenomena under confinement: small-angle neutron scattering studis of CO_2 in aerogel
Journal of Molecular Liquids, **120** (2005), 7

Meyer, R.; Guo, X.; Waser, R.
Nonlinear electrical properties of grain boundaries in oxygen ion conductors
Electrochemical and Solid State Letters, **8** (2005), 10, E67

Meyer, R.; Liedtke, R.; Waser, R.
Oxygen vacancy migration and time-dependent leakage current behavior of $Ba_{0.3}Sr_{0.7}TiO_3$ thin films
Applied Physics Letters, **86** (2005), 112904

Meyer, R.; Waser, R.; Prume, K.; Schmitz, T.; Tiedke, S.
Dynamic leakage current compensation in ferroelectric thin-film capacitor structures
Applied Physics Letters, **86** (2005), 142907

Mi, S.B.; Jia, C. L.; Heeg, T.; Trithaveesak, O.; Schubert, J.; Urban, K.
Heterostructures of $BaTiO_3$ bilayer films grown on $SrTiO_3$ (001) under different oxygen pressures
Journal of Crystal Growth, **283** (2005), 425 - 430

Moert, M.; Mikolajick, T.; Schindler, G.; Nagel, N.; Kasko, I.; Hartner, W.; Dehm, C.; Kohlstedt, H.; Waser, R.
Integration of stacked capacitor module with ultra-thin ferroelectric $SrBi_2Ta_2O_9$film for high density ferroelectric random access memory applications at low voltage operation
Thin Solid Films, **473** (2005), 328

Mokrousov, Y.; Atodiresei, N.; Bihlmayer, G.; Blügel, S.
Magnetism in Molecular Vanadium-Benzene Sandwiches
Electronic Properties of Novel Nanostructures : XIX International Winterschool/Euroconference on Electronic Properties of Novel Materials / ed.: H. Kuzmany ∑ - AIP, 2005. - (American Institute of Physics conference proceedings ; 786). - 0-7354-0275-2. - S. 444

Mokrousov, Y.; Bihlmayer, G.; Blügel, S.
Full-potential linearized augmented plane-wave method for one-dimensional systems: Gold nanowire and iron monowires in a gold tube
Physical Review B, **72** (2005), 045402

Monkenbusch, M.; Holderer, O.; Frielinghaus, H.; Byelov, D.; Allgaier, J.; Richter, D.
Bending moduli of microemulsions; comparison of results from small angle neutron scattering and neutron spin-echo spectroscopy
Journal of Physics: Condensed Matter, **17** (2005), s2903 - s2909

Mussawisade, K.; Ripoll, M.; Winkler, R. G.; Gompper, G.
Dynamics of Polymers in a Particle-Based Mesoscopic Solvent
Journal of Chemical Physics, **123** (2005), 144905

Mönig, H.; Sun, J.; Koroteev, Y.M.; Bihlmayer, G.; Wells, J.; Chulkov, E. V.; Pohl, K.; Hofmann, Ph.
Structure of the (111) surface of bismuth: LEED analysis and first-principles calculations
Physical Review B, **72** (2005), 085410

Müller-Krumbhaar, H.; Gutheim, F.; Pütter, C.
Roughening transition of an SOS-model with elastic interactions
Journal of Crystal Growth, **275** (2005), 51

Müller-Meskamp, L.; Lüssem, B.; Karthäuser, S.; Waser, R.
Rectangular (3x23) superlattice of a dodecanethiol self-assembled monolayer on Au(111) observed by ultra-high-vacuum scanning tunneling microscopy
Journal of Physical Chemistry B, **109** (2005), 23, 11424 - 11426

Nagarajan, V.; Aggarwal, S.; Gruverman, A.; Ramesh, R.; Waser, R.
Nanoscale polarization relaxation in a polycrystalline ferroelectric thin film: role of local environments
Applied Physics Letters, **86** (2005), 262910

Nagarajan, V.; Jia, C. L.; Kohlstedt, H.; Waser, R.; Misirlioglu, I.B.; Alpay, S. P.; Ramesh, R.
Misfit dislocations in nanoscale ferroelectric heterostructures
Applied Physics Letters, **86** (2005), 192910

Nandy, B.; Baumgaertner, A.
Competing polymerization of actin skeleton explains relation between network polarity and cell movements
Journal of Physics: Condensed Matter, **17** (2005), s1871 - s1879

Narros, A.; Arbe, A.; Alvarez, F.; Colmenero, J.; Zorn, R.; Schweika, W.; Richter, D.
Partial structure factors in 1,4-Polybutadiene. A combined neutron scattering and molecular dynamics study
Macromolecules, **38** (2005), 9847 - 9853

Neeb, A. V.; Stanzel, J.; Pontius, N.; Eberhardt, W.; Lüttgens, G.; Bechthold, P. S.; Friedrich, C.
Time-resolved photoelectron spectra of $Pt_2(N_2)$-
Journal of Electron Spectroscopy and Related Phenomena, **144-147** (2005), 91 - 96

Niu, A. Z.; Stellbrink, J.; Allgaier, J.; Willner, L.; Radulescu, A.; Richter, D.; Koenig, B. W.; May, R. P.; Fetters, L. J.
An in situ study of the t-butyllithium initiated polymerization of butadiene in d-heptane via small angle neutron scattering and 1H-NMR
Journal of Chemical Physics, **122** (2005), 134906

Noguchi, H.; Gompper, G.
Dynamics of Fluid Vesicles in Shear Flow: Effect of Membrane Viscosity and Thermal Fluctuations
Physical Review E, **72** (2005), 011901

Noguchi, H.; Gompper, G.
Shape Transitions of Fluid Vesicles and Red Blood Cells in Capillary Flows
Proceedings of the National Academy of Sciences of the United States of America, 102 (2005), 14159 - 14164

Nägele, G.; Dhont, J. K. G.; Meier, G.
Diffusion in Colloidal and Polymeric Systems
Diffusion in Condensed Matter / eds.: P. Heitjans, J. Kärger. - Berlin, Springer, 2005. - 2. Aufl. - 3-540-20043-6. - S. 619 - 715

Ohl, M.; Monkenbusch, M.; Kozielewski, T.; Laatsch, B.; Tiemann, Ch.; Richter, D.
Correction elements for ultra-high resolutions NSE spectrometer
Physica B: Condensed Matter, **356** (2005), 234 - 238

Okumu, J.; Dahmen, C.; Luysberg, M.; von Plessen, G.; Wuttig, M.
Photocromic silver nanoparticles fabricated by sputter deposition
Journal of Applied Physics, **97** (2005), 094305

Pappas, C.; Mezei, F.; Triolo, A.; Zorn, R.
Going to the limits of NSE
Physica B: Condensed Matter, **356** (2005), 206 - 212

Paul, A.; Buchmeier, M.; Bürgler, D. E.; Grünberg, P.
Quantitative investigation of FeMn-based spin-valves by rotating field magnetoresistance measurements
Journal of Magnetism and Magnetic Materials, **286** (2005), 258 - 261

Paul, A.; Buchmeier, M.; Bürgler, D. E.; Grünberg, P.
Rotating-field magnetoresistance of exchange-biased spin valves
Journal of Applied Physics, **97** (2005) , 023910-1 - 023910-6

Paul, A.; Bürgler, D. E.; Grünberg, P.
Enhanced exchange bias in ferromagnet/antiferromagnet multilayers
Journal of Magnetism and Magnetic Materials, **286** (2005), 216 - 219

Paul, A.; Kentzinger, E.; Rücker, U.; Bürgler, D. E.; Grünberg, P.
Nonuniform and sequential magnetization reversal via domain structure formation for multilayered system with grain size enhanced exchange bias
European Physical Journal B, **45** (2005), 249 - 260

Paul, A.; Kentzinger, E.; Rücker, U.; Bürgler, D. E.; Grünberg, P.
Polarized neutron scattering from polycristalline, exchange-biased magnetic multilayers
Physica B: Condensed Matter, **356** (2005), 26

Paul, A.; Kentzinger, E.; Rücker, U.; Bürgler, D.; Grünberg, P.
Measurement and simulation of polarised neutron reflectivity and off-specular scattering from evolving magnetic domain structure in Co/Cu multilayers
Physica B: Condensed Matter, **356** (2005), 31 - 35

Paul, A.; Kentzinger, E.; Rücker, U.; Bürgler, D.; Grünberg, P.
Polarised neutron scattering from polycrystalline, exchange-biased magnetic multilayers
Physica B: Condensed Matter, **356** (2005), 26 - 30

Peressadko, A.G.; Hosoda, N.; Persson, B. N. J.
Influence of surface roughness on the adhesion between elastic bodies
Physical Review Letters, **95** (2005), 124301

Persson, B. N. J.; Albohr, O.; Heinrich, G.; Ueba, H.
Crack propagation in rubber-like materials
Journal of Physics: Condensed Matter, **17** (2005), R1071

Persson, B. N. J.; Albohr, O.; Tartaglino, U.; Volokitin, A. I.; Tosatti, E.
On the nature of surface roughness with application to contact mechanics, sealing, rubber friction and adhesion
Journal of Physics: Condensed Matter, **17** (2005), R1

Persson, B. N. J.; Brener, E. A.
Crack propagation in viscoelastic solids
Physical Review E, **71** (2005), 036123

Persson, B. N. J.; Tartaglino, U.; Albohr, O.; Tosatti, E.
Rubber friction on wet rough substrate at low sliding velocity: the sealing effect
Physical Review B, **71** (2005), 035428

Peter, F.; Rüdiger, A.; Dittmann, R.; Waser, R.; Szot, K.; Reichenberg, B.; Prume, K.
Analysis of shape effects on the piezoresponse in ferroelectric nanograins with and without adsorbates
Applied Physics Letters, **87** (2005), 8, 082901

Peter, F.; Rüdiger, A.; Waser, R.; Szot, K.; Reichenberg, B.
Comparison of in-plane and out-of-plane optical amplification in AFM measurements
Review of Scientific Instruments, **76** (2005), 4, 046101

Peter, F.; Rüdiger, A.; Waser, R.; Szot, K.; Reichenberg, B.
Contributions to in-plane piezoresponse on axially symmetrical samples
Review of Scientific Instruments, **76** (2005), 106108

Pipich, V.; Schwahn, D.; Willner, L.
Composition fluctuations in a homopolymer-diblock copolymer mixture covering the three-dimensional Ising, isotropic Lifshitz, and Brasovskii classes of critical universality
Journal of Chemical Physics, **123** (2005), 124904

Pipich, V.; Schwahn, D.; Willner, L.
Ginzburg number of a homopolymer/diblock copolymer mixture covering 3d-Ising, isotropic Lifshitz and Brasovskii class of critical universality
Physical Review Letters, **94** (2005), 117801

Pithan, C.; Shiratori, Y.; Dornseiffer, J.; Haegel, J.; Magrez, A.; Waser, R.
Microemulsion mediated synthesis of nanocrystalline $(K_x,Na_{1-x})NbO_3$ powders
Journal of Crystal Growth, **280** (2005), 191 - 200

Plonka, R.; Dittmann, R.; Pertsev, N. A.; Vasco, E.; Waser, R.
Impact of the top-electrode material on the permittivity of single-crystalline $Ba_{0.7}Sr_{0.3}TiO_3$ thin films
Applied Physics Letters, **86** (2005), 202908

Poghossian, A.; Cherstvy, A.; Ingebrandt, S.; Offenhäusser, A.; Schöning, M. J.
Possibilities and limitations of label-free detection of DNA hybridization with field-effect-based devices
Sensors and Actuators B, **111-112** (2005), 470 - 480

Popescu, V.; Ebert, H.; Papanikolaou, N.; Zeller, R.; Dederichs, P. N.
Influence of spin-orbit coupling on the transport properties of magnetic tunnel junctions
Physical Review B, **72** (2005), 184427

Popkov, V.; Salerno, M.; Schütz, G. M.
Entangling power of permutation invariant quantum states
Physical Review A, **72** (2005), 032327

Poppe, U.; Faley, M.; Gareev, R. R.; Weides, O. H.; Zimmermann, E.; Glaas, W.; Urban, K.
Applications of a High Temperature Superconductor SQUID Microscope with Soft-magnetic Flux Guide
Proceedings of the Workshop on Nanoelectronics Days, Forschungszentrum Jülich, 09.02.2005-11.02.2005. - 2005. - S. 137 - 138

Postnikov, A. V.; Galakhov, A.V.; Blügel, S.
Magnetic interactions in a Cu-containing heterospin polymer
Phase Transitions, **78** (2005), 689

Postnikov, A. V.; Pagès, O.; Hugel, J. A.
Lattice dynamics of the mixed semiconductors (Be, Zn)Se from first-principles calculations
Physical Review B, **71** (2005), 115206

Prado, L.; Goerigk, G.; Ponce, M. L.; Garamus, V. M.; Wittich, H.; Willumeit, R.; Schulte, K.; Nunes, S. P.
Characterization of Proton-Conducting Organic-Inorganic Polymeric Materials by ASAXS
Journal of Polymer Science B - Polymer Physics, **43** (2005), 2981 - 2992

Prager, M.; Baumert, J.; Press, W.; Plazanet, M.; Tse, J.S.; Klug, D.D.
Rotational tunneling of disordered methyl groups of CH_3F encaged in cubic I water clathrate
Physical Chemistry Chemical Physics, **7** (2005), 1228 - 1234

Prager, M.; Grimm, H.; Kirstein, O.
Using phase-space transformation for an improved hybrid cold time-of-flight spectrometer
Nuclear Instruments and Methods in Physics Research Section A, **554** (2005), 415 - 426

Prager, M.; Grimm, H.; Natkaniecz, I.
Rotational potentials of methyl groups and structures of low temperature phases or mesitylene: a neutron scattering study
Physical Chemistry Chemical Physics, **7** (2005), 2587 - 2593

Prager, M.; Pawlukojc, A.; Sobczyk, L.; Grech, E.; Grimm, H.
Inelastic neutron scattering study of tetramethylpyrazine in the complex with chloranilic acid
Journal of Physics: Condensed Matter, **17** (2005), 5725

Puchalla, J.; Hoffmann-Eifert, S.; Cattaneo, L.; Carella, S.; Waser, R.
MOCVD growth of (Pb, Ba) (Zr, Ti) O_3 thin films for memory applications
Integrated Ferroelectrics, **75** (2005), 225 - 233

Rader, O.; Lezaic, M.; Blügel, S.; Fujimori, A.; Kimura, A.; Kamakura, N.; Kakizaki, A.; Miyanishi, S.; Akinaga, H.
Spin-polarized surface state of MnSb(0001)
New Journal of Physics, **7** (2005), 111

Rakos, A.; Schütz, G. M.
Current distribution and random matrix ensembles for an integrable asymmetric fragmentation process
Journal of Statistical Physics, **118** (2005), 3/4, 511 - 530

Rathgeber, S.; Pakula, T.; Wilk, A.; Matyjaszewski, K.; Beers, K. L.
On the shape of bottle-brush macromolecules: Systematic variation of architectural parameters
Journal of Chemical Physics, **122** (2005), 124904-1 - 124904-13

Regnery, S.; Ding, Y.; Jia, C. L.; Szot, K.; Thomas, R.; Waser, R.
Metal organic chemical vapor deposition of $(Ba,Sr)TiO_3$: Nucleation and growth on Pt-(111)
Journal of Applied Physics, **98** (2005), 084904-1 - 084904-12

Regnery, S.; Thomas, R.; Ehrhart, P.; Waser, R.
$SrTa_2O_6$ thin films for high-K dielectric applications grown by chemical vapor deposition on different substrates
Journal of Applied Physics, **97** (2005), 073521

Reichenberg, B.; Tiedke, S.; Peter, F.; Waser, R.; Tappe, S.; Schneller, T.
Contact mode potentiometric measurements with an atomic force microscope on high resistive perovskite thin films
Journal of the European Ceramic Society, **25** (2005), 12, 2353

Renner, U.; Schütz, G. M.; Vojta, G.
Diffusion on fractals
Diffusion in Condensed Matter / eds.: P. Heitjans, J. Kärger. - Berlin, Springer, 2005. - 2. Aufl. - 3-540-20043-6. - S. 793 - 811

Richter, D.
Viscoelasticity and microscopic motion in dense polymer systems
Diffusion in Condensed Matter / eds.: P. Heitjans, J. Kärger. - Berlin, Springer, 2005. - 2. Aufl. - 3-540-20043-6. - S. 513 - 554

Richter, D.; Monkenbusch, M.; Arbe, A.; Colmenero, J.
Neutron spin echo in polymer systems
Berlin, Springer, 2005
Advances in Polymer Science ; 174; - 3-540-22862-4

Ripoll, M.; Ernst, M. H.
Power law tails of time correlations in a mesoscopic fluid model
Physical Review E, **72** (2005), 011101

Ripoll, M.; Ernst, M. H.
Model system for classical fluids out of equilibrium
Physical Review E, **71** (2005), 041104

Ripoll, M.; Mussawisade, K.; Winkler, R. G.; Gompper, G.
Dynamic Regimes of Fluids Simulated by Multi-Particle-Collision Dynamics
Physical Review E, **72** (2005), 016701

Rodriguez Contreras, J.; Kohlstedt, H.; Petraru, A.; Gerber, A.; Hermanns, B.; Haselier, H.; Nagarajan, N.; Schubert, J.; Poppe, U.; Buchal, C.; Waser, R.
Improved $PbZr_{0.52}Ti_{0.48}O_3$ film quality on $SrRuO_3/SrTiO_3$ substrates
Journal of Crystal Growth, **277** (2005), 210 - 217

Roke, S.; Buitenhuis, J.; van Miltenburg, J. C.; Bonn, M.; van Blaaderen, A.
Interface-solvent effects during colloidal phase transitions
Journal of Physics: Condensed Matter, **17** (2005), s3469 - s3479

Rücker, U.
Magnetisation Configurations and Dynamics
Magnetism goes nano : electron correlations, spin transport, molecular magnetism ; lecture manuscripts of the 36th Spring School of the Institute of Solid State Research ... / eds.: S. Blügel, T. Brückel, C. M. Schneider. - Jülich, 2005. - (Schriften des Forschungszentrums Jülich . Reihe Materie und Material / Matter and Material ; 26). - 3-89336-381-5. - S. D4.1 - D4.30

Rüdiger, A.; Schneller, T.; Roelofs, A.; Tiedke, S.; Schmitz, T.; Waser, R.
Nanosize ferroelectric oxides - tracking down the superparaelectric limit
Applied Physics A, **80** (2005), 1247

Rüdiger, R.
Comment on: 'Ferroelectricity of single-crystalline, monodisperse lead zirconate nanoparticles of 9 nm in diameter'
Applied Physics Letters, **86** (2005), 256101

Sato, K.; Katayama-Yoshida, H.; Dederichs, P. N.
High Curie Temperature and Nano-Scale Spinodal Decomposition Phase in Dilute Magnetic Semiconductors
Japanese Journal of Applied Physics Part 2: Letters, **44** (2005), 30, L948 - L951

Sawka-Dobrowolska, W.; Bator, G.; Sobczyk, L.; Pawlukojc, A.; Ptasiewicz-Bak, H.; Rundloef, H.; Jagielski, P.; Janik, J.A.; Krawczyk, J.; Nowina-Konopka, M.; Steinsvoll, O.; Grech, E.; Nowicka-Scheibe, J.; Prager, M.
Elastic, quasielastic and inelastic neutron scattering studies on the CT hexamethylbenzene-acyanoquinodimethane complex
Journal of Chemical Physics, **123** (2005), 124305

Schedler, R.; Witte, U.; Rotter, M.; Loewenhaupt, M.; Schmidt, W.
Field dependence of the magnon dispersion in the Kondo lattice $CeCu_2$ up to 12T
Journal of Applied Physics, **97** (2005), 10A911-1

Schenk, T.; Nguyen Thi, H.; Gastaldi, J.; Reinhart, G.; Cristiglo, V.; Mangelinck-Noel, N.; Klein, H.; Härtwig, B; Grushko, B.; Billa, B.; Baruchel, J.
Application of synchrotron X-ray imaging to the study of directional solidification of aluminium-based alloys
Journal of Crystal Growth, **275** (2005), 201 - 208

Schindlmayr, A.
Magnetic Excitations
Magnetism goes nano : electron correlations, spin transport, molecular magnetism ; lecture manuscripts of the 36th Spring School of the Institute of Solid State Research ... / eds.: S. Blügel, T. Brückel, C. M. Schneider. - Jülich, 2005. - (Schriften des Forschungszentrums Jülich . Reihe Materie und Material / Matter and Material ; 26). - 3-89336-381-5. - S. D1.1 - D1.20

Schmidt, W.; Ohl, M.
A new instrumental set-up for polarized neutron scattering experiments
Physica B: Condensed Matter, **356** (2005), 1/4, 192 - 196

Schneider, C. M. (Ed.); Blügel, S. (Ed.); Brückel, Th. (Ed.)
Introduction
Magnetism goes nano : electron correlations, spin transport, molecular magnetism ; lecture manuscripts of the 36th Spring School of the Institute of Solid State Research ... / eds.: S. Blügel, T. Brückel, C. M. Schneider. - Jülich, 2005. - (Schriften des Forschungszentrums Jülich . Reihe Materie und Material / Matter and Material ; 26). - 3-89336-381-5. - S. I-1 - I-12

Schneider, C. M.; Kuksov, A.; Krasyuk, A.; Oelsner, A.; Nepijko, S. A.; Schönhense, G.
Time-resolved X-ray photoemission electron microscopy: imaging magnetodynamics on the 100 ps scale and below
Journal of Electron Spectroscopy and Related Phenomena, **144-147** (2005), 967 - 971

Schneider, S.; Gompper, G.
Shapes of crystalline domains on spherical fluid vesicles
Europhysics Letters, **70** (2005), 136 - 142

Schober, T.
Composites of ceramic high-temperature proton conductors with inorganic compounds
Electrochemical and Solid State Letters, **8** (2005), 4, A199 - A200

Schober, T.
Transformation of an oxygen ion conductor to a proton conductor by solid state reaction
Solid State Ionics, **176** (2005), 29/30, 2275 - 2277

Schober, T.; Grover Coors, W.
Entry and exit of water vapor in bulk ceramic proton conductors
Solid State Ionics, **176** (2005), 357 - 362

Schorn, P.J.; Schneller, T.; Böttger, U.; Waser, R.
Characterization of chemical solution deposition-derived lead hafnate titanate thin films
Journal of the American Ceramic Society, **88** (2005), 1312 - 1314

Schroeder, K.
Magnetism in Atoms
Magnetism goes nano: electron correlations, spin transport, molecular magnetism; lecture manuscripts of the 36th Spring School of the Institute of Solid State Research ... / eds.: S. Blügel, T. Brückel, C. M. Schneider. - Jülich, 2005. - (Schriften des Forschungszentrums Jülich . Reihe Materie und Material / Matter and Material ; 26). - 3-89336-381-5. - S. A1.1 - A1.16

Schwahn, D.
Critical to mean field crossover in polymer blends
Phase Behavior of Polymer Blends / ed.: K. Freed. - Springer, 2005. - (Advances in Polymer Science ; 183). - 3-540-25680-6. - S. 1 - 61

Schweika, W.
Magnetic Excitations and Scattering Experiments
Magnetism goes nano : electron correlations, spin transport, molecular magnetism ; lecture manuscripts of the 36th Spring School of the Institute of Solid State Research ... / eds.: S. Blügel, T. Brückel, C. M. Schneider. - Jülich, 2005. - (Schriften des Forschungszentrums Jülich . Reihe Materie und Material / Matter and Material ; 26). - 3-89336-381-5. - S. D3.1 - D3.16

Schweika, W.
Polarisation Analysis
Neutron scattering : lectures of the laboratory course held at the Forschungszentrum Jülich / ed.: T. Brückel ... - Jülich, Forschungszentrum, 2005. - (Schriften des Forschungszentrums Jülich, Reihe Material und Materie ; 28). - 3-89336-395-5. - S. 4-1 - 4-25

Schönhals, A.; Goering, H.; Schick, Ch.; Frick, B.; Zorn, R.
Polymers in nanocomposites: What can be learned from relaxation and scattering experiments?
Journal of Non-Crystalline Solids, **351** (2005), 2668 - 2677

Schönherr, G.
Hard rod gas with long-range interactions: Exact predictions for hydrodynamic properties of continuum systems from discrete models
Physical Review E, **71** (2005), 026122

Schütz, G. M.
Single-file diffusion far from equilibrium
Diffusion Fundamentals : Leipzig 2005 / ed.: J. Kärger, F. Grinberg, P. Heitjans. - Leipzig, Universitätsverl., 2005. - 3-86583-073-0. - S. 49 - 67

Seeck, O.; Kentzinger, E.
Continuum Description: Grazing Incidence Neutron Scattering
Neutron scattering : lectures of the laboratory course held at the Forschungszentrum Jülich / ed.: T. Brückel ... - Jülich, Forschungszentrum, 2005. - (Schriften des Forschungszentrums Jülich, Reihe Material und Materie ; 28). - 3-89336-395-5. - S. 6-1 - 6-26

Seiler, O.; Burschka, C.; Schwahn, D.; Tacke, R.
Behavior of Tri(n-butyl)ammonium Bis[citrato(3-)-O_1,O_3,O_6] silicate in Aqueous Solution: Analysis of a Sol-Gel Process by Small-Angle Neutron Scattering
Inorganic Chemistry, **44** (2005), 7, 2318

Shiratori, Yu.; Tietz, F.; Penkalla, H. J.; He, J. Q.; Shiratori, Yo.; Stöver, D.
Influence of impurities on the conductivity of composites in the system $(3YSZ)_{1-x}$-$(MgO)_x$
Journal of Power Sources, **148** (2005), 32 - 42

Singer, R.; Fähnle, M.; Bihlmayer, G.
Constrained spin-density functional theory for excited magnetic configurations in an adiabatic approximation
Physical Review B, **71** (2005), 214435

Slebarski, E. C.; Szot, K.; Gamza, M.; Penkalla, H. J.; Breuer, U.
Influence of grain-boundary defects on electric transport in CeRhSn with a non-Fermi-liquid ground state
Physical Review B, **72** (2005), 8, 085443-1 - 085443-6

Spatschek, R.
Auf Biegen und Brechen
Wissenschaft im Zeichen der Zeit / ed.: R. Ball. - Jülich, 2005. - (Schriften des Forschungszentrums Jülich . Reihe Allgemeines / General ; 4). - 3-89336-411-0. - S. 147 - 152

Spatschek, R.; Brener, E. A.
Fracture and the Grinfeld instability
Journal of Crystal Growth, **275** (2005), e307 - e311

Sternemann, C.; Huotari, S.; Vanko, G.; Volmer, M.; Monaco, G.; Gusarov, A.; Lustfeld, H.; Sturm, K.; Schuelke, W.
Correlation-Induced Double-Plasmon Excitation in Simple Metals Studied by Inelastic X-Ray Scattering
Physical Review Letters, **95** (2005), 157401

Su, Y.
Ordering Phenomena in Complex Transition-Metal Oxides (CTMO)
Magnetism goes nano : electron correlations, spin transport, molecular magnetism ; lecture manuscripts of the 36th Spring School of the Institute of Solid State Research ... / eds.: S. Blügel, T. Brückel, C. M. Schneider. - Jülich, 2005. - (Schriften des Forschungszentrums Jülich . Reihe Materie und Material / Matter and Material ; 26). - 3-89336-381-5. - S. A8.1 - A8.22

Tatchev, D.; Goerigk, G.; Valova, M. J.; Dille, J.; Kranold, R.; Armyanov, S.; Delplancke, J.-L.
Investigation of the primary crystallization of Ni_{17} at.% P alloy by ASAXS
Journal of Applied Crystallography, **38** (2005), 787 - 794

Teren, A. R.; Thomas, R.; He, J.; Ehrhart, P.
Comparison of precursors for pulsed metal-organic chemical vapor deposition of HfO_2 high-k dielectric thin films
Thin Solid Films, **478** (2005), 206

Thomas, R.; Patil, U.; Ehrhart, P.; Devi, A.; Waser, R.
Zirconium dioxide thin films for high-K applications by MOCVD from novel mononuclear precursors
15th European Conference on Chemical Vapor Deposition / ed.: A. Devi ... - 2005. - (Proceedings of the Electrochemical Society ; 2005-09). - 1-56677-427-6. - S. 944 - 951

Thomas, R.; Regnery, S.; Ehrhart, P.; Waser, R.; Patil, U.; Bhakta, R.; Devi, A.
High-k dielectric materials by metalorganic chemical vapor deposition: growth and characterization
Ferroelectrics, **327** (2005), 111

Tillmann, R. G. E.; Thust, A.; Gerber, A.; Weides, M. P.; Urban, K.
Atomic structure of beta-tantalum nanocrystallites
Microscopy and Microanalysis, **11** (2005), 534 - 544

Torma, V.; Peterlik, N. A.; Bauer, U.; Rupp, W.; Hüsing, N.; Bernstorff, S.; Steinhart, M.; Goerigk, G.; Schubert, U.
Mixed Silica Titania Materials Prepared from a Single-Source Sol-Gel Precursor: A Time-Resolved SAXS Study of the Gelation, Aging, Supercritical Drying, and Calcination Processes
Chemistry of Materials, **17** (2005), 12, 3146 - 3153

Triolo, A.; Russina, O.; Hardacre, C.; Nieuwenhuyzen, M.; Gonzalez, M.A.; Grimm, H.
Relaxation processes in room temperature ionic liquids: The case of 1-methyl-3-butyl imidazolium hexafluorophosphate
Journal of Physical Chemistry B, **109** (2005), 22061 - 22066

Tuinier, R.; Taniguchi, T.
Polymer depletion-induced slip near an interface
Journal of Physics: Condensed Matter, **17** (2005), 2, L9 - L14

Udyansky, A.; Bugaev, V. N.; Schweika, W.; Shchyglo, O.; Reichert, H.; Dosch, H.
Analytical correlation correction of the chemical potential of solid solutions
Physical Review B, **71** (2005), 140201-1 - 140201-4

Ueba, H.; Mii, T.; Lorente, N.; Persson, B. N. J.
Adsorbate motions induced by inelastic-tunneling current: Theoretical scenarios of two-electron processes
Journal of Chemical Physics, **123** (2005), 084707

Vangeyte, P.; Leyh, B.; Rojas, O.J.; Claessen, P. M.; Heinrich, M.; Auvray, L.; Willet, N.; Jerome, R.
Adsorption of poly(ethylene oxide)-b-poly(epsilon-caprolactone) copolymers at the silica-water interface
Langmuir, **21** (2005), 2930 - 2940

Vasco, E.
Theoretical optimization of the self-organized growth of nanoscale arrays through a figure of merit
Applied Physics Letters, **85** (2004), 17, 3714 - 3716

Vasco, E.; Karthäuser, S.; Dittmann, R.; He, J.-Q.; Jia, C.-L.; Szot, K.; Waser, R.
$SrZrO_3$ nanopatterning using self-organizing $SrRuO_3$ as a template
Advanced Materials, **17** (2005), 3, 281

Vass, S.; Grimm, H.; Bányai, I.; Meier, G.; Gilányi, T.
Slow Water Diffusion in Micellar Solutions
Journal of Physical Chemistry B, **109** (2005), 11870 - 11874

Vogel, J.; Kuch, W.; Hertel, R.; Camarero, J.; Fukumoto, K.; Romanens, F.; Pizzini, S.; Bonfim, M.; Petroff, F.; Fontaine, A.; Kirschner, J.
Influence of domain wall interactions on nanosecond switching in magnetic tunnel junctions
Physical Review B, **72** (2005), 220402®

Volokitin, A. I.; Persson, B. N. J.
Adsorbate-Induced Enhancement of Electrostatic Noncontact Friction
Physical Review Letters, **94** (2005), 086104

Vrij, A.; Tuinier, R.
Structure of concentrated colloidal dispersions
Particulate Colloids / J. Lyklema. - Elsevier, 2005. - (Fundamentals of Interface and Colloid Science ; 4). - 0-12-460529-X. - S. 5.1 - 5.10

Wiebe, J.; Meier, F.; Hashimoto, K.; Bihlmayer, G.; Blügel, S.; Ferriani, P.; Heinze, S.; Wiesendanger, R.
Unoccupied surface state on Pt(111) revealed by scanning tunneling spectroscopy
Physical Review B, **72** (2005), 193406

Willmann, R. D.; Schütz, G. M.; Grosskinsky, S.
Dynamical origin of spontaneous symmetry breaking in a field-driven nonequilibrium system
Europhysics Letters, **71** (2005), 542 - 548

Winkler, R. G.; Ripoll, M.; Mussawisade, K.; Gompper, G.
Simulation of Complex Fluids by Multi-Particle-Collision Dynamics
Computer Physics Communications, **169** (2005), 326 - 330

Wischnewksi, A.
Polymers makes a new move
"Highlights of ILL Research : A review of ILL Research into Complex Everyday Materials ; Neutrons and Soft Matter". - Institut Laue Langevin, Grenoble, 2005. - S. 8

Woudenberg, F. C. M.; Sager, W. F. C.; ten Elshof, J. E.; Verweij, H.
Nanostructured barium titanate thin films from nanoparticles obtained by an emulsion precipitation method
Thin Solid Films, **471** (2005), 134 - 139

Yao, Z.; Liu, C.; Jung, P.
Diffusion and permeation of deuterium in EUROFER97: Effect of irradiation and of implanted helium
Fusion Science and Technology, **48** (2005), 1285 - 1291

Zamponi, M.
Polymere - Molekulare Entfesselungskünstler
Wissenschaft im Zeichen der Zeit : Preisträger des Leibfried-Preises im Forschungszentrum Jülich 2000 - 2005 / ed.: R. Ball. - Jülich, Forschungszentrum, Zentralbibliothek, 2005. - (Schriften des Forschungszentrum Jülich . Reihe Allgemeines / General ; 4). - 3-89336-411-0. - S. 183 - 189

Zamponi, M.; Monkenbusch, M.; Willner, L.; Wischnewski, A.; Farago, B.; Richter, D.
Contour length fluctuations in polymer melts: A direct molecular proof
Europhysics Letters, **72** (2005), 6, 1039 - 1044

Zeller, R.
Lloyd's formula in multiple-scattering calculations with finite temperature
Journal of Physics: Condensed Matter, **17** (2005), 5367

Zembilgotov, A. G.; Pertsev, N. A.; Böttger, U.; Waser, R.
Effect of anisotropic in-plane strains on phase states and dielectric properties of epitaxial ferroelectric thin films
Applied Physics Letters, **86** (2005), 052903

Zembilgotov, G.; Pertsev, N. A.; Waser, R.
Phase states of nanocrystalline ferroelectric ceramics and their dielectric properties
Journal of Applied Physics, **97** (2005), 114315

Zhang, Z.; Buitenhuis, J.
Synthesis of well-defined colloidal dispersions of poly(ethylene glycol)-grafted silica particles
6th Liquid Matter Conference of the European Physical Society : Abstracts Book. - 2005. - 2-914771-29-0. - S. 151

Appendix

Conferences and Schools

Physics meets Biology: From Soft Matter to Cell Biology
35th Spring School, Institute of Solid State Research
March 22 – April 2, 2004; Jülich, Germany
organized by G. Gompper, U. B. Kaupp, J. K. G. Dhont, D. Richter, R. G. Winkler

8th Laboratory Course - Neutron Scattering
Sep 13 - Sep 24, 2004; Jülich, Germany
Organized by T. Brückel, G. Heger, D. Richter, R. Zorn

Jülich Soft Matter Days 2004
November 16 – November 19, 2004; Congresscentrum Rolduc, Kerkrade, Netherlands
Organized by J.K.G. Dhont, D. Richter, G. Gompper

Colloids in External Fields
II Transregio SFB Workshop
September 28 – September 29, 2004; Jülich, Germany

Nanomagnetism: New Insights with Synchrotron Radiation
338th WEH-Seminar, Jan 5 – Jan 7, 2005; Bad Honnef, Germany
organized by C. M. Schneider and K. Starke

nanoelectronic days 2005
Feb 09 – Feb 11, 2005; Jülich, Germany
organized by R. Waser and W. Albrecht

Magnetism goes Nano: Electron Correlations, Spin Transport, Molecular Magnetism
36th Spring School, Institute of Solid State Research
Feb 14 – Feb 25, 2005; Jülich, Germany
organized by C. M. Schneider, S. Blügel, T. Brückel

9th Laboratory Course - Neutron Scattering
Sep 12 - Sep 23, 2005; Jülich, Germany
organized by T. Brückel, G. Heger, D. Richter, R. Zorn

40 Years of the GW Approximation for the Electronic Self-Energy: Achievements and Challenges
356th WEH Seminar Sep 12 - Sep 15, 2005; Physikzentrum Bad Honnef, Germany
Organized by A. Schindlmayer, N. Vast, M. Palummo, O. Pulci, P. Garcia-Gonzalez

10th Conference on Frontiers of Electron Microscopy in Materials Science
Sep 25 - Sep 30, 2005; Kasteel Vaalsbroek, Netherlands
organized by K. Urban, J. Mayer, M. Luysberg, K. Tillmann

Nanospintronics
ESF Exploratory Workshop, Sep 29 - Sep 30, 2005; Wegberg-Wildenrath, Germany
organized by C. M. Schneider

Jülich Soft Matter Days 2005
Nov 01 – Nov 04, 2005; Gustav-Stresemann-Institut, Bonn, Germany
organized by J.K.G. Dhont, G. Gompper, D. Richter

Advances and Prospects in Molecular Magnetism
362nd WEH-Seminar, Nov 13 – Nov 16, 2005; Bad Honnef, Germany
organized by R. Fink, P. Müller, S. Blügel, J. Schnack

Teaching Activities at Universities 2004/2005

Lecturer	University
Dr. Baumgärtner	Duisburg
Prof. Bechthold	Köln
Prof. Blügel	Aachen
Dr. Bringer	Düsseldorf
Prof. Brückel	Aachen
Prof. Dhont	Düsseldorf
Dr. Ebert	Aachen
Dr. Ehrhart	Aachen
Prof. Eisenriegler	Düsseldorf
Prof. Gompper	Köln
Dr. Hertel	Halle-Wittenberg
Dr. Kohlstedt	Köln
Dr. Lustfeld	Duisburg
Prof. Müller-Krumbhaar	Aachen
Prof. Nägele	Konstanz
Prof. Richter	Münster
Prof. C.M. Schneider	Duisburg-Essen
Prof. H. Schroeder	Aachen
Prof. K. Schroeder	Aachen
Dr. Schütz	Bonn
Dr. Schweika	Aachen
Prof. Szot	Katowice
Prof. Urban	Aachen
Prof. Waser	Aachen
Dr. Wiegand	Köln
Prof. Winkler	Ulm
Dr. Zorn	Münster

Institut für